

**Dielectrometry Measurements of Moisture Diffusion and
Temperature Dynamics in Oil Impregnated Paper Insulated
Electric Power Cables**

by

Zachary M. Thomas
B.S., Syracuse University, 2003
M.S., Massachusetts Institute of Technology 2005

Submitted to the Department of Electrical Engineering and Computer Science
in partial fulfillment of the requirements for the degree of

Doctor of Philosophy in Electrical Engineering and Computer Science

at the

MASSACHUSETTS INSTITUTE OF TECHNOLOGY

June 2007

© Massachusetts Institute of Technology 2007. All rights reserved.

Author
Department of Electrical Engineering and Computer Science
May 4, 2007

Certified by
Markus Zahn
Professor of Electrical Engineering
Thesis Supervisor

Accepted by
Arthur C. Smith
Chairman, Department Committee on Graduate Students

to my grandparents

Casmier & Veronica Midura

Dielectrometry Measurements of Moisture Diffusion and Temperature Dynamics in Oil Impregnated Paper Insulated Electric Power Cables

by

Zachary M. Thomas

B.S., Syracuse University, 2003

M.S., Massachusetts Institute of Technology 2005

Submitted to the Department of Electrical Engineering and Computer Science
on May 4, 2007, in partial fulfillment of the
requirements for the degree of
Doctor of Philosophy in Electrical Engineering and Computer Science

Abstract

Paper insulated lead covered (PILC) cables have played an important role in underground power distribution for a hundred years. Replacing aged PILC before failure is critical to managing power distribution. Three prominent failure mechanisms accelerate cable aging: temperature stresses, moisture ingress, and partial discharge. The research focuses on the effect of temperature and moisture on the effective (complex) permittivity of the cable insulation. Measurements are performed using cylindrical dielectrometry sensors designed to be wrapped around the cable. The lead sheath of the cable is removed so that the sensors can be placed directly in contact with the insulation. From the measurements, the electrical properties of the material as a function of temperature and transient moisture diffusion are found.

A theoretical treatment of the interdigital dielectrometry sensors with a cylindrical geometry is presented. Two classes of the geometry are studied. The ϕ periodic sensor geometry has electrodes aligned with the cylindrical axis and periodic around the circumference. The z periodic sensor geometry has the electrodes forming rings around the cylinder that are periodic along the cylindrical axis. The material is modeled by concentric rings of homogeneous materials. The electric field solution consists of an infinite summation of Fourier series terms. In finding the field solution and as a consequence of it, the potential, electric field lines, and the impedance between the driving and sensing electrodes are found. A generalized solution to the planar dielectrometry sensor topology is also presented. This solution allows for an arbitrary placement and excitation of electrodes, providing the analytical tools for a new generation of sensors.

Dielectrometry sensors for use in ϕ and z periodic geometries are designed and manufactured on a 4 mil PTFE substrate. An experimental setup is designed and built to provide a temperature and humidity controlled environment for measurements. Special clamping mechanisms are used to secure the sensor to the sample. Custom built hardware is used to excite the sensor at frequencies ranging from 0.005 Hz to 10,000 Hz (over six decades), measure and record the response, and deliver it to a computer for storage and analysis.

Steady state measurements are performed at temperatures ranging from room temperature to 100 °C. Plastics, woods, and the PILC cable samples are measured. Using the theoretical model, the effective permittivity is estimated from the measurements. An Arrhenius temperature dependence is observed for several materials including the PILC cables. We characterize the temperature dependence of these materials by a master curve and activation energy. Together they give a complete description of the effective permittivity's frequency and temperature dependence.

Transient measurements of moisture diffusion are made at constant temperatures for several

materials. For some experiments the boundary conditions limit the diffusion of moisture to one direction. When the z periodic sensor is used, six independent measurements are taken along the direction of diffusion. From the initial and final conditions and the theoretical model, a mapping between the electrical properties and the insulation moisture content is formed. Moisture concentration along the direction of diffusion is estimated and in some cases characterized by a simple diffusion coefficient. The diffusion experiments provide evidence that moisture can move rapidly through the stranded conductors of the cables, delivering moisture to locations far removed from an initial breach.

The experimental results show the electrical properties of the cable insulation is highly sensitive to the presence of moisture and changes in temperature. While using these sensors for field measurements may not be practical because they require the cable sheath to be removed, the technology provides a valuable, low cost tool for assessing cable health in an off-line setting.

Thesis Supervisor: Markus Zahn
Title: Professor of Electrical Engineering

Acknowledgments

The work presented in this thesis was performed in the Laboratory for Electromagnetic and Electronic Systems (LEES) and was sponsored by the Electric Power Research Institute (EPRI). Through a Graduate Research Fellowship the National Science Foundation provided support for a portion of my tenure. Special thanks to Ansoft for providing valuable software tools. Special thanks to the EPRI Cable Testing Network (ECTN) committee and member utilities for conversations and discussions during the March 2007 meetings.

I am grateful for the support of so many people who made this thesis possible and to so many more who have made my time at MIT a joy. I thank Professor Markus Zahn for his commitment to me as a student, his guidance through the research process, and the depth of knowledge and resources he has provided as my thesis supervisor. Special thanks to David Otten who helped keep some of my experimental hardware working like it was built yesterday, not yesteryear. I want to thank Professor Wuqiang Yang from the University of Manchester, for the pleasure of working with him on a paper. I wish to thank Professor Jeffrey H. Lang and Professor David J. Perreault for their participation in my thesis committee.

The staff at LEES has been tremendous in making this so positive an experience. Thanks to Kiyomi Boyd who helped me be comfortable in LEES from the very beginning; Dimonika Bizi, for always making me feel like her favorite student to have around the office; Wayne Ryan, for his help getting me setup at HVRL. Thanks also to Gary DesGroseilliers and Miwa Suzuki and their help.

While the building that is home to HVRL isn't the most esthetic on campus, HVRLers have certainly helped me overcome its grim shape. Very special thanks to Dr. Se-Hee Lee, Dr. Shihab Elborai, Dr. Tony He, Frank Schubert, Clint Lawler, Uzoma Orji, and Hsin-Fu Huang, who helped in making N10 a fun place to work. Thanks also to Dr. Chathan Cooke for the kindness he extended to me.

I'd also like to thank Professor Zahn's students whom I didn't share the HVRL lab with but certainly commiserated with: Frank O'Sullivan, and Padraig J. Cantillon-Murphy.

Thanks to those at EPRI who helped make this project possible, Robert Keefe, Walter Zenger, and Matthew Olearczyk.

I'd like to thank Prof. Jin Au Kong for allowing me to TA 6.632 to help meet my graduation requirements, and to my fellow TA Dr. Brandon Kemp for taking much of the load. It was a great deal of fun to go back to refresh myself on some of my masters thesis work in wave theory. In addition to Brandon I'd like to thank some of the other members of Prof. Kong's research group including my master thesis coadvisor Dr. Tomasz Grzegorzczak, and the students I shared the lab

with: Prof. Xudong Chen, Bill Herrington, Dr. James Chen, and Dr. Christopher Moss. I'd also like to thank Dr. Benjamin Barrowes, another student of Prof. Kong whom coincidentally produced a MATLAB to Mathematica interface I found on the web which was quite useful in my research.

Nearly my entire time at MIT I was fortunate enough to serve as the resident advisor at Delta Kappa Epsilon. Living at Δ KE has been as ideal an arrangement as I could have ever expected. The benefits have far exceeded the burden. Special thanks to the brothers for selecting me, especially Brandon Holm, the president at the time. Extra special thanks to Tom Egan, the cook who for four years has kept me well fed and to Lew Gosmon the house father, who's humorous vulgarity will be impossible to forget. I'd also like to thank members of the Fraternities, Sororities and Independent Living Groups (FSILG) office for providing support and guidance over the years, in particular Dean David Rogers, Kaya Miller, and Fran Miles.

The Tech Catholic Community has provided a spiritual home during my time at MIT. Special thanks to the chaplans over the years, Father Paul A. Reynolds CSP and Father Richard Clancy. Many thanks to those members whom I've become friends with including Anna Morys, Bill Jacobs, Andrew Lauer, Ana Posada, and Joel Fernandez.

I'd like to thank Bro. Tom Purcell, OFM Conv., Father Tim Mulligan, OFM Conv., and Bro. Jim Moore, OFM Conv. and the many other Conventual Franciscan Friars who have provided support and prayers over the years.

Thanks to Murat Celik for his dedication and help while serving as TA for 6.640. I'd also like to thank Prof. Joel Schindall the director of LEES and who assisted by serving on my RQE committee.

Any acknowledgements wouldn't be complete if I didn't include my mentors at Syracuse University, Prof. Jay Kyoon Lee, and Prof. Lisa Ann Osadciw. I'd also like to thank Prof. Fred Phelps who recognized my talents and encouraged me at Syracuse.

Physical activity has been one of the ways I've been able to keep most of my sanity while a student. Special thanks to Brandon Pierquet and Emily Fox who introduced me to the crazy idea of actual playing ice hockey. The past two seasons have been incredible, and I hope to play as often as possible for many years to come. Thanks to my mountain biking partners Matt Hartman, Liz Mitchell, and James Mann. They also happen to be members of my kickball team which is full of great friends. I'd like to thank Ariane Theriault, Lisa Curtin, John Pascucci, Avrah Brandes, and Danielle Bergeron for being great teammates and friends.

I'd like to thank my brother in Phi Kappa Psi, Peter Romano who came to Boston with me and has been such a great friend. I wish him and his fiance Theresa Foyer the best in their marriage.

I'd also like to thank my good friends from back home in Buffalo. Those that are still there make home feel like home: Michael Niro, Jerid Williams, Christopher Bresette, Timothy Sentman, Jason

Fiedler, and Dr. Richard Dombrowski who beat me to it by a few months.

I've also like to thank my friends at MIT, many of whom have already been mentioned but also Laura Zager, Keith and Maggy Herring, Cem Hatipoglu and Holly Waisanen-Hatipoglu, Shubham Mukherjee, and Vasanth Sarathy.

Lastly I'd like to thank my family without whose love and prayers this would not have been possible. Thank you to my parents Isaac and Christine, to my sister Margot, and my Aunt, Sister Jeremy Midura, CSSF. Thanks to Uncle Richard and Aunt Tina, and my cousins Joe, Greg, and Missy Bruggeman. Thanks to my Uncle Larry and Aunt Jackie Thomas. And thanks to my paternal grandparents Ike and Kathy Thomas. A very special thanks to my grandparents whom have passed away during my time at MIT and to whom this thesis is dedicated, Casey and Veronica Midura.

Contents

1	Introduction	29
1.1	Motivation	29
1.2	Thesis Overview	30
1.3	Thesis Outline	30
1.4	Thesis Conventions	32
1.5	Table of Experimental Measurements	33
2	An Overview of PILC Cables	35
2.1	Historical Perspective	35
2.1.1	Cable Types	36
2.2	Ageing Mechanism for Power Cables	36
2.3	Measurement Techniques from Previous Research	38
2.4	EPRI Cable Samples	39
2.4.1	Description of the Cables	39
2.4.2	Cable Handling	40
2.5	Non-Intrusive Cable Measurements	40
2.6	Chapter Summary	43
3	Dielectrometry Sensor Theory	45
3.1	Introduction to Dielectrometry	45
3.1.1	Solving the Forward Problem Solutions	50
3.2	Planar Periodic Sensors	51
3.2.1	Surface Capacitance Density	52
3.2.2	Collocation Points	53
3.2.3	Electrode Surface Boundary Condition	54
3.2.4	Transcapacitance	55

3.3	Cylindrical ϕ Periodic Sensors	56
3.3.1	Laplace's Equation in Cylindrical Coordinates	56
3.3.2	Surface Capacitance Density	58
3.3.3	Collocation Points	62
3.3.4	Boundary Condition at r_e	65
3.3.5	Calculating the Transadmittance	66
3.4	Cylindrical z Periodic Sensors	68
3.4.1	Surface Capacitance Density	69
3.4.2	Completing the Solution	72
3.5	Generalized Planar Periodic Sensors	72
3.5.1	Collocation Points	73
3.5.2	Surface Capacitance Density	74
3.5.3	Fourier Coefficients	76
3.5.4	Boundary Conditions	78
3.5.5	Admittance Matrix	80
3.5.6	Lossy Media and Time Harmonic Sources	81
3.6	Planar Dual Periodic Sensors	81
3.6.1	General Solution to Laplace Equation	82
3.6.2	Fourier Transform in Two Dimensions	84
3.6.3	Surface Capacitance Density	86
3.6.4	Collocation Points	87
3.6.5	Boundary Conditions Part I	90
3.6.6	Fourier Coefficients at $z = 0$	92
3.6.7	Boundary Conditions Part II	100
3.7	Electric Potential Solution	101
3.8	Field Lines	105
3.8.1	Planar Sensor Field Lines	105
3.8.2	ϕ Periodic Sensor Field Lines	107
3.8.3	z Periodic Sensor Field Lines	108
3.9	Chapter Summary	110
4	Dielectrometry Sensor Design	111
4.1	Comparison of Cylindrical and Planar Sensors	111
4.1.1	Planar Sensor Geometry Simulations	112

4.1.2	ϕ Periodic Sensor	115
4.1.3	z Periodic Sensor	120
4.1.4	Potential in the Solution Region	122
4.1.5	Field Lines in the Solution Region	128
4.1.6	Lossy Materials	139
4.1.7	Comparison of Analytical and Theoretical Solution Techniques	139
4.2	Sensor Designs	142
4.2.1	Practical Design Issues	143
4.2.2	Pre-existing Sensor Designs	143
4.2.3	Three Wavelength Sensor (January 2006)	145
4.2.4	Six Channel z Periodic Sensor (December 2006)	150
4.2.5	z Periodic Sensor with End Connections	155
4.2.6	z and ϕ Periodic Sensor	155
4.3	Hydrophilic Sensor	157
4.3.1	Experiment: Dielectric Response of Moist Air	158
4.3.2	Sensitivity of Air Substrate Sensor	159
4.4	Chapter Summary	164
5	Experiment Design	165
5.1	Experiments	165
5.1.1	Steady State Experiments	167
5.1.2	Transient Experiments	168
5.2	Sensing Hardware	169
5.2.1	Controller Box	170
5.2.2	Interface Box	171
5.3	Mounting Hardware	172
5.3.1	Pipe Clamp	172
5.3.2	Hose Clamp	173
5.3.3	Sling Clamp	175
5.4	Environment Control Hardware	175
5.4.1	Vacuum Chambers	175
5.4.2	Temperature Control	178
5.4.3	Pressure Monitoring	179
5.4.4	Humidity Sensors	179

5.4.5	Adding Moisture to the Chamber	184
5.5	Error Analysis	185
5.5.1	Systematic Errors	185
5.5.2	Uncertainty	186
5.6	Chapter Summary	194
6	Steady State Measurements	195
6.1	Diagnostic Measurements of Known Dielectrics	195
6.1.1	Teflon Rod	198
6.1.2	Polycarbonate Rod	200
6.1.3	Polyethylene Rod	202
6.1.4	Acrylic Rod	204
6.2	Wood Rod Measurements	206
6.2.1	Birch Wood Rod	206
6.3	Cable Measurements	210
6.3.1	Single Conductor Cable Measurements	210
6.3.2	Three Conductor Cable Measurements	214
6.4	Chapter Summary	216
7	Dielectric Properties	217
7.1	Introduction to Dielectrics	218
7.1.1	Maxwell's Equations and the Constitutive Laws	218
7.1.2	High Field Effects	220
7.1.3	Impedance Measurements	220
7.2	Dependence on Temperature	223
7.2.1	Estimated the Effective Permittivity from Measurements	223
7.2.2	Arrhenius Temperature Dependence	241
7.3	Dependence on Moisture	263
7.4	Dependence of Dielectric Properties on Cable Age	266
7.5	Chapter Summary	268
8	Transient Measurements	269
8.1	Transient Measurements Using ϕ Periodic Sensors	269
8.1.1	ϕ Periodic Teflon Rod Transient Measurements	270
8.1.2	ϕ Periodic Birch Wood Rod Transient Measurements	274

8.1.3	ϕ Periodic Single Conductor Cable Measurements	277
8.1.4	ϕ Periodic Three Conductor Cable Measurements	284
8.2	Transient Measurements Using z Periodic Sensors	296
8.2.1	z Periodic Birch Wood Rod Transient Measurements	296
8.2.2	z Periodic Maple Wood Rod Transient Measurements	300
8.2.3	z Periodic Single Conductor Cable Transient Measurements	309
8.3	Chapter Summary	312
9	Moisture Diffusion	315
9.1	The Diffusion Equation	315
9.1.1	Derivation of the Diffusion Equation	316
9.1.2	Solution to the Linear 1D Diffusion Equation	317
9.1.3	Small Time or Semi-Infinite Length Diffusion	321
9.1.4	Radial Diffusion	325
9.1.5	Radial and Angular Diffusion	329
9.1.6	Radial and Axial Diffusion	330
9.1.7	Normalized Diffusion Coefficient	331
9.2	Measurements of Moisture Diffusion	332
9.2.1	Air and Paper Moisture Equilibriums	334
9.3	Diffusion Estimates from ϕ Periodic Measurements	334
9.3.1	Birch Rod Diffusion	336
9.4	Diffusion Estimates from z Periodic Measurements	341
9.4.1	Maple Rod Diffusion	342
9.4.2	Birch Rod Diffusion	346
9.4.3	Single Conductor Cable Diffusion	346
9.5	Three Dimensional Diffusion Problems	350
9.5.1	Example 3: Three Conductor Cable	350
9.5.2	Example 2: Three Conductor Cable	354
9.5.3	Example 3: Three Conductor Cable	354
9.6	Chapter Summary	356
10	Multichannel Sensors	357
10.1	Introduction	357
10.2	The Multichannel Sensor	358
10.2.1	Penetration Depth	359

10.2.2 Lateral Changes in Permittivity	366
10.3 Sensing Hardware	369
10.4 Experimental Verification	370
10.5 Capacitive Sensor Arrays	373
10.6 Chapter Summary	374
11 Summary, Conclusions and Suggestions for Future Work	377
11.1 Summary	377
11.1.1 Sensor Theory	378
11.1.2 Sensor Designs	378
11.1.3 Steady State Measurements and Analysis	379
11.1.4 Transient Measurements and Analysis	380
11.1.5 Multichannel Sensors	380
11.2 Conclusion	381
11.2.1 Laboratory Experience	382
11.3 Suggestions for Future Work	383
11.3.1 Theoretical Work	383
11.3.2 Cylindrical Clamping	385
11.3.3 Multichannel Sensing	385
11.3.4 Diffusion Experiments	385
11.3.5 PILC Health Assessment	386
A Miscellanea	387
A.1 Terms and Nomenclature	387
A.2 Temperature Conversion	388
A.3 Controller Box Commands	390
A.4 Acronyms	391
A.5 Symbols & Constants	393
A.6 MATLAB Code	393
B Additional Figures	403
B.1 Steady State Measurements	403
B.1.1 Teflon Rod Constant Temperature Measurements	403
B.1.2 Polycarbonate Rod Constant Temperature Measurements	412
B.1.3 Constant Temperature Polyethylene Rod	415

B.1.4	Acrylic Rod Constant Temperature	418
B.1.5	Constant Temperature Three Conductor Cable	421
B.2	Transient Measurements	427
B.2.1	ϕ Periodic Transient Measurements	427

List of Figures

2-1	Cross-section of three conductor and single conductor cables from EPRI.	39
2-2	Half space transmission problem setup for normal incidence.	41
2-3	Transmitted power into lead half space. Skin depth of lead.	42
3-1	January 2006 three wavelength sensor design.	46
3-2	Dielectrometry sensor cross-section and equivalent circuit.	47
3-3	Floating voltage with ground plane mode circuit model.	48
3-4	Floating voltage with guard plane mode circuit model.	48
3-5	Short circuit current mode circuit model.	50
3-6	Cylindrical sensor geometries with (a) ϕ periodicity, and (b) z periodicity.	51
3-7	Planar dielectrometry sensor cross-section.	52
3-8	Cross-section of cylinder showing key quantities.	58
3-9	Summary of possible electrode configurations for the generalized planar periodic sensor. 73	
3-10	Labeling of selected collocation points for generalized planar periodic sensor solution. 74	
3-11	Planar dual periodic sensor topology.	82
3-12	Planar dual periodic unit cell.	88
3-13	Planar dual periodic sensor collocation points.	89
3-14	Planar dual periodic sensor triangular regions for linear approximations.	89
4-1	Maxwell 2D simulation setup for study of the balloon boundary condition.	113
4-2	Results for the simulation and theory study of balloon boundary condition.	114
4-3	Study of the effect of a top ground plane on the planar sensor.	116
4-4	Cross-section of a ϕ periodic sensor with a center conductor.	117
4-5	Results of the ϕ periodic sensor study where $r_0 = Ar_e$	118
4-6	Results of the ϕ periodic sensor study where $A = r_e - r_0$	119
4-7	Results of the z periodic sensor study where $r_0 = Ar_e$	121

4-8	Results of the z periodic sensor study where $A = r_e - r_0$	122
4-9	Electric potential plot of a 1 mm planar sensor with a top ground plane at 0.5 mm. $\epsilon_r = 1$	124
4-10	Electric potential plot of a 1 mm z periodic sensor with a center conductor. $\epsilon_r = 1$	125
4-11	Cartesian plot of the electric potential of a single period of the ϕ periodic sensor. $\epsilon_r = 1$	126
4-12	Electric potential plot of a 1 mm ϕ periodic sensor with a center conductor.	127
4-13	Electric field lines of a 1 mm planar sensor with a top ground plane at 0.5 mm. $\epsilon_r = 1$	129
4-14	Electric field lines of a 1 mm z periodic sensor with a center conductor. $\epsilon_r = 1$	130
4-15	Cartesian plot of the electric field lines of a single period of the ϕ periodic sensor. $\epsilon_r = 1$	131
4-16	Electric field lines of a 1 mm ϕ periodic sensor with a center conductor.	132
4-17	Field lines for a planar sensor with top ground plane heights of $\lambda/8$, $\lambda/4$, $\lambda/2$, and λ	134
4-18	Field lines for a planar sensor with top ground plane heights of 2λ and infinity.	135
4-19	Field lines for ϕ periodic sensors with a center conductor ($r_0 = 0.1r_e = 0.064$ mm) and without a center conductor.	137
4-20	Field lines for ϕ periodic sensors with center conductors of radii $r_0 = 0.6r_e =$ 0.382 mm, and $r_0 = 0.8r_e = 0.509$ mm.	138
4-21	Calculated conductance and capacitance for lossy material when excited in planar and cylindrical sensors.	140
4-22	Magnitude of voltage in $\lambda = 1$ mm planar sensor with MUT $\epsilon_r = 1$, $\sigma = 10^{-8}$ S/m at selected frequencies.	141
4-23	Three wavelength sensor designed by Y. Du for the SCCM mode.	144
4-24	Three wavelength sensor designed by Y. Du for the FVGPM mode.	144
4-25	January 2006 three wavelength sensor electrode production design.	147
4-26	January 2006 three wavelength sensor back plane production design.	148
4-27	January 2006 via locations for three wavelength sensor production design.	149
4-28	Rendering and photograph of the six channel z periodic sensor.	150
4-29	December 2006 electrode production design.	152
4-30	December 2006 back plane production design.	153
4-31	December 2006 via locations for production design.	154
4-32	Design for a six channel z periodic sensor with end connections.	155
4-33	Cracked sheath experiment concept.	156
4-34	Six channel z and ϕ periodic sensor design.	157
4-35	Dielectrometry measurement of moist air at 155 °F and 34% relative humidity.	160

4-36	Calculated permittivity for the moist air measurements in Fig. 4-35.	161
4-37	Study of air substrate thickness.	162
4-38	Study of air substrate drive and sense electrode width.	163
5-1	Simplified experimental setup with the principle components labeled.	167
5-2	Controller and interface box photographs.	170
5-3	Photographs of the sling clamping and pipe clamp.	173
5-4	Photographs of the hose clamping mechanism for birch and Teflon sample setups. . .	174
5-5	Schematic for the top flange for the small chamber.	176
5-6	Schematic view of the large chamber.	177
5-7	Schematic for the top flange for the large chamber.	177
5-8	Schematic for the side port flanges for the large chamber.	178
5-9	Histogram of temperature measurements using proportional mode in the large vacuum chamber with a set point temperature of 160 °F. Measurements were taken every 5 seconds for 4 days.	179
5-10	Saturation vapor pressure and density for water.	180
5-11	Relative Humidity test using HIH4000 humidity sensors.	183
5-12	Saturation vapor density as calculated from experimental results.	184
5-13	Demonstration of errors in calculated saturation vapor density.	185
5-14	Theoretical permittivity as a function of capacitance and gain for the three standard sensor wavelengths.	187
5-15	Experimental measurement of Teflon using a 5.0 mm sensor at 10 Hz over 11 days. .	188
5-16	Standard deviation of Teflon measurements with drift and with drift removed for two channels.	189
5-17	Drift and probability of less drift due to noise for Teflon measurements.	191
5-18	Error in permittivity estimates due to measurement noise.	192
5-19	Error in dielectric loss as a result of phase errors.	193
6-1	Experimental setup of the Teflon rod for steady state measurements.	197
6-2	Teflon constant temperature dielectric spectroscopy measurements.	199
6-3	Polycarbonate constant temperature dielectric spectroscopy measurements.	201
6-4	Polyethylene constant temperature dielectric spectroscopy measurements.	203
6-5	Acrylic rod constant temperature dielectric spectroscopy measurements.	205
6-6	Moist birch rod constant temperature dielectric spectroscopy measurements.	207
6-7	Dried birch rod constant temperature dielectric spectroscopy measurements.	209

6-8	Moist single conductor cable constant temperature dielectric spectroscopy measurements.	211
6-9	Dry single conductor cable constant temperature dielectric spectroscopy measurements.	213
6-10	Three conductor cable constant temperature dielectric spectroscopy measurements. .	215
7-1	Lossy parallel plate capacitor and circuit model.	222
7-2	Teflon rod effective permittivity as estimated from the steady state temperature measurements in Fig. 6-2.	226
7-3	Polycarbonate rod effective permittivity as estimated from the steady state temperature measurements in Fig. 6-3.	228
7-4	Polyethylene rod effective permittivity as estimated from the steady state temperature measurements in Fig. 6-4.	230
7-5	Acrylic rod effective permittivity as estimated from the steady state temperature measurements in Fig. 6-5.	232
7-6	Moist birch rod effective permittivity as estimated from the steady state temperature measurements in Fig. 6-6.	234
7-7	Dry birch rod effective permittivity as estimated from the steady state temperature measurements in Fig. 6-7.	235
7-8	Moist single conductor cable effective permittivity as estimated from the steady state temperature measurements in Fig. 6-8.	237
7-9	Dry single conductor cable effective permittivity as estimated from the steady state temperature measurements in Fig. 6-9.	238
7-10	Dry three conductor cable effective permittivity as estimated from the steady state temperature measurements in Fig. 6-10.	240
7-11	Acrylic rod logarithmic frequency shifts as a function of inverse absolute temperature.	243
7-12	Acrylic rod master curves.	244
7-13	Dry birch rod logarithmic frequency shifts as a function of inverse absolute temperature.	245
7-14	Dry birch rod shifted measurements for the formation of the master curve.	246
7-15	Dry birch rod master curves.	247
7-16	Moist birch rod logarithmic frequency shifts as a function of inverse absolute temperature.	248
7-17	Moist birch rod shifted permittivity measurements for the formation of the master curve.	249
7-18	Moist birch rod master curves.	250

7-19	Moist single conductor cable logarithmic frequency shifts as a function of inverse absolute temperature.	252
7-20	Moist single conductor cable shifted measurements for the formation of the master curve.	253
7-21	Moist single conductor cable master curves.	254
7-22	Dry single conductor cable logarithmic frequency shifts as a function of inverse absolute temperature.	256
7-23	Dry single conductor cable shifted measurements for the formation of the master curve.	257
7-24	Dry single conductor cable master curves.	258
7-25	Three conductor cable logarithmic frequency shifts as a function of inverse absolute temperature.	260
7-26	Three conductor cable shifted measurements for the formation of the master curve. .	261
7-27	Three conductor cable master curves.	262
7-28	Redrawn ϵ' and ϵ'' curves from Neimanis & Eriksson.	264
7-29	Loss tangent calculated from Neimanis & Eriksson data in Fig. 7-28 [1].	265
7-30	Master curves for the effective permittivity data in Fig. 7-28.	266
7-31	Frequency shifts as a function of moisture content for the master curves in Fig. 7-30.	267
8-1	Teflon rod ϕ periodic sensor diffusion experiment temperature and relative humidity log.	271
8-2	Teflon rod ϕ periodic sensor diffusion experiment gain and phase for selected frequencies.	272
8-3	Teflon rod ϕ periodic sensor diffusion experiment gain and phase for selected times. .	273
8-4	Birch rod ϕ periodic sensor diffusion experiment temperature and relative humidity log.	274
8-5	Birch rod ϕ periodic sensor diffusion experiment gain and phase for selected frequencies.	275
8-6	Birch rod ϕ periodic sensor diffusion experiment gain and phase for selected times. .	276
8-7	Single conductor cable measurement setup photographs.	277
8-8	Single conductor cable ϕ periodic sensor diffusion experiment temperature and relative humidity log.	278
8-9	Unwrapped single conductor gain and phase measurements for a diffusion experiment at 174 °F using a ϕ periodic sensor.	279
8-10	Wrapped single conductor gain and phase measurements for a diffusion experiment at 174 °F using ϕ periodic sensor.	280

8-11 Comparison between wrapped and unwrapped single conductor cable gains on the 2.5 mm sensor.	281
8-12 Single conductor cable with ϕ periodic sensor diffusion experiment temperature and relative humidity log.	282
8-13 Single conductor cable measurements at 147 °F and 20% relative humidity.	283
8-14 Photographs of the experimental setup for the three conductor cable using the ϕ periodic sensor.	284
8-15 Unwrapped three conductor cable ϕ periodic sensor diffusion experiment temperature (101 °F) and relative humidity (81%) log.	285
8-16 Unwrapped three conductor cable ϕ periodic sensor diffusion measurement gain and phase. $T = 101$ °F.	286
8-17 Unwrapped three conductor cable ϕ periodic sensor diffusion experiment temperature (182 °F) and relative humidity (53%) log.	287
8-18 Unwrapped three conductor cable ϕ periodic sensor diffusion measurement gain and phase. $T = 180$ °F.	288
8-19 Unwrapped three conductor cable ϕ periodic sensor diffusion experiment temperature (193 °F) and relative humidity (34%) log.	289
8-20 Unwrapped three conductor cable ϕ periodic sensor diffusion measurement gain and phase. $T = 195$ °F.	290
8-21 Unwrapped three conductor cable ϕ periodic sensor diffusion experiment temperature (174 °F) and relative humidity (46%) log.	291
8-22 Unwrapped three conductor cable ϕ periodic sensor diffusion measurement gain and phase. $T = 174$ °F.	292
8-23 Unwrapped three conductor cable ϕ periodic sensor diffusion experiment temperature (155 °F) and relative humidity (34%) log.	293
8-24 Unwrapped three conductor cables moisture ingress measurements at 155 °F using a ϕ periodic sensor.	294
8-25 Unwrapped three conductor cables moisture egress measurements at 155 °F using a ϕ periodic sensor.	295
8-26 Photographs of a birch rod in the sling clamping mechanism with a z periodic sensor.	296
8-27 Birch rod diffusion experiment transient temperature (128 °F) and relative humidity log for the z periodic sensor measurements.	297
8-28 Birch rod measurements at 130 °F and 100% RH for select frequencies.	298
8-29 Birch rod measurements at 130 °F and 100% RH for select times.	299

8-30 Birch rod relative gain profiles at four frequencies. 300

8-31 Maple rod diffusion experiment transient temperature (98 °F) and relative humidity
 log for the z periodic sensor measurements. 301

8-32 Maple rod measurements at 98 °F for select frequencies. 302

8-33 Maple rod frequency sweeps for select times. $T = 98$ °F 303

8-34 Maple rod relative gain profiles at four frequencies. 304

8-35 Maple rod diffusion experiment transient temperature (127 °F) and relative humidity
 log for the z periodic sensor measurements. 305

8-36 Maple rod measurements at 127 °F for select frequencies. 306

8-37 Maple rod frequency sweeps for select times. $T = 127$ °F 307

8-38 Maple rod relative gain profiles at four frequencies. 308

8-39 Transient % relative humidity during moisture diffusion into the single conductor
 cable using the z periodic sensor. 309

8-40 Single conductor cable measurements at 128 °F for select frequencies. 310

8-41 Single conductor cable measurements at 128 °F for select times. 311

8-42 Single conductor cable relative gain profiles at four frequencies. 312

9-1 Illustration of the one dimensional diffusion problem. 317

9-2 One dimensional diffusion examples 1–4 in Table 9.1. 322

9-3 One dimensional diffusion examples 5–6 in Table 9.1. 323

9-4 Comparison of a linear and nonlinear diffusion process. 324

9-5 Radial diffusion examples. 329

9-6 Jeffries curves for moisture in paper as a function of relative humidity and tempera-
 ture [111]. 335

9-7 Fessler et al. curves of moisture in paper as a function of relative humidity for selected
 temperatures [112]. 335

9-8 Birch rod diffusion initial and final values of permittivity as measured by the 5 mm
 sensor. 337

9-9 Birch rod effective permittivity as a function of the moisture content at 10 Hz. 337

9-10 Calculated per unit length capacitance and conductance as a function of birch rod
 moisture concentration. 338

9-11 Side view of the birch rod and sensor for analysis purposes. 339

9-12 Comparison of the theoretical and experimental capacitance and conductance as a
 function of time for the birch rod. 340

9-13 Comparison of the theoretical and experimental gain and phase as a function of time for the birch rod.	341
9-14 Maple rod moisture mapping for z periodic sensor measurements at 1 Hz.	343
9-15 Maple rod moisture profiles measured using the z periodic sensor.	344
9-16 Maple rod: Measured (black) and theoretical (red) gain and phase for moisture diffusion.	345
9-17 Birch rod moisture mapping for z periodic sensor measurements at 10 Hz.	346
9-18 Birch rod moisture profiles measured using the z periodic sensor.	347
9-19 Single conductor cable moisture mapping for z periodic sensor measurements at 1 Hz.	348
9-20 Single conductor cable moisture profiles measured using the z periodic sensor.	349
9-21 Three conductor cable geometry produced for analysis in Comsol Multiphysics.	351
9-22 Dirichlet boundary conditions on the three conductor cable.	352
9-23 Slices of the moisture concentration in the three conductor cable.	353
9-24 Moisture isosurfaces inside the three conductor cable.	353
9-25 Slices of the moisture concentration in the three conductor cable.	354
9-26 Dirichlet boundary conditions on the three conductor cable.	355
9-27 Moisture isosurfaces inside the three conductor cable.	355
10-1 Multichannel sensor design featuring 32 channels.	359
10-2 Field lines for a 1 mm wavelength sensor.	360
10-3 Comparison of discretized sense electrode capacitance for $\epsilon = \epsilon_o$, and $\epsilon = 10\epsilon_o$ with quarter wavelength air gap.	361
10-4 Simulation results for six electrode penetration depth study.	364
10-5 Potential field for the DDDSSS electrode configuration.	365
10-6 Voltage at the surface of the electrodes for the DDDSSS configuration.	365
10-7 Field Lines for the 5, 10, and 15 mm effective wavelength sensors. The fundamental wavelength is 5 mm.	366
10-8 Multichannel sensor permittivity profile study using Maxwell 2D simulations.	368
10-9 Sense and drive circuit configurations for the multichannel sensor.	370
10-10 Measurement setup for Teflon slab motion.	370
10-11 Total measured capacitance as a function of position from the multichannel sensor experiment.	371
10-12 Photograph of the sensor used in the multichannel sensor experiment.	372
10-13 Measured capacitance as a function of position from the multichannel sensor experi- ments 'A' and 'B'.	372

10-14	Experimental results for a Teflon block moved in the direction of the electrodes. . . .	373
10-15	Five finger capacitive sensor array.	375
10-16	Capacitive sensor array with fifth electrode triggered.	376
11-1	Asymmetric electrode configuration requiring both sine and cosine terms.	384
A-1	Temperature conversion between Fahrenheit, Celsius, Rankine, and Kelvin.	388
B-1	Additional Teflon constant temperature dielectric spectroscopy measurements. . . .	404
B-2	Effective permittivity data for the Teflon rod from the steady state temperature measurements in Fig. B-1.	405
B-3	Additional Teflon constant temperature dielectric spectroscopy measurements. . . .	407
B-4	Effective permittivity data for the Teflon rod from the steady state temperature measurements in Fig. B-3.	408
B-5	Additional Teflon constant temperature dielectric spectroscopy measurements. . . .	410
B-6	Effective permittivity data for the Teflon rod from the steady state temperature measurements in Fig. B-5.	411
B-7	Additional polycarbonate constant temperature dielectric spectroscopy measurements.	413
B-8	Effective permittivity data for the polycarbonate rod from the steady state temperature measurements in Fig. B-7.	414
B-9	Additional polyethylene constant temperature dielectric spectroscopy measurements.	416
B-10	Effective permittivity data for the polyethylene rod from the steady state temperature measurements in Fig. B-9.	417
B-11	Additional acrylic rod constant temperature dielectric spectroscopy measurements. .	419
B-12	Effective permittivity data for the acrylic rod from the steady state temperature measurements in Fig. B-11.	420
B-13	Additional three conductor cable constant temperature dielectric spectroscopy measurements from June 2006.	422
B-14	Effective permittivity data for the three conductor cable from the steady state temperature measurements in Fig. B-13.	423
B-15	Additional three conductor cable constant temperature dielectric spectroscopy measurements from June 2006.	425
B-16	Effective permittivity data for the three conductor cable from the steady state temperature measurements in Fig. B-15.	426

B-17 Transient Teflon experiment calculated effective permittivity from measurements in Section 8.1.1.	427
B-18 Birch rod experiment calculated effective permittivity from measurements in Section 8.1.2.	428
B-19 Unwrapped single conductor cable experiment calculated effective permittivity from measurements in Section 8.1.3, Experiment 1.	429
B-20 Wrapped single conductor cable experiment calculated effective permittivity from measurements in Section 8.1.3, Experiment 1.	430
B-21 Single conductor cable experiment calculated effective permittivity from measurements in Section 8.1.3, Experiment 2.	431
B-22 Three conductor cable experiment calculated effective permittivity from measurements in Section 8.1.4, Experiment 1.	432
B-23 Three conductor cable experiment calculated effective permittivity from measurements in Section 8.1.4, Experiment 2.	433
B-24 Three conductor cable experiment calculated effective permittivity from measurements in section 8.1.4, Experiment 3.	434
B-25 Three conductor cable experiment calculated effective permittivity from measurements in Section 8.1.4, Experiment 4.	435
B-26 Three conductor cable moisture ingress experiment calculated effective permittivity from measurements in Section 8.1.4, Experiment 5.	436
B-27 Three conductor cable moisture egress experiment calculated effective permittivity from measurements in Section 8.1.4, Experiment 5.	437

List of Tables

3.1	Summary of Generalized Planar Periodic Sensor Variables	75
4.1	Balloon Boundary Condition Study: Sensor and Simulation Parameters	113
4.2	Balloon Boundary Condition Study: Simulation Boundary Conditions	113
4.3	ϕ periodic sensor comparison of simulation to theory for $r_0 = Ar_e$ and $2\pi r_e = \lambda = 1$ mm.	118
4.4	ϕ periodic sensor comparison of simulation to theory for select cases of $A = r_e - r_0$.	120
4.5	z Periodic Sensor Solution Methods Comparison	142
5.1	Interface Box Nominal and Measured Feedback Capacitances	172
5.2	Saturation Vapor Pressure for Select Temperatures	181
5.3	Disturbance Factors and Approximate Capacitance Error	186
6.1	Electrical Properties of the Dielectric Test Rods	196
6.2	Teflon Steady State Measurements: Average Temperatures and Standard Deviations	198
6.3	Polycarbonate Steady State Measurements: Average Temperatures and Standard De- viations	200
6.4	Polyethylene Steady State Measurements: Average Temperatures and Standard De- viations	202
6.5	Acrylic Steady State Measurements: Average Temperatures and Standard Deviations	204
6.6	Moist Birch Steady State Measurements: Average Temperatures and Standard Devi- ations	206
6.7	Dried Birch Steady State Measurements: Average Temperatures and Standard Devi- ations	208
6.8	Moist Single Conductor Cable Measurements Steady State Temperature Information	210
6.9	Dry Single Conductor Cable Measurements Steady State Temperature Information .	212
6.10	Three Conductor Cable Measurements Steady State Temperature Information	214

7.1	Activation Energies for Measured Materials	242
7.2	Master Curve Logarithmic Frequency Shifts with Temperature for the Moist Single Conductor Cable	251
7.3	Master Curve Logarithmic Frequency Shifts with Temperature for the Dry Single Conductor Cable	255
7.4	Master Curve Logarithmic Frequency Shifts with Temperature for the Three Conduc- tor Cable	259
9.1	One Dimensional Diffusion Examples. $D_o = 1$	321
9.2	The first nine zero's of the Bessel functions of the first kind of order 0 and 1.	326
9.3	Capacitance for Birch Diffusion Estimate	339
10.1	Possible Sensor Configurations for a 6 Finger Periodicity. D-Drive, S-Sense, G-Ground.	363
10.2	Penetration Depth Study Simulation Parameters	363
10.3	Calculated Capacitance in pF/m for 5 mm Periodicity Example Problems	366
10.4	Table of Capacitances and Gains for 1, 2.5 and 5 mm sensors. Gain assumed 1 nF feedback capacitor and 5 cm electrode length.	367
A.1	Supplies for Cleaning Sensors	389
B.1	Constant Temperature Information for Additional Steady State Teflon Measurement	1 403
B.2	Constant Temperature Information for Additional Steady State Teflon Measurement	2 406
B.3	Constant Temperature Information for Additional Steady State Teflon Measurement	3 409
B.4	Constant Temperature Information for Steady State Polycarbonate Measurements .	412
B.5	Constant Temperature Information for Steady State Polyethylene Measurements . .	415
B.6	Constant Temperature Information for Steady State Acrylic Measurements	418
B.7	Constant Temperature Information for Steady State Three Conductor Cable Mea- surements	421
B.8	Constant Temperature Information for Steady State Three Conductor Cable Mea- surements	424

Chapter 1

Introduction

1.1 Motivation

Underground electric power cables have provided electricity to millions of people for decades. Every major city is home to thousands of miles of cables connecting supply to demand in a complex network reflecting the ongoing effort to respond to the needs of consumers. The cables themselves reflect the technology of their day, and therefore the vast majority of these networks is made up of old technology. Nevertheless, older cables, some dating back over a hundred years, continue to be tremendously useful in power delivery.

While the cable designs of yesteryear were intended to meet the demands of their day, they provide a significant foundation in meeting the demands of today. With a significant portion of underground power being supplied by antiquated cables, there is significant motivation for geriatric research into their aging process.

Cable aging and eventual failure is attributed primarily to temperature fluctuations, moisture ingress, and partial discharges (PD). Understanding these phenomena will lead to a better understanding of how to test cables, determining when to replace unhealthy cables, and will improve cable technology in the future. Properly scheduling cable replacement should lead to a reduction of service outages and the reduction of replacement costs.

While many types and designs of cables exist, our efforts focus on cables with oil-impregnated paper insulation and specifically issues pertaining to temperature fluctuations and moisture ingress. Paper insulated lead covered (PILC) cables have been made available to us by the Electric Power Research Institute (EPRI), the sponsor of the research. The effects of moisture on the electrical properties of the cable are monitored using dielectrometry (dielectric spectroscopy) sensors specifically

designed for the task of measuring moisture profiles as a function of temperature and time.

1.2 Thesis Overview

The thesis presents the results of research work done in developing dielectrometry sensing technology along with cable and other material measurements done with the sensors. The research has focused in three areas: the development of electro-quasistatic (EQS) sensors and field solutions, experimental measurements, and interpreting experimental results.

The development of the EQS “dielectrometry” sensors provides a basic tool for measuring electrical properties of a material. The electrical properties measured are the relative permittivity and conductivity of a medium, or equivalently the medium’s effective permittivity. Theoretical work is presented that provides a semi-analytical solution for the electric field for a number of cylindrical and planar sensor topologies. This can further be used to predict measurable quantities such as the impedance, and complex gain between sensor electrodes.

Physical sensors are manufactured based on the theoretical work. A number of steady state and transient measurements are conducted on various polymers, woods, and the power cables. Temperature, humidity and frequency are varied in a series of experiments providing data for further investigation into the material properties. Using the theoretical solution the effective permittivity is estimated and moisture concentration profiles are estimated.

1.3 Thesis Outline

The thesis is designed to provide an authoritative presentation of our results, and to serve as a useful reference to those working with similar sensing technology or cables. Chapter 2 provides an overview of the history and ageing mechanisms associated with oil-impregnated paper cables. The cable samples available for measurements are presented. An overview is given of past investigations on cable ageing research along with the various technologies used.

Chapter 3 provides the theoretical foundation for dielectric spectroscopy. Dielectrometry sensor theory is presented for the planar sensor, cylindrical ϕ periodic sensor, cylindrical z periodic sensor, a generalized form of the planar sensor, and a planar sensor periodic in two directions. Field solutions are derived as well as the admittance between drive and sense electrodes.

In Chapter 4 the new theoretical solutions for the cylindrical sensors are explored in relation to the planar solution. The expectation that the cylindrical and planar sensor solutions converge as the radius becomes much larger than the sensor wavelength is confirmed. The effect of conductivity in

lossy materials is explored for each geometry. The theoretical solutions are also compared to solutions achieved using finite element solvers. The sensor designs used in measurements are presented and the design choices discussed. A special sensor design for a hydrophilic sensor is explored. The hydrophilic sensor lacks a backplane permitting moisture to pass directly through the substrate and into the material under test (MUT).

Chapter 5 gives an overview of the procedure for the steady state and transient measurements performed for the research. Details of the experimental chamber setup and the environment control hardware are given. The hardware used to excite and measure the sensor response is described. Sources of measurement error due to limitations of the theoretical model and experimental noise are also explored.

Chapter 6 presents steady state measurements on a number of Teflon, polycarbonate, polyethylene, acrylic, birch wood, and cable samples. Measurements are conducted at temperatures ranging from room temperature to approaching the boiling point. The gain and phase measurements are presented and discussed.

Chapter 7 investigates the electrical effect of temperature and moisture content on a sample. Using the theoretical results presented in Chapter 3, the measurements in Chapter 6 are used to estimate the effective permittivity. The temperature dependence is recognized to have the Arrhenius dependence and an activation energy is estimated and a master curve is formed. A study of the moisture dependence of the electrical properties is made in light of the results of Neimanis & Eriksson [1].

Chapter 8 presents the results of moisture diffusion experiments. During each experiment the temperature and relative humidity is recorded. The gain and phase measurements are presented as a function of time at several frequencies. The boundary conditions are stated for each experiment.

Chapter 9 characterizes the diffusion process. The diffusion equation is derived and solved for cartesian and cylindrical coordinates. Examples of linear diffusion are given. Several of the experimental results in Chapter 8 are investigated.

Chapter 10 provides further exploration into the multichannel sensor. The benefits are explored and the technical requirements discussed. Simple experiments demonstrates the utility of such a sensor.

Chapter 11 gives a summary and conclusion of the work. Suggestions are made for continuing efforts in future work related to the topics of the thesis.

Appendix A serves as a quick reference for several miscellaneous items including specialized terms, acronyms, and symbols used in the thesis. Also provided is a brief listing of relevant controller box commands.

Appendix B provides additional measurements and figures not presented in the text itself.

1.4 Thesis Conventions

In an attempt to be consistent throughout the work, we adhere to the following conventions.

The notation for the natural logarithm of x is $\ln(x)$. Engineering notation is used for the common logarithm, *i.e.* base-10. That is $\log_{10}(x)$ may appear explicitly, or with the 10 suppressed such as $\log(x)$.

Units are always given with all quantities requiring them. Generally the author assumes the reader is comfortable with metric and English units. The units of common use are degrees Fahrenheit and Celsius, meters, inches, and mils (1 mil = 0.001 inch). In many cases the choice of units reflects a design specification and the preference to use exact quantities with minimal digits when possible.

A vector field quantity is denoted by a line over a capital letter, \bar{A} . Unit vectors are indicated by hats as follows: in cartesian coordinates, \hat{x} , \hat{y} , and \hat{z} , and in cylindrical coordinates, \hat{r} , $\hat{\phi}$, and \hat{z} .

Matrices are indicated by a bold capital letter, such as \mathbf{A} . Vectors in matrix equations are indicated by a bold lower case letter such as \mathbf{v} . Members of a vector are indexed with a subscript such as ν_m . Indexing may begin at zero or one. Similar indexing is used for matrix elements.

When possible, experimentally measured data is reported with standard deviation in the form $A \pm B$ or $A(B)$. For example the charge on an electron is $-q$, where q is expressed [2]

$$q = 1.602176487 \times 10^{-19} \pm 0.000000040 \times 10^{-19} \text{ C} \quad (1.1)$$

or equivalently,

$$q = 1.602176487(40) \times 10^{-19} \text{ C} \quad (1.2)$$

Numerical data is subject to numerical errors. For numerical computations when practical we solve the problem at two resolutions and report the results of the higher resolution simulation to 1 significant digit past the agreement between the two simulations. For example, if a coarse mesh simulation resulted in a calculation of 5.0244271... pF/m and a fine mesh simulation result in 5.0241715... pF/m, we would report the result as 5.0242 pF/m.

When working with phasor notation, an $e^{j\omega t}$ time dependence is used. The choice is customary in circuit theory, which is based on quasistatic approximations. When referring and comparing to other texts it critical to note the time dependence. While most modern works either choose an $e^{j\omega t}$ (see [3]) or an $e^{-i\omega t}$ (see [4]), several works can be found with an $e^{i\omega t}$ time dependence (for example [5]). Most notably the choice will effect the sign of the imaginary part of the permittivity.

1.5 Table of Experimental Measurements

Experimental measurements are conducted on a number of materials. A summary of all the measurements is given below.

Material	Type	Temp. °F	RH %	Meas. Sec.	Analysis Sec.	Figures
Teflon	Steady State	Table 6.2 (59 to 174)	0	6.1.1	7.2	6-2, 7-2
Teflon	Steady State	Table B.1 (71 to 176)	0	B.1.1	B.1.1	B-1, B-2
Teflon	Steady State	Table B.2 (70 to 174)	0	B.1.1	B.1.1	B-3, B-4
Teflon	Steady State	Table B.3 (70 to 176)	0	B.1.1	B.1.1	B-5, B-6
Polycarbonate	Steady State	Table 6.3 (70 to 175)	0	6.1.2	7.2	6-3, 7-3
Polycarbonate	Steady State	Table B.4 (75 to 174)	0	B.1.2	B.1.2	B-7, B-8
Polyethylene	Steady State	Table 6.4 (71 to 174)	0	6.1.3	7.2	6-4, 7-4
Polyethylene	Steady State	Table B.5 (74 to 175)	0	B.1.3	B.1.3	B-9, B-10
Acrylic*	Steady State	Table 6.5 (72 to 155)	0	6.1.4	7.2	6-5, 7-5
Acrylic	Steady State	Table B.6 (74 to 174)	0	B.1.4	B.1.4	B-11, B-12
Birch* (Moist)	Steady State	Table 6.6 (70 to 176)	NA	6.2.1	7.2	6-6, 7-6
Birch* (Dry)	Steady State	Table 6.7 (77 to 176)	0	6.2.1	7.2	6-7, 7-7

*Additional analysis in Section 7.2.2.

Material	Type	Temp. °F	RH %	Meas. Sec.	Analysis Sec.	Figures
1CC* (Moist)	Steady State	Table 6.8 (81 to 185)	NA	6.3.1	7.2	6-8, 7-8
1CC* (Dry)	Steady State	Table 6.9 (64 to 195)	0	6.3.1	7.2	6-9, 7-9
3CC*	Steady State	Table 6.10 (73 to 194)	0	6.3.2	7.2	6-10, 7-10
3CC*	Steady State	Table B.7 (75 to 213)	0	B.1.5	B.1.5	B-13, B-14
3CC*	Steady State	Table B.8 (70 to 165)	0	B.1.5	B.1.5	B-15, B-16
Teflon	Transient (ϕ)	167	30	8.1.1		8-2, 8-3, B-17
Birch	Transient (ϕ)	99	59	8.1.2	9.3.1	8-5, 8-6, B-18
1CC	Transient (ϕ)	174	27	8.1.3		8-9, 8-10, B-19, B-20
1CC	Transient (ϕ)	147	Various	8.1.3		8-13, B-21
3CC	Transient (ϕ)	101	81	8.1.4		8-16, B-22
3CC	Transient (ϕ)	182	53	8.1.4		8-18, B-23
3CC	Transient (ϕ)	193	34	8.1.4		8-20, B-24
3CC	Transient (ϕ)	174	46	8.1.4		8-22, B-25
3CC	Transient (ϕ)	155	34	8.1.4		8-24, 8-25, B-26, B-27
Birch	Transient (z)	128	60	8.2.1	9.4.2	8-28, 8-29, 8-30
Maple	Transient (z)	98	35	8.2.2		8-32, 8-33, 8-34
Maple	Transient (z)	127	27	8.2.2	9.4.1	8-36, 8-37, 8-38
1CC	Transient (z)	128	40	8.2.3	9.4.3	8-40, 8-41, 8-42

* *Additional analysis in Section 7.2.2.*

Chapter 2

An Overview of Paper Insulated Lead Covered Cables

2.1 Historical Perspective

Paper insulated lead covered (PILC) cables have a long history of use beginning in the 19th century. The first known case of using helically wrapped paper to insulate a wire is attributed to a paper manufacture in Richmond, Virginia named John Wortendyke. In 1872 Wortendyke used a taping machine to helically wrap wire for an electric bell in his home. While Wortendyke never commercialized the process, Edwin McCracken, a former employee of Wortendyke, did further work on the taping machine and was granted a U.S. patent in 1884 for “an electric wire having a covering consisting of a spirally wound and lapping strip or strips of paper composed of pure vegetable fiber and applied in its unchanged fibrous condition to the wire, the paper forming, of itself, the insulating covering for the wire.” The first commercial impregnated paper-insulated, lead sheathed cable was produced for telephony in 1888 by John Barrett of AT&T [6].

Over the next several decades, improvements were made in every aspect of cable construction. Originally the paper taping was made of manila-rope fibers, but shortages during World War I forced manufacturers to turn to washed wood-pulp fibers. Fourdrinier paper making machines became the standard and now are used almost exclusively. Drying and impregnation of oil into the paper developed from McCracken’s immersion technique, to a drying cycle with heat and pressure. Impregnation is also done under pressure. The application of the lead sheath, improvements in its quality and reduction in its thickness also followed. Corrosion preventing jackets were developed by the 1950s [6].

Pre 1960s cables were buried underground only in metropolitan areas or when other practical considerations required it. The initial design of these underground cables used an oil-soaked paper insulation [7]. The aesthetic value of buried cables became more appreciated in the 1960s and the growing market put pressure on the development of less expensive cables with a solid dielectric.

PILC cables are designed to last 30 to 50 years, but many installed in the 1930s and 40s are still in service, well past their design life. These cables continue to be used by utilities without an understanding of the cables condition [8]. With many cables continuing to operate acceptably, research efforts are aimed at reducing the number of outages by providing information for deciding if a cable should be replaced. The nature of these efforts vary significantly in scale. In Gothenburg, Sweden extensive mapping of partial discharges (PD) in the existing power cable network were done over the course of two years [9]. Nearly 2000 km of cable were measured and evaluated. Other efforts have looked closely at aged cables and the effect of moisture on the electrical properties [1,10]. Disposal of exhumed cables has been the topic of other research [11].

Because the nature of the research is highly experimental and modeling the cable requires significant simplifying assumptions, additional research to corroborate or challenge prior publications is tremendously valuable. Cable samples may seem representative, however, the history of cable samples is usually only vaguely known. Additional theoretical and experimental work focusing on the mechanisms of cable breakdown provides a better understanding and basis for cable replacement. The long term goal is to maximize cable life and recognize and replace failing cables with minimal interruption of service.

2.1.1 Cable Types

The literature uses several names for the oil-paper insulated cables we are working with. Some studies deal with both paper and more modern cable technologies. Some references use the acronym PILC to stand for paper-insulated lead cable [6]. Others suggest paper-insulated lead covered [8]. Other common underground cable types found in the literature include cross linked polyethylene cables (XLPE), and self contained fluid filled cables (SCFF) [12]. Dow Corning Corp. has developed a water tree retardant XLPE cable (TR-XLPE) that utilizes a cable restoration technology [7].

2.2 Ageing Mechanism for Power Cables

Ageing in PILC cable systems is primarily caused by three mechanisms: high operating temperature, partial discharge (PD), and moisture ingress [12].

Thermal aging by temperature cycling or high temperatures can result in a decrease in the degree

of polymerization (DP). DP is the average length of a polymer chain. Larger values of DP provide greater mechanical strength. Thermal aging is identified by the formation of carbon monoxide and carbon dioxide, a loss in mechanical integrity, and changes in the chemical structure [13].

Partial Discharge (PD) refers to the localized dielectric breakdown of a small portion of insulation under high voltage stress. Gaps or voids in the insulation can become sites for PD. Voids can be formed during temperature cycling or near leaks. Regions of the insulation with low oil will operate at a higher temperature and PD may occur. PD can result in the release of hydrogen gas and methane [12].

Moisture can enter the insulation of oil-paper insulated cables through leakage in the sheath due to cracking, corrosion, or inadequate sealing. Often damage is caused by mechanical digging equipment such as a backhoe. Water is also formed as a byproduct of the thermal aging of cellulose [1].

There is some disagreement in the literature as to the significance of the effect of moisture in failed cables. Bitam-Megherbi et al. have stated, “among the factors which have a harmful role in electric insulation, moisture remains indisputably the most significant [14].” But the significance has been questioned elsewhere. Bucholz et al. have concluded that “the main degradation process of the examined PILC cables does not seem to be associated to moisture in paper but rather to the aging of oil [15].”

Our own research efforts do not study cable failure directly, but focus on the electrical properties of the cable as temperature and moisture are varied. It will be shown that the dielectric losses have order of magnitude increases with increased temperature and moisture content. Conductivity will decrease the efficiency of power transmission. Total failure occurs when a short develops in the cable, typically in the case of severe PD.

Other forms and sources of cable failure commonly found in underground cable networks include third party damage, joints between cables, and cable terminations. In a study done in Gothenburg, Sweden by Olsson & Bengtsson, which included XLPE and PILC cables, the primary cause of cable failure was the joints of paper insulated cables, followed by third party damage, and then internal faulting in PILC cables [9]. Together these accounted for about 80% of all cable faults.

Cables that have been excavated due to failure or other reasons are typically disassembled to recover the valuable metal content. The insulation is generally considered as waste and sent to landfills. Investigations have been made into energy recovery from the polymer waste [11].

2.3 Measurement Techniques from Previous Research

Studies on the electrical properties of paper have used a variety of measurement technologies. Many of these techniques were developed in part for the analysis of oil impregnated transformer board used in industrial power transformers [16]. In fact this is one of the original applications of dielectrometry [17–19].

One of the simplest forms of dielectric spectroscopy is to form a parallel plate capacitor with the MUT. This technique has been used extensively in the literature under various circuit configurations to maximize the accuracy of the current measurements [14, 18].

The isothermal relaxation current (IRC) test measures the relaxation current after the application of a DC voltage [8, 15]. The leakage current test (LIpaTEST™) measures the leakage current during the application of a DC voltage and relates it to the cable capacitance and the length of the cable [8, 15]. The return voltage method (RVM) has been used to determine the polarization spectra and insulation condition of oil-paper transformers [20], and PILC cables [15].

Using partial discharge measurements as a basis for assessing cable health has been the topic of several investigations [9, 21–23]. Other partial discharge detection sensors have been suggested such as an acoustic sensor [24].

Several sensing technologies may be used to detect moisture. Near infrared spectroscopy has been used to estimate moisture content in impregnated paper [25]. Time domain reflectometry measurements have been used to assess the state of water in oil-impregnated paper [26]. So called differential TDR has been used to detect locations of moisture ingress [10, 27]. Time domain methods have also been used to estimate the dielectric spectra of oil-impregnated cellulose [28]. X-ray computed tomography has been used to monitor moisture in wood and may have applications in paper insulation [29, 30].

The Karl Fischer method is used for the purposes of determining moisture content in solid and liquid samples [1, 15]. It is discussed in Section 7.3.

The experimental measurement technique used in this research is dielectric spectroscopy, otherwise known as dielectrometry with interdigital sensors. This form of dielectrometry has also been referred to as the ‘imposed $\omega - k$ ’ technique. This name however is slightly misleading since the use of k as a wavenumber is usually reserved for propagating and evanescent waves in electromagnetic wave theory. Interdigital dielectrometry has been used extensively for experimental measurements involving transformer board paper, typically to monitor moisture diffusion from oil into a sample. Other applications of interdigital dielectrometry sensors proposed include detection of landmines [31], the detection of dangerous materials for security applications [32], and the monitoring of curing pro-

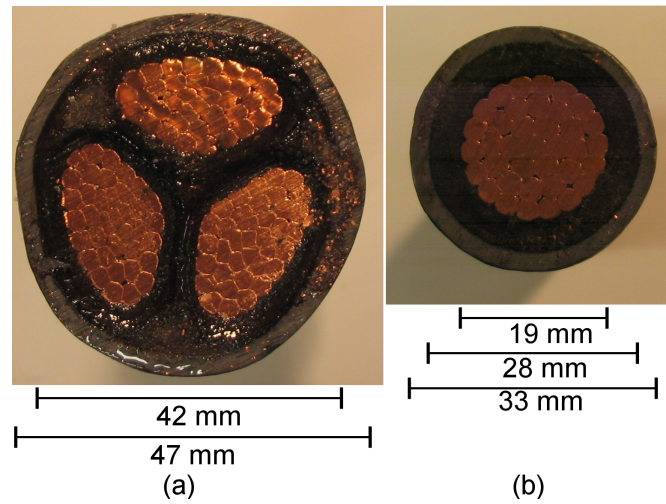


Figure 2-1: Cross-section of the (a) three conductor cable and (b) single conductor power cable supplied by EPRI. The dimensions are of the diameter of the outer conductor and insulation for both cables, and the inner conductor for the single conductor cable. Cables are shown as their actual size.

cesses [33]. Electric Capacitance Tomography (ECT) is a similar measurement system for detection of dielectrics [34].

In view of the expense involved in replacing underground cables, Dow Corning Inc. has developed an injection process for XLPE cable. Phenylmethyldimethoxysilane (PMDMS) is injected in-between the conductor strands of a cable. The fluid travels down the cable and can diffuse into the polyethylene insulation. PMDMS reacts with water to eliminate water and fill damaged voids. The process has been commercialized since 1987 with significant success when applied to both ‘distribution’ (below 46 kV) and ‘transmission’ (above 46 kV) class cables [7, 35]. It is not believed this process has been applied to PILC cables.

2.4 EPRI Cable Samples

2.4.1 Description of the Cables

Two cables samples have been supplied by EPRI for measurements. Originally each cable measured about 2 feet in length prior to being cut for measurements. One cable has three center conductors and the other has a single center conductor. The cross-sections of the cables are pictured in Fig. 2-1.

The three conductor cable consists of three stranded copper conductors separated by an oil-

paper insulation. The cable is protected with a lead sheath. Disassembling the cable reveals that the insulating paper tapes are wound around the individual conductors or phases, and that the belt insulation wraps around all three insulated conductors. The insulation around each phase consists of 15 paper tapes 6 mils thick. The belt insulation has 10 layers 5 mils thick and 2 layers 7 mils thick. The outer diameter of the lead sheath is nominally $1\frac{7}{8}$ " (47 mm). The outer diameter of the insulation (inner diameter of the lead sheath) is nominally $1\frac{5}{6}$ " (42 mm). The lead is approximately 2.5 mm thick.

The single conductor cable shown in Fig. 2-1(b) has a single conductor of stranded copper surrounded by a paper-oil insulation, surrounded by a lead sheath. The outer insulation consists of 28 insulating tapes $\frac{7}{8}$ " wide and 6 mils thick. The outer diameter of the lead sheath is $1\frac{5}{16}$ " (33 mm). The insulation outer diameter is $1\frac{1}{16}$ " (28 mm), and the conductor diameter is $\frac{3}{4}$ " (19 mm).

The three conductor cable is rated for a 6 kV load and the single conductor cable is rated for a 15 kV load [36]. No information was available regarding the age or service of these cable samples.

2.4.2 Cable Handling

In the process of the research a few observations have been made regarding the handling of the provided cables. The oil in the paper has a tendency to leak out of the cable over time particularly when the cable is held in a high temperature environment. This was noted after the initial measurements that an oily film developed at the bottom of the measurement chamber. The outer most paper strips can become dry and begin to unravel after about two or three measurements. Samples are stored horizontally in sealed containers to minimize the egression of oil.

2.5 Non-Intrusive Cable Measurements

In this section we investigate the possibility of penetrating the lead sheath with an electromagnetic sensor. One of EPRI's initial thoughts for this research was to develop an electromagnetic sensor tool to measure the moisture presence through the lead sheath of cables in the field. Measurements and tables have shown that the conductivity of the outside of the lead sheath is highly conducting and any electric field sensor is made impossible by the extremely small electric field transmitted through the lead sheath. The lead sheath acts similarly to electrostatic shielding such that practical electrostatic measurements cannot be made from outside the sheath. There are many ways to demonstrate this.

While lead is a relatively poor conductor, with a conductivity roughly 13 times smaller than copper, the relaxation time is still many over orders of magnitude smaller than the excitation peri-

odicity.

$$\tau = \frac{\epsilon}{\sigma} = \frac{8.85 \times 10^{-12}}{4.5 \times 10^6} = 1.9 \times 10^{-18} \text{ sec.} \quad (2.1)$$

We can therefore treat the lead sheath as a perfect electrical conductor (PEC). When an electromagnetic field is introduced to the outside of the sheath, a time varying surface charge forms on the conductors surface to satisfy boundary conditions. The fields inside the sheath will be practically unaffected by external fields.

Another demonstration of the electric fields inability to penetrate lead is to consider a plane wave from air normally incident on a lead half space as shown in Fig. 2-2. The incident wave is of the form $\mathbf{E}(z, t) = \mathbf{Re}\{E_0 e^{-jk_z z} e^{j\omega t}\}$, where E_0 is the field amplitude, ω is the angular frequency, k_z is the wavenumber, and t is time. The total complex amplitude electric field in the air half space, using time harmonic notation is

$$E_y = RE_0 e^{jk_z z} + E_0 e^{-jk_z z}. \quad (2.2)$$

R is the reflection coefficient and the choice of \hat{y} as the direction of polarization is arbitrary. The transmitted electric field is

$$E_{ty} = TE_0 e^{-jk_{tz} z} \quad (2.3)$$

where T is the transmission coefficient and k_{tz} is the wavenumber in lead. We note that finding the corresponding magnetic field can easily be done using Faraday's Law.

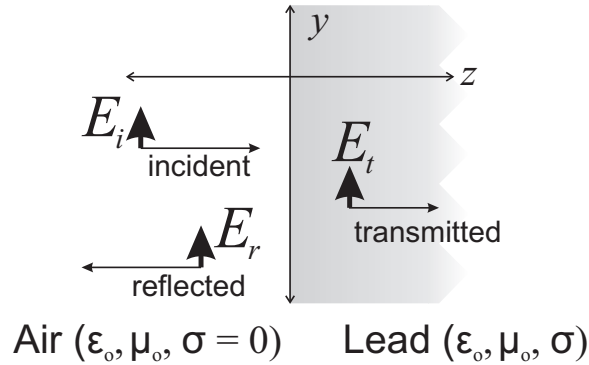


Figure 2-2: A half space transmission problem with normal incidence. E_i , E_r and E_t represent the incident, reflected, and transmitted fields respectively. The left medium is air and the right is lead.

Solving for the transmission coefficient is straight forward [4].

$$T = \frac{2}{1 + \frac{k_{tz}}{k_z}} \quad (2.4)$$

The wavenumber in lead is

$$k_{tz} = \omega \sqrt{\mu_0 \epsilon^*} \quad (2.5)$$

We have taken the permeability of lead to be μ_0 , and the effective permittivity to be

$$\epsilon^* = \epsilon_0 - j \frac{\sigma}{\omega} \quad (2.6)$$

The time average transmitted power is

$$\langle \overline{S}_t \rangle = \hat{z} \frac{1}{2} \mathbf{Re} \left\{ \sqrt{\frac{\epsilon^*}{\mu_0}} \right\} |T|^2 |E_0|^2 \quad (2.7)$$

We can plot the transmitted power as a function of frequency and normalized by the incident power, $|E_0|^2/2\eta_0$, where $\eta_0 = \sqrt{\mu_0/\epsilon_0}$ is the intrinsic impedance of free space. The normalized transmitted power and the skin depth are shown as a function of frequency in Fig. 2-3. Despite a significant skin depth at low frequencies the transmitted power is negligible because $|T| \ll 1$. If we go to higher frequencies, the skin depth becomes infinitesimally small.

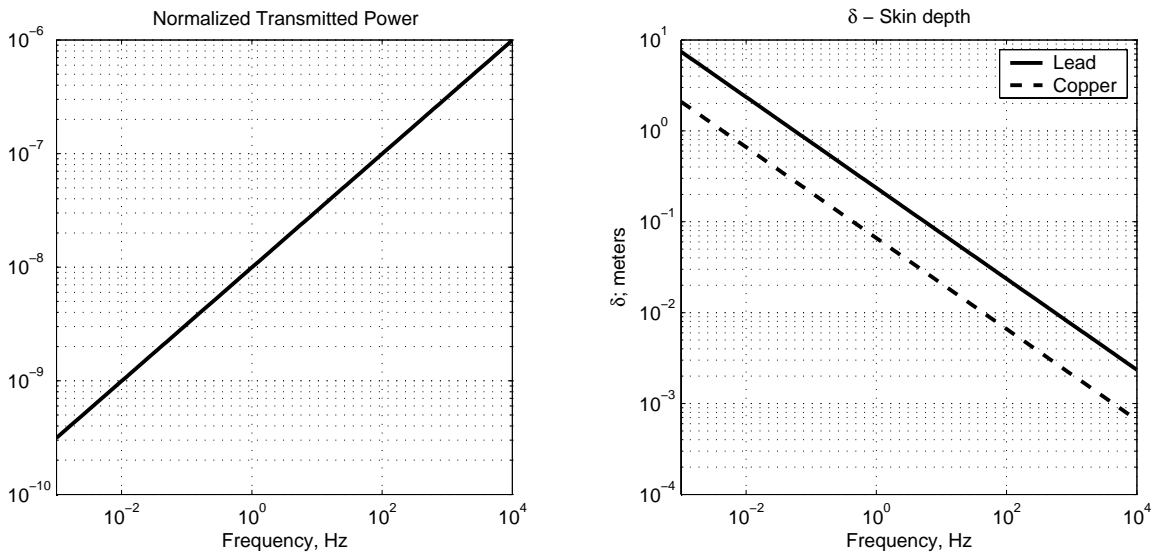


Figure 2-3: Normalized transmitted power into a lead half space from normal incidence and skin depth for lead. The skin depth of copper is shown for comparison.

The lead sheath of the cable prevents any practical quasistatic or electromagnetic field penetration. Even if a magnetostatic sensor could produce a magnetic field that penetrates the lead, the fields are unaffected by the permittivity of the material. Because moisture and temperature fluctuations produce changes in the electrical conductivity and permittivity rather than the magnetic

permeability, the magnetostatic sensor, while able to produce a field, is still unable to sense the electric properties of the insulation within.

As a final test, the sensor was placed directly on the surface of the lead sheath. The measured gain saturated the hardware, confirming our expectations. The results here are expected and there is perhaps little surprise that an electrostatic sensor cannot penetrate an electrostatic shield. The dielectrometry measurements of the cable insulation must be done with direct access to the cable insulation. Although removing the lead sheath, even temporarily, is impractical for field measurements, dielectrometry measurements in a laboratory setting provide detailed information on how the electrical properties of the insulation are affected by changes in the cable environment.

2.6 Chapter Summary

This chapter has provided an overview of the paper insulated lead covered (PILC) cables. The extensive use of PILC for underground power distribution has been discussed. Three primary ageing mechanisms have been identified: high operating temperatures, partial discharge, and moisture ingress. We have provided references for a number of tests used in assessing cable health and electrical properties. The cable samples provided by EPRI have also been described.

We demonstrate that using a dielectrometry sensor to estimate the dielectric properties of the insulation through the lead sheath is not practical. This is because the measurement signal is severely attenuated by the lead sheath. Thus, all measurements in this thesis have removed the lead sheath.

Chapter 3

Dielectrometry Sensor Theory

3.1 Introduction to Dielectrometry

Dielectrometry is the measurement of impedance for the purpose of determining the effective permittivity of a material under test (MUT). For most materials the effective permittivity is a frequency dependent quantity and a dielectrometry measurement system must be designed to interrogate the MUT over a range of frequencies. By controlling other parameters such as the temperature and humidity a series of measurements can be made to characterize the MUT with variations in these parameters.

The simplest form of a dielectrometry sensor is a parallel plate capacitor with surface area A , separated by the dielectric material to be characterized having thickness ℓ . The unknown parameters of the dielectric are the relative permittivity ϵ and the conductivity σ which can be combined to form an effective permittivity, ϵ^* , as defined in eq. 2.6. By properly exciting the capacitors terminals the effective permittivity can be determined [3].

In this research a more sophisticated sensor than the parallel plate capacitor is used. It requires access to only one surface of the sample and can produce a profile of the samples electrical properties. The sensor shown in Fig. 3-1 is a typical form of the interdigital dielectrometry sensor we have described. The sensor consists of a series of alternating *drive* and *sense* electrodes electroplated on a dielectric substrate. The MUT is placed on top of the sensor. The bottom of the sensor substrate has a ground plane, confining the fields and thus preventing other materials from affecting the measurements. The sensor shown in the figure actually has three sensors on a single substrate. Each single sensor has different sensing characteristics based on its geometry. In this case the sensors have different *wavelengths* [37], or spatial periods which affects the sensitivity to material properties

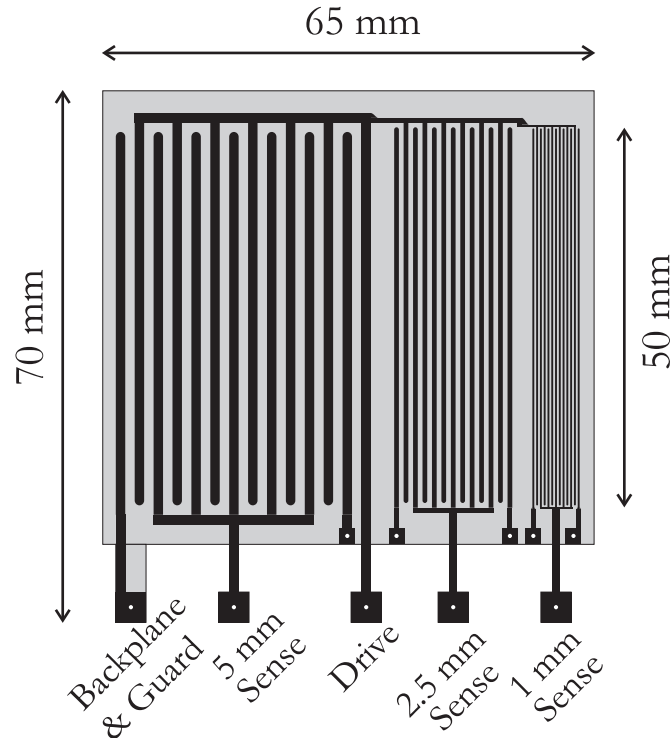


Figure 3-1: A typical three-wavelength (5, 2.5, and 1 mm) interdigital sensor. White dots indicate electrical vias that can serve as contact points for the coaxial leads, or simply as a means of connecting the guard fingers to ground. The terminals from left to right are backplane/guard, 5 mm sense, drive, 2.5 mm sense, and 1 mm sense. Sensor shown is actual size. Sensor design is discussed in Section 4.2.3.

further away from the plane of the electrodes. This design has been used extensively for determining permittivity profiles normal to the surface of the electrodes [19, 31, 38–40]. Care should be used in estimating material properties far away from the sensor. Cantrell et al. have performed uncertainty analysis on the traditional estimation techniques and found they can lead to significant estimation errors that increase with layer depth [41]. A number of planar geometries have been considered to provide different sensing characteristics [42, 43].

The impedance measured by small wavelengths are predominantly determined by the material properties very close to the sensor. Larger wavelengths are also affected by the material properties close to the sensor, but are also affected by the material properties deeper into the material. This phenomena roughly describes the penetration depth – the depth into the MUT, as measured from the surface of the electrodes, at which a change in material properties can be detected by the sensor. The penetration depth is related to how fast the fields decay into the MUT which is determined by the sensor wavelength. For sensors that are identical in all respects besides scale, longer wavelength

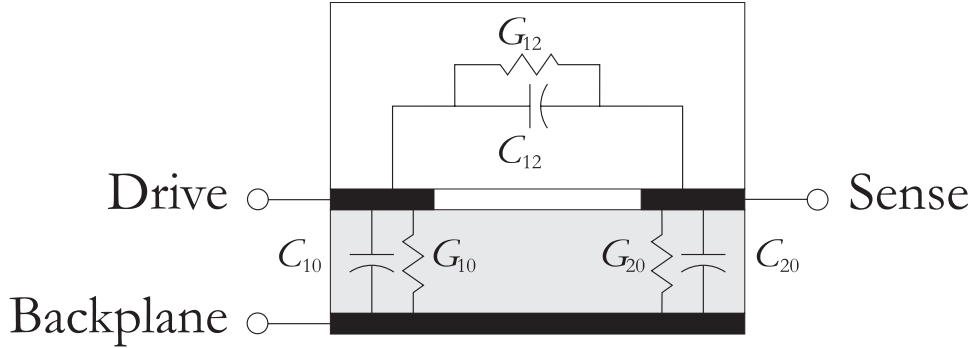


Figure 3-2: A half-wavelength cross-section of the sensor detailing the equivalent circuit between the terminals.

sensors will have deeper penetration depths.

The interdigital dielectrometry sensor has three terminals. The drive terminal is typically excited by a sinusoidal voltage source. The sense terminal is connected to the output circuitry, and the backplane/guard terminal is driven at the sensing electrode voltage for voltage mode sensing, or grounded for current mode sensing, depending on the chosen mode of operation. Properties of the MUT are determined through analysis based on comparing the driving signal to the signal measured at the sense electrode.

The circuit model of a half wavelength of the sensor is shown in Fig. 3-2. In the model every pair of terminals is connected by a resistance and capacitance in parallel. The mutual partial capacitance and conductance between the drive and sense electrodes is often referred to as the *transcapacitance* and *transconductance* respectively [44]. The *guard* terminals in Fig. 3-1 are not included in the model because infinite periodicity is assumed for analytical work.

There are several modes of operation for making measurements with the sensors that have been developed and are detailed extensively in [32]. Here we present the configuration and the transfer function. The original mode of operation is the *Floating Voltage with Ground Plane Mode* (FVGrPM) which connects a load capacitance, C_L , between the sense terminal and ground, and grounds the backplane [17,45,46]. The drive terminal is connected directly to a sinusoidal source. The FVGrPM circuit model is shown in Fig. 3-3. The system transfer function is

$$\frac{V_{Sense}}{V_{Drive}} = \frac{j\omega C_{12} + G_{12}}{j\omega (C_{12} + C_{20} + C_L) + G_{12} + G_{20}} \quad (3.1)$$

This mode is underdetermined since the complex transfer function can only be solved for two variables, yet there are in fact four unknowns (C_{12} , G_{12} , C_{20} , and G_{20}). Generally the transfer function depends on the frequency in such a way that the capacitances and conductances themselves depend

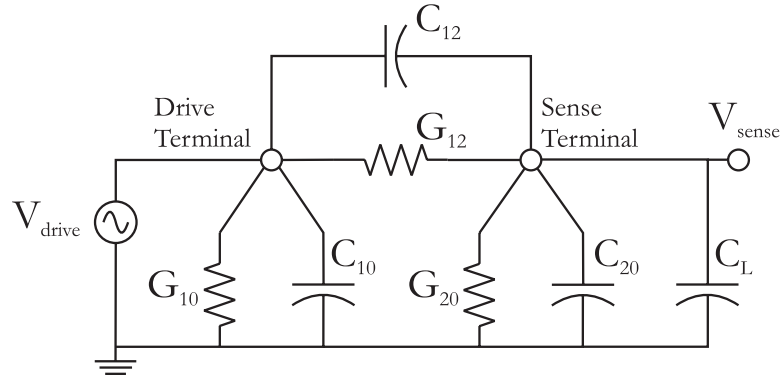


Figure 3-3: Floating voltage with ground plane mode circuit model. In general the capacitances C_{nm} and conductances G_{nm} are frequency dependent. C_L is a lumped element load capacitor.

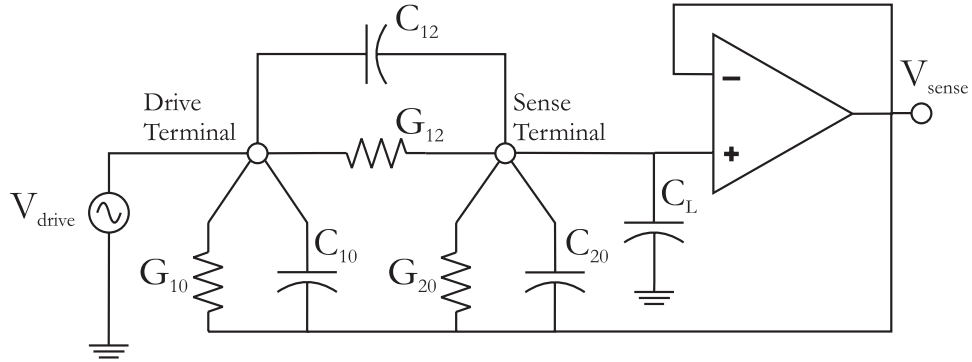


Figure 3-4: Floating voltage with guard plane mode circuit model. In general the capacitances C_{nm} and conductances G_{nm} are frequency dependent. C_L is a lumped element load capacitor.

on frequency.

The *Floating Voltage with Guard Plane Mode* (FVGPM) was designed to eliminate the problem of too many unknowns by driving the backplane at the sense voltage [44, 47]. This was done using a voltage follower circuit to prevent the current through C_{10} and G_{10} from affecting the measurement which would occur if the backplane and sense terminals were directly connected together. The FVGPM circuit model is shown in Fig. 3-4. The transfer function for this mode is

$$\frac{V_S}{V_D} = \frac{j\omega C_{12} + G_{12}}{j\omega (C_{12} + C_L) + G_{12}} \quad (3.2)$$

Notice that this equation is identical to eq. 3.1 with the C_{20} and G_{20} terms set to zero.

If measurements are to be made simultaneously at multiple wavelengths, the backplane of each wavelength must be distinct in the FVGPM mode as in general the sensing voltage is different

for each wavelength. The *Short Circuit Current Mode* (SCCM) eliminates the need for separate backplanes. The SCCM mode first introduced in [48], is presently the mode of choice and is used exclusively in this research. Under this configuration the drive fingers of the sensor are attached to a voltage source, and the sense terminals are fed into the input of an operational amplifier with a feedback capacitance, C_f . The backplane/guard terminals are grounded. The complex gain is defined as the ratio of the sensing output signal, V_S , and the input drive signal, V_D . The circuit model is shown in Fig. 3-5. The transfer function and complex gain of the circuit is

$$\frac{V_S}{V_D} = -\frac{j\omega C_{12}(\omega) + G_{12}(\omega)}{j\omega C_f} \quad (3.3)$$

The measured gain and phase are

$$\text{Gain} = 20 \log_{10} \left| \frac{V_S}{V_D} \right| = 20 \log_{10} \left(\frac{\sqrt{\omega^2 C_{12}^2 + G_{12}^2}}{\omega C_f} \right) \quad (3.4)$$

$$\phi = \angle \left(\frac{V_S}{V_D} \right) = \arctan \left(-\frac{G_{12}}{\omega C_{12}} \right) + \pi \quad (3.5)$$

In our measurements and calculations, gain and phase are reported in decibels ($20 \log |V_S/V_D|$), and degrees ($\angle \left(\frac{V_S}{V_D} \right)$) respectively.

From the measured gain and phase we can determine the values of $G_{12}(\omega)$ and $C_{12}(\omega)$.

$$C_{12}(\omega) = -C_f \mathbf{Re} \left\{ \frac{V_S}{V_D} \right\} = -C_f \left| \frac{V_S}{V_D} \right| \cos \phi \quad (3.6)$$

$$G_{12}(\omega) = \omega C_f \mathbf{Im} \left\{ \frac{V_S}{V_D} \right\} = \omega C_f \left| \frac{V_S}{V_D} \right| \sin \phi \quad (3.7)$$

Since all other circuit elements are eliminated by the choice of the SCCM mode we refer to C_{12} and G_{12} as C_T and G_T . “ T ” is chosen to stand for “transcapacitance” or “transconductance.” For low loss material at high frequencies it is difficult to accurately estimate G_{12} because of the measurements sensitivity to small phase errors. In Chapter 7 estimates of the imaginary part of the effective permittivity, a quantity related to G_{12} , clearly show a noise floor.

It should be noted that the feedback impedance is chosen as a capacitance for the SCCM mode. The transfer function is still easily manipulated if a more sophisticated feedback impedance is chosen. It is conceivable this might be done to provide a frequency variable gain to allow a wide swath of frequency measurements to be made without reaching the noise floor, or exceeding the capabilities of the amplifier.

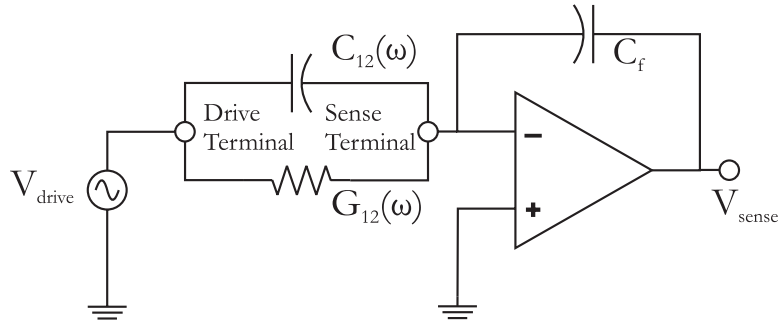


Figure 3-5: Short circuit current mode circuit model. The sensor and MUT are represented by the C_{12} and G_{12} sub-circuit. The backplane is grounded.

3.1.1 Solving the Forward Problem Solutions

Semi-analytic methods have been developed with several assumptions to predict the measured complex gain. The first paper on the subject by Zaretsky et al. addressed the forward problem in a planar geometry [37]. Efforts since then by Lesieutre et al. have eliminated the assumption of zero thickness electrodes [49]. Sheiretov & Zahn added the effect of a zero order term [50] erroneously dismissed in [37].

In order to achieve analytical results, these methods all assume the sensors to be of infinite periodicity and the electrodes to be of infinite length. Further, the MUT may consist only of stratified homogeneous layers on top of the sensor. Variation in material properties is assumed to be only in the direction perpendicular to the sensor surface. Electrode thickness is also ignored in [37] and [50].

In addition to a planar geometry, a “cylindrical” geometry has been considered by Sheiretov & Zahn to eliminate the assumptions of infinite length and periodicity [43]. The design is appropriate for measuring planar, layered materials, or perhaps a cylindrical rod on end.

In this chapter we present the results of Sheiretov & Zahn for the planar geometry [50], and then proceed to use a similar approach to solve for two cylindrical sensor geometries. Figure 3-6(a) shows a cylindrical sensor with electrodes periodic in the ϕ direction. Figure 3-6(b) shows a similar sensor, but with electrodes periodic in the z direction. In both cases the substrate and backplane are removed for clarity. Generally these sensors will be looking inward, towards the axis of the cylinder, however, it is obvious from our derivations that this orientation is not necessary. Once the theory presented here is understood, it is almost a trivial matter to consider a multi-layer substrate, or a substrate without a ground plane. If these two circumstances are permitted it is equivalent to saying the sensor can be outward looking since the only thing that generally distinguishes the MUT from

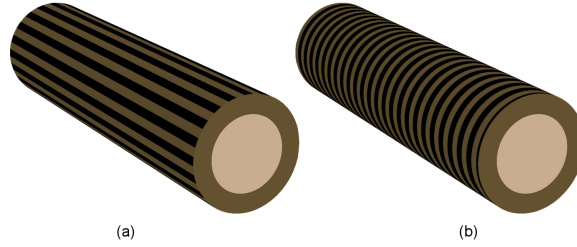


Figure 3-6: Cylindrical sensor geometries with (a) ϕ periodicity, and (b) z periodicity.

the substrate is that the substrate is of known thickness and electrical properties, while the MUT has at least one unknown property.

We also present a general form of the planar sensor solution that allows a series of sensor electrodes to be driven and sensed in an arbitrary manner. This derivation is a powerful generalization of the topology since it allows us to design sensors of arbitrary cross-section and excitation pattern. The response of sensors with finite periodicity can be estimated. Multiple penetration depth sensors can be designed by electronically varying which electrodes are driven, grounded and sensed. Such a sensor eliminates the need to print several differently sized sensors on a substrate and allows for truly collocated measurements. Finally a planar dual periodic sensor derivation is introduced. The sensor is periodic in both directions of the plane.

3.2 Planar Periodic Sensors

We begin by presenting the derivation done by Sheiretov & Zahn in [50] with a slightly different notation, and corrections to small errors in that paper. The material is presented with greater detail in Sheiretov's thesis [51]. The planar results serve as a comparison to the results for cylindrical geometry in the subsequent sections. Sheiretov assumes a planar geometry which assumes electrode periodicity in the x direction, uniformity in the y , and MUT layers in the z direction. Cases with and without a top ground plane are considered.

A cross-section of the planar geometry is shown in Fig. 3-7. Because of symmetry the problem can be reduced to solving for the fields in one half wavelength. The center of the drive electrode is chosen as the origin. The electrodes are on a substrate with thickness t_s , the opposite side of which is a grounded backplane. On top of the sensor is the MUT, which consists of P layers of dielectric each with a unique effective permittivity, ϵ_p^* . The interface between layers p and $p + 1$ is at $z = z_p$. By definition $z_0 = 0$. The thickness of layer p is $t_p = z_p - z_{p-1}$. The final layer may extend to $z = \infty$ or be limited by a grounded top plane.

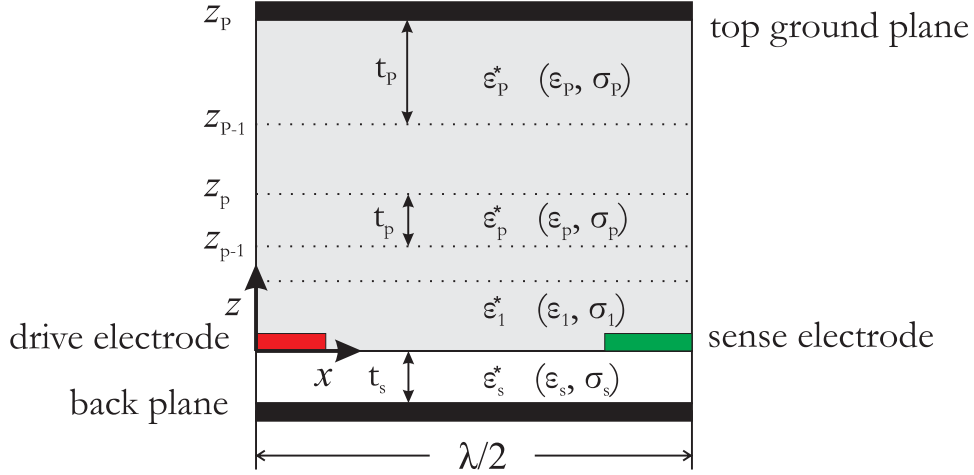


Figure 3-7: Planar dielectrometry sensor cross-section. The origin is at the center of the drive electrode. Above the material under test (MUT) is either a ground plane as shown, or extends to infinity.

Under EQS assumptions, Laplace's equation governs the electric field behavior. The electric potential is

$$\Phi(x, z) = \tilde{\Phi}_0(z) + \sum_{n=1}^{\infty} \tilde{\Phi}_n(z) \cos k_n x, \quad k_n = \frac{2\pi n}{\lambda} \quad (3.8)$$

where λ is the electrode periodicity. The sine terms are eliminated by taking the x axis to be centered on a drive electrode. The field can be found by determining the Fourier coefficients $\tilde{\Phi}_n = \tilde{\Phi}_n(z=0)$.

3.2.1 Surface Capacitance Density

This motivates the definition of the surface capacitance density, $C_n^*(z)$, that can be found at the surface of the electrodes.

$$C_n^*(z) = \frac{\epsilon^*(z) \tilde{E}_{z,n}(z)}{\tilde{\Phi}_n(z)} \quad (3.9)$$

The n th Fourier component of the electric field in the z direction is related to the Fourier coefficient by

$$\tilde{E}_{z,n}(z) = -\frac{d}{dz} \tilde{\Phi}_n(z) \quad (3.10)$$

Once $C_n^*(z)$ is found above and below the surface of the electrodes, the potential at the electrode surface and all other potentials and fields can be found. We define the difference in surface capacitance density above and below the electrodes as

$$C_n^* = \|C_n^*(z)\|_{z=0} = C_n^*(0^+) - C_n^*(0^-) \quad (3.11)$$

We have denoted the jump by double bars. C_n^* is found by first applying boundary conditions at the top of the top layer. That is, at the top ground plane or at $z = \infty$ when no top ground plane is present. $C_n^*(z)$ is found at the bottom of the top layer directly, and a transfer relation is used to find the value at the bottom of every subsequent layer, until the surface of the electrodes is reached. We summarize the results.

At the bottom of a top layer that extends to infinity

$$C_n^*(z_{P-1}) = k_n \epsilon_P^* \quad (3.12)$$

$$C_0(z_{P-1}) = 0 \quad (3.13)$$

If the top of the top layer is a ground plane, the surface capacitance density at the bottom of the top layer is

$$C_n^*(z_{P-1}) = k_n \epsilon_P^* \coth k_n t_P \quad (3.14)$$

$$C_0(z_{P-1}) = \frac{\epsilon_P^*}{t_P} \quad (3.15)$$

A relationship exists between the surface capacitance density at adjacent layer interface. This transfer relation permits us to start with one of the above cases and find C_n^* , the surface capacitance density at the surface of the electrodes. The transfer relations are

$$C_n^*(z_{p-1}) = k_n \epsilon_p^* \frac{C_n^*(z_p) \coth k_n t_p + k_n \epsilon_p^*}{C_n^*(z_p) + k_n \epsilon_p^* \coth k_n t_p} \quad (3.16)$$

$$C_0(z_{p-1}) = \frac{\epsilon_p^* C_0^*(z_p)}{t_p C_0^*(z_p) + \epsilon_p^*} \quad (3.17)$$

3.2.2 Collocation Points

The gap between the drive and sense electrodes is discretized into K collocation points. The 0 th and $K+1$ th collocation points are at the drive and sense electrode edges respectively. The potential at the m th collocation point is ν_m . Using a piecewise-linear approximation between the collocation points to describe $\Phi(x, z = 0)$, the Fourier coefficients can be found in terms of the collocation points

x_m and the collocation potentials, ν_m . The coefficients are

$$\tilde{\Phi}_n = -\frac{4}{\lambda k_n^2} \left\{ \sum_{m=1}^K \nu_m \left[\frac{\cos k_n x_{m+1} - \cos k_n x_m}{x_{m+1} - x_m} - \frac{\cos k_n x_m - \cos k_n x_{m-1}}{x_m - x_{m-1}} \right] + V_D \frac{\cos k_n x_1 - \cos k_n x_0}{x_1 - x_0} \right\} \quad (3.18)$$

$$\tilde{\Phi}_0 = \frac{1}{\lambda} \left[V_D(x_0 + x_1) + \sum_{m=1}^K \nu_m(x_{m+1} - x_{m-1}) \right] \quad (3.19)$$

where V_D is the drive voltage.

3.2.3 Electrode Surface Boundary Condition

The jump in the normal component of $\epsilon^* \bar{E}$ is zero in the gap between the electrodes. We define this quantity as the effective surface charge density, $\sigma_S^*(x)$, since in the absence of ohmic conduction it is precisely the surface charge density.

$$\sigma_S^*(x) = \|\epsilon^* E_z\| = 0 \quad (3.20)$$

The gap is divided into K regions each containing one collocation point. We require the integral of the surface charge over each region equal to zero.

$$\int_{x'_\ell}^{x'_{\ell+1}} \sigma_S^*(x) dx = 0 \quad (3.21)$$

The values x'_ℓ are the points dividing each region. The effective surface charge density is related to the Fourier coefficients and the surface capacitance density as

$$\sigma_S^*(x) = C_0^* \tilde{\Phi}_0 + \sum_{n=1}^{\infty} C_n^* \tilde{\Phi}_n \cos k_n x \quad (3.22)$$

Substituting 3.22 into 3.21 and integrating we find the boundary condition can be written as

$$0 = C_0^* \tilde{\Phi}_0 (x'_{\ell+1} - x'_\ell) + \sum_{n=1}^{\infty} C_n^* \tilde{\Phi}_n \frac{1}{k_n} [\sin k_n x'_{\ell+1} - \sin k_n x'_\ell] \quad (3.23)$$

$$= \sum_{n=0}^{\infty} C_n^* \sum_{m=1}^K M_{\ell,m}^n \nu_m - V_D \sum_{n=0}^{\infty} C_n^* b_\ell^n \quad (3.24)$$

In the last equation, terms that are coefficients of ν_m are grouped into the matrix \mathbf{M}^n with elements $M_{\ell,m}^n$, and those which are not, are grouped in the vector \mathbf{b}^n , with elements b_ℓ^n . The n superscript

is part of the naming convention and is not an exponent. This allows us to write a single matrix equation to solve for the vector of unknown collocation point voltages \mathbf{v} .

$$\mathbf{M}\mathbf{v} = V_D\mathbf{b} \quad (3.25)$$

where

$$\mathbf{M} = \sum_{n=0}^{\infty} C_n^* \mathbf{M}^n \quad (3.26)$$

$$\mathbf{b} = \sum_{n=0}^{\infty} C_n^* \mathbf{b}^n \quad (3.27)$$

The matrix elements of \mathbf{M}^n are

$$M_{\ell,m}^n = -\frac{4}{\lambda k_n^3} [\sin k_n x'_{\ell+1} - \sin k_n x'_{\ell}] \left[\frac{\cos k_n x_{m+1} - \cos k_n x_m}{x_{m+1} - x_m} - \frac{\cos k_n x_m - \cos k_n x_{m-1}}{x_m - x_{m-1}} \right] \quad (3.28)$$

for $n > 0$, and

$$M_{\ell,m}^0 = \frac{1}{\lambda} (x'_{\ell+1} - x'_{\ell}) (x_{m+1} - x_{m-1}) \quad (3.29)$$

The elements of \mathbf{b}^n are

$$b_{\ell}^n = \frac{4}{\lambda k_n^3} [\sin k_n x'_{\ell+1} - \sin k_n x'_{\ell}] \frac{\cos k_n x_1 - \cos k_n x_0}{x_1 - x_0} \quad (3.30)$$

for $n > 0$, and

$$b_{\ell}^0 = -\frac{1}{\lambda} (x'_{\ell+1} - x'_{\ell}) (x_0 + x_1) \quad (3.31)$$

3.2.4 Transcapacitance

Having solved the matrix equation 3.25, the potential at the surface of the electrodes is known. The transcapacitance between the drive and the sense electrode is found for a portion of the sense electrode with length L by integrating the current density over the surface of the sense electrode and using Ohm's Law to find the impedance, which will be purely capacitive when all layer permittivities

are real. The expression for the transcapacitance is found to be.

$$\begin{aligned}
C_T = & -2L \sum_{n=1}^{\infty} C_n^* \sin k_n x_{K+1} \frac{4}{\lambda k_n^3} \left\{ \frac{\cos k_n x_1 - \cos k_n x_0}{x_1 - x_0} \right. \\
& + \left. \sum_{m=1}^K \frac{\nu_m}{V_D} \left[\frac{\cos k_n x_{m+1} - \cos k_n x_m}{x_{m+1} - x_m} - \frac{\cos k_n x_m - \cos k_n x_{m-1}}{x_m - x_{m-1}} \right] \right\} \\
& - \frac{2L}{\lambda} C_0^* \left(\frac{\lambda}{2} - x_{K+1} \right) \left[x_0 + x_1 \sum_{m=1}^K \frac{\nu_m}{V_D} (x_{m+1} - x_{m-1}) \right] \tag{3.32}
\end{aligned}$$

This is twice the capacitance expressed in eq. 52 of [50]. This factor is due to the fact that the integration of the surface current is only over half the sense electrode. Because of the symmetry of the problem the current density is exactly the same over the other half of the electrode, doubling the total capacitance.

3.3 Cylindrical ϕ Periodic Sensors

3.3.1 Laplace's Equation in Cylindrical Coordinates

Research focused on solving for the dielectrometry sensor response have predominantly focused on the planar geometry solution. Our interest however is to place the sensor on a cylindrical surface of constant radius, namely the outside of the cable. Electroquasistatic fields are assumed allowing for the use of Laplace's equation. Laplace's equation in cylindrical coordinates is

$$\nabla^2 \Phi = \frac{1}{r} \frac{\partial}{\partial r} \left(r \frac{\partial V}{\partial r} \right) + \frac{1}{r^2} \frac{\partial^2 V}{\partial \phi^2} + \frac{\partial^2 V}{\partial z^2} = 0 \tag{3.33}$$

It is proposed to use the method of separation of variables to solve the equation and to simplify the form of the solution by assuming periodic variation in the ϕ direction and no variation in the z direction. In Section 3.4 we assume periodic variation in the z direction and no variation in the ϕ direction. The ϕ periodic sensor geometry with substrate and backplane removed is shown in Fig. 3-6(a). We start by proposing a solution to Laplace's equation of the form

$$\Phi = R(r)Q(\phi)Z(z) \tag{3.34}$$

Equation 3.34 is substituted into 3.33 and the entire equation is divided by Φ/r^2 resulting in three terms.

$$\frac{r}{R(r)} \frac{d}{dr} \left(r \frac{dR(r)}{dr} \right) + \frac{1}{Q(\phi)} \frac{d^2 Q(\phi)}{d\phi^2} + \frac{r^2}{Z(z)} \frac{d^2 Z(z)}{dz^2} = 0 \tag{3.35}$$

Then eq. 3.35 can be rewritten as

$$\frac{r}{R(r)} \frac{d}{dr} \left(r \frac{dR(r)}{dr} \right) + \frac{r^2}{Z(z)} \frac{d^2 Z(z)}{dz^2} = -\frac{1}{Q(\phi)} \frac{d^2 Q(\phi)}{d\phi^2} = n^2, \quad (3.36)$$

where n^2 is the separation constant. The solution for $Q(\phi)$ is determined.

$$Q(\phi) = \begin{cases} C_n e^{jn\phi} + D_n e^{-jn\phi} & n > 0 \\ C_0 \phi + D_0 & n = 0 \end{cases} \quad (3.37)$$

Because Φ and thus Q , must have the same value at $\phi = 0$ and 2π , n must be an integer and $C_0 = 0$. The R and Z terms in eq. 3.36 can be rearranged and set equal to a second separation constant, $-k^2$.

$$\frac{1}{rR(r)} \frac{d}{dr} \left(r \frac{dR(r)}{dr} \right) - \frac{n^2}{r^2} = -\frac{1}{Z(z)} \frac{d^2 Z(z)}{dz^2} = -k^2 \quad (3.38)$$

For ϕ periodicity, $d^2 Z(z)/dz^2 = 0$ implies $k = 0$. Equation 3.38 can then be simplified to

$$r \frac{d}{dr} \left(r \frac{dR(r)}{dr} \right) - n^2 R(r) = 0 \quad (3.39)$$

Because ϕ is periodic n must be an integer and the solution to $R(r)$ is

$$R(r) = \begin{cases} A_n r^n + B_n r^{-n} & n > 0 \\ A_0 + B_0 \ln r & n = 0 \end{cases} \quad (3.40)$$

Combining the solutions $R(r)$, $Q(\phi)$, and $Z(z) = Z_0$ by multiplying terms of equal n , and summing over all n we have the general solution for Φ .

$$\Phi(r, \phi) = A_0 + B_0 \ln r + \sum_{n=1}^{\infty} \left[A_n r^n + B_n \frac{1}{r^n} \right] [C_n \cos n\phi + D_n \sin n\phi] \quad (3.41)$$

The sensor wavelength, λ , must be a submultiple of the circumference, $2\pi r_e$.

$$\lambda = \frac{2\pi r_e}{q} \quad (3.42)$$

q is an integer and represents the number of sensor wavelengths needed to completely circumscribe the cylinder. The radius r_e is the distance from the center of the cylinder to the electrode surface.

We define the angular wavelength, θ_λ , and angular half-wavelength, $\theta_{\lambda/2}$ as

$$\theta_\lambda = 2\theta_{\lambda/2} = \frac{\lambda}{r_e} = \frac{2\pi}{q} \quad (3.43)$$

We consider the geometry shown in Fig. 3-8 which consists of P concentric layers of materials. The p th layer has a value of permittivity, ϵ_p , conductivity, σ_p , and an outer radius, r_p associated with it. The inner radius is r_{p-1} . The substrate has an effective permittivity, ϵ_s^* . We consider the two cases where the inner most layer is or is not a grounded perfect electrical conductor (PEC).

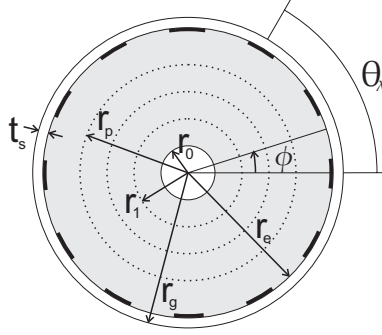


Figure 3-8: Cross-section of cylinder showing key quantities. r_e - radius to electrodes. r_g - radius to ground plane. r_p - radius of p th concentric layer. ϕ - angle around cylinder. θ_λ - angular wavelength. r_0 - radius of center conductor. t_s - substrate thickness.

The allowed values of n can be restricted since the cases where n is not a multiple of the number of wavelengths around the cylinder, q , the coefficients A_n and B_n must be equal to zero. The sine terms can also be dropped by taking the drive electrode to be centered at $\phi = 0$ which insure an even field periodicity.

$$\Phi(r, \phi) = A_0 + B_0 \ln r + \sum_{n=q, 2q, \dots} [A_n r^n + B_n r^{-n}] \cos n\phi \quad (3.44)$$

We can rewrite eq. 3.44 by grouping terms and coefficients.

$$\Phi(r, \phi) = \tilde{\Phi}_0(r) + \sum_{n=q, 2q, \dots} \tilde{\Phi}_n(r) \cos n\phi \quad (3.45)$$

By inspection of eq. 3.44 we determine the values of $\tilde{\Phi}_0(r)$ and $\tilde{\Phi}_n(r)$.

$$\tilde{\Phi}_0(r) = A_0 + B_0 \ln r \quad (3.46)$$

$$\tilde{\Phi}_n(r) = A_n r^n + B_n r^{-n} \quad (3.47)$$

3.3.2 Surface Capacitance Density

As an intermediate step we calculate the surface capacitance density at the electrode surface. We later use this information to solve for the potential between the electrodes, which can then be used

to determine the Fourier coefficients in eq. 3.45. We define the surface capacitance density at radius r as

$$C_n^*(r) = \frac{\epsilon^*(r)\tilde{E}_{r,n}(r)}{\tilde{\Phi}_n(r)} \quad (3.48)$$

$\epsilon^*(r)$ is the effective permittivity at radius r and is related to the layer permittivities and conductivities.

$$\epsilon^*(r) = \begin{cases} \epsilon_1 - j\frac{\sigma_1}{\omega}, & r_0 < r < r_1 \\ \vdots & \vdots \\ \epsilon_p - j\frac{\sigma_p}{\omega}, & r_{p-1} < r < r_p \\ \vdots & \vdots \\ \epsilon_P - j\frac{\sigma_P}{\omega}, & r_{P-1} < r < r_e \end{cases} \quad (3.49)$$

Implicit is an $e^{j\omega t}$ time dependence. At the boundaries the permittivity should be chosen based on the region under consideration. $\tilde{E}_{r,n}(r)$ is the radial electric field Fourier coefficient. The radial electric field is related to the potential.

$$E_r(r, \phi) = \tilde{E}_{r,0}(r) + \sum_{n=q,2q,\dots} \tilde{E}_{r,n}(r) \cos n\phi = -\frac{d}{dr}\Phi(r, \phi) \quad (3.50)$$

The Fourier coefficients of the electric field can be determined directly from the potential Fourier coefficients.

$$\tilde{E}_{r,n}(r) = -\frac{d}{dr}\tilde{\Phi}_n(r) \quad (3.51)$$

$C_n^*(r)$ is continuous across material interfaces (other than at the electrodes), because $\epsilon^*(r)\tilde{E}_{r,n}(r)$ and $\tilde{\Phi}_n(r)$ are continuous.

Intermediate Layer p , $n \neq 0$ Terms

Consider the intermediate layer p , with an inner radius of r_{p-1} and an outer radius of r_p . Writing $\tilde{\Phi}_n(r)$ in terms of its values at the inner and outer radius we have.

$$\tilde{\Phi}_n(r_{p-1}) = A_n r_{p-1}^n + B_n r_{p-1}^{-n} \quad (3.52)$$

$$\tilde{\Phi}_n(r_p) = A_n r_p^n + B_n r_p^{-n} \quad (3.53)$$

From eq. 3.52 and 3.53 we can solve for A_n and B_n . Substituting these values into eq. 3.47 we have an expression for the $\tilde{\Phi}_n(r)$ in the p th layer in terms of the value of $\tilde{\Phi}_n$ at the layer boundaries.

$$\tilde{\Phi}_n(r) = \left[\frac{r_p^n \tilde{\Phi}_n(r_p) - r_{p-1}^n \tilde{\Phi}_n(r_{p-1})}{r_p^{2n} - r_{p-1}^{2n}} \right] r^n + \left[\frac{r_p^n r_{p-1}^n \left(r_p^n \tilde{\Phi}_n(r_{p-1}) - r_{p-1}^n \tilde{\Phi}_n(r_p) \right)}{r_p^{2n} - r_{p-1}^{2n}} \right] r^{-n}, \quad r_{p-1} \leq r \leq r_p \quad (3.54)$$

From eq. 3.54 we can find $\tilde{E}_{r,n}(r)$. We now can find the surface capacitance density at each interface.

$$C_n^*(r_p) = -n\epsilon_p^* \frac{(r_p^{2n} + r_{p-1}^{2n}) \tilde{\Phi}_n(r_p) - 2r_p^n r_{p-1}^n \tilde{\Phi}_n(r_{p-1})}{r_p (r_p^{2n} - r_{p-1}^{2n}) \tilde{\Phi}_n(r_p)} \quad (3.55)$$

$$C_n^*(r_{p-1}) = n\epsilon_p^* \frac{(r_p^{2n} + r_{p-1}^{2n}) \tilde{\Phi}_n(r_{p-1}) - 2r_p^n r_{p-1}^n \tilde{\Phi}_n(r_p)}{(r_p^{2n} - r_{p-1}^{2n}) r_{p-1} \tilde{\Phi}_n(r_{p-1})} \quad (3.56)$$

Note that eq. 3.56 uses ϵ_p^* rather than ϵ_{p-1}^* . This is because we used the solution for $\tilde{\Phi}_n(r)$ in the p th region to calculate $\tilde{E}_{r,n}(r_{p-1})$ and then $C_n^*(r_{p-1})$. As noted earlier, $C_n^*(r)$ is continuous between material layers. We now eliminate $\tilde{\Phi}_n(r_p)$ and $\tilde{\Phi}_n(r_{p-1})$ from the expression.

$$C_n^*(r_p) = -\frac{n\epsilon_p^* (r_p^{2n} - r_{p-1}^{2n}) n\epsilon_p^* - (r_p^{2n} + r_{p-1}^{2n}) r_{p-1} C_n^*(r_{p-1})}{r_p (r_p^{2n} + r_{p-1}^{2n}) n\epsilon_p^* - (r_p^{2n} - r_{p-1}^{2n}) r_{p-1} C_n^*(r_{p-1})} \quad (3.57)$$

This equation may need to be rewritten for numerical evaluation to avoid numerical errors. The following form has proven effective.

$$C_n^*(r_p) = -\frac{n\epsilon_p^*}{r_p} \left[\frac{n\epsilon_p^* - r_{p-1} C_n^*(r_{p-1})}{\alpha_1 n\epsilon - \alpha_2 r_{p-1} C_n^*(r_{p-1})} - \frac{n\epsilon_p^* + r_{p-1} C_n^*(r_{p-1})}{\alpha_3 n\epsilon_p^* - \alpha_4 r_{p-1} C_n^*(r_{p-1})} \right] \quad (3.58)$$

We have used $\alpha_{1,2,3,4}$ as place holders for

$$\alpha_1 = 1 + \left(\frac{r_{p-1}}{r_p} \right)^{2n} \quad (3.59)$$

$$\alpha_2 = 1 - \left(\frac{r_{p-1}}{r_p} \right)^{2n} \quad (3.60)$$

$$\alpha_3 = 1 + \left(\frac{r_p}{r_{p-1}} \right)^{2n} \quad (3.61)$$

$$\alpha_4 = -1 + \left(\frac{r_p}{r_{p-1}} \right)^{2n} \quad (3.62)$$

Intermediate Layer p , $n = 0$ Terms

The $n = 0$ terms can be solved for by considering two concentric cylinders with radii r_{p-1} and r_p at potential $\tilde{\Phi}_0(r_{p-1})$ and $\tilde{\Phi}_0(r_p)$ respectively. The form of the solution is known to be that of eq. 3.46. Solving for the Fourier coefficients we have

$$\tilde{\Phi}_0(r) = \frac{[\tilde{\Phi}_0(r_p) - \tilde{\Phi}_0(r_{p-1})] \ln r + \tilde{\Phi}_0(r_{p-1}) \ln r_p - \tilde{\Phi}_0(r_p) \ln(r_{p-1})}{\ln(r_p/r_{p-1})}, \quad r_{p-1} \leq r \leq r_p \quad (3.63)$$

The electric field coefficient is found by direct application of eq. 3.51.

$$\tilde{E}_{r,0}(r) = -\frac{d}{dz} \tilde{\Phi}_0(r) = \frac{\tilde{\Phi}_0(r_{p-1}) - \tilde{\Phi}_0(r_p)}{r \ln \frac{r_p}{r_{p-1}}} \quad (3.64)$$

The surface capacitance densities at each surface are found and rearranged such that $C_0^*(r_p)$ is expressed strictly in terms of physical quantities and $C_0^*(r_{p-1})$.

$$C_0^*(r_p) = \frac{\epsilon_p^* \tilde{\Phi}_0(r_{p-1}) - \tilde{\Phi}_0(r_p)}{r_p \tilde{\Phi}_0(r_p) \ln \frac{r_p}{r_{p-1}}} \quad (3.65)$$

$$C_0^*(r_{p-1}) = \frac{\epsilon_p^* \tilde{\Phi}_0(r_{p-1}) - \tilde{\Phi}_0(r_p)}{r_{p-1} \tilde{\Phi}_0(r_{p-1}) \ln \frac{r_p}{r_{p-1}}} \quad (3.66)$$

$$C_0^*(r_p) = \frac{\epsilon_p^*/r_p}{\epsilon_p^*[r_{p-1}C_0^*(r_{p-1})]^{-1} - \ln \frac{r_p}{r_{p-1}}} \quad (3.67)$$

Cylinder with a Grounded Center Conductor

When the center of the cylinder has a grounded PEC with radius r_0 the potential $\Phi(r_0, \phi)$ is zero. From eqs. 3.56 and 3.66 we find that $|C_n^*(r_0)| \rightarrow \infty$ for all n . We can find $C_n^*(r_1)$ and $C_0^*(r_1)$ in this limit from eqs. 3.57 and 3.67.

$$C_n^*(r_1) = -\frac{n\epsilon_1^*}{r_1} \left(\frac{r_1^{2n} + r_0^{2n}}{r_1^{2n} - r_0^{2n}} \right) \quad (3.68)$$

$$C_0^*(r_1) = \frac{\epsilon_1^*}{r_1 \ln \frac{r_0}{r_1}} \quad (3.69)$$

For computational purposes it may be useful to rewrite eq. 3.68.

$$C_n^*(r_1) = -\frac{n\epsilon_1^*}{r_1} \left(\frac{1}{1 - \left(\frac{r_0}{r_1}\right)^{2n}} + \frac{1}{\left(\frac{r_1}{r_0}\right)^{2n} - 1} \right) \quad (3.70)$$

Cylinder Without a Center Conductor, $r_0 = 0$

For the case of a cylinder without a center conductor the potential must be finite at $r = 0$. This implies $B_n = 0$ in the $p = 1$ layer. We can write the form of the field and potential as

$$\tilde{\Phi}_n(r) = \tilde{\Phi}_n(r_1) \left(\frac{r}{r_1} \right)^n, \quad r \leq r_1 \quad (3.71)$$

$$\tilde{E}_{r,n}(r) = -\frac{n}{r_1} \tilde{\Phi}_n(r_1) \left(\frac{r}{r_1} \right)^{n-1}, \quad r \leq r_1 \quad (3.72)$$

Using eq. 3.48 we find $C_n^*(r_1)$.

$$C_n^*(r_1) = -\frac{n\epsilon_1^*}{r_1} \quad (3.73)$$

To find the $C_0^*(r_1)$ term we take the limit $r_0 \rightarrow 0$ in eq. 3.65. The natural logarithm approaches infinity while all other terms remain finite.

$$C_0^*(r_1) = 0 \quad (3.74)$$

Surface Capacitance Density at Electrodes

There is a discontinuity in the surface capacitance density at the sensor electrodes. Assuming that there is in fact a ground plane at a radius r_g we can determine $C_n^*(r_e^+)$ from eq. 3.56 and 3.66 by substituting r_e for r_{p-1} and r_g for r_p , and letting $\tilde{\Phi}_n(r_g) \rightarrow 0$ and $\tilde{\Phi}_0(r_g) \rightarrow 0$.

$$C_n^*(r_e^+) = -\frac{n\epsilon_s^*}{r_e} \left(\frac{r_e^{2n} + r_g^{2n}}{r_e^{2n} - r_g^{2n}} \right) \quad (3.75)$$

$$C_0^*(r_e^+) = \frac{\epsilon_s^*}{r_e \ln \frac{r_g}{r_e}} \quad (3.76)$$

Recall that ϵ_s^* is the effective permittivity of the substrate. Equation 3.75 can be rewritten for computational purposes as

$$C_n^*(r_e^+) = -\frac{n\epsilon_s^*}{r_e} \left(\frac{1}{1 - \left(\frac{r_g}{r_e}\right)^{2n}} + \frac{1}{\left(\frac{r_e}{r_g}\right)^{2n} - 1} \right) \quad (3.77)$$

3.3.3 Collocation Points

We introduce a discrete set of points at the radius r_e between a set of drive and sense electrodes at which we will calculate the potential, $\Phi(r_e, \phi)$. Let there be $K + 2$ collocation points between the

drive and sense electrodes. The m th point is at an angle ϕ_m measured from the center of the drive electrode, $m = 0, 1, \dots, K + 1$. By symmetry about the drive electrodes

$$\Phi(r, \phi) = \Phi(r, -\phi). \quad (3.78)$$

That is the potential is an even function with respect to ϕ when $\phi = 0$ is taken to be the center of a drive electrode. We interpolate the value of Φ in-between collocation points by a piecewise-linear fit

$$\Phi(r_e, \phi) = \frac{(\phi_{m+1} - \phi)\nu_m + (\phi - \phi_m)\nu_{m+1}}{\phi_{m+1} - \phi_m} \quad \text{for } \begin{cases} \phi_m < \phi < \phi_{m+1} \\ m = 0, 1, \dots, K \end{cases} \quad (3.79)$$

where $\nu_m = \Phi(r_e, \phi)$.

The selection of the points of ϕ_m is arbitrary except for the requirement that ϕ_0 and ϕ_{K+1} correspond to the edge of the drive and sense electrode respective. Concentrating the points in regions where the field is changing the fastest will improve the overall accuracy of the solution for a particular value of K . We suggest using the cosinusoidal distribution

$$\phi_m = \left(\frac{c}{2} + \frac{\lambda - c - d}{4} \left[1 - \cos \left(\frac{\pi m}{K + 1} \right) \right] \right) r_e^{-1} \quad (3.80)$$

c and d are the linear width of the drive and sense electrodes respectively. In order to find the values of the potentials at the ν_m we integrate the appropriate boundary conditions over a set of K intervals delimited by the points ϕ'_ℓ , where $\ell = 0, 1, \dots, K$. We define the values of ϕ'_ℓ .

$$\phi'_\ell = \begin{cases} \phi_0 & \ell = 0 \\ (\phi_{\ell+1} + \phi_\ell)/2 & \ell = 1, 2, \dots, K - 1 \\ \phi_{K+1} & \ell = K \end{cases} \quad (3.81)$$

From Fourier transform theory we know the Fourier series coefficients, $\tilde{\Phi}_n(r)$ to be

$$\tilde{\Phi}_n(r) = \frac{2}{\theta_{\lambda/2}} \int_0^{\theta_{\lambda/2}} \Phi(r, \phi) \cos(n\phi) d\phi \quad (3.82)$$

We defined $\theta_{\lambda/2}$ in eq. 3.43. When $r = r_e$, we can write this as

$$\begin{aligned} \tilde{\Phi}_n(r_e) &= \frac{2}{\theta_{\lambda/2}} \left[\int_0^{\phi_0} V_D \cos(n\phi) d\phi \right. \\ &\quad \left. + \sum_{m=0}^K \int_{\phi_m}^{\phi_{m+1}} \cos(n\phi) \frac{(\phi_{m+1} - \phi)\nu_m + (\phi - \phi_m)\nu_{m+1}}{\phi_{m+1} - \phi_m} d\phi \right] \end{aligned} \quad (3.83)$$

$$\begin{aligned} \tilde{\Phi}_n(r_e) &= \frac{2}{n\theta_{\lambda/2}} \left\{ V_D \sin(n\phi) \right. \\ &\quad \left. + \sum_{m=0}^K \frac{1}{n} \frac{\nu_{m+1} - \nu_m}{\phi_{m+1} - \phi_m} [\cos n\phi_{m+1} - \cos n\phi_m] \right. \\ &\quad \left. + \sum_{m=0}^K [\nu_{m+1} \sin n\phi_{m+1} - \nu_m \sin n\phi_m] \right\} \end{aligned} \quad (3.84)$$

The last summation of terms cancel each other on a term by term bases except for the first and last term, but the ν_0 term cancels with the first term in eq. 3.84, and the ν_{K+1} term is 0 because $\nu_{K+1} = 0$. Rewriting the expression with these simplifications we have

$$\begin{aligned} \tilde{\Phi}_n(r_e) &= -\frac{2}{n^2\theta_{\lambda/2}} \left\{ V_D \frac{\cos n\phi_1 - \cos n\phi_0}{\phi_1 - \phi_0} \right. \\ &\quad \left. + \sum_{m=1}^K \nu_m \left[\frac{\cos n\phi_{m+1} - \cos n\phi_m}{\phi_{m+1} - \phi_m} - \frac{\cos n\phi_m - \cos n\phi_{m-1}}{\phi_m - \phi_{m-1}} \right] \right\} \end{aligned} \quad (3.85)$$

Solving for the $n = 0$ term is done similarly. The zero order term of the Fourier series of $\Phi(r, \phi)$ is

$$\tilde{\Phi}_0(r) = \frac{1}{\theta_{\lambda/2}} \int_0^{\theta_{\lambda/2}} \Phi(r, \phi) d\phi. \quad (3.86)$$

Equation 3.79 is substituted into eq. 3.86 and can be simplified by cancellations.

$$\tilde{\Phi}_0(r_e) = \frac{1}{\theta_{\lambda/2}} \left[\int_0^{\phi_0} V_D d\phi + \sum_{m=0}^K \int_{\phi_m}^{\phi_{m+1}} \frac{(\phi_{m+1} - \phi)\nu_m + (\phi - \phi_m)\nu_{m+1}}{\phi_{m+1} - \phi_m} d\phi \right] \quad (3.87)$$

$$= \frac{1}{2\theta_{\lambda/2}} \left[V_D(\phi_0 + \phi_1) + \sum_{m=1}^K \nu_m(\phi_{m+1} - \phi_{m-1}) \right] \quad (3.88)$$

3.3.4 Boundary Condition at r_e

The discontinuity in the normal component of $\epsilon^* \bar{E}$ at the electrode surface ($r = r_e$) is defined as the effective surface charge density, $\sigma_S^*(\phi)$.

$$\sigma_S^*(\phi) = \epsilon^*(r_e^+) E_r(r_e^+, \phi) - \epsilon^*(r_e^-) E_r(r_e^-, \phi) \quad (3.89)$$

We define the surface capacitance density discontinuity

$$C_n^* = C_n^*(r_e^+) - C_n^*(r_e^-) \quad (3.90)$$

Using the definition of surface capacitance density we find the coefficients of the Fourier series expansion of $\sigma_S^*(\phi)$.

$$\sigma_{S_n}^* = C_n^* \tilde{\Phi}_n(r_e) \quad (3.91)$$

This allows us to write $\sigma_S^*(\phi)$ as

$$\sigma_S^*(\phi) = C_0^* \tilde{\Phi}_0(r_e) + \sum_{n=q, 2q, \dots} C_n^* \tilde{\Phi}_n(r_e) \cos n\phi \quad (3.92)$$

In the gap between the electrodes we require there to be no accumulation of charge.

$$\sigma_S^*(\phi) = 0, \quad \phi_0 < \phi < \phi_{K+1} \quad (3.93)$$

Integrating this over each interval $\phi'_\ell < \phi < \phi'_{\ell+1}$ we have

$$\int_{\phi'_\ell}^{\phi'_{\ell+1}} \sigma_S^*(\phi) d\phi = \int_{\phi'_\ell}^{\phi'_{\ell+1}} C_0^* \tilde{\Phi}_0(r_e) d\phi + \sum_{n=q, 2q, \dots} \int_{\phi'_\ell}^{\phi'_{\ell+1}} C_n^* \tilde{\Phi}_n(r_e) \cos(n\phi) d\phi \quad (3.94)$$

$$= C_0^* \tilde{\Phi}_0(r_e) (\phi'_{\ell+1} - \phi'_\ell) + \sum_{n=q, 2q, \dots} \frac{C_n^* \tilde{\Phi}_n(r_e)}{n} [\sin n\phi'_{\ell+1} - \sin n\phi'_\ell] \quad (3.95)$$

By substituting eq. 3.85 and 3.88 into eq. 3.95 we can group terms that have ν_m as a coefficient and those that do not.

$$\int_{\phi'_\ell}^{\phi'_{\ell+1}} \sigma_S^*(\phi) d\phi = \sum_{n=0, q, \dots} C_n^* \sum_{m=1}^K M_{\ell, m}^n \nu_m - V_D \sum_{n=0, q, \dots} C_n^* b_\ell^n = 0 \quad (3.96)$$

Let \mathbf{M}^n be the $K \times K$ matrix of elements $M_{\ell, m}^n$, ($\ell = 0, 1, \dots, K-1$; $m = 1, 2, \dots, K$) and \mathbf{b}^n be the vector length K of terms that are independent of ν_m . If we consider all intervals simultaneously

we can write an equivalent matrix form.

$$\mathbf{M}\mathbf{v} = V_D\mathbf{b} \quad (3.97)$$

Here \mathbf{v} is the vector, length K , of *unknown* potentials ν_m . We exclude the known values v_0 and v_{K+1} . The matrix \mathbf{M} can be derived from eq. 3.95 and is also $K \times K$.

$$\mathbf{M} = \sum_{n=0,q,\dots} C_n^* \mathbf{M}^n \quad (3.98)$$

We find by substitution the elements of \mathbf{M}^n .

$$M_{\ell,m}^n = -\frac{2}{n^3\theta_{\lambda/2}} [\sin n\phi'_{\ell+1} - \sin n\phi'_\ell] \times \left[\frac{\cos n\phi_{m+1} - \cos n\phi_m}{\phi_{m+1} - \phi_m} - \frac{\cos n\phi_m - \cos n\phi_{m-1}}{\phi_m - \phi_{m-1}} \right] \quad \text{for } n > 0 \quad (3.99)$$

and

$$M_{\ell,m}^0 = \frac{1}{2\theta_{\lambda/2}} (\phi_{m+1} - \phi_{m-1})(\phi'_{\ell+1} - \phi'_\ell) \quad (3.100)$$

\mathbf{b} can be written as

$$\mathbf{b} = \sum_{n=0,q,\dots} C_n^* \mathbf{b}^n \quad (3.101)$$

The elements of \mathbf{b}^n are

$$b_\ell^n = \frac{2}{n^3\theta_{\lambda/2}} \left[\frac{\cos n\phi_1 - \cos n\phi_0}{\phi_1 - \phi_0} \right] [\sin n\phi'_{\ell+1} - \sin n\phi'_\ell] \quad \text{for } n > 0 \quad (3.102)$$

and

$$b_\ell^0 = -\frac{1}{2\theta_{\lambda/2}} (\phi_0 + \phi_1)(\phi'_{\ell+1} - \phi'_\ell) \quad (3.103)$$

Solving eq. 3.97 for \mathbf{v} gives an approximation of $\Phi(r_e, \phi)$.

3.3.5 Calculating the Transadmittance

The entire system can be reduced to a two terminal circuit element with a frequency dependent admittance, Y_T . The transadmittance is related to the transcapacitance and transconductance by

$$Y_T = G_T + j\omega C_T \quad (3.104)$$

Here the quantities G_T and C_T are equivalent to G_{12} and C_{12} respectively in Fig. 3-2. The transadmittance is the ratio of the current flowing through the sense electrode to the drive electrode voltage.

$$Y_T = I_S/V_D \quad (3.105)$$

The current in a single sense electrode is found from the discontinuity in the normal component of the total current density.

$$I_S = 2Lr_e \int_{\phi_{K+1}}^{\theta_{\lambda/2}} [J_{r_e^+}(\phi) - J_{r_e^-}(\phi)] d\phi \quad (3.106)$$

The factor of two is introduced because the integration is only over half the electrode cross-section. L is the total length of all the sensing electrodes. The factor of r_e also needed because the integration is over angle, not distance.

By Ampere's law, the sum of the conduction and displacement current densities is related to the electric field.

$$\mathbf{J} = \mathbf{J}_C + \mathbf{J}_D = \sigma \mathbf{E} + j\omega \epsilon \mathbf{E} \quad (3.107)$$

$$= j\omega \left(\epsilon - j \frac{\sigma}{\omega} \right) \mathbf{E} \quad (3.108)$$

$$= j\omega \epsilon^* \mathbf{E} \quad (3.109)$$

The discontinuity in the total current density can now be related to the effective surface charge density.

$$[J_{r_e^+}(\phi) - J_{r_e^-}(\phi)] = j\omega \sigma_S^*(\phi) \quad (3.110)$$

From a series of substitutions involving eqs. 3.92, 3.110, 3.106, and 3.105 we have

$$Y_T = \frac{j\omega 2Lr_e}{V_D} \left[\sum_{n=q,2q,\dots} \int_{\phi_{K+1}}^{\theta_{\lambda/2}} C_n^* \tilde{\Phi}_n(r_e) \cos(n\phi) d\phi + \int_{\phi_{K+1}}^{\theta_{\lambda/2}} C_0^* \tilde{\Phi}_0(r_e) d\phi \right] \quad (3.111)$$

Finally using the known values of $\tilde{\Phi}_n(r_e)$ and $\tilde{\Phi}_0(r_e)$ we have.

$$\begin{aligned} Y_T = & j\omega 2Lr_e \sum_{q,2q,\dots} C_n^* \sin(n\phi_{K+1}) \frac{2}{n^3 \theta_{\lambda/2}} \left\{ \frac{\cos n\phi_1 - \cos n\phi_0}{\phi_1 - \phi_0} + \right. \\ & \left. \sum_{m=1}^K \frac{\nu_m}{V_D} \left[\frac{\cos n\phi_{m+1} - \cos n\phi_m}{\phi_{m+1} - \phi_m} - \frac{\cos n\phi_m - \cos n\phi_{m-1}}{\phi_m - \phi_{m-1}} \right] \right\} \\ & + j\omega \frac{L}{\theta_{\lambda/2}} C_0^*(\theta_{\lambda/2} - \phi_{K+1}) \left[\phi_0 + \phi_1 + \sum_{m=1}^K \frac{\nu_m}{V_D} (\phi_{m+1} - \phi_{m-1}) \right] \end{aligned} \quad (3.112)$$

The transcapacitance and transconductance are

$$C_T = \mathbf{Im}\{Y_T\}/\omega \quad (3.113)$$

$$G_T = \mathbf{Re}\{Y_T\} \quad (3.114)$$

3.4 Cylindrical z Periodic Sensors

In the case of z periodicity, Φ is independent of ϕ . Since $d^2Q(\phi)/d\phi^2 = 0$, we rewrite eq. 3.35 as

$$\frac{1}{rR(r)} \frac{d}{dr} \left(r \frac{dR(r)}{dr} \right) = -\frac{1}{Z(z)} \frac{d^2Z(z)}{dz^2} = k^2 \quad (3.115)$$

where k^2 is the separation constant. The solution of $Z(z)$ is periodic with fundamental periodicity λ . We write Z in terms of k_n

$$Z(z) = \begin{cases} F_n e^{jk_n z} + G_n e^{-jk_n z} & n > 0 \\ F_0 z + G_0 & n = 0 \end{cases} \quad k_n = \frac{2n\pi}{\lambda} \quad (3.116)$$

where n is an integer. Because Φ must be finite as $z \rightarrow \infty$, $F_0 = 0$. To solve for $R(r)$ in eq. 3.115 we multiply by $r^2 R(r)$, carry out the differentiation, and move all terms to the left hand side.

$$r^2 \frac{d^2 R}{dr^2} + r \frac{dR}{dr} - r^2 k_n^2 R = 0 \quad (3.117)$$

Using the substitution of $u_n = k_n r$, and the chain rule we have

$$u_n^2 \frac{d^2 R}{du_n^2} + u_n \frac{dR}{du_n} - u_n^2 R = 0. \quad (3.118)$$

For $n \neq 0$ we recognize this as the modified Bessel equation of order zero with solutions of the modified Bessel functions of the first and second kind of order zero [52].

$$R(r) = \begin{cases} A_n I_0(k_n r) + B_n K_0(k_n r) & n > 0 \\ A_0 + B_0 \ln r & n = 0 \end{cases} \quad k_n = \frac{2n\pi}{\lambda} \quad (3.119)$$

Absorbing the redundant constants we find the general solution for Φ to be

$$\Phi(r, z) = A_0 + B_0 \ln r + \sum_{n=1}^{\infty} [A_n I_0(k_n r) + B_n K_0(k_n r)] [F_n \cos k_n z + G_n \sin k_n z] \quad (3.120)$$

Setting the center of a drive electrode to $z = 0$ forces the potential to be an even function in z , eliminating the sine term.

$$\Phi(r, z) = A_0 + B_0 \ln r + \sum_{n=1}^{\infty} [A_n I_0(k_n r) + B_n K_0(k_n r)] \cos k_n z \quad (3.121)$$

We can rewrite this equation using a similar notation to eq. 3.45.

$$\Phi(r, z) = \tilde{\Phi}_0(r) + \sum_{n=q, 2q, \dots} \tilde{\Phi}_n(r) \cos k_n z \quad (3.122)$$

where

$$\tilde{\Phi}_0(r) = A_0 + B_0 \ln r \quad (3.123)$$

$$\tilde{\Phi}_n(r) = A_n I_0(k_n r) + B_n K_0(k_n r) \quad (3.124)$$

3.4.1 Surface Capacitance Density

The surface capacitance density is defined as

$$C_n^*(r) = \frac{\epsilon^*(r) \tilde{E}_{r,n}(r)}{\tilde{\Phi}_n(r)} \quad (3.125)$$

We now calculate the surface capacitance density equations for the intermediate and inner layers.

Intermediate Layer p , $n \neq 0$ Terms

We begin by considering the p th layer and calculate the n th Fourier potential coefficients at the boundaries.

$$\tilde{\Phi}_n(r_{p-1}) = A_n I_0(k_n r_{p-1}) + B_n K_0(k_n r_{p-1}) \quad (3.126)$$

$$\tilde{\Phi}_n(r_p) = A_n I_0(k_n r_p) + B_n K_0(k_n r_p) \quad (3.127)$$

Solving for A_n and B_n and substituting into eq. 3.124 we have an expression for $\tilde{\Phi}_n(r)$ in terms of the boundary values.

$$\tilde{\Phi}_n(r) = \left[\frac{\tilde{\Phi}_n(r_p) K_0(k_n r_{p-1}) - \tilde{\Phi}_n(r_{p-1}) K_0(k_n r_p)}{I_0(k_n r_{p-1}) K_0(k_n r_p) - I_0(k_n r_p) K_0(k_n r_{p-1})} \right] I_0(k_n r) + \left[\frac{\tilde{\Phi}_n(r_{p-1}) I_0(k_n r_p) - \tilde{\Phi}_n(r_p) I_0(k_n r_{p-1})}{I_0(k_n r_{p-1}) K_0(k_n r_p) - I_0(k_n r_p) K_0(k_n r_{p-1})} \right] K_0(k_n r) \quad (3.128)$$

By the definition of the surface capacitance density and eq. 3.51 we can find its value at the boundaries.

$$C_n^*(r_p) = \frac{\left[k_n \epsilon_p^* I_1(k_n r_p) \left(\tilde{\Phi}_n(r_p) K_0(k_n r_{p-1}) - \tilde{\Phi}_n(r_{p-1}) K_0(k_n r_p) \right) + k_n \epsilon_p^* K_1(k_n r_p) \left(\tilde{\Phi}_n(r_p) I_0(k_n r_{p-1}) - \tilde{\Phi}_n(r_{p-1}) I_0(k_n r_p) \right) \right]}{\left[K_0(k_n r_p) \left(\tilde{\Phi}_n(r_p) I_0(k_n r_{p-1}) - \tilde{\Phi}_n(r_{p-1}) I_0(k_n r_p) \right) + I_0(k_n r_p) \left(\tilde{\Phi}_n(r_{p-1}) K_0(k_n r_p) - \tilde{\Phi}_n(r_p) K_0(k_n r_{p-1}) \right) \right]} \quad (3.129)$$

$$C_n^*(r_{p-1}) = \frac{\left[k_n \epsilon_p^* I_1(k_n r_{p-1}) \left(\tilde{\Phi}_n(r_p) K_0(k_n r_{p-1}) - \tilde{\Phi}_n(r_{p-1}) K_0(k_n r_p) \right) + k_n \epsilon_p^* K_1(k_n r_{p-1}) \left(\tilde{\Phi}_n(r_p) I_0(k_n r_{p-1}) - \tilde{\Phi}_n(r_{p-1}) I_0(k_n r_p) \right) \right]}{\left[K_0(k_n r_{p-1}) \left(\tilde{\Phi}_n(r_p) I_0(k_n r_{p-1}) - \tilde{\Phi}_n(r_{p-1}) I_0(k_n r_p) \right) + I_0(k_n r_{p-1}) \left(\tilde{\Phi}_n(r_{p-1}) K_0(k_n r_p) - \tilde{\Phi}_n(r_p) K_0(k_n r_{p-1}) \right) \right]} \quad (3.130)$$

Because of the length of the expression the second term in both the numerator and denominator are wrapped. Using eqs. 3.129 and 3.130 we find $C_n^*(r_p)$ in terms of $C_n^*(r_{p-1})$.

$$C_n^*(r_p) = \frac{\left[k_n \epsilon_p^* I_1(k_n r_p) \left(C_n^*(r_{p-1}) K_0(k_n r_{p-1}) - k_n \epsilon_p^* K_1(k_n r_{p-1}) \right) + k_n \epsilon_p^* K_1(k_n r_p) \left(C_n^*(r_{p-1}) I_0(k_n r_{p-1}) + k_n \epsilon_p^* I_1(k_n r_{p-1}) \right) \right]}{\left[\left(C_n^*(r_{p-1}) I_0(k_n r_{p-1}) + k_n \epsilon_p^* I_1(k_n r_{p-1}) \right) K_0(k_n r_p) + I_0(k_n r_p) \left(k_n \epsilon_p^* K_1(k_n r_{p-1}) - C_n^*(r_{p-1}) K_0(k_n r_{p-1}) \right) \right]} \quad (3.131)$$

Intermediate Layer p , $n = 0$ Term

Comparing eq. 3.123 to eq. 3.46 we notice that $\tilde{\Phi}_0(r)$ is the same for both the z and ϕ periodic cases. The expression from eq. 3.67 for $C_0^*(r_p)$ is exactly the same in both cases. We repeat it here for convenience.

$$C_0^*(r_p) = \frac{\epsilon_p^*/r_p}{\epsilon_p^* [r_{p-1} C_0^*(r_{p-1})]^{-1} - \ln \frac{r_p}{r_{p-1}}} \quad (3.132)$$

Cylinder with a Grounded Center Conductor, $r_0 = 0$

Taking the limit as $\tilde{\Phi}_n(r_0) \rightarrow 0$ in eqs. 3.130 and 3.66 we find $|C_n^*(r_1)| \rightarrow \infty$ for $n > 0$. We can find $C_n^*(r_1)$ and $C_0^*(r_1)$ in this limit from eqs. 3.131 and 3.132.

$$C_n^*(r_1) = \frac{k_n \epsilon_1^* (I_1(k_n r_1) K_0(k_n r_0) + I_0(k_n r_0) K_1(k_n r_1))}{I_0(k_n r_0) K_0(k_n r_1) - I_0(k_n r_1) K_0(k_n r_0)} \quad (3.133)$$

$$C_0^*(r_1) = \frac{\epsilon_1^*}{r_1 \ln \frac{r_0}{r_1}} \quad (3.134)$$

Cylinder Without a Center Conductor

We know that $K_0(r)$ is infinite at zero, and therefore we require $B_n = 0$ in the $p = 1$ layer. We can solve for $\tilde{\Phi}_n(r)$ for $r < r_1$ in terms of $\tilde{\Phi}_n(r_1)$. We use eq. 3.125 to find the surface capacitance density in terms of known constants.

$$\tilde{\Phi}_n(r) = \tilde{\Phi}_n(r_1) \frac{I_0(k_n r)}{I_0(k_n r_1)}, \quad r \leq r_1 \quad (3.135)$$

$$\tilde{E}_{r,n}(r) = -\frac{k_n \tilde{\Phi}_n(r_1)}{I_0(k_n r_1)} I_1(k_n r), \quad r \leq r_1 \quad (3.136)$$

$$C_n^*(r_1) = -\frac{\epsilon_1^* k_n I_1(k_n r_1)}{I_0(k_n r_1)} \quad (3.137)$$

To find the $C_0^*(r_1)$ term we take the limit $r_0 \rightarrow 0$ in eq. 3.65. The natural logarithm approaches infinity while all other terms stay finite.

$$C_0^*(r_1) = 0 \quad (3.138)$$

By means of the eq 3.132 we find

$$C_0^*(r_p) = 0 \quad (3.139)$$

for all p in the absence of a grounded center conductor.

Surface Capacitance Density at Electrodes

Assuming that there is a ground plane at radius r_g we can determine $C_n^*(r_e^+)$ from eq. 3.130 and 3.66 by substituting r_e for r_{p-1} and r_g for r_p , and letting $\tilde{\Phi}_n(r_g) \rightarrow 0$ and $\tilde{\Phi}_0(r_g) \rightarrow 0$.

$$C_n^*(r_e^+) = \frac{k_n \epsilon_s^* (I_1(k_n r_e) K_0(k_n r_g) + I_0(k_n r_g) K_1(k_n r_e))}{I_0(k_n r_g) K_0(k_n r_e) - I_0(k_n r_e) K_0(k_n r_g)} \quad (3.140)$$

$$C_0^*(r_e^+) = \frac{\epsilon_s^*}{r_e \ln \frac{r_g}{r_e}} \quad (3.141)$$

3.4.2 Completing the Solution

At this point we can calculate $C_n^*(r)$ at all boundaries. The same method applied for the ϕ periodic geometry of assigning collocation points, applying boundary conditions, and solving for the transcapacitance is similarly done and detailed explicitly in Section 3.2.2 and Section 3.2.3 as well as in [50]. The only substitution needed is to exchange x with z .

3.5 Generalized Planar Periodic Sensors

In this section we generalize the result for the planar sensor to the case when the sensor has an arbitrary, but even symmetric half wavelength. One application for this geometry is to drive a small wavelength sensor at a larger effective wavelength, by forming groups of drive and sense electrodes. We require that there be an even symmetry to eliminate the sine term and simplify the derivation and numerical computation. The results found in this section are particularly powerful, and prompt the design of a new generation of dielectrometry sensors. We explore the consequences of these results and next generation sensors in Chapter 10.

We consider the planar case where the sensor is periodic in the x direction, infinite in the y , and periodic in the z . The solution to the potential is Laplace's equation which has the general form

$$\Phi(x, z) = (C_0 + D_0 z) + \sum_{n=1}^{\infty} (C_n e^{k_n z} + D_n e^{-k_n z}) \cos k_n x \quad (3.142)$$

in cartesian coordinates when even symmetry in x has been assumed. The derivation proceeds by finding the surface capacitance density, defining a set of collocation points, and finally finding the Fourier coefficients at the surface of the electrodes. The entire field solution can be found once the potential on this surface is known. The surface capacitance density is independent of electrode characteristics and is unchanged from the results in Section 3.2. The collocation points, however, need to be redefined since there are an arbitrary number of regions where collocation points are needed. We begin the derivation by defining the collocation points, and then find the Fourier coefficients at the electrode surface ($z = 0$). The solution matrix is defined and the admittance is found.

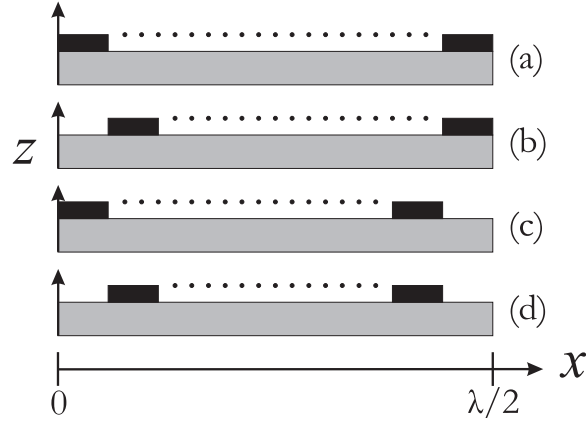


Figure 3-9: Summary of possible electrode configurations. Dots indicate a region of arbitrary electrode configuration. (a) edge electrodes touch $x = 0$ and $x = \lambda/2$ boundaries. (b) edge electrodes touch $x = \lambda/2$ boundary only. (c) edge electrodes touch $x = 0$ boundary only. (d) edge electrodes touch neither boundary.

3.5.1 Collocation Points

Numerous electrode combinations are possible but each falls into one of four categories as shown in Fig. 3-9. Depending on the configuration the sensor half wavelength may not fall on the center of the electrode so a region may exist before the first electrode as in cases (b) and (d). Also possible is a solution region beyond the last electrode as in cases (c) and (d).

Let there be Γ electrodes in the half wavelength. The x position of the beginning and end of the γ th electrode is $\alpha_{\gamma,1}$ and $\alpha_{\gamma,2}$ respectively. The electrode voltage is V_γ . The number of collocation points between the γ and $\gamma + 1$ electrode is $K_\gamma + 2$. If the first electrode does not begin at $x = 0$ then there are $K_0 + 2$ collocation points between from $x = 0$ to $\alpha_{\gamma,1}$. If the last electrode does not end at the half wavelength ($\alpha_{\Gamma,2} \neq \lambda/2$), then there are $K_\Gamma + 2$ collocation points between from $x = \alpha_{\Gamma,2}$ to $\lambda/2$. Note that throughout Section 3.5 K_γ is simply an integer and has no relation to the modified Bessel functions of the second kind which were used in Section 3.4.

Let $x_{\gamma,m}$ be the m th collocation point in the γ th region. The first and last collocation points in each gap are defined $x_{\gamma,0} = \alpha_{\gamma,2}$ and $x_{\gamma,K_\gamma+1} = \alpha_{\gamma+1,1}$. The exact definition of the location of the collocation points is not critical to the derivation, but a cosinusoidal distribution is typically chosen.

$$x_{\gamma,m} = \alpha_{\gamma,2} + \frac{\alpha_{\gamma+1,1} - \alpha_{\gamma,2}}{2} \left(1 - \cos \left(\frac{m\pi}{K_\gamma + 1} \right) \right) \quad \text{for } 0 \leq m \leq K_\gamma + 1 \quad (3.143)$$

The voltage at the $x_{\gamma,m}$ collocation point is defined as $\nu_{\gamma,m}$. Obviously $\nu_{\gamma,0} = V_\gamma$ and $\nu_{\gamma,K_\gamma+1} = V_{\gamma+1}$, which leaves K_γ unknown voltages in the gap to be solved for.

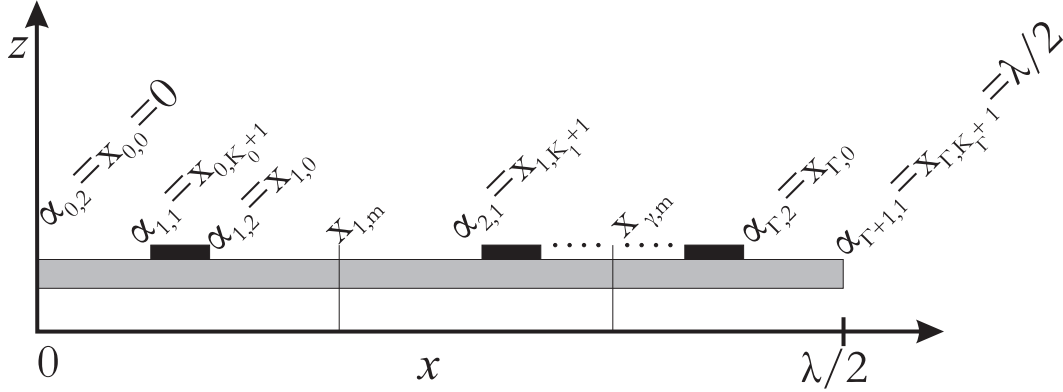


Figure 3-10: Labeling of selected collocation points. The figure shows key collocation points at the beginning and end of electrodes, half wavelength boundaries, and intermediate points in the electrode gaps. Dots indicate an arbitrary electrode layout.

In each gap K_γ integration intervals are defined each enclosing one collocation point. The end points of the intervals are defined as

$$x'_{\gamma,\ell} = \begin{cases} 0 & \ell = 0, \gamma = 0 \\ x_{\gamma,0} = \alpha_{\gamma,2} & \ell = 0, \gamma > 0 \\ (x_{\gamma,\ell+1} + x_{\gamma,\ell})/2 & \ell = 1, 2, \dots, K_\gamma - 1 \\ x_{\gamma,K_\gamma+1} = \alpha_{\gamma+1,1} & \ell = K_\gamma, \gamma < \Gamma \\ \lambda/2 & \ell = K_\gamma, \gamma = \Gamma \end{cases} \quad (3.144)$$

A piecewise linear representation of the voltage between collocation points allows us to define the voltage everywhere on the surface of the electrodes. The interpolated voltage is

$$\Phi(x) = \frac{\nu_{\gamma,m}(x_{\gamma,m+1} - x) + \nu_{\gamma,m+1}(x - x_{\gamma,m})}{x_{\gamma,m+1} - x_{\gamma,m}} \quad \text{for } x_{\gamma,m} < x < x_{\gamma,m+1} \quad (3.145)$$

These details are summarized in Fig. 3-10. Table 3.1 summarizes the defined variables.

3.5.2 Surface Capacitance Density

The surface capacitance density is independent of the electrode configuration and is the same found in Section 3.2.1. The expressions allow us to find the surface capacitance density at the surface of the electrodes. We modify the notation slightly for clarity. The surface capacitance density describes

Table 3.1: Summary of Generalized Planar Periodic Sensor Variables

Quantity	Description
$\bar{\alpha} = \begin{bmatrix} \alpha_{1,1} & \alpha_{1,2} \\ \vdots & \vdots \\ \alpha_{\Gamma,1} & \alpha_{\Gamma,2} \end{bmatrix}$	Beginning and end points of electrodes. Define $\alpha_{0,2} = 0$, and $\alpha_{\Gamma+1,1} = \lambda/2$.
$\bar{K} = [K_0 \ K_1 \ \dots \ K_\Gamma]$	Number of collocation points between the γ th and $(\gamma + 1)$ th electrode. Define $x_{\gamma,0} = \alpha_{\gamma,2}$ and $x_{\gamma,K_\gamma+1} = \alpha_{\gamma+1,1}$. No relation to modified Bessel functions of the 2nd kind.
$\bar{V} = [V_1 \ \dots \ V_\Gamma]$	Voltage of the γ th electrode.
$x_{\gamma,m}$	m th collocation point past γ th electrode.
$\nu_{\gamma,m}$	Voltage at $x_{\gamma,m}$ collocation point.
$x'_{\gamma,\ell}$	Integration interval limits defined by eq. 3.144.

all the material properties of the materials under test. It is defined as

$$C_n^*(z) = \frac{\epsilon^*(z)\tilde{E}_{z,n}(z)}{\tilde{\Phi}_n(z)} \quad (3.146)$$

Let there be P layers with the interface between layers p and $p + 1$ at z_p . Let $z_0 = 0$ designate the surface of the electrodes, z_1 the surface between the 1st and 2nd layer, etc. We first consider the terms where $n \neq 0$. Without a top ground plane the potential must be finite at infinity. The potential in the semi-infinite layer with interface at z_{P-1} is

$$\tilde{\Phi}_n(z) = \tilde{\Phi}_n(z_{P-1})e^{-k_n(z-z_{P-1})} \quad \text{for } z_{P-1} \leq z < \infty \quad (3.147)$$

Since $\tilde{E}_{z,n}(z) = -d\tilde{\Phi}_n(z)/dz$ we find

$$C_n^*(z_{P-1}) = k_n\epsilon_P^* \quad (3.148)$$

We now seek an equation to relate the surface capacitance density at the p th boundary to the $p+1$ th boundary. This is found to be

$$C_n^*(z_p) = k_n\epsilon_{p+1}^* \frac{C_n^*(z_{p+1}) \coth(k_n(z_{p+1} - z_p)) + k_n\epsilon_{p+1}^*}{C_n^*(z_{p+1}) + k_n\epsilon_{p+1}^* \coth(k_n(z_{p+1} - z_p))} \quad (3.149)$$

With $C_n^*(z_{P-1})$ known, we apply eq. 3.149 repeatedly until the surface of the electrodes is reached revealing $C_n^*(0)$.

In the case of $n = 0$ the relationship between the surface capacitance density at z_{p+1} and z_p is

$$C_0^*(z_p) = \frac{\epsilon_{p+1}^* C_0^*(z_{p+1})}{(z_{p+1} - z_p) C_0^*(z_{p+1}) + \epsilon_{p+1}^*} \quad (3.150)$$

If no top ground plane is present $(z_P - z_{P-1}) \rightarrow \infty$ implies

$$C_0^*(0) = 0 \quad (3.151)$$

If a ground plane is present the potential is zero at its surface ($z = z_P$), and the normal electric field is finite. At the surface of the top ground plane $C_n^*(z_P) \rightarrow \infty$. From eq. 3.149 and eq. 3.150 the surface capacitance density at z_{P-1} is determined.

$$C_n^*(z_{P-1}) = k_n \epsilon_P^* \coth(k_n(z_P - z_{P-1})) \quad (3.152)$$

$$C_0^*(z_{P-1}) = \frac{\epsilon_P^*}{(z_P - z_{P-1})} \quad (3.153)$$

We have assumed that the material under test consists of a number of homogeneous layers, each with isotropic properties ϵ_p^* . Because the field at the far boundary is known, we have been able to find $C_n^*(z)$ at the material interfaces without full knowledge of the field. It would be ideal to be able to write $C_n^*(z = 0)$ in terms of a continuous effective permittivity function, $\epsilon^*(z)$ and a boundary condition at z_P . A solution in this form has not yet presented itself and may not be possible. We can approximate $\epsilon^*(z)$ by discretizing the MUT into an arbitrary number of layers.

3.5.3 Fourier Coefficients

With the collocation points and surface voltage defined we now find the Fourier coefficients for the voltage at the surface of the electrodes. The Fourier coefficients are defined as

$$\tilde{\Phi}_n(z) = \frac{4}{\lambda} \int_0^{\lambda/2} \Phi(x, z) \cos k_n x dx \quad (3.154)$$

$$\tilde{\Phi}_0(z) = \frac{2}{\lambda} \int_0^{\lambda/2} \Phi(x, z) dx \quad (3.155)$$

For simplicity we let $\tilde{\Phi}_n = \tilde{\Phi}_n(z = 0)$. We now write an expression for the Fourier coefficients in terms of the voltages, $\nu_{\gamma,m}$.

$$\tilde{\Phi}_n = \frac{4}{\lambda} \left\{ \sum_{\gamma=1}^{\Gamma} \int_{\alpha_{\gamma,1}}^{\alpha_{\gamma,2}} V_{\gamma} \cos k_n x dx + \sum_{\gamma=0}^{\Gamma} \sum_{m=0}^{K_{\gamma}} \int_{x_{\gamma,m}}^{x_{\gamma,m+1}} \frac{\nu_{\gamma,m}(x_{\gamma,m+1} - x) + \nu_{\gamma,m+1}(x - x_{\gamma,m})}{x_{\gamma,m+1} - x_{\gamma,m}} \cos k_n x dx \right\} \quad (3.156)$$

When either or both half wavelength boundaries are touched by an electrode (at $x = 0, \lambda/2$), K_0 or K_{Γ} are defined as 0. The integration limits are the same in these cases and the second term is eliminated in this region. Taking the integral we have

$$\tilde{\Phi}_n = -\frac{4}{\lambda k_n^2} \sum_{\gamma=0}^{\Gamma} \sum_{m=1}^{K_{\gamma}} \nu_{\gamma,m} \left[\frac{\cos k_n x_{\gamma,m+1} - \cos k_n x_{\gamma,m}}{x_{\gamma,m+1} - x_{\gamma,m}} - \frac{\cos k_n x_{\gamma,m} - \cos k_n x_{\gamma,m-1}}{x_{\gamma,m} - x_{\gamma,m-1}} \right] + V_{\gamma} \frac{\cos k_n x_{\gamma,1} - \cos k_n \alpha_{\gamma,2}}{x_{\gamma,1} - \alpha_{\gamma,2}} - V_{\gamma+1} \frac{\cos k_n \alpha_{\gamma+1,1} - \cos k_n x_{\gamma,K_{\gamma}}}{\alpha_{\gamma+1,1} - x_{\gamma,K_{\gamma}}} \quad (3.157)$$

We would like to write this in a form such that all the V_{γ} 's are known by the electrode voltages. When the first and last electrode do not start at $x = 0$ and $x = \lambda/2$ respectively, V_0 and $V_{\gamma+1}$ are unknown.

$$\tilde{\Phi}_n = -\frac{4}{\lambda k_n^2} \left\{ \sum_{\gamma=0}^{\Gamma} \sum_{m=1}^{K_{\gamma}} \nu_{\gamma,m} \left[\frac{\cos k_n x_{\gamma,m+1} - \cos k_n x_{\gamma,m}}{x_{\gamma,m+1} - x_{\gamma,m}} - \frac{\cos k_n x_{\gamma,m} - \cos k_n x_{\gamma,m-1}}{x_{\gamma,m} - x_{\gamma,m-1}} \right] + \sum_{\gamma=1}^{\Gamma} V_{\gamma} \left[\frac{\cos k_n x_{\gamma,1} - \cos k_n \alpha_{\gamma,2}}{x_{\gamma,1} - \alpha_{\gamma,2}} - \frac{\cos k_n \alpha_{\gamma,1} - \cos k_n x_{\gamma-1,K_{\gamma-1}}}{\alpha_{\gamma,1} - x_{\gamma-1,K_{\gamma-1}}} \right] + \nu_{0,0} \frac{\cos k_n x_{0,1} - 1}{x_{0,1}} - \nu_{\Gamma,K_{\Gamma}+1} \frac{(-1)^n - \cos k_n x_{\Gamma,K_{\Gamma}}}{\lambda/2 - x_{\Gamma,K_{\Gamma}}} \right\} \quad (3.158)$$

We now notice that both of the last two terms approach zero for a reasonable choice of collocation points. We drop these terms, which eliminates two unknowns from this equation.

$$\begin{aligned} \tilde{\Phi}_n = & -\frac{4}{\lambda k_n^2} \left\{ \sum_{\gamma=0}^{\Gamma} \sum_{m=1}^{K_\gamma} \nu_{\gamma,m} \left[\frac{\cos k_n x_{\gamma,m+1} - \cos k_n x_{\gamma,m}}{x_{\gamma,m+1} - x_{\gamma,m}} - \right. \right. \\ & \left. \left. \frac{\cos k_n x_{\gamma,m} - \cos k_n x_{\gamma,m-1}}{x_{\gamma,m} - x_{\gamma,m-1}} \right] + \right. \\ & \left. \sum_{\gamma=1}^{\Gamma} V_\gamma \left[\frac{\cos k_n x_{\gamma,1} - \cos k_n \alpha_{\gamma,2}}{x_{\gamma,1} - \alpha_{\gamma,2}} - \frac{\cos k_n \alpha_{\gamma,1} - \cos k_n x_{\gamma-1,K_{\gamma-1}}}{\alpha_{\gamma,1} - x_{\gamma-1,K_{\gamma-1}}} \right] \right\} \end{aligned} \quad (3.159)$$

The $n = 0$ terms are found.

$$\begin{aligned} \tilde{\Phi}_0 = & \frac{1}{\lambda} \sum_{\gamma=1}^{\Gamma} V_\gamma [\alpha_{\gamma,2} - \alpha_{\gamma,1} + x_{\gamma,1} - x_{\gamma-1,K_{\gamma-1}}] + \\ & \frac{1}{\lambda} \left[\nu_{0,0} x_{0,1} + \nu_{\Gamma,K_{\Gamma+1}} \left(\frac{\lambda}{2} - x_{\Gamma,K_\Gamma} \right) \right] + \\ & \frac{1}{\lambda} \sum_{\gamma=0}^{\Gamma} \sum_{m=1}^{K_\gamma} \nu_{\gamma,m} (x_{\gamma,m+1} - x_{\gamma,m-1}) \end{aligned} \quad (3.160)$$

We are again able to drop the $\nu_{0,0}$ and $\nu_{\Gamma,K_{\Gamma+1}}$ terms eliminating two unknowns and reducing the equation to

$$\begin{aligned} \tilde{\Phi}_0 = & \frac{1}{\lambda} \left\{ \sum_{\gamma=1}^{\Gamma} V_\gamma [\alpha_{\gamma,2} - \alpha_{\gamma,1} + x_{\gamma,1} - x_{\gamma-1,K_{\gamma-1}}] + \right. \\ & \left. \sum_{\gamma=0}^{\Gamma} \sum_{m=1}^{K_\gamma} \nu_{\gamma,m} (x_{\gamma,m+1} - x_{\gamma,m-1}) \right\} \end{aligned} \quad (3.161)$$

3.5.4 Boundary Conditions

We require that the effective surface charge density, $\sigma_S^*(x)$, defined as the discontinuity in the normal component of $\epsilon^* \bar{E}$ at $z = 0$, be zero in all gaps between the electrodes (see eq. 3.20). To enforce this condition we require

$$\int_{x'_{\gamma,\ell}}^{x'_{\gamma,\ell+1}} \sigma_S^*(x) dx = 0 \quad (3.162)$$

The effective surface charge density can be written as a Fourier series where each Fourier coefficient is multiplied by the corresponding surface capacitance density term. It follows from the definition

that

$$\int_{x'_{\gamma,\ell}}^{x'_{\gamma,\ell+1}} \sigma_S^*(x) dx = \sum_{n=1}^{\infty} \int_{x'_{\gamma,\ell}}^{x'_{\gamma,\ell+1}} C_n^* \tilde{\Phi}_n \cos k_n x dx + \int_{x'_{\gamma,\ell}}^{x'_{\gamma,\ell+1}} C_0^* \tilde{\Phi}_0 dx \quad (3.163)$$

$$= \sum_{n=1}^{\infty} C_n^* \tilde{\Phi}_n \frac{1}{k_n} [\sin k_n x'_{\gamma,\ell+1} - \sin k_n x'_{\gamma,\ell}] + C_0^* \tilde{\Phi}_0 (x'_{\gamma,\ell+1} - x'_{\gamma,\ell}) \quad (3.164)$$

$$= \sum_{n=0}^{\infty} C_n^* \sum_{\gamma=0}^{\Gamma} \sum_{m=1}^{K_\gamma} M_{(\gamma,\ell),(\gamma,m)}^n \nu_{\gamma,m} - \sum_{n=0}^{\infty} C_n^* b_{(\gamma,\ell)}^n = 0 \quad (3.165)$$

The last line is arrived at by substituting in eqs. 3.159 and 3.161 into eq. 3.164 and grouping terms that are and are not coefficients of $\nu_{\gamma,m}$. The n superscript is part of the naming convention and is not an exponent. We can now write a matrix equation of the form

$$\mathbf{M}\mathbf{v} = \mathbf{b} \quad (3.166)$$

In this equation \mathbf{v} represents the unknown collocation point voltages. Because we have eliminated the voltages $\nu_{0,0}$ and $\nu_{\Gamma,K_{\Gamma+1}}$ from the equations there are H unknown voltages to solve for which is exactly the number of available equations.

$$H = \sum_{\gamma=0}^{\Gamma} K_\gamma \quad (3.167)$$

The matrix \mathbf{M} is defined

$$\mathbf{M} = \sum_{n=0}^{\infty} C_n^* \mathbf{M}^n \quad (3.168)$$

The elements of \mathbf{M}^n are $M_{(\gamma,\ell),(\gamma,m)}^n = M_{R,Q}^n$ where R and Q are defined

$$R = \begin{cases} \ell + \sum_{\beta=0}^{\gamma-1} K_\beta & \gamma > 0 \\ \ell & \gamma = 0 \end{cases} \quad (3.169)$$

$$Q = \begin{cases} m + \sum_{\beta=0}^{\gamma-1} K_\beta & \gamma > 0 \\ m & \gamma = 0 \end{cases} \quad (3.170)$$

In each gap $0 \leq \ell \leq K_\gamma - 1$, and $1 \leq m \leq K_\gamma$. Similarly the matrix \mathbf{b} is defined

$$\mathbf{b} = \sum_{n=0}^{\infty} C_n^* \mathbf{b}^n \quad (3.171)$$

The elements of \mathbf{b}^n are $b_{(\gamma,\ell)}^n = b_R^n$, where R has been defined in eq. 3.169.

We are now able to substitute the expressions for $\tilde{\Phi}_n$ and find $M_{(\gamma,\ell),(\gamma,m)}^n$ and $b_{(\gamma,\ell)}^n$. For $n \neq 0$

$$M_{(\gamma,\ell),(\gamma,m)}^n = -\frac{4}{\lambda k_n^3} (\sin k_n x'_{\gamma,\ell+1} - \sin k_n x'_{\gamma,\ell}) \times \left(\frac{\cos k_n x_{\gamma,m+1} - \cos k_n x_{\gamma,m}}{x_{\gamma,m+1} - x_{\gamma,m}} - \frac{\cos k_n x_{\gamma,m} - \cos k_n x_{\gamma,m-1}}{x_{\gamma,m} - x_{\gamma,m-1}} \right) \quad (3.172)$$

$$b_{(\gamma,\ell)}^n = \frac{4}{\lambda k_n^3} (\sin k_n x'_{\gamma,\ell+1} - \sin k_n x'_{\gamma,\ell}) \times \sum_{\xi=1}^{\Gamma} V_{\xi} \left(\frac{\cos k_n x_{\xi,1} - \cos k_n \alpha_{\xi,2}}{x_{\xi,1} - \alpha_{\xi,2}} - \frac{\cos k_n \alpha_{\xi,1} - \cos k_n x_{\xi-1,K_{\xi-1}}}{\alpha_{\xi,1} - x_{\xi-1,K_{\xi-1}}} \right) \quad (3.173)$$

For $n = 0$

$$M_{(\gamma,\ell),(\gamma,m)}^0 = \frac{1}{\lambda} (x'_{\gamma,\ell+1} - x'_{\gamma,\ell}) (x_{\gamma,m+1} - x_{\gamma,m-1}) \quad (3.174)$$

$$b_{(\gamma,\ell)}^0 = -(x'_{\gamma,\ell+1} - x'_{\gamma,\ell}) \sum_{\xi=1}^{\Gamma} \frac{V_{\xi}}{\lambda} [\alpha_{\xi,2} - \alpha_{\xi,1} + x_{\xi,1} - x_{\xi-1,K_{\xi-1}}] \quad (3.175)$$

Solving the matrix equations results in full knowledge of the potential at the surface of the electrodes. The potential and electric field can then be determined in all space.

3.5.5 Admittance Matrix

The admittance between a set of drive electrodes and sense electrodes offers valuable insight into the properties of the material above the electrode surface. In the applications considered here, three groups of electrodes are formed: drive, sense, and guard. The drive electrodes are all given the drive signal V_D . The sense electrodes are held at ground potential, and the sense electrode current I_S is measured. The guard electrodes are connected to ground. The ratio I_S/V_D gives the admittance Y . In order to have a meaningful admittance the drive electrodes must all be excited at the same voltage.

Let $\bar{\gamma}_S$ be the vector of sense electrode indexes. The current through the sense electrodes is

$$I_S = -2L \sum_{\xi=\bar{\gamma}_S} \int_{\alpha_{\xi,1}}^{\alpha_{\xi,2}} \|J_z(x)\| dx \quad (3.176)$$

We have used $\xi = \bar{\gamma}_S$ to indicate that the summation is over all the components of the vector. The double bars indicate that this is the jump in the normal component of the total current density, $J_z(x)$. The meander length, L , is defined as the “total number of wavelengths times the length of a single electrode.” The factor of two is introduced here to account for the fact that only a half wavelength is simulated. If a single electrode is to be sampled, the factor of two should be

removed *unless* the electrode is at the half wavelength boundary; that is if $\alpha_{\xi,1} = \alpha_{1,1} = 0$, or $\alpha_{\xi,2} = \alpha_{\Gamma,2} = \lambda/2$. Using the relation

$$i\omega\sigma_S^*(x) = \|J_z(x)\| \quad (3.177)$$

and eq. 3.22 we find

$$I_S = -2j\omega L \sum_{\xi=\bar{\gamma}_S} \left[\int_{\alpha_{\xi,1}}^{\alpha_{\xi,2}} C_0^* \tilde{\Phi}_0 dx + \sum_{n=0}^{\infty} \int_{\alpha_{\xi,1}}^{\alpha_{\xi,2}} C_n^* \tilde{\Phi}_n \cos k_n x dx \right] \quad (3.178)$$

Carrying out the integration and dividing by V_D we have

$$Y = -\frac{j2\omega L}{V_D} \sum_{\xi=\bar{\gamma}_S} \left[C_0^* \tilde{\Phi}_0 (\alpha_{\xi,2} - \alpha_{\xi,1}) + \sum_{n=0}^{\infty} \frac{C_n^* \tilde{\Phi}_n}{k_n} (\sin k_n \alpha_{\xi,2} - \sin k_n \alpha_{\xi,1}) \right] \quad (3.179)$$

3.5.6 Lossy Media and Time Harmonic Sources

This derivation is valid for the electroquasistatic problem with lossy media (finite conductivity), and time harmonic sources with an $e^{j\omega t}$ time dependence. The surface capacitance density terms will become complex because the effective permittivities, which they depend on will be complex. We can also drive electrodes with arbitrary phase angles by making the components of \bar{V} complex. Possible benefits of a sophisticated excitation scheme are not immediately obvious.

3.6 Planar Dual Periodic Sensors

In this section we present the developments of a solution for a planar sensor that is periodic in two directions. The basic sensor topology is shown in Fig. 3-11. The sensor is intended to provide sensitivity to changes in effective permittivity in the x and y directions which may have different wavelengths, λ_x and λ_y , respectively. In the figure λ_x is drawn longer than λ_y . Assuming the sensor is infinitely periodic allows us to use Fourier theory in finding an analytical solution. The solution space can be reduced first to a single unit cell which is shown in the box in Fig. 3-11. By tiling the unit cell the entire sensor can be built.

Finding the transcapacitance between the drive and sense electrodes requires knowledge of the voltage at the surface of the electrodes. The voltage on the electrodes themselves are known with the drive at voltage V_D and the sense at zero volts. The voltage elsewhere in each unit cell will be the same, and further the unit cell has a voltage profile that is flip symmetric about the diagonal connecting opposite electrodes of the same type. The region of unique voltages is confined to the

pattern region in the figure.

The task at hand is to provide a solution to the voltage at the surface of the electrodes. The assumptions of a multilayered MUT and substrate with grounded backplane are used here as in previous derivations.

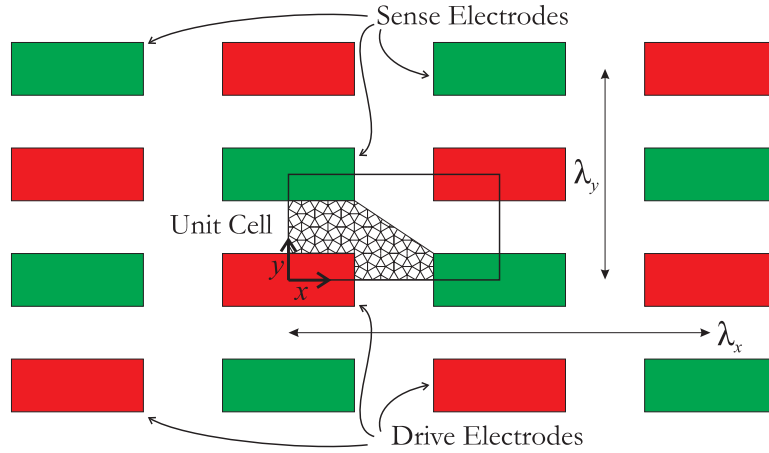


Figure 3-11: Planar dual periodic sensor topology. Sensor features different wavelengths in x and y directions. The design is a repetition of the boxed unit cell. The smallest unique region of unknown voltages is the patterned region.

3.6.1 General Solution to Laplace Equation

We begin by asserting that the solution to the fields is Laplace's equation and we assume a separable form of the solution.

$$\nabla^2 V = 0 \quad (3.180)$$

$$V = X(x)Y(y)Z(z) \quad (3.181)$$

$$\nabla^2 V = \frac{\partial^2 V}{\partial x^2} + \frac{\partial^2 V}{\partial y^2} + \frac{\partial^2 V}{\partial z^2} \quad (3.182)$$

Plugging in the separable form we have

$$\frac{1}{X(x)} \frac{d^2 X(x)}{dx^2} + \frac{1}{Y(y)} \frac{d^2 Y(y)}{dy^2} + \frac{1}{Z(z)} \frac{d^2 Z(z)}{dz^2} = 0 \quad (3.183)$$

Introducing the separation constant k^2 we can find the solution for $Z(z)$.

$$\frac{1}{Z(z)} \frac{d^2 Z(z)}{dz^2} = k^2 \quad (3.184)$$

$$\frac{1}{X(x)} \frac{d^2 X(x)}{dx^2} + \frac{1}{Y(y)} \frac{d^2 Y(y)}{dy^2} = -k^2 \quad (3.185)$$

$$Z(z) = \begin{cases} Ae^{+kz} + Be^{-kz} & k \neq 0 \\ A_0 z + B_0 & k = 0 \end{cases} \quad (3.186)$$

A second separation constant is introduced to assist in solving for $X(x)$ and $Y(y)$.

$$\frac{1}{X(x)} \frac{d^2 X(x)}{dx^2} + \frac{1}{Y(y)} \frac{d^2 Y(y)}{dy^2} + k^2 = 0 \quad (3.187)$$

$$\frac{1}{X(x)} \frac{d^2 X(x)}{dx^2} = -k_x^2 \quad (3.188)$$

$$\frac{1}{Y(y)} \frac{d^2 Y(y)}{dy^2} + k^2 - k_x^2 = 0 \quad (3.189)$$

For convenience a third separation constant is introduced that is dependent on the other two.

$$k_y^2 = k^2 - k_x^2 \quad (3.190)$$

The $k_{x,y} \neq 0$ solutions to $X(x)$ and $Y(y)$ are sines and cosines. It is convenient to assume that the origin is centered on a drive electrode such that the solution is even in both x and z . This eliminates the sine terms completely.

$$X(x) = \begin{cases} A \cos k_x x & k \neq 0 \\ A_0 x + B_0 & k = 0 \end{cases} \quad (3.191)$$

$$Y(y) = \begin{cases} A \cos k_y y & k \neq 0 \\ A_0 y + B_0 & k = 0 \end{cases} \quad (3.192)$$

We require that $V(x + \lambda_x, y, z) = V(x, y, z)$ and $V(x, y + \lambda_y, z) = V(x, y, z)$. This can be achieved only if

$$k_{x,n} = \frac{2\pi n}{\lambda_x} \quad (3.193)$$

$$k_{y,m} = \frac{2\pi m}{\lambda_y} \quad (3.194)$$

$$k_{n,m}^2 = k_{x,n}^2 + k_{y,m}^2 \quad (3.195)$$

where n and m are integers. We have renamed the separation constants to include the integers they depend on. The potential can not grow uninhibited, and therefore the linear terms for $k_x, k_z = 0$ are zero ($A_0 = 0$ for $X(x)$ and $Y(y)$). If $k = 0$ then $k_x = k_y = 0$ which implies $n = m = 0$.

Total solution for V has 4 terms to be added forming the total solution.

$$\text{Term 1} \rightarrow A_0 z + B_0 \quad n = m = 0 \quad (3.196)$$

$$\text{Term 2} \rightarrow \sum_{n=1}^{\infty} \sum_{m=1}^{\infty} (A_{n,m} e^{k_{n,m} z} + B_{n,m} e^{-k_{n,m} z}) \cos k_{x,n} x \cos k_{y,m} y \quad n, m \neq 0 \quad (3.197)$$

$$\text{Term 3} \rightarrow \sum_{n=1}^{\infty} (A_{n,0} e^{k_{n,0} z} + B_{n,0} e^{-k_{n,0} z}) \cos k_{x,n} x \quad n \neq 0, m = 0 \quad (3.198)$$

$$\text{Term 4} \rightarrow \sum_{m=1}^{\infty} (A_{0,m} e^{k_{0,m} z} + B_{0,m} e^{-k_{0,m} z}) \cos k_{y,m} y \quad n = 0, m \neq 0 \quad (3.199)$$

This can be written more concisely by absorbing terms 3 and 4 into term 2 and absorbing B_0 from term 1 into the summation by adjusting the indexes. When $n = m = 0$ the summation is simply $A_{0,0} + B_{0,0}$. Taking $B_{0,0} = 0$ maintains generality.

$$V(x, y, z) = A_0 z + \sum_{n=0}^{\infty} \sum_{m=0}^{\infty} (A_{n,m} e^{k_{n,m} z} + B_{n,m} e^{-k_{n,m} z}) \cos k_{x,n} x \cos k_{y,m} y \quad (3.200)$$

3.6.2 Fourier Transform in Two Dimensions

We now digress to generalize the Fourier series into two dimensions [53]. Consider the function $f(\bar{r})$ where \bar{r} is a vector in two dimensions (x and y). We require

$$f(\bar{r} + \bar{R}) = f(\bar{r}) \quad (3.201)$$

where $\bar{R} = \hat{x} m_1 \lambda_x + \hat{y} m_2 \lambda_y$. m_1 and m_2 take all integer values. We can write such a function as

$$f(\bar{r}) = \sum_{n=-\infty}^{\infty} \sum_{m=-\infty}^{\infty} C_{n,m} e^{i \bar{k}_{n,m} \cdot \bar{r}} \quad (3.202)$$

which is called the Fourier series expansion. Here we have taken

$$\bar{k}_{n,m} = \hat{x} k_{k,n} + \hat{y} k_{y,m} = \hat{x} \frac{2\pi n}{\lambda_x} + \hat{y} \frac{2\pi m}{\lambda_y} \quad (3.203)$$

We wish to solve for the coefficients $C_{n,m}$ in the special case where $f(\bar{r})$ has even periodicity in both x and y . This implies that $C_{n,m} = C_{-n,-m} = C_{-n,m} = C_{n,-m}$. We can now write

$$f(\bar{r}) = \sum_{n=-\infty}^{\infty} \sum_{m=-\infty}^{\infty} C_{n,m} e^{i\bar{k}_{n,m} \cdot \bar{r}} \quad (3.204)$$

$$= \sum_{n=0}^{\infty} \sum_{m=0}^{\infty} C_{n,m} \left(e^{i(k_{x,n}x + k_{y,m}y)} + e^{-i(k_{x,n}x + k_{y,m}y)} + e^{i(k_{x,n}x - k_{y,m}y)} + e^{-i(k_{x,n}x - k_{y,m}y)} \right) \quad (3.205)$$

$$= \sum_{n=0}^{\infty} \sum_{m=0}^{\infty} 2C_{n,m} [\cos(k_{x,n}x + k_{y,m}y) + \cos(k_{x,n}x - k_{y,m}y)] \quad (3.206)$$

$$= \sum_{n=0}^{\infty} \sum_{m=0}^{\infty} 4C_{n,m} \cos k_{x,n}x \cos k_{y,m}y \quad (3.207)$$

The solution to $C_{n,m}$ can be shown to be [53]

$$C_{n,m} = \frac{1}{\lambda_x \lambda_y} \int_{-\frac{\lambda_y}{2}}^{\frac{\lambda_y}{2}} \int_{-\frac{\lambda_x}{2}}^{\frac{\lambda_x}{2}} f(\bar{r}) e^{-i\bar{k}_{n,m} \cdot \bar{r}} dx dy \quad (3.208)$$

$$= \frac{4}{\lambda_x \lambda_y} \int_0^{\frac{\lambda_y}{2}} \int_0^{\frac{\lambda_x}{2}} f(\bar{r}) e^{-i\bar{k}_{n,m} \cdot \bar{r}} dx dy \quad (3.209)$$

In the second equation we have applied the symmetry condition. Adding the solutions to $C_{n,m}$, $C_{-n,-m}$, $C_{-n,m}$, and $C_{n,-m}$ we have

$$C_{n,m} = \frac{1}{\lambda_x \lambda_y} \int_0^{\frac{\lambda_y}{2}} \int_0^{\frac{\lambda_x}{2}} f(\bar{r}) \left(e^{i(k_{x,n}x + k_{y,m}y)} + e^{-i(k_{x,n}x + k_{y,m}y)} + e^{i(k_{x,n}x - k_{y,m}y)} + e^{-i(k_{x,n}x - k_{y,m}y)} \right) dx dy \quad (3.210)$$

$$= \frac{4}{\lambda_x \lambda_y} \int_0^{\frac{\lambda_y}{2}} \int_0^{\frac{\lambda_x}{2}} f(\bar{r}) \cos(k_{x,n}x) \cos(k_{y,m}y) dx dy \quad n, m > 0 \quad (3.211)$$

We must treat the terms with zero separately since using the above equation results in double counting the zero terms.

$$C_{0,0} = \frac{4}{\lambda_x \lambda_y} \int_0^{\frac{\lambda_y}{2}} \int_0^{\frac{\lambda_x}{2}} f(\bar{r}) dx dy \quad (3.212)$$

$$2C_{n,0} = \frac{8}{\lambda_x \lambda_y} \int_0^{\frac{\lambda_y}{2}} \int_0^{\frac{\lambda_x}{2}} f(\bar{r}) \cos k_{x,n}x dx dy \quad (3.213)$$

$$2C_{0,m} = \frac{8}{\lambda_x \lambda_y} \int_0^{\frac{\lambda_y}{2}} \int_0^{\frac{\lambda_x}{2}} f(\bar{r}) \cos k_{y,m}y dx dy \quad (3.214)$$

We now rewrite the solution to $V(x, y, z)$ as

$$V(x, y, z) = A_0 z + \sum_{n=0}^{\infty} \sum_{m=0}^{\infty} \Phi_{n,m}(z) \cos k_{x,n} x \cos k_{y,m} y \quad (3.215)$$

We recognize $\Phi_{n,m}(z)$ as the Fourier coefficients which we now have the solution for.

$$\Phi_{n,m}(z) = \frac{16}{\lambda_x \lambda_y} \int_0^{\frac{\lambda_y}{2}} \int_0^{\frac{\lambda_x}{2}} V(x, y, z) \cos(k_{x,n} x) \cos(k_{y,m} y) \, dx dy \quad n, m > 0 \quad (3.216)$$

$$\Phi_{0,0}(z) = \frac{4}{\lambda_x \lambda_y} \int_0^{\frac{\lambda_y}{2}} \int_0^{\frac{\lambda_x}{2}} V(x, y, z) \, dx dy \quad (3.217)$$

$$\Phi_{n,0}(z) = \frac{8}{\lambda_x \lambda_y} \int_0^{\frac{\lambda_y}{2}} \int_0^{\frac{\lambda_x}{2}} V(x, y, z) \cos k_{x,n} x \, dx dy \quad n \neq 0 \quad (3.218)$$

$$\Phi_{0,m}(z) = \frac{8}{\lambda_x \lambda_y} \int_0^{\frac{\lambda_y}{2}} \int_0^{\frac{\lambda_x}{2}} V(x, y, z) \cos k_{y,m} y \, dx dy \quad m \neq 0 \quad (3.219)$$

The Fourier coefficients can be summarized by use of the Kronecker delta function.

$$\Phi_{n,m}(z) = \left(1 - \frac{\delta_{n,0}}{2}\right) \left(1 - \frac{\delta_{m,0}}{2}\right) \frac{16}{\lambda_x \lambda_y} \int_0^{\frac{\lambda_y}{2}} \int_0^{\frac{\lambda_x}{2}} V(x, y, z) \cos(k_{x,n} x) \cos(k_{y,m} y) \, dx dy \quad (3.220)$$

The Kronecker delta function is defined as

$$\delta_{n,m} = \begin{cases} 1 & \text{for } n = m \\ 0 & \text{for } n \neq m \end{cases} \quad (3.221)$$

3.6.3 Surface Capacitance Density

The surface capacitance density is defined as

$$C_{n,m}^*(z) = \frac{\epsilon^*(z) E_{z,(n,m)}(z)}{\Phi_{n,m}(z)} \quad (3.222)$$

where $\epsilon^*(z)$ is the effective permittivity, $E_{z,(n,m)}(z)$ is the Fourier coefficient of the electric field in the z direction, and $\Phi_{n,m}(z)$ is the Fourier coefficient of the potential. It is straight forward to see that all the solutions in Section 3.2 and Section 3.2.2 will apply with the substitutions $C_n^*(z) \rightarrow C_{n,m}^*(z)$ and $k_n \rightarrow k_{n,m}$. Let there be P layers with the interface between layers p and $p + 1$ at z_p . Let $z_0 = 0$ designate the surface of the electrodes. Restating the previous results using the appropriate

notation we have

$$C_{n,m}^*(z_{P-1}) = k_{n,m}\epsilon^* \quad \text{bottom of infinite layer} \quad (3.223)$$

$$C_{0,0}^*(z_0) = 0 \quad \text{for infinite layer} \quad (3.224)$$

$$C_{n,m}^*(z_{P-1}) = k_{n,m}\epsilon_P^* \coth(k_{n,m}(z_P - z_{P-1})) \quad \text{layer below top ground plane} \quad (3.225)$$

$$C_{0,0}^*(z_{P-1}) = \frac{\epsilon_P^*}{(z_P - z_{P-1})} \quad \text{layer below top ground plane} \quad (3.226)$$

$$C_{n,m}^*(z_{p-1}) = k_{n,m}\epsilon_P^* \frac{C_{n,m}^*(z_p) \coth(k_{n,m}(z_p - z_{p-1})) + k_{n,m}\epsilon_P^*}{C_{n,m}^*(z_p) + k_{n,m}\epsilon_P^* \coth(k_{n,m}(z_p - z_{p-1}))} \quad \text{transition eq.} \quad (3.227)$$

$$C_{0,0}^*(z_{p-1}) = \frac{\epsilon_P^* C_{0,0}^*(z_p)}{(z_p - z_{p-1})C_{0,0}^*(z_p) + \epsilon_P^*} \quad \text{transition eq.} \quad (3.228)$$

Assuming a substrate with an effective permittivity ϵ_s^* and thickness t_s we find the surface capacitance density just below the surface of the electrodes to be

$$C_{n,m}^*(z = 0^-) = -k_{n,m}\epsilon_s^* \coth k_{n,m}t_s, \quad \text{for } n \neq 0 \text{ or } m \neq 0 \quad (3.229)$$

$$C_{0,0}^*(z = 0^-) = -\frac{\epsilon_s^*}{t_s} \quad (3.230)$$

3.6.4 Collocation Points

We now minimize the region we need to solve for. We look at the unit cell shown in Fig. 3-12. The four gray rectangles represent the electrodes. The black lines indicate the periodicity grid. We have assumed that the drive and sense electrodes are the same size. The only region with a unique voltage is in the lightly gray shaded region. The other half is simply a rotation of the solution in the light gray region. The field lines are “cartoon”, that is drawn to give some indication of the field directions.

Having found the region we need to solve the field in we now proceed to assign collocation points to the region as illustrated in Fig. 3-13. Our method is to assign a number of points and spacing along three lines. The first is along the top edge of the drive electrode from $\{0, w_y/2\}$ to $\{w_x/2, w_y/2\}$ (A to B) where there are $K_1 + 2$ points. The second edge extends from $\{w_x/2, 0\}$ to $\{w_x/2, w_y/2\}$ (C to B) where there are $K_2 + 2$ points. Along the diagonal from $\{w_x/2, \lambda_y/2 - w_y/2\}$ to $\{\lambda_x/2 - w_x/2, w_y/2\}$ (F to E) there are $K_3 + 2$ points.

The method requires no restriction on the spacing except that the first and last points correspond with the appropriate end points. The accuracy may be highly affected by the choice of spacing, and points should be more closely clustered in regions with high potential gradients. A grid is formed by extending these initial points in the x and y directions and forming a grid which is shown in

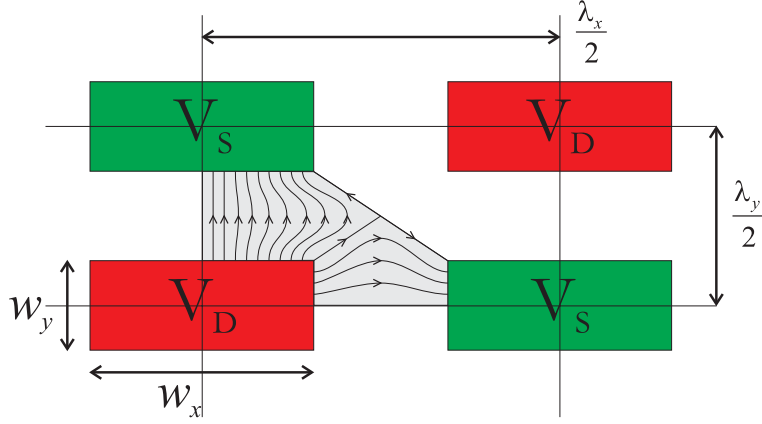


Figure 3-12: Planar dual periodic unit cell. The region to be solved for is shown in light grey with cartoon lines to demonstrate the field lines. The origin is the lower left corner of the unit cell which is the center of the lower left drive electrode.

Fig. 3-13. Three regions are identified for reference. Region one and two refer to the rectangular regions between the drive and sense electrodes, and region three is the triangular region. The naming convention is straightforward and several key points are detailed in Fig. 3-13. The grid points will generally be referred to as $\{x_\alpha, y_\beta\}$ or equivalently as $\bar{x}_{\alpha,\beta}$.

Voltage at the Electrode Surface, $z = 0$

We assign the voltage $\nu_{\alpha,\beta}$ at the point $\bar{x}_{\alpha,\beta}$ and $z = 0$. We use a linear approximation of the voltage in-between collocation points by defining a surface from the three closest points on which a surface can be defined.

Let $x_\alpha \leq x \leq x_{\alpha+1}$ and $y_\beta \leq y \leq y_{\beta+1}$. We define

$$\bar{P} = \hat{x}(x_{\alpha+1} - x_\alpha) + \hat{z}(\nu_{\alpha+1,\beta} - \nu_{\alpha,\beta}) \quad (3.231)$$

$$\bar{Q} = \hat{y}(y_{\beta+1} - y_\beta) + \hat{z}(\nu_{\alpha,\beta+1} - \nu_{\alpha,\beta}) \quad (3.232)$$

Because \bar{P} and \bar{Q} are both vectors in the surface of the plane, $\bar{N} = \bar{P} \times \bar{Q}$ is a vector normal to the surface. Let \bar{R} be the vector from $\{x_\alpha, y_\beta, \nu_{\alpha,\beta}\}$ to $\{x, y, V(x, y)\}$.

$$\bar{N} = -\hat{x}P_zQ_y - \hat{y}P_xQ_z + \hat{z}P_xQ_y \quad (3.233)$$

$$\bar{R} = \hat{x}(x - x_\alpha) + \hat{y}(y - y_\beta) + \hat{z}(V(x, y) - \nu_{\alpha,\beta}) \quad (3.234)$$

If $\{x, y, V(x, y)\}$ is in the plane then $\bar{R} \cdot \bar{N} = 0$. Taking the dot product and solving for $V(x, y)$ we

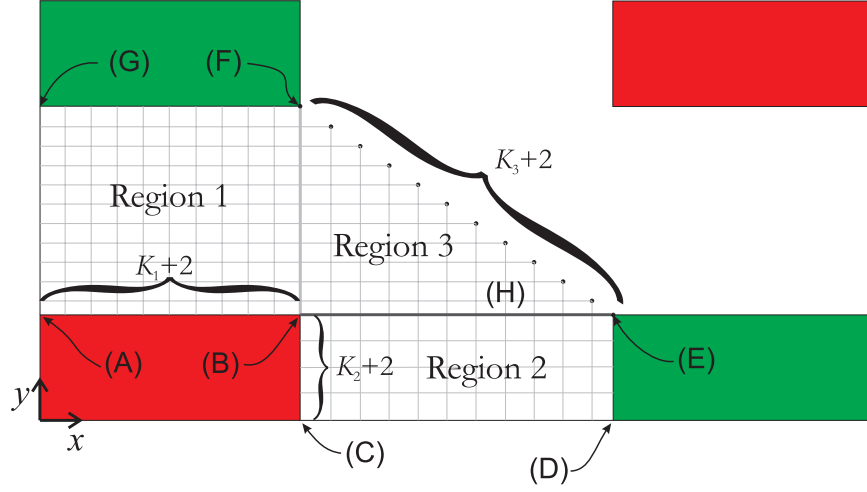


Figure 3-13: Unit cell of planar dual periodic sensor with selected collocation points labeled. (A) $\{x_0, y_{K_2+1}\}$, (B) $\{x_{K_1+1}, y_{K_2+1}\}$, (C) $\{x_{K_1+1}, y_0\}$, (D) $\{x_{K_1+K_3+2}, y_0\}$, (E) $\{x_{K_1+K_3+2}, y_{K_2+1}\}$, (F) $\{x_{K_1+1}, y_{K_2+K_3+2}\}$, (G) $\{x_0, y_{K_2+K_3+2}\}$, (H) $\{x_\alpha, y_\beta\}$

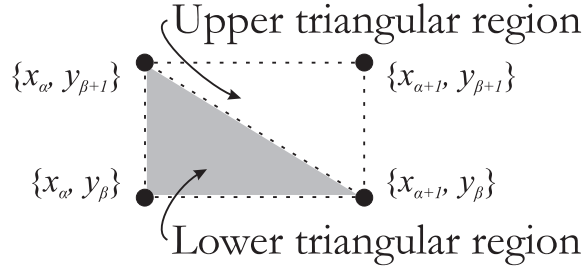


Figure 3-14: Planar dual periodic sensor triangular regions for linear approximations.

have

$$V(x, y) = \nu_{\alpha, \beta} + (\nu_{\alpha+1, \beta} - \nu_{\alpha, \beta}) \frac{x - x_\alpha}{x_{\alpha+1} - x_\alpha} + (\nu_{\alpha, \beta+1} - \nu_{\alpha, \beta}) \frac{y - y_\beta}{y_{\beta+1} - y_\beta} \quad (3.235)$$

which is valid in the lower triangular region where

$$x_\alpha \leq x \leq x_{\alpha+1}$$

and

$$y_\beta \leq y \leq -\frac{y_{\beta+1} - y_\beta}{x_{\alpha+1} - x_\alpha} (x - x_\alpha) + y_{\beta+1}$$

In the upper triangular region the solution is

$$V(x, y) = \nu_{\alpha+1, \beta+1} + (\nu_{\alpha, \beta+1} - \nu_{\alpha+1, \beta+1}) \frac{x - x_{\alpha+1}}{x_\alpha - x_{\alpha+1}} + (\nu_{\alpha+1, \beta} - \nu_{\alpha+1, \beta+1}) \frac{y - y_{\beta+1}}{y_\beta - y_{\beta+1}} \quad (3.236)$$

where the region is constrained to

$$x_\alpha \leq x \leq x_{\alpha+1}$$

and

$$-\frac{y_\beta - y_{\beta+1}}{x_\alpha - x_{\alpha+1}}(x - x_{\alpha+1}) + y_\beta \leq y \leq y_{\beta+1}$$

3.6.5 Boundary Conditions Part I

We define the effective surface charge density $\sigma_S^*(x, y)$ as

$$\sigma_S^*(x, y) = \|\epsilon^* E_z(x, y)\| \quad (3.237)$$

We require the effective surface charge density at the surface of the electrodes ($z = 0$) to be zero everywhere except over the electrodes themselves.

$$\sigma_S^*(x, y) = 0 \quad (3.238)$$

We can write $\sigma_S^*(x, y)$ as a Fourier series at $z = 0$.

$$\sigma_S^*(x, y) = \sum_{n=0}^{\infty} \sum_{m=0}^{\infty} \sigma_{S(n,m)}^* \cos k_{x,n} x \cos k_{y,m} y \quad (3.239)$$

We introduce $C_{n,m}^*$ as the difference in surface capacitance density at $z = 0^+$ and $z = 0^-$.

$$C_{n,m}^* = C_{n,m}^*(0^+) - C_{n,m}^*(0^-) \quad (3.240)$$

By using equations 3.237 and 3.222 we find the Fourier coefficients $\sigma_{S(n,m)}^*$ are

$$\sigma_{S(n,m)}^* = C_{n,m}^* \Phi_{n,m}(0) \quad (3.241)$$

To enforce the boundary condition, and in effect solve for the voltages at the collocation points, we integrate the effective surface charge density over a surface enclosing each interior collocation point and set it equal to zero. This produces one equation for each interior collocation point. Therefore, the number of unknowns must be equal to the number of interior collocation points. The number of interior collocation points is

The edges between region one and three, and two and three have been included in the region one and two totals respectively. The $3K_3$ edge points along the lines $x = 0$, $y = 0$, and along the diagonal, have not been included to limit the number of unknowns. Any expression involving these

$$\begin{aligned}
\text{Region 1} &\rightarrow K_3(K_1 + 1) \\
\text{Region 2} &\rightarrow K_3(K_2 + 1) \\
\text{Region 3} &\rightarrow (K_3^2 - K_3)/2
\end{aligned}$$

terms must be forced towards zero to be eliminated from the final expression. This can be achieved by placing the adjacent points sufficiently close to the edge. The total number of unknowns, H , is then

$$H = K_3 \left(K_1 + K_2 + \frac{K_3}{2} + \frac{3}{2} \right) \quad (3.242)$$

The integration region enclosing collocation point $\bar{x}_{\gamma,\delta}$ is a rectangular region with lower corner $\bar{x}'_{\gamma-1,\delta-1}$ and upper corner $\bar{x}'_{\gamma,\delta}$. These boundaries are

$$\bar{x}'_{\gamma,\delta} = \begin{cases} \{x_0, y_{K_2+1}\} & \gamma = 0, \delta = K_2 + 1 \\ \{x_{K_1+1}, y_0\} & \gamma = K_1 + 1, \delta = 0 \\ \{x_0, (y_{\delta+1} + y_\delta)/2\} & \gamma = 0, K_2 + 2 \leq \delta \leq K_2 + K_3 - 1 \\ \{(x_{\gamma+1} + x_\gamma)/2, y_0\} & K_1 + 2 \leq \gamma \leq K_1 + K_3 - 1, \delta = 0 \\ \{(x_{\gamma+1} + x_\gamma)/2, y_{K_2+K_3+2}\} & 1 \leq \gamma \leq K_1, \delta = K_2 + K_3 + 1 \\ \{(x_{\gamma+1} + x_\gamma)/2, y_{K_2+1}\} & 1 \leq \gamma \leq K_1, \delta = K_2 + 1 \\ \{x_{K_1+1}, (y_{\delta+1} + y_\delta)/2\} & \gamma = K_1 + 1, 1 \leq \delta \leq K_2 \\ \{x_{K_1+K_3+2}, (y_{\delta+1} + y_\delta)/2\} & \gamma = K_1 + K_3 + 1, 1 \leq \delta \leq K_2 \\ \{(x_{\gamma+1} + x_\gamma)/2, (y_{\delta+1} + y_\delta)/2\} & \text{otherwise} \end{cases} \quad (3.243)$$

The x and y components of $\bar{x}'_{\gamma,\delta}$ are $x'_{\gamma,\delta}$ and $y'_{\gamma,\delta}$. Notice that both γ and δ are needed. The integral of the effective surface charge density is then

$$\int_{x'_{\gamma-1,\delta-1}}^{x'_{\gamma,\delta}} \int_{y'_{\gamma-1,\delta-1}}^{y'_{\gamma,\delta}} \sigma_S^*(x, y) dy dx = 0 \quad (3.244)$$

Expressing $\sigma_S^*(x, y)$ in terms of its Fourier series we have

$$0 = \sum_{n=0}^{\infty} \sum_{m=0}^{\infty} \int_{x'_{\gamma-1,\delta-1}}^{x'_{\gamma,\delta}} \int_{y'_{\gamma-1,\delta-1}}^{y'_{\gamma,\delta}} \sigma_{S(n,m)}^* \cos k_{x,n} x \cos k_{y,m} y dy dx \quad (3.245)$$

$$= \sum_{n=0}^{\infty} \sum_{m=0}^{\infty} \int_{x'_{\gamma-1,\delta-1}}^{x'_{\gamma,\delta}} \int_{y'_{\gamma-1,\delta-1}}^{y'_{\gamma,\delta}} C_{n,m}^* \Phi_{n,m}(0) \cos k_{x,n} x \cos k_{y,m} y dy dx \quad (3.246)$$

We wish to express eq. 3.246 as a matrix equation which can be solved for \bar{v} , the vector of unknown potentials. We have already solved for the $C_{n,m}^*$ coefficients. Before writing this in matrix form we solve for the Fourier series coefficients, $\Phi_{n,m}(0)$.

3.6.6 Fourier Coefficients at $z = 0$

We now have all the information we need to solve for the Fourier coefficients. We introduce the notation $\tilde{\Phi}_{n,m} = \Phi_{n,m}(z = 0)$ for convenience. We begin with the simplest coefficient Fourier expression and proceed towards the most complicated. The integration regions in all cases is only half of that in eq. 3.220 because of symmetry. A factor of two is introduced to account for this.

Fourier Coefficients for $n = m = 0$

We begin with eq. 3.217 and expand it to include all the individual integration regions.

$$\begin{aligned}
\tilde{\Phi}_{0,0} = & \frac{8}{\lambda_x \lambda_y} \left\{ \int_0^{\frac{w_y}{2}} \int_0^{\frac{w_x}{2}} V_D dx dy + \right. & (3.247) \\
& \sum_{\alpha=0}^{K_1} \sum_{\beta=K_2+1}^{K_2+K_3+1} \int_{x_\alpha}^{x_{\alpha+1}} \int_{y_\beta}^{y_{\beta+1}} V(x, y) dy dx + \\
& \sum_{\alpha=K_1+1}^{K_1+K_3+1} \sum_{\beta=0}^{K_2} \int_{x_\alpha}^{x_{\alpha+1}} \int_{y_\beta}^{y_{\beta+1}} V(x, y) dy dx + \\
& \left. \sum_{\alpha=K_1+1}^{(K_1+K_3)} \sum_{\beta=K_2+1}^{(K_1+K_2+K_3+1-\alpha)} \int_{x_\alpha}^{x_{\alpha+1}} \int_{y_\beta}^{y_{\beta+1}} V(x, y) dy dx + \right. \\
& \left. \sum_{\alpha=K_1+1}^{(K_1+K_3+1)} \int_{x_\alpha}^{x_{\alpha+1}} \int_{y_{\beta(\alpha)}}^{-\frac{y_{\beta(\alpha)+1} - y_{\beta(\alpha)}}{x_{\alpha+1} - x_\alpha} (x - x_\alpha) + y_{\beta(\alpha)+1}} V(x, y) dy dx \right\}
\end{aligned}$$

where

$$\beta(\alpha) = K_1 + K_2 + K_3 + 2 - \alpha \quad (3.248)$$

The first term represents the integral over the drive electrode and is trivial. The second and third terms represent the integral over regions one and two respectively. The last two terms represent the integral over region three. This integral covers the entire area, but we must reduce this to eliminate any expressions involving the edge voltages, since there are not enough equations to solve for these terms. The edge voltages at the electrode edges are known of course, but along the left boundary of region one, the lower boundary of region two, and the diagonal boundary of region three the voltages are unknown and must be eliminated to prevent an excess of unknown voltages. We revise 3.247 to

eliminate these terms.

$$\begin{aligned}
\tilde{\Phi}_{0,0} = & \frac{8}{\lambda_x \lambda_y} \left\{ \int_0^{\frac{w_y}{2}} \int_0^{\frac{w_x}{2}} V_D dx dy + \right. \\
& \sum_{\alpha=1}^{K_1} \sum_{\beta=K_2+1}^{K_2+K_3+1} \int_{x_\alpha}^{x_{\alpha+1}} \int_{y_\beta}^{y_{\beta+1}} V(x, y) dy dx + \\
& \sum_{\alpha=K_1+1}^{K_1+K_3+1} \sum_{\beta=1}^{K_2} \int_{x_\alpha}^{x_{\alpha+1}} \int_{y_\beta}^{y_{\beta+1}} V(x, y) dy dx + \\
& \sum_{\alpha=K_1+1}^{(K_1+K_3)} \sum_{\beta=K_2+1}^{(K_1+K_2+K_3-\alpha)} \int_{x_\alpha}^{x_{\alpha+1}} \int_{y_\beta}^{y_{\beta+1}} V(x, y) dy dx + \\
& \left. \sum_{\alpha=K_1+1}^{(K_1+K_3+1)} \int_{x_\alpha}^{x_{\alpha+1}} \int_{y_{\beta(\alpha)}}^{-\frac{y_{\beta(\alpha)+1}-y_{\beta(\alpha)}}{x_{\alpha+1}-x_\alpha}(x-x_\alpha)+y_{\beta(\alpha)+1}} V(x, y) dy dx \right\}
\end{aligned} \tag{3.249}$$

where

$$\beta(\alpha) = K_1 + K_2 + K_3 + 1 - \alpha \tag{3.250}$$

We can now integrate each term individually. Disregarding the coefficient the V_D term is simply

$$\frac{w_x}{2} \frac{w_y}{2} V_D \tag{3.251}$$

The middle terms must be broken into the upper triangular integration region, and the lower triangular integration region and the appropriate expression for $V(x, y)$ must be substituted. For the lower triangular region we substitute in eq. 3.235 and get

$$\int_{x_\alpha}^{x_{\alpha+1}} \int_{y_\beta}^{y_{\alpha,\beta}(x)} \left(\nu_{\alpha,\beta} + (\nu_{\alpha+1,\beta} - \nu_{\alpha,\beta}) \frac{x - x_\alpha}{x_{\alpha+1} - x_\alpha} + (\nu_{\alpha,\beta+1} - \nu_{\alpha,\beta}) \frac{y - y_\beta}{y_{\beta+1} - y_\beta} \right) dy dx \tag{3.252}$$

where the integration limit is

$$y_{\alpha,\beta}(x) = -\frac{y_{\beta+1} - y_\beta}{x_{\alpha+1} - x_\alpha} (x - x_\alpha) + y_{\beta+1} \tag{3.253}$$

The expression is integrated and found to be

$$\frac{1}{6} (x_\alpha - x_{\alpha+1}) (y_\beta - y_{\beta+1}) (\nu_{\alpha,\beta} + \nu_{\alpha+1,\beta} + \nu_{\alpha,\beta+1}) \tag{3.254}$$

For the upper triangular region we substitute in eq. 3.236 and get

$$\int_{x_\alpha}^{x_{\alpha+1}} \int_{y_{\alpha,\beta}(x)}^{y_{\beta+1}} \left(\nu_{\alpha+1,\beta+1} + (\nu_{\alpha,\beta+1} - \nu_{\alpha+1,\beta+1}) \frac{x - x_{\alpha+1}}{x_\alpha - x_{\alpha+1}} + (\nu_{\alpha+1,\beta} - \nu_{\alpha+1,\beta+1}) \frac{y - y_{\beta+1}}{y_\beta - y_{\beta+1}} \right) dy dx \quad (3.255)$$

where the integration limit

$$y_{\alpha,\beta}(x) = -\frac{y_\beta - y_{\beta+1}}{x_\alpha - x_{\alpha+1}}(x - x_{\alpha+1}) + y_\beta \quad (3.256)$$

The expression is evaluated to be

$$\frac{1}{6}(x_\alpha - x_{\alpha+1})(y_\beta - y_{\beta+1})(\nu_{\alpha+1,\beta+1} + \nu_{\alpha+1,\beta} + \nu_{\alpha,\beta+1}) \quad (3.257)$$

The last term in eq. 3.249 is simply a lower triangular integration. The solution is the same as eq. 3.254 with $\beta \rightarrow \beta(\alpha)$, where $\beta(\alpha)$ is given by eq. 3.250.

$$\frac{1}{6}(x_\alpha - x_{\alpha+1})(y_{\beta(\alpha)} - y_{\beta(\alpha)+1})(\nu_{\alpha,\beta(\alpha)} + \nu_{\alpha+1,\beta(\alpha)} + \nu_{\alpha,\beta(\alpha)+1}) \quad (3.258)$$

The total expression for $\tilde{\Phi}_{0,0}$ is

$$\begin{aligned} \tilde{\Phi}_{0,0} = & \frac{4}{3\lambda_x\lambda_y} \left\{ \frac{3w_x w_y}{2} V_D + \right. & (3.259) \\ & \sum_{\alpha=1}^{K_1} \sum_{\beta=K_2+1}^{K_2+K_3+1} (x_\alpha - x_{\alpha+1})(y_\beta - y_{\beta+1})(\nu_{\alpha,\beta} + 2\nu_{\alpha+1,\beta} + 2\nu_{\alpha,\beta+1} + \nu_{\alpha+1,\beta+1}) + \\ & \sum_{\alpha=K_1+1}^{K_1+K_3+1} \sum_{\beta=1}^{K_2} (x_\alpha - x_{\alpha+1})(y_\beta - y_{\beta+1})(\nu_{\alpha,\beta} + 2\nu_{\alpha+1,\beta} + 2\nu_{\alpha,\beta+1} + \nu_{\alpha+1,\beta+1}) + \\ & \sum_{\alpha=K_1+1}^{(K_1+K_3)} \sum_{\beta=K_2+1}^{(K_1+K_2+K_3-\alpha)} (x_\alpha - x_{\alpha+1})(y_\beta - y_{\beta+1})(\nu_{\alpha,\beta} + 2\nu_{\alpha+1,\beta} + 2\nu_{\alpha,\beta+1} + \nu_{\alpha+1,\beta+1}) + \\ & \left. \sum_{\alpha=K_1+1}^{(K_1+K_3+1)} (x_\alpha - x_{\alpha+1})(y_{\beta(\alpha)} - y_{\beta(\alpha)+1})(\nu_{\alpha,\beta(\alpha)} + \nu_{\alpha+1,\beta(\alpha)} + \nu_{\alpha,\beta(\alpha)+1}) \right\} \end{aligned}$$

where $\beta(\alpha)$ is given by eq. 3.250. The key feature is to notice that all the ν terms have coefficients that are dependent only on known constants. No term involves the product of two ν terms. This feature will allow us to later write a matrix equation.

Fourier Coefficients for $n \neq 0$, $m = 0$

We begin with eq. 3.218 and dissect the integral into the same regions as for the previous case.

$$\begin{aligned}
\tilde{\Phi}_{n,0} = & \frac{16}{\lambda_x \lambda_y} \left\{ \int_0^{\frac{w_y}{2}} \int_0^{\frac{w_x}{2}} V_D \cos(k_{x,n}x) \, dx dy + \right. \\
& \sum_{\alpha=1}^{K_1} \sum_{\beta=K_2+1}^{K_2+K_3+1} \int_{x_\alpha}^{x_{\alpha+1}} \int_{y_\beta}^{y_{\beta+1}} V(x,y) \cos(k_{x,n}x) \, dy dx + \\
& \sum_{\alpha=K_1+1}^{K_1+K_3+1} \sum_{\beta=1}^{K_2} \int_{x_\alpha}^{x_{\alpha+1}} \int_{y_\beta}^{y_{\beta+1}} V(x,y) \cos(k_{x,n}x) \, dy dx + \\
& \sum_{\alpha=K_1+1}^{(K_1+K_3)} \sum_{\beta=K_2+1}^{(K_1+K_2+K_3-\alpha)} \int_{x_\alpha}^{x_{\alpha+1}} \int_{y_\beta}^{y_{\beta+1}} V(x,y) \cos(k_{x,n}x) \, dy dx + \\
& \left. \sum_{\alpha=K_1+1}^{(K_1+K_3+1)} \int_{x_\alpha}^{x_{\alpha+1}} \int_{y_{\beta(\alpha)}}^{-\frac{y_{\beta(\alpha)+1}-y_{\beta(\alpha)}}{x_{\alpha+1}-x_\alpha}(x-x_\alpha)+y_{\beta(\alpha)+1}} V(x,y) \cos(k_{x,n}x) \, dy dx \right\} \tag{3.260}
\end{aligned}$$

Again $\beta(\alpha)$ is given by eq. 3.250. The first integral can easily be evaluated.

$$V_D \frac{w_y}{2} \frac{\sin(k_{x,n} \frac{w_x}{2})}{k_{x,n}} \tag{3.261}$$

The solution to the intermediate integrals are

$$K_{\alpha,\beta} \nu_{\alpha,\beta} + K_{\alpha+1,\beta} \nu_{\alpha+1,\beta} + K_{\alpha,\beta+1} \nu_{\alpha,\beta+1} + K_{\alpha+1,\beta+1} \nu_{\alpha+1,\beta+1} \tag{3.262}$$

where

$$K_{\alpha,\beta} = \frac{(y_\beta - y_{\beta+1})}{2(x_\alpha - x_{\alpha+1})^2 k_{x,n}^3} \left(-2 \sin(x_\alpha k_{x,n}) + 2 \sin(x_{\alpha+1} k_{x,n}) + \right. \tag{3.263}$$

$$\left. (x_\alpha - x_{\alpha+1}) k_{x,n} (2 \cos(x_\alpha k_{x,n}) + \sin(x_\alpha k_{x,n})(x_\alpha - x_{\alpha+1}) k_{x,n}) \right)$$

$$K_{\alpha+1,\beta} = \frac{(y_\beta - y_{\beta+1})}{2(x_\alpha - x_{\alpha+1})^2 k_{x,n}^3} \left(2(\sin(x_\alpha k_{x,n}) - \sin(x_{\alpha+1} k_{x,n})) + \right. \tag{3.264}$$

$$\left. (x_\alpha - x_{\alpha+1}) k_{x,n} (\sin(x_{\alpha+1} k_{x,n})(x_{\alpha+1} - x_\alpha) k_{x,n} - 2 \cos(x_\alpha k_{x,n})) \right)$$

$$K_{\alpha,\beta+1} = \frac{(y_\beta - y_{\beta+1})}{2(x_\alpha - x_{\alpha+1})^2 k_{x,n}^3} \left(2(\sin(x_\alpha k_{x,n}) - \sin(x_{\alpha+1} k_{x,n})) \right. \tag{3.265}$$

$$\left. + (x_\alpha - x_{\alpha+1}) k_{x,n} (\sin(x_\alpha k_{x,n})(x_\alpha - x_{\alpha+1}) k_{x,n} - 2 \cos(x_{\alpha+1} k_{x,n})) \right)$$

$$K_{\alpha+1,\beta+1} = \frac{(y_\beta - y_{\beta+1})}{2(x_\alpha - x_{\alpha+1})^2 k_{x,n}^3} \left(-2 \sin(x_\alpha k_{x,n}) + 2 \sin(x_{\alpha+1} k_{x,n}) \right. \tag{3.266}$$

$$\left. + (x_\alpha - x_{\alpha+1}) k_{x,n} (2 \cos(x_{\alpha+1} k_{x,n}) + \sin(x_{\alpha+1} k_{x,n})(x_{\alpha+1} - x_\alpha) k_{x,n}) \right)$$

The final integral in eq. 3.260 has a different set of coefficients since it is only an integration over the lower region.

$$K_{\alpha,\beta(\alpha)}\nu_{\alpha,\beta(\alpha)} + M_{\alpha+1,\beta(\alpha)}\nu_{\alpha+1,\beta(\alpha)} + M_{\alpha,\beta(\alpha)+1}\nu_{\alpha,\beta(\alpha)+1} \quad (3.267)$$

where $K_{\alpha,\beta(\alpha)}$ is the same as in eq. 3.263 and

$$M_{\alpha+1,\beta(\alpha)} = \frac{(y_{\beta(\alpha)} - y_{\beta(\alpha)+1})}{(x_{\alpha} - x_{\alpha+1})^2 k_{x,m}^3} \left(2 (\sin(x_{\alpha} k_{x,m}) - \sin(x_{\alpha+1} k_{x,m})) - \right. \quad (3.268)$$

$$\left. (\cos(x_{\alpha} k_{x,m}) + \cos(x_{\alpha+1} k_{x,m})) (x_{\alpha} - x_{\alpha+1}) k_{x,m} \right)$$

$$M_{\alpha,\beta(\alpha)+1} = \frac{(y_{\beta(\alpha)} - y_{\beta(\alpha)+1})}{2(x_{\alpha} - x_{\alpha+1})^2 k_{x,m}^3} \left(-2 \sin(x_{\alpha} k_{x,m}) + 2 \sin(x_{\alpha+1} k_{x,m}) + \right. \quad (3.269)$$

$$\left. (x_{\alpha} - x_{\alpha+1}) k_{x,m} (2 \cos(x_{\alpha} k_{x,m}) + \sin(x_{\alpha} k_{x,m}) (x_{\alpha} - x_{\alpha+1}) k_{x,m}) \right)$$

We are now prepared to write the solution to $\tilde{\Phi}_{n,0}$

$$\tilde{\Phi}_{n,0} = \frac{16}{\lambda_x \lambda_y} \left\{ V_D \frac{w_y}{2} \frac{\sin(k_{x,n} \frac{w_x}{2})}{k_{x,n}} + \right. \quad (3.270)$$

$$\sum_{\alpha=1}^{K_1} \sum_{\beta=K_2+1}^{K_2+K_3+1} K_{\alpha,\beta} \nu_{\alpha,\beta} + K_{\alpha+1,\beta} \nu_{\alpha+1,\beta} + K_{\alpha,\beta+1} \nu_{\alpha,\beta+1} + K_{\alpha+1,\beta+1} \nu_{\alpha+1,\beta+1} +$$

$$\sum_{\alpha=K_1+1}^{K_1+K_3+1} \sum_{\beta=1}^{K_2} K_{\alpha,\beta} \nu_{\alpha,\beta} + K_{\alpha+1,\beta} \nu_{\alpha+1,\beta} + K_{\alpha,\beta+1} \nu_{\alpha,\beta+1} + K_{\alpha+1,\beta+1} \nu_{\alpha+1,\beta+1} +$$

$$\sum_{\alpha=K_1+1}^{(K_1+K_3)} \sum_{\beta=K_2+1}^{(K_1+K_2+K_3-\alpha)} K_{\alpha,\beta} \nu_{\alpha,\beta} + K_{\alpha+1,\beta} \nu_{\alpha+1,\beta} + K_{\alpha,\beta+1} \nu_{\alpha,\beta+1} + K_{\alpha+1,\beta+1} \nu_{\alpha+1,\beta+1} +$$

$$\left. \sum_{\alpha=K_1+1}^{(K_1+K_3+1)} K_{\alpha,\beta(\alpha)} \nu_{\alpha,\beta(\alpha)} + M_{\alpha+1,\beta(\alpha)} \nu_{\alpha+1,\beta(\alpha)} + M_{\alpha,\beta(\alpha)+1} \nu_{\alpha,\beta(\alpha)+1} \right\}$$

where $\beta(\alpha)$ is given by eq. 3.250.

Fourier Coefficients for $n = 0$, $m \neq 0$

We begin with eq. 3.219 and dissect the integral into the same regions as for the previous case.

$$\begin{aligned}
\tilde{\Phi}_{0,m} = & \frac{16}{\lambda_x \lambda_y} \left\{ \int_0^{\frac{w_y}{2}} \int_0^{\frac{w_x}{2}} V_D \cos(k_{y,m}y) \, dx dy + \right. & (3.271) \\
& \sum_{\alpha=1}^{K_1} \sum_{\beta=K_2+1}^{K_2+K_3+1} \int_{x_\alpha}^{x_{\alpha+1}} \int_{y_\beta}^{y_{\beta+1}} V(x,y) \cos(k_{y,m}y) \, dy dx + \\
& \sum_{\alpha=K_1+1}^{K_1+K_3+1} \sum_{\beta=1}^{K_2} \int_{x_\alpha}^{x_{\alpha+1}} \int_{y_\beta}^{y_{\beta+1}} V(x,y) \cos(k_{y,m}y) \, dy dx + \\
& \sum_{\alpha=K_1+1}^{(K_1+K_3)} \sum_{\beta=K_2+1}^{(K_1+K_2+K_3-\alpha)} \int_{x_\alpha}^{x_{\alpha+1}} \int_{y_\beta}^{y_{\beta+1}} V(x,y) \cos(k_{y,m}y) \, dy dx + \\
& \left. \sum_{\alpha=K_1+1}^{(K_1+K_3+1)} \int_{x_\alpha}^{x_{\alpha+1}} \int_{y_{\beta(\alpha)}}^{-\frac{y_{\beta(\alpha)+1}-y_{\beta(\alpha)}}{x_{\alpha+1}-x_\alpha}(x-x_\alpha)+y_{\beta(\alpha)+1}} V(x,y) \cos(k_{y,m}y) \, dy dx \right\}
\end{aligned}$$

Again $\beta(\alpha)$ is given by eq. 3.250. The first integral can easily be evaluated.

$$V_D \frac{w_x}{2} \frac{\sin(k_{y,m} \frac{w_y}{2})}{k_{y,m}} \quad (3.272)$$

The intermediate integrals are now found to be in the same form as eq. 3.262, where the coefficients are now

$$K_{\alpha,\beta} = \frac{(x_\alpha - x_{\alpha+1})}{2(y_\beta - y_{\beta+1})^2 k_{y,m}^3} \left(-2 \sin(y_\beta k_{y,m}) + 2 \sin(y_{\beta+1} k_{y,m}) + \right. \quad (3.273)$$

$$\left. (y_\beta - y_{\beta+1}) k_{y,m} (2 \cos(y_\beta k_{y,m}) + \sin(y_\beta k_{y,m}) (y_\beta - y_{\beta+1}) k_{y,m}) \right)$$

$$K_{\alpha+1,\beta} = \frac{(x_\alpha - x_{\alpha+1})}{2(y_\beta - y_{\beta+1})^2 k_{y,m}^3} \left(2 (\sin(y_\beta k_{y,m}) - \sin(y_{\beta+1} k_{y,m})) + \right. \quad (3.274)$$

$$\left. (y_\beta - y_{\beta+1}) k_{y,m} (\sin(y_\beta k_{y,m}) (y_\beta - y_{\beta+1}) k_{y,m} - 2 \cos(y_{\beta+1} k_{y,m})) \right)$$

$$K_{\alpha,\beta+1} = \frac{(x_\alpha - x_{\alpha+1})}{2(y_\beta - y_{\beta+1})^2 k_{y,m}^3} \left(2 (\sin(y_\beta k_{y,m}) - \sin(y_{\beta+1} k_{y,m})) + \right. \quad (3.275)$$

$$\left. (y_\beta - y_{\beta+1}) k_{y,m} (\sin(y_{\beta+1} k_{y,m}) (y_{\beta+1} - y_\beta) k_{y,m} - 2 \cos(y_\beta k_{y,m})) \right)$$

$$K_{\alpha+1,\beta+1} = \frac{(x_\alpha - x_{\alpha+1})}{2(y_\beta - y_{\beta+1})^2 k_{y,m}^3} \left(-2 \sin(y_\beta k_{y,m}) + 2 \sin(y_{\beta+1} k_{y,m}) + \right. \quad (3.276)$$

$$\left. (y_\beta - y_{\beta+1}) k_{y,m} (2 \cos(y_{\beta+1} k_{y,m}) + \sin(y_{\beta+1} k_{y,m}) (y_{\beta+1} - y_\beta) k_{y,m}) \right)$$

The final integral in eq. 3.271 has a solution of the form in eq. 3.267. Again $K_{\alpha,\beta(\alpha)}$ is the same as in eq. 3.273 and

$$M_{\alpha+1,\beta} = \frac{(x_\alpha - x_{\alpha+1})}{2(y_\beta - y_{\beta+1})^2 k_{y,m}^3} \left(-2 \sin(y_\beta k_{y,m}) + 2 \sin(y_{\beta+1} k_{y,m}) + \right. \quad (3.277)$$

$$\left. (y_\beta - y_{\beta+1}) k_{y,m} (2 \cos(y_\beta k_{y,m}) + \sin(y_\beta k_{y,m}) (y_\beta - y_{\beta+1}) k_{y,m}) \right)$$

$$M_{\alpha,\beta+1} = \frac{(x_\alpha - x_{\alpha+1})}{(y_\beta - y_{\beta+1})^2 k_{y,m}^3} \left(2 (\sin(y_\beta k_{y,m}) - \sin(y_{\beta+1} k_{y,m})) - \right. \quad (3.278)$$

$$\left. (\cos(y_\beta k_{y,m}) + \cos(y_{\beta+1} k_{y,m})) (y_\beta - y_{\beta+1}) k_{y,m} \right)$$

We can now write the solution to $\tilde{\Phi}_{0,m}$

$$\tilde{\Phi}_{0,m} = \frac{16}{\lambda_x \lambda_y} \left\{ V_D \frac{w_x}{2} \frac{\sin(k_{y,m} \frac{w_y}{2})}{k_{y,m}} + \right. \quad (3.279)$$

$$\sum_{\alpha=1}^{K_1} \sum_{\beta=K_2+1}^{K_2+K_3+1} K_{\alpha,\beta} \nu_{\alpha,\beta} + K_{\alpha+1,\beta} \nu_{\alpha+1,\beta} + K_{\alpha,\beta+1} \nu_{\alpha,\beta+1} + K_{\alpha+1,\beta+1} \nu_{\alpha+1,\beta+1} +$$

$$\sum_{\alpha=K_1+1}^{K_1+K_3+1} \sum_{\beta=1}^{K_2} K_{\alpha,\beta} \nu_{\alpha,\beta} + K_{\alpha+1,\beta} \nu_{\alpha+1,\beta} + K_{\alpha,\beta+1} \nu_{\alpha,\beta+1} + K_{\alpha+1,\beta+1} \nu_{\alpha+1,\beta+1} +$$

$$\sum_{\alpha=K_1+1}^{(K_1+K_3)} \sum_{\beta=K_2+1}^{(K_1+K_2+K_3-\alpha)} K_{\alpha,\beta} \nu_{\alpha,\beta} + K_{\alpha+1,\beta} \nu_{\alpha+1,\beta} + K_{\alpha,\beta+1} \nu_{\alpha,\beta+1} + K_{\alpha+1,\beta+1} \nu_{\alpha+1,\beta+1} +$$

$$\left. \sum_{\alpha=K_1+1}^{(K_1+K_3+1)} K_{\alpha,\beta(\alpha)} \nu_{\alpha,\beta(\alpha)} + M_{\alpha+1,\beta(\alpha)} \nu_{\alpha+1,\beta(\alpha)} + M_{\alpha,\beta(\alpha)+1} \nu_{\alpha,\beta(\alpha)+1} \right\}$$

where $\beta(\alpha)$ is given by eq. 3.250.

Fourier Coefficients for $n, m \neq 0$

We begin with eq. 3.216 and dissect the integral into the same regions as for the previous case.

$$\begin{aligned}
\tilde{\Phi}_{n,m} = & \frac{16}{\lambda_x \lambda_y} \left\{ \int_0^{\frac{w_y}{2}} \int_0^{\frac{w_x}{2}} V_D \cos(k_{x,n}x) \cos(k_{y,m}y) \, dx dy + \right. \\
& \sum_{\alpha=1}^{K_1} \sum_{\beta=K_2+1}^{K_2+K_3+1} \int_{x_\alpha}^{x_{\alpha+1}} \int_{y_\beta}^{y_{\beta+1}} V(x, y) \cos(k_{x,n}x) \cos(k_{y,m}y) \, dy dx + \\
& \sum_{\alpha=K_1+1}^{K_1+K_3+1} \sum_{\beta=1}^{K_2} \int_{x_\alpha}^{x_{\alpha+1}} \int_{y_\beta}^{y_{\beta+1}} V(x, y) \cos(k_{x,n}x) \cos(k_{y,m}y) \, dy dx + \\
& \sum_{\alpha=K_1+1}^{(K_1+K_3)} \sum_{\beta=K_2+1}^{(K_1+K_2+K_3-\alpha)} \int_{x_\alpha}^{x_{\alpha+1}} \int_{y_\beta}^{y_{\beta+1}} V(x, y) \cos(k_{x,n}x) \cos(k_{y,m}y) \, dy dx + \\
& \left. \sum_{\alpha=K_1+1}^{(K_1+K_3+1)} \int_{x_\alpha}^{x_{\alpha+1}} \int_{y_{\beta(\alpha)}}^{-\frac{y_{\beta(\alpha)+1}-y_{\beta(\alpha)}}{x_{\alpha+1}-x_\alpha} (x-x_\alpha)+y_{\beta(\alpha)+1}} V(x, y) \cos(k_{x,n}x) \cos(k_{y,m}y) \, dy dx \right\}
\end{aligned} \tag{3.280}$$

The first term in eq. 3.280 is found

$$\frac{\sin\left(\frac{1}{2}w_x k_{x,n}\right) \sin\left(\frac{1}{2}w_y k_{y,m}\right) V_D}{k_{x,n} k_{y,m}} \tag{3.281}$$

Again we can write the solution to the intermediate integrals in the form of eq. 3.262.

While the expressions are of unreasonable length for inclusion here, it is evident from the form of $V(x, y)$ that all the integrals will result in expressions where $\nu_{\alpha,\beta}$ has coefficients that depend only on the collocation points $(\bar{x}_{\alpha,\beta})$, and the wave numbers, $k_{x,n}$, and $k_{y,m}$. Using the same notation as before we have the solution to $\tilde{\Phi}_{n,m}$.

$$\begin{aligned}
\tilde{\Phi}_{n,m} = & \frac{16}{\lambda_x \lambda_y} \left\{ \frac{\sin\left(\frac{1}{2}w_x k_{x,n}\right) \sin\left(\frac{1}{2}w_y k_{y,m}\right) V_D}{k_{x,n} k_{y,m}} + \right. \\
& \sum_{\alpha=1}^{K_1} \sum_{\beta=K_2+1}^{K_2+K_3+1} K_{\alpha,\beta} \nu_{\alpha,\beta} + K_{\alpha+1,\beta} \nu_{\alpha+1,\beta} + K_{\alpha,\beta+1} \nu_{\alpha,\beta+1} + K_{\alpha+1,\beta+1} \nu_{\alpha+1,\beta+1} + \\
& \sum_{\alpha=K_1+1}^{K_1+K_3+1} \sum_{\beta=1}^{K_2} K_{\alpha,\beta} \nu_{\alpha,\beta} + K_{\alpha+1,\beta} \nu_{\alpha+1,\beta} + K_{\alpha,\beta+1} \nu_{\alpha,\beta+1} + K_{\alpha+1,\beta+1} \nu_{\alpha+1,\beta+1} + \\
& \sum_{\alpha=K_1+1}^{(K_1+K_3)} \sum_{\beta=K_2+1}^{(K_1+K_2+K_3-\alpha)} K_{\alpha,\beta} \nu_{\alpha,\beta} + K_{\alpha+1,\beta} \nu_{\alpha+1,\beta} + K_{\alpha,\beta+1} \nu_{\alpha,\beta+1} + K_{\alpha+1,\beta+1} \nu_{\alpha+1,\beta+1} + \\
& \left. \sum_{\alpha=K_1+1}^{(K_1+K_3+1)} K_{\alpha,\beta(\alpha)} \nu_{\alpha,\beta(\alpha)} + M_{\alpha+1,\beta(\alpha)} \nu_{\alpha+1,\beta(\alpha)} + M_{\alpha,\beta(\alpha)+1} \nu_{\alpha,\beta(\alpha)+1} \right\}
\end{aligned} \tag{3.282}$$

where $\beta(\alpha)$ is given by eq. 3.250.

All of the expressions for $\tilde{\Phi}_{n,m}$ are of the general form

$$\tilde{\Phi}_{n,m} = F_{n,m} + \sum_{\alpha=1}^{K_1+K_3+1} \sum_{\beta=1}^{K_2+K_3+1} K_{\alpha,\beta} \nu_{\alpha,\beta} + K_{\alpha+1,\beta} \nu_{\alpha+1,\beta} + K_{\alpha,\beta+1} \nu_{\alpha,\beta+1} + K_{\alpha+1,\beta+1} \nu_{\alpha+1,\beta+1} \quad (3.283)$$

where $F_{n,m}$ is the constant term. In fact this form can be compacted even further by consolidating the coefficients.

$$\tilde{\Phi}_{n,m} = F_{n,m} + \sum_{\alpha=1}^{K_1+K_3+1} \sum_{\beta=1}^{K_2+K_3+1} K_{\alpha,\beta} \nu_{\alpha,\beta} \quad (3.284)$$

In this form many of the $K_{\alpha,\beta}$ coefficients will be zero since they do not correspond to an actual collocation point. Nevertheless we see that the form is quite simple and the complexity is only in the length of the expressions for the coefficients.

3.6.7 Boundary Conditions Part II

Having found the Fourier coefficients we can now proceed by reshaping the boundary condition equation into a matrix equation. Restating eq. 3.246 and integrating we have

$$0 = \sum_{n=0}^{\infty} \sum_{m=0}^{\infty} \int_{x'_{\gamma-1,\delta-1}}^{x'_{\gamma,\delta}} \int_{y'_{\gamma-1,\delta-1}}^{y'_{\gamma,\delta}} C_{n,m}^* \tilde{\Phi}_{n,m} \cos k_{x,n} x \cos k_{y,m} y dy dx \quad (3.285)$$

$$\begin{aligned} &= \sum_{n=1}^{\infty} \sum_{m=1}^{\infty} C_{n,m}^* \tilde{\Phi}_{n,m} \frac{\sin k_{x,n} x'_{\gamma,\delta} - \sin k_{x,n} x'_{\gamma-1,\delta-1}}{k_{x,n}} \frac{\sin k_{y,m} y'_{\gamma,\delta} - \sin k_{y,m} y'_{\gamma-1,\delta-1}}{k_{y,m}} \quad (3.286) \\ &+ \sum_{m=1}^{\infty} C_{0,m}^* \tilde{\Phi}_{0,m} (x'_{\gamma,\delta} - x'_{\gamma-1,\delta-1}) \frac{\sin k_{y,m} y'_{\gamma,\delta} - \sin k_{y,m} y'_{\gamma-1,\delta-1}}{k_{y,m}} \\ &+ \sum_{n=1}^{\infty} C_{n,0}^* \tilde{\Phi}_{n,0} \frac{\sin k_{x,n} x'_{\gamma,\delta} - \sin k_{x,n} x'_{\gamma-1,\delta-1}}{k_{x,n}} (y'_{\gamma,\delta} - y'_{\gamma-1,\delta-1}) \\ &+ C_{0,0}^* \tilde{\Phi}_{0,0} (x'_{\gamma,\delta} - x'_{\gamma-1,\delta-1}) (y'_{\gamma,\delta} - y'_{\gamma-1,\delta-1}) \end{aligned}$$

The terms in this expression can be grouped as depending on or independent of $\nu_{\alpha,\beta}$.

$$0 = \sum_{n=0}^{\infty} \sum_{m=0}^{\infty} C_{n,m}^* \sum_{\alpha=1}^{K_1+K_3+1} \sum_{\beta=1}^{K_2+K_3+1} M_{\alpha,\beta,\gamma,\delta}^{n,m} \nu_{\alpha,\beta} - \sum_{n=0}^{\infty} \sum_{m=0}^{\infty} C_{n,m}^* b_{\gamma,\delta}^{n,m} \quad (3.287)$$

One equation results from every boundary condition equation for a total of H equations which equals the number of unknown voltages. We write these equations in matrix form.

$$\mathbf{M}\mathbf{v} = \mathbf{b} \quad (3.288)$$

The complete solution to the potential at the surface of the electrodes is found by solving the matrix equation for \mathbf{b} . Once the surface voltage is known it is possible to find the complete electric field, potential distribution, and related quantities such as the impedance between the drive and sense electrodes.

The solution to the two dimensional planar problem follows conceptually from the solution to the previous problems. The difficulties are primarily in book keeping, that is keeping track of the collocation points and integration boundaries, and in the required algebraic manipulation. Because of the complexity of this problem a computer implementation has not been developed. Memory limitations are expected at this time even for simple problems.

3.7 Electric Potential Solution

In addition to calculating the transcapacitance, it is interesting to find the potential as a function of the spatial coordinates. By solving for the transcapacitance we have already solved for the potential at each collocation point, ν_m . Using eqs. 3.85 and 3.88 we are able to find the Fourier coefficients at the surface of the electrodes. Using eqs. 3.46 and 3.47 for the ϕ periodic case, and eqs. 3.123 and 3.124 for the z periodic case, in addition to the boundary conditions at each layer we can solve for the potential inside the cylinder.

The boundary conditions at the interface of the p and $p - 1$ layers are

$$\hat{r} \cdot (\epsilon_p^* \bar{E}_p - \epsilon_{p-1}^* \bar{E}_{p-1})|_{r=r_{p-1}} = 0 \quad (3.289)$$

$$\hat{r} \times (\bar{E}_p - \bar{E}_{p-1})|_{r=r_{p-1}} = 0 \quad (3.290)$$

Using eqs. 3.50 and 3.51, we can rewrite the first boundary condition as:

$$\epsilon_p^* \frac{d}{dr} \tilde{\Phi}_n(r)|_{r_{p-1}^+} = \epsilon_{p-1}^* \frac{d}{dr} \tilde{\Phi}_n(r)|_{r_{p-1}^-} \quad (3.291)$$

The superscript for r_{p-1} indicates which layer $\tilde{\Phi}_n$ should be calculated in. The form of $\tilde{\Phi}_n$ is known from eqs. 3.46, 3.47, and 3.124, and using each respectively we have

$$0 = \epsilon_{p-1}^* B_{p-1,0} - \epsilon_p^* B_{p,0} \quad (3.292)$$

$$0 = \epsilon_{p-1}^* r_{p-1}^n A_{p-1,n} - \epsilon_{p-1}^* r_{p-1}^{-n} B_{p-1,n} - \epsilon_p^* r_{p-1}^n A_{p,n} + \epsilon_p^* r_{p-1}^{-n} B_{p,n} \quad (3.293)$$

$$0 = \epsilon_{p-1}^* I_1(k_n r_{p-1}) A_{p-1,n} - \epsilon_{p-1}^* K_1(k_n r_{p-1}) B_{p-1,n} - \epsilon_p^* I_1(k_n r_{p-1}) A_{p,n} + \epsilon_p^* K_1(k_n r_{p-1}) B_{p,n} \quad (3.294)$$

The corresponding equations for the planar case are

$$0 = \epsilon_{p-1}^* B_{p-1,n} - \epsilon_p^* B_{p,n} \quad (3.295)$$

$$0 = \epsilon_{p-1}^* e^{k_n z_{p-1}} A_{p-1,n} - \epsilon_{p-1}^* e^{-k_n z_{p-1}} B_{p-1,n} - \epsilon_p^* e^{k_n z_{p-1}} A_{p,n} + \epsilon_p^* e^{-k_n z_{p-1}} B_{p,n} \quad (3.296)$$

The second boundary condition, eq. 3.290 can be written as

$$E_\phi(r_{p-1}^+, \phi) = E_\phi(r_{p-1}^-, \phi) \quad (3.297)$$

$$E_z(r_{p-1}^+, z) = E_z(r_{p-1}^-, z) \quad (3.298)$$

for the ϕ , and z periodic cases respectively. We can write $E_\phi(r, \phi)$ and $E_z(r, z)$ in terms of $\tilde{\Phi}_n(r)$.

$$E_\phi(r, \phi) = -\frac{1}{r} \frac{\partial}{\partial \phi} \Phi(r, \phi) = \frac{1}{r} \sum_{n=q, 2q, \dots} n \tilde{\Phi}_n(r) \sin n\phi \quad (3.299)$$

$$\tilde{E}_{\phi,n}(r) = \frac{n}{r} \tilde{\Phi}_n(r) \quad (3.300)$$

$$E_z(r, z) = -\frac{\partial}{\partial z} \Phi(r, z) = \sum_{n=1}^{\infty} k_n \tilde{\Phi}_n(r) \sin k_n z \quad (3.301)$$

$$\tilde{E}_{z,n}(r) = k_n \tilde{\Phi}_n(r) \quad (3.302)$$

In both cases, the boundary condition can be written as

$$\tilde{\Phi}_n(r_{p-1}^+) = \tilde{\Phi}_n(r_{p-1}^-) \quad (3.303)$$

Again using the form of $\tilde{\Phi}_n$ known from eqs. 3.46, 3.47, and 3.124, we have

$$0 = A_{p-1,0} + \ln(r_{p-1}) B_{p-1,0} - A_{p,0} - \ln(r_{p-1}) B_{p,0} \quad (3.304)$$

$$0 = r_{p-1}^n A_{p-1,n} + r_{p-1}^{-n} B_{p-1,n} - r_{p-1}^n A_{p,n} - r_{p-1}^{-n} B_{p,n} \quad (3.305)$$

$$0 = I_0(k_n r_{p-1}) A_{p-1,n} + K_0(k_n r_{p-1}) B_{p-1,n} - I_0(k_n r_{p-1}) A_{p,n} - K_0(k_n r_{p-1}) B_{p,n} \quad (3.306)$$

The corresponding equations for the planar case are

$$0 = A_{p-1,0} + z_{p-1} B_{p-1,0} - A_{p-1,0} - z_{p-1} B_{p-1,0} \quad (3.307)$$

$$0 = e^{k_n z_{p-1}} A_{p-1,n} + e^{-k_n z_{p-1}} B_{p-1,n} - e^{k_n z_{p-1}} A_{p,n} - e^{-k_n z_{p-1}} B_{p,n} \quad (3.308)$$

Finally we must apply the boundary conditions at $r = r_e$, and $r = r_0$. Let there be P layers

such that $r_p = r_e$. At r_p we have

$$\tilde{\Phi}_0(r_e) = A_{p,0} + B_{p,0} \ln r_p \quad (3.309)$$

$$\tilde{\Phi}_n(r_e) = r_p^n A_{p,n} + r_p^{-n} B_{p,n} \quad (3.310)$$

$$\tilde{\Phi}_n(r_e) = I_0(k_n r_p) A_{p,n} + K_0(k_n r_p) B_{p,n} \quad (3.311)$$

In the case of a grounded center conductor of radius r_0 we have $\tilde{\Phi}_n(r) = 0$ for all n .

$$0 = A_{1,0} + B_{1,0} \ln r_0 \quad (3.312)$$

$$0 = r_0^n A_{1,n} + r_0^{-n} B_{1,n} \quad (3.313)$$

$$0 = I_0(k_n r_0) A_{1,n} + K_0(k_n r_0) B_{1,n} \quad (3.314)$$

In the case without a center conductor we require $B_{1,n} = 0$ to prevent each expression from exploding as $r_0 \rightarrow 0$ (r_0^{-n} , $\ln r_0$, $K_0(k_n r_0)$).

We can combine these expressions into a matrix form to solve for the coefficients $A_{p,n}$ and $B_{p,n}$ in each layer. As an example we show the matrix for $n \neq 0$ for ϕ periodic, and a grounded center conductor.

$$\begin{bmatrix} r_1^n & r_1^{-n} & -r_1^n & -r_1^{-n} & \dots & \dots & \dots & \dots & \dots & \dots & 0 \\ \epsilon_1^* r_1^n & -\epsilon_1^* r_1^{-n} & -\epsilon_2^* r_1^n & \epsilon_2^* r_1^{-n} & \dots & \dots & \dots & \dots & \dots & \dots & 0 \\ \dots & \dots & \dots & \dots & \dots & \dots & \dots & \dots & \dots & \dots & \dots \\ 0 & \dots & \dots & \dots & \dots & r_{P-1}^n & r_{P-1}^{-n} & -r_{P-1}^n & -r_{P-1}^{-n} & \dots & 0 \\ 0 & \dots & \dots & \dots & \dots & \epsilon_{P-1}^* r_{P-1}^n & -\epsilon_{P-1}^* r_{P-1}^{-n} & -\epsilon_P^* r_{P-1}^n & \epsilon_P^* r_{P-1}^{-n} & \dots & 0 \\ r_0^n & r_0^{-n} & \dots & \dots & \dots & \dots & \dots & \dots & \dots & \dots & 0 \\ 0 & \dots & \dots & \dots & \dots & \dots & r_P^n & r_P^{-n} & \dots & \dots & 0 \\ 0 & \dots & \dots & \dots & \dots & \dots & \dots & \dots & r_{P+1}^n & r_{P+1}^{-n} & \dots \\ 0 & \dots & \dots & \dots & \dots & \dots & \dots & \dots & r_P^n & r_P^{-n} & \dots \\ 0 & \dots & \dots & \dots & \dots & \dots & \dots & \dots & \dots & r_P^n & r_P^{-n} \end{bmatrix} \begin{bmatrix} A_{1,n} \\ B_{1,n} \\ A_{1,n} \\ B_{2,n} \\ \vdots \\ A_{P-1,n} \\ B_{P-1,n} \\ A_{P,n} \\ B_{P,n} \\ A_{P+1,n} \\ B_{P+1,n} \end{bmatrix} = \begin{bmatrix} 0 \\ 0 \\ 0 \\ 0 \\ \vdots \\ 0 \\ 0 \\ 0 \\ \tilde{\Phi}_n(r_e) \\ 0 \\ \tilde{\Phi}_n(r_e) \end{bmatrix} \quad (3.315)$$

As a second example we show the matrix for $n \neq 0$ for a z periodic cylindrical sensor with a

grounded center conductor.

$$\begin{bmatrix} I_0(k_n r_1) & K_0(k_n r_1) & -I_0(k_n r_1) & -K_0(k_n r_1) & \dots & \dots & \dots & \dots & \dots & \dots & 0 \\ \epsilon_1^* I_1(k_n r_1) & -\epsilon_1^* K_1(k_n r_1) & -\epsilon_2^* I_1(k_n r_1) & \epsilon_2^* K_1(k_n r_1) & \dots & \dots & \dots & \dots & \dots & \dots & 0 \\ \dots & \dots & \dots & \dots & \dots & \dots & \dots & \dots & \dots & \dots & \dots \\ 0 & \dots & \dots & \dots & I_0(k_n r_{P-1}) & K_0(k_n r_{P-1}) & -I_0(k_n r_{P-1}) & -K_0(k_n r_{P-1}) & \dots & \dots & 0 \\ 0 & \dots & \dots & \dots & \epsilon_{P-1}^* I_1(k_n r_{P-1}) & -\epsilon_{P-1}^* K_1(k_n r_{P-1}) & -\epsilon_P^* I_1(k_n r_{P-1}) & \epsilon_P^* K_1(k_n r_{P-1}) & \dots & \dots & 0 \\ I_0(k_n r_0) & K_0(k_n r_0) & \dots & \dots & \dots & \dots & \dots & \dots & \dots & \dots & 0 \\ 0 & \dots & \dots & \dots & \dots & \dots & I_0(k_n r_P) & K_0(k_n r_P) & \dots & \dots & 0 \\ 0 & \dots & \dots & \dots & \dots & \dots & \dots & \dots & \dots & I_0(k_n r_{P+1}) & K_0(k_n r_{P+1}) \\ 0 & \dots & \dots & \dots & \dots & \dots & \dots & \dots & \dots & I_0(k_n r_P) & K_0(k_n r_P) \end{bmatrix}$$

$$\times \begin{bmatrix} A_{1,n} \\ B_{1,n} \\ A_{1,n} \\ B_{2,n} \\ \vdots \\ A_{P-1,n} \\ B_{P-1,n} \\ A_{P,n} \\ B_{P,n} \\ A_{P+1,n} \\ B_{P+1,n} \end{bmatrix} = \begin{bmatrix} 0 \\ 0 \\ 0 \\ 0 \\ \vdots \\ 0 \\ 0 \\ 0 \\ \tilde{\Phi}_n(r_e) \\ 0 \\ \tilde{\Phi}_n(r_e) \end{bmatrix} \quad (3.316)$$

The first $2(P-1)$ equations are the boundary conditions between the layers. The next two equations are boundary conditions at the center conductor and at the inside of the electrodes. The final two equations are the boundary conditions for the substrate layer at the electrodes and at the ground plane. All values except the coefficients vector are known. A similar matrix can be formed for the $n = 0$ case.

3.8 Field Lines

In the case where there is no free charge and a spatially uniform permittivity

$$\nabla \times \bar{E} = 0 \quad (3.317)$$

$$\nabla \cdot \bar{E} = 0 \quad (3.318)$$

since $\bar{D} = \epsilon \bar{E}$. Using the identity that the divergence of the curl of a vector is zero we define the electric vector potential, \bar{F} .

$$\bar{E} = -\nabla \times \bar{F} = -\nabla \Phi \quad (3.319)$$

Φ is the electric scalar potential which we have solved for already.

3.8.1 Planar Sensor Field Lines

We can find \bar{F} from Φ

$$\Phi = A_0 + B_0 z + \sum_{n=1}^{\infty} \cos k_n x (A_n e^{k_n z} + B_n e^{-k_n z}) \quad (3.320)$$

$$\begin{aligned} -\nabla \Phi &= \hat{x} \left(\sum_{n=1}^{\infty} k_n \sin k_n x (A_n e^{k_n z} + B_n e^{-k_n z}) \right) + \\ &\quad \hat{z} \left(-B_0 - \sum_{n=1}^{\infty} k_n \cos k_n x (A_n e^{k_n z} - B_n e^{-k_n z}) \right) \end{aligned} \quad (3.321)$$

Taking the curl of \bar{F} we have

$$-\nabla \times \bar{F} = -\hat{x} \left(\frac{\partial F_z}{\partial y} - \frac{\partial F_y}{\partial z} \right) - \hat{y} \left(\frac{\partial F_x}{\partial z} - \frac{\partial F_z}{\partial x} \right) - \hat{z} \left(\frac{\partial F_y}{\partial x} - \frac{\partial F_x}{\partial y} \right) \quad (3.322)$$

Since $E_y = 0$ we attempt a solution where F_x and F_z are both zero.

$$\bar{E} = -\nabla \times \bar{F} = \hat{x} \left(\frac{\partial F_y}{\partial z} \right) - \hat{z} \left(\frac{\partial F_y}{\partial x} \right) \quad (3.323)$$

We now equate each of the vector components.

$$\frac{\partial F_y}{\partial z} = \sum_{n=1}^{\infty} k_n \sin k_n x (A_n e^{k_n z} + B_n e^{-k_n z}) \quad (3.324)$$

$$\frac{\partial F_y}{\partial x} = B_0 + \sum_{n=1}^{\infty} k_n \cos k_n x (A_n e^{k_n z} - B_n e^{-k_n z}) \quad (3.325)$$

We integrate both equations to find two expressions for F_y .

$$F_y = C(x) + \sum_{n=1}^{\infty} \sin k_n x (A_n e^{k_n z} - B_n e^{-k_n z}) \quad (3.326)$$

$$F_y = D(z) + B_0 x + \sum_{n=1}^{\infty} \sin k_n x (A_n e^{k_n z} - B_n e^{-k_n z}) \quad (3.327)$$

$C(x)$ and $D(z)$ are integration constants. These equations are the same when $D(z) = 0$ and $C(x) = B_0 x$.

$$F_y(x, z) = B_0 x + \sum_{n=1}^{\infty} \sin k_n x (A_n e^{k_n z} - B_n e^{-k_n z}) \quad (3.328)$$

By definition the electric field lines are

$$\frac{dz}{dx} = \frac{E_z}{E_x} \quad (3.329)$$

We know from equation 3.323 the relationship between $E_{x,z}$ and F_y

$$\frac{dz}{dx} = -\frac{\partial F_y / \partial x}{\partial F_y / \partial z} \quad (3.330)$$

Rearranging we find that terms can be equated to the total differential of F_y .

$$\frac{\partial F_y}{\partial z} dz + \frac{\partial F_y}{\partial x} dx = dF_y = 0 \quad (3.331)$$

$$F_y(x, z) = F_y(x_0, z_0) \quad (3.332)$$

We conclude that the electric vector potential is constant along each field line. A direct expression for the field line cannot be written from eq. 3.328, however we can find what the constant is for a field line that passes through a point $\{x_0, z_0\}$. In practice this is sufficient for plotting the desired field lines. When plotting field lines that continue from one material layer to another, such as at the interface between the substrate and the first material, the constants A_n and B_n in the expression for the electric vector potential change. Further the constant $F_y(x_0, z_0)$ that defines the field line also changes. This is expected since in deriving eq. 3.318 from Gauss' law, we assumed the permittivity is spatially invariant. To continue the field line into the layer we must evaluate F_y at the point on the interface between the two materials at which the field line ended. This serves as the new constant that the field line follows.

In Section 4.1.4 we present a number of studies where we plot the potential in the solution region.

3.8.2 ϕ Periodic Sensor Field Lines

We can find \bar{F} from Φ

$$\Phi = A_0 + B_0 \ln r + \sum_{n=q,2q,\dots}^{\infty} (A_n r^n + B_n r^{-n}) \cos n\phi \quad (3.333)$$

Taking the negative gradient of Φ we have

$$-\nabla\Phi = -\hat{r} \left\{ \frac{B_0}{r} + \sum_{n=q,2q,\dots}^{\infty} n (A_n r^{n-1} + B_n r^{-n-1}) \cos n\phi \right\} \quad (3.334)$$

$$+\hat{\phi} \sum_{n=q,2q,\dots}^{\infty} n (A_n r^{n-1} + B_n r^{-n-1}) \sin n\phi \quad (3.335)$$

The negative curl of \bar{F} is

$$-\nabla \times \bar{F} = -\hat{r} \left(\frac{1}{r} \frac{\partial F_z}{\partial \phi} - \frac{\partial F_\phi}{\partial z} \right) - \hat{\phi} \left(\frac{\partial F_r}{\partial z} - \frac{\partial F_z}{\partial r} \right) - \hat{z} \frac{1}{r} \left(\frac{\partial(rF_\phi)}{\partial r} - \frac{\partial F_r}{\partial \phi} \right) \quad (3.336)$$

Since $E_z = 0$ we attempt a solution where F_ϕ and F_r are both zero.

$$-\nabla \times \bar{F} = -\hat{r} \frac{1}{r} \frac{\partial F_z}{\partial \phi} + \hat{\phi} \frac{\partial F_z}{\partial r} \quad (3.337)$$

Setting the components of the vectors equal we have

$$\frac{1}{r} \frac{\partial F_z}{\partial \phi} = \frac{B_0}{r} + \sum_{n=q,2q,\dots}^{\infty} n (A_n r^{n-1} + B_n r^{-n-1}) \cos n\phi \quad (3.338)$$

$$\frac{\partial F_z}{\partial r} = \sum_{n=q,2q,\dots}^{\infty} n (A_n r^{n-1} + B_n r^{-n-1}) \sin n\phi \quad (3.339)$$

Solving both equations for F_z by integration we have

$$F_z = B_0 \phi + C(r) + \sum_{n=q,2q,\dots}^{\infty} (A_n r^n - B_n r^{-n}) \sin n\phi \quad (3.340)$$

$$F_z = D(\phi) + \sum_{n=q,2q,\dots}^{\infty} (A_n r^n - B_n r^{-n}) \sin n\phi \quad (3.341)$$

Equating the two solutions we determine $C(r) = 0$ and $D(\phi) = B_0 \phi$.

$$F_z = B_0 \phi + \sum_{n=q,2q,\dots}^{\infty} (A_n r^n - B_n r^{-n}) \sin n\phi \quad (3.342)$$

The electric field lines satisfy the following equation

$$\frac{dr}{rd\phi} = \frac{E_r}{E_\phi} \quad (3.343)$$

Substituting for E_r and E_ϕ in terms of F_z we have

$$\frac{dr}{rd\phi} = -\frac{\partial F_z / \partial \phi}{r \partial F_z / \partial r} \quad (3.344)$$

Rearranging we have the equation for the total differential of F_z

$$\frac{\partial F_z}{\partial r} dr + \frac{\partial F_z}{\partial \phi} d\phi = dF_z = 0 \quad (3.345)$$

We therefore conclude that a field line that passes through the point $\{r_o, \phi_o\}$ must satisfy

$$F_z(r, \phi) = F_z(r_o, \phi_o) \quad (3.346)$$

3.8.3 z Periodic Sensor Field Lines

We can find \bar{F} from Φ

$$\Phi = A_0 + B_0 \ln r + \sum_{n=1}^{\infty} \cos k_n z (A_n I_0(k_n r) + B_n K_0(k_n r)) \quad (3.347)$$

Using the following identities

$$\frac{d}{dx} [x^{-n} I_n(x)] = x^{-n} I_{n+1}(x) \quad (3.348)$$

$$\frac{d}{dx} [x^{-n} K_n(x)] = -x^{-n} K_{n+1}(x) \quad (3.349)$$

$$\frac{d}{dx} G(ax) = a \frac{d}{d(ax)} G(ax) \quad (3.350)$$

and the gradient in cylindrical coordinates we have

$$\begin{aligned} -\nabla\Phi &= \hat{r} \left(-\frac{B_0}{r} - \sum_{n=1}^{\infty} k_n \cos k_n z (A_n I_1(k_n r) - B_n K_1(k_n r)) \right) + \\ &\quad \hat{z} \left(\sum_{n=1}^{\infty} k_n \sin k_n z (A_n I_0(k_n r) + B_n K_0(k_n r)) \right) \end{aligned} \quad (3.351)$$

Taking the curl of \bar{F} we have

$$-\nabla \times \bar{F} = -\hat{r} \left(\frac{1}{r} \frac{\partial F_z}{\partial \phi} - \frac{\partial F_\phi}{\partial z} \right) - \hat{\phi} \left(\frac{\partial F_r}{\partial z} - \frac{\partial F_z}{\partial r} \right) - \hat{z} \frac{1}{r} \left(\frac{\partial(rF_\phi)}{\partial r} - \frac{\partial F_r}{\partial \phi} \right) \quad (3.352)$$

Since $E_\phi = 0$ we can attempt a solution where F_r and F_z are both zero.

$$\bar{E} = -\nabla \times \bar{F} = \hat{r} \left(\frac{\partial F_\phi}{\partial z} \right) - \hat{z} \frac{1}{r} \left(\frac{\partial(rF_\phi)}{\partial r} \right) \quad (3.353)$$

We would proceed by equating the vector components to those in eq. 3.351.

$$\frac{\partial F_\phi}{\partial z} = -\frac{B_0}{r} - \sum_{n=1}^{\infty} k_n \cos k_n z (A_n I_1(k_n r) - B_n K_1(k_n r)) \quad (3.354)$$

$$-\frac{1}{r} \frac{\partial(rF_\phi)}{\partial r} = \sum_{n=1}^{\infty} k_n \sin k_n z (A_n I_0(k_n r) + B_n K_0(k_n r)) \quad (3.355)$$

We integrate the first equation with respect to z and have

$$F_\phi = C(r) - \frac{B_0}{r} z - \sum_{n=1}^{\infty} \sin k_n z (A_n I_1(k_n r) - B_n K_1(k_n r)) \quad (3.356)$$

We would like to integrate the second equation to find an expression for F_ϕ and resolve the constants so that both equations are satisfied. While the first equation is trivial to integrate, the second equation is quite challenging to do so directly. Instead we simply substitute the solution for the first equation as F_ϕ in the second. The result is an equation for the constant $C(r)$.

$$C(r) + r \frac{dC(r)}{dr} = 0 \quad (3.357)$$

The solution $C(r) = A/r$ where A is a constant, or $C(r) = 0$. We see from eq. 3.353 that neither solution has an effect on the electric field and choose $C(r) = 0$ for simplicity.

By definition the electric field lines are

$$\frac{dz}{dr} = \frac{E_z}{E_r} \quad (3.358)$$

We know from equation 3.353 the relationship between E_r and E_z and F_ϕ

$$\frac{dz}{dr} = -\frac{1}{r} \frac{\partial(rF_\phi)/\partial r}{\partial F_\phi/\partial z} \quad (3.359)$$

Rearranging the terms and replacing with the total differential we have

$$r \frac{\partial F_\phi}{\partial z} dz + \frac{\partial(rF_\phi)}{\partial r} dr = 0 \quad (3.360)$$

$$r \frac{\partial F_\phi}{\partial z} dz + \left(r \frac{\partial F_\phi}{\partial r} + F_\phi \right) dr = 0 \quad (3.361)$$

This form is equivalent to

$$d(rF_\phi) = 0 \quad (3.362)$$

We therefore conclude that a field line that passes through the point $\{r_o, z_o\}$ must satisfy

$$F_\phi(r, z) = \frac{r_o F_\phi(r_o, z_o)}{r} \quad (3.363)$$

In Section 4.1.5 we present a number of studies using the electric field lines.

3.9 Chapter Summary

In this chapter we have introduced the interdigital dielectrometry sensor. We have illustrated several methods of exciting and measuring the sensor response and have shown that the short-circuit current mode (SCCM) provides the greatest accuracy and ease of use. We then provided a derivation for the transmittance for the planar (Section 3.2), ϕ periodic (Section 3.3), and z periodic sensors (Section 3.4). We have generalized the planar sensor so that an arbitrary topology and excitation can be considered (Section 3.5). A planar dual periodic sensor has also been considered (Section 3.6). In this case the electrodes are rectangular patches forming a sensor that is periodic in two directions.

In addition to finding the transmittance, all field quantities can be found including the electric potential and electric field. The procedure for finding the potential is described in Section 3.7. The electric field can be found directly from the potential, however, it is also interesting to illustrate the field using field lines. We provide a method to determine the electric field lines in Section 3.8.

Chapter 4

Dielectrometry Sensor Design

Interdigital dielectrometry sensors provide a means to measure a materials dielectric properties with minimal intrusion. In principle, dielectrometry sensors only require access to one face of the material to be tested. Taking meaningful measurements begins with properly designing sensors. Significant efforts have been made in previous research to perform parameter studies where every design choice is considered over a range of practical values for an application [54]. Sensor design involves understanding the tradeoffs between penetration depth, measurement sensitivity, dynamic range, and noise tolerance [55].

In this chapter we verify the theoretical results for the z and ϕ periodic cylindrical sensors. The cylindrical sensor response is compared to the equivalent planar sensor case. As the radius of the cylinder becomes large compared to the wavelength we find that the behavior of the cylindrical geometry sensors approaches that of the planar geometry sensors.

4.1 Comparison of Cylindrical and Planar Sensors

In this section, the new results for the ϕ and z periodic cylindrical sensors derived in the previous chapter are compared to the planar dielectrometry sensor solution and results from finite element simulations. For both the ϕ and z periodic sensors, as the distance from the cylinder's axis to the surface of the electrodes is increased, the geometry approaches that of the planar sensor. This can be seen directly from the equations in sections 3.3 and 3.4 when the limit is taken as r_e approaches infinity. This limit serves in part as a verification of the theoretical results.

In order to compute results for the formulations in Chapter 3, a software implementation has been developed using MATLAB [56], Mathematica [57], and the Mathematica Symbolic Toolbox for

MATLAB [58]. For planar problems the stand alone executable *GETGP* (“Get Gain and Phase”), developed by Yanko Sheiretov is used [59,60]. Obviously only a finite number of Fourier terms and collocation points can be calculated in finite time. Most problems converge acceptably well with about 500 Fourier terms and 50 collocation points. Problems solved using these parameters can be solved in a few seconds. When greater accuracy is required the number of Fourier terms and collocation points can be increased.

4.1.1 Planar Sensor Geometry Simulations

We begin our comparison by first considering the results for planar simulations using Maxwell 2D and compare it to the results calculated using MATLAB code and *GETGP*. Similar to the derivation in Chapter 3 the sensor can be reduced to a half wavelength in Maxwell with the appropriate choice of boundary conditions. Two issues exist that cause the derivation and the simulation to differ. A finite electrode thickness is required, a feature not taken account for in the theoretical calculations. Also when no top ground plane is present, the solution space extends to infinity which cannot be simulated in finite element software. To maintain a finite solution space, Maxwell provides a balloon boundary condition which attempts to reproduce the same result. We begin by investigating the effectiveness of the balloon boundary condition.

Maxwell Study of Balloon Boundary Condition

We begin with a study of the size of the simulation space in Maxwell 2D. The setup is shown in Fig. 4-1. The distance from the sensor to the top of the simulation space, H , is varied. Theoretically this has no effect, however, at the top surface the balloon boundary condition is used for simulation. Ideally the balloon should act as an extension of the simulation space, however we find the results depend dramatically on the choice of distance to the balloon. To demonstrate, 1 and 5 mm sensors are simulated. The sensor and simulation parameters used in the simulation are listed in Table 4.1. The choice of substrate permittivity and thickness match those of the Teflon substrate available from Polyflon Company who manufactured the sensors for experiments [61]. The boundary conditions are summarized in Table 4.2. The convergence condition was an energy error of less than 0.001% [62].

Figure 4-2 shows the numerical and simulation results for the 1 and 5 mm sensors. The size of the simulation space clearly has a dramatic effect if kept too small. In fact, a fortunate choice of H could cause the illusion of perfect agreement with theory. We notice that a larger ratio of H to λ is needed for the 1 mm sensor than the 5 mm sensor. Solid lines are superimposed on the figures indicating the theoretical capacitance as calculated from the MATLAB code and *GETGP*. The theoretical lines are not subject to any variation with H since it is not a parameter in the

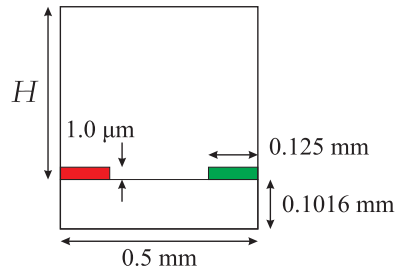


Figure 4-1: Maxwell 2D simulation setup for study of the balloon boundary condition. A half wavelength is simulated and the calculated capacitance per unit length is doubled. Numeric values are for the $\lambda = 1$ mm sensor case. This figure is not to scale.

Table 4.1: Balloon Boundary Condition Study: Sensor and Simulation Parameters

Sensor Parameters		
Sensor Wavelength	λ	1, 5 mm
Substrate Relative Permittivity	ϵ_s	2.1
Substrate Thickness	t_s	.1016 mm (4 mils)
Drive electrode width		$\lambda/4$
Sense electrode width		$\lambda/4$
Electrode Thickness (Theory)		0 μm
Electrode Thickness (Maxwell 2D)		1 μm
Permittivity of MUT		ϵ_0
Conductivity of MUT		0
Simulation Parameters		
Number of Fourier Terms	N	1000
Number of Collocation Points	K	50

Table 4.2: Balloon Boundary Condition Study: Simulation Boundary Conditions

Surface of Volume	Boundary Condition
Top of Bounding Box (BB):	Balloon (Voltage)
Right and Left Sides of BB:	Even Symmetric
Bottom of BB:	Value, 0.0 V
Drive Electrode:	Voltage, 1.0 V
Sense Electrode:	Voltage, 0.0 V

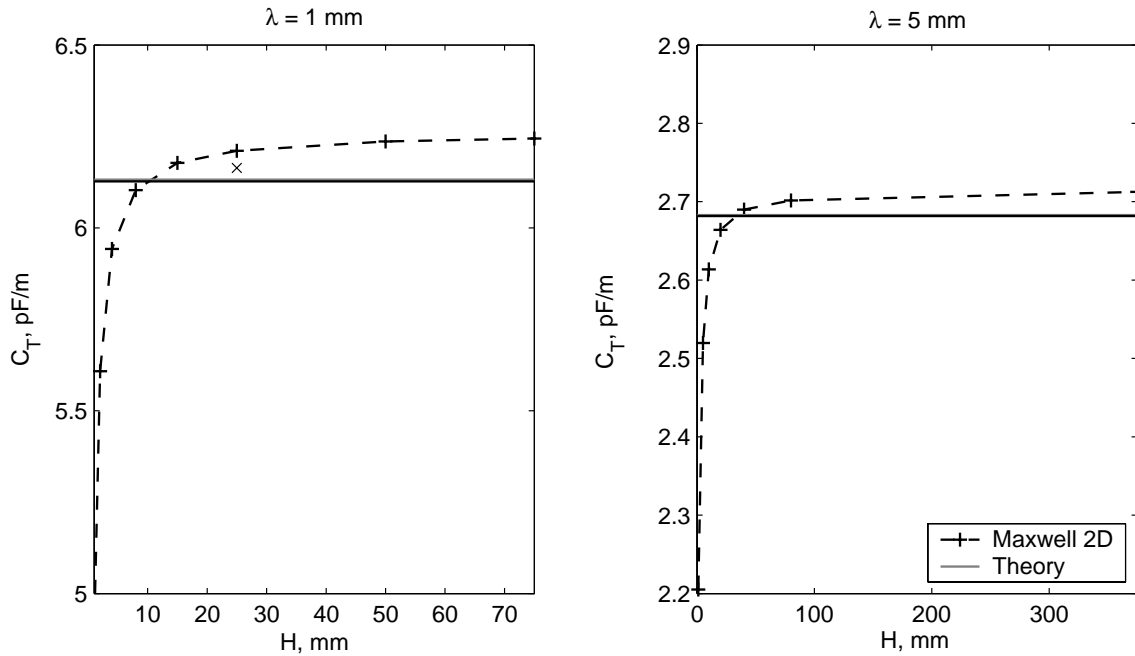


Figure 4-2: Results for the simulation and theory study of balloon boundary condition. The solid lines indicate the theoretical capacitance value which is independent of H . The Maxwell 2D simulation results are shown as dashed lines with data points indicated by a +. The \times at $H = 25$ in the 1 mm figure indicates the capacitance when the electrode thickness is reduced to $0.5 \mu\text{m}$.

theoretical formulation. The MATLAB code was solved using 1,000 Fourier terms while *GETGP*, which is faster, solved for 3,000 Fourier terms.

Above a certain H the capacitance is no longer varying indicating a sufficiently sized simulation space. As expected, the finite thickness of the electrodes in simulation increases the capacitance. We find for the largest H simulated (75 and 375 mm), this results in an error from theory of 1.83%, and 1.09% for the 1 and 5 mm sensors respectively. This is much larger than the simulation error allowing us to attribute the difference to the electrode thickness. To further demonstrate this, we show the capacitance can be reduced by reducing the electrode thickness. Maxwell 2D limits the ratio of the largest dimension to the smallest dimension in a simulation. We demonstrate by reducing the electrode thickness to $0.5 \mu\text{m}$ when $H = 25$ mm ($25 \text{ mm}/0.5 \mu\text{m} = 50,000$). The result is plotted as an \times in Fig. 4-2 and shows a reduction in “error” by about a factor of 2.

The actual electrode thickness for production sensors is about 17 microns (0.7 mils). This additional thickness increases the capacitance by 22% to 7.458 pF/m for the 1 mm sensor, but only by 8.8% to 2.918 pF/m for a 5 mm sensor. If we use theory which assumes no electrode thickness this corresponds to the capacitance if the MUT permittivity was $1.20\epsilon_0$ for the 1 mm sensor, but

only $1.08\epsilon_0$ for the 5 mm sensor. Note that the retrieved permittivity has a nonlinear relationship to the capacitance when the MUT and substrate are of different permittivities.

This study has highlighted the necessity of maximizing the simulation space because of the limitations of the balloon boundary condition, and has also drawn attention to the effect electrode thickness has on the measured capacitance.

Capacitance Study with Varying Top Ground Plane Height

In the previous study we saw that placing an artificial limit on the size of the simulation space can have a significant consequence on simulation results in Maxwell 2D. Placing a ground plane on top of the MUT places a physical limit on the fields, and we expect simulation and theoretical results to be in agreement. Any differences are to be attributed to the finite electrode thickness. The sensor and simulation parameters are the same as in Table 4.1, and the boundary conditions are the same as in Table 4.2, with the exception of the top of the bounding box which is now an equipotential surface at zero volts (Value, 0.0 V).

Figure 4-3 shows the simulation and theoretical results. The capacitance between the drive and sense electrode is related to the number of field lines that begin on the drive electrode and terminate on the sense electrode. The presence of the substrate ground plane and the top ground plane, forces several field lines to terminate on these surfaces reducing the drive-sense capacitance. As the distance increases and approaches infinity, the geometry is identical to the case without a top ground plane, since by definition the potential at infinity is zero.

We see once again that the 1 mm sensor is more sensitive to the electrode thickness than the 5 mm sensor. The black curve shows the theoretical value while the grey curve shows the value from simulation using a 1 μm electrode thickness. The dashed line shows the results for the practical electrode thickness of 17 μm .

4.1.2 ϕ Periodic Sensor

We now study the behavior of the ϕ periodic sensor introduced in section 3.3 and shown in Fig. 3-6(a). Again we note that the wavelength must be an integer multiple of the circumference for the theoretical solution. The circumference serves as the upper bound for the wavelength.

We present two studies. In the first, the radius of the center conductor, r_0 is proportional to the electrode radius, r_e , that is $r_0 = Ar_e$. The study considers several values of A , as the circumference is varied from 1 to 150 wavelengths. In the second study, the distance between the center conductor and the electrodes is fixed, $A = r_e - r_0$. The 1 mm sensor parameters given in Table 4.1 are used in simulation. The ϕ periodic sensor results are compared to the equivalent planar sensor results. The

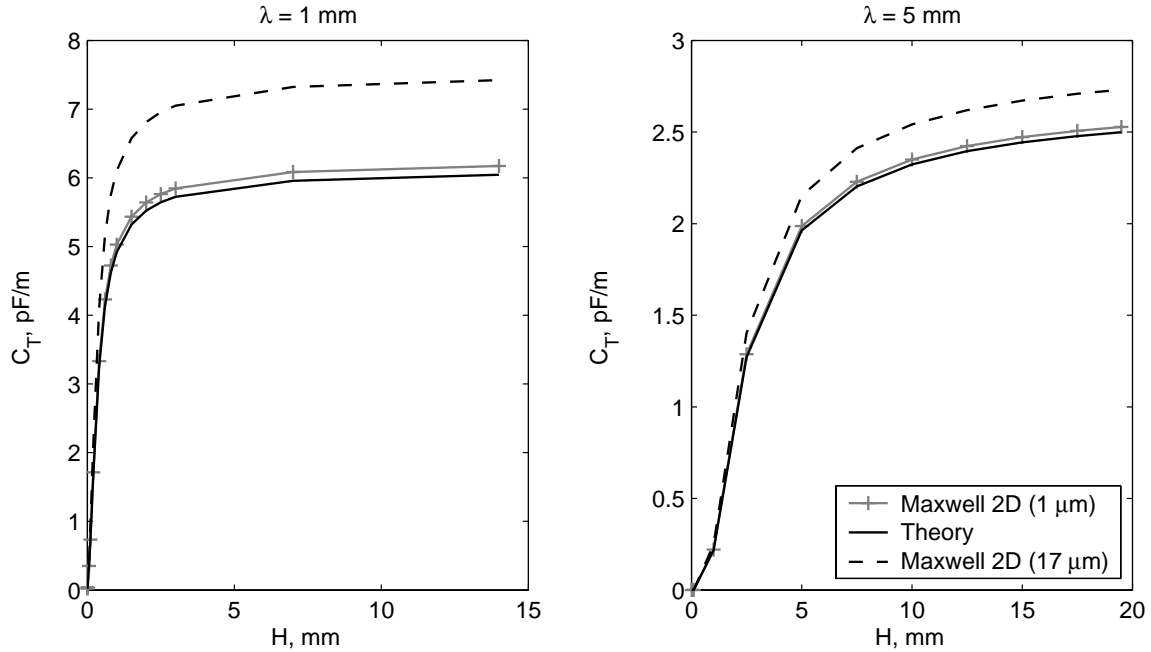


Figure 4-3: Theoretical and simulation results for a planar sensor where the distance, H , to the top ground plane is varied. The results for the practical electrode thickness of $17 \mu\text{m}$ are also shown.

equivalent planar sensor is equivalent in that all material dimensions are matched by the coordinate transformation, $z = -(r - r_e)$ and $x = \phi r$.

Simulation of this geometry in Maxwell 2D is generally not practical for large ratios of circumference to wavelength since it does not seem possible to simulate a single “pie slice” of the geometry. The entire cylinder must be simulated. The reason is that symmetric boundary conditions cannot be applied along angular boundaries. Several simulations with small ratios are done to verify the theoretical results.

ϕ Periodic Sensor Study: $r_0 = Ar_e$

In our first demonstration we place a grounded center conductor in the center of a cylindrical air rod and vary the radius of the electrodes and the center conductor, while holding the ratio constant. Ratio’s of 0 (no center conductor), 0.1, 0.6, 0.8, 0.9, and 0.95 are simulated. The circumference ($2\pi r_e$) is varied from one wavelength (1 mm) to 150 wavelengths. Figure 4-4 shows an example setup where the circumference is six wavelengths. Theoretical capacitances are calculated using the ϕ periodic sensor formulation and compared with the equivalent planar sensor. The results are shown in Fig. 4-5. The solid lines represent the cylindrical sensor capacitance values and the dotted

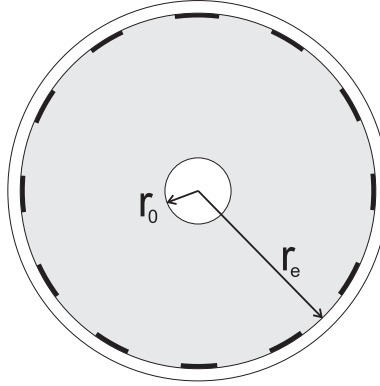


Figure 4-4: Cross-section of a ϕ periodic sensor with a center conductor. The radius of the center conductor is r_0 and the radius of the electrodes is r_e . In this image the circumference equals six wavelengths and $r_0 = 0.2r_e$. In the first study the ratio r_0/r_e is held constant. In the second study the difference $r_e - r_0$ is held constant.

lines represent the capacitance for the equivalent planar sensor. Note that the capacitance is per meter of sense electrode, *not* per meter of rod. This could be determined by multiplying by the number of sense electrodes or equivalently the circumference to wavelength ratio.

We see that for ratios close to one, the difference between the cylindrical sensor and the planar sensor is quite small. As A is decreased, the difference becomes more significant, particularly when the circumference is only a few wavelengths. As the circumference increases, the distance between the electrodes and the center conductor also increases. For all choices of A , as $r_e \rightarrow \infty$ the capacitance will converge to the same value, since the distance to the top ground plane also approaches infinity. Figure 4-5 also presents the convergence of the ϕ periodic cylindrical sensor to the equivalent planar capacitances. Convergence is defined as

$$\text{Convergence} = \frac{C_\phi - C_x}{C_x} \quad (4.1)$$

where C_ϕ and C_x are the capacitances of the ϕ periodic and planar sensors respectively. The results clearly show convergence at large ratios of circumference to wavelength, but different behaviors at lower ratios.

To further verify the results, Maxwell 2D simulations are done for the six different ratios for the $2\pi r_e/\lambda = 1$ cases. The electrode thickness in the simulation was $0.1 \mu\text{m}$. Each result is shown as an \times in Fig. 4-5 and is in good agreement with the theoretical result. A numerical comparison is shown in Table 4.3. In most cases the difference between simulation and theory is only a few percent. As the capacitance decreases, it becomes more difficult to estimate numerically.

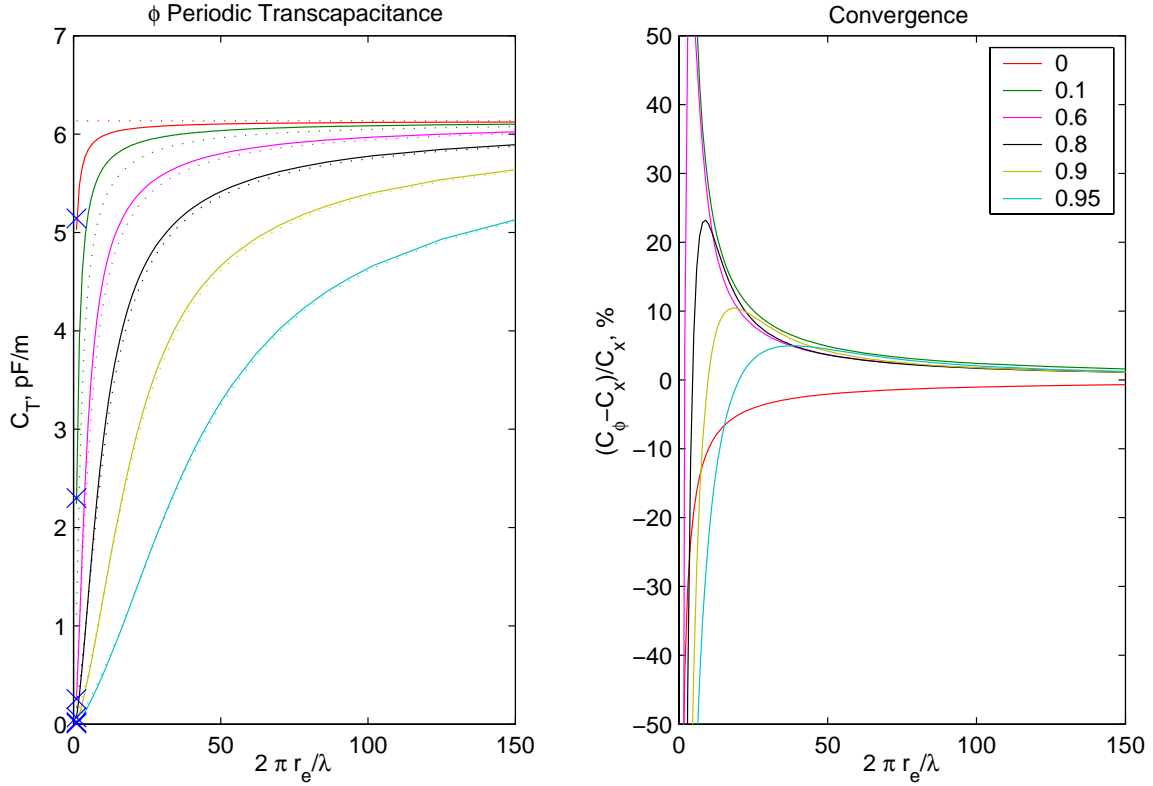


Figure 4-5: Capacitance of ϕ periodic sensor when the ratio of the center conductor diameter to the electrode radius is held constant, $r_0 = Ar_e$. Legend indicates the values of A . The left figure shows the calculated capacitance for the ϕ periodic case (solid) and the equivalent planar case (dotted) as the ratio of the circumference to the wavelength is varied. Each \times represents the corresponding result from Maxwell 2D simulations. The percent difference is shown in the right figure. Simulation parameters are summarized in Table 4.1 ($\lambda = 1$ mm).

Table 4.3: ϕ periodic sensor comparison of simulation to theory for $r_0 = Ar_e$ and $2\pi r_e = \lambda = 1$ mm.

r_o	C_T Maxwell (pF/m)	C_T Theory (pF/m)	% Difference
$0r_e$	5.142	5.0242	2.3
$0.1r_e$	2.300	2.2372	2.8
$0.6r_e$	0.256	0.2460	4.1
$0.8r_e$	0.069	0.0655	5.3
$0.9r_e$	0.020	0.0187	7.0
$0.95r_e$	0.006	0.005	20

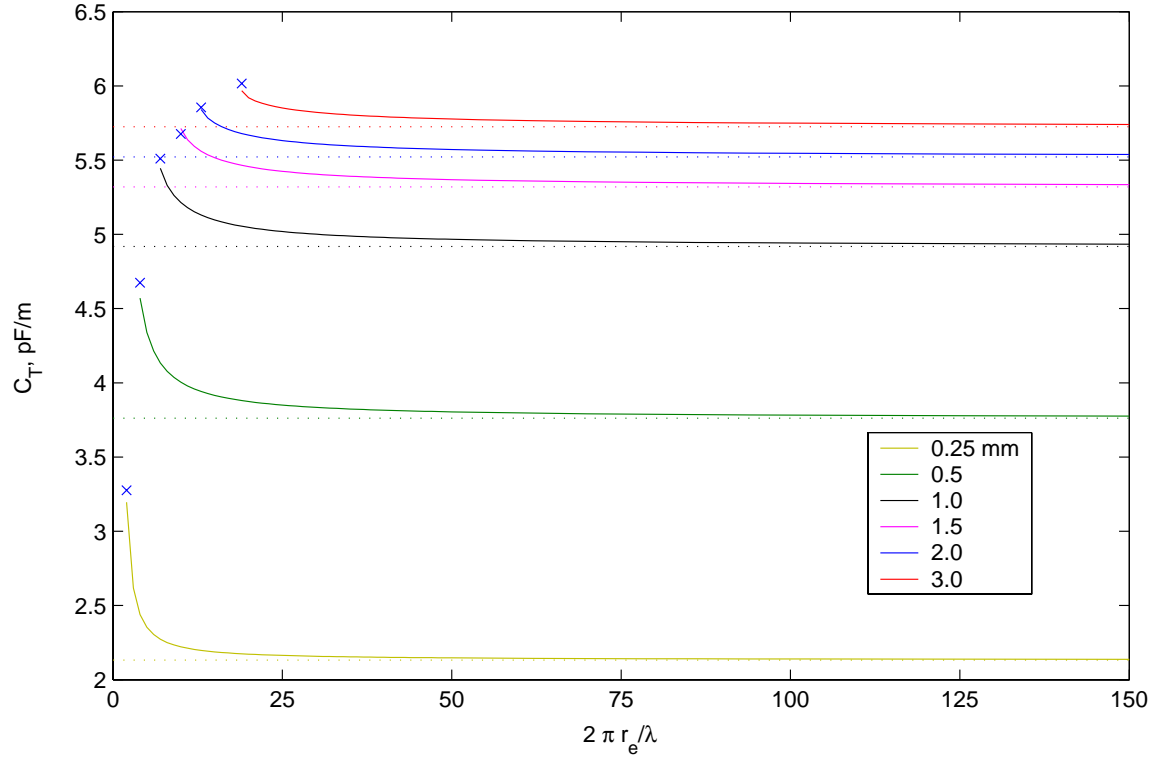


Figure 4-6: Capacitance calculated from theory for the ϕ periodic sensor with center conductors a fixed distance from the electrodes, $A = r_e - r_0$. The legend indicates the value of A . The dotted curves are the planar equivalent capacitances. Each \times represents the corresponding result from Maxwell 2D simulations. Simulation parameters are summarized in Table 4.1 ($\lambda = 1$ mm).

ϕ **Periodic:** $A = r_e - r_0$

We now set the distance between the electrodes and the center conductor constant (see Fig. 4-4). Depending on the choice of distance this may require a circumference of several wavelengths to achieve. Figure 4-6 shows the results from the ϕ periodic sensor theory (solid) for several different choices of $r_e - r_0$. The dotted lines are for the equivalent planar case which does not vary with $2\pi r_e/\lambda$. Simulations in Maxwell 2D are done for the minimum circumference cases with an electrode thickness of $0.1 \mu\text{m}$. Each result from Maxwell 2D is plotted as an \times in the figure. A numerical comparison of the ϕ periodic theory and the Maxwell 2D result is given in Table 4.4. The simulation results are in excellent agreement with the theoretical results.

Table 4.4: ϕ periodic sensor comparison of simulation to theory for select cases of $A = r_e - r_0$.

$r_e - r_0$	r_0	$2\pi r_e/\lambda$	C_T Maxwell	C_T Theory	Difference
0.25 mm	0.068 mm	2	3.276 pF/m	3.1953 pF/m	2.53 %
0.5	0.137	4	4.673	4.5706	2.24
1.0	0.114	7	5.510	5.4452	1.19
1.5	0.092	10	5.676	5.7139	-0.66
2.0	0.069	13	5.854	5.8417	0.21
3.0	0.024	19	6.015	5.9677	0.80

4.1.3 z Periodic Sensor

The z periodic sensor is easily simulated in Maxwell 2D as a device with axial symmetry. Maxwell 2D again permits the use of symmetric boundary conditions. Unlike the ϕ periodic case, the geometry is easily varied with the use of the parametric sweep feature.

The same tests used for the ϕ periodic cylindrical sensor are used here. In this case the circumference need not be an integer number of wavelengths. There is no restriction on the radius, r_e . Again the 1 mm sensor parameters are assumed from Table 4.1.

z Periodic: $r_0 = Ar_e$

The ratio of r_0/r_e is held constant, and the ratio of circumference to the wavelength is varied from 0 to 100. The expected behavior is convergence to the planar air capacitance as the radius becomes sufficiently large. The results shown in Fig. 4-7 clearly show this tendency. The results are quite similar to the ϕ periodic case. The dotted curves representing the equivalent planar case are the same as in the ϕ periodic case and reproduced here for comparison. Maxwell 2D simulations are done for the case $r_0 = 0.8r_e$ for several different radii. While the simulated values are slightly higher than the theoretical values as expected from the finite electrode thickness, the agreement is still excellent.

z Periodic: $A = r_e - r_0$

In this set of simulations the distance between the center conductor and electrodes is held constant. This sets the minimum radius. The simulation results are shown in Fig. 4-8. The first point of each curve is for the minimum radius and no center conductor is present. The second point increases the radius slightly so that the center conductor has a radius of 1.6 μm . The characteristic shape is slightly different than that observed for the ϕ periodic response in Fig. 4-6. In that case the response monotonically decreased as the radius increased until the planar response was reached. In

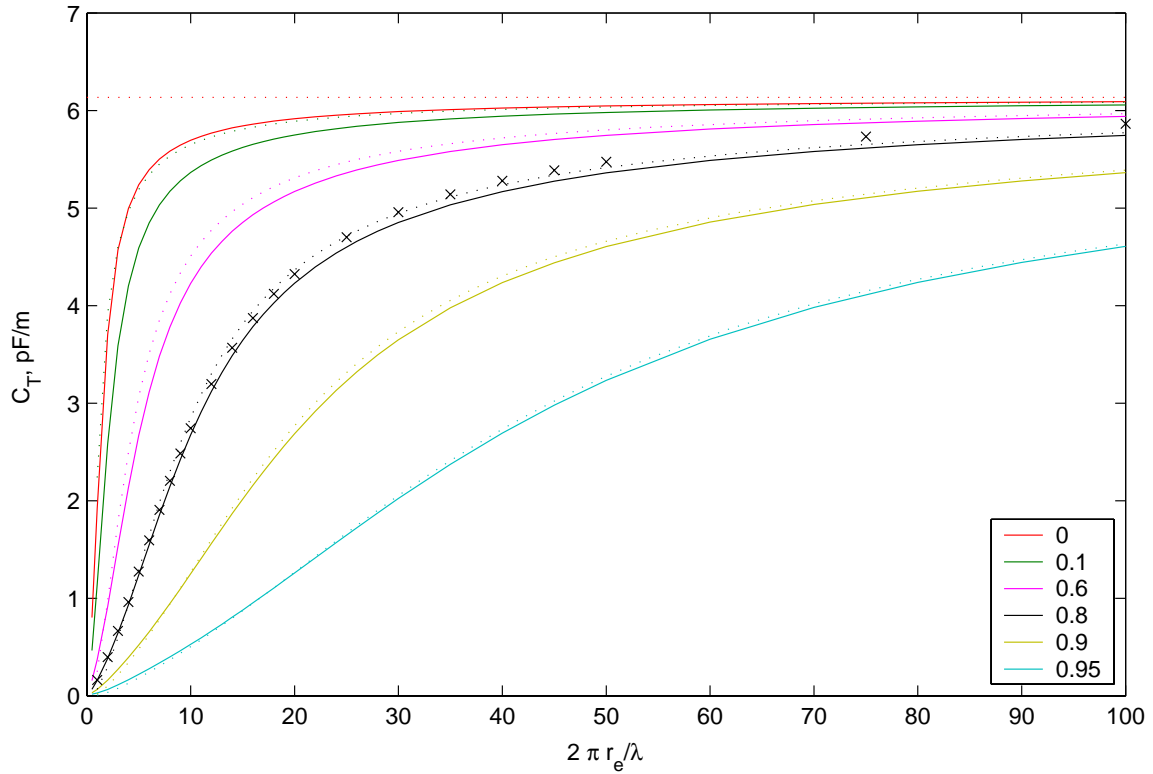


Figure 4-7: Capacitance of Z periodic sensor when the ratio of the center conductor diameter to the electrode radius is held constant, $r_0 = Ar_e$. Legend indicates the values of A . The calculated capacitance for the z periodic case is shown (solid) as well as the equivalent planar case (dotted). Each \times represents data from Maxwell 2D simulations for the $r_0 = 0.8r_e$ case. Simulation parameters are summarized in Table 4.1 ($\lambda = 1$ mm).

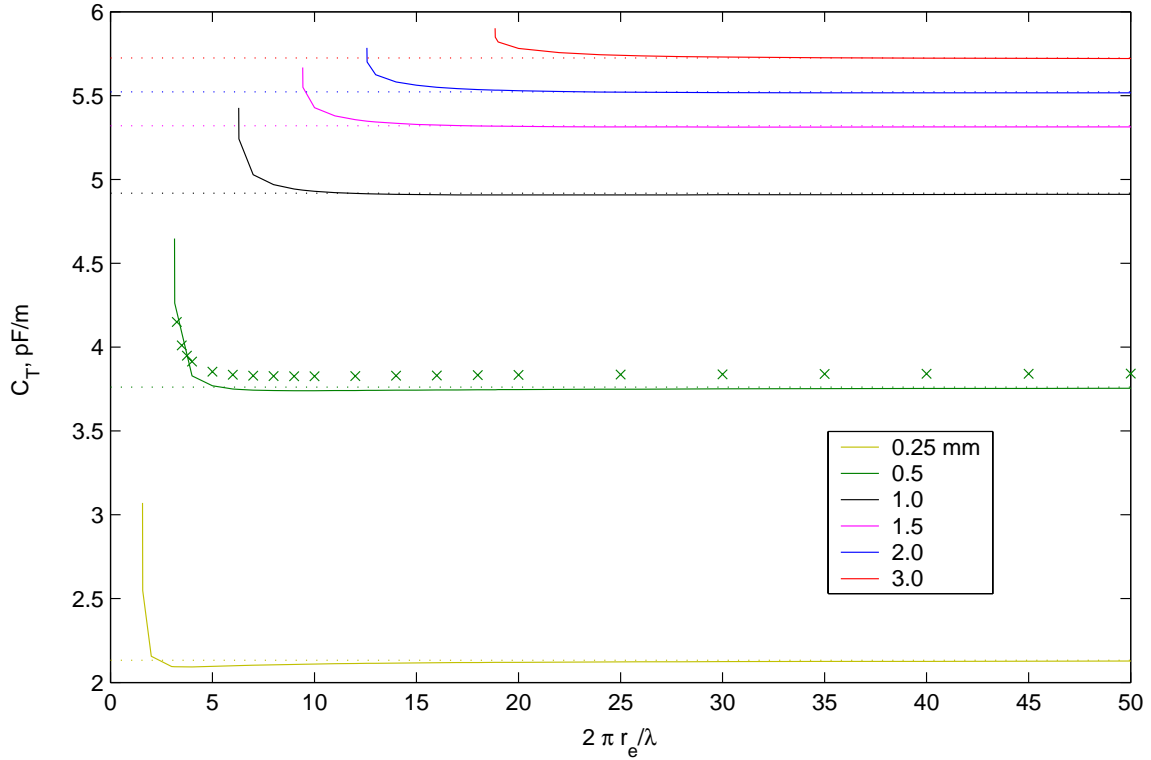


Figure 4-8: Capacitance for z periodic sensor with center conductors a fixed distance from the electrodes, $A = r_e - r_0$. The legend indicates the value of A . The calculated capacitance for the z periodic case is shown (solid) as well as the equivalent planar case (dotted). Each \times represents data from Maxwell 2D simulations for the $r_e - r_0 = 0.5$ mm case. Simulation parameters are summarized in Table 4.1 ($\lambda = 1$ mm).

this case however, the response initially is higher than the planar case. As the radius is increased the capacitance drops below that of the planar case, and then approaches it by increasing. The Maxwell simulated case, shown with crosses, is slightly higher than the theoretical value. This is again due to the thickness of the electrodes. It has the same shape characteristics described for the theoretical curves.

4.1.4 Potential in the Solution Region

In order to find the admittance of the sensor/MUT system we find the potential at the surface of the electrodes. Knowing the potential at this surface allows us to find the potential everywhere inside the solution region. This is done by applying boundary conditions and solving for the coefficients of each spatial Fourier mode as described in Section 3.7. We plot the amplitude of the potential inside all the materials to further demonstrate the consistency of the theoretical and simulation solutions.

As an example we consider the case with a top ground plane $\lambda/2$ away from the surface of the electrodes. For the ϕ and z periodic sensor we choose the radius $r_e = 2\lambda/\pi$, corresponding to a four wavelength circumference. Using $\lambda = 1$ mm this corresponds to $r_0 = 0.215r_e = 0.137$ mm. The remaining parameters are summarized in Table 4.1. The theoretical results are plotted in Figs. 4-9, 4-10, 4-11 and 4-12. The Maxwell 2D simulation results are not shown because they are indistinguishable from the theoretical results. Note that only the solution space is plotted. The bordering white in each figure, and the center of the cylinder in Fig. 4-12 are outside the solution space, where the potential is of no interest. We also note that the capacitance per unit length is per unit length of a *single* sense electrode. To calculate the total capacitance for all the sense electrodes we would multiply by the number of sense electrodes, 4, and the total sensor length.

Looking at the potential, provides insight about the relative capacitances for the different sensors. Notice the slight difference between the planar and z periodic potentials. The constant potential lobes in the z periodic plot extend slightly further towards the sense electrode. This suggests that the electric field is more concentrated near the sense electrode. More field lines terminate on the sense electrode accounting for the larger capacitance. The ϕ periodic potential is shown for comparison in Fig. 4-11. In comparing the ϕ periodic potential to the z periodic and planar potentials we see that the equal potential surfaces extend much further over the sense electrode in the ϕ periodic case, accounting for the significantly larger value of capacitance.

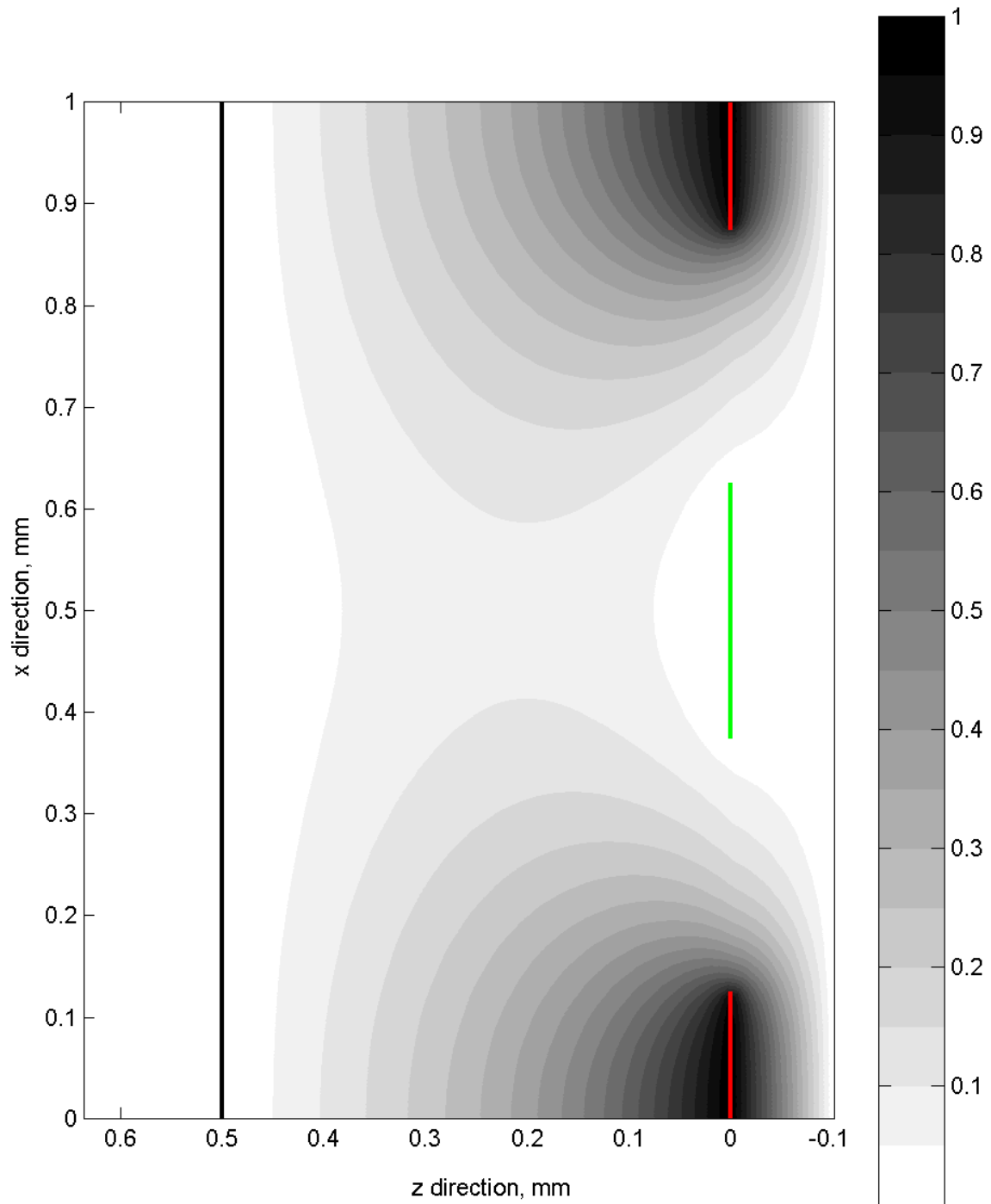


Figure 4-9: Single period of the planar 1 mm sensor potential (Φ/V_D) as a function of x and z . The red lines indicate the location of the drive electrodes, and the green line the location of the sense electrode. $C_T = 3.7612$ pF/m. Simulation parameters are summarized in Table 4.1 ($\lambda = 1$ mm).

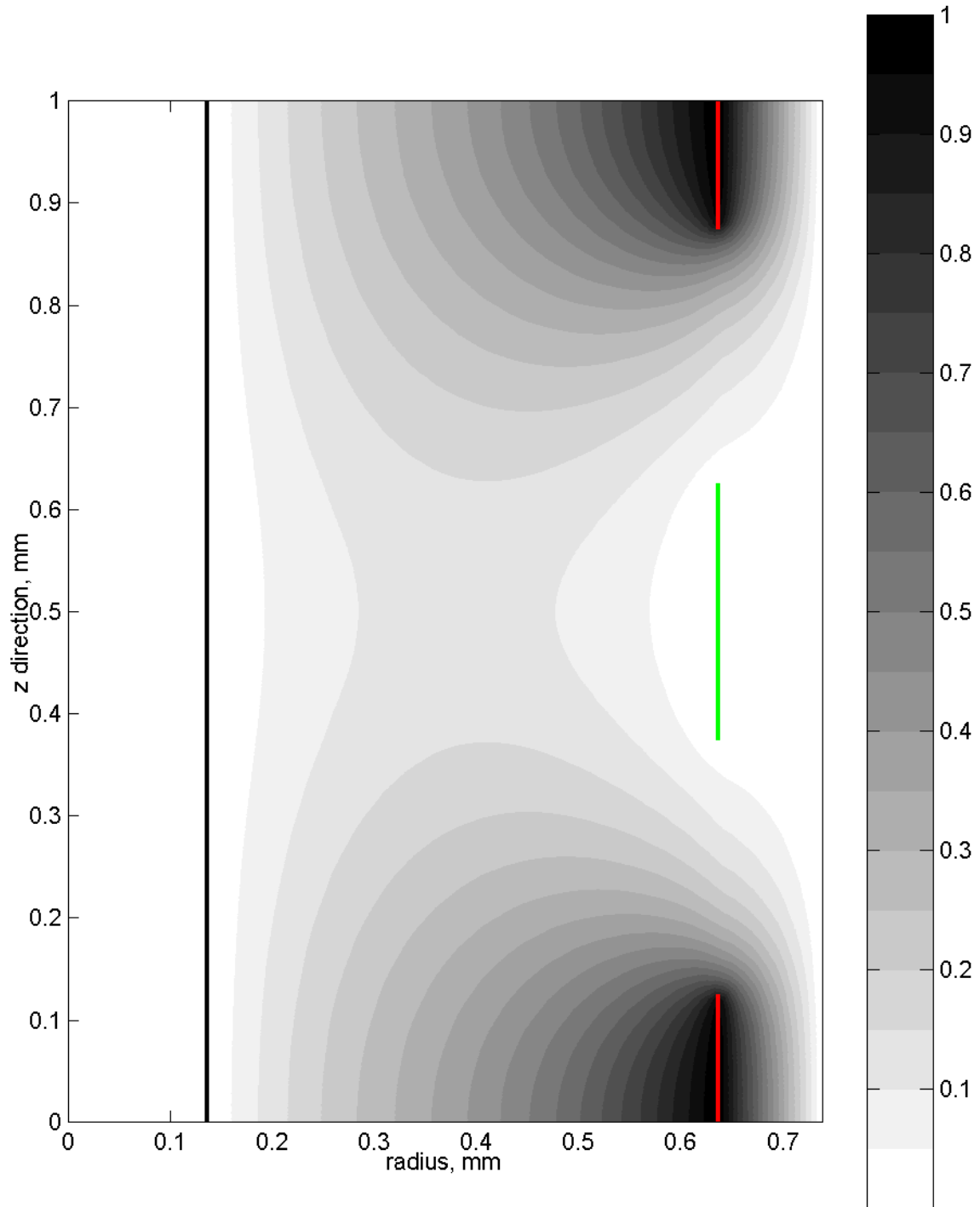


Figure 4-10: Single period of the cylindrical z periodic 1 mm sensor potential (Φ/V_D) as a function of radius and z . The red lines indicate the location of the drive electrodes, and the green line the location of the sense electrode. $C_T = 3.8280$ pF/m. Simulation parameters are summarized in Table 4.1 ($\lambda = 1$ mm).

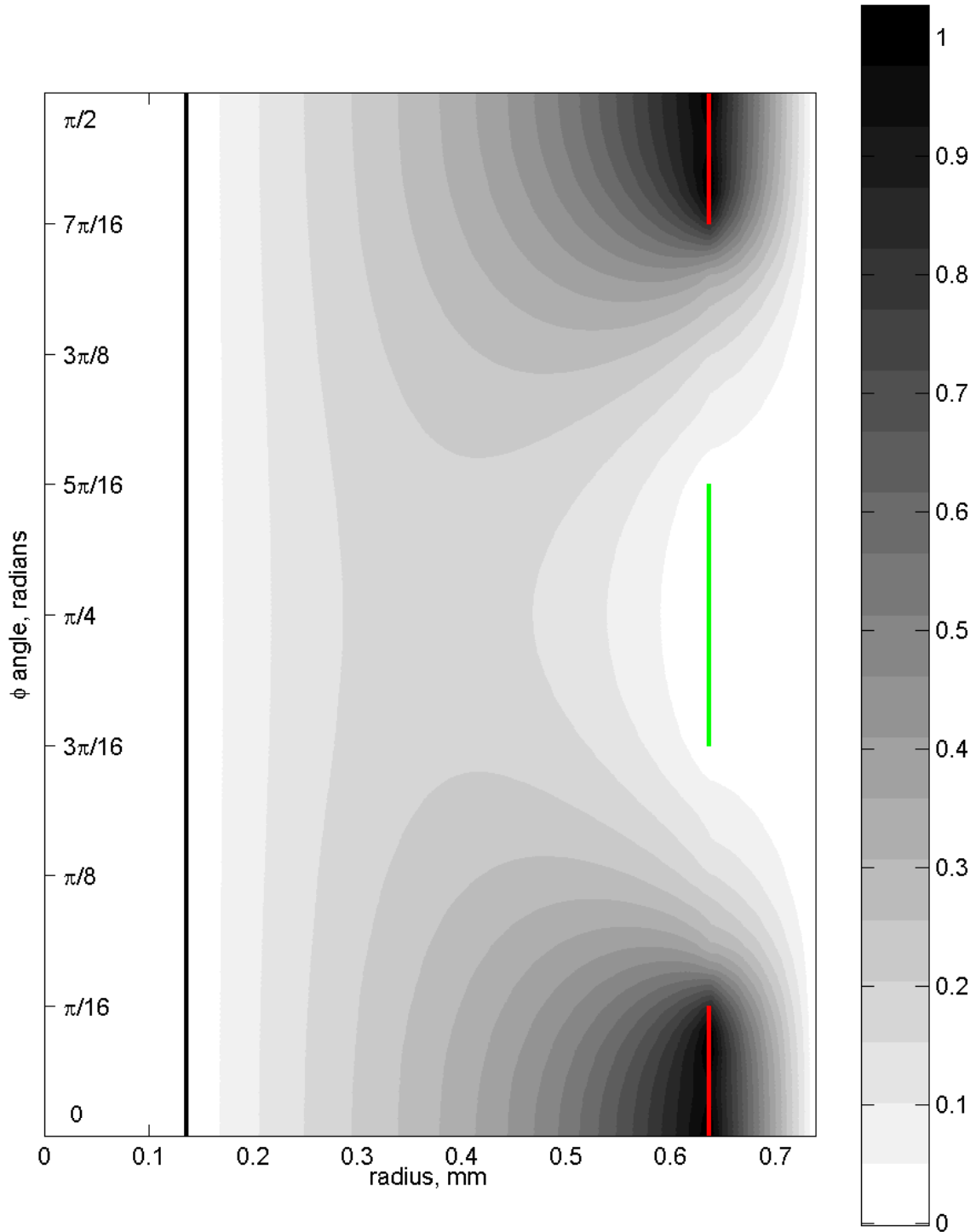


Figure 4-11: Cartesian plot of the electric potential of a single period of the cylindrical ϕ periodic 1 mm sensor potential (Φ/V_D) as a function of r and ϕ . The red lines indicate the location of the drive electrodes, and the green line the location of the sense electrode. $C_T = 4.5706$ pF/m. Figure 4-12 shows the same potential with the correct proportions. Simulation parameters are summarized in Table 4.1 ($\lambda = 1$ mm).

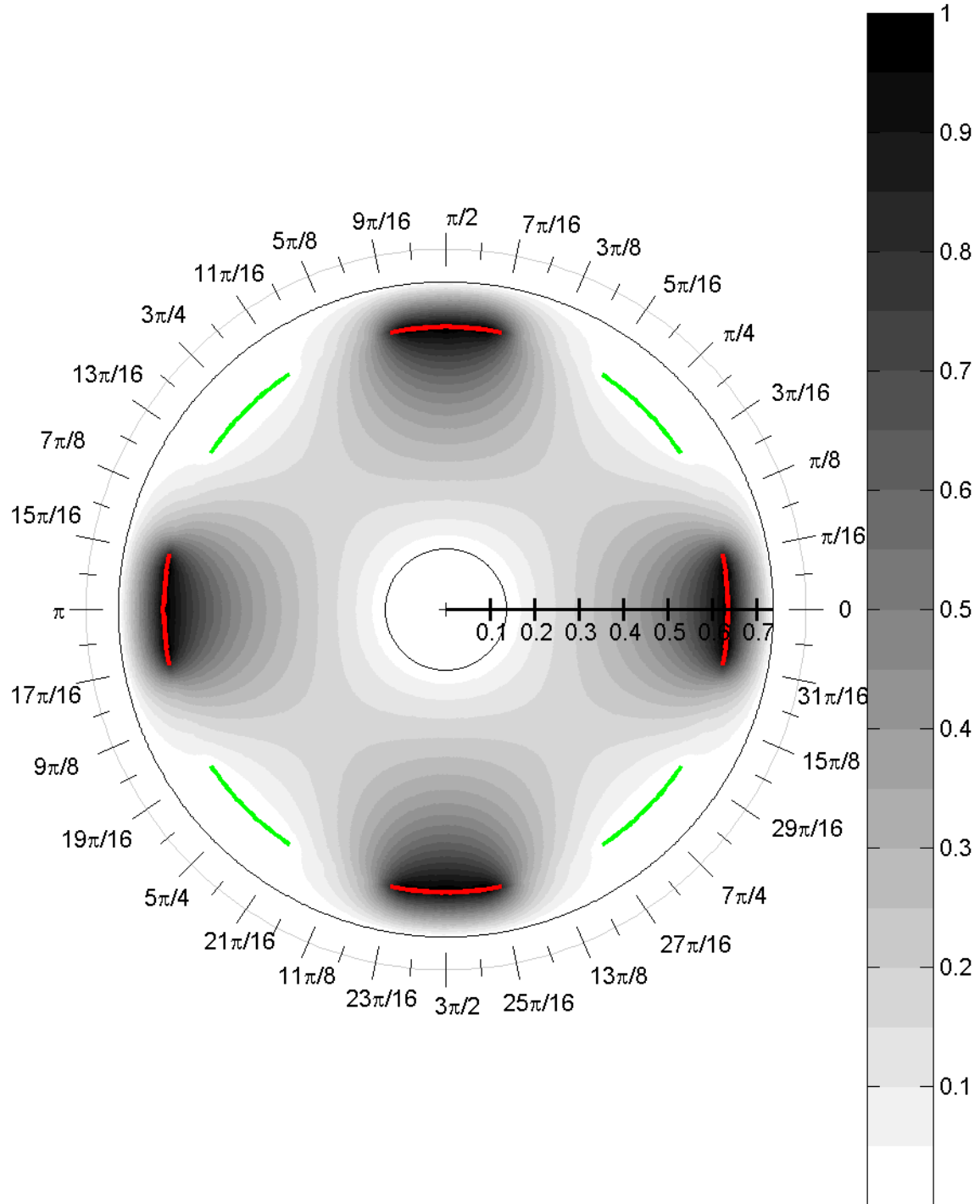


Figure 4-12: Electric potential (Φ/V_D) plot of a 1 mm ϕ periodic sensor with a center conductor. $\epsilon_r = 1$. The circumference is 4 mm, which corresponds to 4 wavelengths. The red lines indicate the location of the drive electrodes, and the green lines the location of the sense electrodes. $C_T = 4.5706$ pF/m. Figure 4-11 shows the same potential in cartesian coordinates. Simulation parameters are summarized in Table 4.1 ($\lambda = 1$ mm).

4.1.5 Field Lines in the Solution Region

We now compare the field lines in the solution region for the examples in Section 4.1.4. The field line plots are generated using the theory presented in Section 3.8. The examples plotted in Figs. 4-13, 4-14, 4-15, and 4-16 correspond with the figures in the previous section.

In generating the field solutions 501 Fourier terms and 52 collocation points are used. There is no difficulty in increasing these numbers, however these values are sufficient for these problems. In finding the solution to the $A_{p,n}$ and $B_{p,n}$ coefficients (see Section 3.7) as many coefficients as numerically possible are solved for. In these examples the coefficients up to $n = 198$, $n = 86$, and $n/q = 11$ were found for the planar, z , and ϕ periodic problems respectively.

It may seem surprising and suspicious that so few terms are used, particularly for the ϕ periodic example. The reason so few terms for the ϕ periodic solution are calculated is that for $n/q = 12$, some of the terms become extremely large (10^{185}), and others extremely small (10^{-186}). The matrix is singular to MATLAB's working precision and inversion leads to erroneous results.

In fact 12 terms (11 Fourier and a DC) proves sufficient to give accurate field lines. Part of the reason is that the Fourier coefficients, $\tilde{\Phi}_n(r_e)$, needed for the solution to solve for $A_{p,n}$ and $B_{p,n}$ are extremely accurate. They are calculated directly from the voltages at the collocation points. The choice of a large number of Fourier terms and collocation points is essential to insuring the collocation point voltages are calculated accurately.

In order to allow fair comparison between each of the field line plots the field lines all were picked to pass through the same relative locations on the drive, sense, and back plane electrodes. The results are even more elucidating than the potential plots. Notice how the field lines appear to be pinched towards the center for the z and particularly ϕ periodic sensors when compared to the planar sensor. This implies more field lines are terminating on the sense electrodes, which is reflected in the increased capacitance measurements.

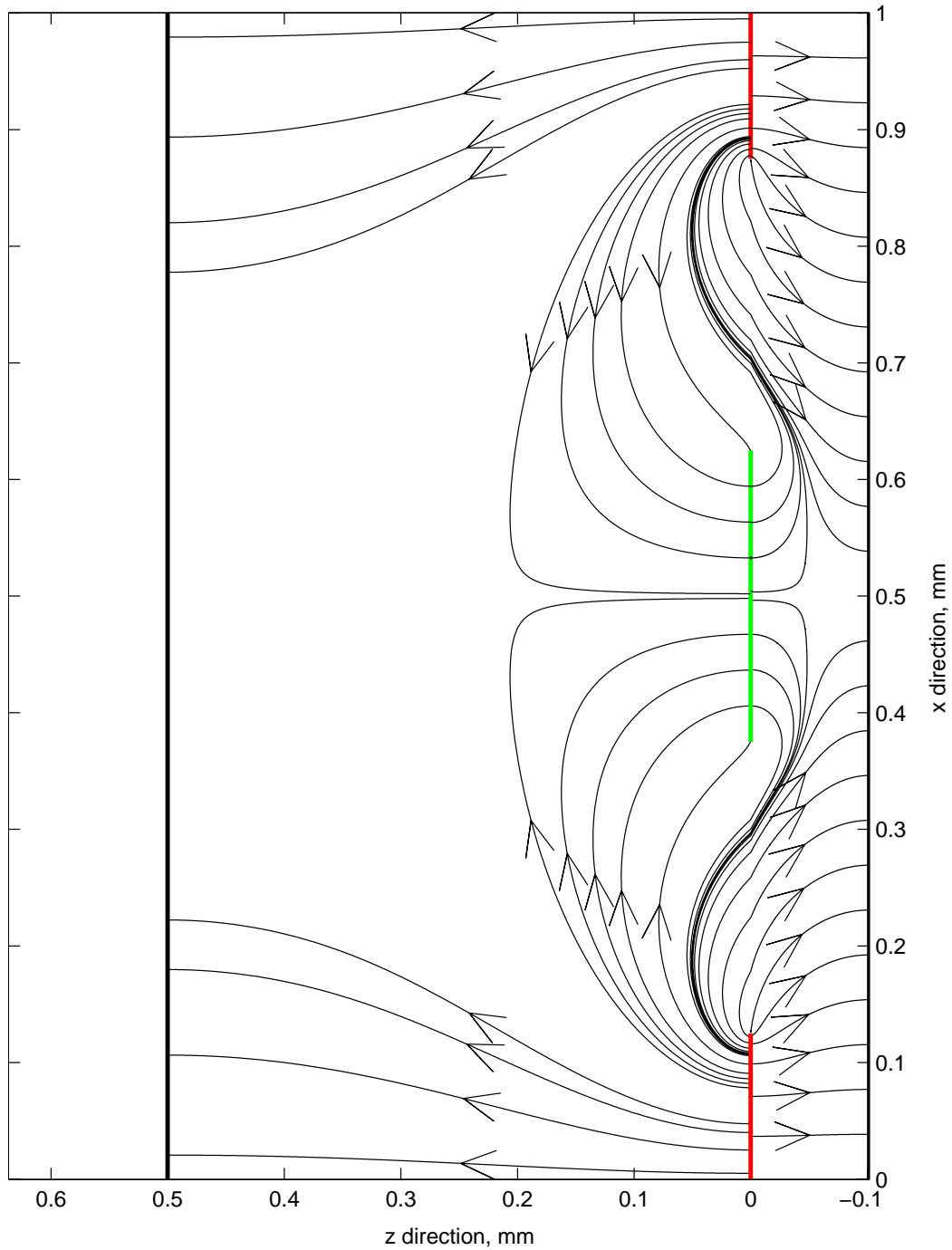


Figure 4-13: Electric field lines of a 1 mm planar sensor with a top ground plane at 0.5 mm; $\epsilon_r = 1$, $\epsilon_s = 2.1$. Figure 4-9 shows the potential plot for the same configuration. The red and green lines indicate the location of the drive and sense electrodes respectively. Simulation parameters are summarized in Table 4.1 ($\lambda = 1$ mm).

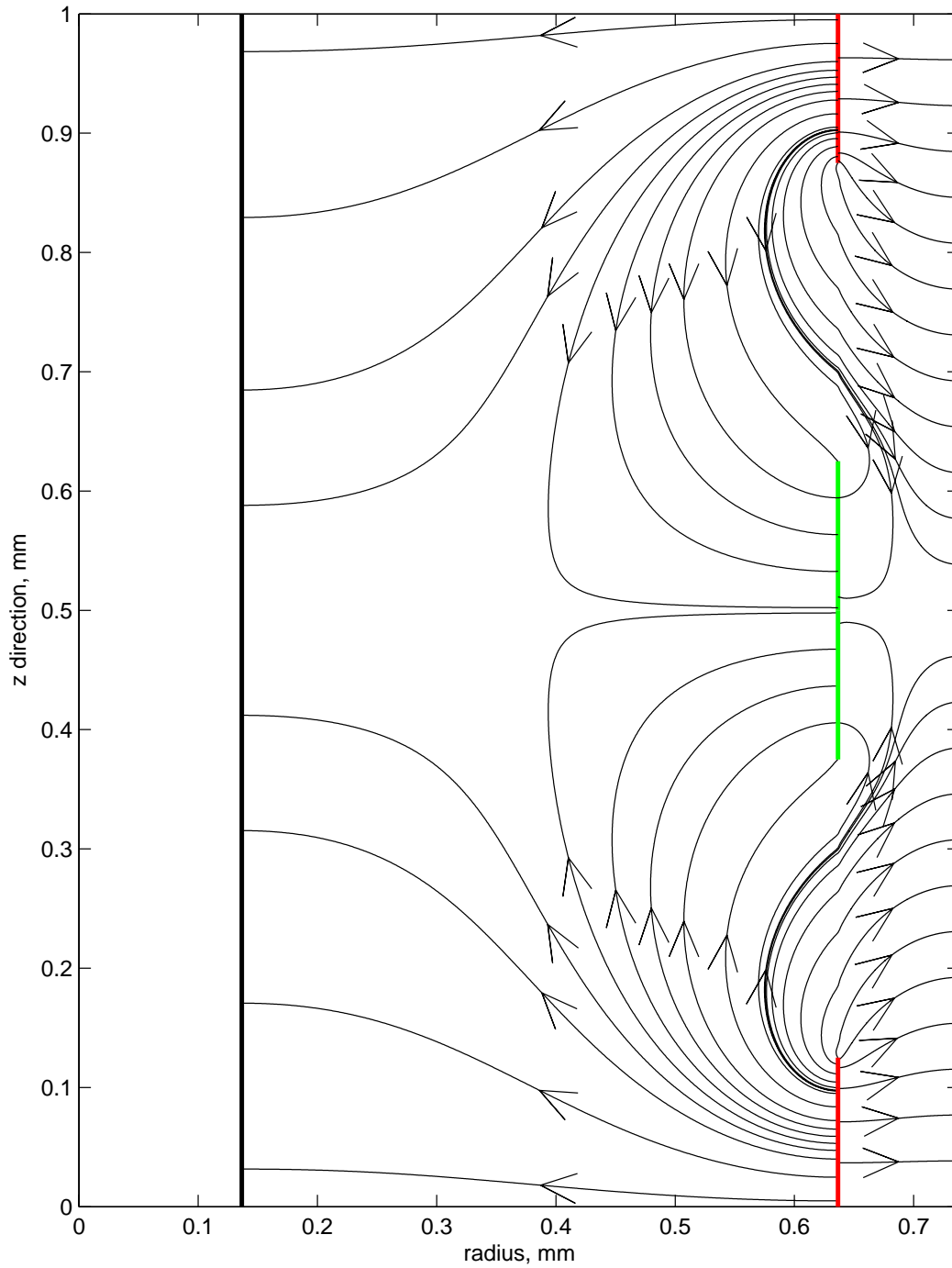


Figure 4-14: Electric field lines of a 1 mm z periodic sensor with a center conductor; $\epsilon_r = 1$, $\epsilon_s = 2.1$, $r_0 = 0.137$ mm. Figure 4-10 shows the potential plot for the same configuration. The red and green lines indicate the location of the drive and sense electrodes respectively. Simulation parameters are summarized in Table 4.1 ($\lambda = 1$ mm).

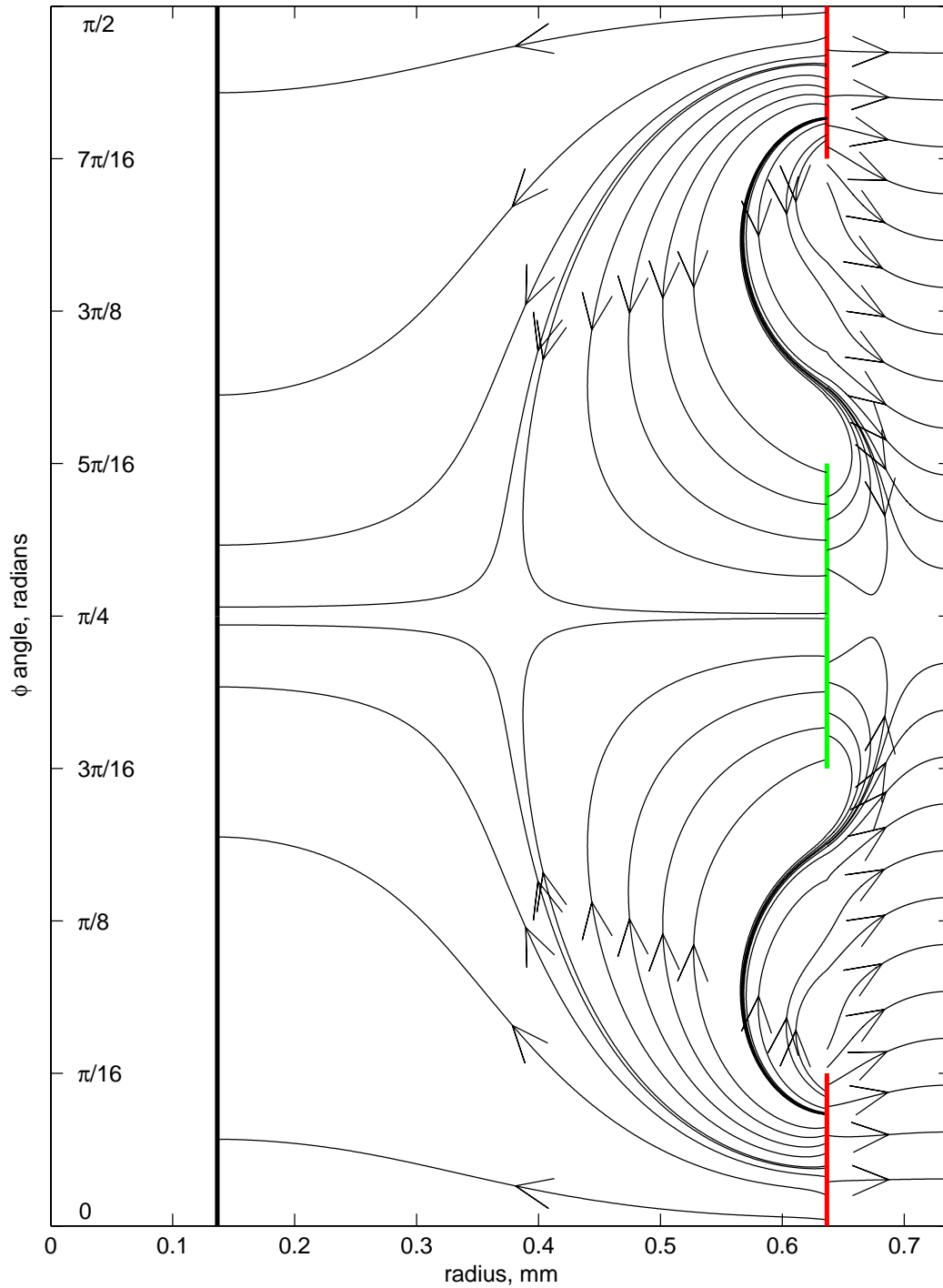


Figure 4-15: Cartesian plot of the electric field lines of a single period of the ϕ periodic sensor; $\epsilon_r = 1$, $\epsilon_s = 2.1$, $r_0 = 0.137$ mm. The field lines are plotted in the true proportions in Fig. 4-16. Figure 4-11 shows the potential plot for the same configuration. The red and green lines indicate the location of the drive and sense electrodes respectively. Simulation parameters are summarized in Table 4.1 ($\lambda = 1$ mm).

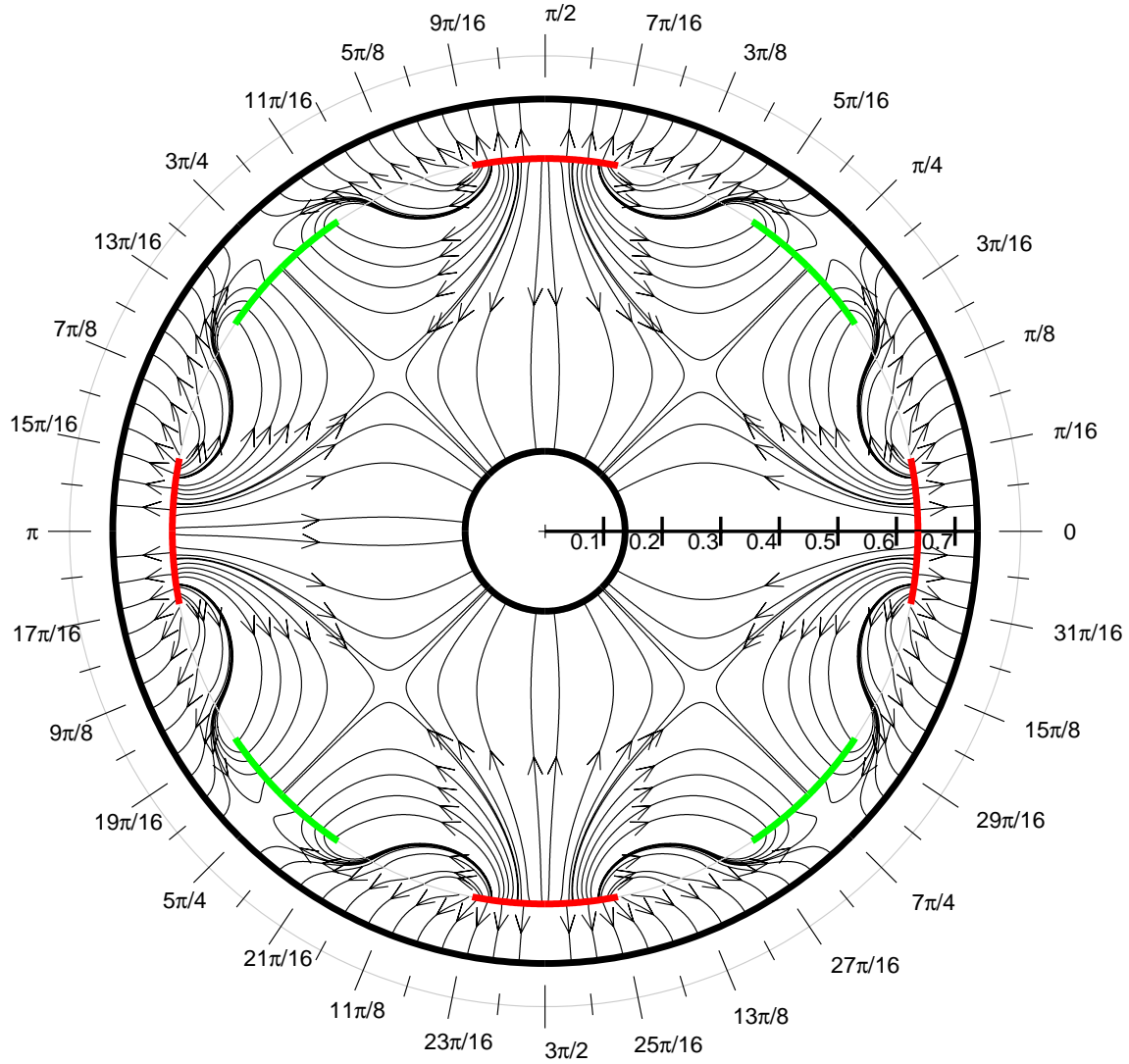


Figure 4-16: Electric field lines of a 1 mm ϕ periodic sensor with a center conductor; $\epsilon_r = 1$, $\epsilon_s = 2.1$, $r_0 = 0.137$ mm. The circumference is 4 mm, which corresponds to 4 wavelengths. The field lines are plotted in the cartesian coordinates in Fig. 4-15. Figure 4-12 shows the potential plot for the same configuration. The red and green lines indicate the location of the drive and sense electrodes respectively. Simulation parameters are summarized in Table 4.1 ($\lambda = 1$ mm).

Planar Sensor Study on Ground Plane Height

We now illustrate the field lines for a planar 1 mm wavelength sensor as the ground plane height is increased from $\lambda/8$ to infinity. The capacitance as a function of ground plane height was plotted in Fig. 4-3. We again use the parameters from Table 4.1. Figures 4-17 illustrates the field lines for heights of $\lambda/8$, $\lambda/4$, $\lambda/2$, and λ . Figure 4-18 illustrates the fields lines for heights of 2λ , and infinity.

The field line plots indicate what portion of the drive electrode is coupling with the sense electrode. When the top ground plane is very close, only the very edge of the drive electrode couples with the sense electrode. Because the potential gradient is so weak near the sense electrode, particularly between the backplane and sense electrode, it is difficult to calculate the field lines in this region. A numerical problem also exists when the potential lines are nearly parallel to the interface between the substrate and MUT, making it difficult to trace some field lines through the interface.

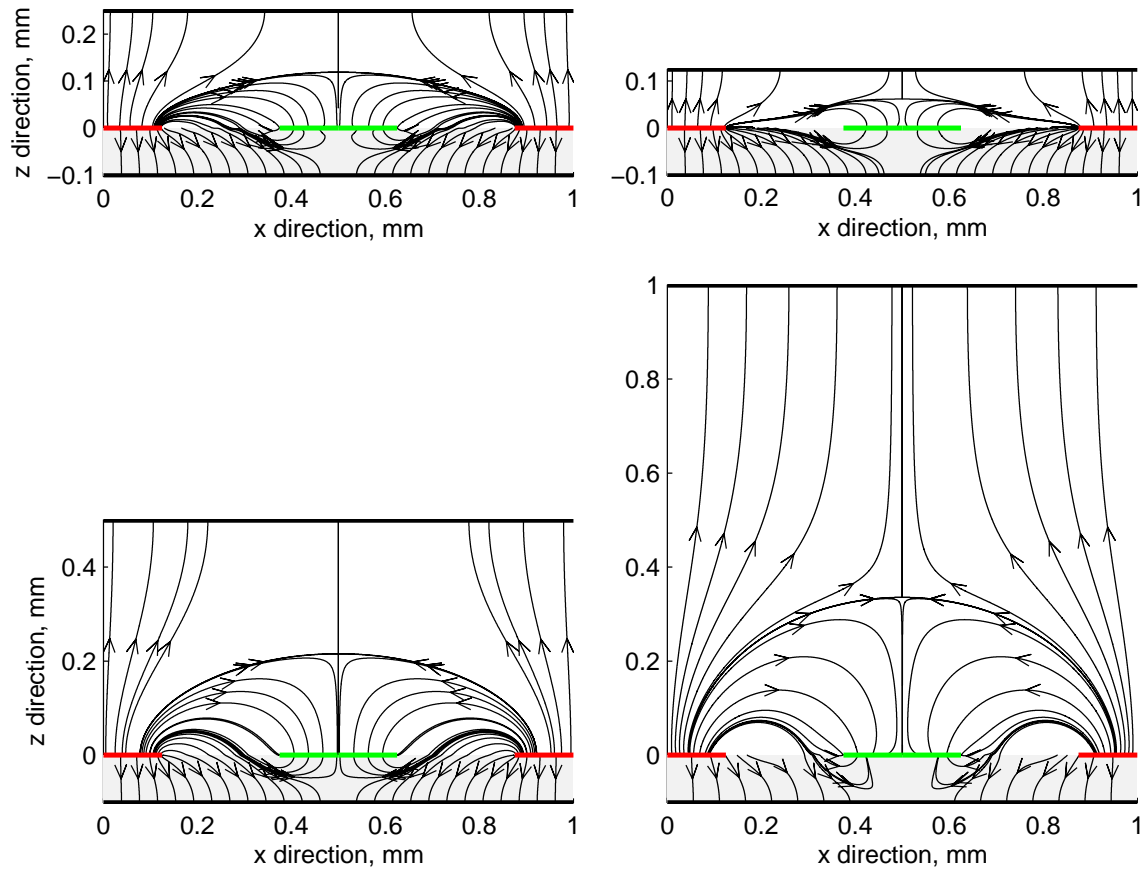


Figure 4-17: Field lines for a planar sensor with top ground plane heights of $\lambda/8$ (top right), $\lambda/4$ (top left), $\lambda/2$ (bottom left), and λ (bottom right). $\epsilon_r = 1$, $\epsilon_s = 2.1$. All field lines originate on drive electrodes (red) and terminate on ground planes or sense electrodes (green). Simulation parameters are summarized in Table 4.1 ($\lambda = 1$ mm).

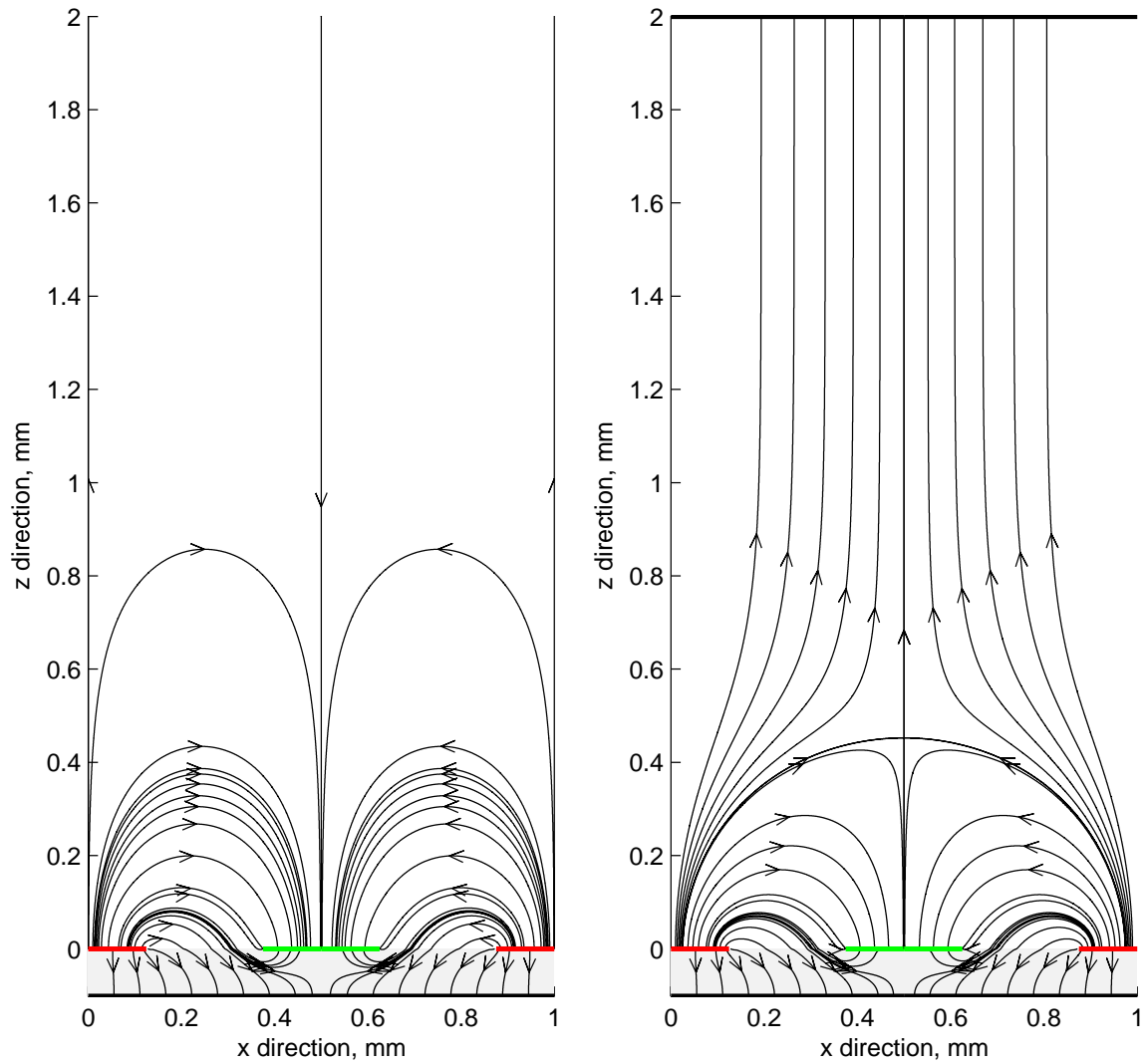


Figure 4-18: Field lines for a planar sensor with top ground plane heights of 2λ (right) and infinity (left). $\epsilon_r = 1$, $\epsilon_s = 2.1$. All field lines originate on drive electrodes (red) and terminate on ground planes or sense electrodes (green). Simulation parameters are summarized in Table 4.1 ($\lambda = 1$ mm).

ϕ Periodic Sensor Study on Center Conductor Radius

The effect of a center conductor on a 1 mm ϕ periodic sensor field is now studied. The circumference is four wavelengths corresponding to $r_e = 0.637$ mm. The remaining parameters are taken from Table 4.1. Figure 4-19 shows the field lines when there is no center conductor and when the center conductor radius is $r_0 = 0.1r_e = 0.064$ mm. Figure 4-20 shows the field lines when the center conductor radius is $r_0 = 0.6r_e = 0.382$ mm, and $r_0 = 0.8r_e = 0.509$ mm. A fifth case can be found in Fig. 4-16 where $r_0 = 0.215r_e = 0.137$ mm.

As the radius, r_0 , is increased, more and more field lines terminate on the ground planes rather than on the sense electrodes. This results in a reduction of capacitance. It becomes increasingly difficult to resolve the field lines in the substrate as the center conductor radius increases.

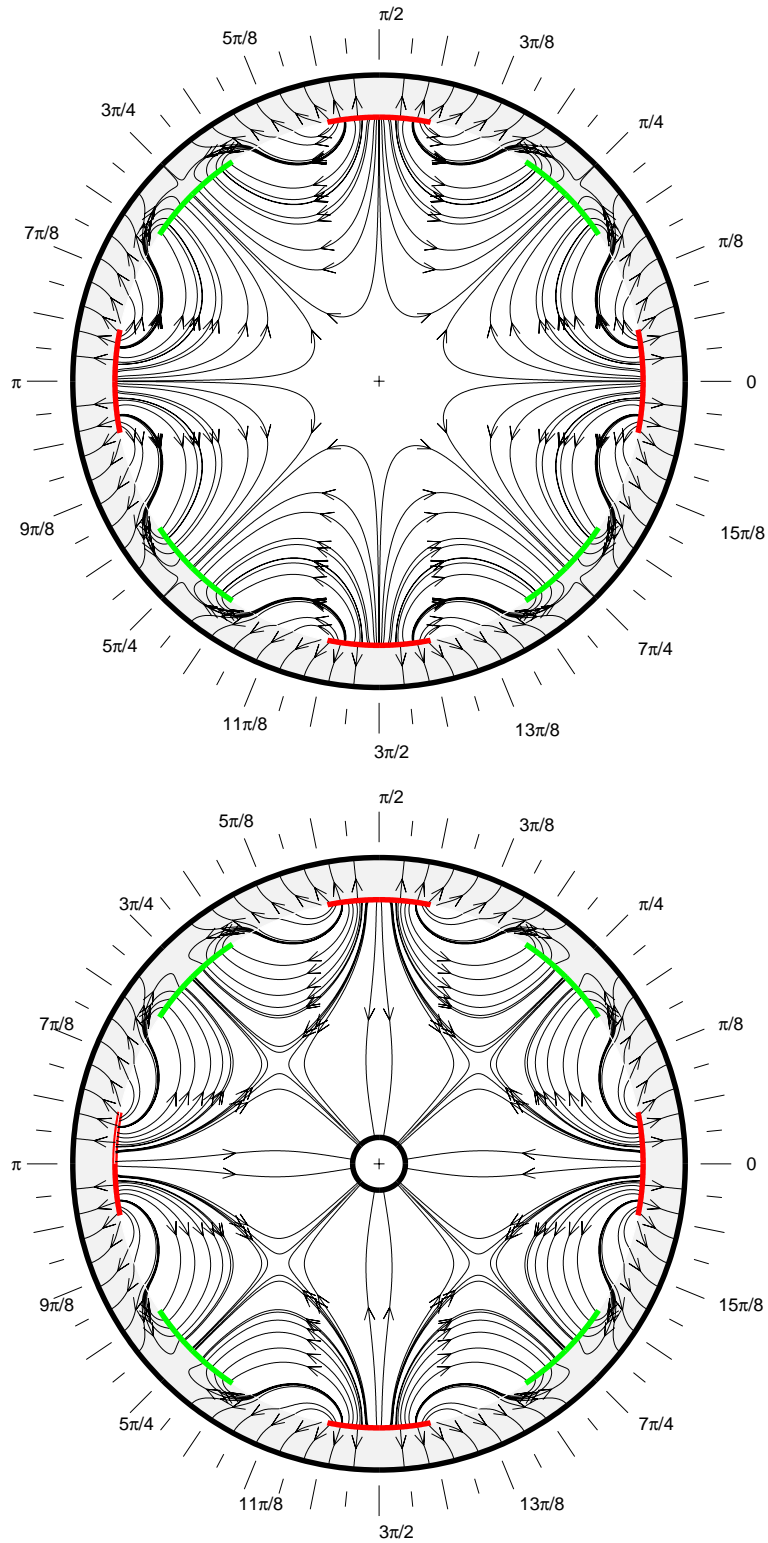


Figure 4-19: Field lines for ϕ periodic sensors with a center conductor (bottom, $r_0 = 0.1r_e = 0.064$ mm) and without (top) a center conductor. $\epsilon_r = 1$, $\epsilon_s = 2.1$. Simulation parameters are summarized in Table 4.1 ($\lambda = 1$ mm).

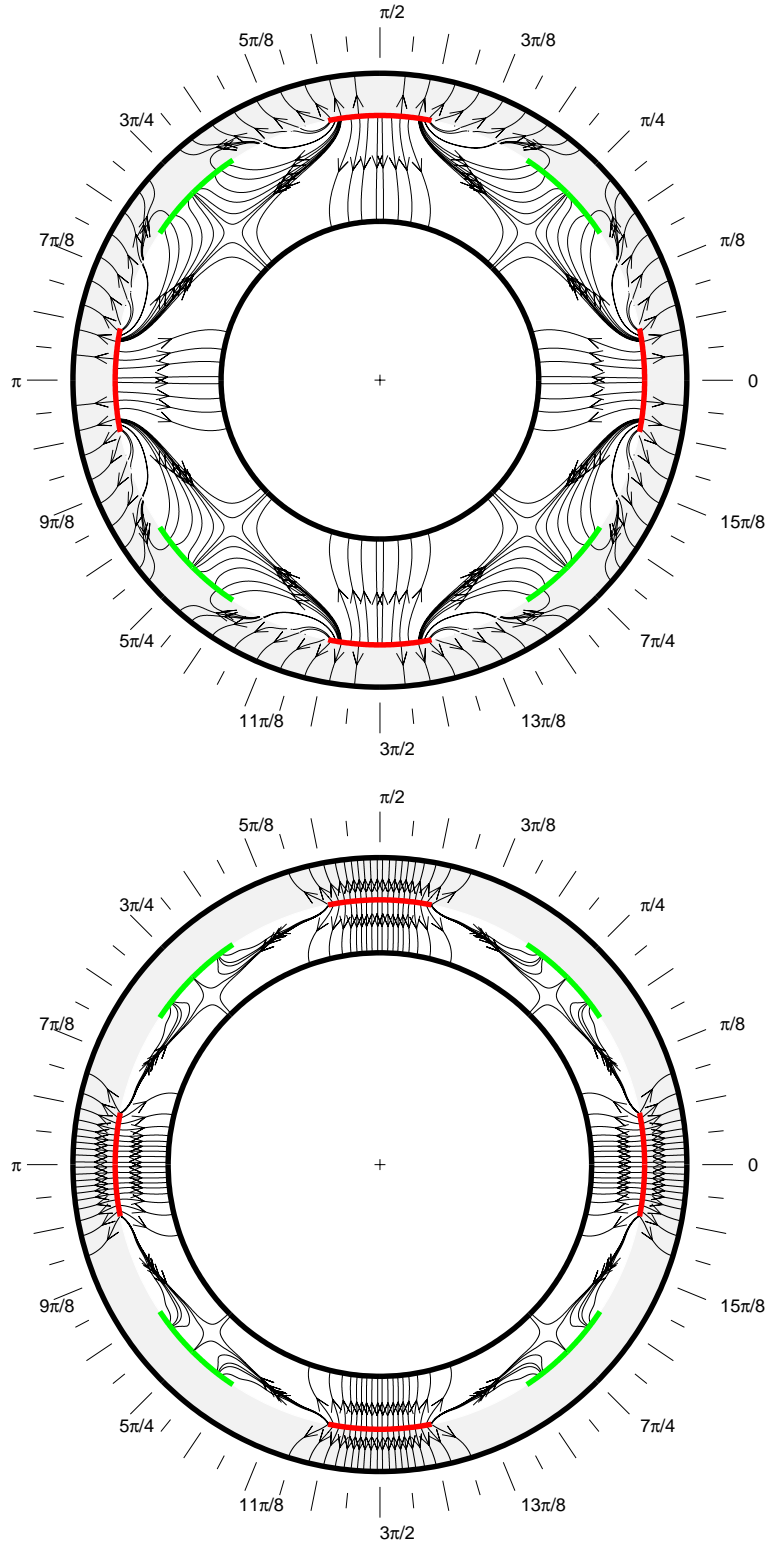


Figure 4-20: Field lines for ϕ periodic sensors with center conductors of radii $r_0 = 0.6r_e = 0.382$ mm (top), and $r_0 = 0.8r_e = 0.509$ mm (bottom). $\epsilon_r = 1$, $\epsilon_s = 2.1$. Simulation parameters are summarized in Table 4.1 ($\lambda = 1$ mm).

4.1.6 Lossy Materials

We now consider cases where the MUT conductivity is non-zero. This will introduce a conductance term making the admittance complex. The sensor response will be frequency dependent. In order to study the effect of conductivity we simulate a frequency sweep over several decades. At high frequency we expect the susceptance term to dominate the sensor admittance. At low frequency the conductance terms should dominate. The transition region can be estimated by setting the conductance and susceptance terms of the admittance equal, and solving for the frequency.

$$G_{12} = \omega C_{12} \quad (4.2)$$

$$G_{12} \propto \sigma \quad (4.3)$$

$$C_{12} \propto \epsilon \quad (4.4)$$

$$f \approx \frac{\sigma}{2\pi\epsilon} \quad (4.5)$$

The proportionality constant is determined from the geometry and is the same for both conductance and capacitance. We recognize eq. 4.5 as $(2\pi)^{-1}$ times the reciprocal of the relaxation time.

As an example we consider an infinite MUT (no top ground plane) with permittivity $\epsilon = \epsilon_0$ F/m, and conductivity $\sigma = 10^{-8}$ S/m. Our estimate of the transition frequency is 1.8×10^2 Hz. We consider the z and ϕ periodic cylindrical sensors, and the planar sensor with no center conductor or top ground plane. For the cylindrical cases we take 4λ (4 mm) as the circumference. The frequency is swept from 0.1 Hz to 10 kHz. All other parameters are given in Table 4.1. The results are shown in Fig. 4-21. Figure 4-22 shows the magnitude of the voltage for selected frequencies for the 1 mm planar sensor case.

The results show good agreement in all cases. Differences may be primarily attributed to the finite electrode thickness. Notice that the transition frequency estimate marks the start of the transition region. Not only are the values highly frequency dependent, the transcapacitance can take negative values. This is perfectly acceptable. A discussion of this issue and a simple demonstration showing how this is possible can be found in [47,54]. In theory this system could be represented by a network of lumped element resistors and capacitors. This is avoided by reducing the network to a frequency dependent parallel conductance and capacitance where the capacitance can take negative values.

4.1.7 Comparison of Analytical and Theoretical Solution Techniques

In this section we simulate a z periodic geometry using all the solution techniques at our disposal. These include the theoretical model, Ansoft Maxwell 2D, Ansoft Maxwell 3D version 11.1, and 2D

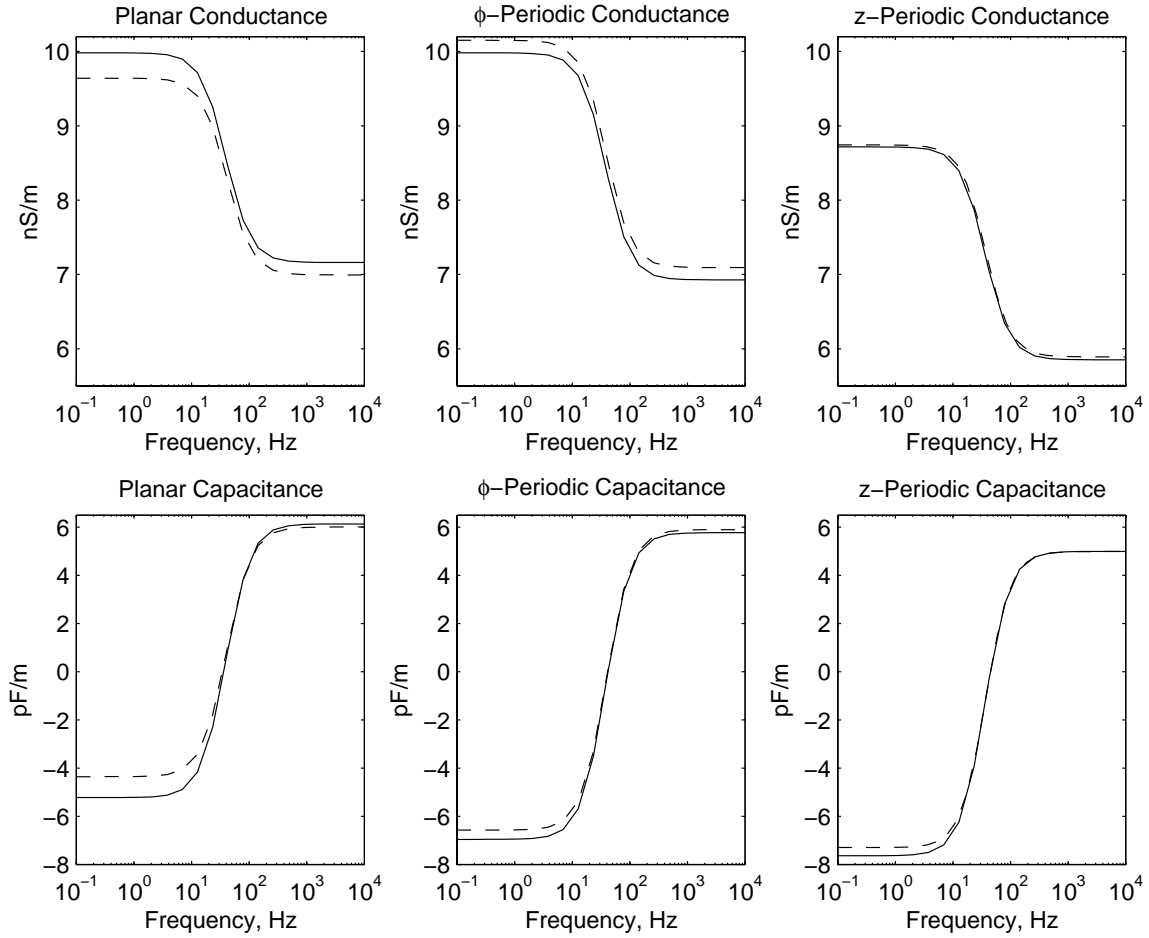


Figure 4-21: Frequency sweep for the three sensor geometries when the MUT has $\epsilon_r = 1$, and $\sigma = 10^{-8}$ S/m. The solid lines show the theoretical values, while the dashed lines show the results calculated from Maxwell 2D (Planar and ϕ periodic) and Multiphysics (z periodic). Simulation parameters are summarized in Table 4.1 ($\lambda = 1$ mm).

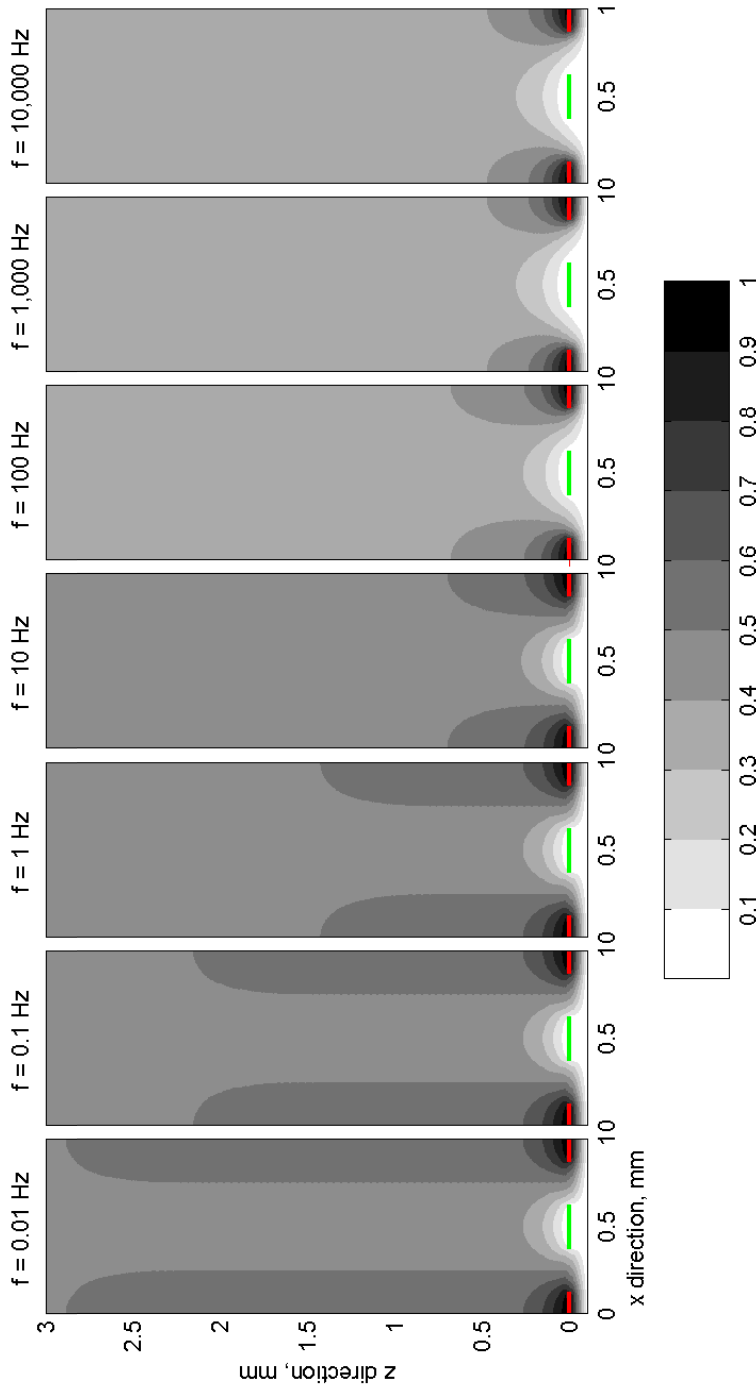


Figure 4-22: Magnitude of voltage in $\lambda = 1$ mm planar sensor with MUT $\epsilon_r = 1$, $\sigma = 10^{-8}$ S/m at selected frequencies. There is no top ground plane. Additional simulation parameters are given in Table 4.1 ($\lambda = 1$ mm).

Table 4.5: z Periodic Sensor Solution Methods Comparison.

Method	Capacitance, pF	% Difference	Notes
Theoretical	0.5413	×	$N = 2500, K = 200$
Maxwell 2D	0.5479	+1.22%	electrode height: 1 μm , 20 passes
Maxwell 3D	0.5791	+6.99%	869,416 elements, 26 passes
Multiphysics 2D	0.5434	+0.39%	9,724 elements
Multiphysics 3D	0.5097	-5.84%	193,013 elements

and 3D solutions from Comsol Multiphysics version 3.3 with the AC/DC Module. A Teflon rod with radius 1.4 cm is simulated with electrodes periodic in z . The standard Teflon substrate is used having a 4 mil thickness (.1016 mm) and a 5.0 mm wavelength sensor is used. Symmetric boundary conditions are used to reduce the size of the simulation region. The results are summarized in Table 4.5 compares the estimated capacitance for a single sense ring which is equivalent to a meander length of $2\pi r_e \approx 8.8$ cm. The theoretical simulation is done for several values of N and K . The full numeric results are 0.5403318... pF for $N = 1000$ and $K = 100$, 0.5416318... pF for $N = 2000$ and $K = 150$, and 0.5413117... pF $N = 2500$ and $K = 200$. An attempt to execute $N = 3000$ and $K = 200$ resulted in an out of memory error. We conclude our theoretical analysis has uncertainty in the fourth digit. We characterize the error of the finite element methods based on the theoretical result.

In principle the only geometry that is physically different is the Maxwell 2D geometry which requires a finite electrode thickness. This is not necessary in the 3D modelers or in the Multiphysics 2D geometry. The 3D tools result in the largest difference between the nominal value and the theoretical value. The closest agreement was between the Multiphysics 2D simulation. This gives us increased confidence in the validity of the theoretical solution and the MATLAB implementation.

4.2 Sensor Designs

During the course of the research several sensor designs were considered and a few were manufactured for experimental measurements. The manufactured dielectrometry sensors used for measurements are typically etched on CuFlon by Polyflon Company, a company based in Norwalk, CT. CuFlon is a Teflon substrate with copper electroplated onto the top and bottom surfaces. Both sides can be etched to high precision and several Teflon and copper thicknesses are available [61]. In this section we present the manufactured sensor designs and some sensors ready for production but never manufactured.

4.2.1 Practical Design Issues

Many of the theoretical assumptions must be violated to produce a practical sensor. Some efforts have been made to quantify the error introduced by each of these assumptions, and methods have been developed to minimize the error by design such as the inclusion of a guard electrode. Mamishev et al. have shown by sensitivity analysis that the error due to non-ideal contact between the MUT and the sensor can be reduced by filling the air gap with a dielectric liquid such as castor and transformer oil [63]. In our own measurements of the oil impregnated cables, an air gap does not seem to be an issue. The oil in the paper fills in the gaps adequately enough to provide consistent measurement results provided sufficient pressure is applied to the sensor.

Studies have been done on planar sensors to characterize the effect of cross coupling between sensors, the effect of electrode thickness, the effect of finite length electrodes, the use of guard electrodes, and other issues [47,54]. Modeling errors are further discussed in Section 5.5.

4.2.2 Pre-existing Sensor Designs

The initial research efforts made use of remaining sensors available from previous research projects. Figure 4-23 shows the sensor designed for the Couette Facility measurements conducted by Y. Du [64, 65]. The sensor was also used by Jason Sears in his research on dangerous materials sensing [32]. This is a three wavelength sensor (1, 2.5 and 5 mm) each with 25 cm of meander length and a metallization ratio of 0.5. The design features a 10 mil (254 μm) Teflon substrate. The copper electrodes are approximately 14 μm thick (1/3 oz. cladding). The compact design features dual grounding contacts for the sense electrodes. The leads used to connect these sensors are made from RG179B/U coaxial cable. These cables have a 7 strand inner conductor and an outer diameter of 0.1" [66].

A second sensor design previously manufactured is shown in Fig. 4-24. It appears this particular design may have been the efforts of both A. Mamishev and Y. Du around 1996. The sensor has three separate backplanes for use excitation by the FVGPM mode introduced in Section 3. This feature was used to physically separate the sensors so that each wavelength could be used individually. The electrode thickness is 14 μm and the Teflon substrate is 10 mils thick. This design is believed to have been first introduced in [67], and used in numerous subsequent papers.

The first several months of research was done using these sensor designs. In this time several flaws emerged. The most significant problem is the choice of coaxial cable. RG179 is an excellent SMA male to SMA male connection cable, but in our setup the cable is soldered to the sensor at one end. With sensors only having a weight around 4 grams, the kinks and turns of the cable place

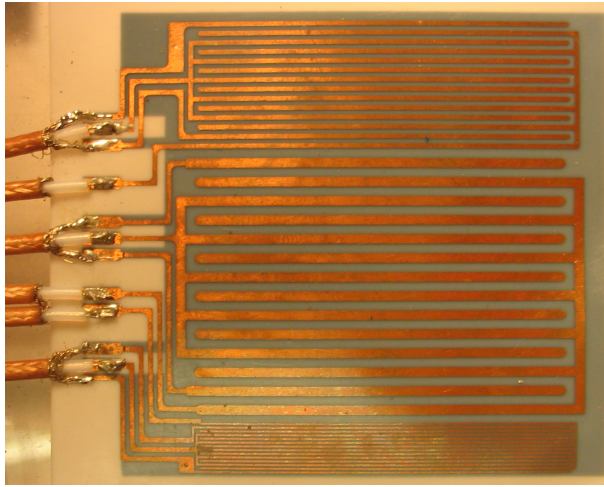


Figure 4-23: Three wavelength sensor designed by Y. Du for the Couette facility. Sensor wavelengths are 1.0 (bottom), 2.5 (top), and 5.0 mm (middle). The sensor design is relatively compact to fit in the facility. Sensor shown is the actual size.

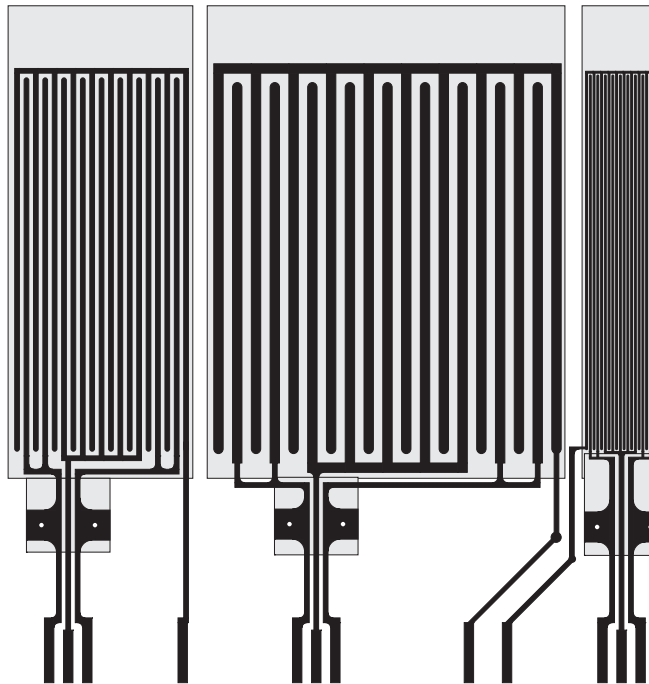


Figure 4-24: Three wavelength sensor designed by A. Mamishev for the floating voltage with guard plane mode (see Section 3). Sensor wavelengths are 1.0 (right), 2.5 (left), and 5.0 mm (center). The backplane is shown in light gray. Because the width is so large the sensors were cut apart for rod measurements. Sensor shown is the actual size.

a great deal of stress on the connection pads. Typically after a few hours of manipulation, some of the leads would tear off, taking the electrode pad with them. Without a pad, and given the small size of the sensor, it is impractical to resolder the connection. The affected wavelength of the sensor can no longer be used.

Generally the spacing between contact pads was found to be prohibitively small. Achieving a good solder connection and avoiding bridges with the relatively heavy RG179 cable provided significant challenge in the laboratory.

Another problem that emerged was the frequent, microscopic cracking of the electrodes when wrapped around a cylindrical surface. The cracking is not apparent under visual inspection. An ohm meter is used to isolate the location of these cracks by trial and error. Soldering a short at the crack often yielded aberrant results. Sensors with cracked electrodes should be discarded as most repair attempts prove unsatisfactory.

4.2.3 Three Wavelength Sensor (January 2006)

In response to the struggles experienced with the available sensors, a three wavelength sensor designed specifically for cylindrical geometries was developed. The design is shown in Fig. 3-1. The top surface of the sensor is shown in black and forms the interdigital fingers for a 1, 2.5, and 5 mm sensor. Each wavelength has five sense fingers each of 5 cm length for a total meander length of 25 cm. A single guard finger is included on each side to keep the overall sensor width below 3.4 inches, so that there is no overlap when wrapped around the single conductor cable. The ground plane covers much of the back of the sensor and is illustrated by the gray box surrounding the interdigital finger area. Vias connecting the front and back plane are shown as white circles. The design features a 4 mil (101.6 μm) Teflon substrate with $1/2$ ounce copper cladding (0.7 mils thick). The design choice of a thinner substrate and thicker electrode than the previous generation of sensors was made to maximize sensor flexibility and lifetime. Extra large pads have been used to reduce peeling when coaxial cables are connected to the sensor. The sensors feature a single drive channel, which reduces the number of SMA connections needed on the vacuum chamber for each sensor from six to four. RG178 coaxial cable is used to connect the interface box to the sensor because of its lightness and flexibility [68]. The cable has an outer diameter of 75 mils. The connection typically is done by threading the center conductor through the via and soldering to pads on the back side of the sensor.

Nine of these sensors were manufactured in January 2006 with the only variation being a left to right mirroring for some of the sensors as shown in Figures 4-25, 4-26, and 4-27. The sensors have proved to have satisfactory physical characteristics. Copper peeling or cracking, both problems in

test measurements using pre-existing sensors have not been a problem with the new sensors. The only problem thus far has been cables breaking off at the via due to excessive flexing of the center conductor. This problem will exist regardless of the connection and could be reduced by using a cable with a thicker center conductor. If the cable is too heavy however, the copper pad may peel off the substrate. The fix only requires removing solder from the via and reinserting a clean cable. This can often be done with the sensor still in place on the MUT. Cleaning oil off the sensors after cable measurements proved difficult. Once a sensor was used with a cable it was from then on only used for cable measurements.

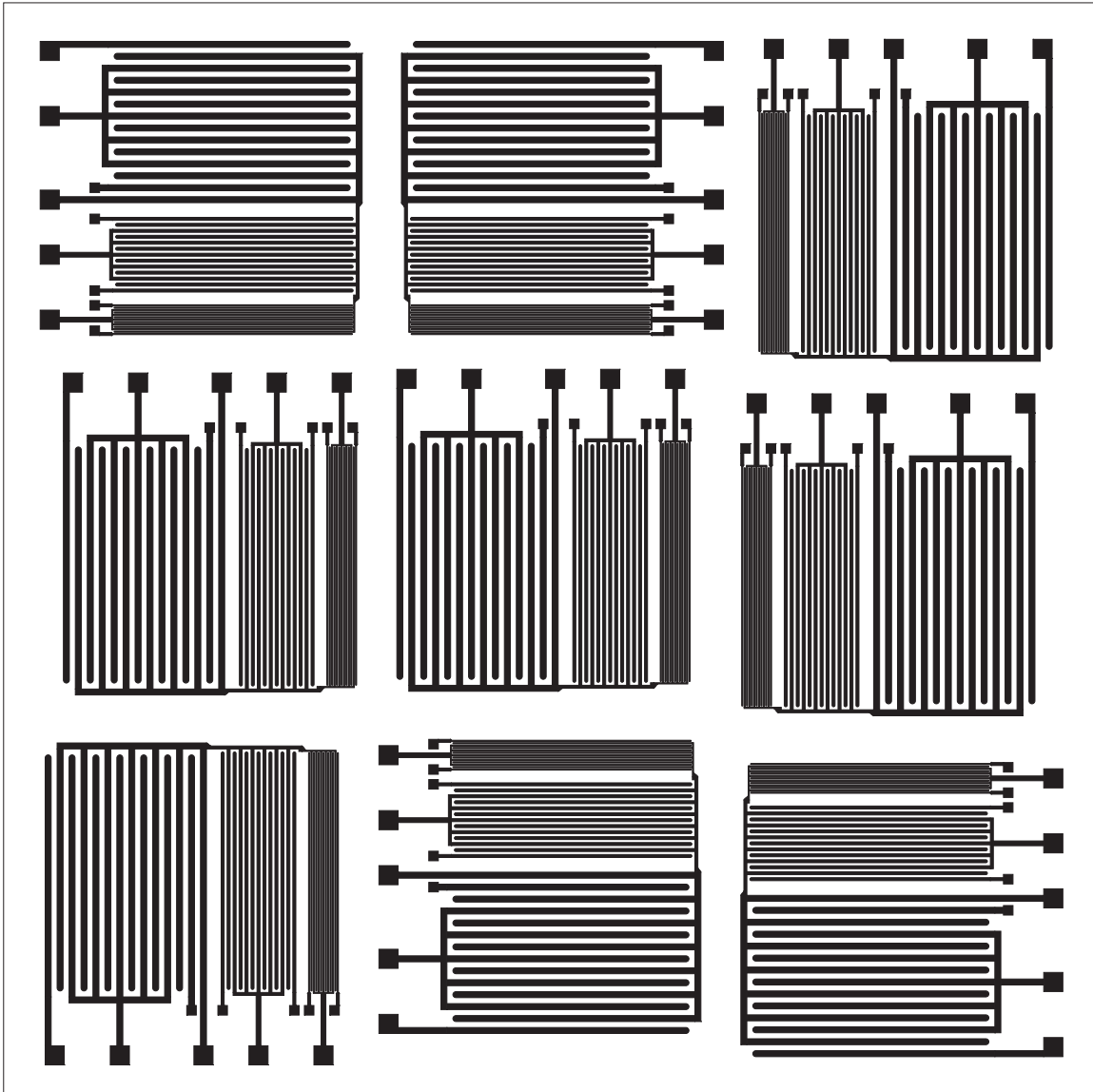


Figure 4-25: January 2006 three wavelength sensor electrode production design. The orientation is flipped for four of the sensors relative to that shown in Fig. 3-1. The dimensions of the bounding square is 9×9 inches.

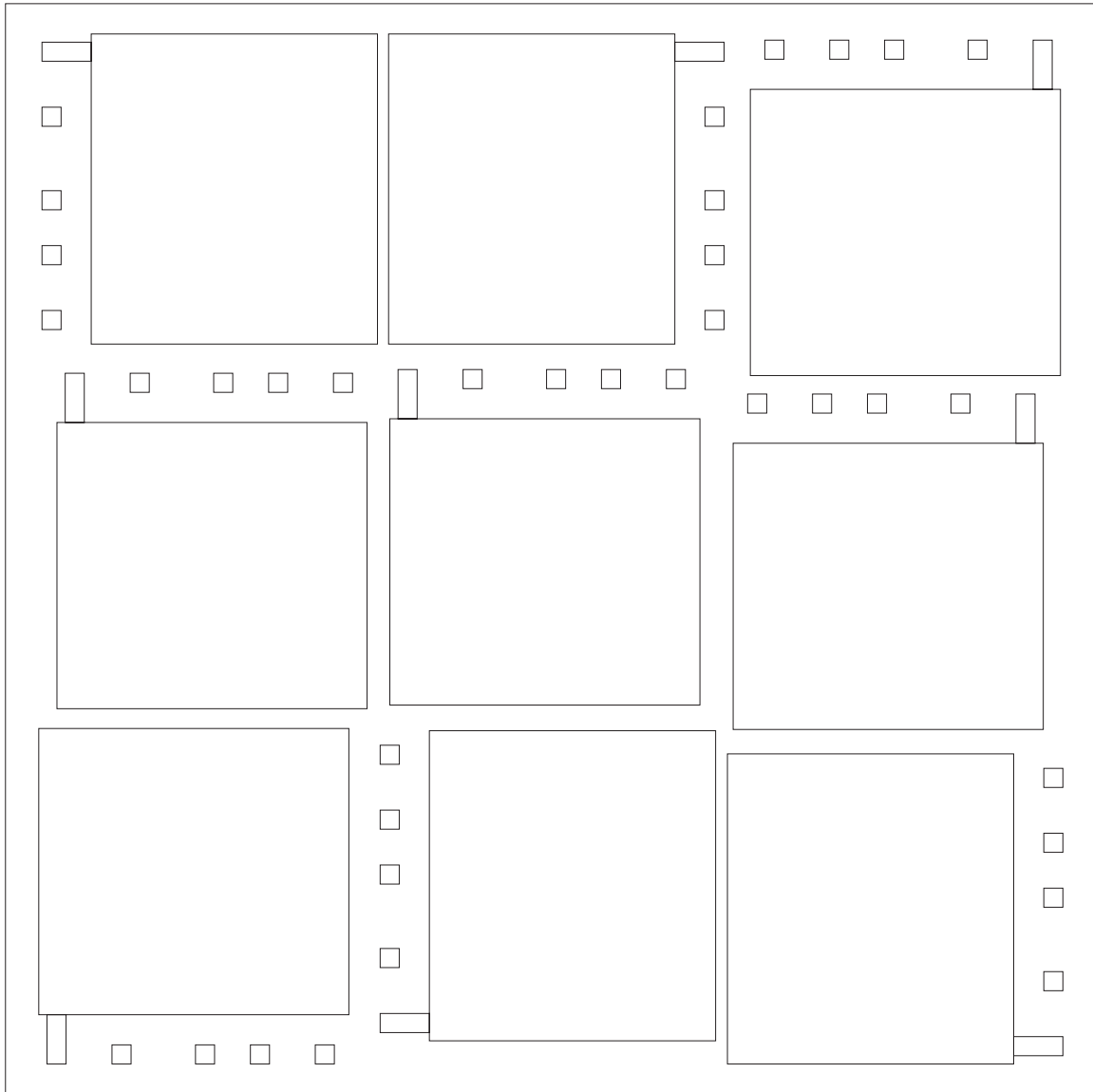


Figure 4-26: January 2006 three wavelength sensor back plane production design. The dimensions of the bounding square is 9×9 inches.

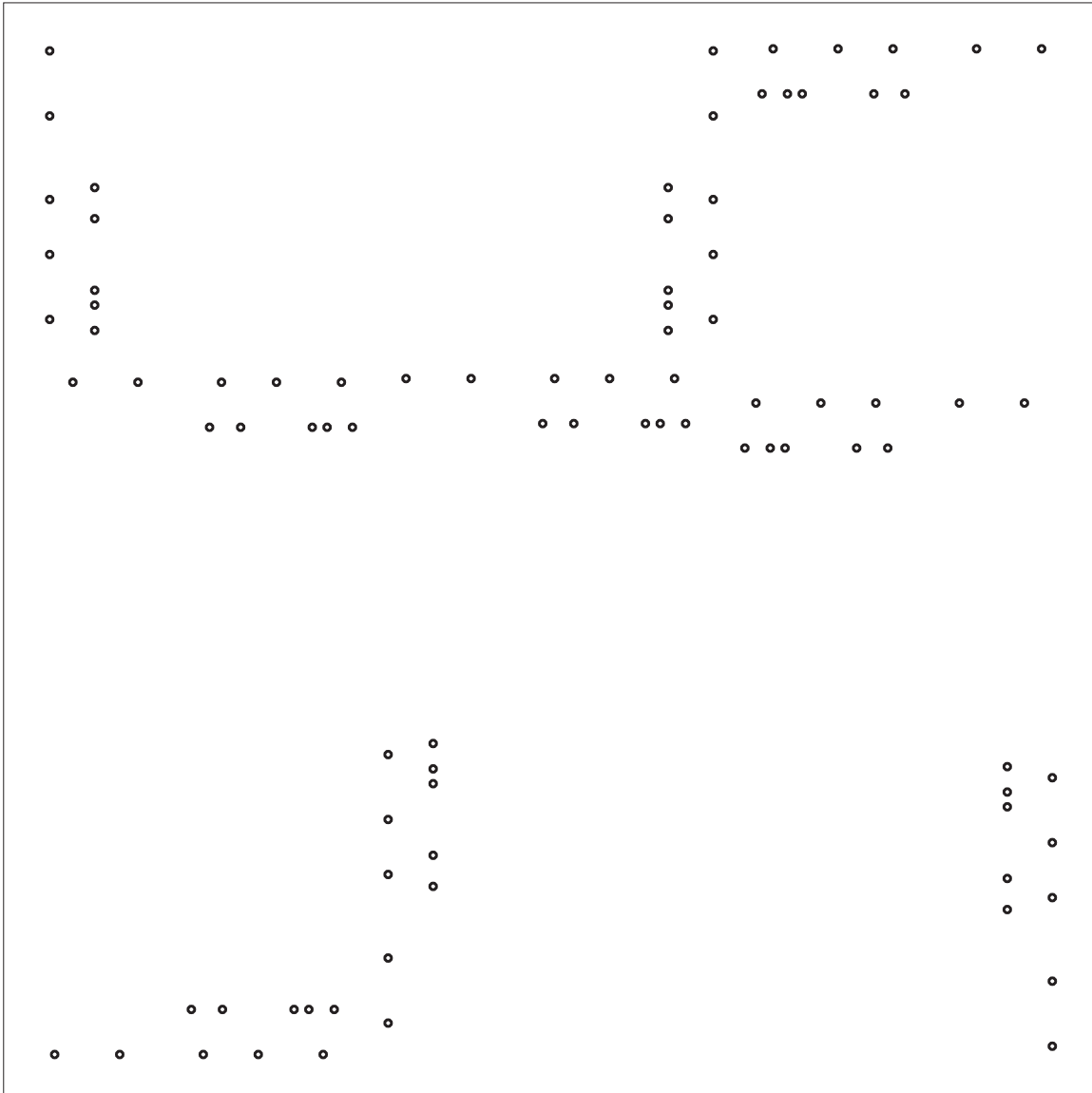


Figure 4-27: December 2006 via locations for three wavelength sensor production design. The vias are shown oversized to clarify their location. The actual via is a circle with a 0.56 mm diameter. The dimensions of the bounding square is 9×9 inches.

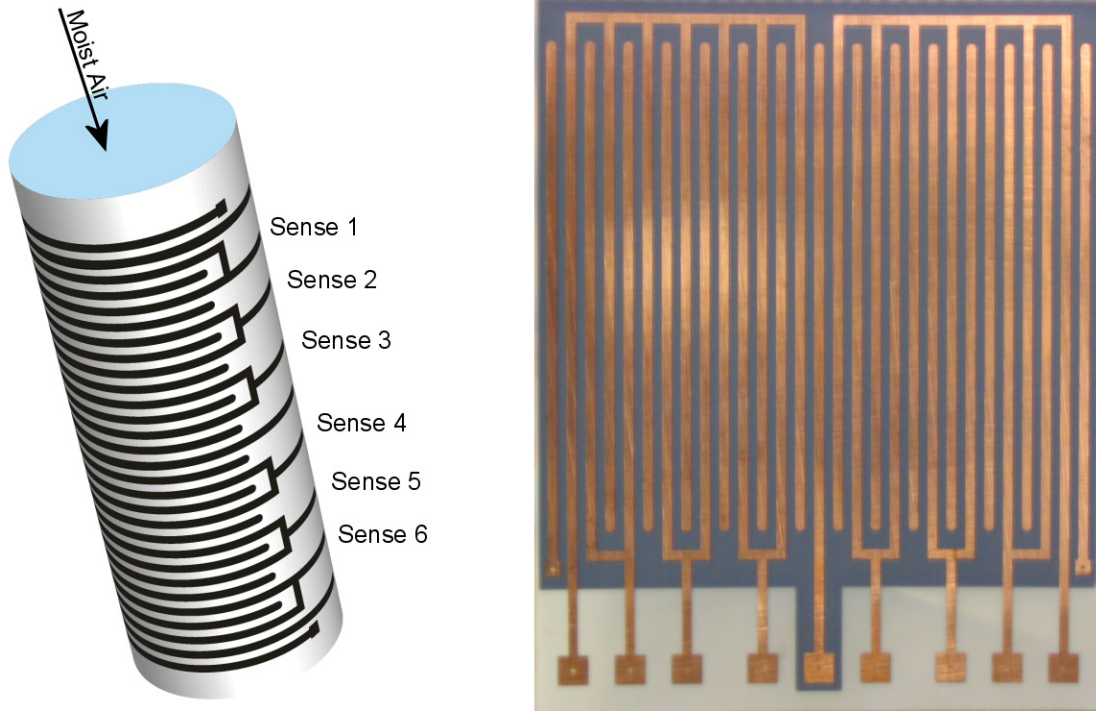


Figure 4-28: Left: Rendering of the six channel z periodic sensor in a typical measurement scenario. Right: Photograph of the z periodic sensor (actual size).

4.2.4 Six Channel z Periodic Sensor (December 2006)

The six channel z periodic sensor manufactured in December 2006 is specifically designed for experiments where moisture is diffusing into the MUT from one end as shown in Fig. 4-28. The figure also shows an actual size photograph of the sensor designed for use on the single conductor cable. The sensor is designed for use with two controller boxes simultaneously so that six measurement channels are possible. Each channel is attached to a two finger 5 mm wavelength sensor. The manufactured design is shown in Figures 4-29, 4-30, and 4-31. The electrode length is determined by the circumference of the cable to be measured. The top three sensors are for the three conductor cable and have electrode lengths of 10 cm. The lower three are for the single conductor cable and have electrode lengths of 6.7 cm.

The spacing of the channel location is 1 cm except at the gap between channels four and five where a guard electrode has been introduced to allow for the independent operation of channels 1-3 and 4-6. This is necessary because the interface boxes only support three channels each and two interface boxes must be used with this sensor.

We associate a position with each measurement so that a profile can be formed. Taking the first

channel as being at position zero the effective channel positions are 0.0, 1.0, 2.0, 3.5, 4.5, and 5.5 cm. The channel is assumed to be located at the midway point between the two sense electrodes. These channel positions allow us to create a profile of any process moving in z , the direction of electrode periodicity.

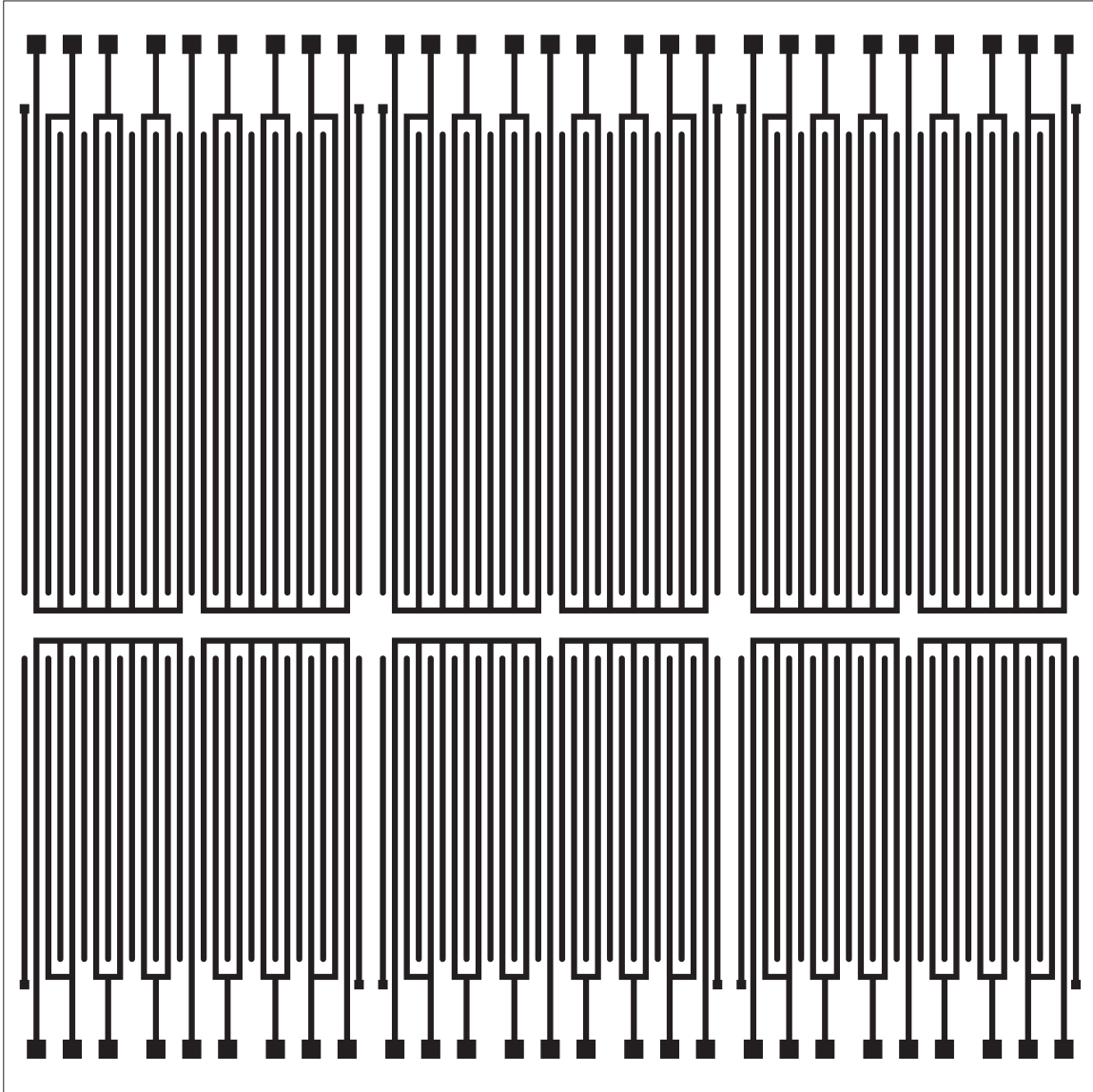


Figure 4-29: December 2006 electrode production design. The larger sensors are for the three conductor cable, and the smaller sensors are for the single conductor cable. The dimensions of the bounding square is 9×9 inches.

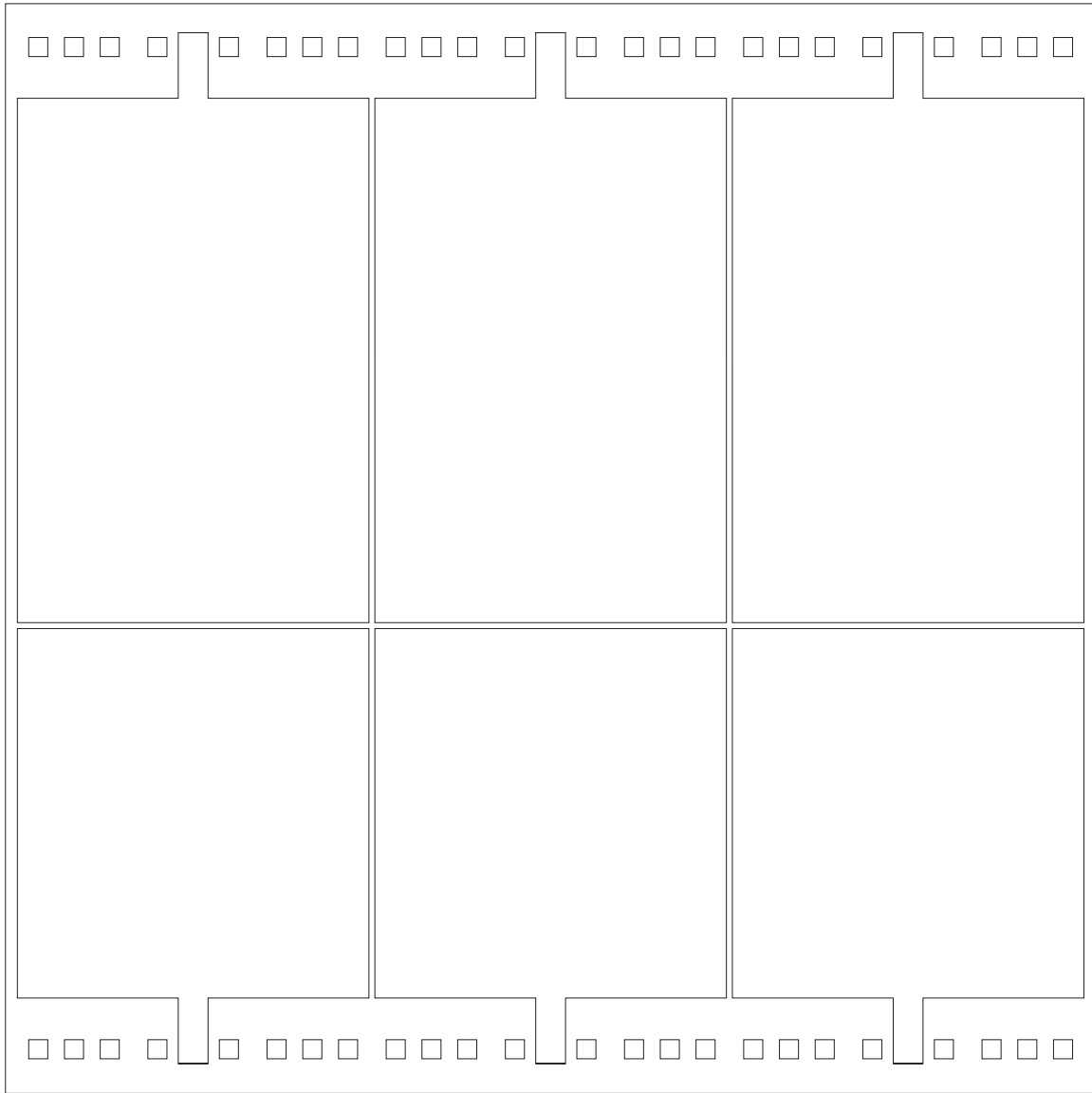


Figure 4-30: January 2006 back plane production design. The actual dimensions of the bounding square is 9×9 inches.

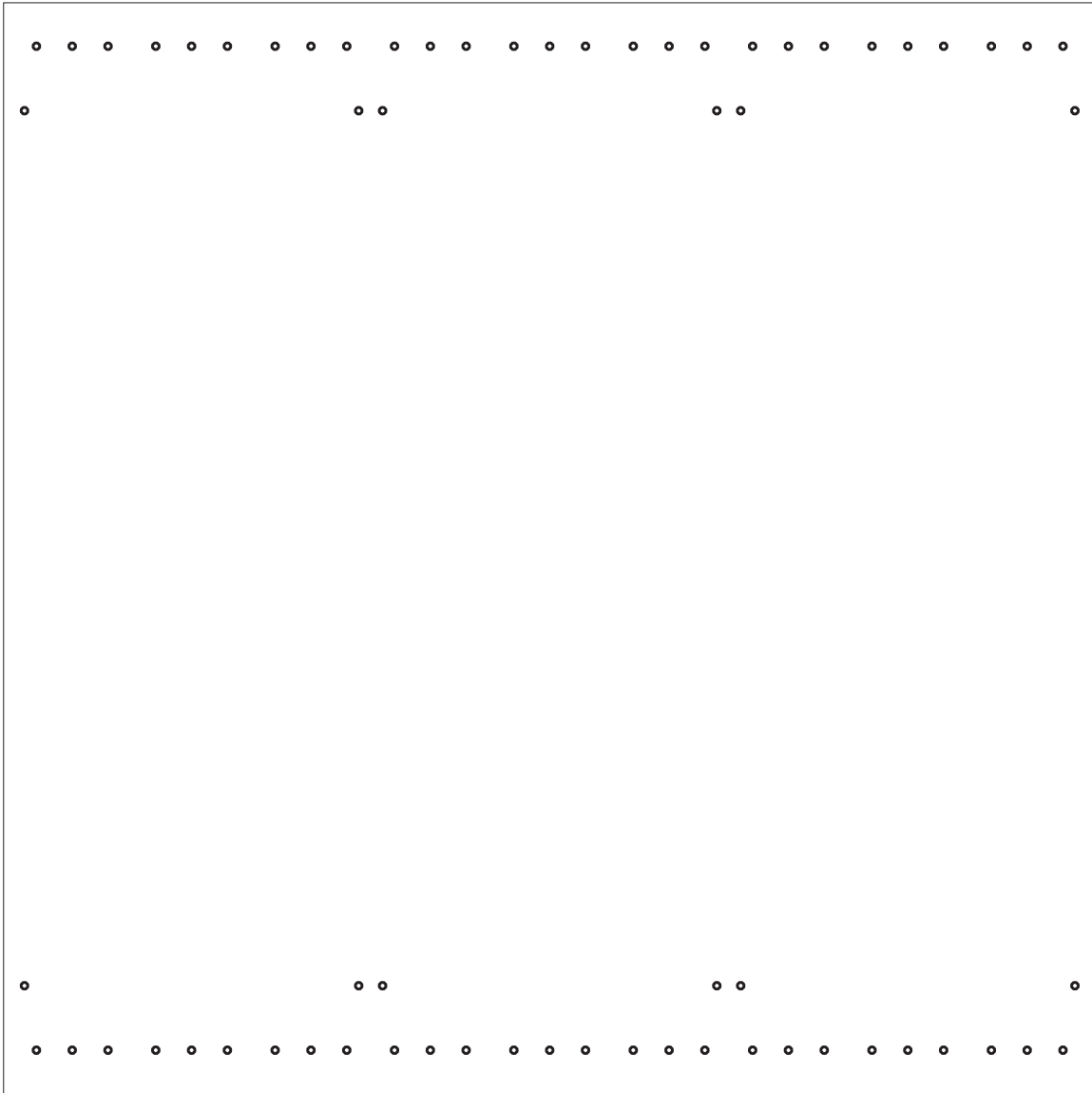


Figure 4-31: January 2006 via locations for production design. The vias are shown oversized to clarify their location. The actual via is a circle with a 0.56 mm diameter. The actual dimensions of the bounding square is 9×9 inches.

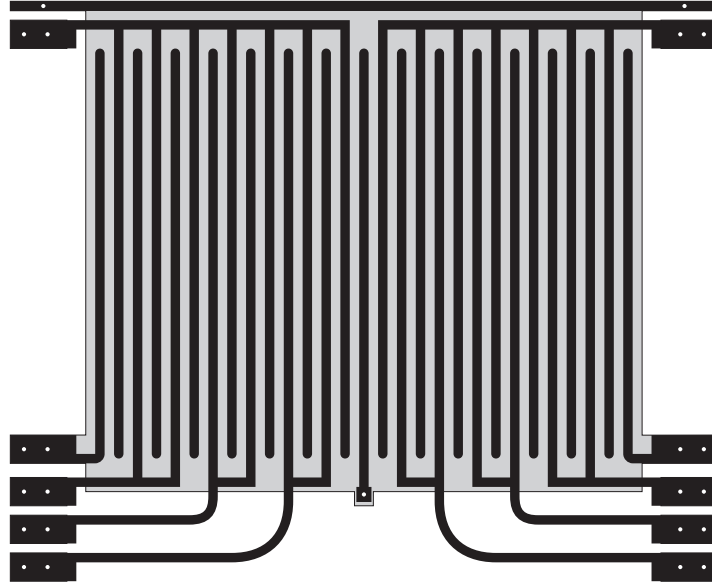


Figure 4-32: Design for a six channel z periodic sensor with end connections. The electrode periodicity is 5 mm. Sensor shown is the actual size.

4.2.5 z Periodic Sensor with End Connections

A sensor with end connections serves as an alternative design to the six channel sensor. The sensor is shown in Fig. 4-32. All electrical connections can be made at the ends eliminating the need for access along the side of the cylinder. It is believed that the better clamping mechanisms require 360° access to the sides, and by placing all connections to the ends, the intimacy of the contact between sensor and MUT can be improved. Again a 5 mm wavelength has been used here. The design is for the single conductor cable. Access is required to both ends of the cable. Notice the inclusion of a grounded strip along the top to minimize coupling between the drive pads and sense pads. This sensor has not been manufactured.

4.2.6 z and ϕ Periodic Sensor

A z and ϕ periodic sensor could monitor diffusion from a small crack. The concept is illustrated in Fig. 4-33. Moisture is allowed to enter from a small region between a z and ϕ periodic sensor. Ideally symmetry demands the diffusion process be symmetric about this point so that the combination of the two sensor measurements can be used to describe the diffusion process.

The proposed sensor is shown in Fig. 4-34. The location of the moisture entrance point should be somewhere along the line where the sensors meet. In this case the wavelength for both sensors is 4 mm. A different number of electrodes appears on each channel since the moisture gradient

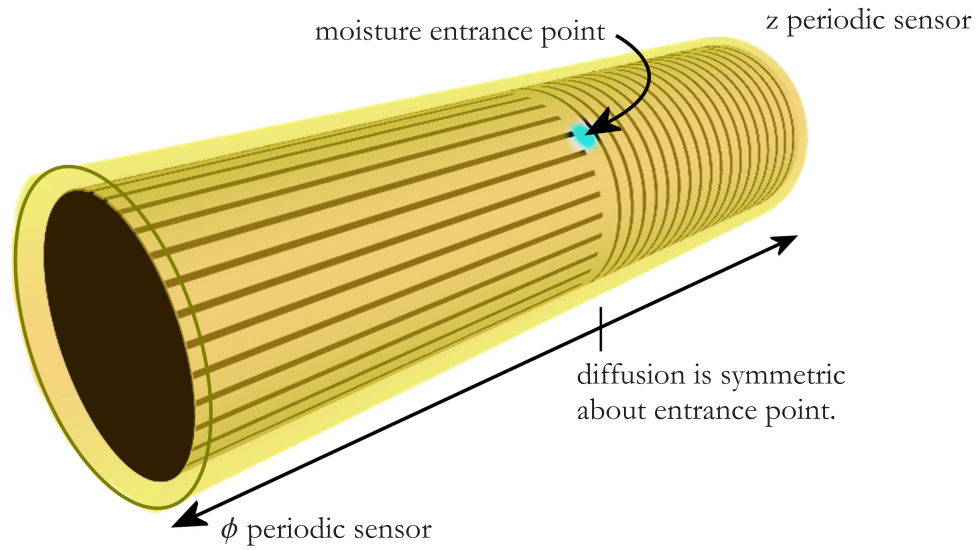


Figure 4-33: Cracked sheath experiment concept. The combination of a z and ϕ periodic sensor is used to monitor moisture diffusion from the moisture ingress point.

will be very large near the crack site, tailing off away from the crack. This sensor has not been manufactured.

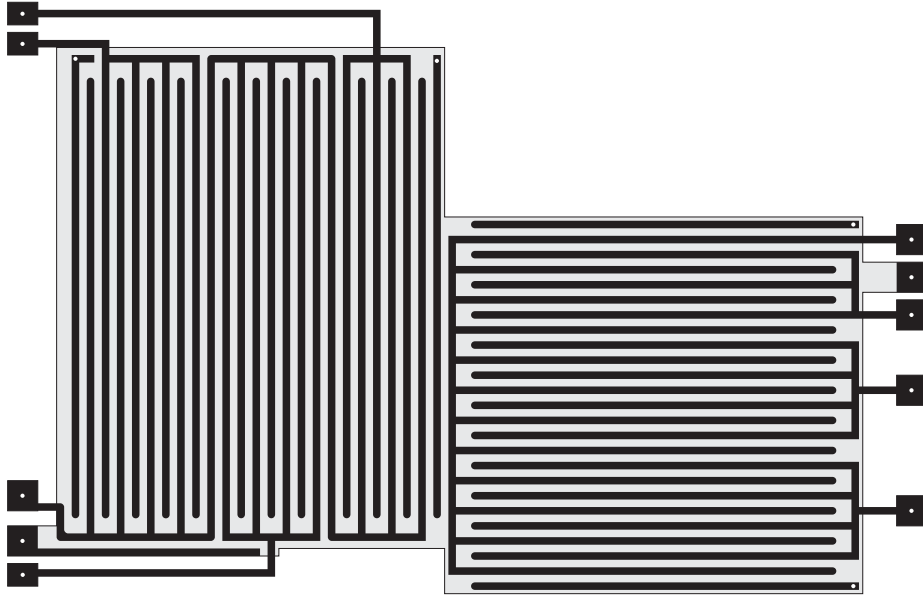


Figure 4-34: Six channel z and ϕ periodic sensor design. The sensor wavelength is 4 mm. Sensor shown is the actual size.

4.3 Hydrophilic Sensor

The presence of the sensor substrate limits the measurement configurations of the dielectrometry sensor. The substrate used in our designs is Teflon, chosen for its low conductivity and hydrophobic properties. Because Teflon does not absorb water, its electrical properties do not change during moisture diffusion experiments. At the same time it dictates an insulating boundary condition anywhere it is in contact with the MUT. It would be useful to be able to achieve a concentration boundary condition at the surface of the electrodes and the MUT. In order for this setup to exist, a hydrophilic sensor substrate is needed.

In early dielectrometry research Kapton, a polyimide film, and silicon dioxide were used as a sensor substrate [17, 69, 70]. Both are hydrophilic, and the substrate can absorb moisture. The problem is that the electrical properties of the substrate change when moisture is in it. In both cases a thin parylene coating was used to prevent contaminants from entering the substrate and dominating the response.

A useful hydrophilic substrate cannot become dominantly conducting if measurements of the MUT are to remain possible. Ideally the substrate must provide a constant moisture concentration at sufficient levels as to provide moisture to be absorbed by the MUT. That is it has an infinite diffusion coefficient. Ideally the substrate is non-conducting, even with the presence of moisture,

and has a dielectric constant of one to maximize the amount of field passing through the MUT.

In fact our description of an ideal hydrophilic substrate is very similar to air. Moist air can freely enter the MUT through the gaps between the electrodes, permitting a diffusion experiment not possible using a traditional sensor. Depending on the temperature and level of humidity, the moisture in the air may have an insignificant effect on the permittivity. The diffusion of moisture in the air is generally orders of magnitude faster than any material to be measured. The primary difficulty is that air offers no structural support for electrodes. The electrodes must be secured to the MUT. Depending on the MUT various solutions are possible. For many materials metal plating can be applied as it is for CuFlon and other materials. Other possible approaches include painting metal electrodes on or using a copper tape. For the purposes of theory the surrounding air serves as the substrate.

4.3.1 Experiment: Dielectric Response of Moist Air

How the presence of moisture in air affects the dielectric properties will in part determine the efficacy of such a sensor. By simultaneously monitoring air temperature, relative humidity, and dielectric properties we can observe how the former affect the later.

The dielectric properties of moist air can be monitored using the three wavelength sensor introduced in Section 4.2.3. The sensor is placed inside a vacuum chamber along with a temperature and humidity sensor. The temperature is set to 155 °F and the chamber is thoroughly dried using a vacuum pump. The relative humidity is then increased to 34% (see Fig. 8-23) and the response is monitored for about 13 days. The measurements are shown in Fig. 4-35. The initial response to moisture reaches its peak on the 1 mm and 2.5 mm sensors in less than 30 minutes, a time scale too small to be visible on the plot. The permittivity and conductivity calculated for each wavelength and frequency are shown in Fig. 4-36.

The 2.5 mm sensor gain returns to the baseline measurement at 100, 1,000, and 10,000 Hz after about one day. The phase for the 1 and 10 kHz measurements are normal after two days. The 10 Hz channel takes nearly 8 days to recover the baseline gain, and the phase doesn't return to the baseline until the chamber is evacuated after 13 days. The 1 mm sensor gain and phase is dramatically affected by the moisture step and only the measurements at 10 kHz recover before the chamber is evacuated. The 5 mm sensor gain and phase does not change throughout the experiment.

Our interpretation of these results is that a partial film of water formed on the sensor during the humidification process leading to the different responses observed. This is possible because of non-uniformities in the temperature during this time. This partial film of water on the sensor leads to conduction paths from the drive to sense electrode predominantly affecting the smaller wavelengths

at the lowest measurement frequencies. For the 5 mm wavelength the conduction paths are not formed and the film is effectively too thin to be detected at this wavelength.

4.3.2 Sensitivity of Air Substrate Sensor

It is necessary to consider the sensitivity of an air substrate sensor to changes in the electrical properties of the MUT, and compare them to traditional sensor technology. In order to determine the sensor sensitivity we study the effect of removing the substrate. Figure 4-37 shows the effect of changing the substrate permittivity to ϵ_0 and then increasing the distance between the ground plane and the electrodes. The ϕ periodic sensor theory is used with the single conductor cable dimensions ($r_e = 1.4$ cm, $r_0 = 0.95$ cm). In order to eliminate C_f and show the difference in sensitivity to various MUTs, the gain is normalized to 0 dB for a MUT of $\epsilon_r = 1$. Overall the effect of eliminating the substrate is to increase the capacitance. This is primarily due to the removal of the ground plane. Now the field lines all terminate on the electrodes. A larger capacitance is more easily measured. The rate of change in capacitance with MUT permittivity is approximately the same for all cases. This results in an apparent reduction of the dynamic range of the voltage measurements, however, overall the Gain will be significantly higher, improving noise tolerance.

The width of the electrodes is an important physical consideration in the sensor design. The narrower the electrodes, the more uniform the moisture diffusion into the cable will be. Thinner electrodes, however, may pose greater challenges in mechanically affixing the sensor to the MUT. Figure 4-38 illustrates clearly that the thickness has a significant impact on the measured capacitance. Electrode widths of 0.7, 1.25, 1.5, and 2.0 mm are shown as examples. The $\epsilon_r = 2.1$, $t_s = 10$ mil is again shown (blue) for reference. The standard sensor electrode width is $\lambda/4$ (1.25 mm). Overall the wider the electrode the greater the capacitance measurement. The rate of change in capacitance with permittivity also increases, but the dynamic range is practically unchanged.

The penetration depth should also be considered. If possible, multiple penetration depths should be used to provide greater details to changes in MUT properties perpendicular to the sensor. Narrow electrodes generally result in an increase in penetration depth.

We conclude that the air substrate sensor may be an effective way of measuring moisture diffusion into materials. The critical challenge lies in constructing the sensors physically. Wires leading to and from the sensor electrodes will certainly affect the field since they must exist in the solution region. Development of a practical sensor requires the effect to be negligible or otherwise accounted for.

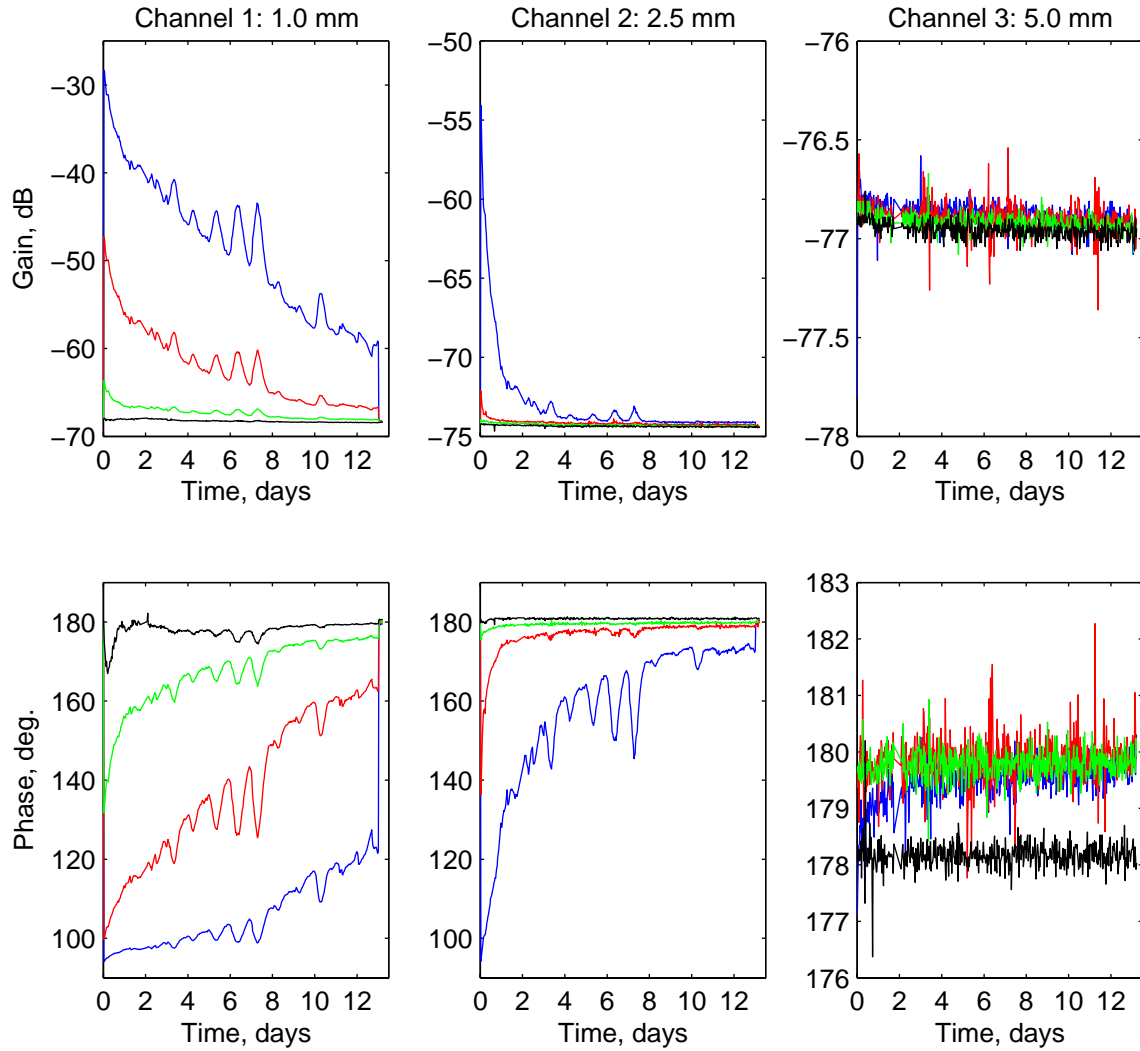


Figure 4-35: Dielectrometry measurement of moist air at 155 °F and 34% relative humidity. The initial response to moisture peaks on the 1 and 2.5 mm sensors in less than 30 minutes. The 5 mm channel appears unaffected. Measurements are shown at 10 (blue), 100 (red), 1,000 (green), and 10,000 (black) Hz for the 1, 2.5, and 5 mm dielectrometry sensors. $C_f = 5nF$ on all channels. This measurement was conducted from July 5 to July 26, 2006.

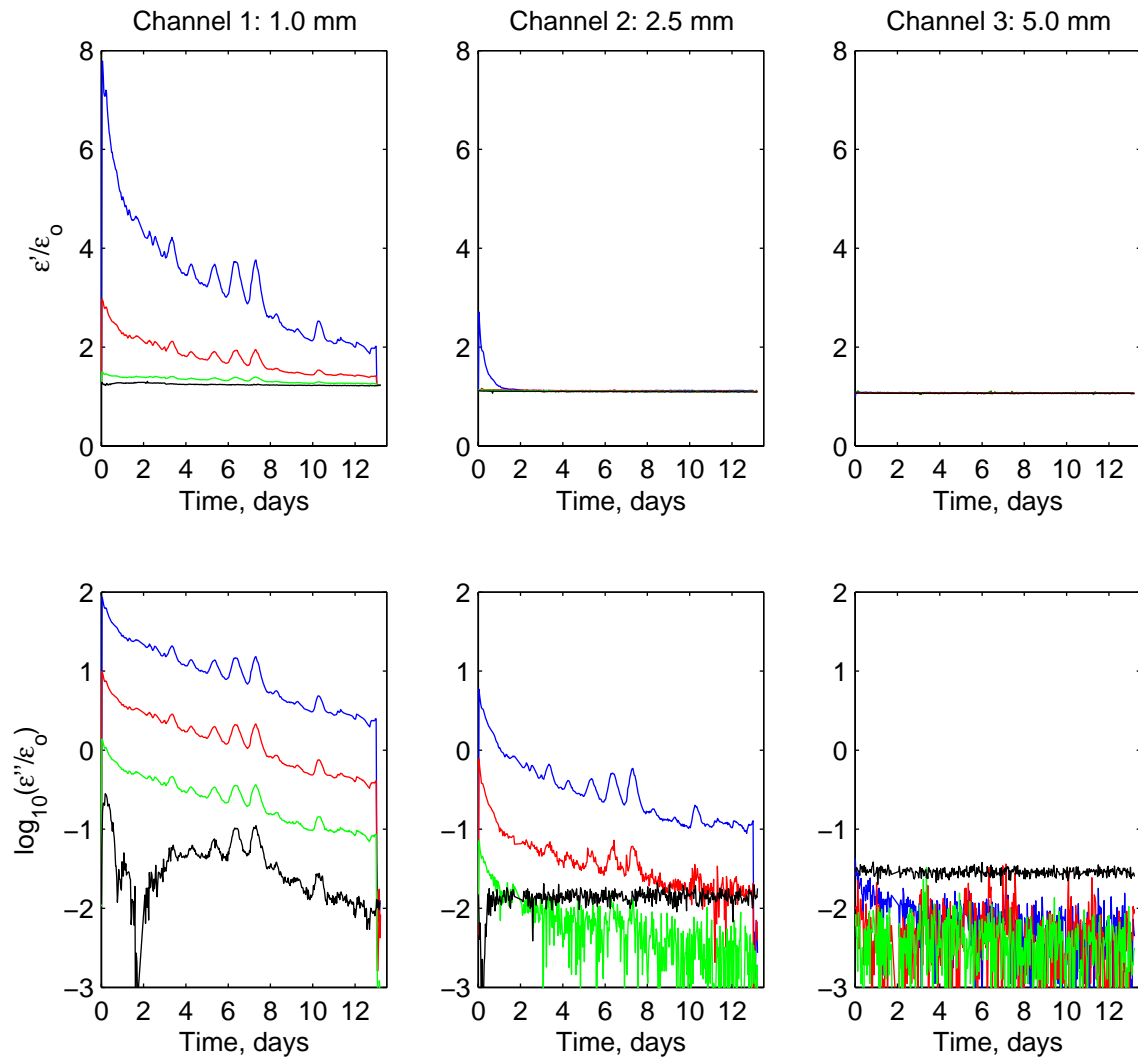


Figure 4-36: Calculated permittivity for the moist air measurements in Fig. 4-35. Calculated values are for measurements at 10 (blue), 100 (red), 1,000 (green), and 10,000 (black) Hz for the 1, 2.5, and 5 mm dielectrometry sensors.

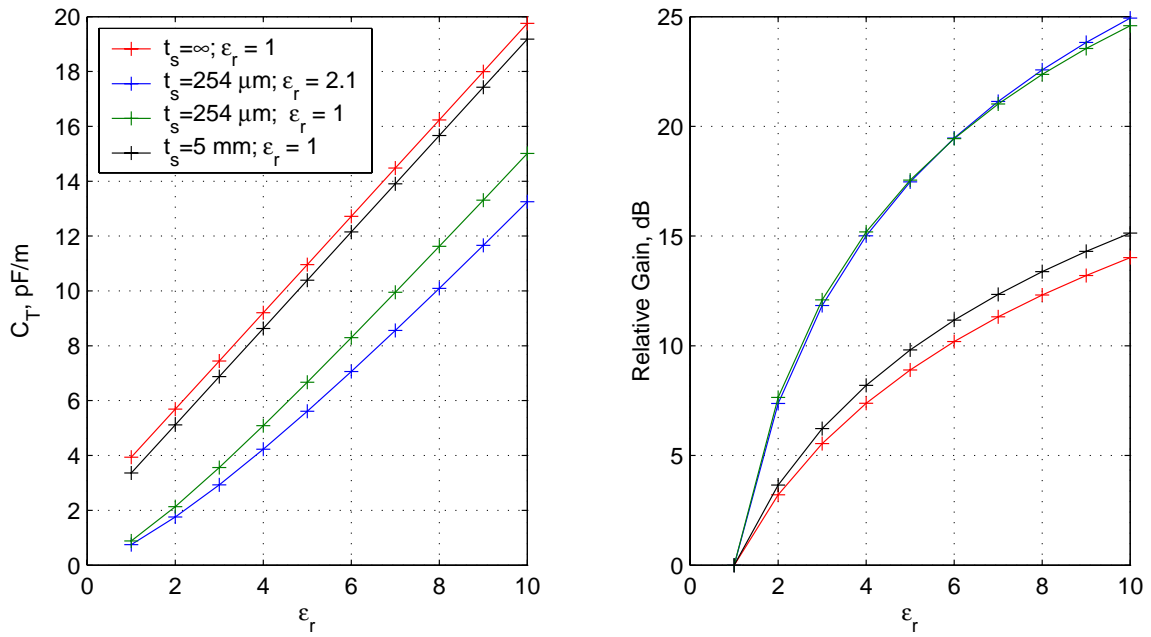


Figure 4-37: Study of the effects of substrate thickness on transcapacitance and sensor gain as MUT permittivity is varied. The single conductor cable dimensions are used for r_e and the center conductor diameter. Relative gains are calculated by subtracting the gain calculated for $\epsilon_r = 1$. $\lambda = 5 \text{ mm}$.

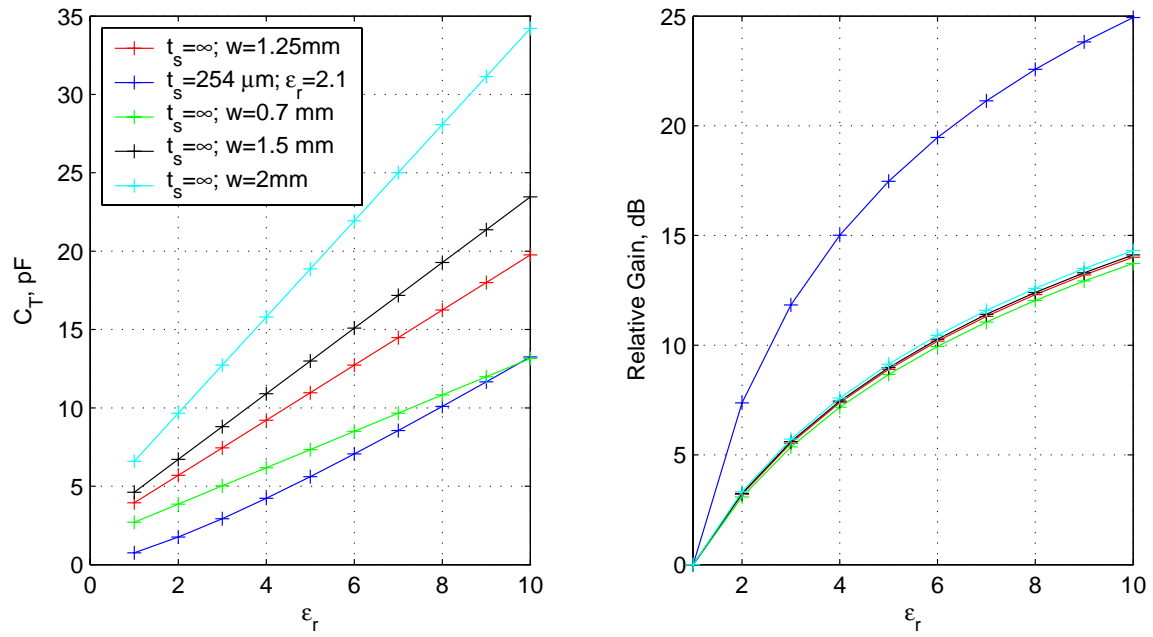


Figure 4-38: Study of the effects of drive and sense electrode thickness on transcapacitance and sensor gain as MUT permittivity is varied. The wavelength is 5.0 mm and the electrode width is w . For the blue curve, $w = 1.25$ mm. The single conductor cable conductor and insulator radii are used. Relative gains are calculated by subtracting the gain calculated for $\epsilon_r = 1$.

4.4 Chapter Summary

In this chapter we have verified through numeric case studies the derivations completed in Chapter 3. A series of comparisons have been made between the ϕ periodic and planar sensor, and the z periodic and planar sensor. As anticipated, as the ratio of the sensor radius to sensor wavelength becomes large, the behavior of the cylindrical sensors and the planar sensors becomes identical.

Several case studies are made to illustrate the potential (Section 4.1.4) and electric field lines (Section 4.1.5) inside the solution region. The theory is capable of considering lossy materials as well. To illustrate the frequency dependence of the transmittance for lossy materials, examples are considered for the planar, ϕ periodic, and z periodic geometries (Section 4.1.6).

Several sensor designs were manufactured for experimental measurements. In Section 4.2 each of the sensors used is illustrated. For possible future applications, several new sensor designs that were not manufactured are also presented.

Finally, in Section 4.3 a hydrophilic sensor design is presented. This sensor could be printed directly onto the material under test, eliminating the need for a sensor substrate. The advantage of this sensor is that it allows moisture to pass through it, enabling experiments to be performed that are not possible with a hydrophobic substrate such as Teflon.

Chapter 5

Experiment Design

Our efforts to determine the electrical properties of the PILC cable insulation require experimental tests to be conducted. In this chapter we outline the types of experiments to be conducted and present the measurement hardware and software used. All our experiments fall into one of two categories: transient measurements, where a diffusion process is typically being monitored, or steady state measurements, typically a frequency scan at a stabilized temperature and relative humidity.

The hardware can be broken into three categories: the sensing hardware, the mounting hardware, and the environment control hardware. The sensing hardware includes the interface and controller boxes which excite and measure the response of the dielectrometry sensors. The mounting hardware is what holds the sensor in contact with a cylindrical MUT. The environment control hardware maintains and monitors the desired temperature and moisture environment for the experiment.

In addition to presenting the measurement equipment, we also present some independent analysis of the capabilities of the measurement hardware. The choice of experimental procedure is also discussed in light of its evolution during the course of the research. Finally sources of measurement error are discussed. A study is conducted to estimate measurement noise.

5.1 Experiments

The experiments to be conducted are designed to provide information on the electrical properties of the power cables oil-impregnated paper insulation. The moisture diffusion properties of the material are also determined by monitoring various diffusion processes.

Before beginning anything other than the simplest measurements we must first determine what the dielectric properties of the insulation depend on. Clearly if a dependence is found on a parameter

not recorded during a measurements, it is difficult to attribute changes in the properties, and the measurements become quite ambiguous. The premise of the choice of the interdigital dielectrometry sensor is that the dielectric properties will change with the presence of moisture in the insulation. It is also known that the dielectric properties will vary with temperature. The pressure of the ambient air is not expected to play a significant role in the dielectric properties by itself. What it can effect are the moisture levels in the air and in turn the boundary conditions and air-MUT equilibrium moisture levels.

Other parameters that may effect dielectrometry measurements include the orientation of the cable itself in the experiment. Gravity will tend to draw the oil out of the cable over time. While an experiment extending over several months may be able to detect this change, the time constant is very long. (This is a problem for vertical installations of PILC which can fail at the top due to dry paper.) Our experiments are typically conducted over lengths of time which this effect can be ignored. Nevertheless, while over an individual experiment this effect may be ignored, fresh cable samples should be used as often as possible to avoid any cumulative effect that may accrue over several months.

In order to provide a temperature and humidity controlled environment a vacuum chamber is used. The chamber has connections necessary for the dielectrometry hardware and the environmental control and monitoring hardware. A simplified view of the experimental setup is shown in Fig. 5-1. The dielectrometry measurement system consists of a controller box, which provides the excitation signal and measures the response, and an interface box, which provides amplification to the drive signal, and the current to voltage converter operational amplifier circuit in Fig. 3-5. A temperature controller connected to a thermocouple temperature probe and heat tape regulates the chambers temperature. Various methods are used to introduce moisture into the chamber. Shown is a setup where humidified nitrogen gas is bubbled through water and then into the chamber. A relative humidity sensor is placed inside the chamber and the measurements are logged by PC. Humidity can be removed from the chamber by evacuating the chamber using a connected vacuum pump. A pressure gauge provides a means of measuring the chamber pressure to determine the quality of isolation from the ambient environment.

The measurement and environmental monitors and controls are connected to a PC operating LabVIEW version 8.0 prior to December 2006, and version 8.2 thereafter. LabVIEW provides a means to initiate measurements, record measurement results, control and record temperature, and monitor the relative humidity and pressure.

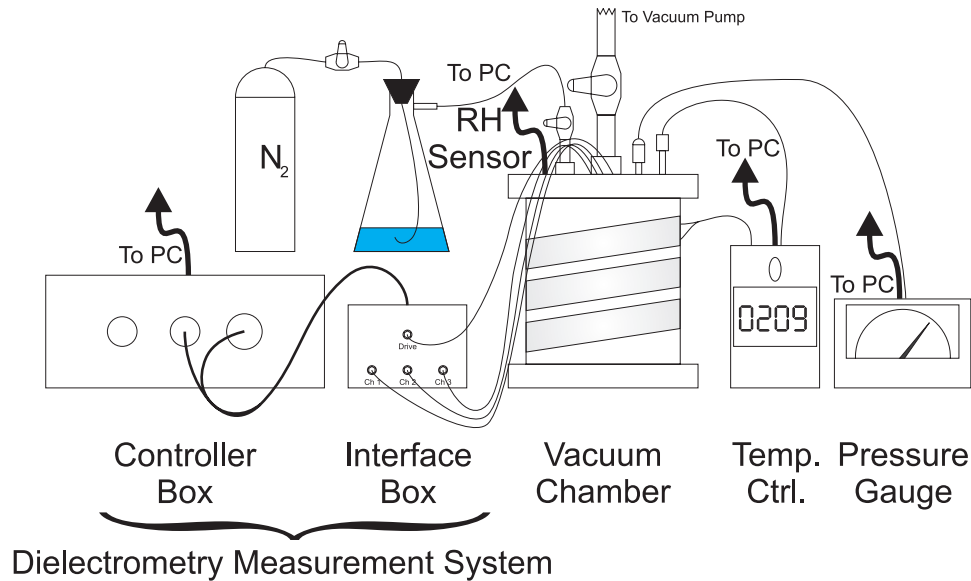


Figure 5-1: Simplified experimental setup with the principle components labeled.

5.1.1 Steady State Experiments

The temperature dependence of the dielectrometry response of the power cables can be explored by measuring the response at fixed temperatures. The response is measured for frequencies from 10^{-2} to 10^4 Hz. The temperature is regulated during the measurement to minimize variation. Since the conditions are steady state, the temperature is uniform throughout the cable sample. Measurements are automated and are taken sequentially at increasing or decreasing temperatures depending on the initial temperature and the range of temperature set points. After the completion of a measurement, the temperature set point is adjusted and allowed to stabilize before the next measurement is initiated. Typically a stabilization time of 30 minutes or more is used depending on the material under test.

The temperature controller is typically used in proportional mode for these measurements since it provides excellent temperature stability with minimal calibration effort. A consequence of this is that the set point temperature is never actually reached. This and other issues involving the temperature controller are discussed in Section 5.4.2.

The relative humidity for the majority of these measurements is 0%. The vacuum pump can be run throughout the experiment to prevent moisture from entering the MUT at any time. Because the moisture diffusion time is much longer than the heat diffusion time, experiments involving moisture are generally measured as transients. The experimental results of the steady state measurements are presented in Chapter 6.

5.1.2 Transient Experiments

In principle either the temperature or humidity could be changed to provide a basis for a transient measurement. A temperature transient measurement has a number of difficulties. Essentially the boundary conditions on the cable are not well known. First the temperature inside the chamber cannot be changed in a uniform way. Second, heat transfers through all the materials, including the sensor, clamping mechanism, rubber linings, etc. is unknown. Each material has its own thermal conductivity, specific heat, and density, which in general must be determined before solving the heat equation. To interpret the results these parameters must be known for all the materials. The setup is difficult to model analytically and a detailed 3D model would be needed. Finally, because the temperature transients are on the order of minutes, the profile will change during the course of a frequency measurement. The controller box requires a minimum of three sinusoidal oscillations before declaring a gain and phase measurement for a given frequency. A single measurement at 10^{-2} Hz takes at least five minutes. The heat distribution could be dramatically different from the start to end of such a measurement making its usefulness uncertain.

A moisture transient is significantly easier to model because hydrophobic materials having moisture diffusion coefficients much smaller than the MUT are readily available. The boundary conditions can be controlled and tailored for different experiments. The diffusion process typically takes several days to weeks, to months, making the time it takes to make a single measurement insignificant. The transient experiments presented in Chapter 8 are all moisture transient measurements.

Moisture transient experiments typically begin with no moisture at a fixed temperature. Prior to beginning the transient period, an initially steady state is achieved. Often this is done by removing moisture from the environment and sample by using a vacuum pump. When the vacuum pump is running and the dielectric response is stable, it is assumed that the moisture has been removed from the sample. Typically this takes anywhere from a day to a week, depending on the sample and temperature. Having reached a steady measurement, the vacuum pump is turned off and the chamber is flooded with the ambient air. Because the chamber temperature is typically well above the ambient temperature, the relative humidity of this air that flows into the chamber quickly drops as the air reaches the chamber temperature. The relationship could be predicted using a psychrometric chart. Because this typically results in a relative humidity lower than desired, additional moisture must be introduced to the chamber. Two methods have been used. The first involves heating and humidifying nitrogen gas which is forced through the tank for a period of a few minutes. This can sometimes result in excessive moisture, and condensation within the chamber. A second method injects a predetermined amount of water into the chamber with a syringe.

After the moisture has been introduced to the chamber, the chamber is sealed. The temperature

continues to be regulated, and the relative humidity is monitored, but not regulated. Typically the relative humidity decreases during the course of an experiment as a certain amount of the moisture diffuses into the MUT. If the temperature is not uniform throughout the chamber, some moisture may condense. This can occur in extremities such as pipes and other connections that have significant surface area exposed. Finally moisture can always be lost through any leaks in the chamber.

The experiment is allowed to continue until sensor failure or steady state is reached. In many experiments, the vacuum pump is activated to extract the moisture at this point. Ideally over time the sensor response should return to the initial state. When this occurs it verifies that the initial state has been reached and that the cable has no “memory.” That is, the current state has no dependence on the previous state of the cable.

5.2 Sensing Hardware

The complex gain is most generally a function of frequency and therefore measurements must be taken over a frequency range. The choice of frequency range should be made to capture both the capacitive and conductive behavior of the MUT. At “low” frequency the conductive behavior of the MUT dominates. The phase angle is near 90° and the gain decreases 20 dB per decade. At high frequency the capacitive behavior dominates and the phase angle is near 180° and the gain is independent of frequency. There is a transition frequency band where the behavior switches from conductive at low frequency to capacitive at high frequency. The transition frequency is nominally $\sigma/2\pi\epsilon$, as given by eq. 4.5. For the materials of interest, this typically puts us in a frequency band from 10^{-2} to 10^4 Hz.

The sensing hardware used consists of a controller box to generate the excitation and measure the response, and the interface box to amplify the signal and interface with the sensor itself. The controller box was originally developed by David Otten in 1989 and was later modified by Darrell Schlicker to accommodate additional applications using the short circuit current mode [48,54]. The controller box is designed to automatically take complex gain measurements in a frequency sweep. David Otten, a principal research engineer in the Laboratory for Electromagnetic and Electronic Systems (LEES) designed the original hardware and has refurbished and maintained the hardware. The present interface box was developed in 1997 by Darrell Schlicker. In addition to implementing the operational amplifier circuit in Fig. 3-5, it amplifies the input signal. The interface box connects directly to an individual sensor. The controller and interface boxes are pictured in Fig. 5-2.

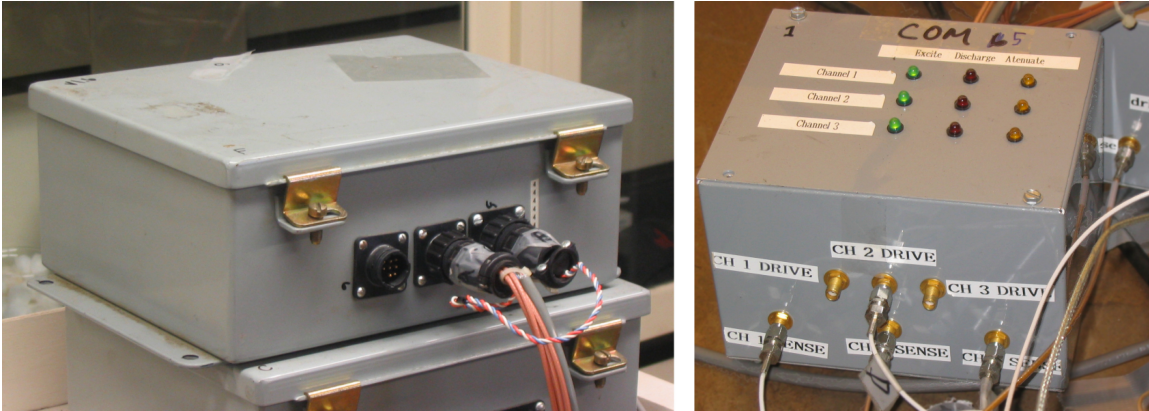


Figure 5-2: Controller (left) and interface (right) box photographs.

5.2.1 Controller Box

The controller box is capable of taking complex gain measurements from .005 to 10,000 Hz ($10^{-2.3}$ to 10^4 Hz). The user may specify any subset within this range for measurement. Measurements are made at ten frequencies per decade with approximately logarithmic spacing. A full spectrum scan has a total of 64 measurements. The controller box natively supports four measurement channels, however, the interface box supports only three. The box can communicate over a RS-232 serial port connection. Commands can be sent over telnet, and measurement data can be downloaded from the controller. The excitation signal is a one volt peak sine wave. Gain and phase measurements are with respect to this input signal. The controller box has a limited memory capacity (256 kb), enabling it to store a limited number of frequency sweeps depending on the number of enabled channels. Under most circumstances data is immediately fed to the PC after the completion of a frequency sweep. The sense signal is buffered using a ± 5 Volt op-amp limiting the gain to $20 \log(5) \approx +14$ dB. The hardware implements a variable gain amplification of the measured signal to use the full dynamic range of the hardware. If the measured signal has a DC component, this will reduce the amplification that can be used, and reduces the quality of the measurement as a result. In addition to reporting the gain and phase for each channel and frequency, the controller box hardware reports the DC offset voltage and the variable amplification used. The latter two pieces of data provide a mechanism for evaluating the reliability of the measurement results. Software version 1.7 supports the functionality of the interface box and is used throughout the research. A description of all the commands needed can be found in [71] and [72]. A summary is given in Section A.3. Details on how to connect and communicate with the box using a telnet program can be found in [32]. LabVIEW is used primarily to send commands and receive and record measurement data from the controller

box. The controller box is photographed in Fig. 5-2 (left).

In some measurements the phase measurements at high frequency tend to increase above 180° . This is due to bandwidth limitations in the preamplifier used to buffer signals in the controller box [71]. The effect is a timing error. The software supports adding a frequency dependent time delay so that a particular phase angle can be achieved. Generally the feature was not used due to some difficulties in calibration. Also, for the vast majority of materials the phase is 180° for high frequency and the error is easily recognized.

The controller box reports gain and phase to two decimal points.

5.2.2 Interface Box

The interface box is connected to the controller box and has three channels for measurements. The design shows efforts to support a 4th channel, however, this feature was never fully implemented. Each channel has two feedback capacitors, one that is always enabled, and a second that can be added in parallel in the feedback loop if the “attenuate” feature is enabled. Ideally this feature would be used to increase the feedback capacitance if the gain became too high, and may saturate the sense buffer op-amp in the controller box. A feature such as this is not currently implemented in the controller or interface box software or hardware. To make use of the attenuate feature practically, the measurement would need to be taken and then checked to see if the controller box was saturated during the measurement. If it was, “attenuate” could be turned on and the measurement retaken.

The interface box is properly initialized by enabling “excite” on the measurement channels. This simply indicates that the drive signal is being sent to the channel.

The “discharge” feature enables the use of a relay to short out the feedback capacitances after each measurement and is controlled by a bat switch on the interface box. The indicator lights on the top of the interface box case labeled “discharge” should be ignored, as software control was never implemented. The bat switch exists on the rear of the interface box so that the discharge feature can be controlled mechanically. A distinct sound of the reed relay can be heard after each measurement. The drive signal from the controller box is amplified by -10 , inverting the original signal. The controller box is unaware of this modification to the drive signal, and to appropriately interpret the gain and phase measurements recorded by the controller box, all gain and phase measurements must be shifted down by 20 dB, and phase shifted by 180° . This correction has been made on every measurement in this thesis. Our inventory includes four working interface boxes. A prototype box exists, however, it lacks several of the features included in the final version. The primary feedback capacitances (C_f in Fig. 3-5) in the four working boxes are summarized in Table 5.1. The capacitances were measured using a Meterman CR50 capacitance tester [73]. The test frequency is

Table 5.1: Interface Box Nominal and Measured Feedback Capacitances

Interface Box	Channel	Nominal Value (nF)	Measured Value (nF)
1	1	5	4.99
	2	5	4.89
	3	5	5.00
2	1	3	3.03
	2	10	9.83
	3	3	3.00
3	1	5	4.90
	2	5	5.08
	3	5	4.94
4	1	5	4.91
	2	5	4.93
	3	5	4.89

850 Hz. An interface box is photographed in Fig. 5-2 (right).

5.3 Mounting Hardware

During the course of the research several different mounting mechanisms have been used to secure the dielectrometry sensor to the sample. Cylindrical mounting is substantially more difficult than the simple pressing needed in planar geometry problems. Ideally, the applied pressure should be uniform over the entire surface of the sensor. It should not cause bunching, folding, or shear forces on the sensor or cylindrical sample. The mounting hardware also must act as a hydrophobic seal in the moisture diffusion measurements. In most cases it is desired that the seal cover the entire cylindrical surface of the rod. The mounting mechanism must also facilitate the connection of electrical leads to the sensor terminals.

It is difficult to meet all of these requirements simultaneously, nor has it been immediately obvious when a particular mounting mechanism has worked well or poorly as it is difficult to isolate the mounting hardware performance from other measurement problems.

5.3.1 Pipe Clamp

The pipe clamp was the first mounting hardware used for experimental measurements. It is shown in Fig. 5-3. It features a large bolt that can be tightened easily. Electrodes can easily be connected at the end of the cylinder. Connection along the gap was never attempted due to poor contact pressure at the necessary angles. The clamp as purchased from McMaster-Carr features a ribbed rubber liner

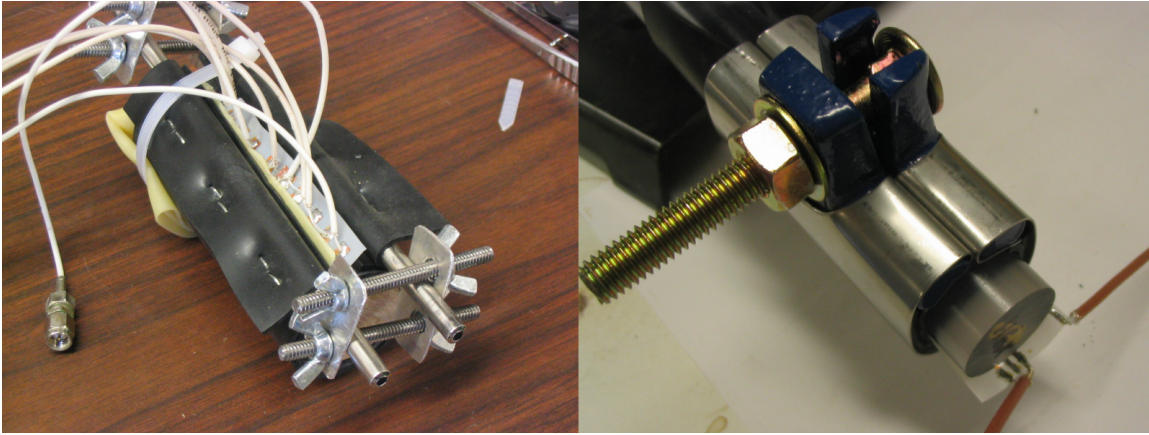


Figure 5-3: Photographs of the sling clamping (left) and pipe clamp (right).

that is glued to the metal sheath. The ribbing is undesirable and a second piece of rubber liner insert is inserted to help produce an even distribution of pressure on the sensor. The pipe clamp design produces significant shear forces away from the bottom of the clamp which has contributed to electrode micro-cracking in some of the older sensor designs. These cracks are invisible to the naked eye yet can easily be detected using an Ohm meter. Once a sensor has suffered micro-cracking it is essentially destroyed and should be discarded. This problem can be reduced by hand tightening the bolt and not using the lever arm of the ratchet.

The pipe clamp does not achieve good 360° pressure on the sample. In the region closest to the bolt, often no pressure is applied at all. Irregularities were sometimes noted in sensor responses for any sensor placed in the 180° closest to the securing bolt. Generally the practice is to avoid this region when possible. If the sensor length is greater than half the circumference, only the longest wavelength should be allowed to extend into this region. Because of this issue, it cannot be claimed to act as a hydrophobic layer protecting the MUT from moisture. This limits our analysis of the diffusion problems performed with this mounting hardware.

Ultimately this sensor mounting hardware does not provide a consistently stable platform for measurements. The hose clamp and sling clamp provide superior results.

5.3.2 Hose Clamp

The hose clamp is an ad hoc attempt to overcome many of the problems with the pipe clamp mounting hardware. It is pictured in Fig. 5-4. The hose clamp design features a series of hose camps in close proximity buffered by one or more layers of rubber linings. The hose clamp proves nearly uniform pressure over 360°. By offsetting the screw position of the individual hose clamps



Figure 5-4: Photographs of the hose clamping mechanism for birch (left) and Teflon (right) sample setups.

the pressure distribution is likely to be more regular. Because of its nature, electrical leads can only be connected at the end of the cylinder.

One of the initial challenges is the buckling of the rubber liners during tightening. The liner must be cut to precisely the correct length to avoid an overlap or significant gap. It has been found that using a single liner (typically 1/8 inch thickness) does not provide an adequate buffer from the features of the hose clamp. When a single liner is used the sensor tends to conform to the shape of the buckle, and the gaps between adjacent clamps can swell.

In the most recent experiments, a triple liner is used. Immediately surrounding the sensor a latex sleeve is applied. The sleeve is formed from a single finger of a latex surgical glove. The latex provides its own tension and does not bunch up. It acts as a moisture barrier on one end of the cylinder in addition to along the cylindrical surface. A rubber layer is then cut to a length slightly smaller than the circumference of the MUT. This layer is wrapped around the cable such that the gap where the edges meet is not supporting the sensor. Finally, a second rubber liner of slightly longer length is wrapped so that its edge is opposite that of the edge of the middle layer.

Achieving this configuration by hand can be an arduous process sometimes leading to sensor leads breaking off. However, once the clamp is secured the leads can easily be reattached. The measurements suggest this is the best method for achieving Neumann boundary conditions on the cylindrical surface of the rod. Latex is not truly a hydrophobic substance, but it appears the rate of moisture diffusion is sufficiently small. A more suitable sheath has not presented itself.

5.3.3 Sling Clamp

The sling clamp is another ad hoc technique developed with the primary purpose of allowing the z periodic sensor connections to be easily attached. It is pictured in Fig. 5-3. The clamp is made of two quarter inch pipes and a rubber sheet. The ends of the rubber are folded down and stapled as shown to provide a guide for the pipes similar to a pole stretcher. The MUT and sensor are placed inside the bed which must be custom cut to the correct length for the sample. Typically, room is allowed for a rubber insert to provide additional padding from the staples.

To tighten the clamp the pipes are squeezed together. The hardware at each end features two plates with holes drilled allowing a threaded rod to slide through. The pipes are placed between the plates and four wing nuts are used to adjust the tightness. Both sides must be adjusted simultaneously to achieve a uniform clamp.

This clamp has proven reasonably successful. The rubber has a tendency to rip at high temperatures if too few staples are used. A wide variety of rubber liners of various thicknesses have been tested. The primary challenge is in achieving a good moisture seal along the top of the sensor. In a future design it should be attempted to have a sensor that tucks the sensor edge, rather than allows it to come up as in the picture.

5.4 Environment Control Hardware

Our primary experimental goal is to take complex gain measurements at various frequencies in a temperature and humidity controlled environment. We would like to monitor and/or control the temperature and relative humidity. For some experiments chamber pressure is also of interest. Our setup consists of the temperature controller, pressure gauge, vacuum pump, humidifier, relative humidity sensors, and a personal computer running LabVIEW. In this section we discuss the purpose, capabilities, and some limitations of each piece of equipment. How the hardware is implemented is also discussed.

5.4.1 Vacuum Chambers

Two vacuum chambers have been modified to run the humidity and temperature controlled experiments. The “small chamber” is cylindrical in shape with a $6\frac{1}{2}$ inch inner height and an inner diameter of $5\frac{3}{4}$ inches. Eight inch flanges cover both ends. Figure 5-5 shows the schematic for the top flange of the small chamber. The top flange has a removable center portion where 4 SMA connectors are seated. Humidity can be introduced through the humidity release valve or by removing the vacuum connection from the quick connect. Vacuum pressures of approximately 0.06 to 0.1 torr

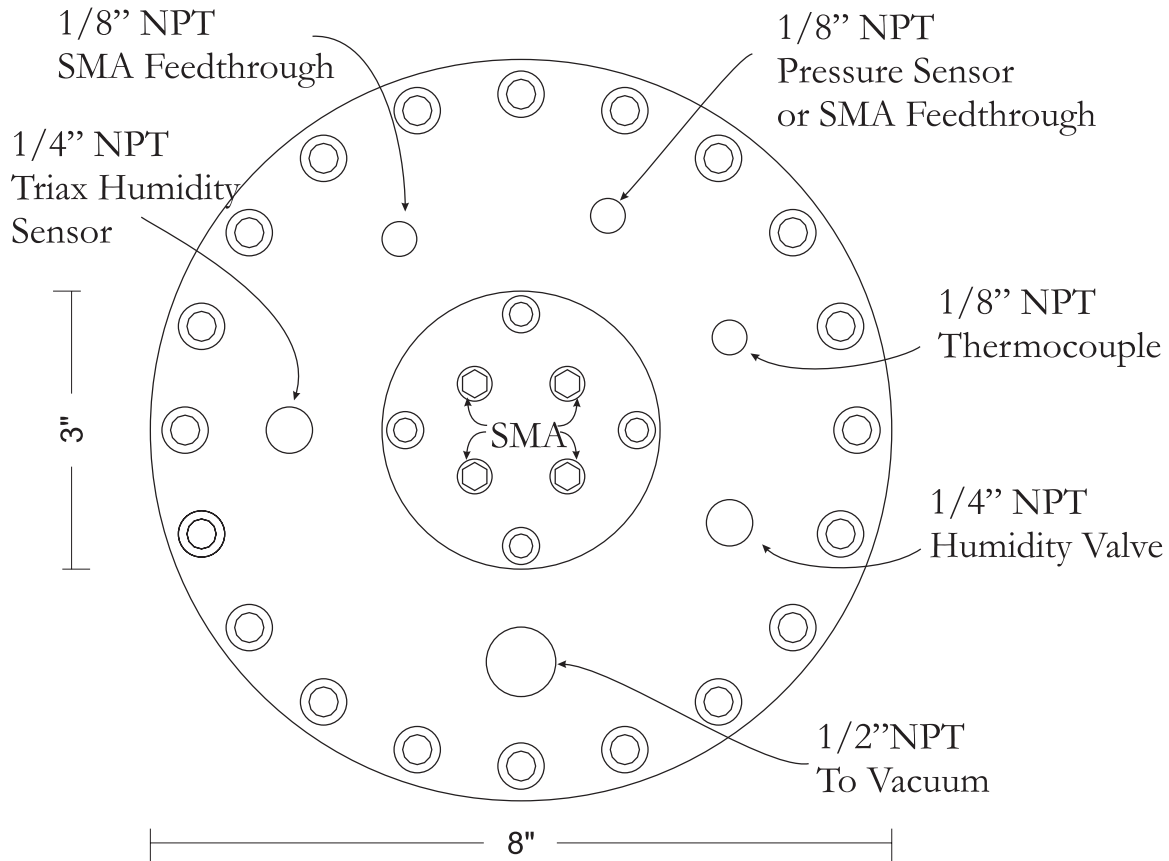


Figure 5-5: Schematic for the top flange for the small chamber. The flange is attached with 20 bolts.

are typically reached, but can only be sustained by continually running the vacuum pump. In some experiments the pressure sensor is removed and replaced with two SMA feedthroughs. This allows for the operation of up to six measurement channels simultaneously.

The “large chamber” is capable of housing two cable samples simultaneously. The chamber is $8\frac{1}{2}$ inches deep with two $2\frac{3}{4}$ inch side ports and top and bottom 10 inch flanges. The vacuum chamber is illustrated in Fig. 5-6. The internal diameter is $7\frac{3}{4}$ inches. The top flange shown in Fig. 5-7 is fitted with the temperature, pressure, and humidity system inputs. The two side flanges shown in Fig. 5-8 have the SMA connections for the dielectrometry sensors.

The top flange is recycled from a previous project and features several input ports, including two isolated BNC connections which have a tendency to leak. This was mitigated by using vacuum grease which allowed us to reduce the pressure to 0.5 torr. This is sufficient to limit moisture leakage. This chamber has the problem that the side ports act as extremities and tend to be cooler than the rest of the chamber. This can result in condensation on the sensor’s SMA connectors which

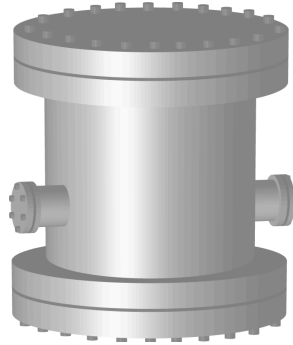


Figure 5-6: Schematic view of the large chamber. The two side ports are visible. The small chamber lacks the side ports.

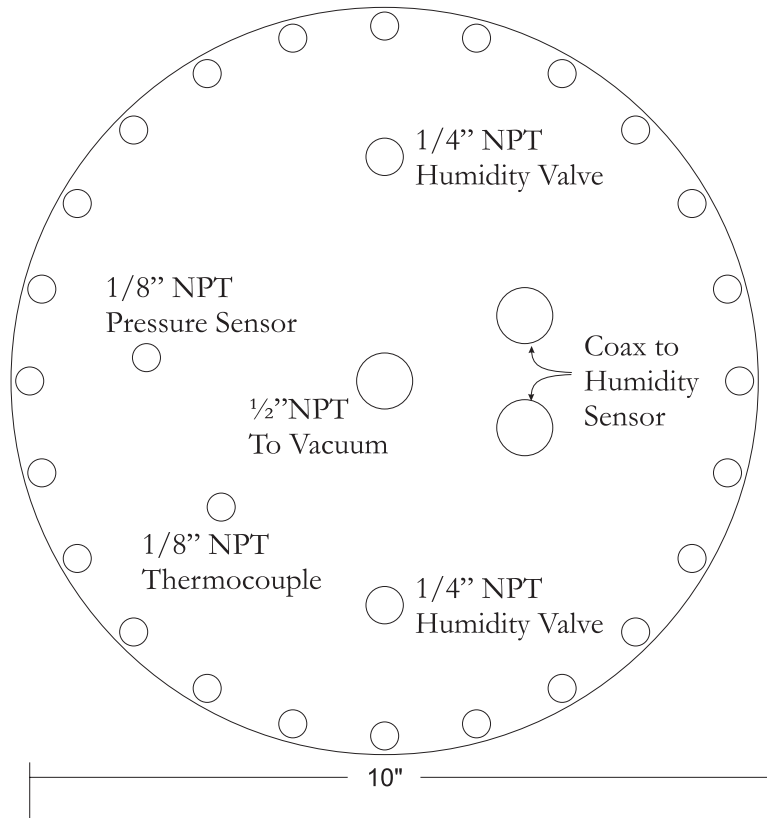


Figure 5-7: Schematic for the top flange for the large chamber. The flange is attached with 24 bolts.

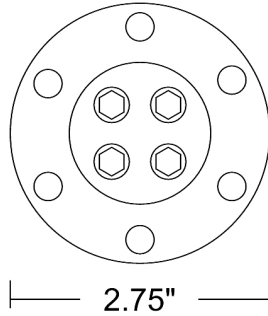


Figure 5-8: Schematic for the side port flanges for the large chamber. In the center are four SMA connectors. The flange is attached with 6 bolts.

feed through the these ports. In some cases this resulted in a short circuit in the connector, and sensor failure.

5.4.2 Temperature Control

An Omega Engineering CN77344-C2 temperature controller is used to regulate the temperature within the vacuum chamber. A T type thermocouple is used to measure the inside temperature of the chamber. A heating tape is wrapped around the chamber. An Omega Engineering SSR240DC25 relay is connected to the temperature controller and the heat tape to insure that the appropriate amount of current can be supplied to the tape. Originally, the controller was configured to Proportional-Integral-Derivative Control (PID) mode, however this often resulted in significant oscillations and was difficult to calibrate. When simply the “proportional” mode is used the temperature stability improves significantly. With the proportional feedback method the applied power, W , is proportional to the difference of the set point and measured temperature.

$$W = \begin{cases} P \times (T_s - T_o) & T_o < T_s \\ 0 & T_o > T_s \end{cases} \quad (5.1)$$

In eq. 5.1, T_s is the set point temperature, T_o is the measured temperature, and P is the proportional gain. With low gain the system is overdamped, but as the gain is increased the system becomes underdamped and can eventually become unstable. Our primary goal is to minimize oscillations

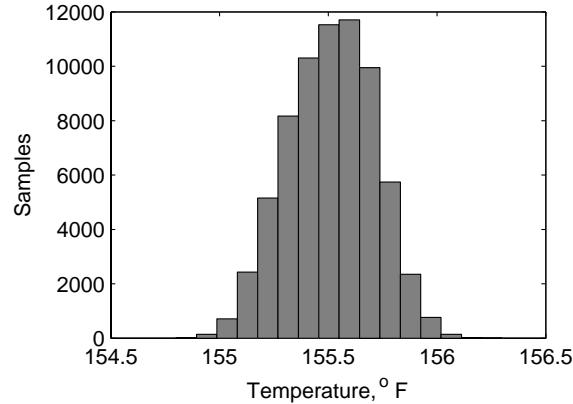


Figure 5-9: Histogram of temperature measurements using proportional mode in the large vacuum chamber with a set point temperature of 160 °F. Measurements were taken every 5 seconds for 4 days.

so an overdamped system is generally preferred. The steady state temperature difference between the set point and the actual temperature is not a problem since in most cases achieving a specific temperature is unnecessary.

Figure 5-9 is a histogram showing temperature measurements taken over a four day period every 5 seconds for a set temperature of 160 °F, on the large, two sensor vacuum chamber. The mean, median, and standard deviation are 155.51, 155.5, and 0.214 °F respectively. The temperature controller reports Fahrenheit temperature to one decimal place.

5.4.3 Pressure Monitoring

In many experiments during chamber evacuation, the pressure inside the vacuum chamber is monitored for the purpose of characterizing the success of establishing a closed system. A Varian Model 531 vacuum gauge thermocouple with a 1/8" NPT fitting is used in these cases. This is connected to a Varian Model 801 controller. The controller has a 0 to 11 mV output that is recorded by LabVIEW. The 531 vacuum gauge has a pressure range from 1×10^{-3} to 2 torr. This is well below atmospheric pressure (1 atm = 760 torr) and therefore is used only when running the vacuum pump to determine how tight the chamber is.

5.4.4 Humidity Sensors

There is a dance between pressure, temperature, and humidity described by the science of thermodynamics. While temperature and pressure can easily be measured without need for knowing the other

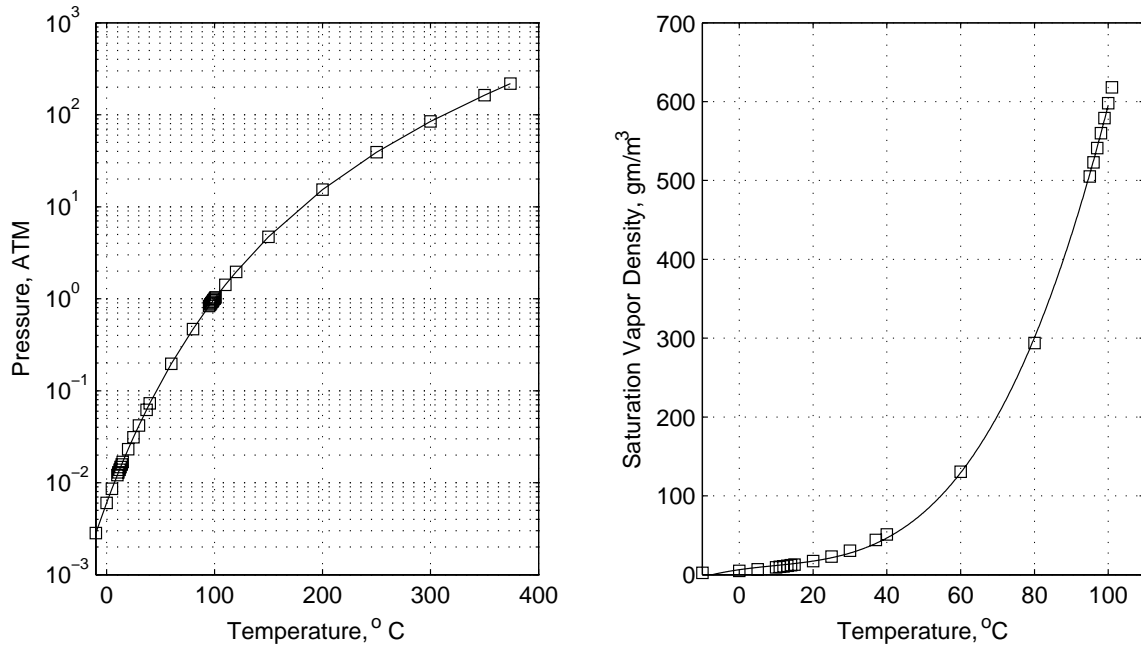


Figure 5-10: Saturation vapor pressure or boiling pressure (right) and saturation vapor density (left) for water at various temperatures.

two, humidity is slightly vague. Most sensors report the *relative* humidity. Relative humidity is the ratio of the actual vapor density (m_v), to the saturation density (m_{sat}), or equivalently the actual vapor pressure (P_v), to the saturation vapor pressure (P_{sat}). It is usually reported as a percentage.

$$RH = \frac{m_v}{m_{sat}} = \frac{P_v}{P_{sat}} \quad (5.2)$$

The saturation vapor pressure and density can easily be found from tables and graphs such as Fig. 5-10, which is a plot of the saturation vapor pressure and saturation vapor density for various temperatures [74]. A full curve would include temperatures that go all the way down to absolute zero, but 374.14 °C is the highest temperature at which there is a corresponding saturation pressure (217 atm). Above this temperature there is no distinct phase change process. The saturation pressures are reported numerically in Table 5.2. It is interesting to note that the boiling point for a given pressure is simply the saturation vapor temperature.

The actual vapor pressure can exceed the saturation vapor pressure, but only when the temperature is above the boiling temperature. In this case the vapor is superheated and relative humidity sensors will not provide meaningful results and may in fact be misleading. In a fixed volume chamber filled with only water (no air), the saturation vapor pressure can be found by measuring the equilib-

Table 5.2: Saturation Vapor Pressure for Select Temperatures

Temp. °C	P_{sat} (ATM)	Temp. °C	P_{sat} (ATM)
-10.0	0.0028	95.0	0.8342
0.0	0.0060	96.0	0.8658
5.0	0.0086	97.0	0.8974
10.0	0.0121	98.0	0.9303
11.0	0.0129	99.0	0.9645
12.0	0.0138	100.0	1.0000
13.0	0.0148	101.0	1.0368
14.0	0.0158	110.0	1.4139
15.0	0.0168	120.0	1.9592
20.0	0.0231	150.0	4.6997
25.0	0.0313	200.0	15.3408
30.0	0.0418	250.0	39.2401
37.0	0.0619	300.0	84.7570
40.0	0.0728	350.0	163.1285
60.0	0.1966	373.14	217.7547
80.0	0.4672		

rium pressure in the chamber. This requires that there always be some condensation in the chamber. By measuring the pressure at each temperature the curves in Fig. 5-10 could be found. The key is that there must always be some condensation and only water and vapor are in the chamber, but no air. If air is present in the chamber its partial pressure must be known. The partial pressure of the air at different temperatures can be predicted based on the ideal gas law. The volume is also changing as a pool of water is formed, but this issue may be ignored depending on the required accuracy. For example, at 200 °C the vapor in saturated air will take up less than 1% of the volume when completely condensed.

Two types of humidity sensors have been used for experiments, the HIH-3610, and HIH-4000, both products of Honeywell [75, 76]. They are three terminal devices taking a 5 V supply and producing an output voltage proportional to the relative humidity. Several equations are provided to calculate the relative humidity based on the output voltage and possibly temperature as well. The HIH-4000 sensors include a linear calibration fit at 25 °C. Our testing has deemed the temperature compensated conversion equation to be the most reliable. The temperature compensated conversion from output voltage to relative humidity for the HIH-4000 sensor is

$$RH = \frac{V_o - (0.9237 - 0.0041C + 0.000040C^2)}{0.0305 + 0.000044C - 0.0000011C^2} \quad (5.3)$$

where V_o is the output voltage and C is the temperature in °C [76].

Several tests were conducted on the HHH-4000 series moisture sensors. Tests were conducted inside a closed vacuum chamber with a fixed amount of moisture inside. If there is no condensation and the temperature is uniform throughout the chamber, the moisture should all be vaporized, and the vapor density should be constant.

The experiment is conducted in the small vacuum chamber. The vacuum pump valve is removed and replaced with an NPT plug. The humidity valve is also removed and plugged. All connections are made through the SMA ports. Inside the chamber on a breadboard three of the HHH-4000 sensors are properly wired. A small computer fan is also placed in the chamber to help circulate the vapor.

After the chamber is sealed the temperature and humidity are allowed to stabilize. At a steady state of 125.5 °F and approximately 82% relative humidity the chamber temperature is increased steadily to 170 °F. This temperature change takes about 11 minutes. From the saturation vapor density values plotted in Fig. 5-10 and given in Table 5.2, the actual vapor density is calculated using eq. 5.2. The results are plotted in Fig. 5-11. The top graph shows the measured relative humidity, the lowest graph shows the measured temperature, and the middle graph shows the calculated saturated vapor density. Ideally the vapor density should be constant. We have selected this region because it characterizes the accuracy of the sensors. Sensors #33 and #34 indicate a rise in vapor pressure, while sensor #30 at first indicates a slight drop and then slight rise. The sensors are all located in the center of the chamber within about two inches of each other suggesting that this is about the maximum agreement to be expected.

A second way of characterizing the response is to calculate the saturation vapor pressure by assuming the vapor pressure is constant in eq. 5.2. As the temperature is varied the measured saturation vapor density can be compared to the literature values. Taking the initial vapor density as constant the saturation vapor density is calculated. The results are plotted as a function of temperature in Fig. 5-12.

In other experiments the temperature is cycled. Drifting occurs suggesting that the temperature in the chamber is not constant everywhere and that in some places there may be condensation. As an example of this consider Fig. 5-13. The saturation vapor density is fixed to a point about 30 minutes into the experiment as indicated by the black square in the figure. As the temperature is cycled the experiment times are noted. The initial temperature is about 170 °F. The temperature is lowered to about 135 °F then raised again to 170 °F. Finally the chamber is allowed to cool until the end of the experiment after 105 minutes. Notice how the predicted saturated vapor density decreases from about $t = 47$ to $t = 82$ minutes while the temperature is nominally constant. This indicates the relative humidity is increasing suggesting condensed moisture in the chamber is evaporating. It appears the looping is caused by condensation which is due to the lack of uniformity in the chamber

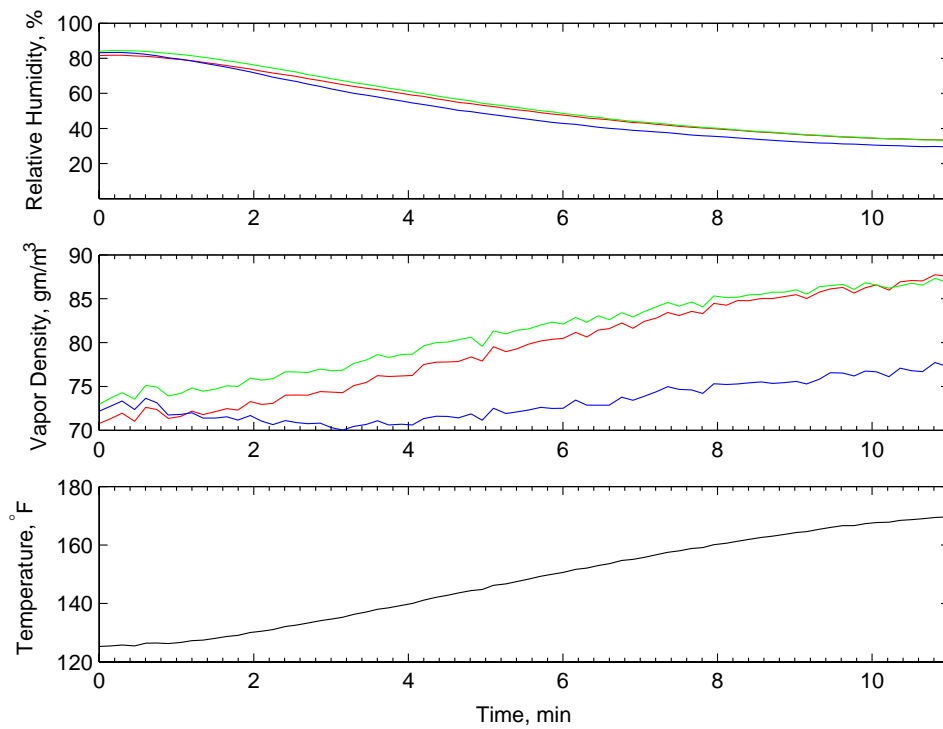


Figure 5-11: Relative Humidity test using HIH4000 humidity sensors. The temperature is controlled and the RH is monitored. The vapor density in the chamber is calculated. Sensor Serial Numbers: red - #34, green - #33, blue - #30.

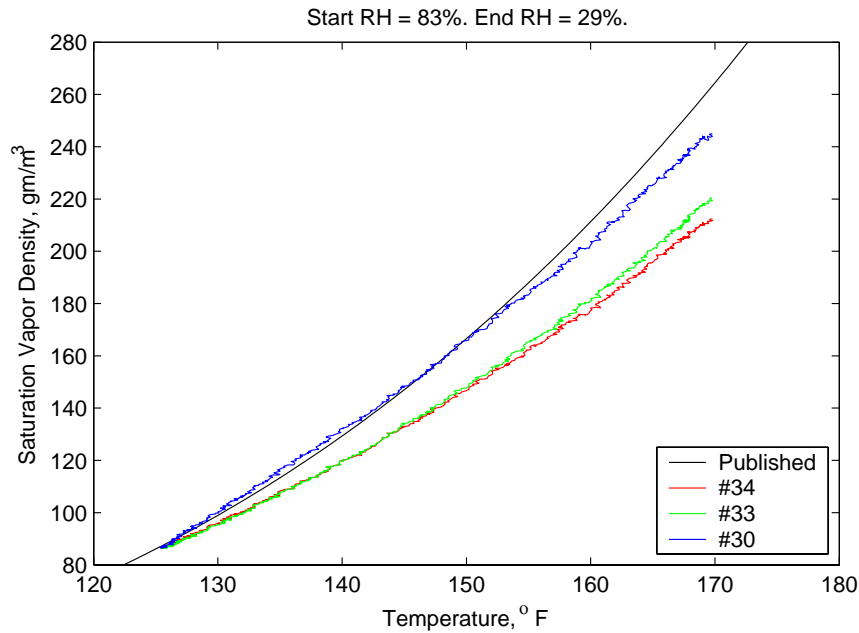


Figure 5-12: Saturation vapor density as implied by the experimental temperature and relative humidity measurements in Fig. 5-11 assuming constant vapor density. The results have been forced to agree at 125 °F. This agreement diverges as the temperature is increased.

temperature.

The conclusion of these experiments has generally been to take the relative humidity sensors as accurate and assume inconsistencies in vapor density are due to condensation, absorption by materials, or leakage. Unfortunately this prevents us from calculating the moisture absorbed by the MUT since this is not the only moisture sink.

5.4.5 Adding Moisture to the Chamber

Moisture is added to the chamber in one of two ways. In the early experiments moisture is added to the system by forcing nitrogen gas bubbled through water into the chamber. After allowing the bubbling to proceed for several minutes the gas is turned off and the chamber sealed. This is the setup illustrated in Fig. 5-1.

It was eventually determined that this method reduced the chamber temperature too much, often resulting in too much moisture being added to the chamber. This sometimes formed condensate on the cables, sensors and connectors and resulted in sensor failure. Later experiments primarily used a syringe to inject water into the chamber in a controlled amount. The time it takes for the moisture to evaporate and relative humidity to stabilize is typically far less than an hour, a very short period

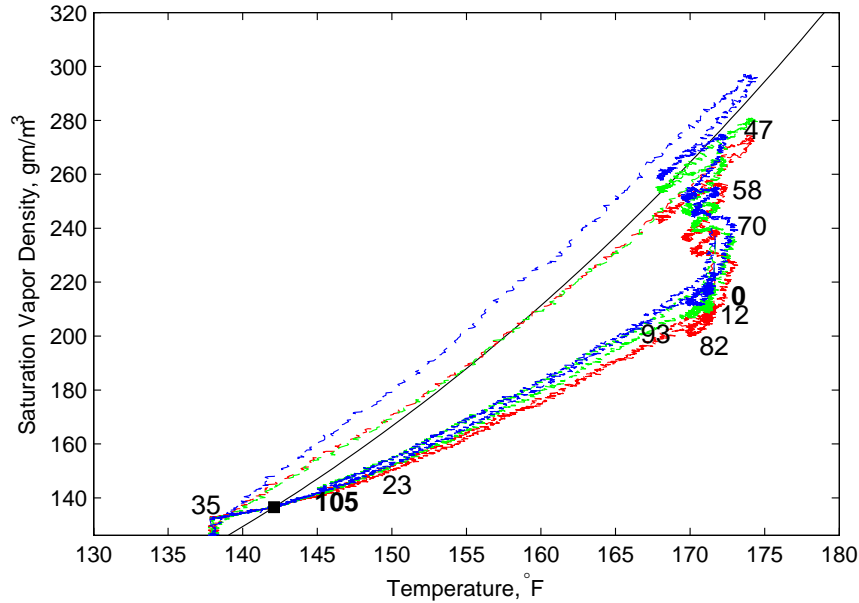


Figure 5-13: Demonstration of errors in calculated saturation vapor density. The saturation vapor density is fixed at the point indicated by the black square. The numbers represent the experiment time in minutes.

of time compared to the length of typical experiments.

5.5 Error Analysis

The subsequent chapters consist primarily of temperature, relative humidity, and complex gain measurements. Each of these measurements is subject to uncertainty and systematic error.

5.5.1 Systematic Errors

During the course of the research we have worked to eliminate systematic measurement errors to the extent practical. For example, thermocouple probes are calibrated with more reliable thermometers. Independent data loggers are often placed inside the chamber to compare with online readings [77].

Assumptions of the theoretical model produce systematic errors in effective permittivity estimates. For example, non-zero electrode thickness, finite periodicity, and finite electrode length, are all realities of the sensors not considered in the theoretical model. Quantifying the errors introduced by the model have been explored in part by A. Mamishev in Chapter 6 of his thesis [54], however each sensor design is likely to introduce a unique set of systematic errors that have some dependence on the MUT. Table 5.3 summarizes the error in the capacitance calculation resulting from

Table 5.3: Disturbance Factors and Approximate Capacitance Error

Disturbance Factor	$\lambda = 1.0$ mm	$\lambda = 2.5$ mm	$\lambda = 5.0$ mm
Finite Length	+0.5%	+1.2%	+2.4%
Finite Periodicity	-4%	-4%	-4%
Electrode Thickness	+13%	+9%	+6%
Total	+9.5%	+6.2%	+4.4%

disturbance factors, *i.e.*, differences between the theoretical model and the manufactured sensor. The percentages indicate the increase in measured capacitance using the real sensor over the ideal sensor. These should be considered ballpark figures since every MUT will have unique disturbance characteristics. This is because the electric field changes due to the different material properties of the MUT and substrate. This is opposed to a parallel plate capacitor for instance where the electric field is the same (V/d) regardless of the MUT permittivity.

We see from the table that in general the capacitance will be over estimated. The relationship between the measured capacitance and the MUT permittivity is nonlinear and must be solved using the theoretical model or by numerical methods. For a lossless MUT and for the standard sensor wavelengths the relationship is plotted in Fig. 5-14. Overestimating capacitance will lead to over estimating the permittivity.

Other sources of systematic error primarily affect calculation of diffusion profiles in the MUT. Here the boundary conditions and sometimes material properties must be assumed. While electromagnetic properties are extensively published for a multitude of materials, there is relatively little information about moisture diffusion. We therefore do not estimate the error in the boundary conditions directly but qualitatively assess their quality based on the characteristics of the measured data.

5.5.2 Uncertainty

In this section σ is used to represent standard deviation.

The measurement apparatus itself is limited by system and environmental noise. In order to characterize the measurements in terms of noise error, we take steady state experimental data and estimate the standard deviation of the noise. Additive gaussian noise is assumed. We use a constant temperature measurement of Teflon as the basis of our analysis. (While the relative humidity is changing it has no affect on Teflon which is hydrophobic.) The measurements are presented under a different context in Section 8.1.1, Fig. 8-2. Ideally the recorded measurements would be unchanging during the 11 days of the experiment. This is substantially the case for the 2.5 and 5.0 mm channels

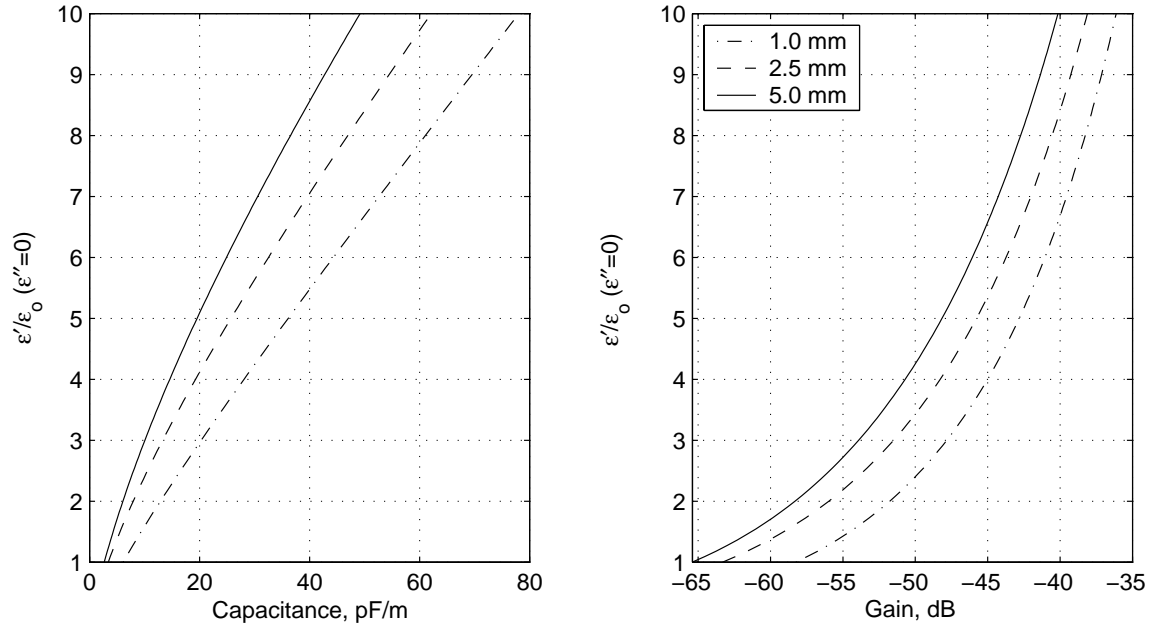


Figure 5-14: Permittivity as a function of capacitance (left) and gain (right) for the three standard sensor wavelengths. Additional parameters: $\sigma = 0$ (conductivity), $t_s = 4$ mil, $\epsilon_s = 2.1\epsilon_0$, metallization ratio 50%, $C_f = 5$ nF.

but not for the 1 mm channel, therefore we only consider the longer wavelength results.

We would like to estimate the standard deviation of the gain and phase measurements as a function of frequency. We begin by considering the 5.0 mm wavelength sensor measurement at 10 kHz in Fig. 5-15. The top and bottom figures are for the gain and phase measurements respectively. The right hand figures show the actual measurement data which is taken at 705 sample times. The left figures shows a histogram of each measurement value. This is easily done since the measurement is limited to two decimal places by the controller box. A gaussian curve with the sample mean and variance is superimposed over the histogram. It is scaled to the maximum histogram count.

If the experimental conditions were truly steady state, the “signal” (measurement less the noise) would be constant. If the experimental conditions are changing ever so slowly during the experiment, the signal will drift with the conditions that affect it. The presence of noise makes it impossible to ascertain with certainty if the measurement changes are due to noise or to drift in the signal, but we can estimate the likelihood of either case. We assume the signal is linear with slope zero if in true steady state. If the true measurement is slowly changing the drift is the value of the non-zero slope.

We fit the measurement data with a straight line. Because we have only a finite number of samples the slope may be due to noise or drift. The standard deviation is calculated after subtracting the

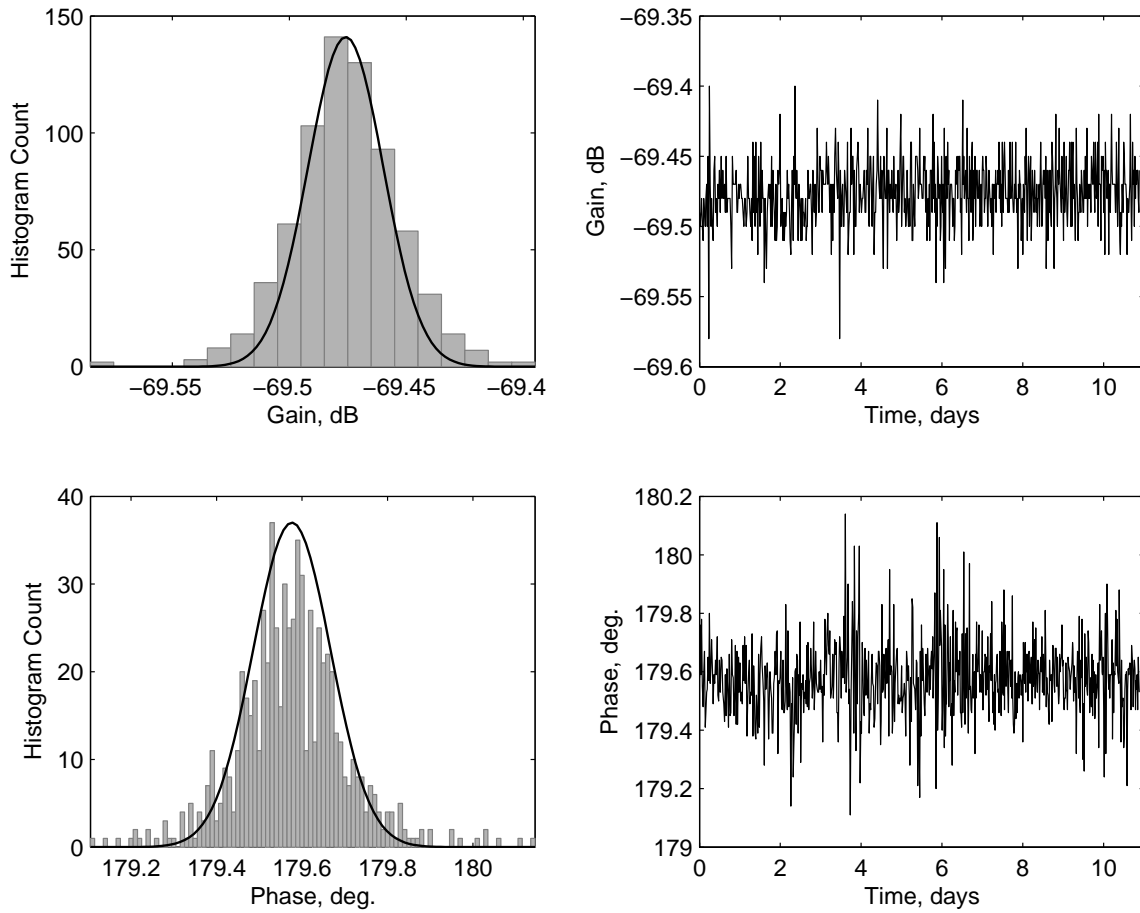


Figure 5-15: Experimental measurement of Teflon using a 5.0 mm sensor at 10 Hz over 11 days. The left figures show the histogram counts of each measurement while the right figures show the measurements themselves. Also show are the gaussian curve fits. There are 705 total samples.

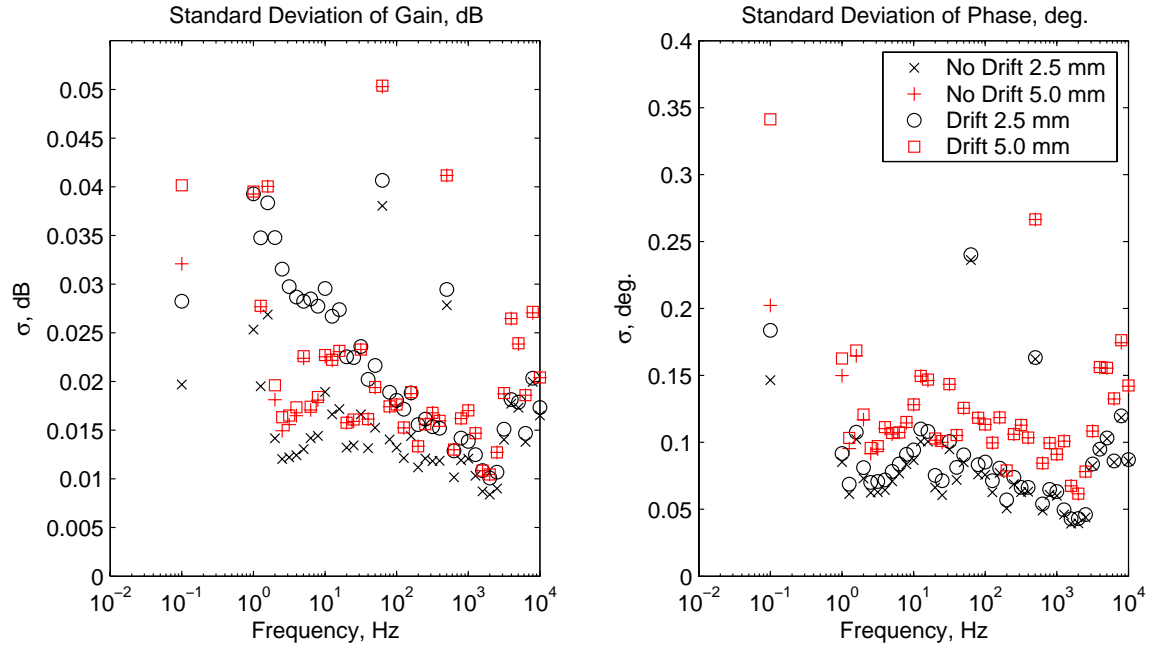


Figure 5-16: Standard deviation of Teflon measurements with drift and with drift removed for two channels. Removing drift reduces the standard deviation. 705 samples were used for each frequency.

apparent signal drift leaving us in principle with only noise. The calculated standard deviation as a function of frequency is plotted in Fig. 5-16. When compared to the standard deviation calculated when the drift has not been subtracted we see that it is always smaller.

We next calculate the probability the apparent drift is “real” and not an artifact of finite sampling, but due to changes in the actual signal. The signal is taken to be a straight line of the form

$$y = Ax + B \quad (5.4)$$

where A and B are random variables that satisfy the least-squares fitting of the measurement data $\{t_1, Y_1\} \dots \{t_j, Y_j\} \dots \{t_n, Y_n\}$. Here t_j is the measurement time which is assumed to be a number (zero variance) and Y_j is the measurement less the mean ($\mathbf{E}[Y_j] = 0$) at the corresponding time having additive noise such that $\text{var}[Y_j] = \sigma^2$. The least squares solution for A and B is found from the matrix equation

$$\begin{bmatrix} z_1 & z_3 \\ n & z_1 \end{bmatrix} \begin{bmatrix} A \\ B \end{bmatrix} = \begin{bmatrix} Z_2 \\ Z_4 \end{bmatrix} \quad (5.5)$$

where

$$z_1 = \sum_{j=1}^n t_j \quad Z_2 = \sum_{j=1}^n Y_j \quad z_3 = \sum_{j=1}^n t_j^2 \quad Z_4 = \sum_{j=1}^n t_j Y_j$$

The values of z_1 and z_3 are constants, while Z_2 and Z_4 are zero mean random variables with variances $n\sigma^2$ and $z_3\sigma^2$ respectively. Solving for A and B we find

$$A = \frac{nZ_4 - z_1Z_2}{nz_3 - z_1^2} \quad (5.6)$$

$$B = \frac{Z_4z_1 - z_3Z_2}{z_1^2 - nz_3} \quad (5.7)$$

Finding the variances of A and B we have

$$\sigma_A^2 = \text{var}[A] = \sigma^2 \frac{z_3n^2 + z_1^2n}{(z_3n - z_1^2)^2} \quad (5.8)$$

$$\sigma_B^2 = \text{var}[B] = \sigma^2 \frac{z_1^2z_3 + z_3^2n}{(z_1^2 - z_3n)^2} \quad (5.9)$$

As expected we find that increasing the number of samples for the same time reduces the variance in A and B which tend towards zero as $n \rightarrow \infty$.

Using the standard deviations from Fig. 5-16 for σ , we determine the probability the drift is due to noise by means of the error function defined as

$$\text{erf}(x) = \frac{2}{\sqrt{\pi}} \int_0^x e^{-t^2} dt \quad (5.10)$$

For a normal distribution with standard deviation σ and expected value 0 the probability a sample is between $-x$ and $+x$ is

$$\text{erf}\left(\frac{|x|}{\sigma\sqrt{2}}\right) \quad (5.11)$$

We can use eq. 5.11 to calculate the likelihood a second set of noise samples would produce less apparent drift by letting x equal the observed measured drift A , and σ_A from eq. 5.8. For noise without drift the expected value is obviously 50%. We plot the drift and probabilities in Fig. 5-17. The symbols correspond to the standard deviation data taken from Fig. 5-16. Notice how assuming all drift is due to noise and using the calculated standard deviation results in extremely low probabilities. This indicates that it is highly likely that the standard deviation is overstated.

Using the standard deviation σ_A clearly identifies the 2.5 mm sensor as having drift since the likelihood of achieving less drift from a second set of noise samples is almost certain. The probability of less drift for the 5.0 mm sensor measurements is all over the range indicating that we have a good estimate of the standard deviation, and that there was negligible drift in the signal to start with.

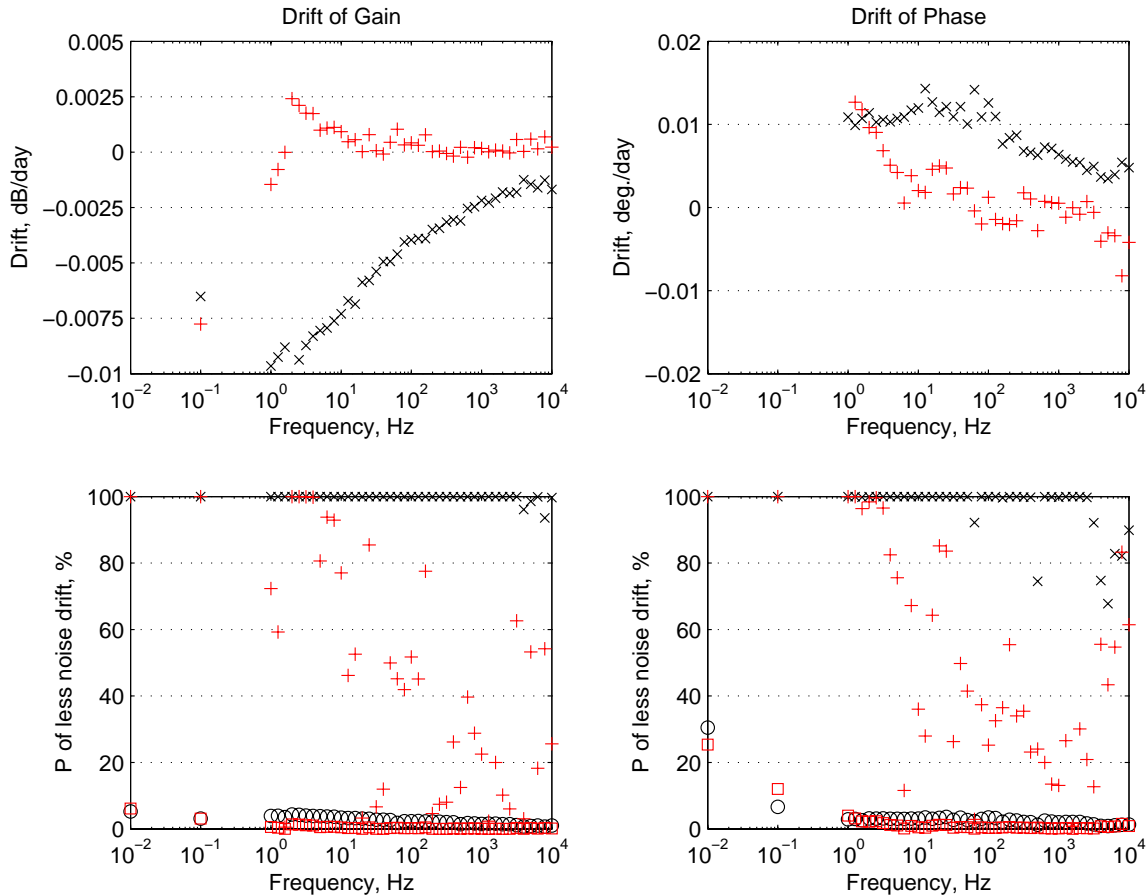


Figure 5-17: Drift and probability of less drift when all drift is due exclusively to noise. Black and red marks indicate the 2.5 and 5.0 mm channels respectively. The legend for the lower figures is the same as Fig 5-16.

Comparing the two standard deviations used for the 5.0 mm sensor as shown in Fig. 5-16 shows they are almost identical when the drift is removed. The probability of less apparent drift is very sensitive to these small changes however. Each of these points is calculated with 705 samples making drift very easy to detect.

This study has provided standard deviation estimates of the noise as a function of measurement frequency. We take the estimated standard deviation of the noise for the 5.0 mm sensor without drift to characterize noise for all our sensors (red + in Fig. 5-16).

We would now like to characterize the error introduced into the calculated effective permittivity as a result of noise. We consider the effects of gain and phase errors separately to simplify our analysis. Generally one error will dominate.

We can determine how gain errors affect the permittivity estimates directly from Fig. 5-14. We

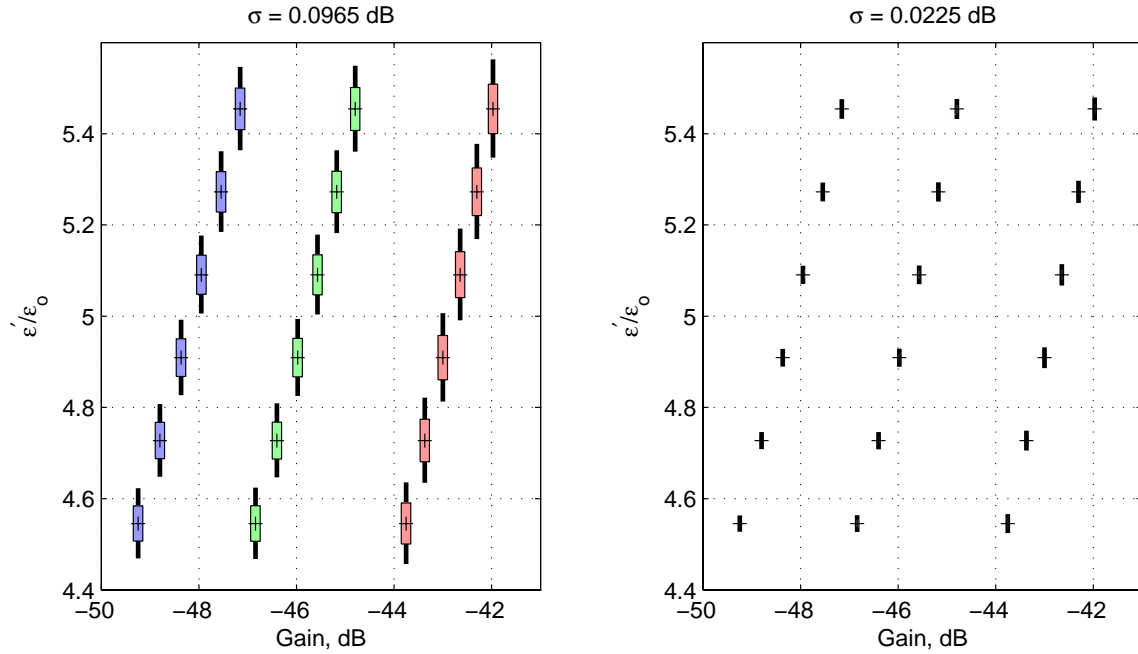


Figure 5-18: Error in permittivity estimates due to measurement noise. Error bars are shown for one and two standard deviations, as colored boxes and bars. ‘+’ indicates nominal value and the colored box width indicates 1σ gain error. The left figure shows the results with the largest observed standard deviation, while the right shows the results using the average over all frequencies. Phase is 180° since the conductivity is zero. $C_f = 5$ nF assumed. Colors: blue – 5.0 mm, green – 2.5 mm, red – 1.0 mm.

begin by taking a nominal value of sensor gain and calculate the permittivity at this value for each sensor wavelength. We then add and subtract one standard deviation to the nominal gain and recalculate the permittivity for the high and low value. Finally we repeat this for two standard deviations. The results are plotted in Fig. 5-18. In the left hand figure $\sigma = 0.0965$ dB. This is the *largest* standard deviation observed at any frequency on the 5.0 mm channel with drift removed (see Fig. 5-16). The right figure shows the error in permittivity when the average standard deviation over all frequencies is used, $\sigma = 0.0225$ dB. It is evident that the gain errors have a very minor effect on the estimated permittivity. As can be seen from Fig. 5-14 (right) higher permittivities are more sensitive to gain errors than smaller permittivities.

To consider the effect of phase error we fix the relative permittivity and vary the conductivity to achieve different phase angles. This is equivalent to sweeping the frequency. In-between 90° and 180° an error in the dielectric loss is very small. As we approach these limits however the error grows substantially. We consider two cases which may be considered typical among our experiments. Near a phase angle of 90° we take the relative permittivity to be 30 and vary the conductivity. The

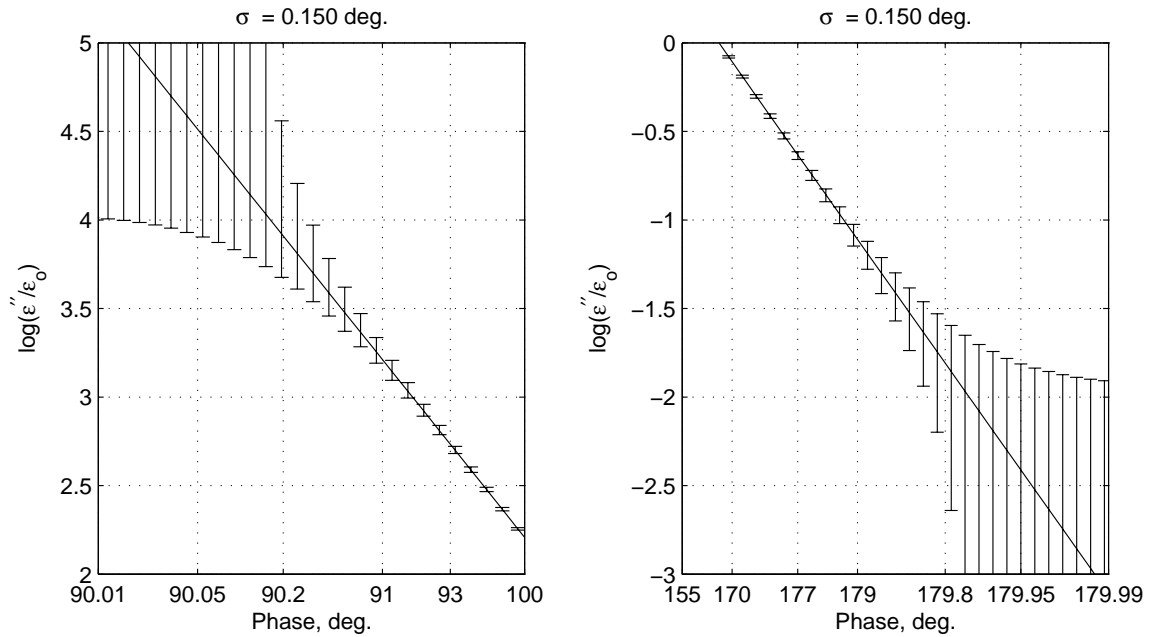


Figure 5-19: Error in dielectric loss as a result of phase errors. Relative permittivity is 30 and 5 for left and right figures respectively. There is no sensitivity to dielectric loss above +4 or less than -2 here. The actual limits depends on the relative permittivity at these phase limits. Note the abscissa's scale is logarithmic about 90° and 180° .

relationship between the phase and dielectric loss ($\log_{10}(\epsilon''/\epsilon_0)$) is plotted in Fig. 5-19 (left). Error bars are shown for $\sigma = 0.150^\circ$. Notice that phase errors essentially limit the maximum dielectric loss that can be measured. The actual saturation limit is dependent on the permittivity. Choosing a relative permittivity of only 5 for example would reduce the saturation point down from 4.0 to about 3.1.

None of the materials we deal with suffer from noise at the high end since usually ϵ' is very large or the feedback capacitance is not small enough and the measurement hardware is saturated. Much more common is reaching the noise floor at 180° . In this case the material is highly insulating and noise essentially limits how low a dielectric loss we can record. For this example we use a relative permittivity of 5 and observe a noise limit around -2 . This is quite consistent with our measurements. The error on lower end extends to negative infinity since the phase angle with noise may exceed 180° .

The conclusion of this analysis is that noise is a limiting factor in the measurement accuracy and must be carefully considered when specific tolerances are expected. Here we conclude that noise makes a minor contribution to measurement error. Systematic errors due to discrepancies

in the model and the physical sensor are much larger sources of error compared to noise, which primarily affects how low of a dielectric loss can be measured. While the measurements can always be reevaluated with greater accuracy using a better model, it is essential to know the noise during the measurement because it places a fundamental limit on the accuracy.

5.6 Chapter Summary

This chapter has served to introduce the experimental procedure followed for transient and steady state temperature and moisture measurements (Section 5.1). Descriptions of all the hardware used for setting up and conducting measurements are presented. The sensing hardware used to excite and measure the sensor response is detailed in Section 5.2. The various types of mounting hardware used to attach the sensor to cylindrical material samples are described in Section 5.3. Each component of the environment control hardware including the vacuum chambers, temperature controllers, pressure monitors, and humidity sensors, is described in Section 5.4. Finally, a study is done on the sources of systematic error and uncertainty in our measurements (Section 5.5). How errors in gain and phase measurements affect the estimates of the dielectric properties is discussed.

Chapter 6

Steady State Measurements

This chapter presents steady state measurements taken on plastic rods, wooden rods, and the power cable samples. The three wavelength sensors introduced in Section 4.2.3 are used for measurements. Many of the tests have been repeated several times; in some cases this is to overcome technical challenges, but in all cases it helps shed light on the repeatability of the measurements. In cases where multiple results are available, the additional results have been placed in appendix B. A description of the measurement procedure can be found in Section 5.1.1. All the measurements have been adjusted to reflect the gain achieved with a 5 nF feedback capacitance. This insures the results from the 1.0, 2.5, and 5.0 sensors can be compared easily against each other and the measurements of other materials.

The measurements presented in this chapter can be used to determine the effective permittivity of the MUT as well as the temperature dependence of the electrical properties. We postpone complete interpretation of the results until the subsequent chapter and focus our discussion the data itself.

6.1 Diagnostic Measurements of Known Dielectrics

We begin presenting the experimental results with a series of diagnostic measurements on known dielectrics. The results illuminate some of the technical issues and challenges of interdigital dielectrometry measurements. These measurements prepare us for some of the technical issues that may present themselves in measuring materials with unknown properties. Table 6.1 reports the dielectric properties of the diagnostic rods used for measurements. Many of the references report the

Table 6.1: Electrical Properties of the Dielectric Test Rods

Material	Rod Diameter	ϵ_r	$\tan \delta$ or σ	Notes
Teflon	1"	2.10	$\sigma = 10^{-17}$ S/m	at 1 kHz [78] [79]
Polycarbonate	1"	2.99 3.00	$\sigma = 10^{-13}$ S/m	[78] [80] [81]
Low Density Polyethylene	1"	2.20 2.28	0.000500 $\sigma = 10^{-16}$ S/m	[78] at 1 MHz [80] [82]
Acrylic	1"	3.70 2.20	0.05 0.03	at 60 Hz [80] at 1 MHz [80]

dissipation factor, also known as the loss tangent, $\tan \delta$. The loss tangent is defined as

$$\tan \delta = \frac{\sigma}{2\pi f \epsilon} \quad (6.1)$$

where σ is the electrical conductivity, ϵ is the permittivity, and f is the frequency. We recognize this as $1/\omega\tau$, where τ is the relaxation time defined in eq. 2.1. We can easily convert dissipation factor to conductivity if the measurement frequency and permittivity are known.

Dielectric spectroscopy measurements are taken from 0.01 Hz to 10 kHz in logarithmic increments of 0.1 for a total of 61 measurements at a fixed temperature. For each material measurements are taken from room temperature to temperatures as high as 193 °F. The gain and phase measurements are reported and discussed. The forward problem is solved using the values from the literature in Table 6.1 and compared to the measured data. Each of these materials is extremely hydrophobic in comparison to the wood and paper insulation measurements in subsequent sections.

In some measurements the phase measurements at high frequency tend to increase above 180°. This is due to bandwidth limitations in the preamplifier used to buffer signals in the controller box (see Section 5.2.1). For example the effect is noticeable on the polyethylene measurements in Fig. 6-4.

A typical experimental setup is shown for a Teflon rod in Fig. 6-1. The orientation of the sensor is ϕ periodic. Hose clamps with a rubber insert are used as the mounting hardware. A detailed photo of the clamping mechanism is shown in Fig. 5-4.

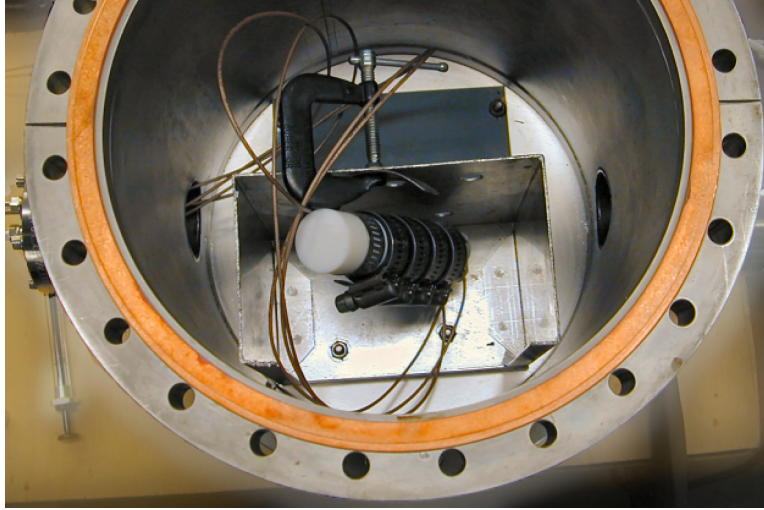


Figure 6-1: Experimental setup of the Teflon rod for steady state measurements. For this measurement the large vacuum chamber is used. The side ports are visible. The Teflon rod and sensor is held with a series of hose clamps. Electrical leads for the drive and sense signals can be seen exiting the left side port.

6.1.1 Teflon Rod

Teflon is the trade name for PTFE, a hydrophobic fluoropolymer with an extremely low coefficient of friction. A one inch diameter Teflon rod is placed inside the temperature controlled chamber. The temperature is stepped from about 60 °F to 174 °F (16 °C to 79 °C). Thirteen total frequency scans are made. During the course of each measurement the temperature is logged at short intervals. The average and standard deviation of the temperature during each frequency scan are recorded in Table 6.2. The experimental results are plotted in Fig. 6-2. The top three axes show the gain measurements for the 1.0, 2.5, and 5.0 mm wavelength sensors. The lower three axes show the phase measurements. Each axis shows the associated dielectric spectroscopy measurements at each temperature. The theoretical values of gain and phase for each channel are given by the solid black curve. The constitutive parameters used for theory are taken from Table 6.1, $\epsilon_r = 2.1$, and $\sigma = 10^{-17}$ S/m.

The traces are color coded to correspond with the temperatures in Table 6.2. In this and the subsequent temperature scans the *jet* colormap from MATLAB is used. The lowest temperatures are colored dark blue. As the temperature increases the colormap ranges through shades of blue, cyan, green, yellow, and red. The highest temperatures is indicated by the darkest red.

With the exception of some of the lowest temperatures on the 1 mm channel, the variation in response is minimal over the measurement range. The difference in level between the theory and

Table 6.2: Teflon Steady State Measurements: Average Temperatures and Standard Deviations

Color							
Avg. Temp. °F	59.2	69.5	78.8	88.5	98.2	108.3	117.8
Std. Dev. °F	0.46	1.04	0.45	0.38	0.31	0.50	0.53
Color							
Avg. Temp. °F	127.4	136.9	146.3	155.6	164.8	173.7	
Std. Dev. °F	0.64	0.67	0.66	0.73	0.25	0.28	

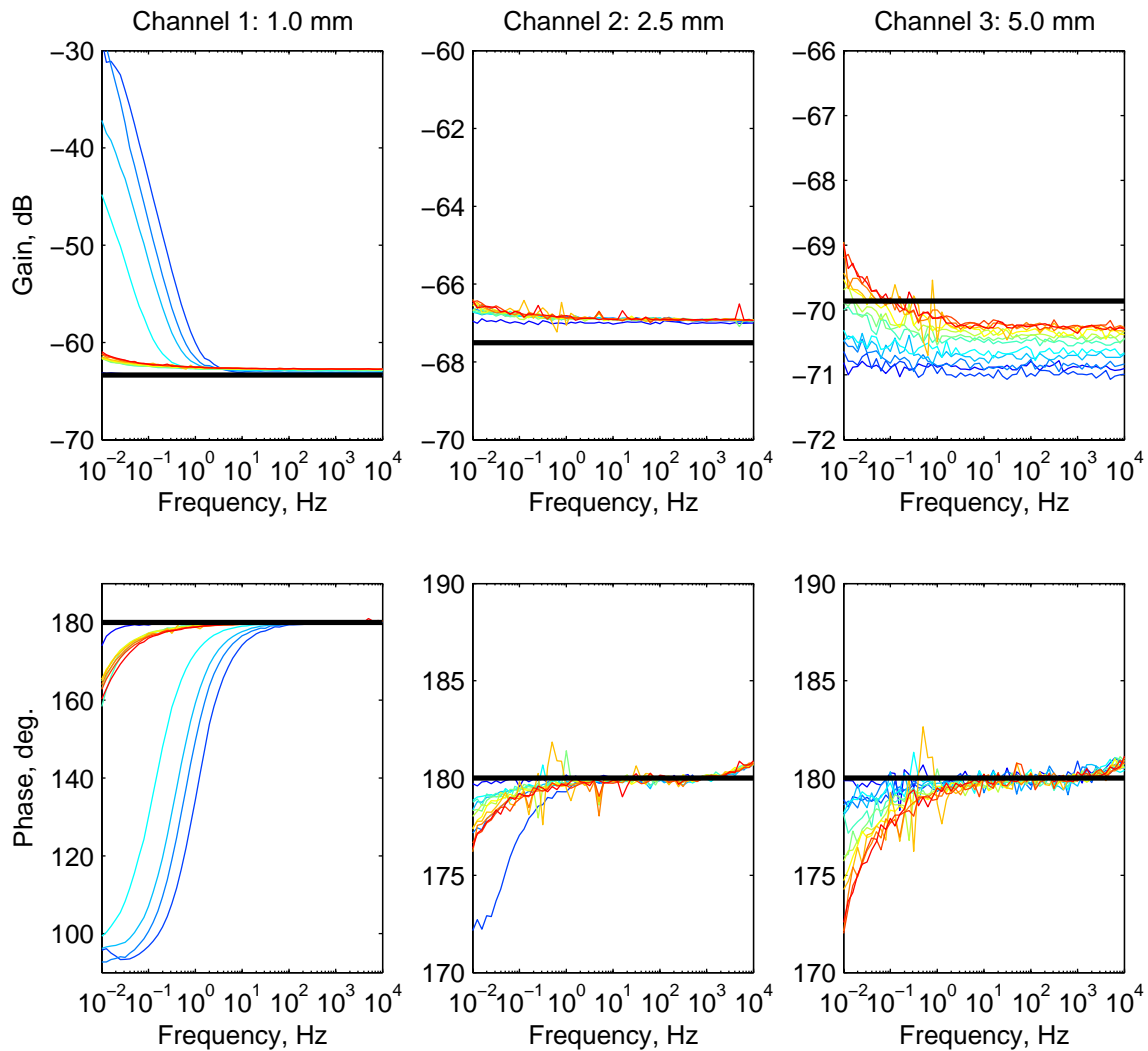


Figure 6-2: Teflon constant temperature dielectric spectroscopy measurements for 13 temperatures using 1, 2.5, and 5 mm wavelength interdigital sensors. Measurement colors correspond to the temperatures listed in Table 6.2. Theoretical results in black assume $\epsilon_r = 2.1$, and $\sigma = 10^{-17}$ S/m (see Table 6.1). Slope in ch. 1 phase at 59.2 °F is -0.9 . Interface box 3 is used. *This measurement was conducted from December 4 to December 5, 2006.*

measurement is notable in the 2.5 mm sensor gain plot. We suspect this is due primarily to the electrode thickness which has not been taken into account when calculating the theoretical gain. Simulation results using Maxwell 2D with an assumed electrode thickness of 17 μm give a gain of -66.46 dB which is very close to the actual measured gain which averages about -66.8 dB. The theoretical gain is -67.48 dB at high frequency. The high frequency gain measurements on the 2.5 mm wavelength channel are predicted by theory when the MUT relative permittivity is 2.25. Calculations of the permittivity based on the measurement results are presented in Chapter 7.

The simulation results for the 1 mm sensor gain is also low, but less visible because of the scale. The 5.0 mm wavelength channel measurements are slightly lower than expected suggesting the presence of small air gaps between the sensor and rod. The effect of the electrode thickness is dominant over the air gap for the smaller wavelengths while for the 5 mm sensor the air gap may have a greater effect.

The 1 mm sensor measurements at 69.5, 78.8, 88.5, and 98.2 $^{\circ}\text{F}$ suggest Teflon is much more conductive than the value in Table 6.2. These results are inconsistent with any reported values, and the dramatic reduction in conductivity at higher temperatures indicates intermittent contamination. This problem is easily identified, but is difficult to avoid entirely. The cause of the offense is likely a dust size particle bridging the narrow gap between drive and sense electrodes that shifts position over time. Beyond simply washing the sensors and MUT, the air quality in our laboratory environment makes further efforts nugatory.

Three additional frequency temperature scans were done on Teflon. They can be found in Section B.1.1.

6.1.2 Polycarbonate Rod

Polycarbonate is a thermoplastic used extensively in injection moldings. In this experiment a one inch diameter polycarbonate rod is measured. The experimental results are presented in a similar fashion as the Teflon measurements in section 6.1.1. The temperature range of the measurements extends from about 70 $^{\circ}\text{F}$ to 165 $^{\circ}\text{F}$ (21 $^{\circ}\text{C}$ to 74 $^{\circ}\text{C}$). Eleven frequency scans are made. The temperatures during the measurement and their standard deviations are reported in Table 6.3. The experimental results are shown in Fig. 6-3. The constitutive parameters used for theory are taken from Table 6.1, $\epsilon_r = 3.00$ and $\sigma = 10^{-13}$ S/m.

The experimental results are in good agreement with the theoretical curves which are within a decibel of the room temperature measurements. The measurement phase indicates that the polycarbonate rod is a good insulator, with most measurements having significant phase shifts only in the lowest decade. Each measurement follows a consistent trend and there is no indication of contami-

Table 6.3: Polycarbonate Steady State Measurements: Average Temperatures and Standard Deviations

Color						
Avg. Temp. °F	70.1	79.4	88.5	98.0	107.6	117.1
Std. Dev. °F	0.53	0.89	0.51	0.58	0.57	0.55
Color						
Avg. Temp. °F	126.6	136.1	145.6	155.1	164.5	
Std. Dev. °F	0.49	0.41	0.32	0.41	0.34	

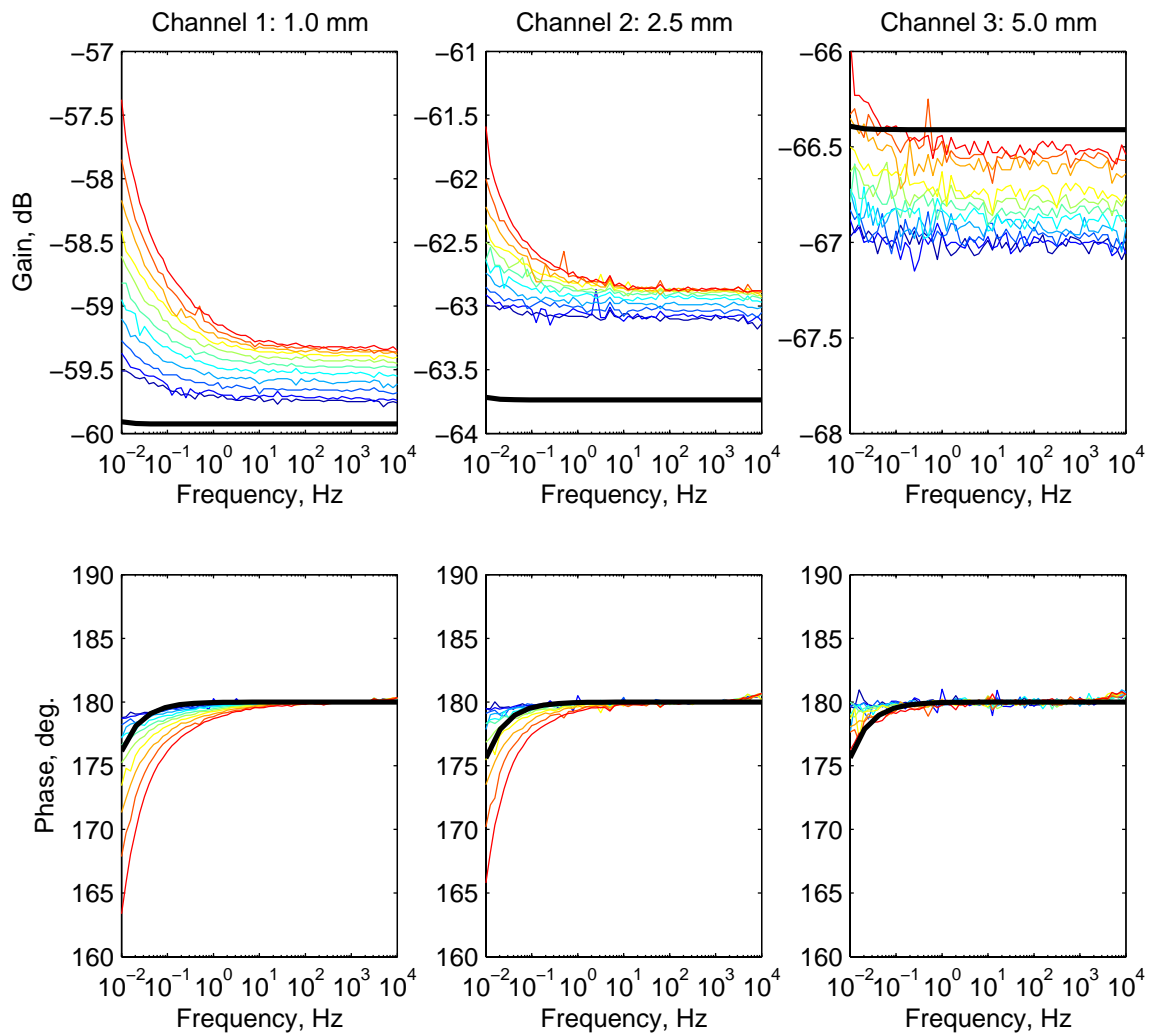


Figure 6-3: Polycarbonate constant temperature dielectric spectroscopy measurements for 11 temperatures using 1, 2.5, and 5 mm wavelength interdigital sensors. Measurement colors correspond to the temperatures listed in Table 6.3. Theoretical results in black assume $\epsilon_r = 3.0$, and $\sigma = 10^{-13}$ S/m (see Table 6.1). Interface box 3 is used. *This measurement was conducted on December 19, 2006.*

Table 6.4: Polyethylene Steady State Measurements: Average Temperatures and Standard Deviations

Color						
Avg. Temp. °F	71.1	79.7	88.7	98.2	107.8	117.2
Std. Dev. °F	1.40	1.08	0.50	0.70	0.67	0.51
Color						
Avg. Temp. °F	126.8	136.1	145.6	155.0	164.4	173.8
Std. Dev. °F	0.46	0.42	0.45	0.40	0.28	0.23

nants in these measurements. The gain has a tendency to increase with temperature indicating an effective increase in permittivity. It is possible that this is due to a physical increase in permittivity, or the reduction of any air gap between the sensor and the MUT. As with Teflon, the electrode thickness causes the measured gain to be larger than expected for the smaller wavelengths, and the presence of the gap causes the measurement to be lower for the 5 mm wavelength.

An additional polycarbonate measurement can be found in Section B.1.2.

6.1.3 Polyethylene Rod

Polyethylene is the thermoplastic used in XLPE cable technology which is used in place of PILC cables in many modern installations. Measurements are taken on a polyethylene rod with a one inch diameter. The experimental results are presented in a similar fashion as the Teflon measurements in section 6.1.1. The temperature range of the measurements extends from about 71 °F to 174 °F (22 °C to 79 °C). Measurements are made at twelve temperatures. The temperatures and their standard deviations are given in Table 6.4. The experimental results are shown in Fig. 6-4. The constitutive parameters used for theory are taken from Table 6.1, $\epsilon_r = 2.20$ and $\sigma = 10^{-16}$ S/m.

The experimental results indicate exceptional frequency stability. The phase shift is less than 3° for all measurements, even at the lowest frequencies. Virtually no shift is detectable in 5 mm sensor measurements. The gain is extremely stable as well within about half of a dB in spread from the lowest to highest temperature measurements on the 1.0 mm and the 5.0 mm channels. The 2.5 mm channel shows almost no variation at all with all temperature measurements within about a tenth of a dB at high frequency.

For both the 1.0 and 2.5 mm channels the predicted gain is significantly lower than the measured gain. The 5.0 mm channel is in excellent agreement. Simulation with Maxwell 2D results in gains of -61.17 dB for the 1.0 mm sensor and -65.96 dB for the 2.5 mm sensor when 17 μ m electrode thicknesses are assumed. In the simulation the gap is assumed to be completely filled with the polyethylene material. In experimental measurements the gap may be partially filled with air,

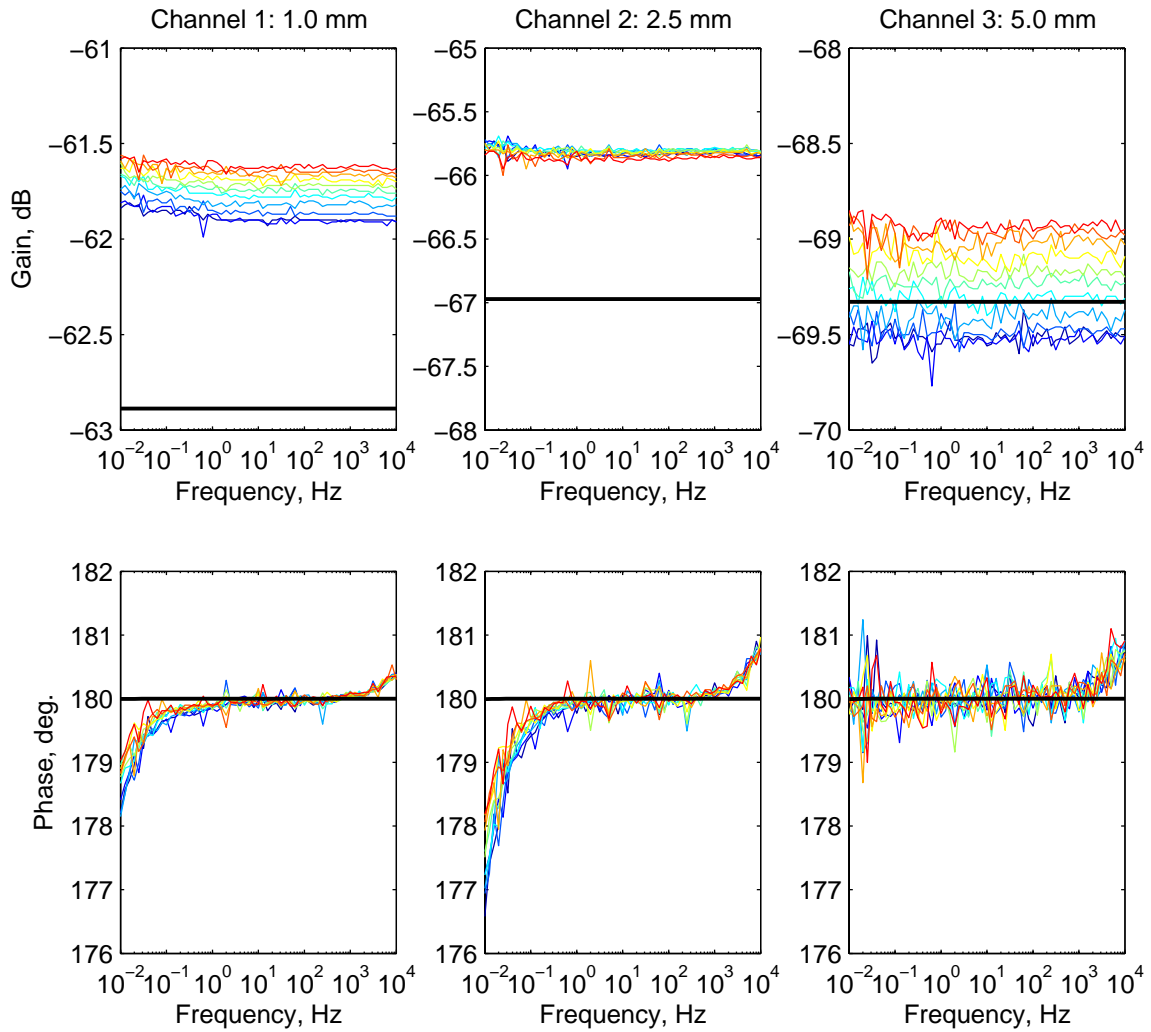


Figure 6-4: Polyethylene constant temperature dielectric spectroscopy measurements for 12 temperatures using 1, 2.5, and 5 mm wavelength interdigital sensors. Measurement colors correspond to the temperatures listed in Table 6.4. Theoretical results in black assume $\epsilon_r = 2.20$, and $\sigma = 10^{-16}$ S/m (see Table 6.1). Interface box 3 is used. *This measurement was conducted December 30, 2006.*

Table 6.5: Acrylic Steady State Measurements: Average Temperatures and Standard Deviations

Color					
Avg. Temp. °F	71.74	79.68	88.66	98.12	107.6
Std. Dev. °F	1.30	1.10	0.53	0.61	0.68
Color					
Avg. Temp. °F	117.1	126.5	136.0	145.4	154.8
Std. Dev. °F	0.49	0.42	0.42	0.40	0.34

which explains the slightly lower gain of the 1.0 mm sensor.

An additional polyethylene measurement can be found in Section B.1.3.

6.1.4 Acrylic Rod

Acrylic (PMMA) is a thermoplastic more commonly known by the tradename Plexiglas®. Measurements are taken on a rod one inch in diameter. The experimental results are presented similarly to the Teflon measurements in section 6.1.1. The temperature range of the measurements extends from about 72 °F to 155 °F (22 °C to 68 °C). The measurement temperatures and their standard deviations are given in Table 6.5. The experimental results are shown in Fig. 6-5. The constitutive parameters used for theory are taken from Table 6.1, $\epsilon_r = 3.70$ and $\sigma = 1.67 \times 10^{-10}$ S/m.

The characteristics of the acrylic rod are unusual in that they do not follow the general trend exhibited by the other materials. The phase appears to be oscillating slightly while the gain is increasing. In general the literature quotes a relatively large range of dielectric properties for acrylic when compared to Teflon for instance. This is due to the dispersive nature of acrylic which makes the measured permittivity highly dependent on the measurement frequency. The simulation values are taken from a measurement conducted at 60 Hz according to Table 6.1. Because of frequency dispersion these measurements are probably not valid at other frequencies as has been assumed by the theoretical model.

An additional acrylic rod measurement can be found in Section B.1.4.

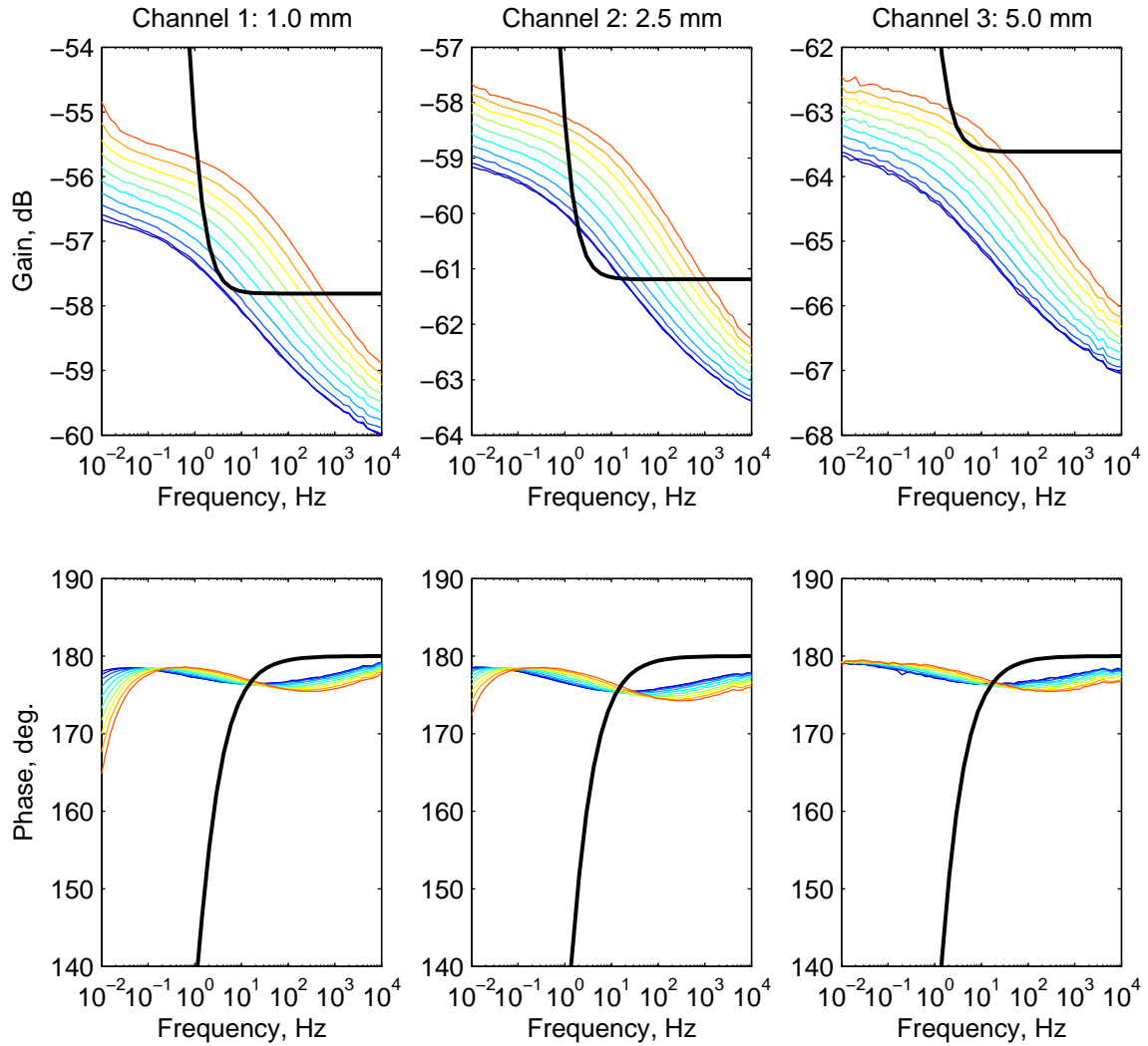


Figure 6-5: Acrylic constant temperature dielectric spectroscopy measurements for 10 temperatures using 1, 2.5, and 5 mm wavelength interdigital sensors. Measurement colors correspond to the temperatures listed in Table 6.5. Theoretical results in black assume $\epsilon_r = 3.70$, and $\sigma = 1.67 \times 10^{-10}$ S/m (see Table 6.1). Interface box 3 is used. *This measurement was conducted January 2, 2007.*

Table 6.6: Moist Birch Steady State Measurements: Average Temperatures and Standard Deviations

Color						
Avg. Temp. °F	70.2	77.7	89.3	98.8	108.4	117.9
Std. Dev. °F	0.21	2.78	0.38	0.48	0.55	0.61
Color						
Avg. Temp. °F	127.6	137.1	146.9	156.5	166.1	175.8
Std. Dev. °F	0.56	0.52	0.47	0.42	0.30	0.29

6.2 Wood Rod Measurements

Wood provides an interesting medium for experimentation with dielectrometry sensors. It can be modeled as homogeneous in the frequency range of interest; it is hydrophilic allowing it to absorb moisture so that a diffusion process can be monitored, and most importantly it is readily available at low cost. Birch, maple and oak rods have been acquired for experimental measurements.

6.2.1 Birch Wood Rod

Measurements are conducted on a birch rod with a 1¹/₄ inch diameter. Birch wood is a hydrophilic material and the amount of moisture in the wood will significantly effect the dielectric properties. A sample of birch rod stored in the laboratory for several days (about 68 °F and 40% relative humidity) is measured.

The initial cycle of measurements are reported as the “moist” birch rod measurements, and the second set as the “dry” birch rod measurements. In the former case measurements are conducted on the rod immediately after sample preparation and placement in the measurement chamber. After the initial temperature cycle from 70 to 176 °F the birch rod is kept in the chamber at approximately 175 °F for sixteen hours before another set of “dry” measurements are taken. The experimental results show significant differences.

Moist Birch

In the first experiment the spectroscopy measurements are taken as the temperature is increased from 70 °F to 176 °F (21 °C to 80 °C). The measurement temperatures and standard deviations are summarized in Table 6.6 and the experimental results are shown in Fig. 6-6. To provide a frame of reference, the black curves represent theoretical results for a material with $\epsilon_r = 3.4$, and $\sigma = 10^{-9}$ S/m. These values do not come from a reference, but are simple estimates chosen based on the experimental data.

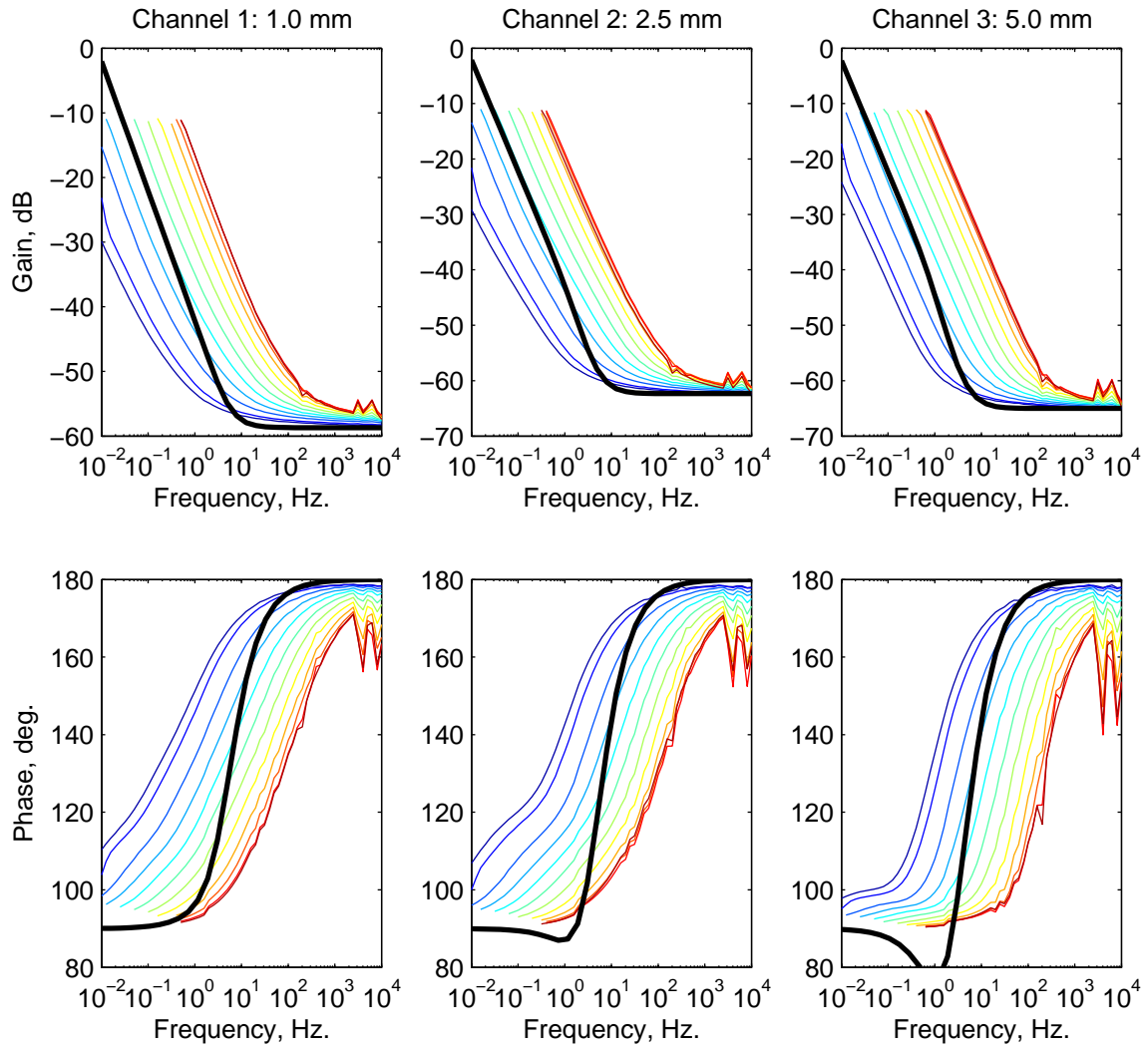


Figure 6-6: Moist birch rod constant temperature dielectric spectroscopy measurements for 12 temperatures using 1, 2.5, and 5 mm wavelength interdigital sensors. Measurement colors correspond to the temperatures listed in Table 6.6. Theoretical results in black assume $\epsilon_r = 3.40$, and $\sigma = 10^{-9}$ S/m. Interface box 1 is used. *This measurement was conducted January 2, 2007.*

Table 6.7: Dried Birch Steady State Measurements: Average Temperatures and Standard Deviations

Color						
Avg. Temp. °F	76.6	84.1	91.4	100.0	109.3	118.8
Std. Dev. °F	0.49	1.15	1.72	1.23	0.82	0.59
Color						
Avg. Temp. °F	128.5	137.9	147.5	157.0	166.6	176.1
Std. Dev. °F	0.59	0.48	0.56	0.55	0.57	0.11

The experimental results are significantly different from the results for the plastic rods. The conductivity is significantly higher, and increase several orders of magnitude as the temperature is increased. At the lowest frequencies the controller box is saturated. This could be avoided by increasing the feedback capacitance resulting in a downward shift of the gain. This comes at the expense of signal to noise ratio, and makes the high frequency measurements where the gain is very low, less reliable.

Notice that the slopes of the low frequency behavior are nominally -20 dB per decade which is predicted from the lossy capacitor model transfer function given in eq. 3.4. At high frequency the gain should approach a constant value determined by the permittivity alone, while the phase approaches 180° . At higher temperatures we see some spiking in the highest decade. We suspect this is possibly due to issues associated with the measurement hardware which have not been observed elsewhere.

The values of permittivity chosen for simulation were selected to match the high frequency gain. The conductivity is clearly varying and the choice for simulation is only to illustrative. The conductivity appears to range from about 10^{-10} S/m for the lowest temperatures, to 3×10^{-8} S/m for the highest.

Dried Birch

After completing the first set of measurements the birch rod is left undisturbed for 16 hours at 176°F allowing much of the moisture in the rod to escape. Measurements are taken starting at 176°F down to 77°F . Twelve frequency scans are made. The temperature information is summarized in Table 6.7. The gain and phase measurements are shown in Fig. 6-7

The measurement results show a significant decrease in overall conductivity. The gain is flat for the highest three decades for the highest temperatures and at the lowest temperature the material shows losses only in the lowest decade. The high frequency gain is down as well suggesting the relative permittivity of about 2.4. The shape is somewhat unusual in that the phase shift never reaches 90°

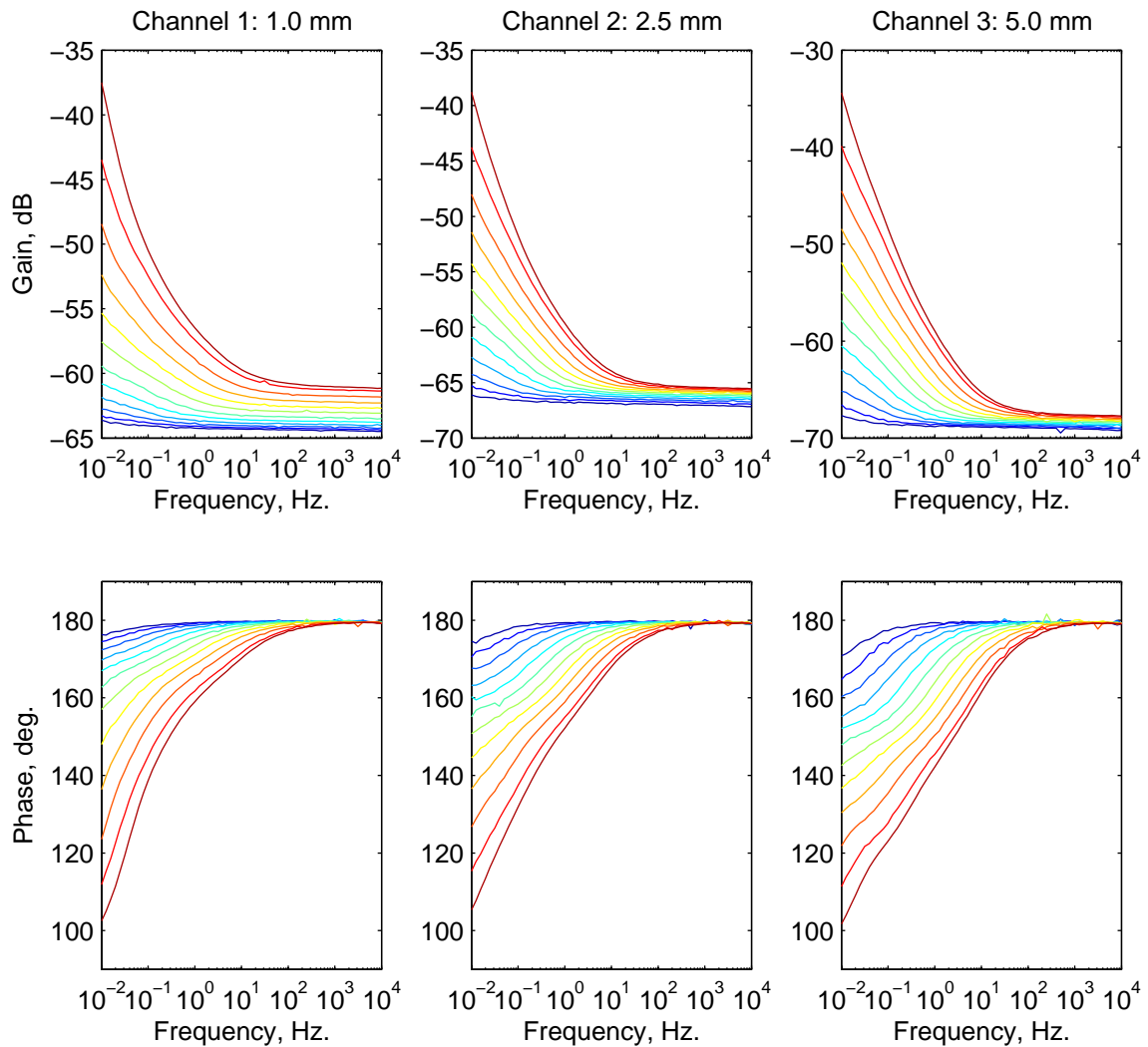


Figure 6-7: Dried birch rod constant temperature dielectric spectroscopy measurements for 12 temperatures using 1, 2.5, and 5 mm wavelength interdigital sensors. Measurement colors correspond to the temperatures listed in Table 6.7. No theoretical curves are given because of the material is highly dispersive. Interface box 1 is used. *This measurement was conducted January 3, 2007.*

Table 6.8: Moist Single Conductor Cable Measurements Steady State Temperature Information

Color						
Avg. Temp. °F	80.6	89.3	99.0	108.7	118.2	127.9
Std. Dev. °F	1.51	0.23	0.29	0.25	0.43	0.47
Color						
Avg. Temp. °F	137.5	147.0	156.6	166.1	175.6	185.2
Std. Dev. °F	0.43	0.40	0.33	0.22	0.20	0.12

even through the transition extends for four decades. This indicates the material is highly dispersive and would not be well approximated by a simple static permittivity and conductivity. A non-dispersive material makes the transition from 90° to 180° in about two decades. The gain is also seen to increase very gently at first, taking several decades to reach a constant slope.

6.3 Cable Measurements

In this section we present measurements of the single and three conductor power cables. We have no prior knowledge of the electrical properties of these cables.

6.3.1 Single Conductor Cable Measurements

In this section we present results for a moist and dry single conductor cable. Prior to measuring the moist cable, a five inch section of cable had been stored at room temperature and relative humidity with the sheath intact. Immediately before the measurements the sheath was removed by a combination of sawing and chiseling with care not to damage the paper insulation.

Moist Single Conductor Cable

A single conductor cable having been exposed to the ambient environment having a temperature of 68°F and a relative humidity of 40%, is measured with a three wavelength sensor. Measurements are made in the small vacuum chamber which is sealed throughout the measurement. The vacuum is never run. The temperature is varied from 80°F to 185°F (27°C to 85°C). Measurements are made at twelve different set point temperatures over the full measurement range of the hardware, 0.005 to 10,000 Hz. The average temperature during each measurement and its standard deviation is recorded in Table 6.8. The experimental results are plotted in Fig. 6-8.

The results have a shape similar to the wood measurements. The transition between conductive and capacitive behavior takes about four decades as the phase moves from 90° to 180° . Increasing

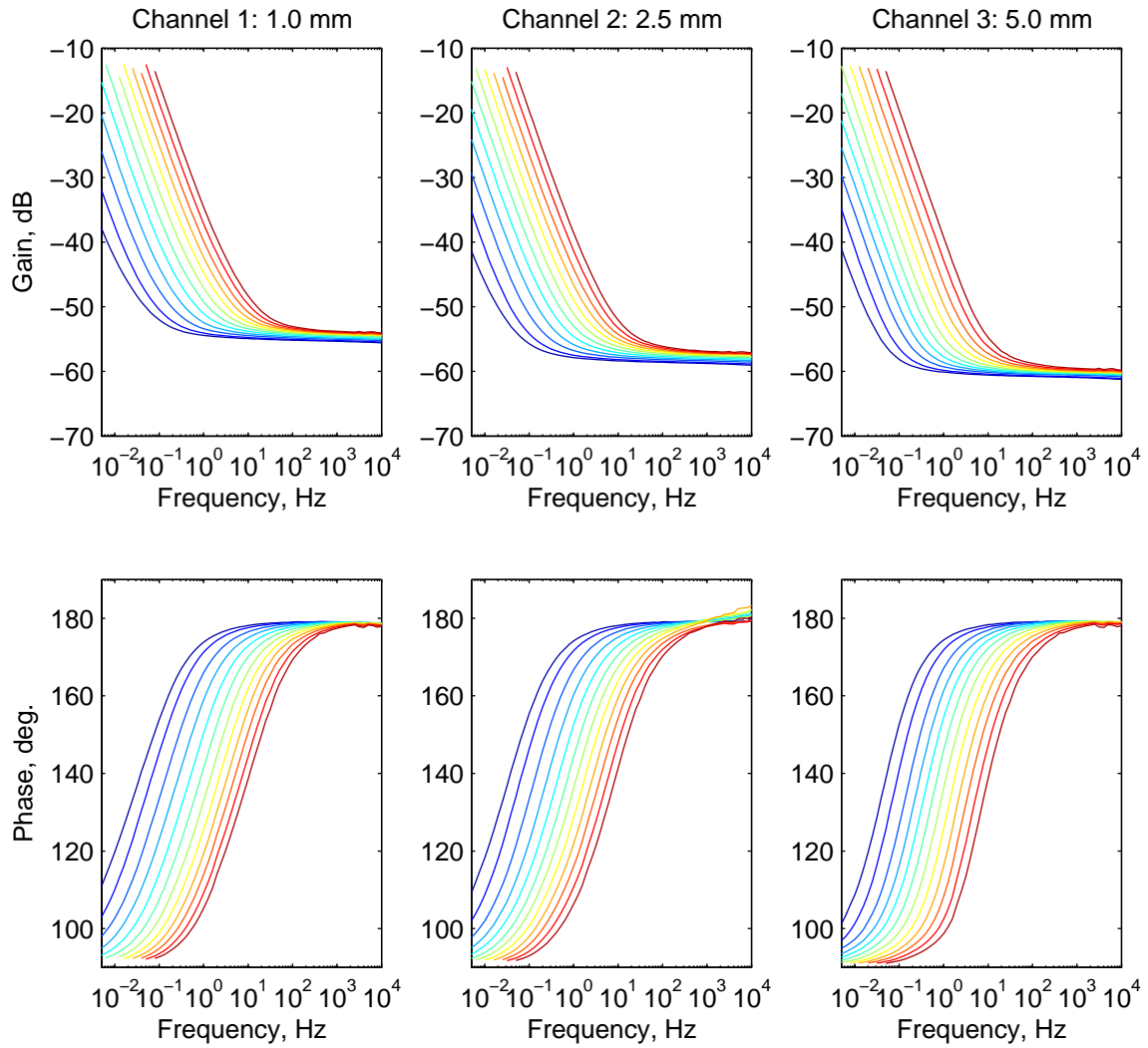


Figure 6-8: Moist single conductor cable constant temperature dielectric spectroscopy measurements for 12 temperatures using 1, 2.5, and 5 mm wavelength interdigital sensors. Measurement colors correspond to the temperatures listed in Table 6.8. Interface box 1 is used. *This measurement was conducted from February 22 to February 23, 2006.*

Table 6.9: Dry Single Conductor Cable Measurements Steady State Temperature Information

Color								
Avg. Temp. °F	63.8	70.0	79.8	89.4	99.0	108.7	118.3	127.9
Std. Dev. °F	0.18	0.15	0.13	0.13	0.15	0.12	0.12	0.12
Color								
Avg. Temp. °F	137.5	147.1	156.8	166.3	175.7	185.3	194.7	
Std. Dev. °F	0.14	0.13	0.11	0.11	0.15	0.14	0.12	

temperature causes the frequency response to shift up in frequency which implies an increasing conductivity. There is also a slight vertical shift in gain with increasing temperature. Gains above about -12 dB result in saturation of the sensing hardware and have been removed for clarity.

Dry Single Conductor Cable

Recognizing the significant conductivity in the moist single conductor cable measurement, a second measurement is made. This time, the measurement chamber with the cable and sensor setup inside is evacuated for several days with the goal of removing all moisture from the cable. The measurement temperature range is increased and the stabilization time is increased to reduce the standard deviation of the temperature. Fifteen steady state temperature measurements are taken. The temperature is varied from 64 °F to 195 °F (18 °C to 90 °C). The temperature data is summarized in Table 6.9 and the measurement results are given in Fig. 6-9.

The results are quite similar to those obtained for the moist cable. The predominant difference is a downward shift in frequency of the measurement curves indicating a reduction in conductivity. The lowest temperature measurements indicate excellent insulation properties with the phase beginning to transition only below 0.1 Hz. The high frequency gain shows only a slight temperature dependence, and is very similar to the moist cable measurements.

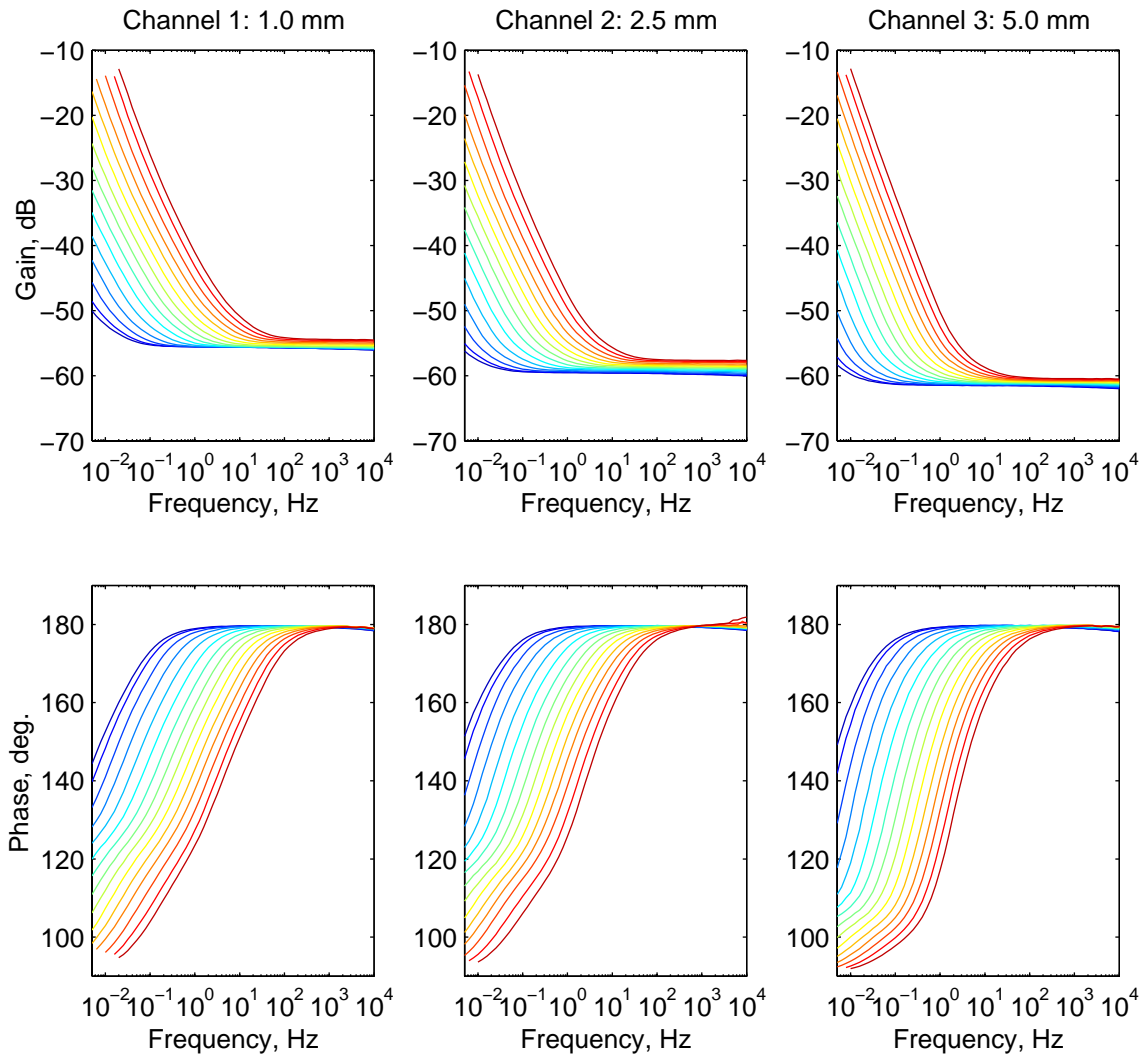


Figure 6-9: Dry single conductor cable constant temperature dielectric spectroscopy measurements for 17 temperatures using 1, 2.5, and 5 mm wavelength interdigital sensors. Measurements are in color (see Table 6.9). Interface box 4 is used. *This measurement was conducted from March 1 to March 2, 2007.*

Table 6.10: Three Conductor Cable Measurements Steady State Temperature Information

Color							
Avg. Temp. °F	73.48	79.84	89.33	98.93	108.5	118	127.5
Std. Dev. °F	0.91	0.32	0.15	0.14	0.14	0.17	0.16
Color							
Avg. Temp. °F	137.1	146.6	156.1	165.5	175	184.4	193.7
Std. Dev. °F	0.11	0.13	0.13	0.11	0.12	0.10	0.10

6.3.2 Three Conductor Cable Measurements

The three conductor cable is measured using the three wavelength sensor in a ϕ periodic orientation. In this experiment the pipe clamping technique described in Section 5.3 is used. The chamber is thoroughly evacuated before beginning the measurement to reduce the cable moisture. The temperature is varied from 73 °F to 194 °F (23 °C to 90 °C) and the vacuum pump is run throughout the measurement. Measurements are made at fourteen different set point temperatures. The average temperature during each measurement and its standard deviation is recorded in Table 6.10. The experimental results are plotted in Fig. 6-10.

The three conductor cable measurements are very similar in shape to the single conductor cable measurements. It appears there may have been slightly more moisture during the measurement or that the paper tapes are simply slightly more conducting than the single conductor cable. The high frequency gain is approximately the same as for the single conductor cable.

Two additional frequency temperature scans done on the three conductor cable are presented in Section B.1.5. *This measurement was conducted from May 18 to May 19, 2006.*

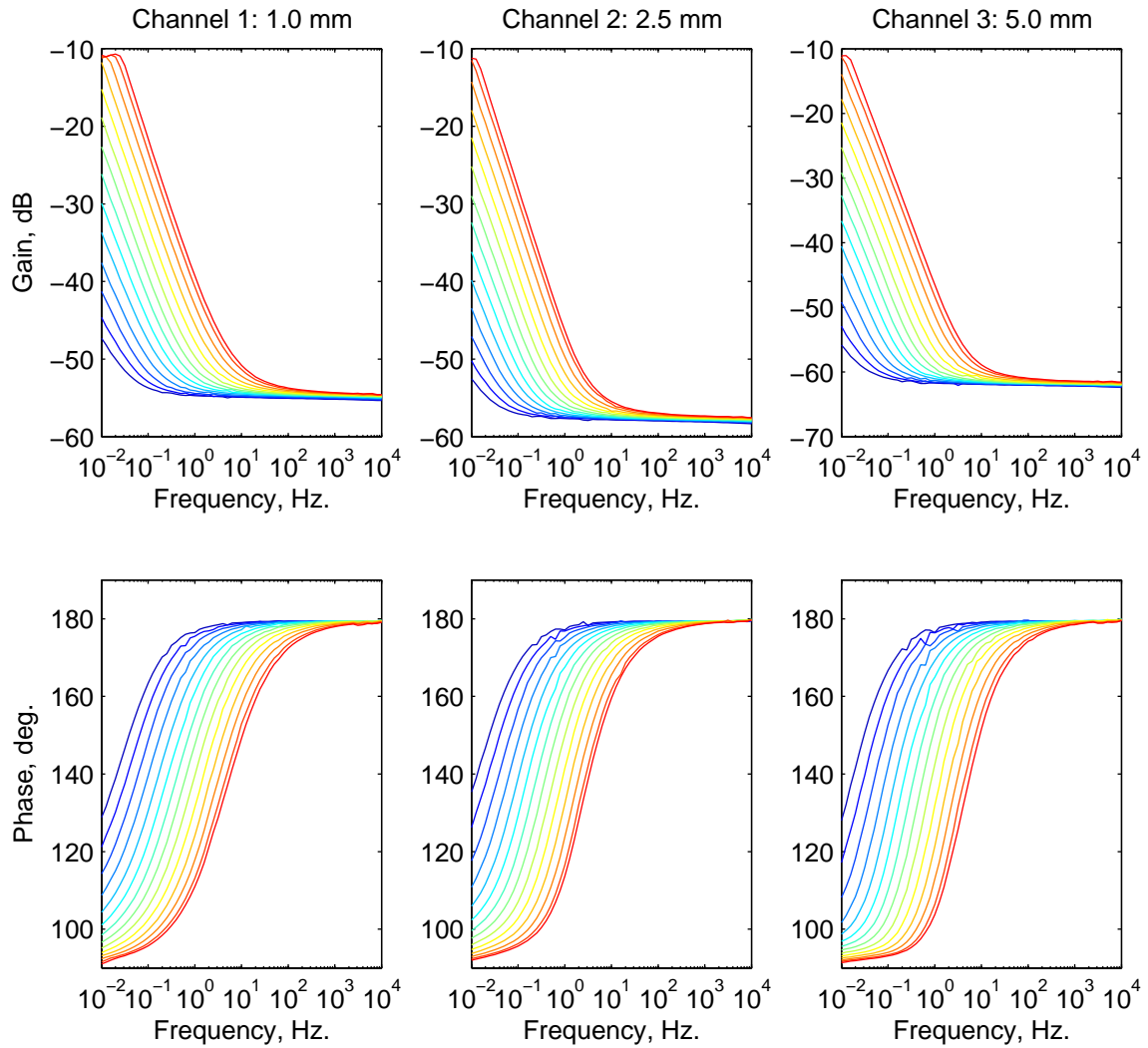


Figure 6-10: Three conductor cable constant temperature dielectric spectroscopy measurements for 14 temperatures using 1, 2.5, and 5 mm wavelength interdigital sensors. Measurement colors correspond to the temperatures listed in Table 6.10. Feedback capacitances are nominally 5 nF. Interface box 4 is used.

6.4 Chapter Summary

In this chapter we have presented steady state measurements on a number of materials at numerous temperatures and in some cases different moisture conditions. The results illustrate a significant temperature dependence for the cable insulation and woods. Most plastics have only a small temperature dependence over the range of measurement temperatures. In the subsequent chapter we provide detailed analysis of the measurements by estimating the dielectric properties. For the cables and other materials, the variation with temperature is shown to be characteristic of an Arrhenius temperature dependence. Additional steady state measurements that repeat some of these experiments are provided in Section B.1.

Chapter 7

Dielectric Properties

In this chapter we investigate the effects of temperature, moisture, and frequency on dielectric materials. We begin with Maxwell's equations and the constitutive laws to clarify some of the many sources of confusion that can exist because of the multiple definitions some terms receive. The basic theory of capacitive measurements is investigated and define the principle characteristics of dielectrics.

In the next section the temperature dependence of dielectric properties is explored. The dielectric measurements presented in Chapter 6 are analyzed using theory from Chapter 3 to estimate the dielectric properties of the measured materials. We then define the Arrhenius temperature dependence and explore its applicability to our own experimental results. For the materials that obey the Arrhenius temperature dependence a master curve may be defined. The Arrhenius temperature dependence is described by a single parameter called the activation energy. In principle the master curve and the activation energy are all that is needed to describe the temperature dependence of a material.

The effect of moisture on dielectric properties is then considered. Neimanis & Eriksson have taken moisture and capacitance measurements on PILC cable insulation similar to our own electric power cables. [1]. We analyze these curves and characterize them by a moisture dependent frequency shift.

7.1 Introduction to Dielectrics

7.1.1 Maxwell's Equations and the Constitutive Laws

The measurement of dielectric properties or simply electric properties of materials is an area of significant efforts in both theory and experimental research. It is worthwhile to begin from the fundamentals and then proceed to avoid, as much as possible, the confusion caused by the ambiguity and duplicity of terms found in the literature.

We begin with Maxwell's equations and the charge conservation equation which are given in eqs. 7.1–7.5. The left hand side shows the general form which are valid for macroscopic phenomena *i.e.*, until the quantum limit is reached and quantum electrodynamic theory must be applied [4]. There is no restriction to linearity or time invariance.

$$\nabla \times \overline{H}(\overline{r}, t) = \frac{\partial \overline{D}(\overline{r}, t)}{\partial t} + \overline{J}(\overline{r}, t) \quad \rightarrow \quad \nabla \times \overline{H}(\overline{r}) = j\omega \overline{D}(\overline{r}) + \overline{J}(\overline{r}) \quad (7.1)$$

$$\nabla \times \overline{E}(\overline{r}, t) = -\frac{\partial \overline{B}(\overline{r}, t)}{\partial t} \quad \rightarrow \quad \nabla \times \overline{E}(\overline{r}) = -j\omega \overline{B}(\overline{r}) \quad (7.2)$$

$$\nabla \cdot \overline{D}(\overline{r}, t) = \rho(\overline{r}, t) \quad \rightarrow \quad \nabla \cdot \overline{D}(\overline{r}) = \rho(\overline{r}) \quad (7.3)$$

$$\nabla \cdot \overline{B}(\overline{r}, t) = 0 \quad \rightarrow \quad \nabla \cdot \overline{B}(\overline{r}) = 0 \quad (7.4)$$

$$\nabla \cdot \overline{J}(\overline{r}, t) = -\frac{\partial \rho(\overline{r}, t)}{\partial t} \quad \rightarrow \quad \nabla \cdot \overline{J}(\overline{r}) = -j\omega \rho(\overline{r}) \quad (7.5)$$

Equations 7.1 through 7.5 are Ampere's Law, Faraday's Law, Gauss' law for electric fields, Gauss' law for magnetic fields, and the law of charge conservation. The field vectors \overline{E} , \overline{H} , \overline{D} , and \overline{B} are the electric field, the magnetic field, the electric displacement, and the magnetic flux density. The source terms \overline{J} and ρ are the electric current density and the electric charge density respectively. The vector \overline{r} is a position vector and t is time. The right hand side shows the time harmonic form in phasor notation assuming an $e^{j\omega t}$ time dependence ($\overline{H}(\overline{r}, t) = \mathbf{Re} \{ \overline{H}(\overline{r}) e^{j\omega t} \}$). This form is applicable for linear time-invariant (LTI) media. For our analysis the time harmonic form of Maxwell's equations is sufficient. We proceed assuming the time harmonic form and suppress the argument \overline{r} for clarity and brevity. The effect of isotropic materials on electromagnetic phenomena is described by the constitutive relations

$$\overline{D} = \epsilon \overline{E} \quad (7.6)$$

$$\overline{B} = \mu \overline{H} \quad (7.7)$$

where ϵ is the permittivity, and μ is the permeability. Analysis throughout assumes materials

are non-magnetic, *i.e.*, $\mu = \mu_o$, the permeability of free space. In some cases the definition of a polarization vector \bar{P} is useful.

$$\bar{D} = \epsilon \bar{E} = \epsilon_o \bar{E} + \bar{P} \quad (7.8)$$

The polarization represents the electric dipole moment per unit volume of the dielectric material. Our interest is in materials where the polarization is related to the electric field by

$$\bar{P} = \epsilon_o \chi \bar{E} \quad (7.9)$$

Here we have defined the electric susceptibility, χ which may be complex and frequency dependent. Under this condition the permittivity is $\epsilon = \epsilon_o(1 + \chi)$. At this point some authors define ϵ' and ϵ'' .

$$\epsilon = \epsilon' - j\epsilon'' \quad (7.10)$$

Both ϵ' and ϵ'' are taken to be real. The choice of the negative sign emphasizes the fact that the imaginary part of ϵ must be negative to satisfy causality [83] (for an $e^{-i\omega t}$ time dependence the imaginary part must be positive).

For ohmic media, the electric current density is related to the electric field by σ , the conductivity of the media.

$$\bar{J} = \sigma \bar{E} \quad (7.11)$$

σ is understood to be real. The total current density, \bar{J}_t , the sum of the displacement current density and the electric current density, is then found from Ampere's law

$$\bar{J}_t = j\omega \bar{D} + \bar{J} \quad (7.12)$$

$$= j\omega \epsilon \bar{E} + \sigma \bar{E} \quad (7.13)$$

$$= j\omega \left(\epsilon - j \frac{\sigma}{\omega} \right) \bar{E} \quad (7.14)$$

$$= j\omega \epsilon^* \bar{E} \quad (7.15)$$

We have defined an effective permittivity ϵ^* which incorporates the conductivity of the media into the permittivity directly. Many authors use the term complex permittivity to refer to ϵ^* , however, this does little to distinguish it from ϵ which may in fact be complex without the consideration of the DC conductivity. Conduction and dielectric phenomenon are grouped together. The effective permittivity includes the effects of ohmic losses and damping. An alternative definition of ϵ' and ϵ'' is

$$\epsilon^* = \epsilon' - j\epsilon'' \quad (7.16)$$

Both ϵ' and ϵ'' are assumed real and again causality requires ϵ'' to be positive. The definition in equation 7.16 is assumed throughout. Finally an effective conductivity, σ , is often defined as $\sigma = \omega\epsilon''$. Again this is a redefinition of σ except when χ is real. Under this definition

$$\epsilon^* = \epsilon' - j\frac{\sigma}{\omega} \quad (7.17)$$

which is the form used in Chapter 3. Experimentally, conduction losses and dielectric damping losses are indistinguishable. The theoretical distinction exists because the physical phenomena are separate. At high frequency, loss is dominated by damping, and at low frequency, loss is dominated by conduction. In general, ϵ'' depends on both mechanisms.

7.1.2 High Field Effects

All real dielectrics are in fact nonlinear since for sufficiently high field intensities their permittivity changes. For sufficiently strong fields the dielectric is “damaged” changing the dielectric properties for other field intensities as well. This refutes both our assumptions of linearity and time-invariance.

In fact this is precisely one of the problems faced in PILC cables. The oil-impregnated paper insulation normally can support the electric field intensities it is subjected to, however, over time the dielectric properties change. The change is exacerbated under conditions of high temperature and high moisture content, both of which lead to increased conductivity, a reduction in dielectric strength, and an increased likelihood of dielectric breakdown. Typically the breakdown phenomena is localized, which is called partial discharge. Eventually this may lead failure of the cable.

Nevertheless theory developed using LTI assumptions is quite powerful in the regime in which it may be applied. Our own experiments are conducted at relatively low voltages and the sensing fields should not damage the insulation.

7.1.3 Impedance Measurements

In the frequency range of interest measurement of dielectric properties are done using a two terminal “capacitive” sensor. This is a slight misnomer since capacitance is a real number and the measurement of lossy dielectrics produce a complex capacitance, which is really simply an impedance or admittance depending on your perspective. The difference leads to an improper derivation which fortuitously leads to a correct result.

The terminals are attached to arbitrarily shaped perfectly conducting plates which are separated by a medium with effective permittivity ϵ^* . Capacitance is defined as the ratio of the charge, Q , induced on the plates to the voltage applied to the plates, V . Using Gauss’ Law for electric fields

(eq. 7.3), the electric constitutive relation (eq. 7.6), and the divergence theorem we can write an expression for charge, Q . The definition of V is the line integral of the electric field from the positive to negative plate. The ratio give us the capacitance.

$$C = \frac{Q}{V} = \epsilon \left[\frac{\oint \bar{E} \cdot d\bar{a}}{\int_+^- \bar{E} \cdot d\bar{\ell}} \right] \quad (7.18)$$

In this equation the Ohmic conductivity plays no role though C may still be complex because of dielectric damping. In order to consider the Ohmic effects we define the impedance Z .

$$Z = \frac{V}{I} = \frac{\int_+^- \bar{E} \cdot d\bar{\ell}}{\oint \bar{J}_t \cdot d\bar{a}} \quad (7.19)$$

The current density is found from eq. 7.15. Assuming ϵ^* is homogeneous we have

$$Z = \frac{V}{I} = \frac{1}{j\omega\epsilon^*} \left[\frac{\int_+^- \bar{E} \cdot d\bar{\ell}}{\oint \bar{E} \cdot d\bar{a}} \right] \quad (7.20)$$

It is incorrect to replace ϵ in eq. 7.18 with ϵ^* . This is inconsistent with the previous definition of C , and is equivalent to the redefining the capacitance, $C = 1/j\omega Z$.

The assumption that the effective permittivity is isotropic and homogeneous was necessary to remove it from the surface integral. The bracketed expression in eqs. 7.18 and 7.20 is a geometric constant independent of the permittivity [5]. If the geometry is not accurately known, an impedance measurement cannot be used to determine the effective permittivity. In this case the loss tangent serves as a partial characterization of the dielectric. The loss tangent is defined to be

$$\tan \delta = \frac{\epsilon''}{\epsilon'} \quad (7.21)$$

The loss angle δ is simply the angle to the point $\{\epsilon', \epsilon''\}$ in the complex plane. Some references refer to the loss tangent as the dissipation factor. The loss tangent can be determined directly from the impedance measurement.

When an impedance measurement produces an electric field that passes through a medium where ϵ^* is spatially varying, the permittivity generally cannot be removed from the surface integral. This is the case with the interdigital dielectrometry sensor since each measurement involves at least two materials, the substrate and the MUT. Interpretation of the sensor measurement in terms of MUT effective permittivity relies on the prior knowledge of the sensor geometry, substrate permittivity, and MUT thickness.

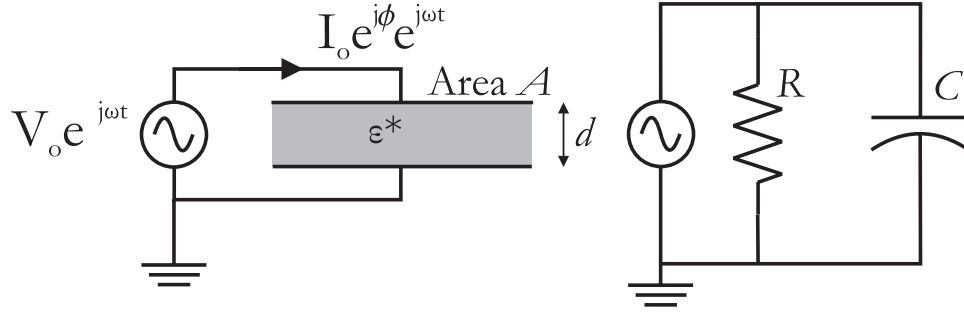


Figure 7-1: Parallel plate capacitor with spacing d , area A , and effective permittivity ϵ^* , excited by voltage $V_o e^{j\omega t}$. Current is $I_o e^{j\phi} e^{j\omega t}$. To the right is the equivalent circuit model.

Example: Parallel Plate Capacitance Measurements

Consider the lossy parallel plate capacitor shown in Fig. 7-1. Using dielectric spectroscopy in the frequency domain, we are able to determine the properties of the dielectric. Our analysis assumes the material is homogeneous the effective permittivity is linear.

We wish to calculate the effective permittivity, effective conductivity and loss tangent from the exciting voltage and resulting current by modeling the lossy capacitor as a capacitor and resistor in parallel.

$$V = V_o e^{j\omega t} \quad (7.22)$$

$$I = I_o e^{j\phi} e^{j\omega t} \quad (7.23)$$

$$V = IZ \quad (7.24)$$

$$Z = \frac{R}{1 + j\omega RC} \quad (7.25)$$

$$Z = \frac{R}{1 + (\omega RC)^2} - j \frac{\omega R^2 C}{1 + (\omega RC)^2} \quad (7.26)$$

$$Z = \frac{V_o}{I_o} e^{-j\phi} = \frac{V_o}{I_o} (\cos \phi - j \sin \phi) \quad (7.27)$$

This gives us two equations and two unknowns.

$$R = \frac{V_o}{I_o} \sec \phi \quad (7.28)$$

$$C = \frac{I_o \sin \phi}{V_o \omega} \quad (7.29)$$

We find the real part of the permittivity and effective conductivity.

$$\epsilon' = \frac{Cd}{A} = \frac{dI_o}{\omega V_o A} \sin \phi \quad (7.30)$$

$$\sigma = \frac{d}{AR} = \frac{dI_o}{V_o A} \cos \phi \quad (7.31)$$

The loss tangent is

$$\tan \delta = \frac{\epsilon''}{\epsilon'} = \frac{\sigma/\omega}{\epsilon} = \frac{1}{\omega RC} = \cot \phi \quad (7.32)$$

Notice that the loss tangent can be determined directly from the phase angle ϕ . This is true regardless of the geometry of the capacitor making it a relatively easy quantity to measure. Some authors prefer treating the lossy capacitor as having a complex capacitance $C = C' - jC''$, which is an equivalent approach.

A wide variety of measurement techniques of dielectric properties are based on the above analysis. Of course additional circuitry is needed to accurately measure the current, which is often done by converting the current to a voltage using an op-amp circuit like that in Fig. 3-5.

7.2 Dependence on Temperature

The experimental results in Chapter 6 clearly show the gain and phase generally shift up in frequency with temperature. While the frequency dependent capacitance and conductance can be calculated directly from eqs. 3.6 and 3.7, it is of great interest to us to use the theory in Chapter 3 to estimate the effective permittivity of the MUT.

After estimating the permittivity we show that some of the materials exhibit the Arrhenius temperature dependence. We estimate the activation energy for these materials and provide a master curve.

7.2.1 Estimated the Effective Permittivity from Measurements

The conversion of gain and phase to the dielectric properties falls into the field of inverse problem solving. The solution to the forward problem is understood. In order to achieve a unique solution for the effective permittivity we take all geometric properties and the dielectric properties of the substrate as given, and focus exclusively on solving for ϵ^* .

The numerical experiments in Chapter 4 indicate that the use of a planar solver should give sufficient accuracy for the ratio of circumference to spatial wavelengths that were measured. Making use of the planar inversion algorithm GETGP [59], we estimate the permittivity and effective con-

ductivity from the gain and phase measurements and the sensor properties. The MUT is assumed to be infinitely thick, an approximation justified by the complete lack of a center conductor, or that the distance from the center conductor from the electrode surface is sufficiently greater than the wavelength that the distance exceeds the sensitivity depth of the sensor. This geometry should lead to single valued complex permittivities. In some planar sensor circumstances, including a top ground plane can lead to multiple solutions for the permittivity [50]. The effective permittivity calculated using GETGP are tested using the ϕ periodic sensor forward problem solution. The calculated gain and phase is in good agreement with the measured gain and phase.

We have chosen to present the effective permittivity data as ϵ'/ϵ_o , which is the relative permittivity, and $\log_{10}(\epsilon''/\epsilon_o)$, which will simply be referred to as the dielectric loss for lack of a better term.

For a non-dispersive material with effective conductivity σ , a log-log plot of ϵ'' versus frequency, will have a slope of -1 since

$$\epsilon''/\epsilon_o = \frac{\sigma}{\omega\epsilon_o} = \frac{\sigma}{2\pi f\epsilon_o} \quad (7.33)$$

$$\log_{10}(\epsilon''/\epsilon_o) = \log_{10} \frac{\sigma}{2\pi\epsilon_o} - \log_{10} f \quad (7.34)$$

$$\frac{d(\log_{10} \epsilon''/\epsilon_o)}{d(\log_{10} f)} = -1 \quad (7.35)$$

A slope other than -1 indicates dispersion, that is the effective permittivity is a function of frequency.

Teflon Rod Permittivity

The Teflon measurements in Section 6.1.1 are converted to effective permittivity and plotted in Fig. 7-2. The results show reasonably good agreement between channels with the relative permittivity estimates between about 1.9 to 2.2 for high frequency. The 1.0 mm and 2.5 mm wavelengths tend to overestimate the value while the 5.0 mm channel underestimates it slightly. The nominal value is known to be about 2.1 to 2.2.

The dielectric loss ($\log_{10}(\epsilon''/\epsilon_o)$), is largely noise on the 2.5 and 5.0 mm wavelengths. The noise floor for the instrumentation appears to be about -2 . The 1.0 mm wavelength was clearly heavily contaminated in some way, causing the conductivity to be at least an order of magnitude higher than the other channels. The correlation seen in the dielectric loss at high frequency is due to a phase error in the measurements due to measurement hardware bandwidth limitations discussed in Section 5.2.1.

Aside from the aberrant behavior observed for some of the 1.0 mm channel measurements, the

temperature dependence is quite small. The 2.5 mm channel shows virtually no dependence while the 5.0 mm channel suggests a slight increase in effective permittivity with temperature.

The conversion results of additional measurements are presented in Section B.1.1, Figs. B-2, B-4, and B-6. The results are largely consistent, with dispersion most noticeable on the 1 mm sensor.

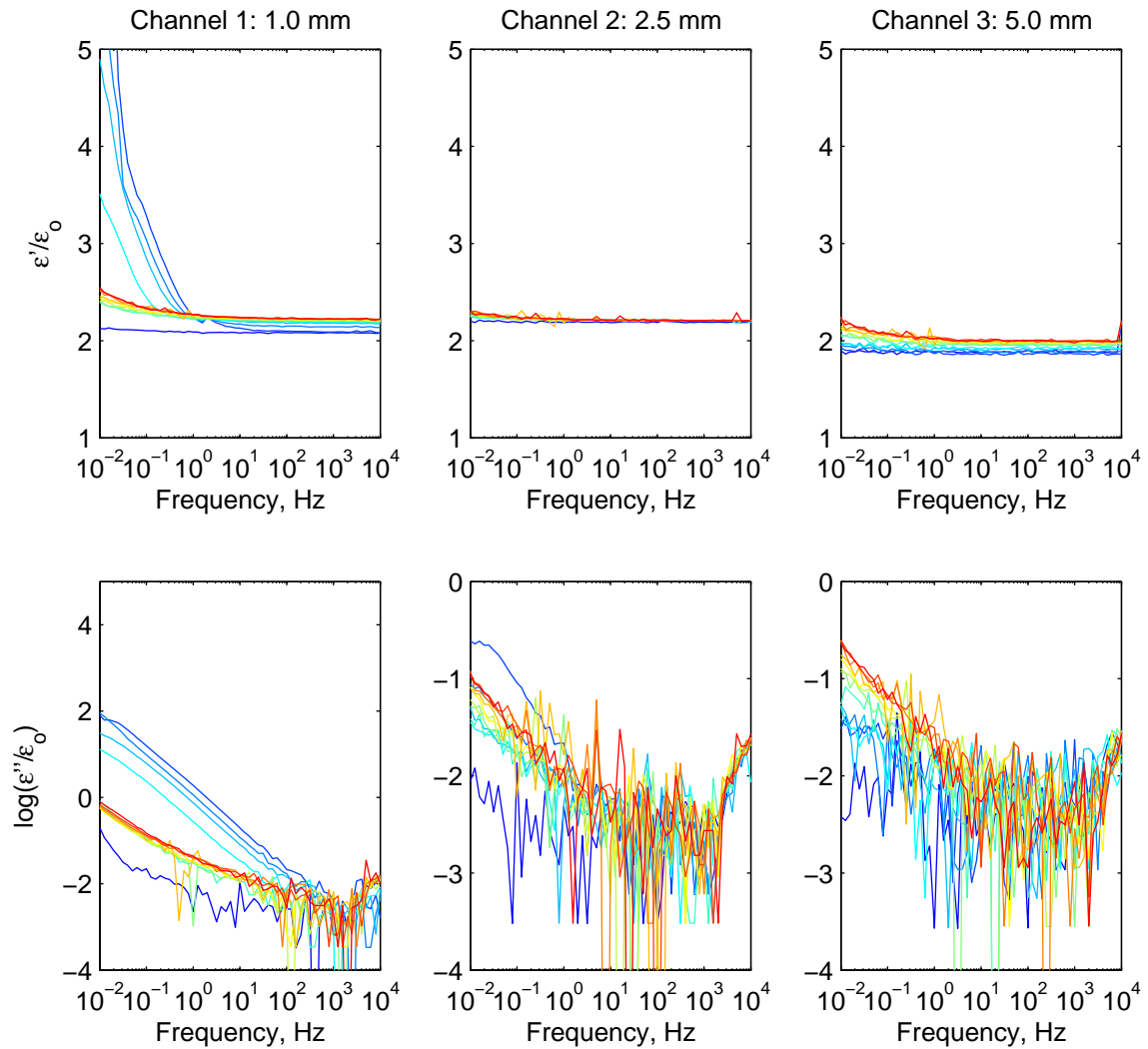


Figure 7-2: Teflon rod effective permittivity as estimated from the steady state temperature measurements in Fig. 6-2. Temperatures vary from 59.2 °F (dark blue) to 173.7 °F (dark red). Measurements are in colors corresponding to the temperatures given in Table 6.2.

Polycarbonate Rod Permittivity

The polycarbonate measurements in Section 6.1.2 are converted to effective permittivity and plotted in Fig. 7-3. The nominal relative permittivity value is 3.0. Again the 1.0, and 2.5 mm channels overestimate the permittivity slightly, while the 5.0 mm channel underestimates it slightly.

The nominal dielectric loss is -0.7 at the lowest measurement frequency of 0.01 Hz. Under the assumption the nominal values are valid throughout the spectrum, the dielectric loss should have a slope of -1 . The losses measured on the 1.0 mm and 2.5 mm sensor are slightly more than expected. The 5.0 mm channel is as expected given the noise limitations. The high frequency correlation of the dielectric loss is due to the bandwidth limitations discussed in Section 5.2.1.

The estimated effective permittivity of an alternate measurement are presented in Section B.1.2. The results are largely consistent with those presented here.

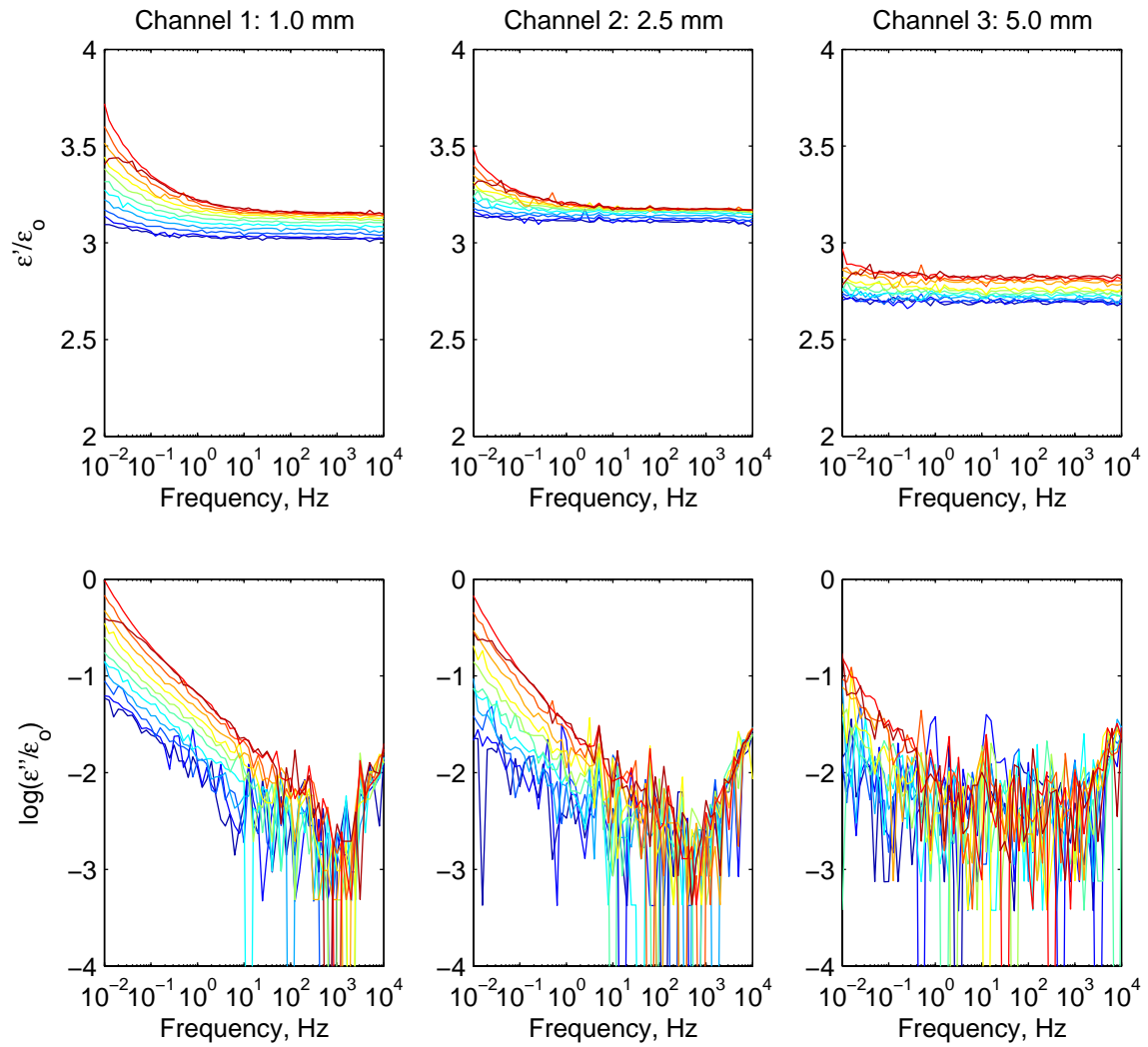


Figure 7-3: Polycarbonate rod effective permittivity as estimated from the steady state temperature measurements in Fig. 6-3. Temperatures vary from 70.1 °F (dark blue) to 164.5 °F (dark red). Measurements are in colors corresponding to the temperatures given in Table 6.3.

Polyethylene Rod Permittivity

The polyethylene measurements in Section 6.1.3 are converted to effective permittivity and plotted in Fig. 7-4. The nominal relative permittivity value is 2.20 to 2.28. The 1.0, and 2.5 mm sensors overestimate the permittivity slightly, while the 5.0 mm sensor covers the nominal value.

The nominal conductivity is so low (10^{-16} S/m) that the dielectric loss should be below the noise level throughout the spectrum. Our measurements show that some conductivity is detected at low frequencies. The high frequency correlation in the dielectric loss is due to the bandwidth limitations discussed in Section 5.2.1.

The estimated effective permittivity of an alternate measurement are presented in Section B.1.3. The results are largely consistent with those presented here.

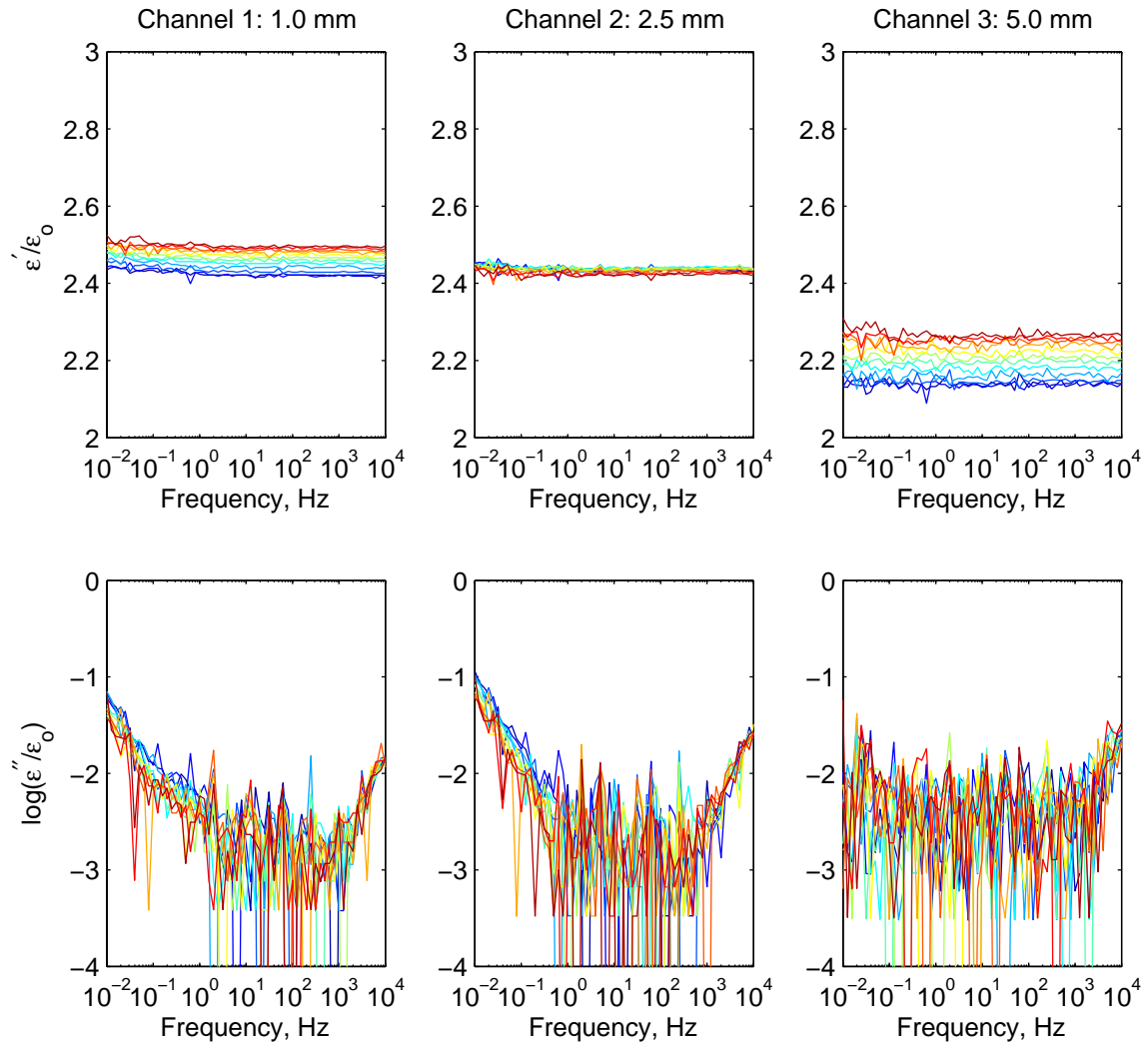


Figure 7-4: Polyethylene rod effective permittivity as estimated from the steady state temperature measurements in Fig. 6-4. Temperatures vary from 71.1 °F (dark blue) to 173.8 °F (dark red). Measurements are in colors corresponding to the temperatures given in Table 6.4.

Acrylic Rod Permittivity

The acrylic rod measurements in Section 6.1.4 are converted to effective permittivity and plotted in Fig. 7-5. The nominal relative permittivity value is 3.7 at 60 Hz and at 1 MHz (10^6 Hz) the nominal value is 2.2. The general trend of the measurements appears with a material that would achieve that value if the two additional decades of measurement range were available to us.

The nominal conductivity is about 6×10^{-10} S/m which corresponds to a dielectric loss of -0.75 at 60 Hz. The behavior is unusual and somewhat inconsistent between the channels particularly at the lowest frequencies. The 5 mm sensor is at its lowest value while the 1.0 and 2.5 mm sensors are at their highest.

This is the first measurement where increasing the temperature clearly shifts the spectrum upwards in frequency. There is also a consistent vertical shift in all the measurements.

The estimated effective permittivity of an alternate measurement are presented in Section B.1.4. The results are largely consistent with those presented here.

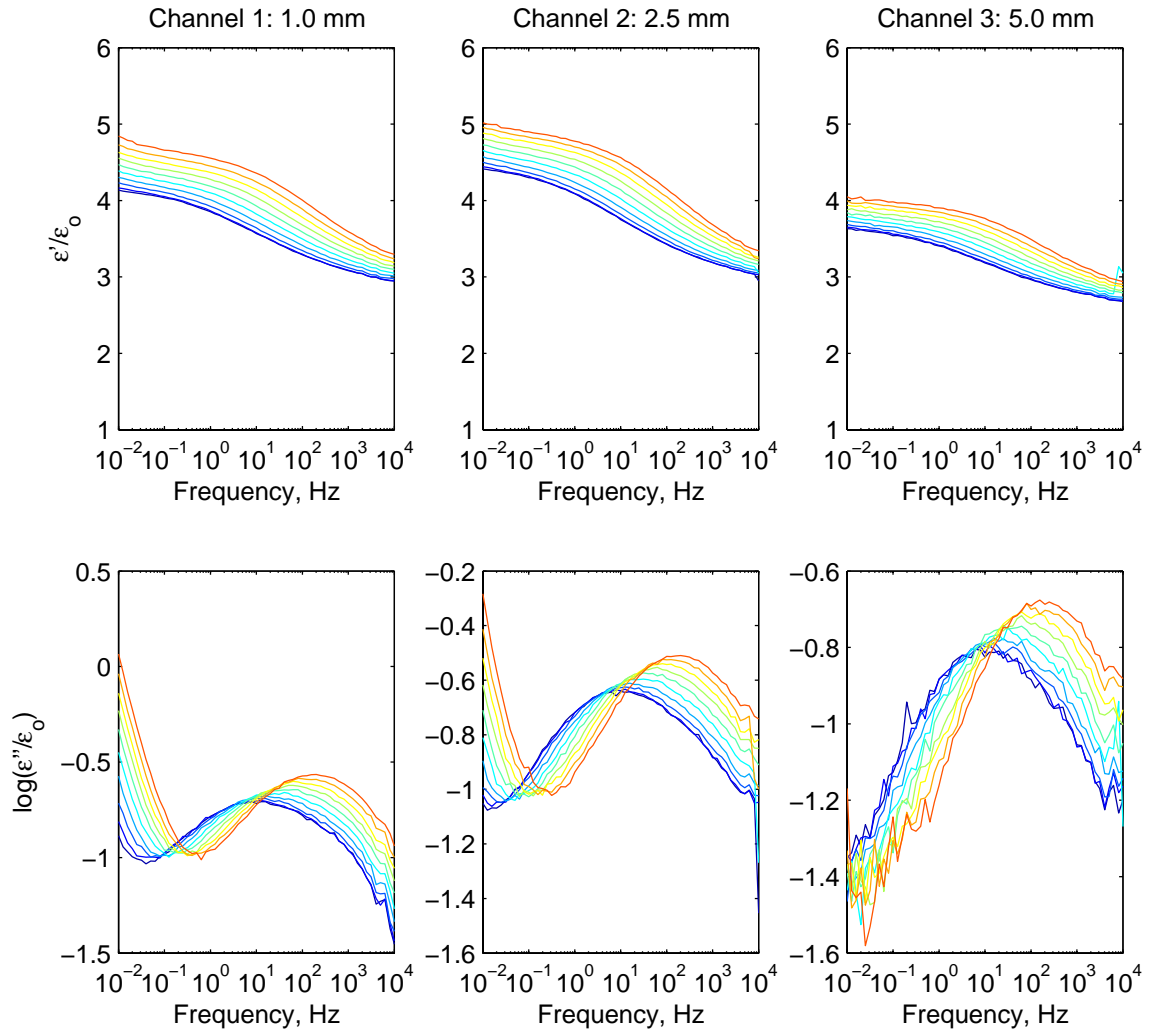


Figure 7-5: Acrylic rod effective permittivity as estimated from the steady state temperature measurements in Fig. 6-5. Temperatures vary from 71.7 °F (dark blue) to 154.8 °F (dark red). Measurements are in colors corresponding to the temperatures given in Table 6.5.

Birch

The birch rod measurements in Section 6.2.1 are converted to effective permittivity and plotted in Figs. 7-6 and 7-7 for the moist and dry measurements respectively. In both cases increasing temperature causes a horizontal shift of the effective permittivity spectrum to higher frequency. A slight upward shift is also noticeable when comparing the high frequency relative permittivity data. We do not have a reference value for the permittivity in this frequency range. Overall agreement from sensor to sensor is considerable.

Drying appears to shift the dielectric properties down in frequency by more than three decades. A vertical shift is also noticed as the high frequency relative permittivity decreases from about 3.5 to 2.2.

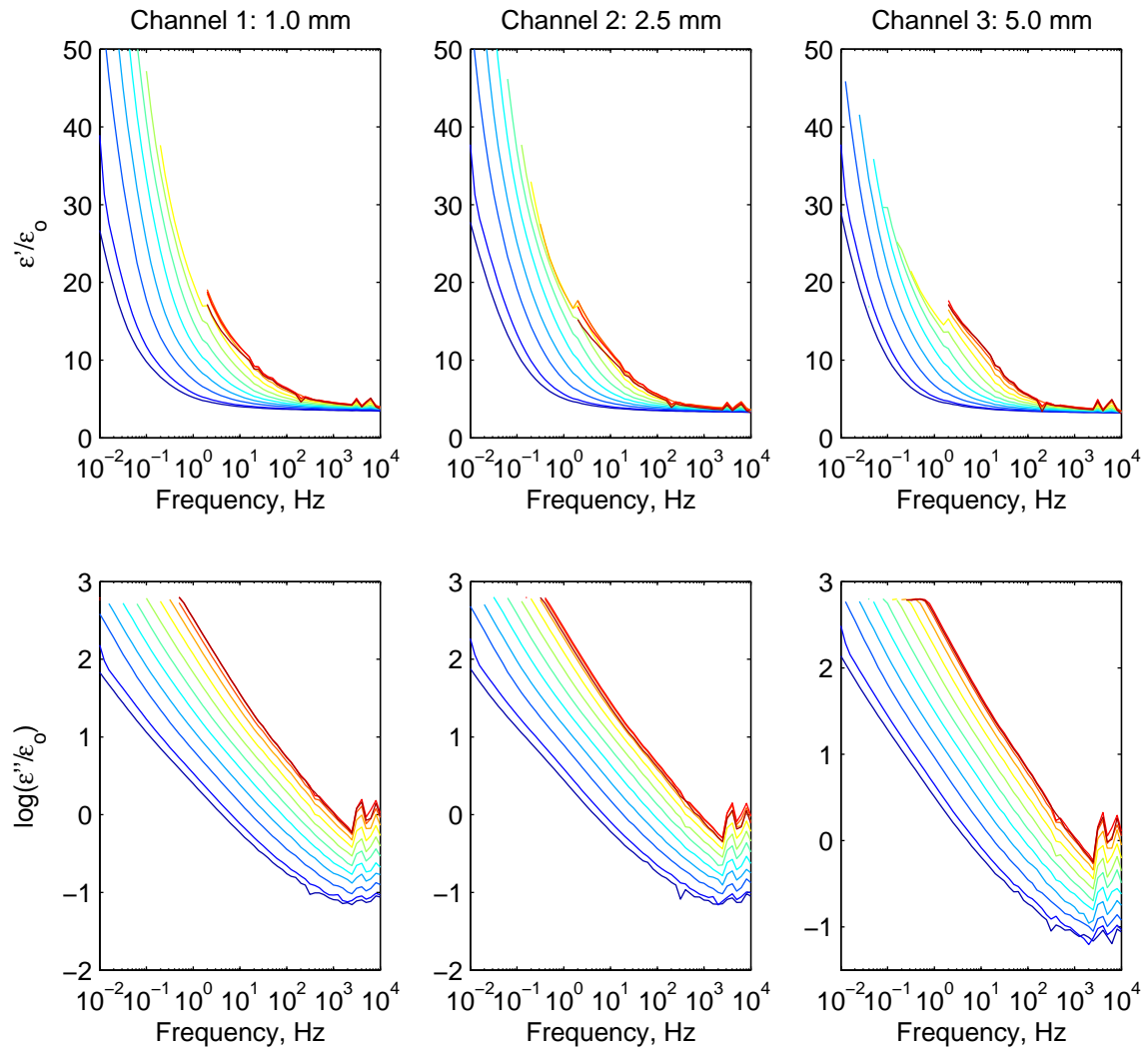


Figure 7-6: Moist birch rod effective permittivity as estimated from the steady state temperature measurements in Fig. 6-6. Temperatures vary from 70.2 °F (dark blue) to 175.8 °F (dark red). Measurements are in colors corresponding to the temperatures given in Table 6.6.

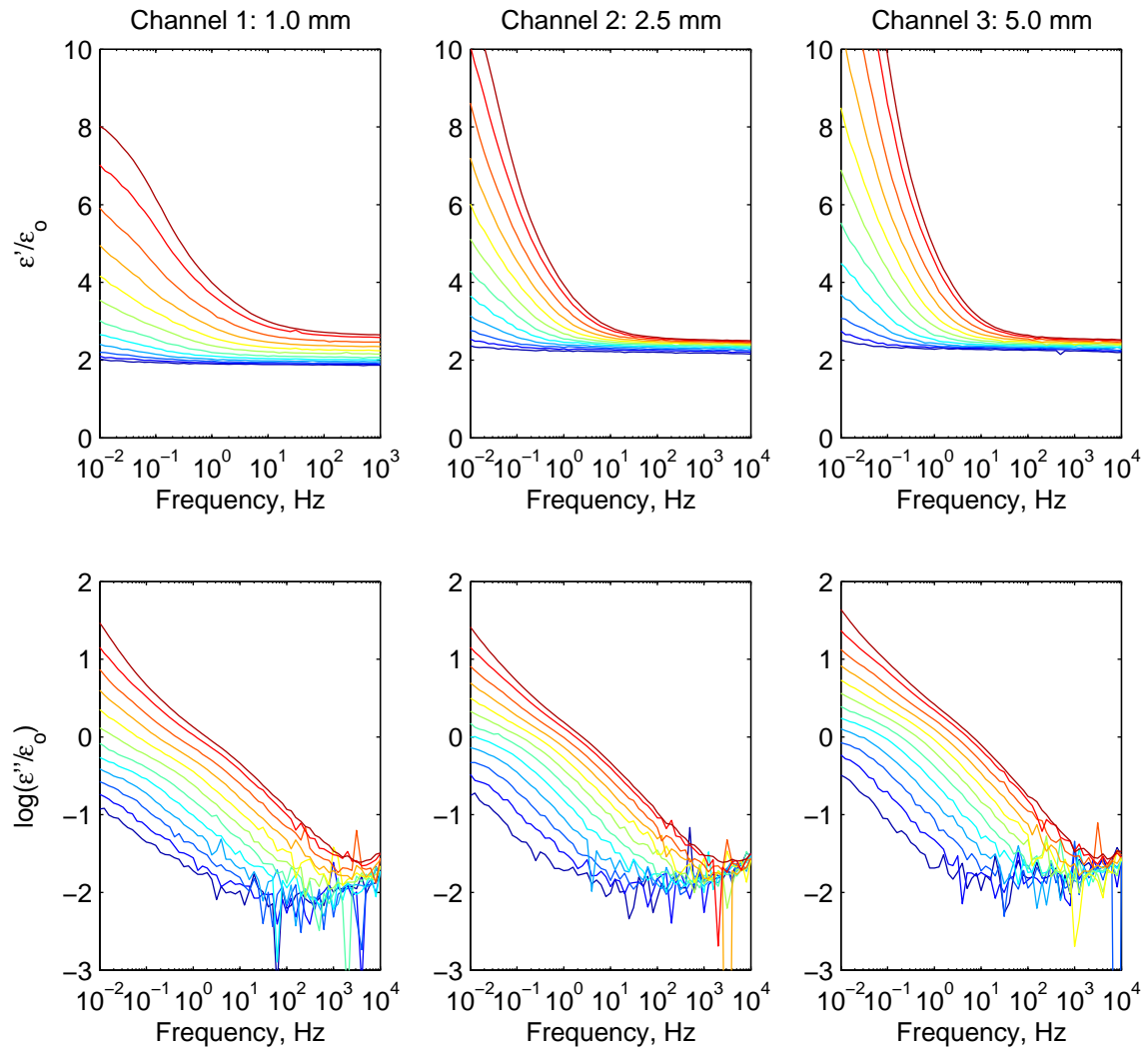


Figure 7-7: Dry birch rod effective permittivity as estimated from the steady state temperature measurements in Fig. 6-7. Temperatures vary from 76.6 °F (dark blue) to 176.1 °F (dark red). Measurements are in colors corresponding to the temperatures given in Table 6.7.

Single Conductor Cable Permittivity

The single conductor cable measurements in Section 6.3.1 are converted to effective permittivity and plotted in Figs. 7-8 and 7-9 for the moist and dry measurements respectively. In both cases increasing temperature causes a horizontal shift of the effective permittivity spectrum to higher frequency. A slight upward shift is also noticeable when comparing the high frequency relative permittivity data. Overall agreement from sensor to sensor is considerable.

The effect of drying appears to cause a shift in frequency of a little more than 2 decades. The vertical shift in relative permittivity at high frequency appears to be about 0.25 down for the dry single conductor cable.

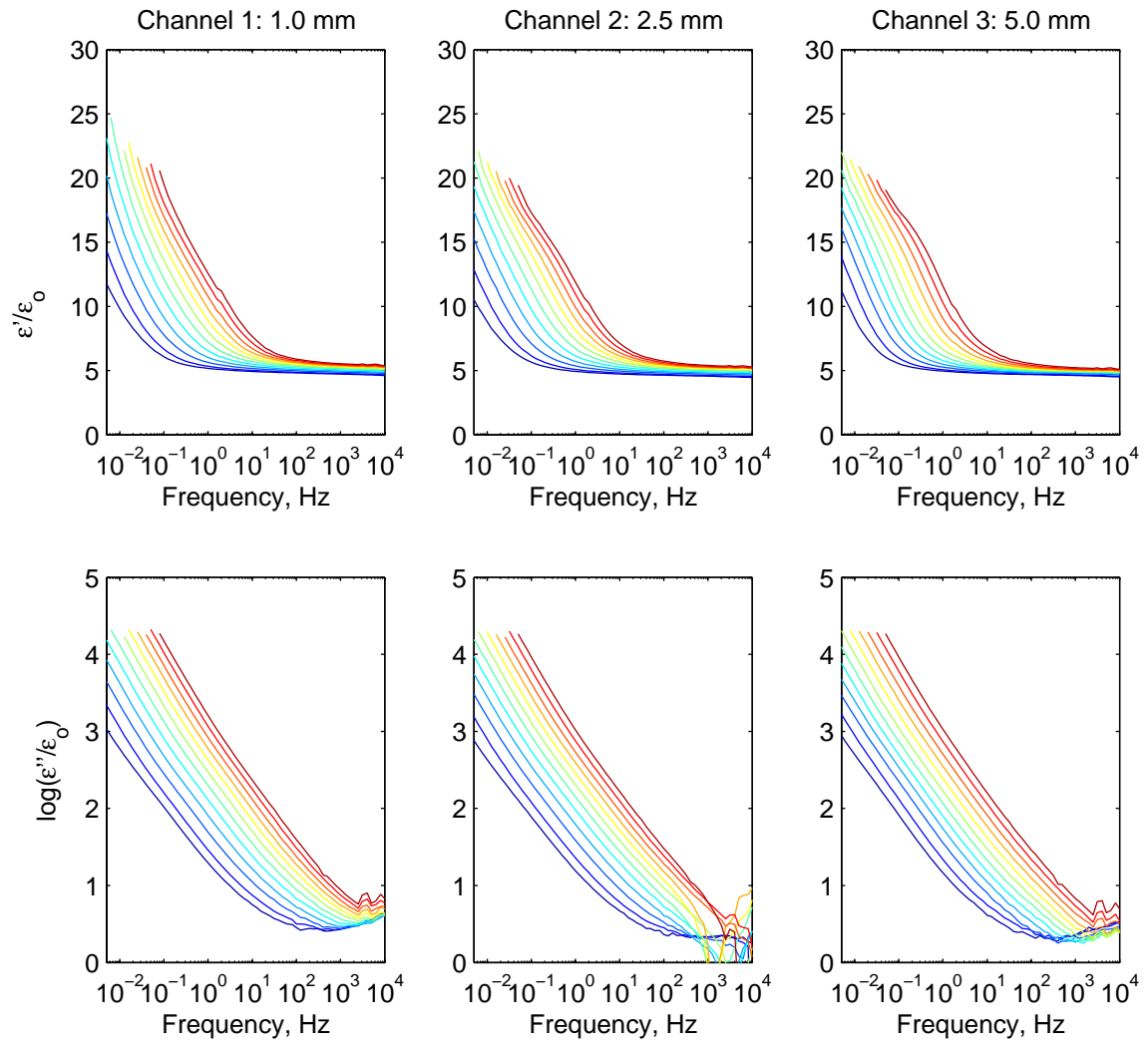


Figure 7-8: Moist single conductor cable effective permittivity as estimated from the steady state temperature measurements in Fig. 6-8. Temperatures vary from 80.6 °F (dark blue) to 185.1 °F (dark red). Measurements are in colors corresponding to the temperatures given in Table 6.8.

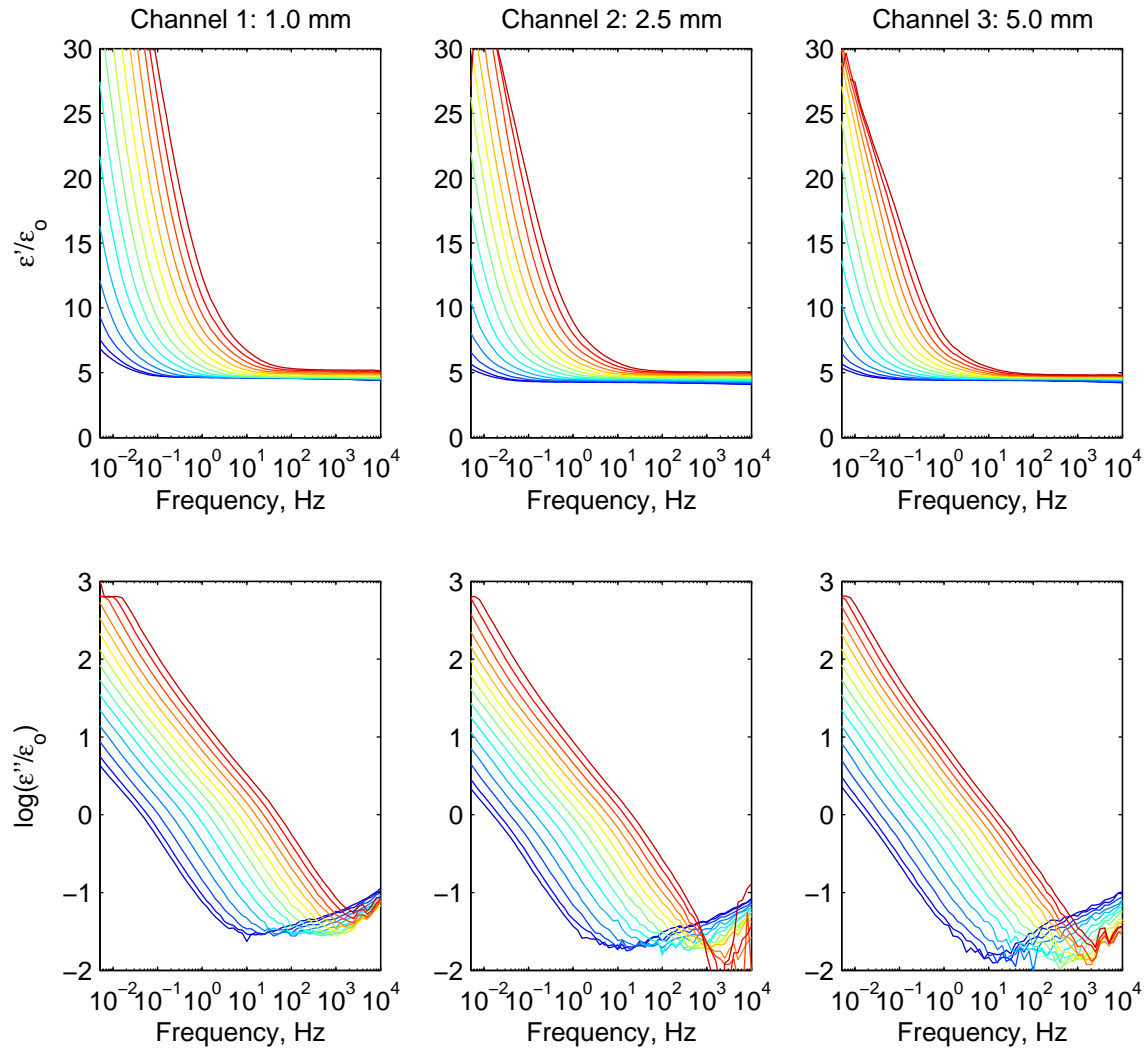


Figure 7-9: Dry single conductor cable effective permittivity as estimated from the steady state temperature measurements in Fig. 6-9. Temperatures vary from 63.8 °F (dark blue) to 194.7 °F (dark red). Measurements are in colors corresponding to the temperatures given in Table 6.9.

Three Conductor Cable Permittivity

The three conductor cable measurements in Section 6.3.2 are converted to effective permittivity and plotted in Fig. 7-10. Increasing temperature causes a horizontal shift of the effective permittivity spectrum to higher frequency. A slight upward shift is also noticeable when comparing the high frequency relative permittivity data. The effective permittivity measurements of the three conductor cable are very similar to those of the dry single conductor cable suggesting that the same paper is used for both cables. Comparing the papers visually, they appear very similar.

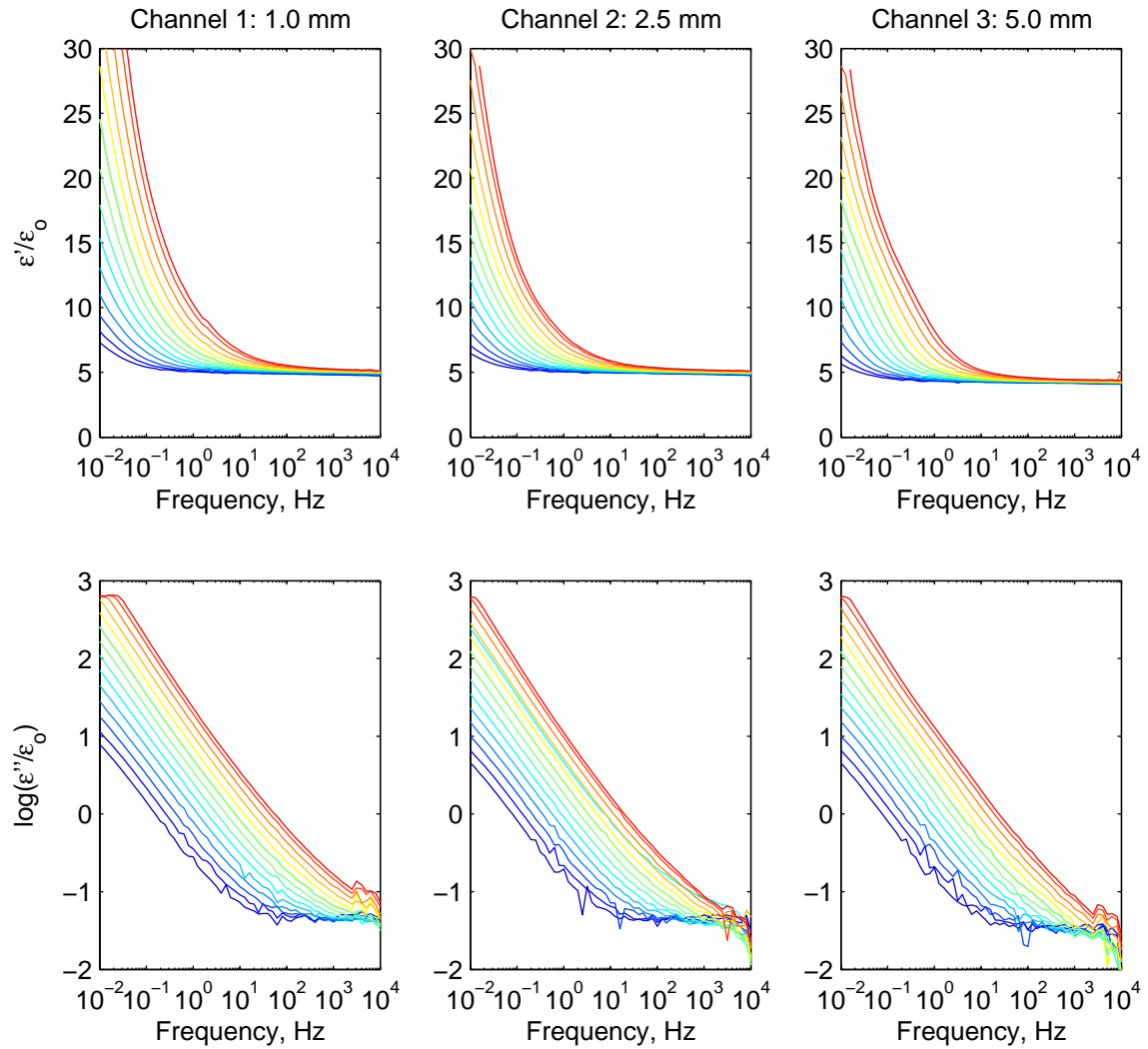


Figure 7-10: Dry three conductor cable effective permittivity as estimated from the steady state temperature measurements in Fig. 6-10. Temperatures vary from 73.5 °F (dark blue) to 193.7 °F (dark red). Measurements are in colors corresponding to the temperatures given in Table 6.10.

7.2.2 Arrhenius Temperature Dependence

The effective permittivity for acrylic, birch, and both cable types exhibit a clear temperature dependence. For an increase in temperature the effective permittivity as a function of frequency shifts linearly on a logarithmic scale. Also observed is a slight increase in the high frequency relative permittivity.

It is possible to describe these materials by a master curve, and an activation energy [5, 18, 84, 85]. The master curve characterizes the frequency dependence of the effective permittivity, and the activation energy characterizes the Arrhenius temperature dependence. The Arrhenius temperature dependence describes the frequency shift of an effective permittivity master curve according to the following relation.

$$10^{\mathcal{F}(1/T)} = e^{-\frac{E_a}{kT}} \quad (7.36)$$

In this equation $\mathcal{F}(1/T)$ is the logarithmic frequency shift, E_a is the activation energy, k is Boltzmann's constant and T is the temperature in Kelvin. The Arrhenius dependence is consistent with the requirements of the Kramers-Kronig relations [5]. If $\epsilon_m^*(f)$ describes the effective permittivity master curve as a function of frequency, for a given temperature the effective permittivity is

$$\epsilon^*(f) = \epsilon_m^*(10^{\log_{10}(f) + \mathcal{F}(1/T)}) \quad (7.37)$$

The master curve describes the effective permittivity for a convenient temperature T_o , such that $\mathcal{F}(1/T_o) = 0$ and $\epsilon^*(f) = \epsilon_m^*(f)$.

The function $\mathcal{F}(1/T)$ must be approximated from the experimental data. Using the substitution $x = 1/T$ we have $\mathcal{F}(1/T) = \mathcal{F}(x)$. If $\mathcal{F}(x)$ can be well fit by a straight line E_a is a constant and the Arrhenius temperature dependence holds.

$$\mathcal{F}(1/T) = -\frac{E_a}{k \ln 10} \frac{1}{T} \quad (7.38)$$

$$\frac{d}{dx} \mathcal{F}(x) = -\frac{d}{dx} \left(\frac{E_a}{k \ln 10} x \right) \quad (7.39)$$

$$E_a = -k \ln 10 \frac{d}{dx} \mathcal{F}(x) \quad (7.40)$$

The quality of this fit can be captured by the norm of the residuals per measurement point.

$$\sqrt{\frac{1}{N} \sum_{n=1}^N \left[\mathcal{F}(x_n) - \left(-\frac{E_a}{k \ln 10} x_n + b \right) \right]^2} \quad (7.41)$$

N is the number of measurement points. Because the offset is determined by the arbitrary choice

Table 7.1: Activation Energies for Measured Materials

Material	Wavelength	E_a eV	Quality
Acrylic Rod	1.0 mm	1.0958(246)	0.0987
	2.5 mm	1.0010(245)	0.0946
	5.0 mm	1.0542(244)	0.1067
Moist Birch Rod	1.0 mm	1.1546(325)	0.0419
	2.5 mm	1.1546(314)	0.0419
	5.0 mm	1.0802(324)	0.0265
Dry Birch Rod	1.0 mm	—	—
	2.5 mm	1.5859(201)	0.1589
	5.0 mm	1.5528(195)	0.1447
Moist Single Conductor Cable	1.0 mm	0.8970(193)	0.0654
	2.5 mm	0.8740(195)	0.0658
	5.0 mm	0.8486(197)	0.0319
Dry Single Conductor Cable	1.0 mm	0.8981(137)	0.0293
	2.5 mm	0.9083(136)	0.0320
	5.0 mm	0.8909(138)	0.0444
Three Conductor Cable	1.0 mm	0.8355(157)	0.0432
	2.5 mm	0.8194(152)	0.0328
	5.0 mm	0.8398(158)	0.0239

of the center temperature, b has no physical significance.

In this section we calculate the activation energy based on the experimental measurements of acrylic, birch, the single conductor cable, and the three conductor cable. To determine the frequency shift, the effective permittivity at each temperature is compared to the effective permittivity at the median temperature. The shift is determined by minimizing the average distance between the two. Logarithmic shifts are made at the measurement resolution of 0.1. The shifts are recorded for each temperature and sensor wavelength. The function $\mathcal{F}(1/T)$ is determined by a straight line fit to the shifts. The activation energy is then calculated from eq. 7.40. Table 7.1 gives the activation energies with standard deviations and the corresponding residual norms for each material. A similar series of temperature measurements were done by Neimanis & Eriksson on similar PILC cables. They reported activation energies of 0.95 to 1.0 eV [1].

We estimate the standard deviation of our activation energy estimates. Because the frequency measurements which were made in logarithmic steps of 0.1, the actual shift could be ± 0.1 from the reported shift. Error analysis is done by adding a uniformly distributed “noise” of width 0.2 to each shift. With the uncertainty added we reevaluate E_a . This is done a thousand or more times to quickly estimate the standard deviation. The results for the cable measurements are largely consistent with each other.

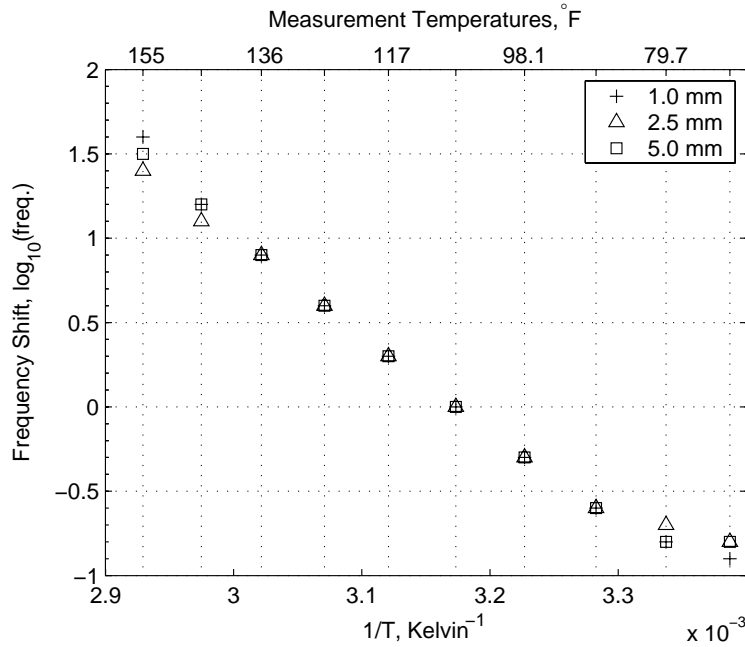


Figure 7-11: Acrylic rod logarithmic frequency shifts as a function of inverse absolute temperature. The shifts are measured relative to the measurement at 108 °F. The measurement temperatures in Fahrenheit are indicated on the top axis.

In order to estimate the master curve, the shifted permittivity plots for each frequency are averaged together to form a single measurement curve. For each experiment a master curve is estimated for the 1.0, 2.5 and 5.0 mm sensors. Ideally for a homogeneous MUT, the master curves for each sensor wavelength should be identical. For each material we present the masters curves and shifts used in calculating the activation energy.

Acrylic Rod

The acrylic rod measurements in Section 6.1.4 have enough correlation to consider the formation of a master curve. The logarithmic frequency shifts are calculated using the above algorithm and are plotted in Fig. 7-11. The values represent the shift of the master curve to return to a particular temperature. Aside from the lowest temperature measurements, the temperature shift of the effective permittivity is quite linear. The activation energies are estimated in Table 7.1.

The effective permittivity curves in Fig. 7-5 are shifted according to Fig. 7-11 and averaged together to form a single effective permittivity curve for each channel. Because the shifts in Fig. 7-11 represent the shift of the master curve, the opposite shift is needed to collapse the original measurements onto a single curve. The master curves are plotted in Fig. 7-12. Overall the shape

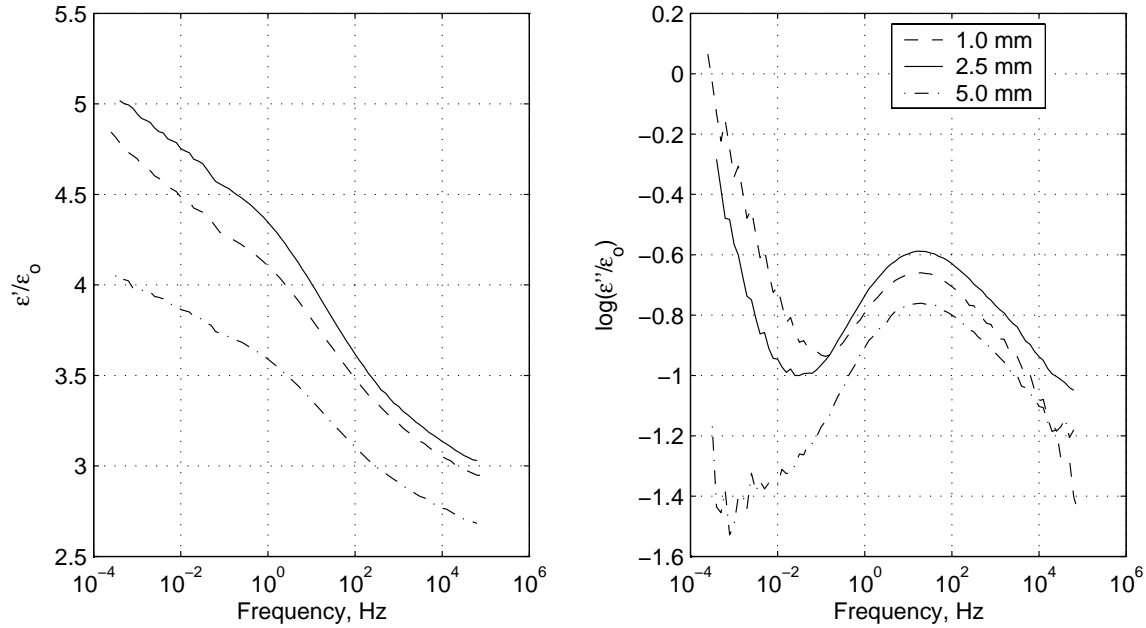


Figure 7-12: Acrylic rod master curves. The curves in Fig. 7-5 are shifted according to Fig. 7-11 (multiplied by -1) and averaged to form a single curve for each channel. The curves for each sensor wavelength are compared.

of the real part of the permittivity is quite comparable between the three channels, although there is an obvious vertical shift. This is due at least in part to disturbance factors such as the electrode thickness (see Section 5.5).

Dry Birch Rod Master Curves

The dry birch rod measured in Section 6.2.1 can be characterized reasonably well by a master curve fit. The frequency shifts for each measurement temperature are calculated using the algorithm described above. The resulting logarithmic frequency shifts are plotted in Fig. 7-13. The data is fit by a linear shifting function $\mathcal{F}(1/T)$, which is calculated based on a least squares fit. The activation energies are estimated in Table 7.1.

The shifted curves are plotted in Fig. 7-14. The effective permittivities for each of the measurement temperatures on the 2.5 and 5.0 mm sensors line up quite well. For these sensor measurements there is very little vertical shifting with temperature.

Because the 1.0 mm channel has a significant vertical shift with temperature it is not included. In principle both horizontal and vertical shifts can be accounted for by aligning the loss peaks for each measurement [86]. Unfortunately the loss peaks occur below the measurable frequency range.

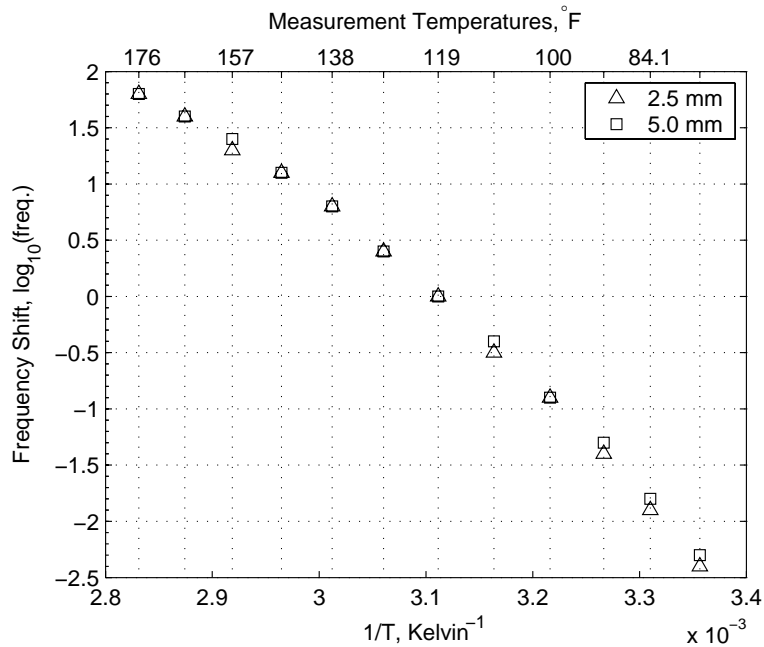


Figure 7-13: Dry birch rod logarithmic frequency shifts as a function of inverse absolute temperature. The shifts are measured relative to the measurement at 128 °F. The measurement temperatures in Fahrenheit are indicated on the top axis.

A master curve is formed by averaging the shifted curves to form a single curve. The master curves for each sensor are compared in Fig. 7-15. Overall the curves follow the same trend, but there is some disagreement as the 5.0 mm curve appears to be a slightly shifted version of the 2.5 mm curve.

There are several possible explanations for this. First the wood is not homogeneous. Each sensor is connected to a different physical location on the wood. The local dielectric properties would be different for each sensor resulting in different measurements. The temperature may not be homogeneous inside the chamber. If one sensor higher on a temperature gradient relative to another the measured conductivity will reflect this.

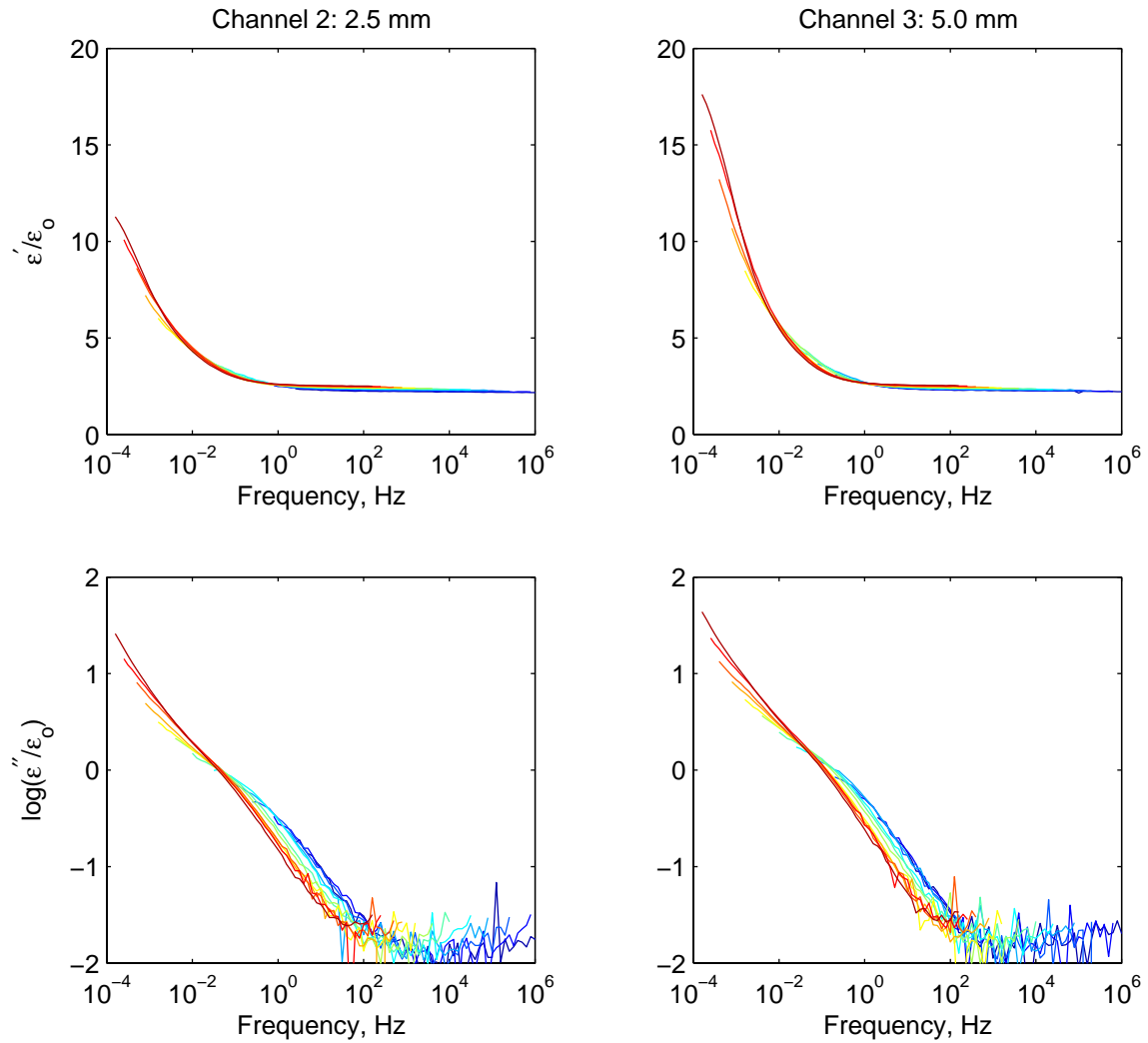


Figure 7-14: Dry birch rod shifted measurements for the formation of the master curve. Each measurement in Fig. 7-7 is shifted according to Fig. 7-13 (multiplied by -1). The quality of the alignment can be seen.

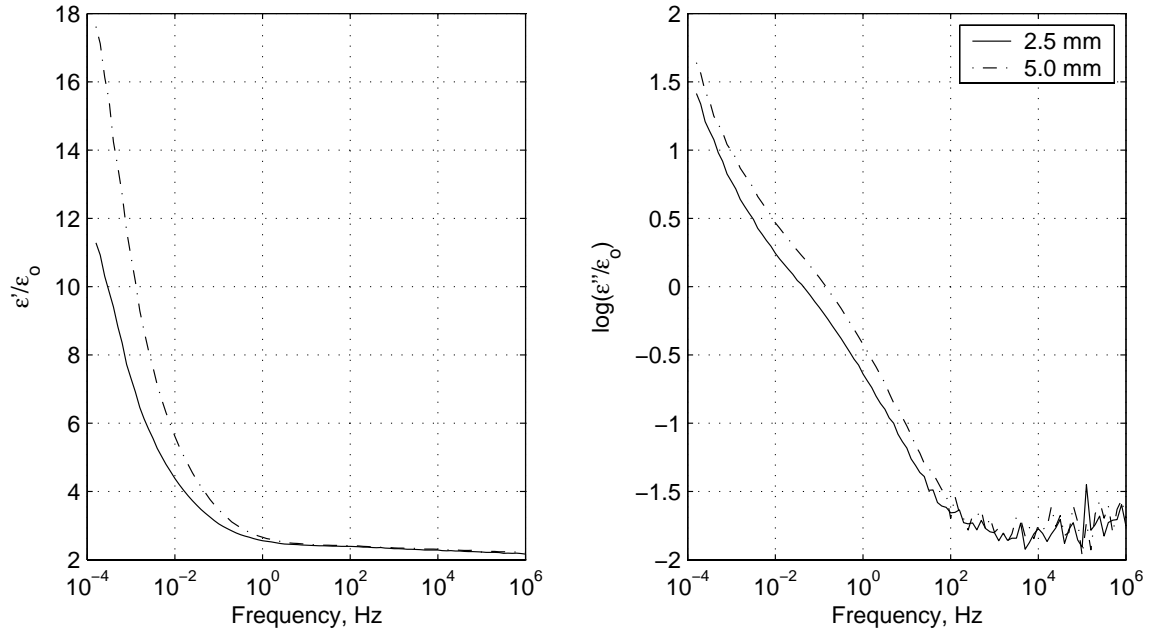


Figure 7-15: Dry birch rod master curves. The curves in Fig. 7-14 are averaged to form a single curve for each channel. The curves for each sensor wavelength are compared.

Moist Birch Rod Master Curves

The moist birch rod measured in Section 6.2.1 can be characterized very well by a master curve fit. The moist birch rod has a significantly lower activation energy than the dry birch rod. This behavior is not surprising since the shape of the permittivity curves are quite different. The logarithmic frequency shifts are plotted in Fig. 7-16. The data is fit by a linear shifting function $\mathcal{F}(1/T)$, which is calculated based on a least squares fit and the activation energies are given in Table 7.1. We have only included the measurements with temperatures up to 137 °F because the behavior is clearly non-Arrhenius for higher temperatures, as can be seen from Fig. 7-6.

The shifted permittivity curves are shown in Fig. 7-17. At high frequency the real part of the permittivity dominates, and at low frequency the imaginary part dominates. As a result there is a noticeable spread in the real permittivity at low frequency and the imaginary part at high frequency. The curves are averaged together to form a single universal curve for each channel. This is plotted in Fig. 7-18. The agreement between all three master curves is excellent for this set of measurements.

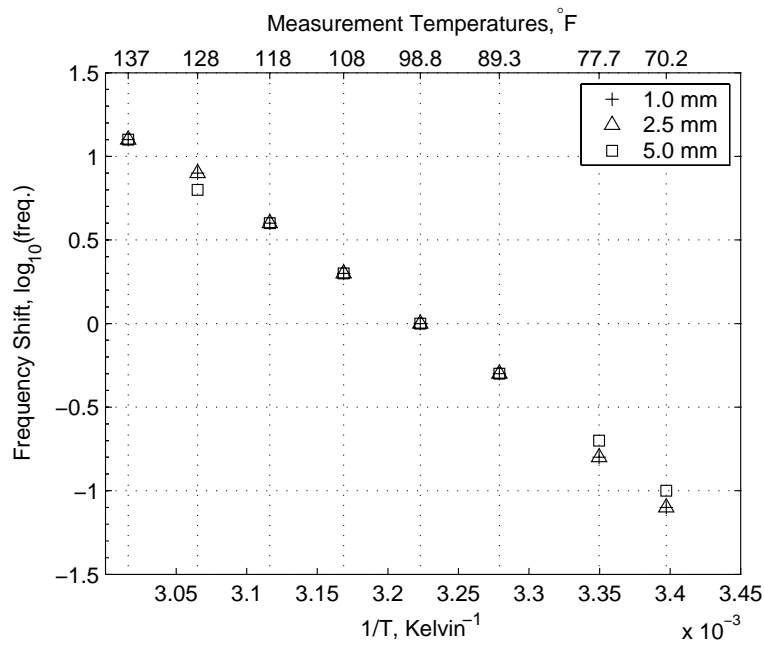


Figure 7-16: Moist birch rod logarithmic frequency shifts as a function of inverse absolute temperature. The shifts are measured relative to the measurement at 99 °F. The measurement temperatures in Fahrenheit are indicated on the top axis.

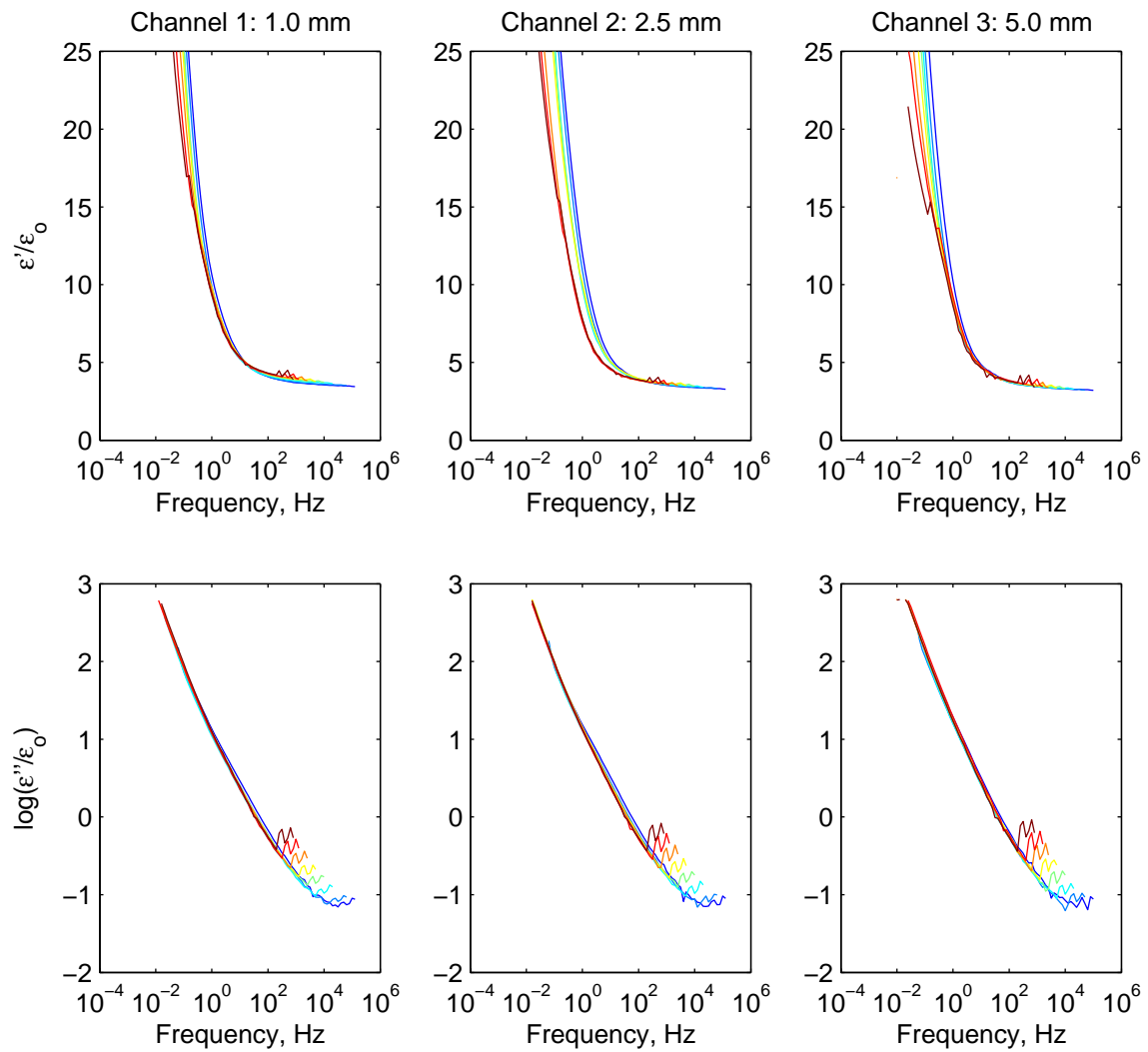


Figure 7-17: Dry birch rod shifted permittivity measurements for the formation of the master curve. Each effective permittivity measurement in Fig. 7-6 is shifted according to Fig. 7-16 (multiplied by -1). The quality of the alignment can be seen.

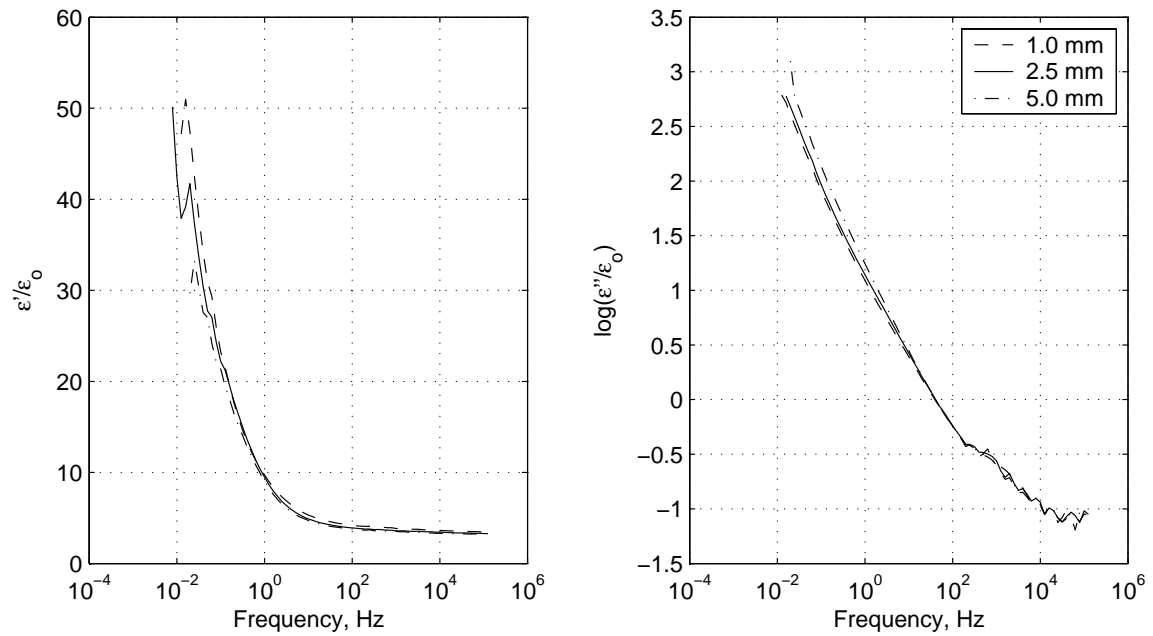


Figure 7-18: Moist birch rod master curves. The curves in Fig. 7-17 are averaged to form a single curve for each channel. The curves for each sensor wavelength are compared.

Table 7.2: Master Curve Logarithmic Frequency Shifts with Temperature for the Moist Single Conductor Cable

Wavelength	80.6 °F	89.3	99.0	108.7	118.2	127.9
1.0 mm	-1.4	-1.1	-0.8	-0.5	-0.2	0
2.5 mm	-1.4	-1	-0.7	-0.5	-0.2	0
5.0 mm	-1.2	-0.9	-0.6	-0.4	-0.2	0
Wavelength	137.5 °F	147.0	156.6	166.1	175.6	185.2
1.0 mm	0.2	0.4	0.6	0.7	0.9	1.1
2.5 mm	0.2	0.4	0.6	0.7	0.9	1.1
5.0 mm	0.2	0.4	0.6	0.8	1	1.2

Moist Single Conductor Cable Master Curves

The moist single conductor cable measured in Section 6.3.1 is described here by a master curve and activation energy. The shifts are calculated using the algorithm described above. The resulting logarithmic frequency shifts are summarized in Table 7.2 and plotted in Fig. 7-19. The shifting function $\mathcal{F}(1/T)$ is calculated based on a straight line fit to the measurements on each channel. The activation energies are estimated in Table 7.1.

The shifted curves are plotted in Fig 7-20. For all three channels the overlap between the different temperature curves is excellent. A master curve is formed by averaging the shifted curves to form a single curve for each channel. The master curves for each sensor wavelength are compared in Fig. 7-21. The agreement is substantially better than for the dry birch rod measurements and comparable to the moist birch rod measurements. The high frequency portion of the curves are in excellent agreement since the dielectric loss, $\log_{10}(\epsilon''/\epsilon_o)$, is near the noise floor. The low frequency portion is also in excellent agreement. The shapes of the three curves are in excellent agreement. Slightly different positions could be due to inhomogeneities in the MUT or small temperature differences within the chamber and MUT.

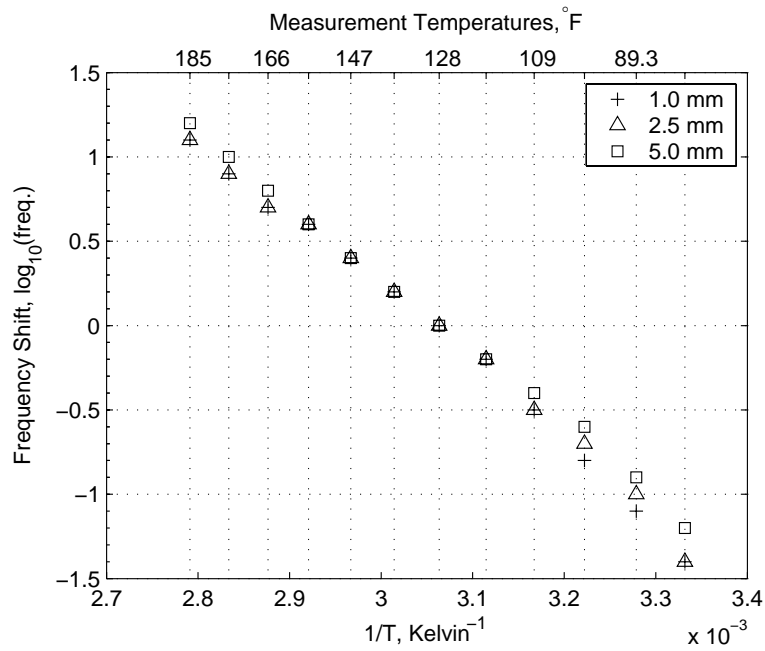


Figure 7-19: Moist single conductor cable logarithmic frequency shifts as a function of inverse absolute temperature. The shifts are measured relative to the measurement at 128 °F. The measurement temperatures in Fahrenheit are indicated on the top axis.

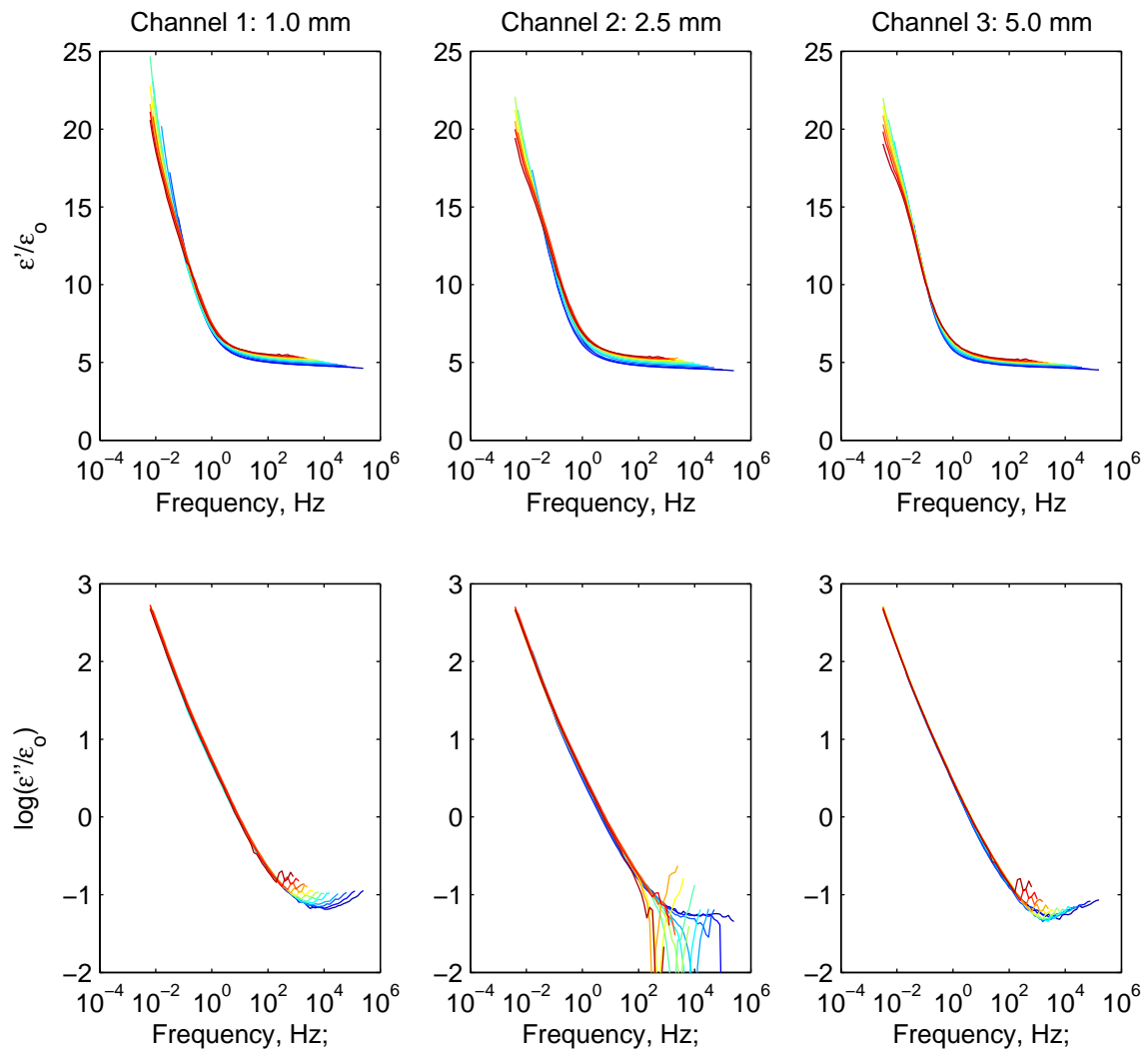


Figure 7-20: Moist single conductor cable shifted measurements for the formation of the master curve. Each effective permittivity measurement in Fig. 7-8 is shifted according to Table 7.2 (multiplied by -1). The quality of the alignment can be seen.

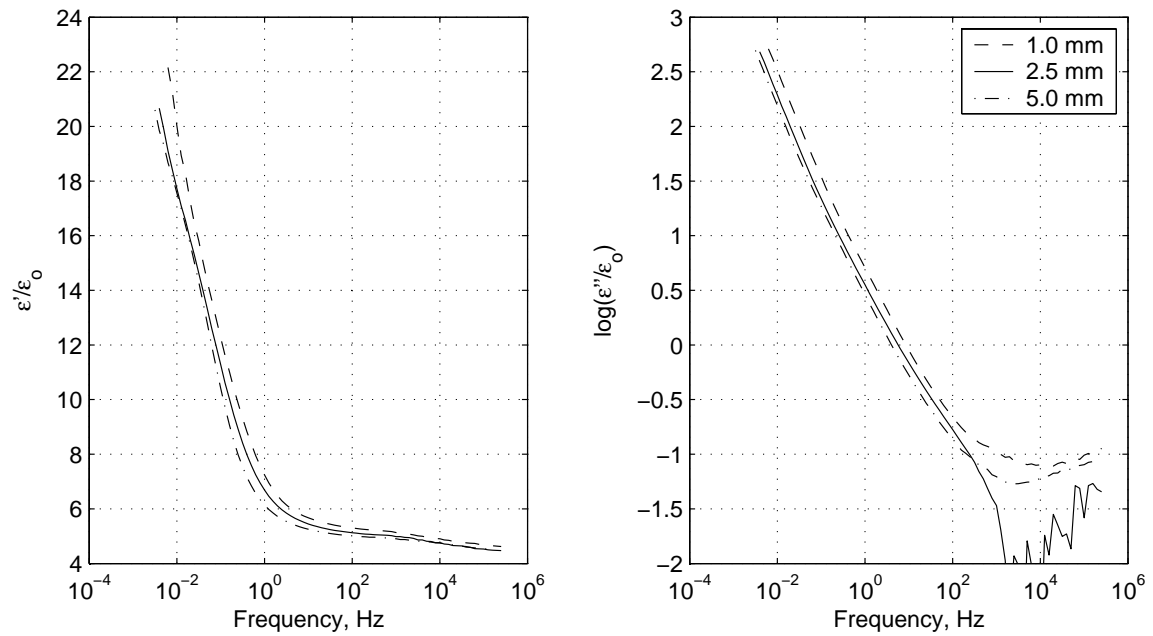


Figure 7-21: Moist single conductor cable master curves. The curves in Fig. 7-20 are averaged to form a single curve for each channel. The curves for each sensor wavelength are compared.

Table 7.3: Master Curve Logarithmic Frequency Shifts with Temperature for the Dry Single Conductor Cable

Wavelength	63.8 °F	70.0	79.8	89.4	99.0	108.7	118.3	
1.0 mm	-1.7	-1.6	-1.3	-1	-0.7	-0.5	-0.2	
2.5 mm	-1.8	-1.6	-1.3	-1	-0.7	-0.5	-0.2	
5.0 mm	-1.8	-1.6	-1.3	-1	-0.7	-0.5	-0.2	
Wavelength	127.9 °F	137.5	147.1	156.8	166.3	175.7	185.3	194.7
1.0 mm	0	0.2	0.4	0.6	0.8	1	1.2	1.4
2.5 mm	0	0.2	0.4	0.6	0.8	1	1.2	1.4
5.0 mm	0	0.2	0.4	0.6	0.8	1	1.1	1.3

Dry Single Conductor Cable Master Curves

The dry single conductor cable measured in Section 6.3.1 is described here by a master curve and activation energy. The shifts are calculated using the algorithm described above. The resulting frequency shifts are summarized in Table 7.3 and plotted in Fig. 7-22. The shifting function $\mathcal{F}(1/T)$ is calculated based on a straight line fit to the measurements on each channel. The activation energies are estimated in Table 7.1. The activation energies are slightly higher for the dry cable than the moist single conductor cable.

The shifted curves are plotted in Fig 7-23. For all three channels the overlap between the different temperature curves is excellent. A master curve is formed by averaging the shifted curves to form a single curve for each channel. The master curves for each sensor wavelength are compared in Fig. 7-24. The agreement is excellent between the 2.5 and 5.0 mm sensor channels. The 1.0 mm sensor appears to suggest a slightly more lossy material. Slightly different conductivities could be explained by inhomogeneities in the MUT or temperature gradients within the chamber and MUT. The high frequency portion of the curves are in excellent agreement.

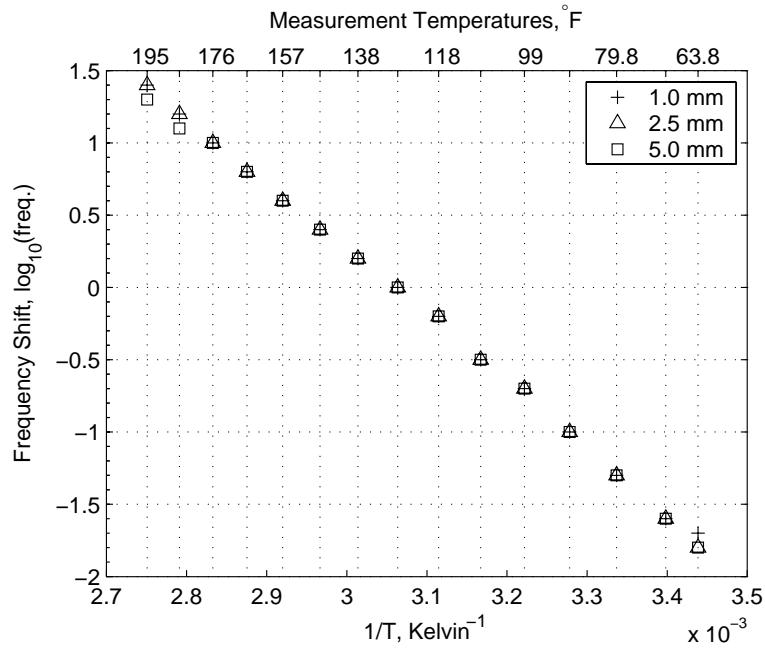


Figure 7-22: Dry single conductor cable logarithmic frequency shifts as a function of inverse absolute temperature. The shifts are measured relative to the measurement at 128 °F. The measurement temperatures in Fahrenheit are indicated on the top axis.

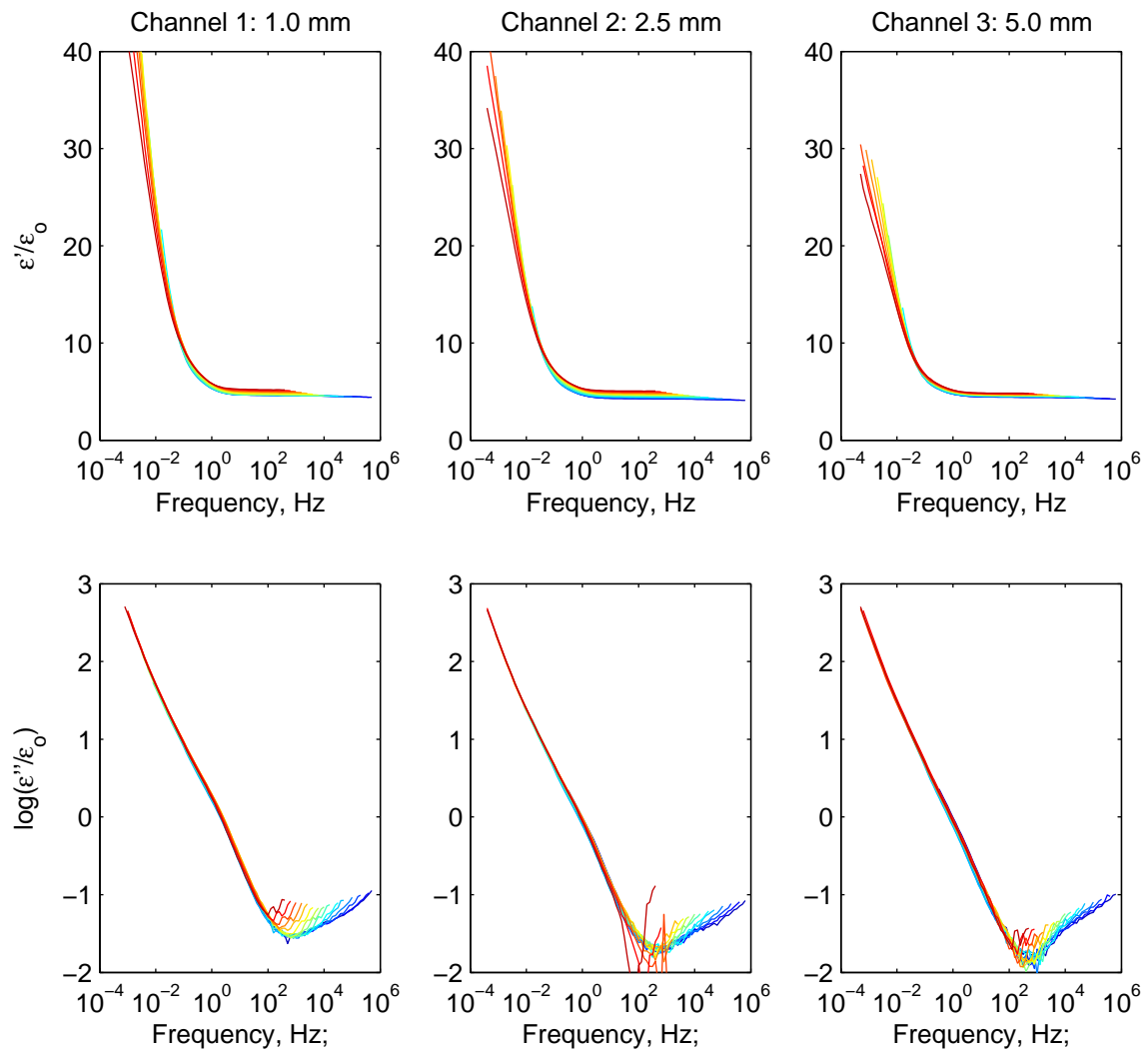


Figure 7-23: Dry single conductor cable shifted measurements for the formation of the master curve. Each effective permittivity measurement in Fig. 7-9 is shifted according to Table 7.3 (multiplied by -1). The quality of the alignment can be seen.

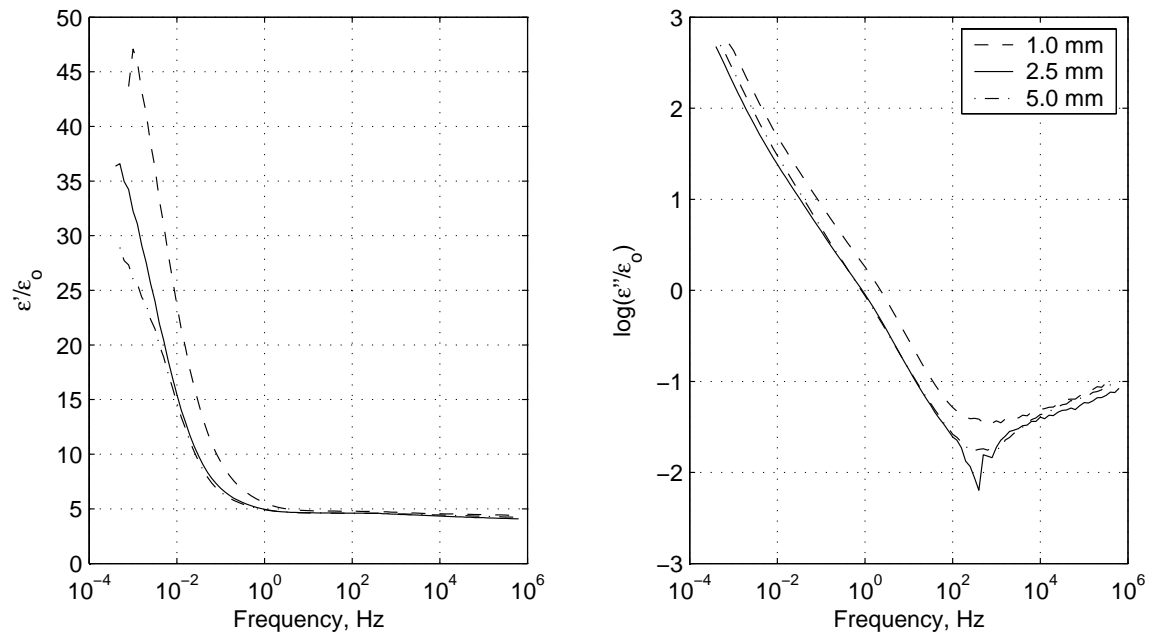


Figure 7-24: Dry single conductor cable master curves. The curves in Fig. 7-23 are averaged to form a single curve for each channel. The curves for each sensor wavelength are compared.

Table 7.4: Master Curve Logarithmic Frequency Shifts with Temperature for the Three Conductor Cable

Wavelength	73.48 °F	79.84	89.33	98.93	108.5	118	127.5
1.0 mm	-1.4	-1.1	-0.9	-0.7	-0.5	-0.2	0
2.5 mm	-1.3	-1.1	-0.9	-0.7	-0.4	-0.2	0
5.0 mm	-1.3	-1.1	-0.9	-0.7	-0.4	-0.2	0
Wavelength	137.1°F	146.6	156.1	165.5	175	184.4	193.7
1.0 mm	0.2	0.4	0.6	0.8	1	1.1	1.2
2.5 mm	0.2	0.4	0.6	0.8	1	1.1	1.2
5.0 mm	0.2	0.4	0.6	0.8	1	1.2	1.3

Three Conductor Cable Master Curves

The three conductor cable measured in Section 6.3.2 is now described by a master curve and activation energy. The frequency shifts are summarized in Table 7.4 and plotted in Fig. 7-25. The shifting function $\mathcal{F}(1/T)$ is calculated based on a straight line fit to the measurements on each channel. The activation energies are estimated in Table 7.1.

The shifted curves are plotted in Fig 7-23. For all three channels the overlap between the different temperature curves is excellent. A master curve is formed by averaging the shifted curves to form a single curve for each channel. The master curves for each sensor are compared in Fig. 7-24. The master curves for the 2.5 and 5.0 mm sensor channels are in excellent agreement for low frequency, while the 1.0 and 2.5 mm channels are in excellent agreement for high frequency. The 1.0 mm sensor appears to suggest a slightly more lossy material. Slightly different conductivities could again be explained by inhomogeneities in the MUT or temperature gradients within the chamber and MUT. The high frequency portion of the curves are in excellent agreement.

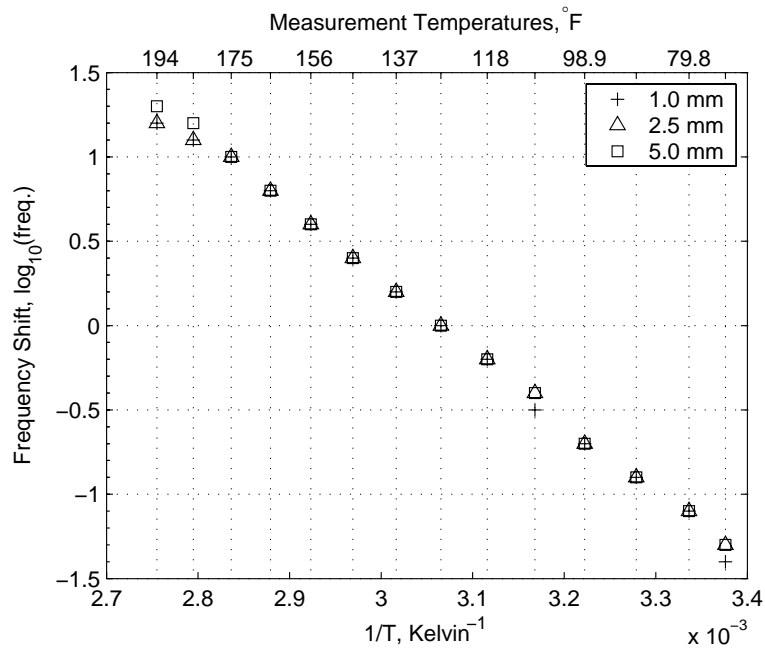


Figure 7-25: Three conductor cable logarithmic frequency shifts as a function of inverse absolute temperature. The shifts are measured relative to the measurement at 128 °F. The measurement temperatures in Fahrenheit are indicated on the top axis.

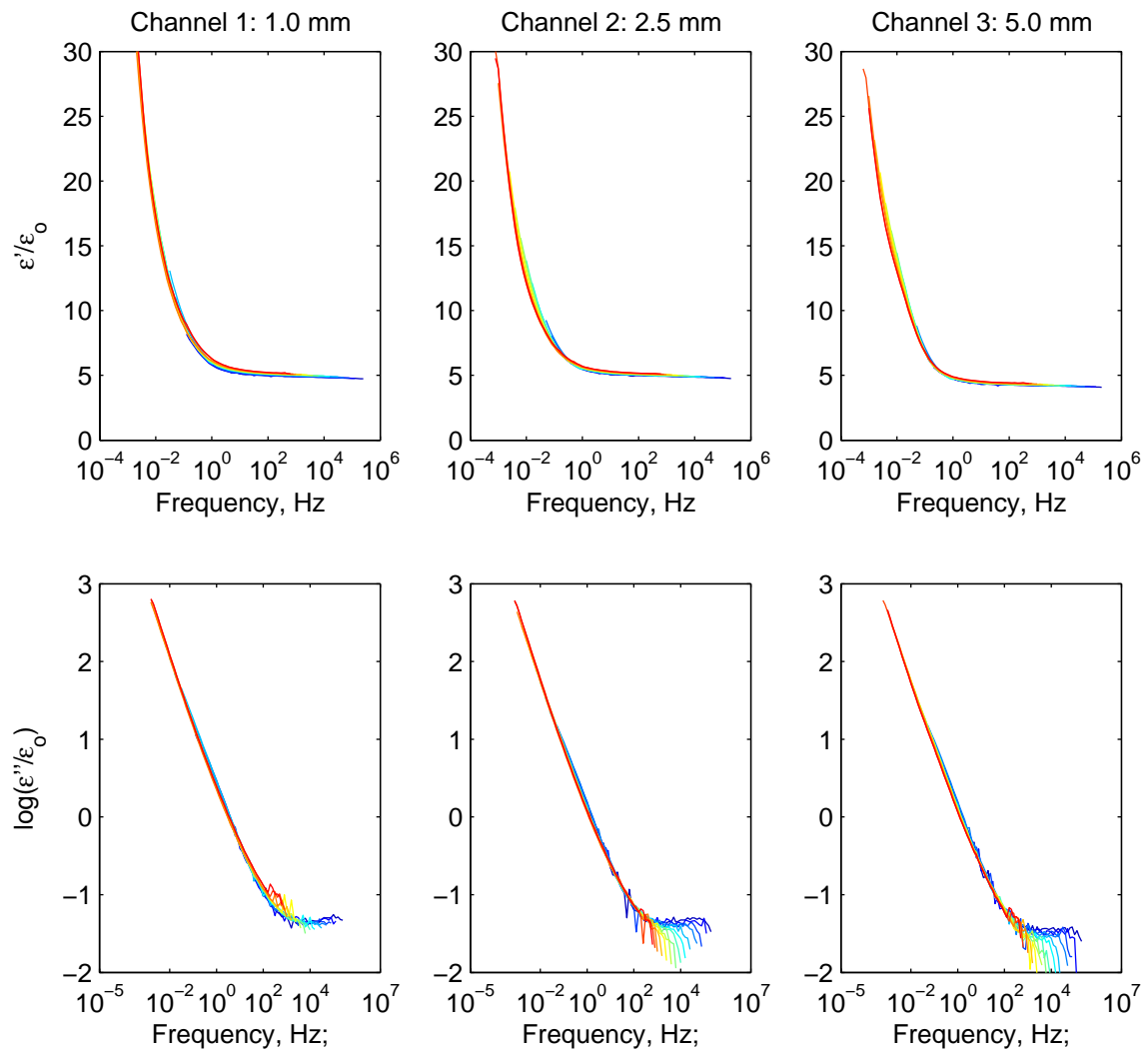


Figure 7-26: Three conductor cable shifted measurements for the formation of the master curve. Each effective permittivity measurement in Fig. 7-10 is shifted according to Table 7.4 (multiplied by -1). The quality of the alignment can be seen.

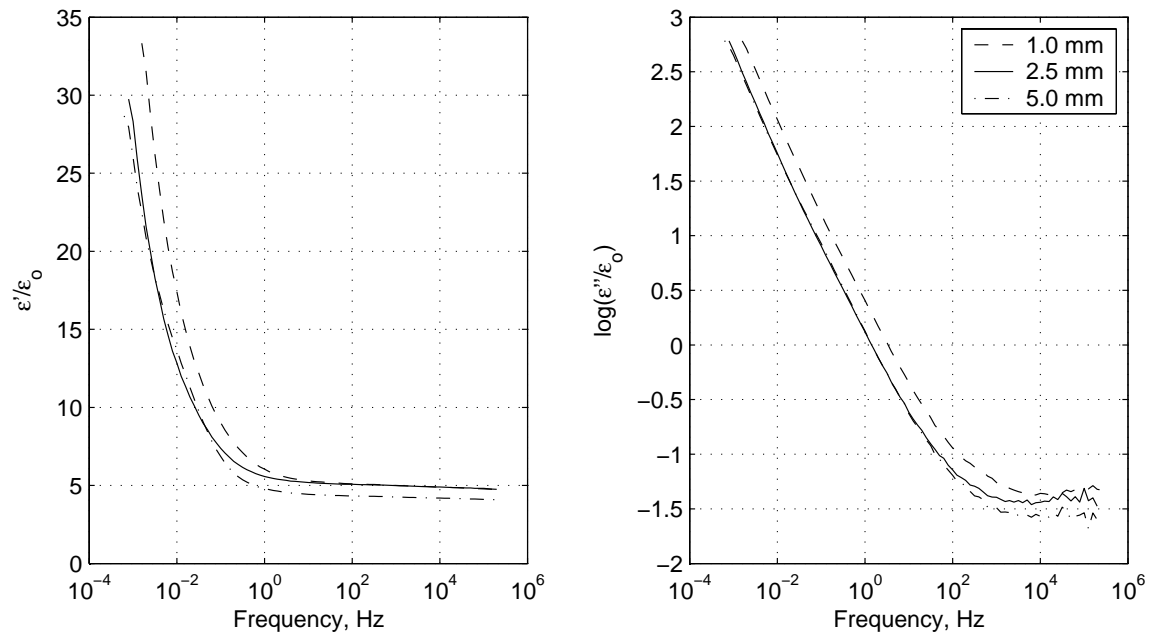


Figure 7-27: Three conductor cable master curves. The curves in Fig. 7-26 are averaged to form a single curve for each channel. The curves for each sensor wavelength are compared.

7.3 Dependence on Moisture

It is clear from the measurements presented thus far that the electrical properties of hydrophilic materials have a significant dependence on the amount of moisture present in the sample. In order to measure the electrical properties of moist materials, samples must be appropriately humidified. The moisture content must then be measured, and finally a capacitive measurement must be made on the sample. The transients associated with moisture diffusion complicate matters because samples must be left in a stable environment long enough to reach a uniform moisture content. Further, during each part of the measuring process the sample must not be allowed to absorb or desorb moisture. In order to find a moisture dependence on the electrical properties, a significant number of samples at different moisture content levels is necessary.

The scope of such an undertaking prevents us from performing our own set of moisture content measurements, however, significant work has been done which may be applied to our own research. Here we present some of the results reported in the literature for use in our own research efforts and perform additional analysis.

Preparing samples for measurement requires achieving a number of different moisture contents in the paper. One technique which has demonstrated reproducible results is to place the paper samples in desiccators with different saturated salt solutions. The salt solutions limit the relative humidity of the air to a specific value [87]. Each different type of salt solution results in a different relative humidity of the air. The amount of water absorbed by the paper is proportional to the relative humidity of the air. Over time, the paper samples reach equilibrium with the moist air. The relationship between the relative humidity of the air and moisture content in the paper is the subject of Section 9.2.1.

Determining the moisture content in the paper samples is often done by coulometric Karl Fischer titrimetry [88, 89]. This is a chemical reaction in which iodine reacts with the water content of the sample. One of the products of the reaction is free charge. The utility of the reaction is that the free charge which can be collected and measured, is directly proportional to the amount of water in the sample. The relationship is 1 mg H₂O yields 10.71 Coulombs [90].

Sheiretov & Zahn conduct parallel plate dielectrometry measurements of oil impregnated pressboard with moisture contents of 1% and 3% (moisture/dry weight) for several temperatures [91, 92]. For the 1% moisture contents a master curve is formed. For the 3% moisture content measurements a different kind of behavior is observed with distinct loss peaks. A similar series of measurements were conducted on paper and pressboard by Ekanayake et al. [93].

Recent work has been done on similar PILC cables by Neimanis & Eriksson [1] to report the

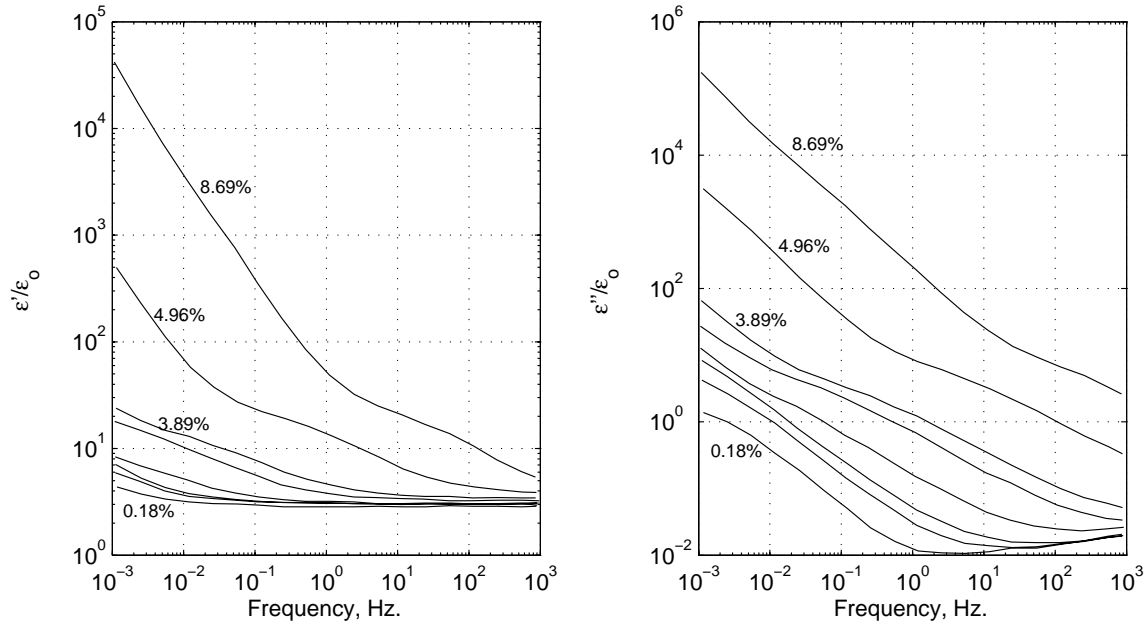


Figure 7-28: Redrawn ϵ' and ϵ'' curves from [1]. Curves from bottom to top represent moisture levels of 0.18%, 1.76%, 2.05%, 2.95%, 3.50%, 3.89%, 4.96%, and 8.69%.

dielectric properties of cable insulation for various moisture levels. The work provides effective permittivity measurements of PILC cable insulation at eight different moisture content levels. Many of the results in [1] had been previously published by Neimanis et al. in [27]. The experimental results presented in this paper have been redrawn in Fig. 7-28 which shows the permittivity as a function of frequency for each moisture content.

Neimanis & Eriksson [1] do not report the temperature at which these measurements were made at, although they are cognisant of the general temperature dependence of paper-oil insulation and therefore it is safe to assume they were all conducted at the same temperature. Further, by comparison to our own results and other portions of [1] we surmise that the measurements were probably done at 20 °C (68 °F). We notice for the lowest moisture content measured the relative permittivity is constant until the 10^{-3} to 10^{-2} decade. This relative low dispersion is seen in our own results for the lowest measured temperature of 73 °F for the three conductor cable where the relative permittivity only increases in the 10^{-2} to 10^{-1} decade. This slight difference could indicate the slightly lower measurement temperature, some trace moisture in our own cable measurements, or is simply due to differences in the insulations.

The high frequency relative permittivity measurements, ranging from 2.9 to 3.6, are lower than our own (about 4.08 to 4.75 for the three conductor cable). By their own admission the results are

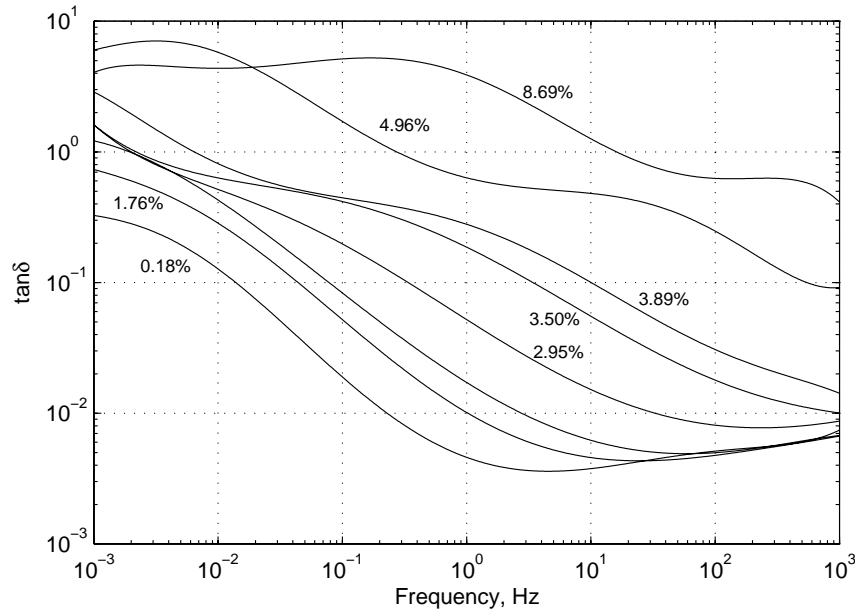


Figure 7-29: Loss tangent calculated from Neimanis & Eriksson data in Fig. 7-28 [1].

low and may be due to the loss of oil, or sample roughness, preventing good contact between the electrodes and sample. Other sources put the relative permittivity between 3.6 and 3.8 [94,95].

From the effective permittivity data the loss tangent can be easily calculated. The loss tangent, shown in Fig. 7-29, are in good agreement with Neimanis' own plot indicating an accurate redrawing of the original data.

A master curve can be formed in a similar way as was done for variations in temperature from the permittivity data in Fig. 7-28. The resulting curve is shown in Fig. 7-30. The frequency shifts used in forming this curve are plotted in Fig. 7-31. The logarithm of the frequency shift, appears to have a linear dependence on the moisture content. The least squares fit line is drawn and has a slope of 0.8257 decades per percent moisture content. This relationship between moisture content and spectral shift has been noted in terms of the shift of the loss peaks by others [86,96]. Sheiretov & Zahn have fit their frequency shift data in [18] (Figure 11) with the functional form $A + \log_{10}(m)$, where A is a constant and m is the percent moisture content, however, the choice is for mathematical convenience. In the least square sense a straight line gives a better fit to their data.

Neimanis & Eriksson [1] find that the minimum value of the loss tangent is related to the moisture content by the functional form

$$m = A + B \min(\tan \delta) \quad (7.42)$$

This form appears to fit reasonably well to the minimum loss tangent data from Fig. 7-29 with

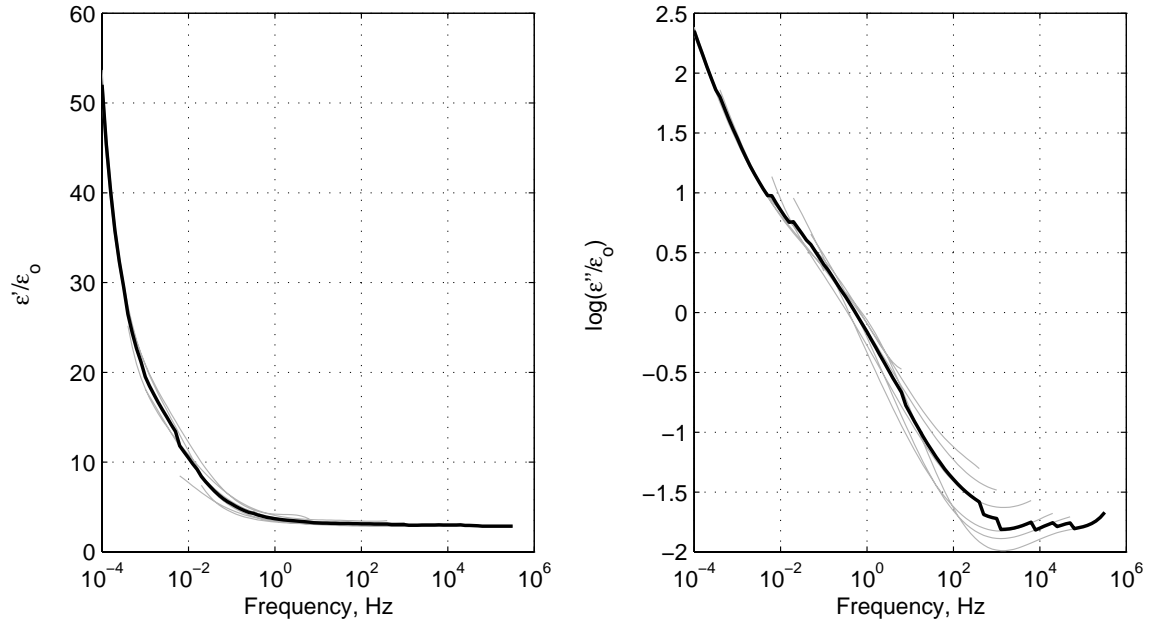


Figure 7-30: Master curves for the effective permittivity data in Fig. 7-28 centered about the 3.50% curve. The solid line shows the averages of all the curves while the shifted curves are shown in light gray.

moisture contents below 3.5%. Several redundant sample measurements are used in their own fit. Research efforts by Bucholz et al. have found no relationship between loss tangent minimums and Karl Fischer titration moisture content measurements [15].

For the purposes of our investigation we assume that the effect of moisture content is a logarithmic frequency shift as illustrated in Fig. 7-31. This permits us to observe a moisture diffusion process and predict the sensor response.

7.4 Dependence of Dielectric Properties on Cable Age

No extensive study has been done regarding the effect of aging on the dielectric properties. It is rare that a research group has had access to comparable samples of different ages. Thärning et al. took loss tangent measurements of XLPE cables that were field aged and artificially aged [97]. The general trend was that aging increased the loss tangent. Neimanis & Eriksson made loss tangent measurements of 20 and 50 year old PILC cables of slightly different designs in 1998 and again 2000 [1]. The shape of the loss tangent measurements (taken from 0.001 to 100+ Hz) is similar, but the older cable is about one decade higher in frequency. Slight differences between the 1998 and 2000 measurements are attributed to a slight difference in measurement temperature, 16 and 18 °C

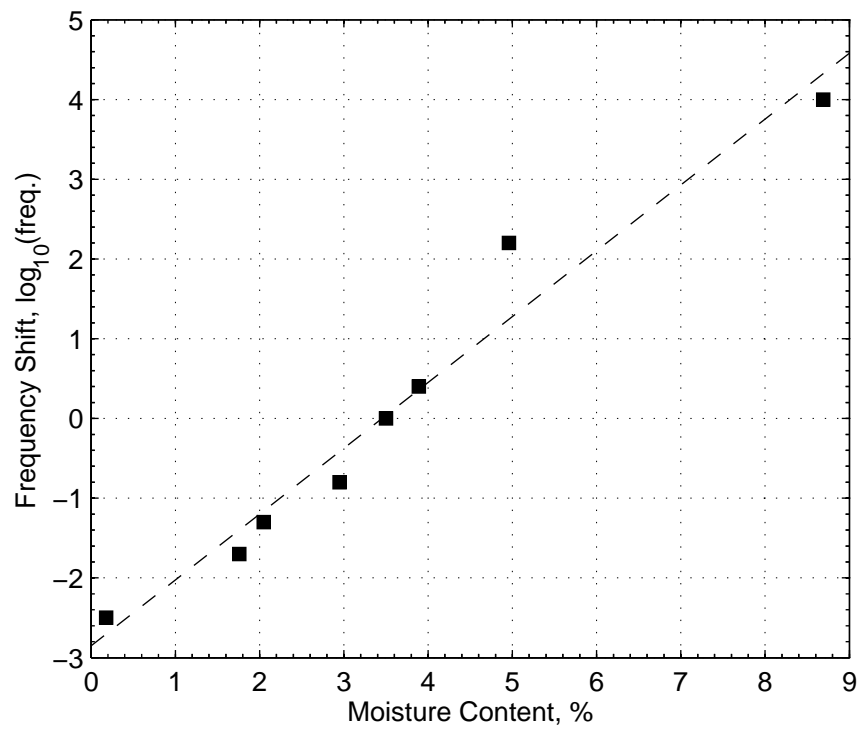


Figure 7-31: Frequency shifts associated with each moisture content for the formation of the master curves in Fig. 7-30. The best fit line having the slope 0.8257 decades per percent moisture content, is drawn.

respectively.

7.5 Chapter Summary

In this chapter we began by providing a thorough description of what is meant by each of the various terms used to describe the dielectric properties of a material. Minor inconsistencies in the terminology used by the literature have been addressed and brought to light.

The experimental measurements in Chapter 6 have been analyzed and the dielectric properties estimated (Section 7.2). For those materials exhibiting strong variations with temperature, the Arrhenius temperature dependence has been used to characterize the response. These materials are described by a master (or universal) curve and an activation energy. Knowing just the master curve, activation energy, and reference temperature, the material properties can be estimated over a large frequency and temperature range.

The dependence of the dielectric properties on moisture content is discussed in Section 7.3. Using the experimental results from Neimanis & Eriksson [1] we show the effect of moisture can be reasonably characterized by a frequency shift of the dielectric properties.

Chapter 8

Transient Measurements

In this chapter we present the results from a series of moisture diffusion experiments using a variety of material samples. The measurements are taken using either the three wavelength sensor (Section 4.2.3) in a ϕ periodic configuration, or the six channel sensor (Section 4.2.4) in a z periodic configuration. With each sensor we conduct measurements on plastics woods and the provided cable samples. The experimental procedure is described in Section 5.1.2.

8.1 Transient Measurements Using ϕ Periodic Sensors

Implementation of the ϕ periodic sensor is significantly easier than using a z periodic sensor because the electrical connections can easily be made at the end of the cable, and a simple clamping mechanism can be used to secure the sensor. Here we present measurements made on a Teflon rod, birch wood, and the single and three conductor cables.

The Teflon measurements as compared to the other material measurements clearly demonstrates a hydrophobic material, as it absorbs a negligible amount of moisture. The wood and cables all absorb a significant amount of moisture and the dielectric properties show a dramatic change due to its presence.

Measurements are taken at constant temperature and are initiated when moisture is introduced into a dry chamber. The experiment proceeds until a new steady state is reached. In many experiments the chamber is evacuated by a vacuum pump and the measurements return to the initial state.

8.1.1 ϕ Periodic Teflon Rod Transient Measurements

Teflon is a hydrophobic material which contributes to its selection as our substrate material. The introduction of moisture into the ambient environment should not effect the sensor response if only the Teflon rod is being measured. The experiment consists of placing a 1 inch diameter Teflon rod in a temperature and humidity controlled environment as described in Section 5.1.2. The hose clamping technique is used to keep the sensor in contact with the Teflon rod, and limits the exposed surface of the Teflon to both ends of the rod. A photograph of the clamping mechanism setup is shown in Fig. 5-4.

Dielectrometry measurements are made using the sensing hardware in three groups of measurements. Measurements are taken from high to low frequency in logarithmic steps of 0.1 (*i.e.* 10^0 , $10^{0.1}$, $10^{0.2}$...). The frequency ranges are 10^0 to 10^4 Hz and at 10^{-1} , and 10^{-2} Hz. A total of 43 frequency measurements are made on each channel before repeating. The reduced sweep is designed to provide a broad spectrum of measurements with a small enough time between sequential measurements at the same frequency to capture the transient details. A full frequency sweep from 10^4 to $10^{-2.3}$, takes about an hour to an hour and a half, while the abbreviated sweep performed here averaged 12:40 on Teflon (min = 10:41, max = 32:21, SD = 4:14).

Prior to time zero, The chamber is first evacuated and allowed to reach an equilibrium temperature of 166 °F. At time zero 1.0 mL of water at room temperature is deposited into the chamber, which is then sealed. The response is measured for several days.

During the course of the experiment the temperature and relative humidity are measured and recorded. This record is shown in Fig. 8-1. We see that the temperature is quite stable throughout the measurement, however, the humidity falls over the course of the week. This is due primarily to condensation in the side ports of the large chamber. These “appendages” to the chamber become cold spots where the moisture can condense.

To present the gain and phase measurements in a useful and meaningful way, two approaches are used. In the first, shown in Fig. 8-2, the measurements are shown as a function of time for the representative measurement frequencies of 0.01, 0.1, 1, 100, and 10,000 Hz (10^{-2} , 10^{-1} , 10^0 , 10^2 , 10^4 Hz). The second approach is to view the entire spectrum of measurements the measurements at fixed times as in Fig. 8-3.

Overall the results are in excellent agreement with the constant temperature measurements on Teflon presented in Section 6.1.1. The 2.5 and 5.0 mm sensors show practically no change during the entire experiment. The lowest frequency measurement has a slightly greater phase measurement than seen previously on Teflon.

The 1.0 mm sensor which we have acknowledged to be the least reliable due to its hypersensitivity

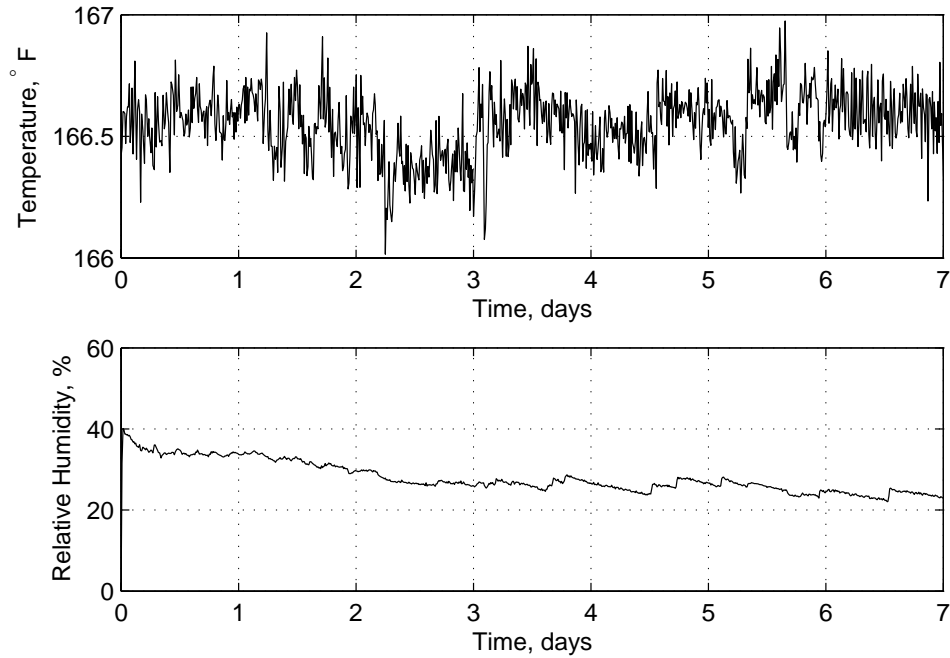


Figure 8-1: Teflon rod ϕ periodic sensor diffusion experiment temperature and relative humidity log.

to contaminants, show significantly more loss than the others. With a perfectly clean sensor and Teflon rod, the conductivity should be undetectable in this measurement range.

The plot of the entire spectrum at selected times give a better idea of the stability of the measurement. Each color represents a particular measurement time following the *jet* color sequence described in Section 6.1.1. Aside from the measurements at 0.01 and 0.1 Hz there is very little variation during the measurement.

The data in Fig. 8-2 has been evaluated by the inverse solver to determine the effective permittivity which has been plotted in appendix B, Fig. B-17.

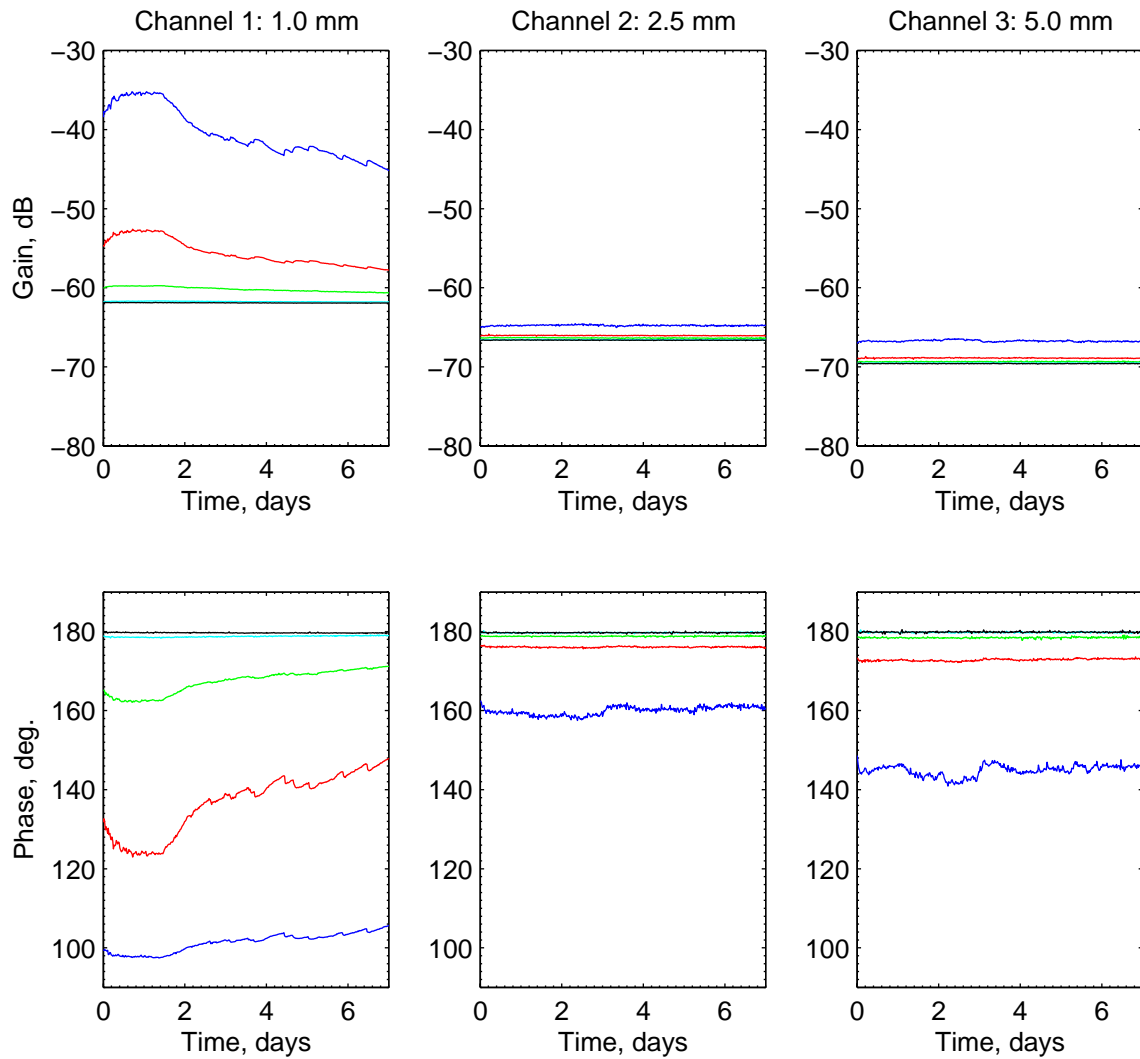


Figure 8-2: Teflon rod ϕ periodic sensor diffusion experiment gain and phase for selected frequencies. Frequencies shown are 0.01 (blue), 0.1 (red), 1.0 (green), 100 (cyan), and 10,000 (black) Hz. *This measurement was conducted from December 18 to December 30, 2006.*

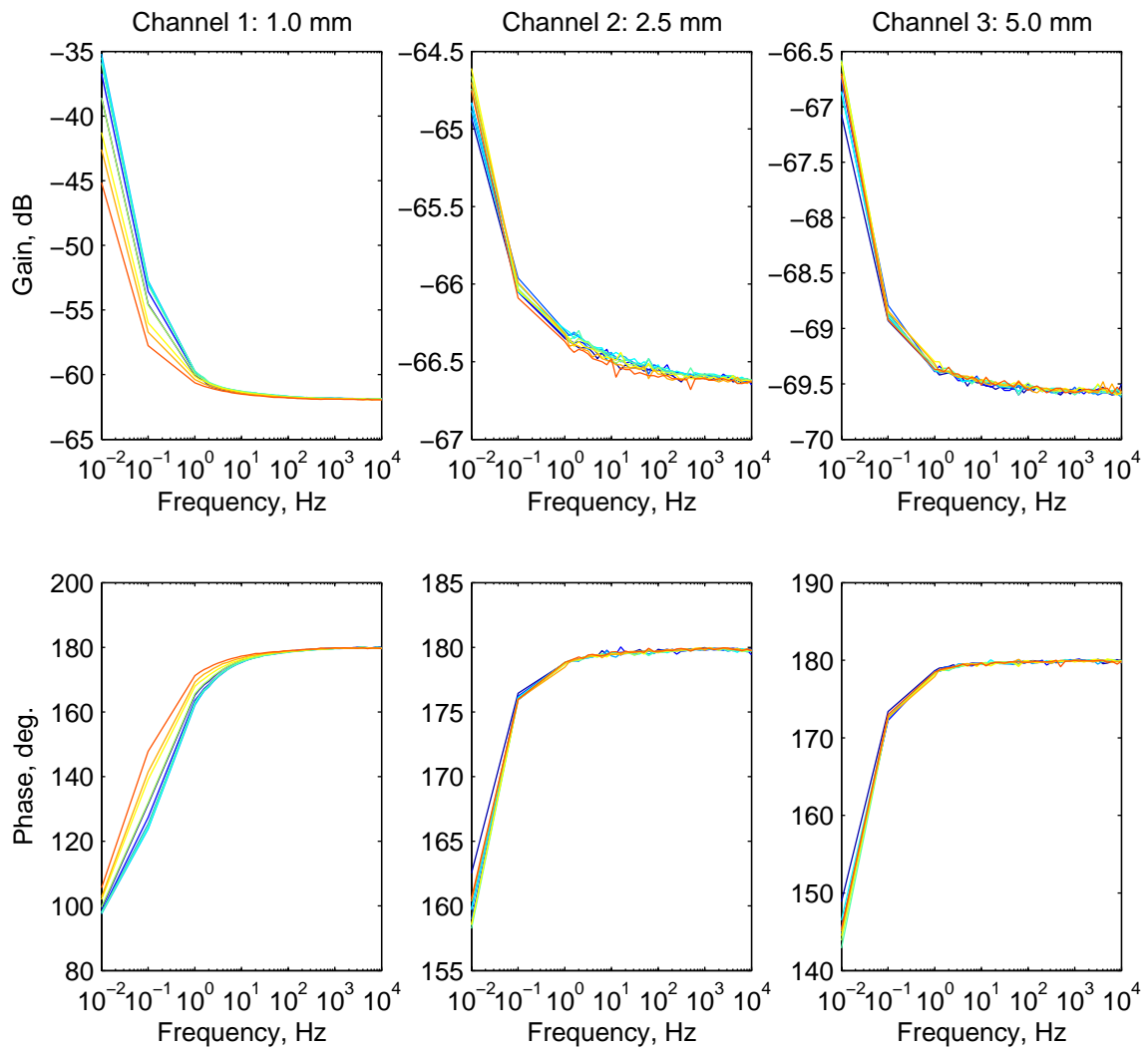


Figure 8-3: Teflon rod ϕ periodic sensor diffusion experiment gain and phase for selected times. Times shown are at $t = 0, 0.2, 0.4, 0.7, 1.0, 1.5, 2.0, 3.0, 5.0,$ and 7.0 days. The color progression is from early to late times (dark blue to yellow to dark red).

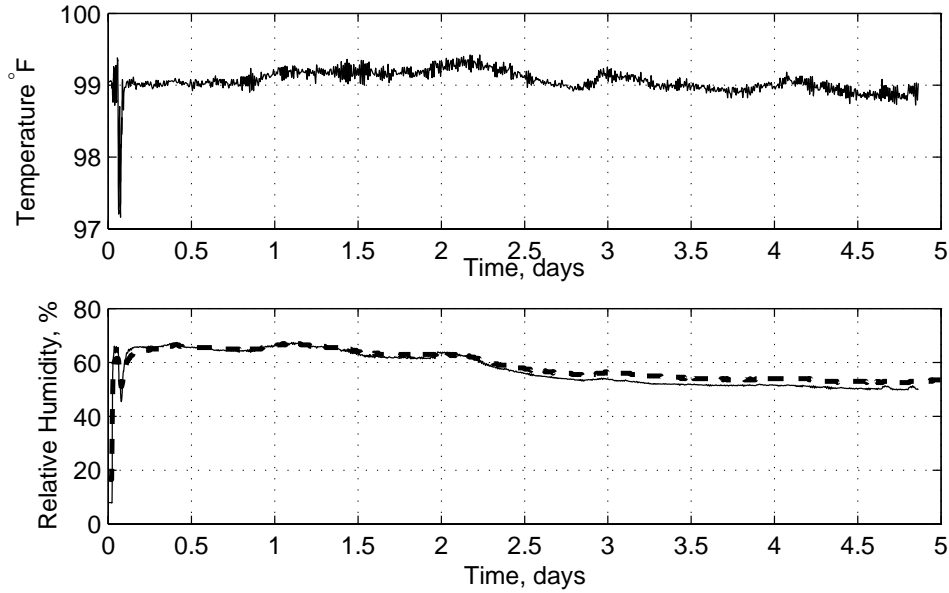


Figure 8-4: Birch rod ϕ periodic sensor diffusion experiment temperature and relative humidity log. Dashed line indicates a second independent relative humidity measurement.

8.1.2 ϕ Periodic Birch Wood Rod Transient Measurements

A birch rod $1\frac{3}{16}$ inches in diameter and $3\frac{1}{2}$ inches in length is measured in a similar way as the Teflon rod. The rod is exposed to the environment at both ends, while the curved surface is in contact with the sensor and hose clamping mechanism.

During the experiment the nominal temperature is 99°F and the relative humidity reaches its peak of 65% shortly after time zero. The transient temperature and humidity details are shown in Fig. 8-4. While the temperature is very constant, there is a noticeable decrease in the relative humidity over the course of the experiment. The average relative humidity is 59%. This is verified by a data logger placed inside the chamber and analyzed after the measurement.

The experimental results are shown in Fig. 8-5 for several frequencies on each channel. Notice that the low frequency channels saturate on all three sensors. Steady state appears to be reached in about three to four days for most channels, although a little drifting still exists on some of the phase measurements.

Figure 8-6 provides an alternative view of the data where all data points are plotted at select times. It is clear that steady state has been reached because of the repetition of the same gain and phase measurements for multiple times.

The electrical properties of the birch rod change dramatically as moisture diffuses into the rod.

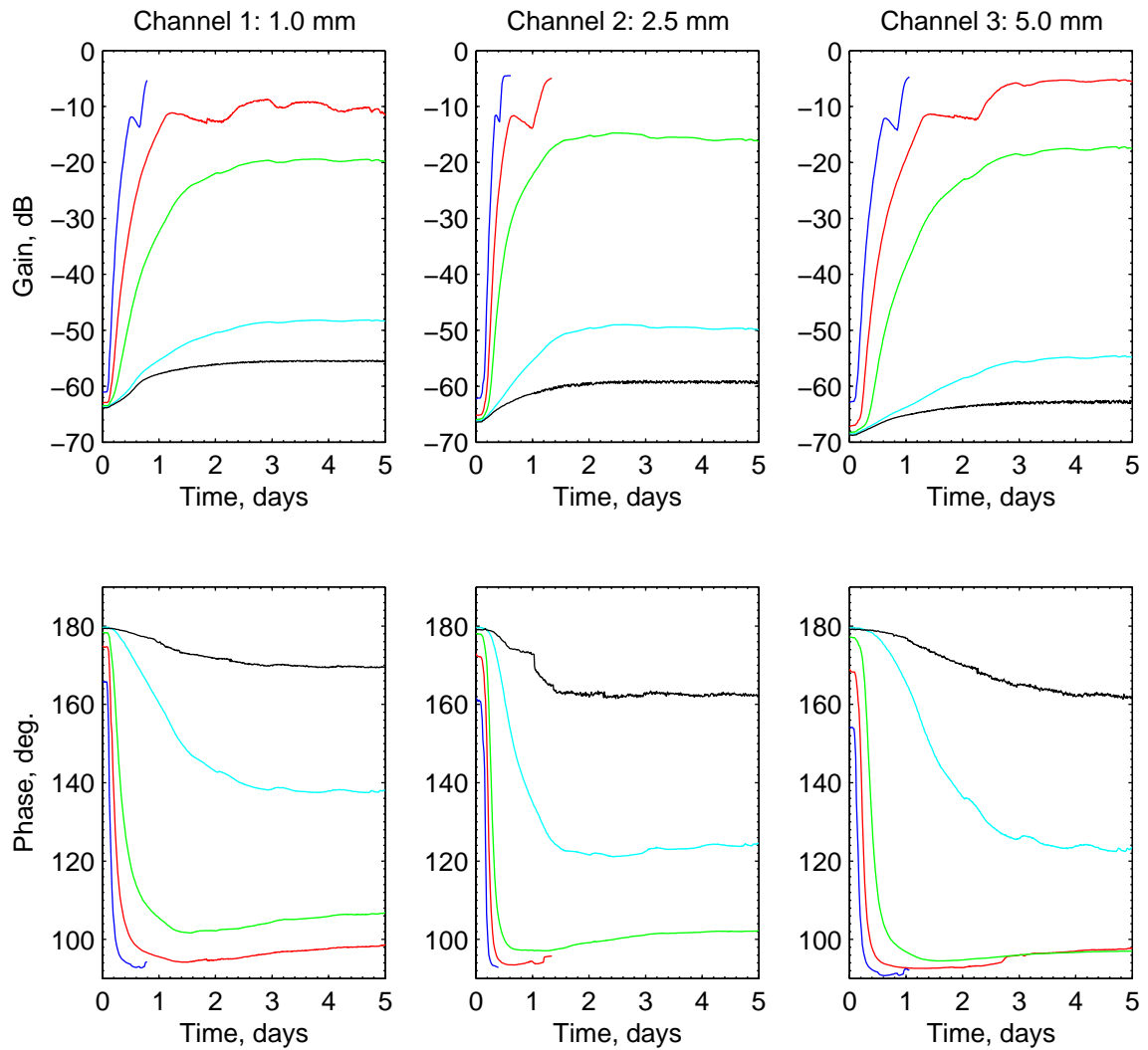


Figure 8-5: Birch rod ϕ periodic sensor diffusion experiment gain and phase for selected frequencies. Frequencies shown are 0.01 (blue), 0.1 (red), 1.0 (green), 100 (cyan), and 10,000 (black) Hz. This measurement was conducted from January 4 to January 9, 2007.

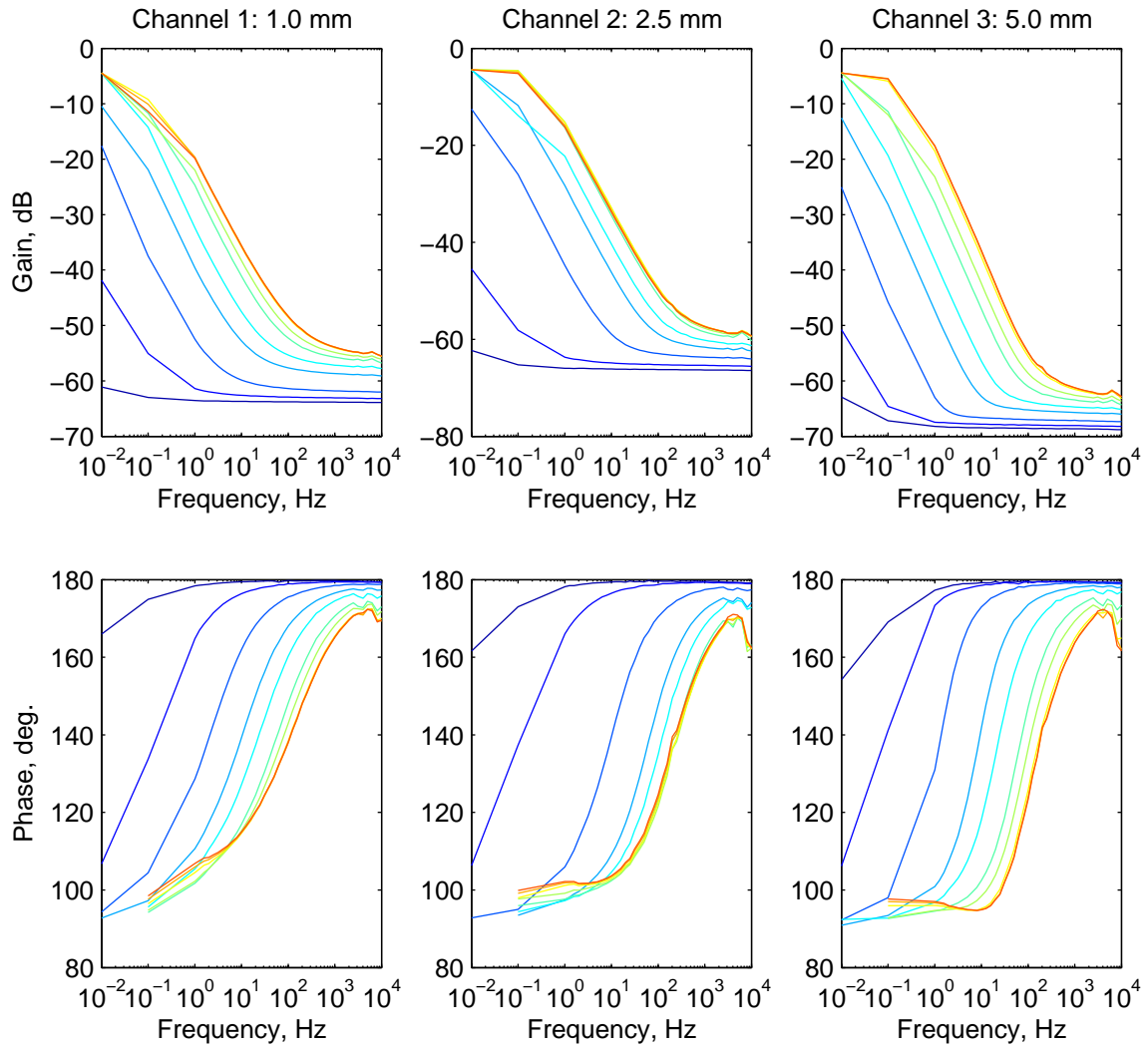


Figure 8-6: Birch rod ϕ periodic sensor diffusion experiment gain and phase for selected times. Times shown are $t = 0, 0.2, 0.4, 0.7, 1.0, 1.5, 2.0, 3.0,$ and 5.0 days. The color progression is from early to late times (dark blue to yellow to dark red).

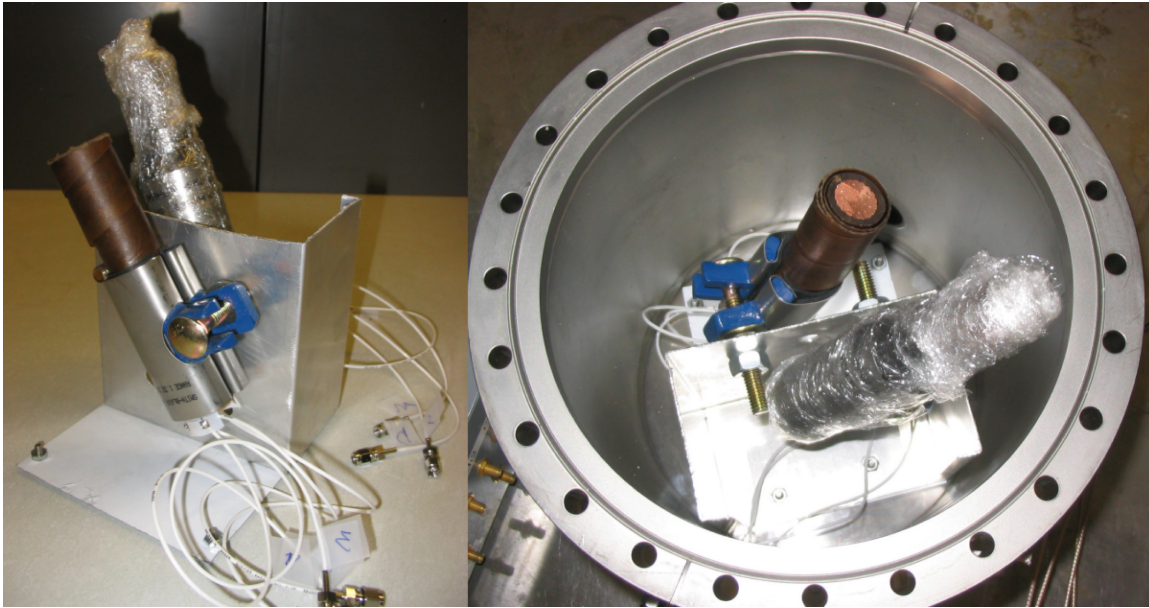


Figure 8-7: Photographs of the single conductor cable measurement setup for two samples. Left: Prepared cable samples in clamping mechanism. Right: Cables inserted into the measurement chamber during preparation for measurements.

The overall trend is an increase in conductivity over several orders of magnitude, while the permittivity change is much smaller. An analysis of these results is presented in Section 9.3.1, where the diffusion coefficient is estimated.

The data in Fig. 8-5 has been evaluated by the inverse solver to determine the effective permittivity which has been plotted in appendix B, Fig. B-18.

8.1.3 ϕ Periodic Single Conductor Cable Measurements

Experiment 1: $T \approx 174$ °F $RH \approx 27\%$

In this experiment two samples of the single conductor cable are measured using the three wavelength sensor. A pipe clamp is used to secure the sensors. One of the samples is “wrapped” with parafilm and plastic wrap such that only the bottom face of the cable is left exposed. The second “unwrapped” sample is left exposed everywhere the clamping mechanism does not touch. This is illustrated in the setup photo shown in Fig. 8-7.

Before the measurement time started the temperature was set and the chamber was evacuated of air and moisture using a vacuum pump. After allowing time for the temperature and measurements to stabilize, the relative humidity was raised by allowing moist air to enter the chamber at time

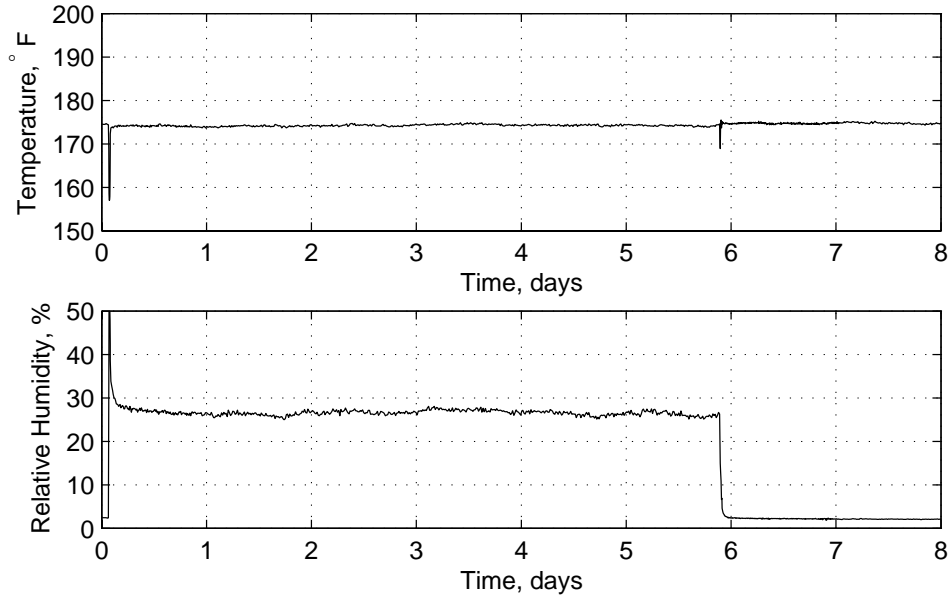


Figure 8-8: Single conductor cable ϕ periodic sensor diffusion experiment temperature and relative humidity log.

zero. During the entire experiment the temperature averaged 174.3°F with a standard deviation of 1.3°F . The relative humidity averaged 27% with a standard deviation of 1.3% during the moisture absorption phase of the experiment. During the humidification process the temperature dropped to about 155°F for about 15 minutes. The transients associated with the temperature drop dissipated much faster than the moisture transients. The temperature and relative humidity log is shown in Fig. 8-8.

The diffusion process is monitored for about six days before the chamber is evacuated. The vacuum was allowed to run for another two days to monitor the desorption process. Throughout the experiment, measurements were taken at 10, 100, 1,000, and 10,000 Hz using the three wavelength sensors on both cables. The results are shown in Fig. 8-9 for the unwrapped cable, and Fig. 8-10 for the wrapped cable.

The measurements show the typical trend of increasing gain and shifting phase with the introduction of moisture into the chamber. Missing data from the unwrapped cable in Fig. 8-9 is due in part to a controller box failure. The controller box was replaced just prior to evacuating the chamber. Sensor failure is also observed on several of the channels

Sensor failure is marked by completely erratic gain and phase measurements and a very large offset voltage (see Section 5.2.1). This data has been suppressed for clarity. Initially the sensor failure had been attributed to moisture condensing on the sensor surface and resulting in near shorting

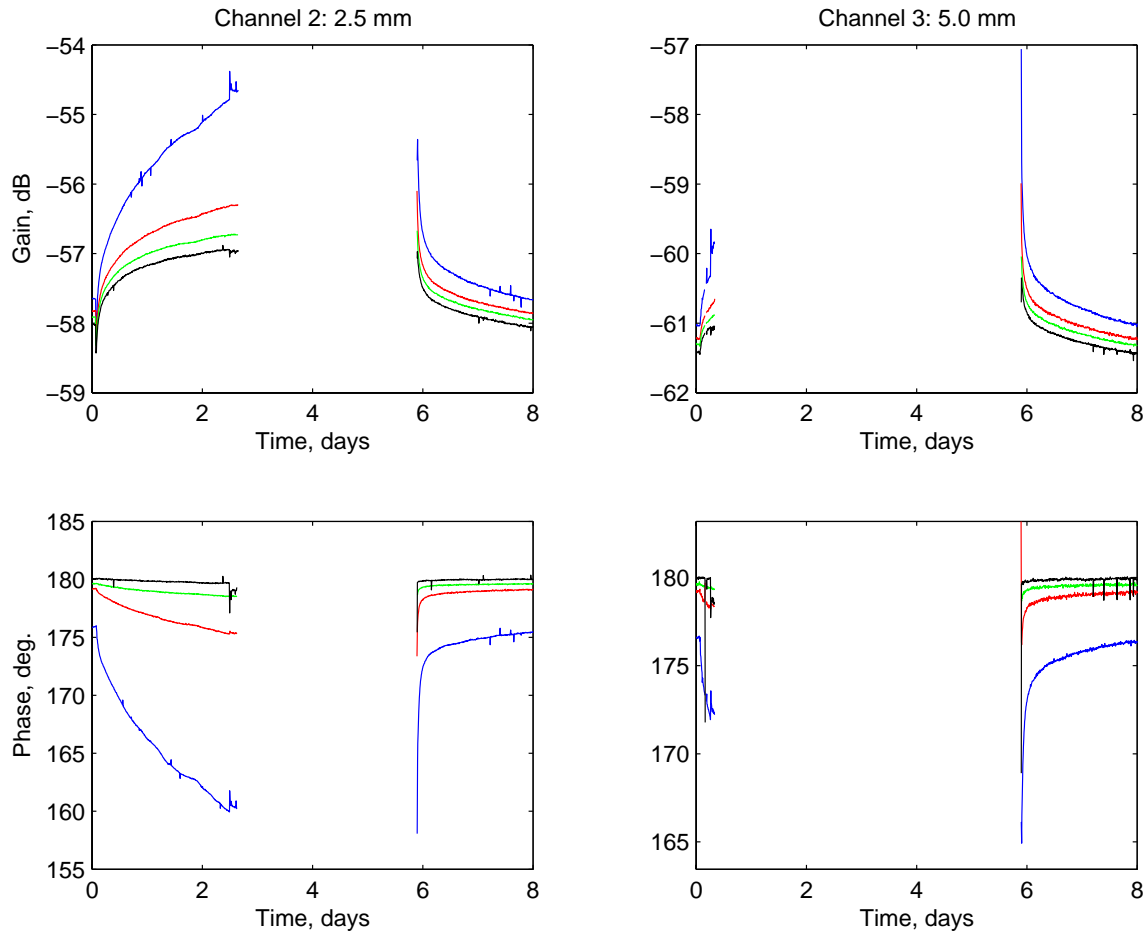


Figure 8-9: Unwrapped single conductor gain and phase measurements for a moisture diffusion experiment at 174 °F using a ϕ periodic sensor. Measurement frequencies are 10 (blue), 100 (red), 1,000 (green), and 10,000 (black) Hz. A failed controller box resulting in missing data was replaced prior to evacuating the chamber at day 6. Interface box 4 is used. *This measurement was conducted from April 4 to April 12, 2006.*

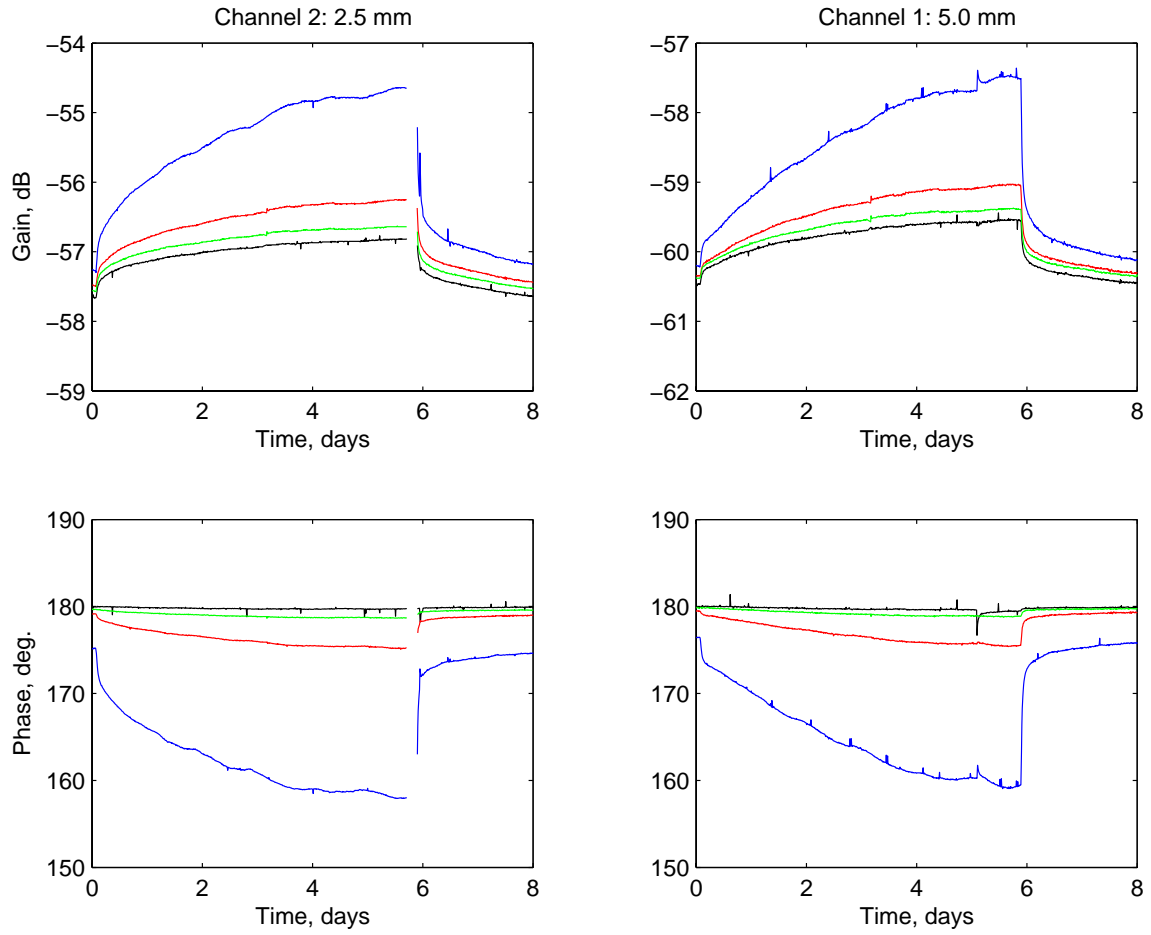


Figure 8-10: Wrapped single conductor gain and phase measurements for a moisture diffusion experiment at 174 °F using a ϕ periodic sensor. Measurement frequencies are 10 (blue), 100 (red), 1,000 (green), and 10,000 (black) Hz. Interface box 3 is used.

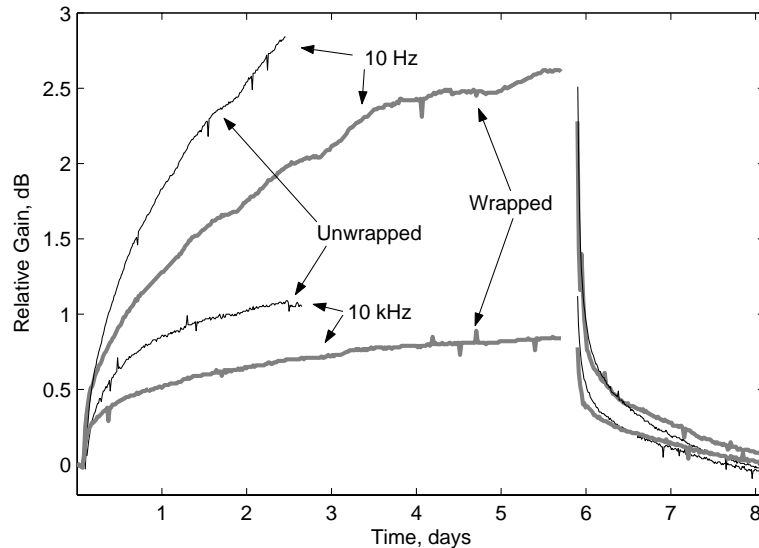


Figure 8-11: Comparison between wrapped and unwrapped single conductor cable relative gains on the 2.5 mm sensor. The unwrapped cable outpaces the response of the wrapped cable as expected.

between the drive and sense electrodes. Because the conductivity of water is so high compared to typical MUTs the feedback capacitance is of insufficient size to prevent the output voltage from saturating. This reason was suspected because of the immediate return of sensor functionality once the evacuation process commenced.

An alternative explanation is that the SMA connectors inside the chamber can be shorted by the water. This is particularly likely on the large chamber with side ports where the temperature in the side ports is significantly lower than the chamber temperature. In one circumstance, upon failure, the sensor was removed without evacuating the chamber. It was found that the SMA connector had a shorted causing the aberrant behavior.

It is appropriate to compare the experimental results for the unwrapped and wrapped channel. We do this for the 2.5 mm sensor measurements. We expect that the diffusion process should be noticeably faster for the unwrapped sensor. We can compare the diffusion times by comparing the change in gain for sensors of the same wavelength on the two cables. For this purpose the relative gains are compared by subtracting the value at time zero. This is necessary since the feedback capacitances are not exactly the same. The experimental results clearly show the unwrapped cable responds faster than the wrapped cable.

The data in Fig. 8-9 and Fig. 8-10 has been evaluated by the inverse solver to determine the effective permittivity which has been plotted in appendix B, Fig. B-19 and Fig. B-20 respectively.

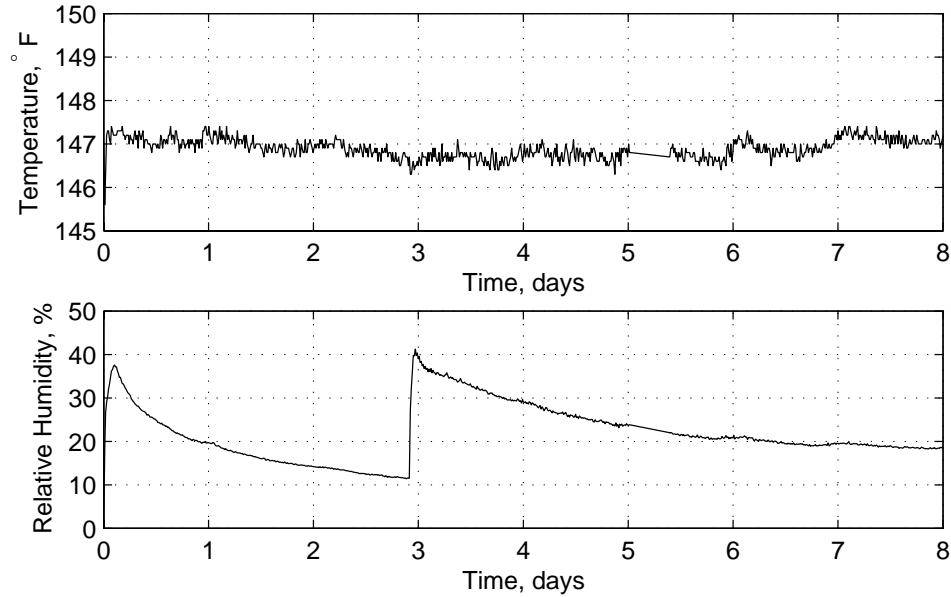


Figure 8-12: Single conductor cable with ϕ periodic sensor diffusion experiment temperature and relative humidity log. Moisture is injected at zero days and nearly three days.

Experiment 2: $T \approx 147$ °F

In this experiment conducted in the small chamber a 3 1/2 inch single conductor cable and ϕ periodic sensor is wrapped with a latex sheath to limit moisture to entering the cable to only one end. The hose clamp technique is used to hold the sensor and sheath in place. The cable is dried for several days at the measurement temperature of 146.9 °F (standard deviation 0.24 °F) before moisture is introduced at time zero. At that time 0.5 mL of water is injected to the chamber, and the chamber is then immediately sealed. The relative humidity rises quickly to about 37%. Over the first three days of the experiment the relative humidity falls to 12% as moisture is absorbed into the cable. After nearly three days, a second injection of 0.5 mL of water is made. The relative humidity quickly peaks at 41%. Over the next five days of the experiment, the relative humidity falls to about 20%. The temperature and relative humidity log are shown in Fig. 8-12. The experimental gain and phase is shown in Fig. 8-13.

The data in Fig. 8-13 has been evaluated by the inverse solver to determine the effective permittivity which has been plotted in appendix B, Fig. B-21.

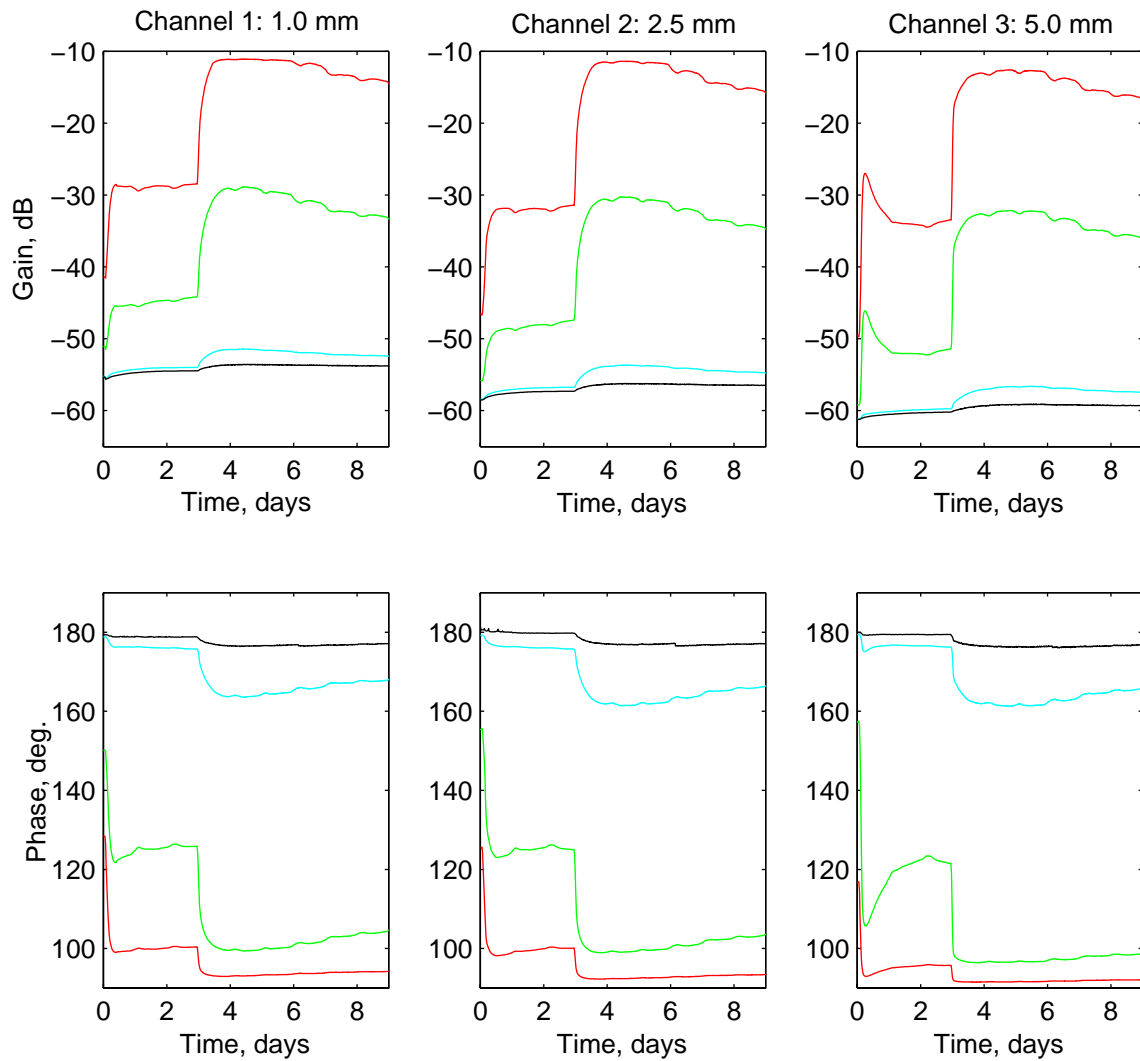


Figure 8-13: Single conductor cable measurements at 147 °F and 20% relative humidity. Measurements are shown for frequencies of 0.1 (red), 1.0 (green), 100 (cyan), and 10,000 (black) Hz. This measurement was conducted from March 3 to March 12, 2007.

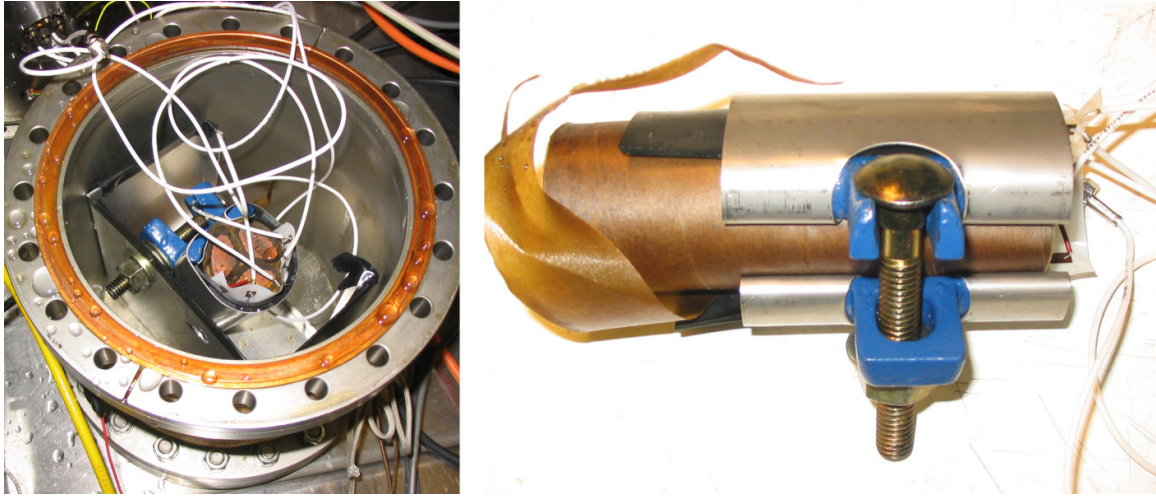


Figure 8-14: Photographs of the experimental setup for the three conductor cable using the ϕ periodic sensor. Left: Cable inside the small chamber after an experiment. Right: View of exposed cable surface.

8.1.4 ϕ Periodic Three Conductor Cable Measurements

Some of the earliest cable measurements were conducted on the three conductor cable using the ϕ periodic sensor. In this section we present many of these early measurements. Only four frequencies are monitored: 10, 100, 1,000 and 10,000 Hz. Nearly all these measurements are made with setup a setup similar to that photographed in Fig. 8-14.

The pipe clamp used does not completely cover the side of the cable, both faces are exposed and an exposed strip exists along the top. This makes solving the diffusion equation difficult but it does give us a good idea as to the time associated with the diffusion process.

For the purposes of comparison, the feedback capacitances in all measurements are “normalized” to 5 nF. To perform the normalization the gain shift due to the actual feedback capacitance is subtracted, then the gain shift expected from a 5 nF feedback capacitance is added. This allows for the comparison of various measurements and channels directly without considering the vertical shifts due to differences in C_f . It is clear from eqs. 3.4 and 3.5 that only the gain is affected by the choice of feedback capacitance.

Experiment 1: $T \approx 101$ °F $RH \approx 81\%$

This experiment on the three conductor cable is done in the small vacuum chamber. The cable and sensor apparatus are dried for about a week using the vacuum pump. At day zero humid air is introduced to the chamber and the vacuum pump turned off. Throughout the experiment the

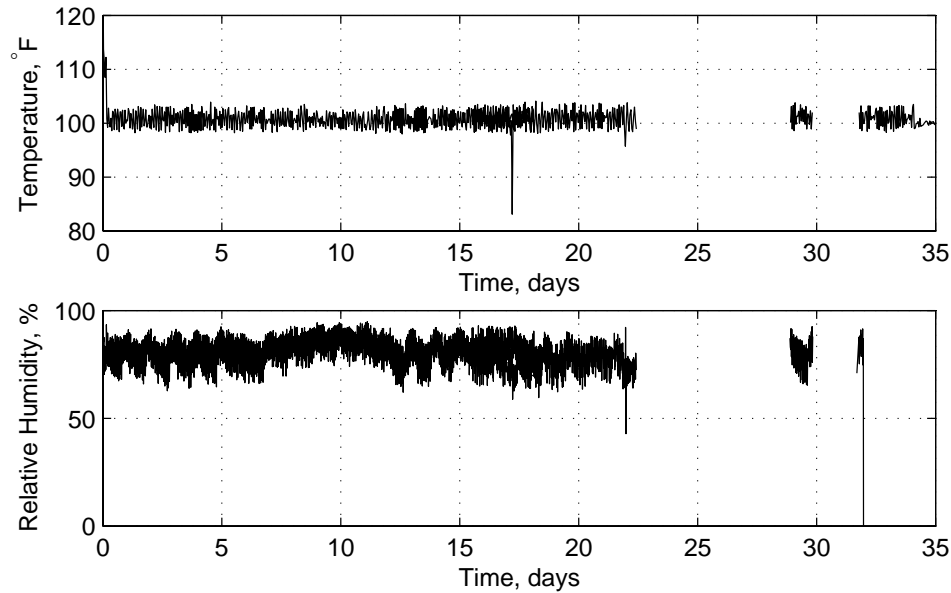


Figure 8-15: Unwrapped three conductor cable ϕ periodic sensor diffusion experiment temperature (101 °F) and relative humidity (81%) log. The logging software was off during the blank periods. The conditions during these periods were consistent with the overall trend.

temperature is regulated. The average temperature is 100.8 °F with standard deviation of 1.9 °F. The average relative humidity during the humidification is 81% with a standard deviation of 7.6%. This variation is larger than in other experiments due to a slightly under damped PID temperature controller. This results in oscillations in the chamber temperature with a period of about 14 minutes. The recorded values of temperature and humidity are plotted in Fig. 8-15.

The moisture diffusion process is allowed to proceed for 32 days before the vacuum pump is again turned on. The moisture evacuation process is recorded for 5 days. The experimental results are shown in Fig. 8-16.

The very slow rate of diffusion is likely due to the relatively low temperature of this experiment. The desorption process is much faster than the absorption process. This is most likely due to the very low pressure during drying. During the evacuation process the pressure is low, lowering the boiling point of water. In fact the chamber temperature is well above the boiling point at the evacuation pressure.

The data in Fig. 8-16 has been evaluated by the inverse solver to determine the effective permittivity which has been plotted in appendix B, Fig. B-22.

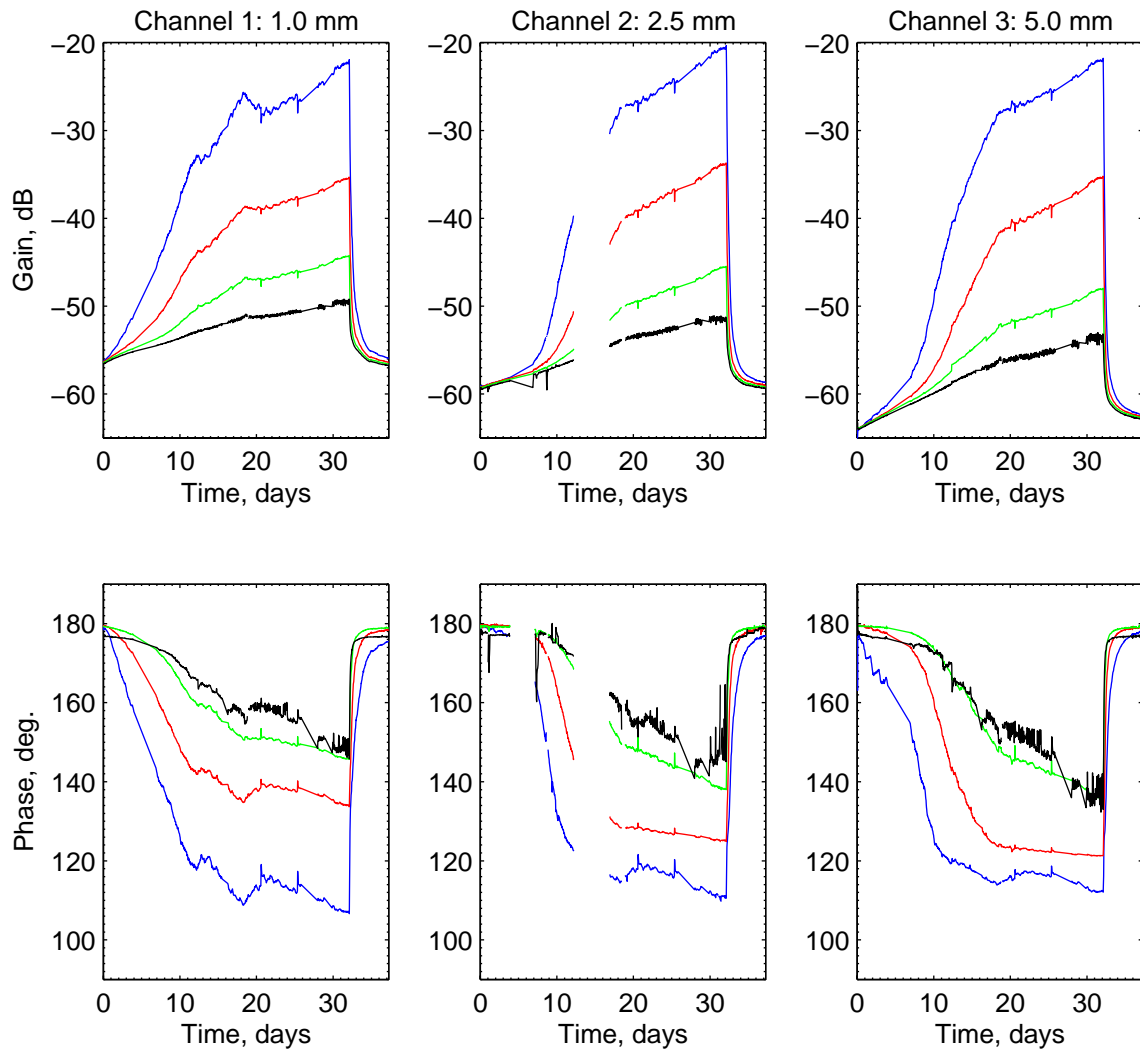


Figure 8-16: Unwrapped three conductor cables diffusion measurement at 100 °F using the ϕ periodic sensor. Measurements are shown for frequencies of 10 (blue), 100 (red), 1,000 (green), and 10,000 (black) Hz. Interface box 2 is used. Feedback capacitances are normalized to 5 nF. *This measurement was conducted from February 6 to March 15, 2006.*

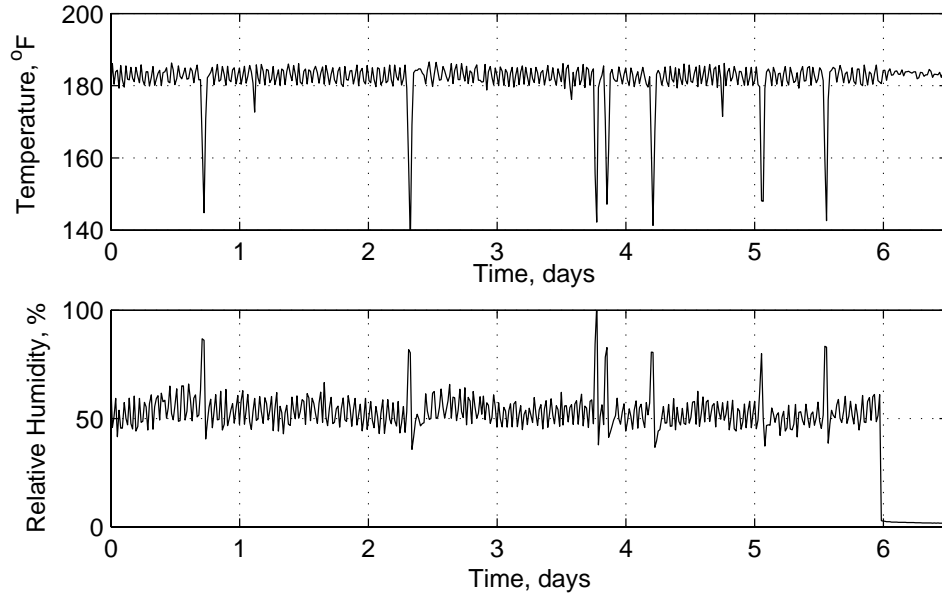


Figure 8-17: Unwrapped three conductor cable ϕ periodic sensor diffusion experiment temperature (182 °F) and relative humidity (53%) log. The drops in temperatures are caused by temporary lapses of the PID temperature controller.

Experiment 2: $T \approx 182$ °F $RH \approx 53\%$

This experiment on the three conductor cable is done in the small vacuum chamber. Immediately following the previous experiment the temperature is raised to 180 °F. After allowing time for the temperature to equilibrate, humidity is introduced at day zero. The diffusion process proceeds for 6 days before the vacuum pump is turned on to reverse the diffusion process. During the experiment the average temperature is 181.5 °F with standard deviation of 7.2 °F. The relative humidity averages 53% with standard deviation 7.9%. The recorded values of temperature and humidity are plotted in Fig. 8-17.

In this experiment there are several spikes that appear to be temporary failures of the temperature controller. This increases the standard deviation substantially. The experimental results shown in Fig. 8-18 are normalized to a 5 nF feedback capacitance. Aside from the temperature drops the results show a smooth development of the gain and phase to steady state values. After about six days the chamber is evacuated.

The data in Fig. 8-18 has been evaluated by the inverse solver to determine the effective permittivity which has been plotted in appendix B, Fig. B-23.

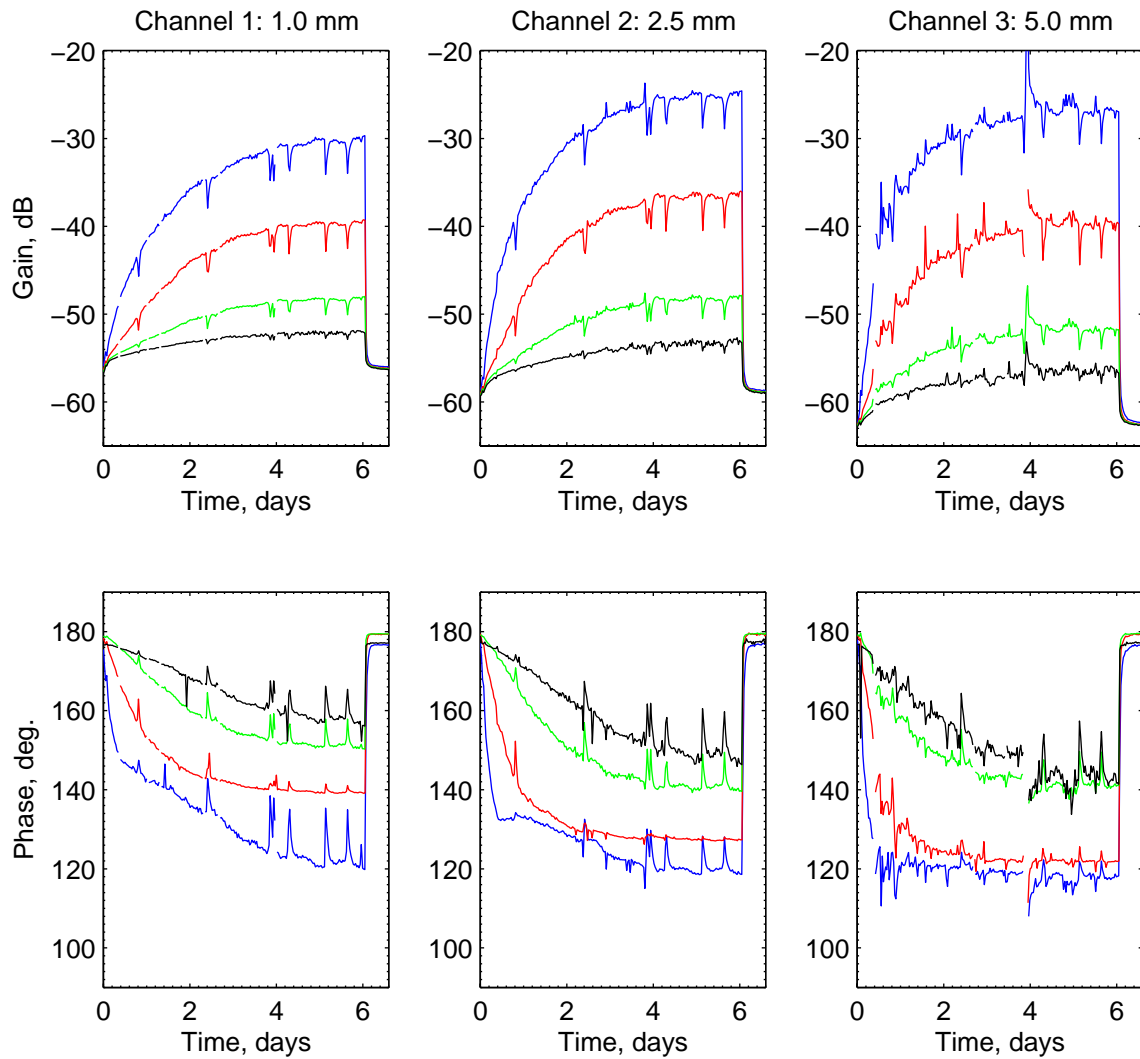


Figure 8-18: Unwrapped three conductor cables diffusion measurement at 180 °F using the ϕ periodic sensor. Measurements are shown for frequencies of 10 (blue), 100 (red), 1,000 (green), and 10,000 (black) Hz. Interface box 2 is used. Feedback capacitances are normalized to 5 nF. *This measurement was conducted from March 15 to March 22, 2006.*

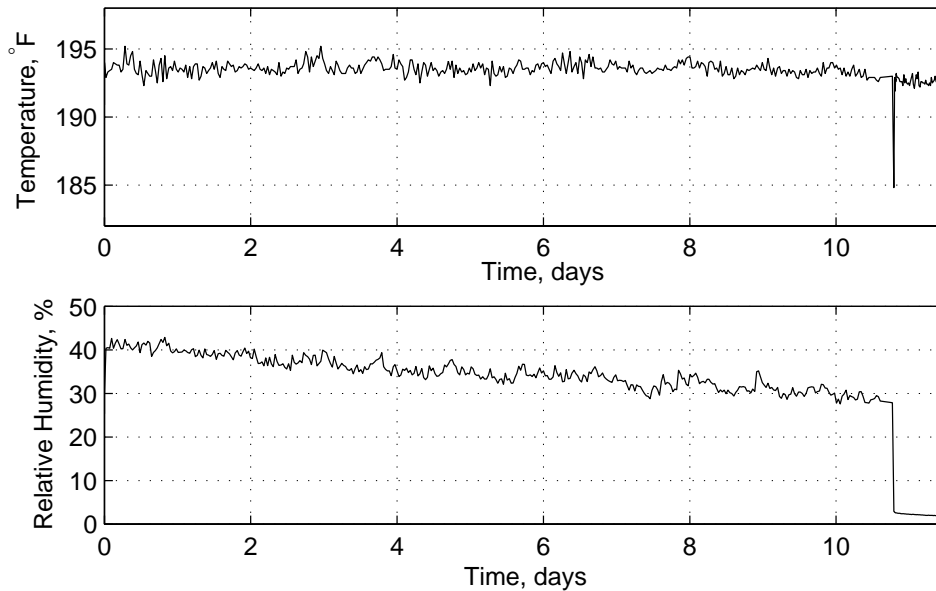


Figure 8-19: Unwrapped three conductor cable ϕ periodic sensor diffusion experiment temperature (193 °F) and relative humidity (34%) log.

Experiment 3: $T \approx 193$ °F $RH \approx 34\%$

This experiment on the three conductor cable is done in the small vacuum chamber. Immediately following the previous measurement the temperature is raised slightly. After allowing time for the temperature to equilibrate humidity is introduced at day zero. The diffusion process proceeds for 11 days before the vacuum pump is turned on to reverse the process. During the experiment the average temperature is 193.3 °F with standard deviation of 0.46 °F. The increased stability is due to the choice of running the temperature controller in proportional mode only. The relative humidity averages 35% with standard deviation 3.6%. The recorded values of temperature and humidity are plotted in Fig. 8-19.

The experimental results are shown in Fig. 8-20. After eleven days the chamber is evacuated. The measurement shows the gain and phase peak and then return towards the initial value. This is consistent with the relative humidity measurements which decrease continuously during the experiment. The reduction is due to absorption by the cable.

The data in Fig. 8-20 has been evaluated by the inverse solver to determine the effective permittivity which has been plotted in appendix B, Fig. B-24.

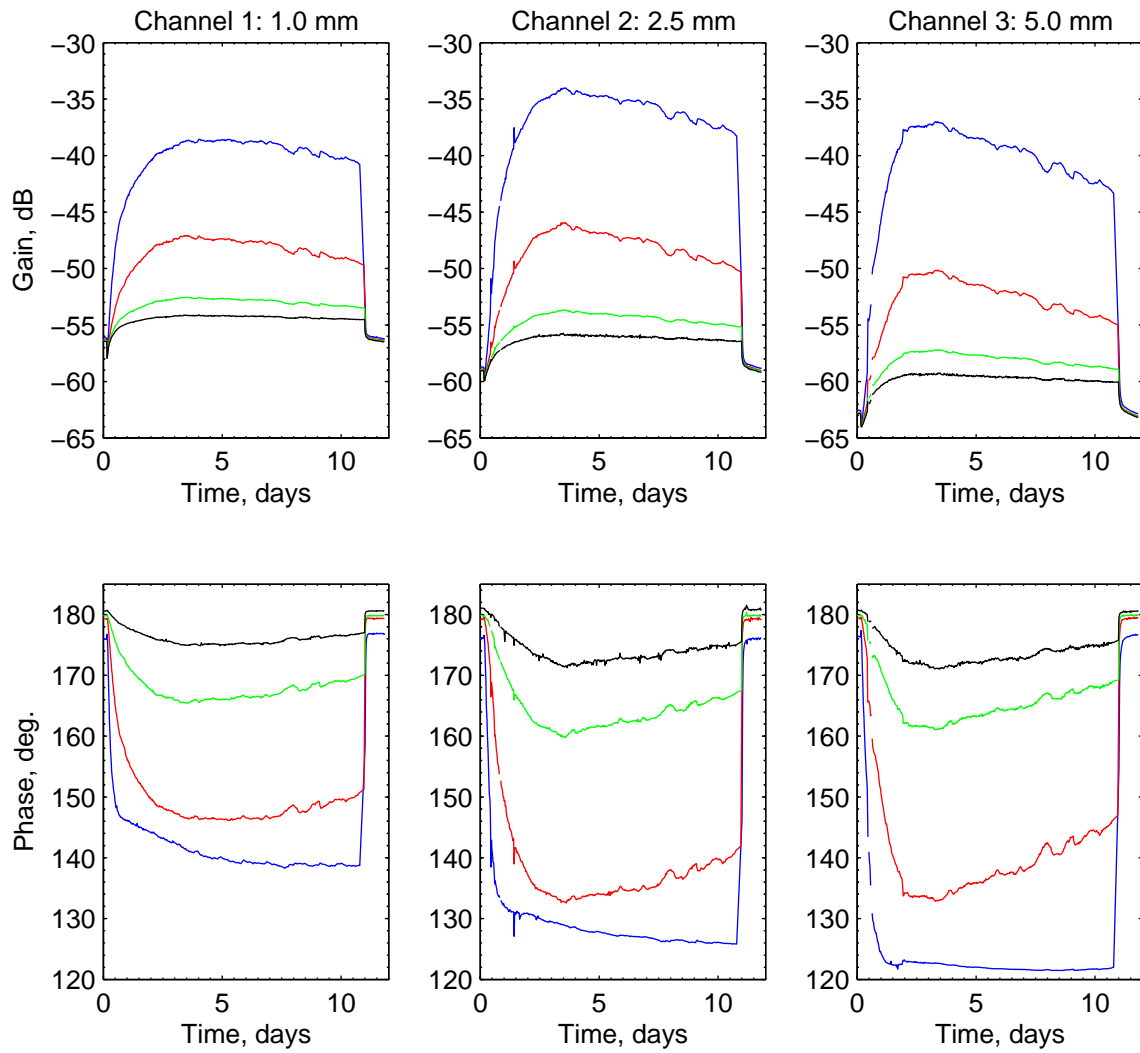


Figure 8-20: Unwrapped three conductor cables diffusion measurement at 195 °F using the ϕ periodic sensor. Measurements are shown for frequencies of 10 (blue), 100 (red), 1,000 (green), and 10,000 (black) Hz. Interface box 2 is used. Feedback capacitances are normalized to 5 nF. *This measurement was conducted from March 23 to April 3, 2006.*

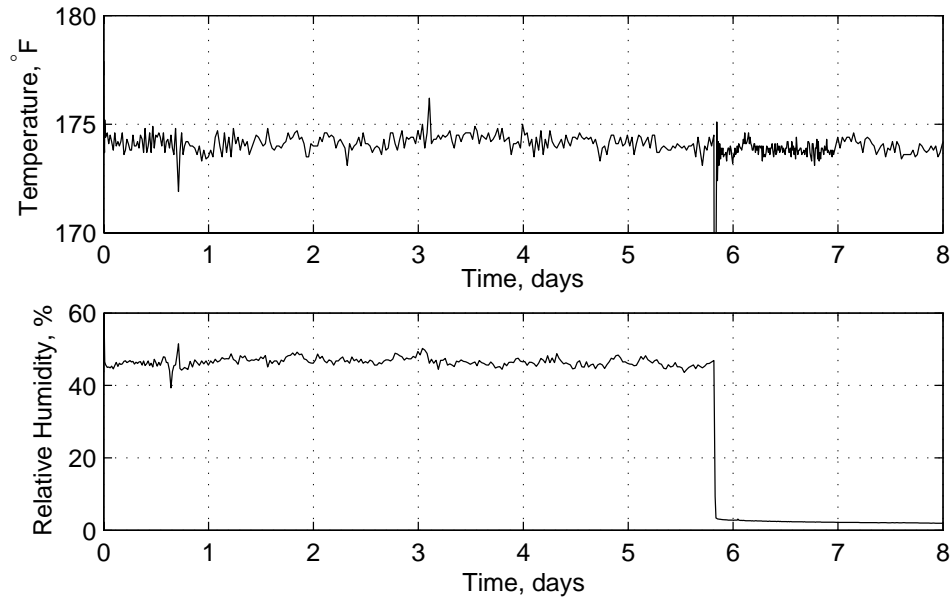


Figure 8-21: Unwrapped three conductor cable ϕ periodic sensor diffusion experiment temperature (174 °F) and relative humidity (46%) log.

Experiment 4: $T \approx 174$ °F $RH \approx 46\%$

This experiment on the three conductor cable is done in the small vacuum chamber. Immediately following the previous measurement the temperature is raised slightly. After allowing time for the temperature to equilibrate, humidity is introduced at day zero. The diffusion process proceeds for 5.8 days before the vacuum pump is turned on to reverse the process. During the experiment the average temperature is 174.0 °F with standard deviation of 1.73 °F. The relative humidity averages 46% with standard deviation 1.4%. The recorded values of temperature and humidity are plotted in Fig. 8-21. The experimental data is presented in Fig. 8-22.

The data in Fig. 8-22 has been evaluated by the inverse solver to determine the effective permittivity which has been plotted in appendix B, Fig. B-25.

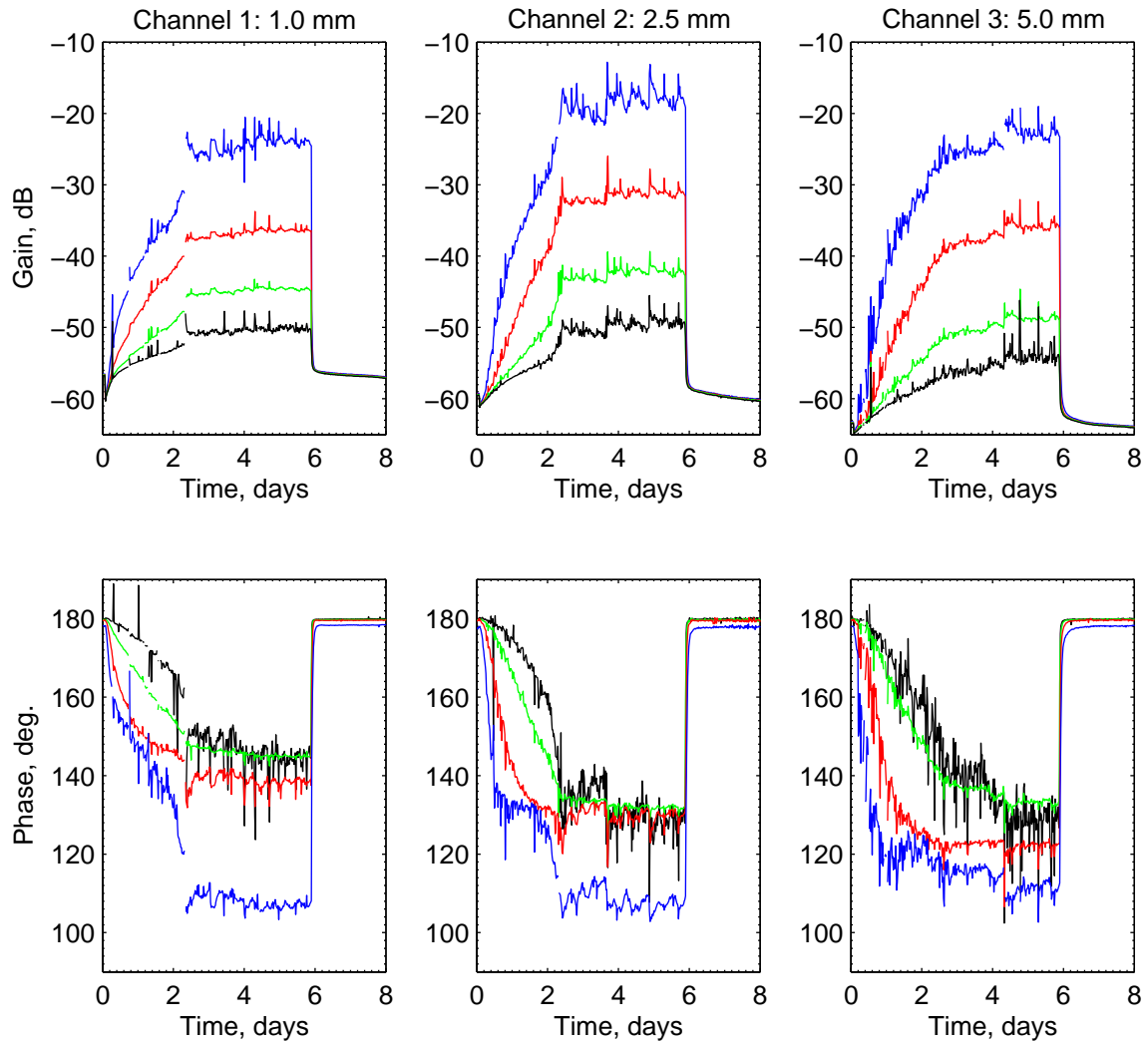


Figure 8-22: Unwrapped three conductor cables diffusion measurement at 174 °F using the ϕ periodic sensor. Measurements are shown for frequencies of 10 (blue), 100 (red), 1,000 (green), and 10,000 (black) Hz. Interface box 2 is used. Feedback capacitances are normalized to 5 nF. *This measurement was conducted from April 4 to April 12, 2006.*

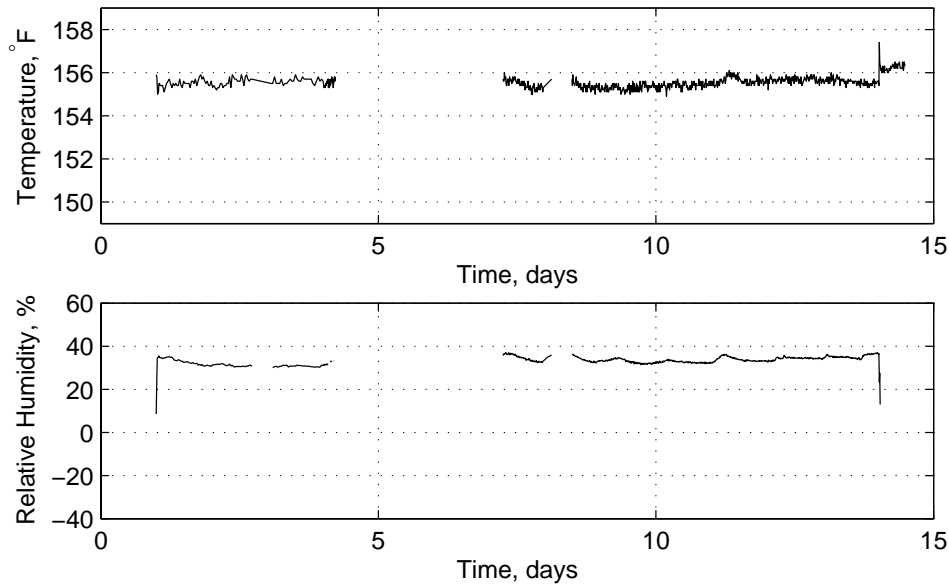


Figure 8-23: Unwrapped three conductor cable ϕ periodic sensor diffusion experiment temperature (155 °F) and relative humidity (34%) log. From about day 4 to day 7 the LabVIEW logger was used for a separate experiment, however, the controller continued to maintain the environmental conditions during this period.

Experiment 5: $T \approx 155$ °F $RH \approx 34\%$

This experiment on the three conductor cable is done in the small vacuum chamber. After allowing time for the temperature to equilibrate, humidity is introduced at day one. The diffusion process proceeds for 13 days before the vacuum pump is turned on to reverse the process. The evacuation process is recorded for four days. During the experiment the average temperature is 155.5 °F with standard deviation of 0.29 °F. The relative humidity averages 34% with standard deviation 1.4%. The recorded values of temperature and humidity are plotted in Fig. 8-23.

The experimental results showing the initial moisture evacuation and the introduction of moisture into the chamber are shown in Fig. 8-24. On day fourteen of the experiment the vacuum pump is turned on and the cable and chamber is dried for four days. The measurement results are shown in Fig. 8-25. To compare the steady state gain and phase before and after the experiment, the steady state values before the introduction in moisture are plotted as dashed lines. The cable response is almost identical before and after the experiment.

The data in Fig. 8-24 and Fig. 8-25 has been evaluated by the inverse solver to determine the effective permittivity which has been plotted in appendix B, Fig. B-26 and Fig. B-27 respectively.

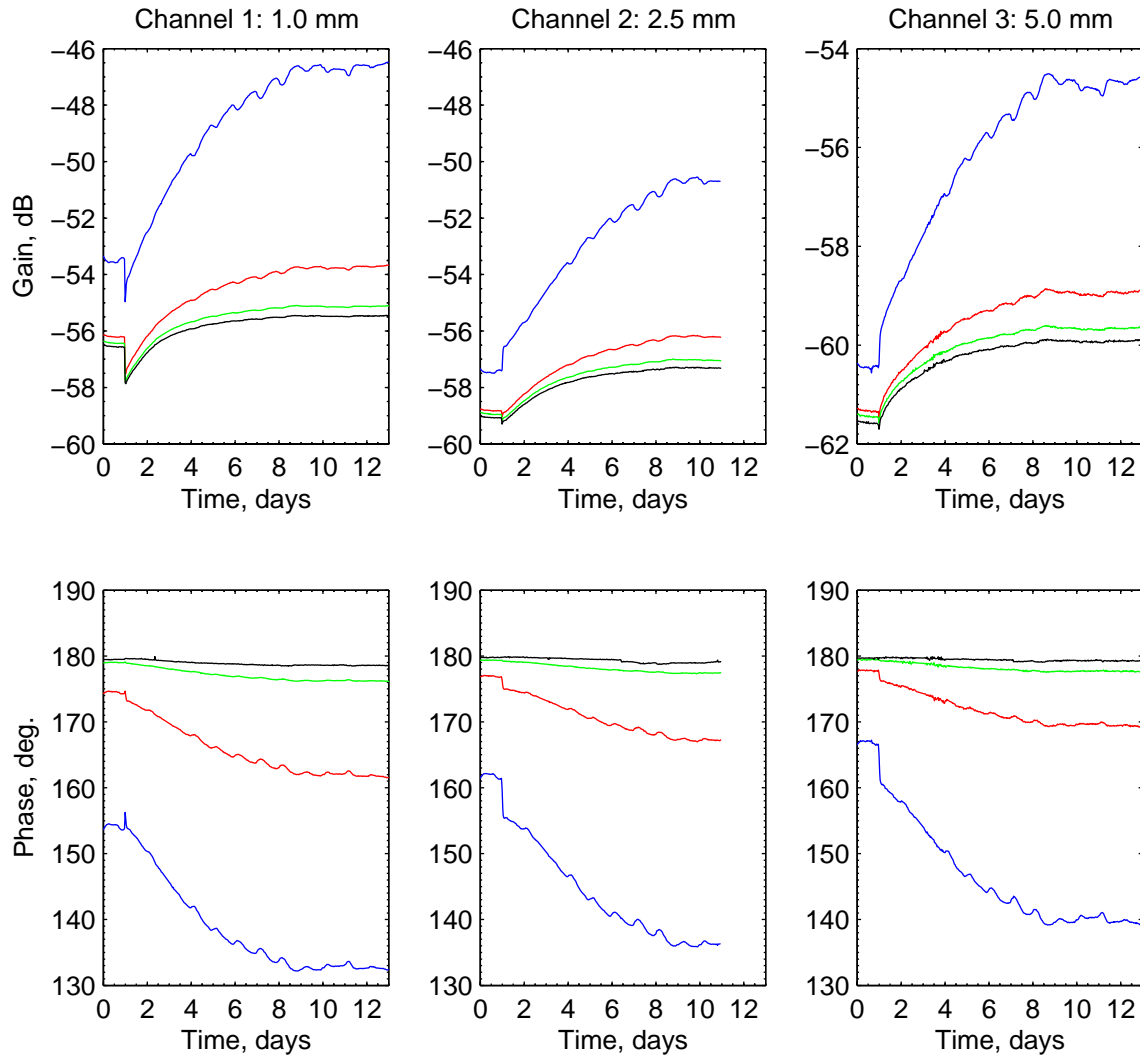


Figure 8-24: Unwrapped three conductor cable moisture ingress measurements at 155 °F using a ϕ periodic sensor. Measurements are shown for frequencies of 10 (blue), 100 (red), 1,000 (green), and 10,000 (black) Hz. Feedback capacitance is 5 nF for each channel. *This measurement was conducted from July 5 to July 26, 2006.*

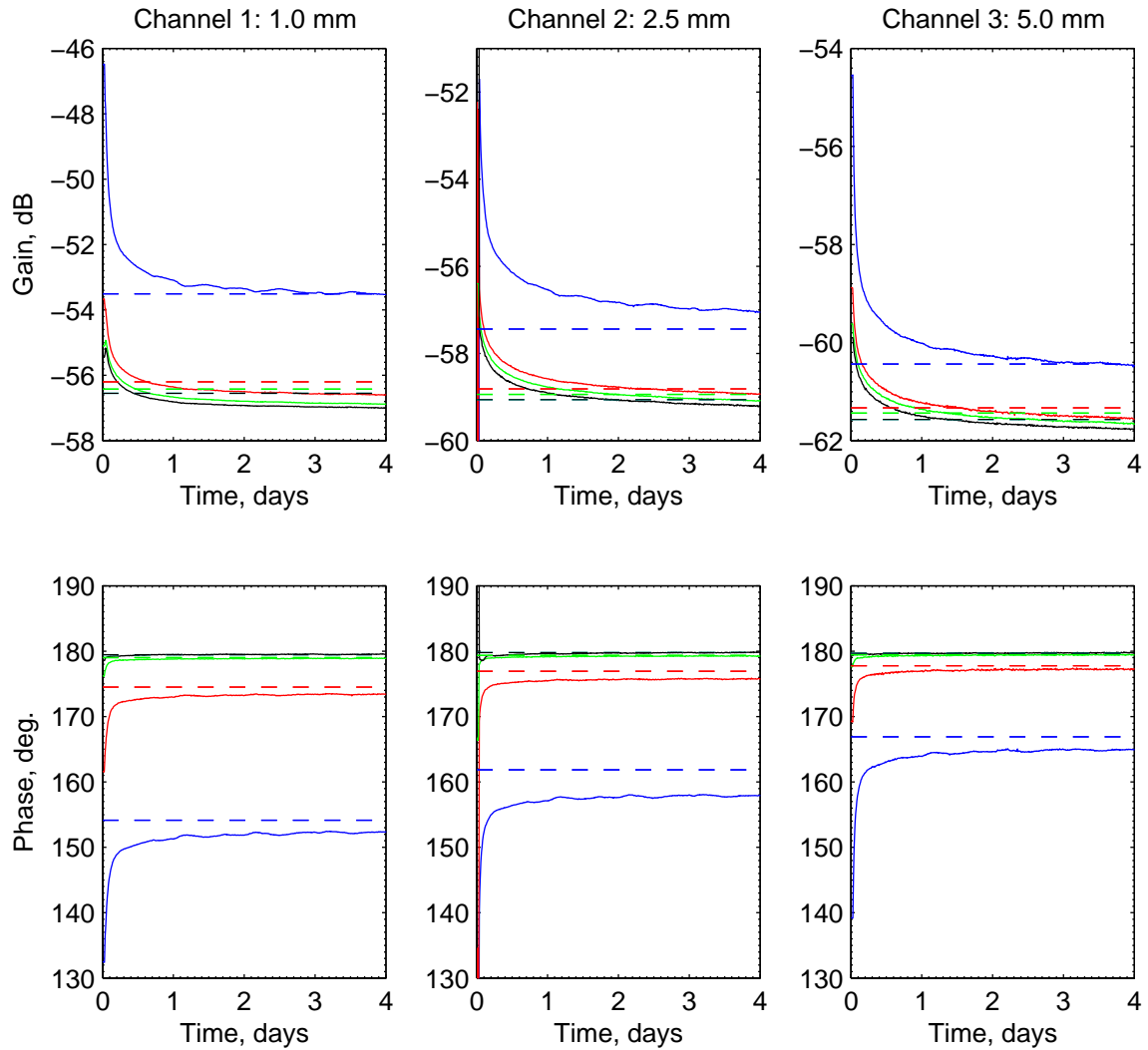


Figure 8-25: Unwrapped three conductor cable moisture egress measurements at 155 °F using a ϕ periodic sensor. To compare the steady state response, before and after the experiment, dashed lines show the response before the experiment ($t = 0$) from Fig. 8-24. Measurements are shown for frequencies of 10 (blue), 100 (red), 1,000 (green), and 10,000 (black) Hz. Feedback capacitance is 5 nF for each channel.



Figure 8-26: Photographs of a birch rod in the sling clamping mechanism with a z periodic sensor. The tightness of the clamp is adjusted by the wing nuts. Several layers of rubber are used to protect the sensor and limit the exposed area to the front surface.

8.2 Transient Measurements Using z Periodic Sensors

The z periodic sensor provides details of the effective permittivity profile along axis of the test material. This is superior to the ϕ periodic sensor which effectively integrates the response of the profile and reports a single measurement. To infer the effective permittivity profiles from the experimental measurements, a diffusion coefficient must be assumed and then verified. Here the profiles are determined directly from measurements and the nature of the diffusion process need not be assumed.

Because the z periodic sensor connections are made along the edge of the cylinder a different clamping mechanism is used. An experimental setup using the z periodic sensor in the sling clamp is shown in Fig. 8-26

In the experiments in this section only one end of the MUT is exposed to the moist air. The curved side and opposite end are covered to prevent moisture flux. Measurements are presented for birch, maple, and the single conductor cable.

8.2.1 z Periodic Birch Wood Rod Transient Measurements

A birch rod with a $1\frac{1}{4}$ inch diameter is measured with the six channel z periodic sensor. The rod is sealed at the back end by wax so that moisture can only enter through the front end of the rod. The relative humidity is maintained at 60% by a small pool at the bottom of the chamber. The average temperature during the measurement is 128.16°F with a standard deviation of 1.3°F . The temperature and humidity log is shown in Fig. 8-27.

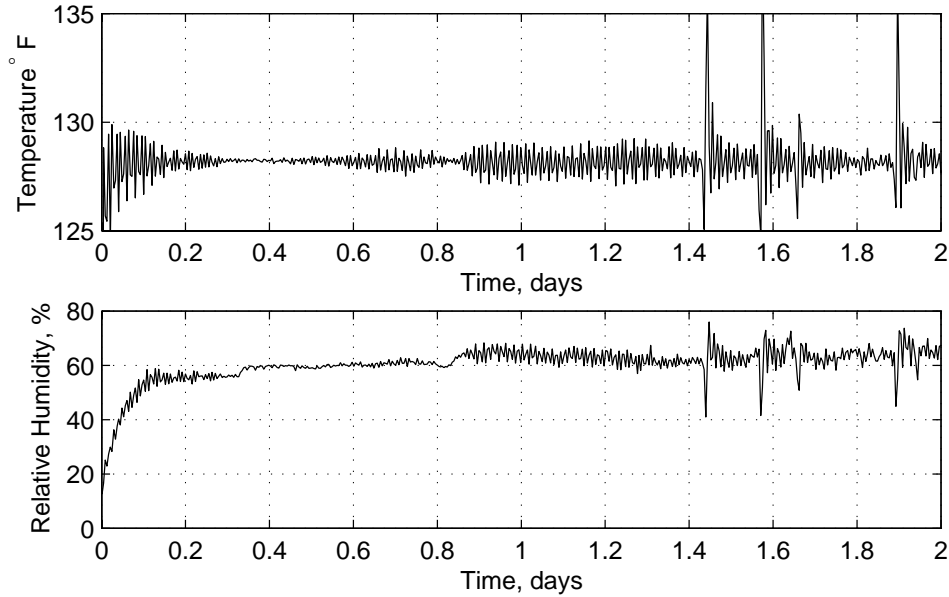


Figure 8-27: Birch rod diffusion experiment transient temperature (128 °F) and relative humidity log for the z periodic sensor measurements.

Measurements are taken using interface boxes two and three for channels 4-6 and 1-3 respectively. All the measurements are normalized to a 5 nF feedback capacitance to allow for head to head comparison. Photographs of the clamp, rod and sensor can be seen in Fig. 8-26.

The measurement results for selected frequencies for the first two days of measurements are shown in Fig. 8-28. The full frequency scan measurements for selected times during the first two days of measurement are shown in Fig. 8-29.

It is difficult to visualize the diffusion process directly from Fig. 8-28. We can present the data as profiles of the measurement at a particular frequency by plotting the measurements at the corresponding locations along the rod. Figure 8-30 shows the relative gain profiles at several times for frequencies of 0.01, 0.1, 400, and 2,500 Hz. The measurements have all been zeroed at the initial time. The open face of the rod corresponds to 0 cm. The data points correspond to the center of the electrode channels.

Measurements at each frequency clearly show a left to right trend, indicative of the movement of moisture into the rod. As the frequency is increased the dynamic range of the relative gain decreases significantly. The changes in the imaginary part of the permittivity is much larger at low frequency leading to a much greater range in values at 0.01 Hz when compared to 2,500 Hz. Later in Section 9.4.2 these results are converted to permittivity which is then related to the moisture content. Profiles are then estimated in terms of moisture content.

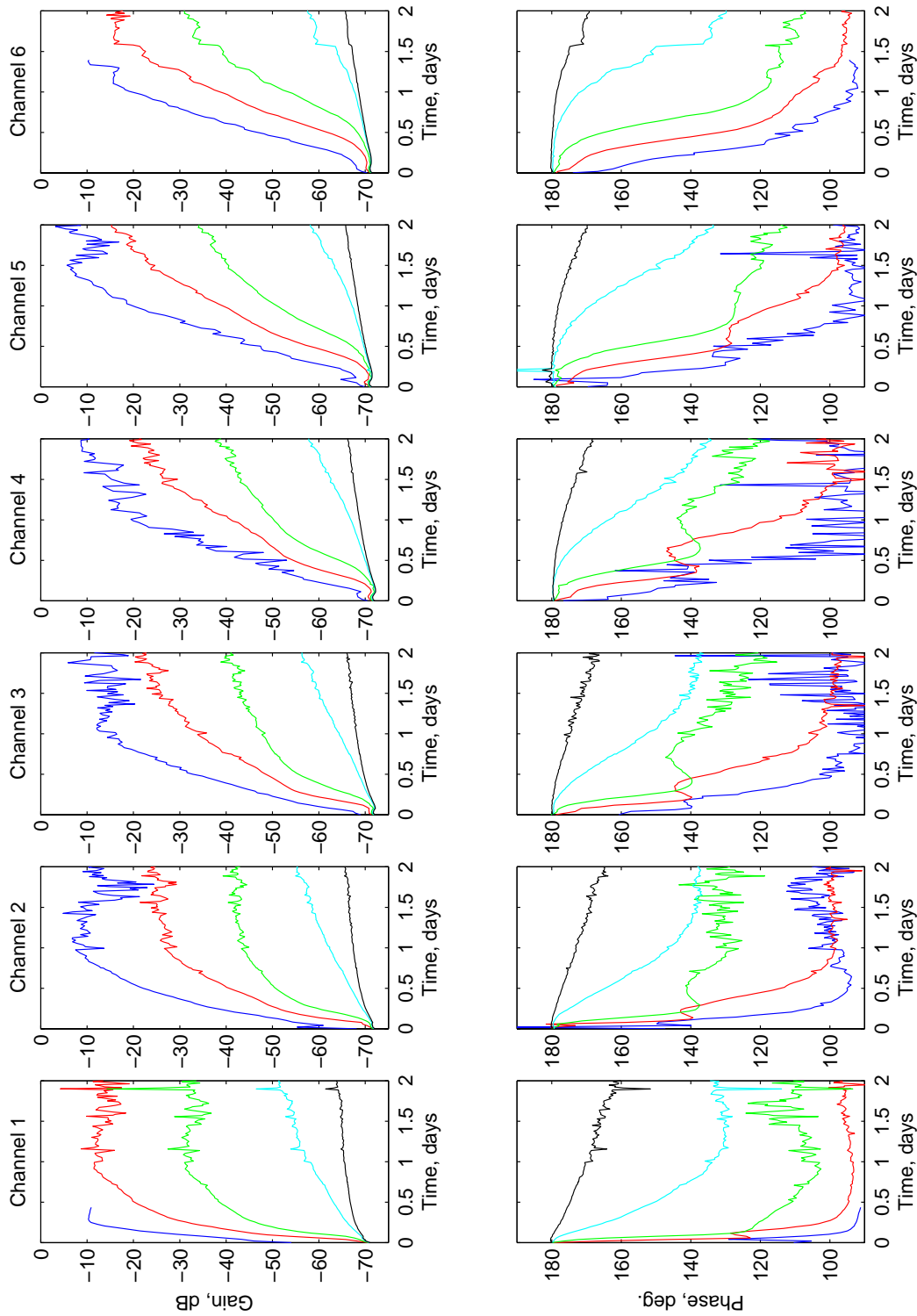


Figure 8-28: Birch rod measurements at 130 °F and 100% RH. Measurements are shown for frequencies of 0.01 (blue), 0.1 (red), 1.0 (green), 100 (cyan), and 2,500 (black) Hz. *This measurement was conducted from January 10 to January 23, 2007.*

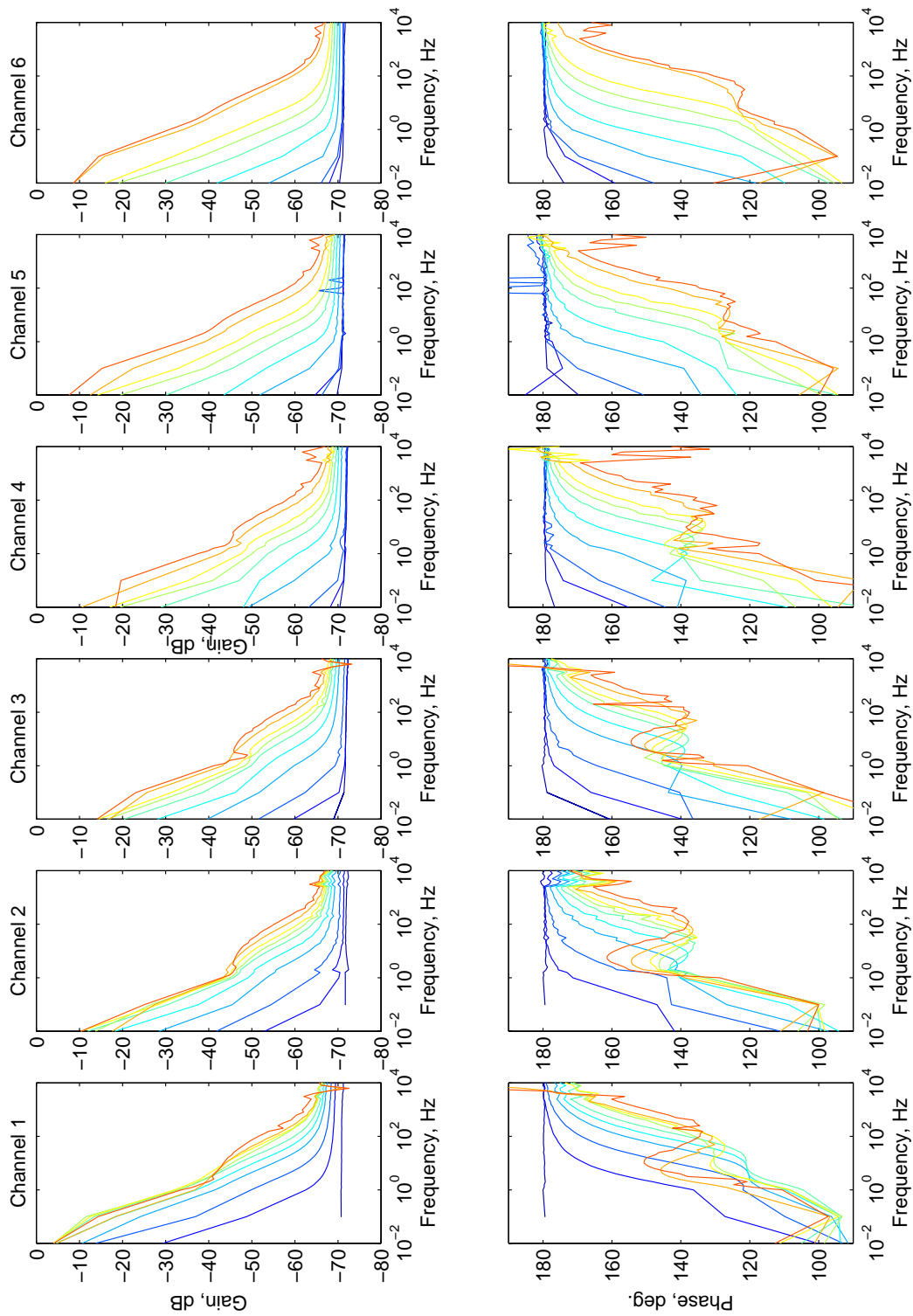


Figure 8-29: Birch rod measurements at 130 °F and 100% RH. Measurements are shown for times 0 (dark blue), 0.1, 0.2, 0.4, 0.6, 0.8, 1.0, 1.2, 1.6, and 2.0 days (red).

We note that the experimental measurements deteriorate in quality after the first 48 hours. This is due to the gradual failure of the clamping mechanism beginning around this time. Upon completion of the experiment the setup was investigated and the failure was noted. In subsequent measurements additional fasteners were used to prevent the problem from reoccurring.

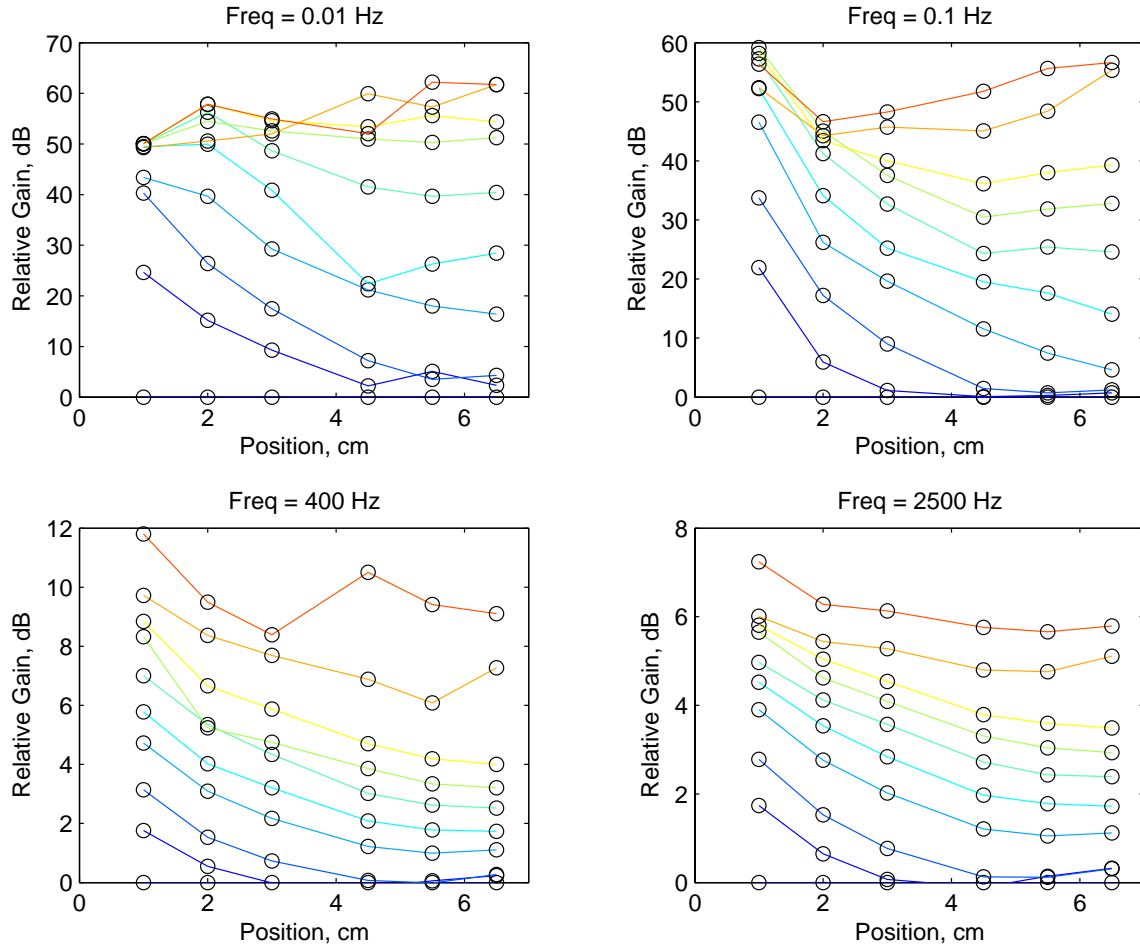


Figure 8-30: Birch rod relative gain profiles at 0.01, 0.1, 400, and 2,500 Hz. Gains have been normalized to 0 dB at time zero. Curve times are 0 (dark blue), 0.1, 0.2, 0.4, 0.6, 0.8, 1.0, 1.2, 1.6, and 2.0 days (red). Position 0 cm corresponds to the open face of the rod.

8.2.2 z Periodic Maple Wood Rod Transient Measurements

Similar measurements are made using a 1 1/4 inch diameter maple rod, 3 1/2 inches in length.

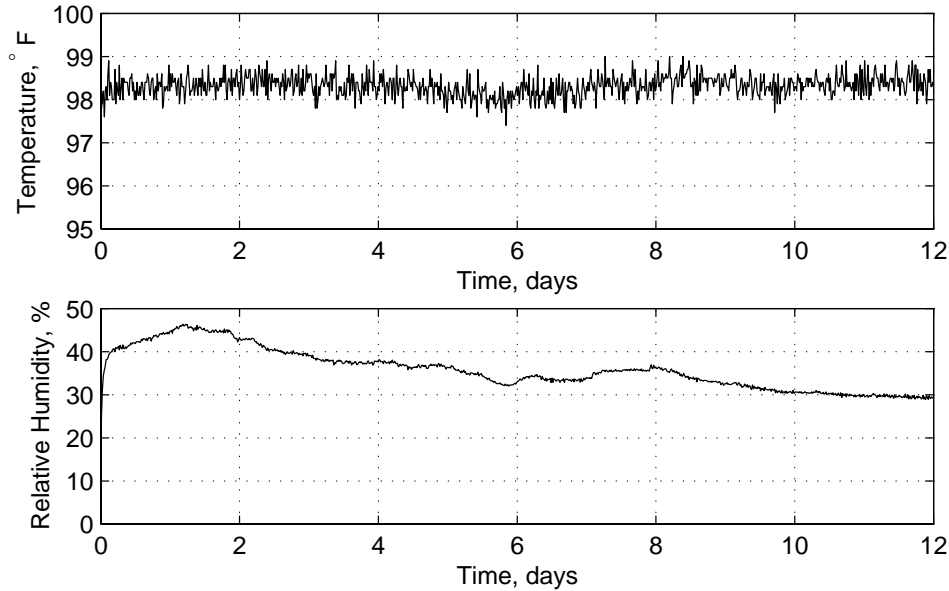


Figure 8-31: Maple rod diffusion experiment transient temperature (98 °F) and relative humidity log for the z periodic sensor measurements.

Experiment 1: $T \approx 98$ °F

During the course of the measurement the temperature averaged 98.31 °F and had a standard deviation of 0.38 °F. At time zero the relative humidity was raised by adding 2 mL of tap water. The relative humidity peaked at 46% and slowly reduced to 29% by day 12. The temperature and relative humidity log are shown in Fig. 8-31.

The six channel sensor measurement results for selected frequencies are shown in Fig. 8-32. The time lag of the response is evident by looking at the 0.01 Hz curve (blue) and noting the shift to the right for the higher channels. Notice also how the lowest frequencies on channel 1 overcompensate in early time until moisture is allowed to seep further into the wood, resulting in the steady reduction in the relative humidity measurement.

An alternate view of the data is to look at all the measured frequencies at a few selected times. This is done in Fig. 8-33 where the complete measured spectrum is plotted at selected times. These measurements make it clear that the lower channels approach steady state much faster as the density of the lines near the final state (upper curves) decreases steadily from channel 1 to 6.

We investigate the profile of the measurements at several times and frequencies. The results shown in Fig. 8-34 demonstrate a clear left to right trend for the vast majority of measurements. The measurement was terminated slightly before steady state was completely reached, but the results

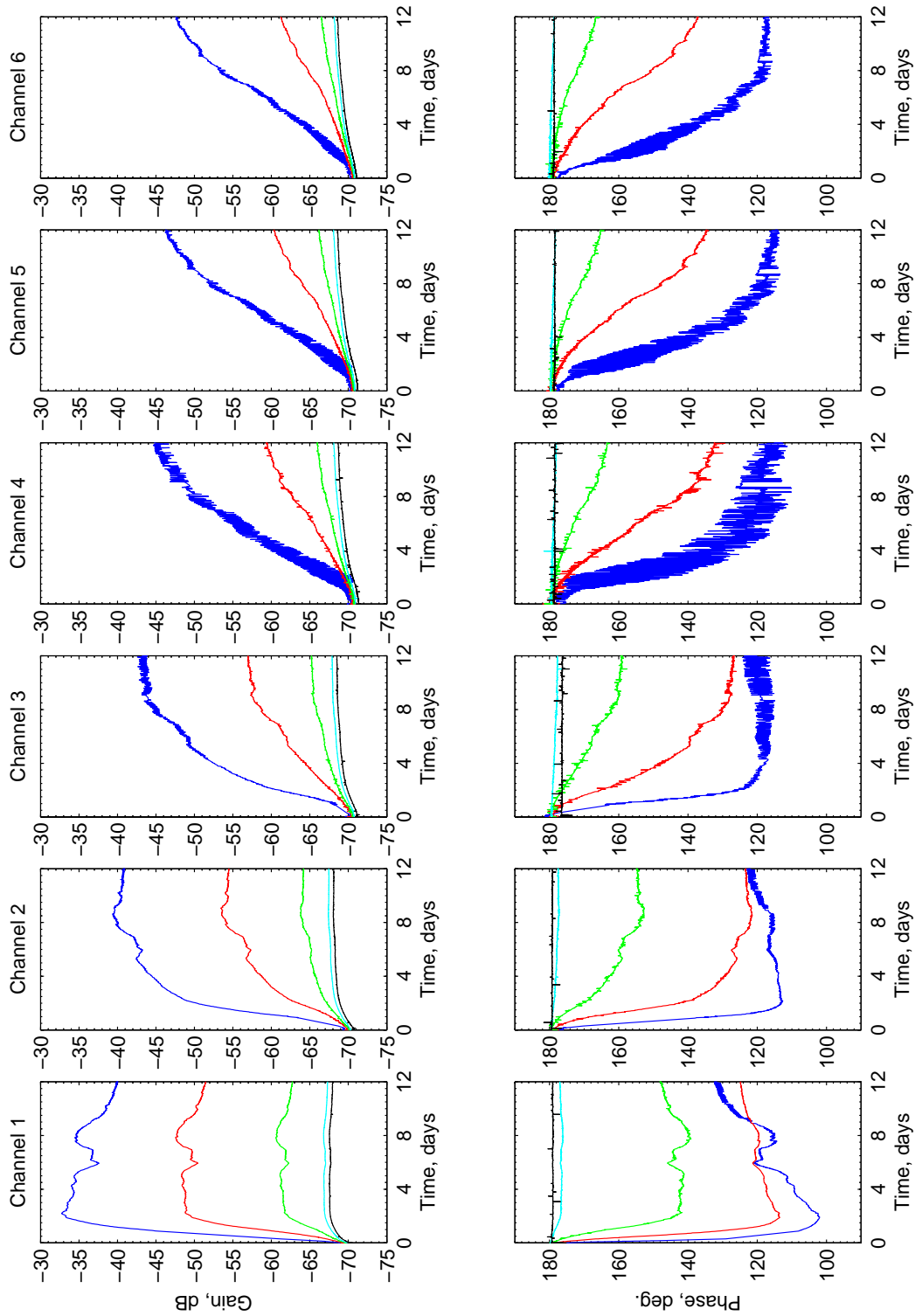


Figure 8-32: Maple rod measurements at 98 °F. Measurements are shown for frequencies of 0.01 (blue), 0.1 (red), 1.0 (green), 100 (cyan), and 10,000 (black) Hz. *This measurement was conducted from January 18 to January 22, 2007.*

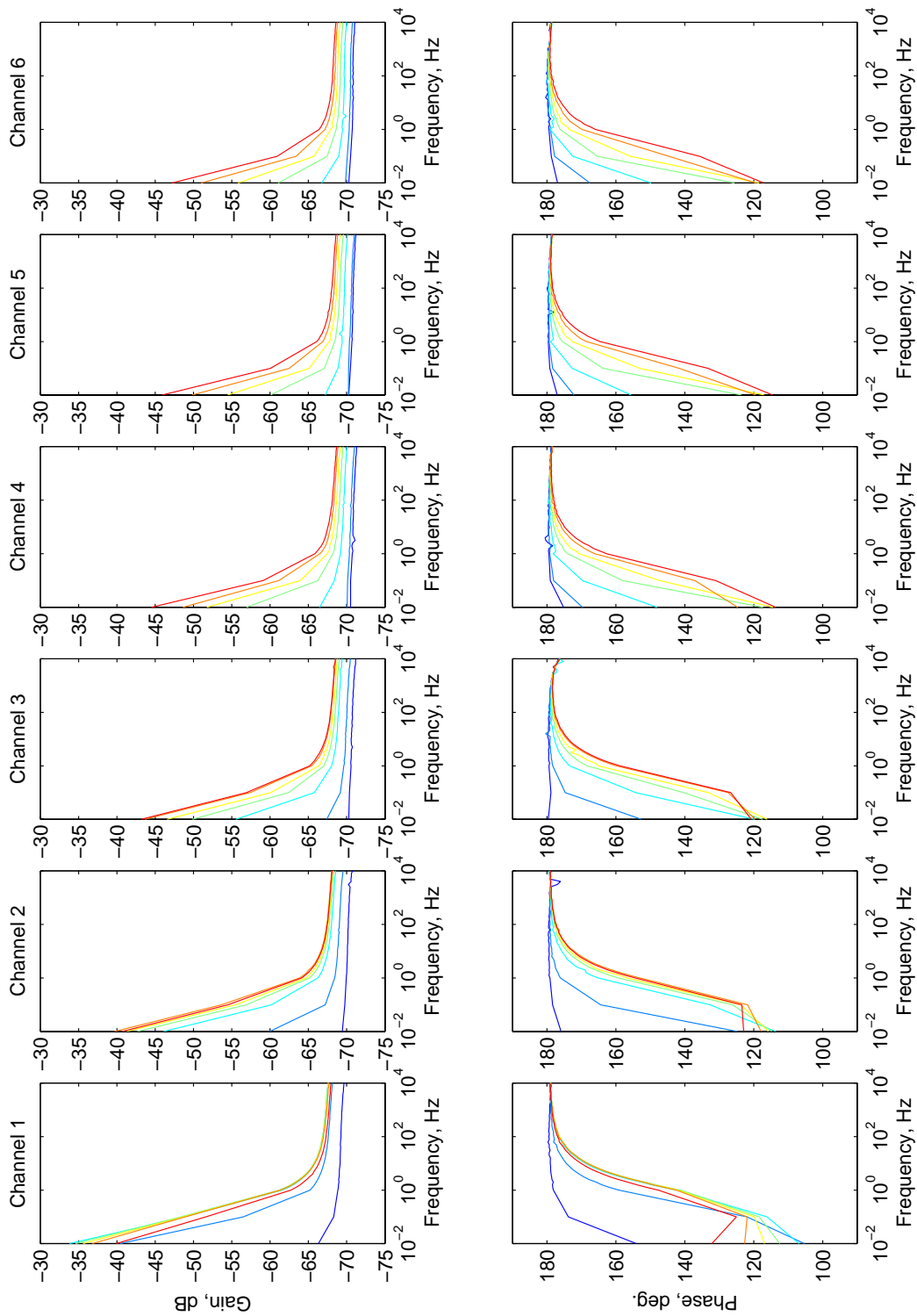


Figure 8-33: Maple rod frequency sweeps. Experiment temperature is 98 °F throughout. Measurement times shown are for 1 (dark blue), 2, 4, 6, 8, 10, and 13 days (red).

clearly show the approach to a new steady state.

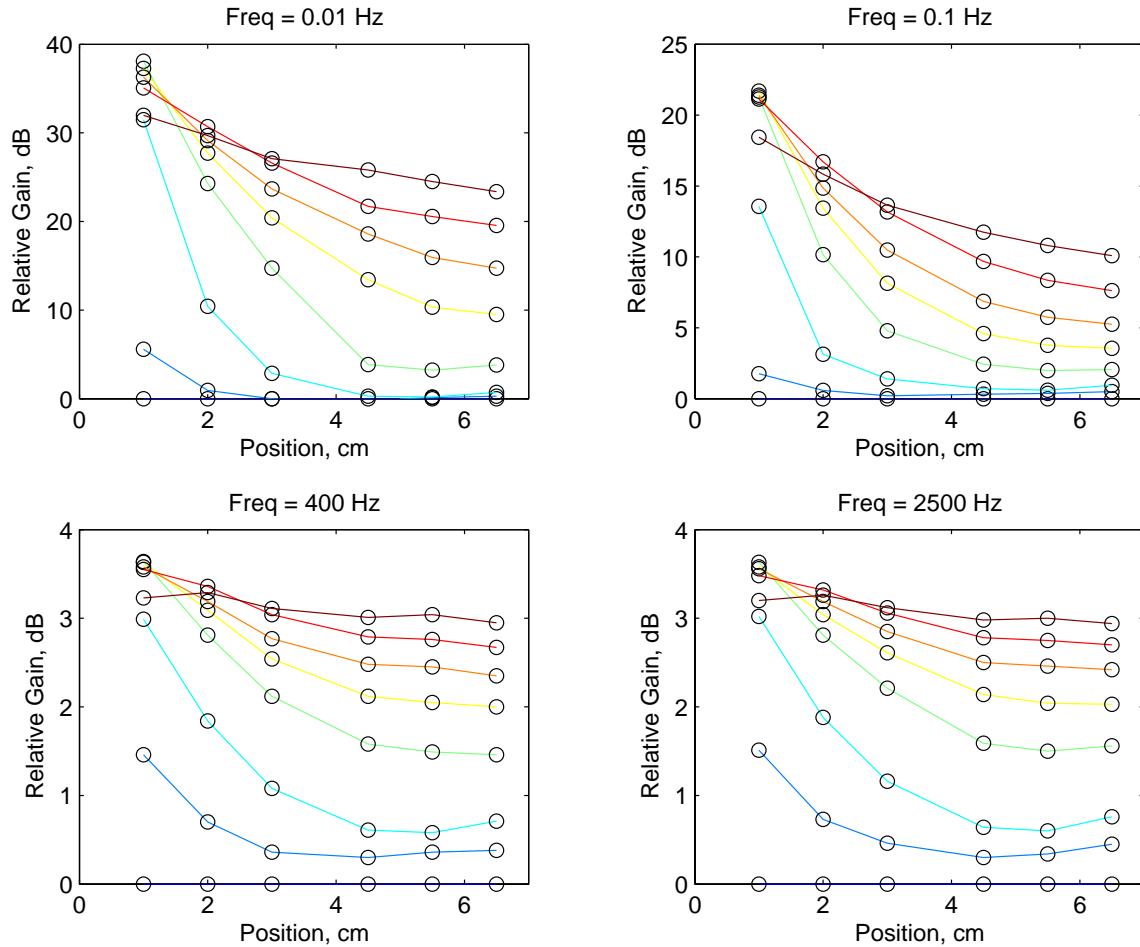


Figure 8-34: Maple rod relative gain profiles at 0.01, 0.1, 400, and 2,500 Hz. Gains have been normalized to 0 dB at time zero. Curve times are 0 (dark blue), 1, 2, 4, 6, 8, 10, and 13 days (red). Position 0 cm corresponds to the open face of the rod.

Experiment 2: $T \approx 127 \text{ }^\circ\text{F}$

During the course of the measurement the temperature averaged $126.6 \text{ }^\circ\text{F}$ and had a standard deviation of $1.6 \text{ }^\circ\text{F}$. At time zero the relative humidity was raised. The relative humidity averaged 27.2% with a standard deviation of 2.3% . The temperature and relative humidity log are shown in Fig. 8-35.

The six channel sensor measurement results for selected frequencies are shown in Fig. 8-36. The time lag of the response is evident by looking at the 0.01 Hz curve (blue) and noting the shift to

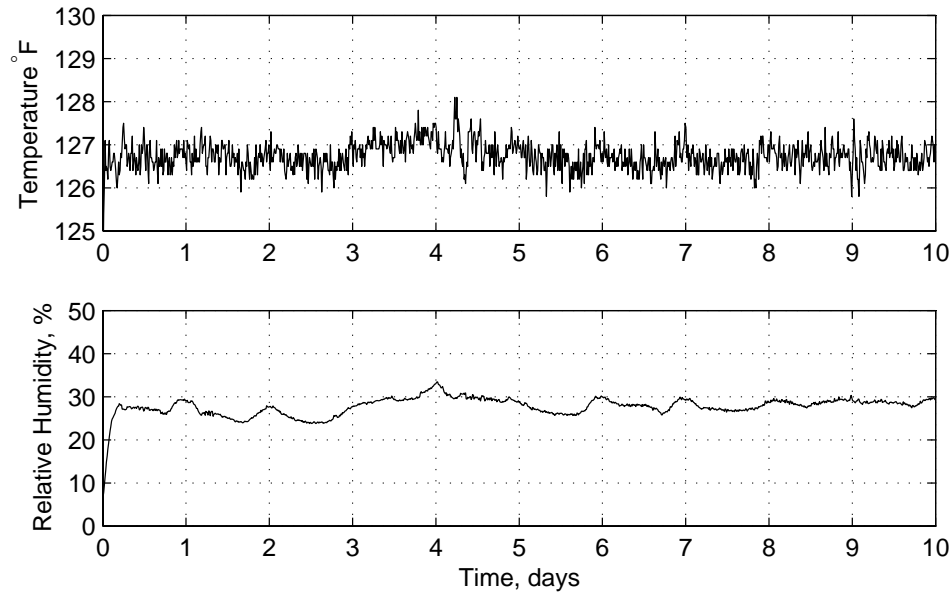


Figure 8-35: Maple rod diffusion experiment transient temperature (127 °F) and relative humidity log for the z periodic sensor measurements.

the right for the higher channels. Because the relative humidity is nearly constant throughout the experiment the gain increases are nearly monotonic.

Figure 8-37 shows the where the complete measured spectrum is plotted at selected times. These measurements make it clear that the lower channels approach steady state much faster as the density of the lines near the final state (upper curves) decreases steadily from the channel 1 to 6.

In Fig. 8-38 the relative gain profiles are plotted at four frequencies for selected times. A very clear left to right trend is visible which corresponds to the direction of moisture transfer. It is clear that the gain is changes most dramatically for the low frequency measurements. Later in Section 9.4.1 these results are converted to permittivity which is then related to the moisture content. Profiles are then estimated in terms of moisture content.

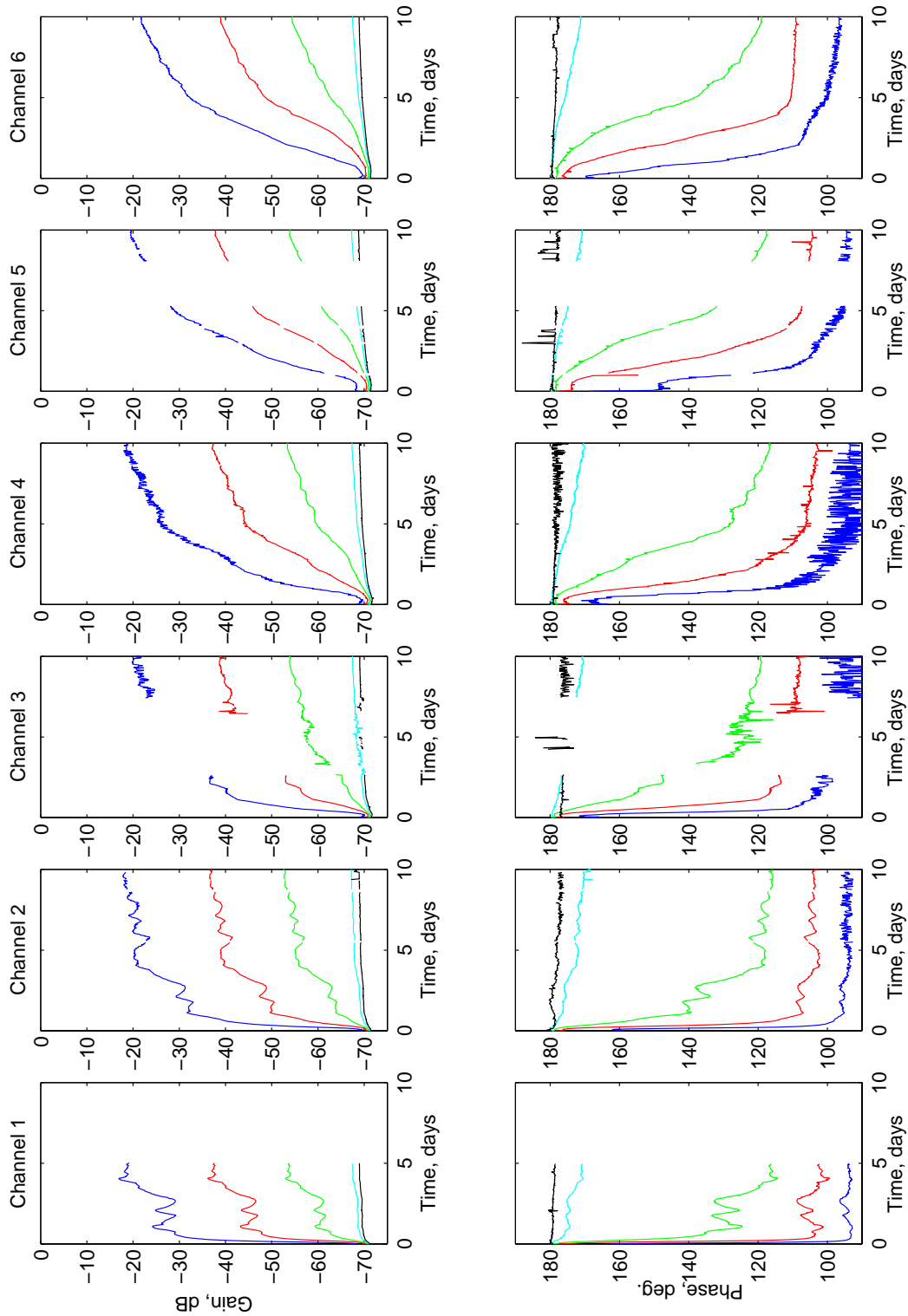


Figure 8-36: Maple rod measurements at 127 °F. Measurements are shown for frequencies of 0.01 (blue), 0.1 (red), 1.0 (green), 100 (cyan), and 10,000 (black) Hz. *This measurement was conducted from January 24 to February 6, 2007.*

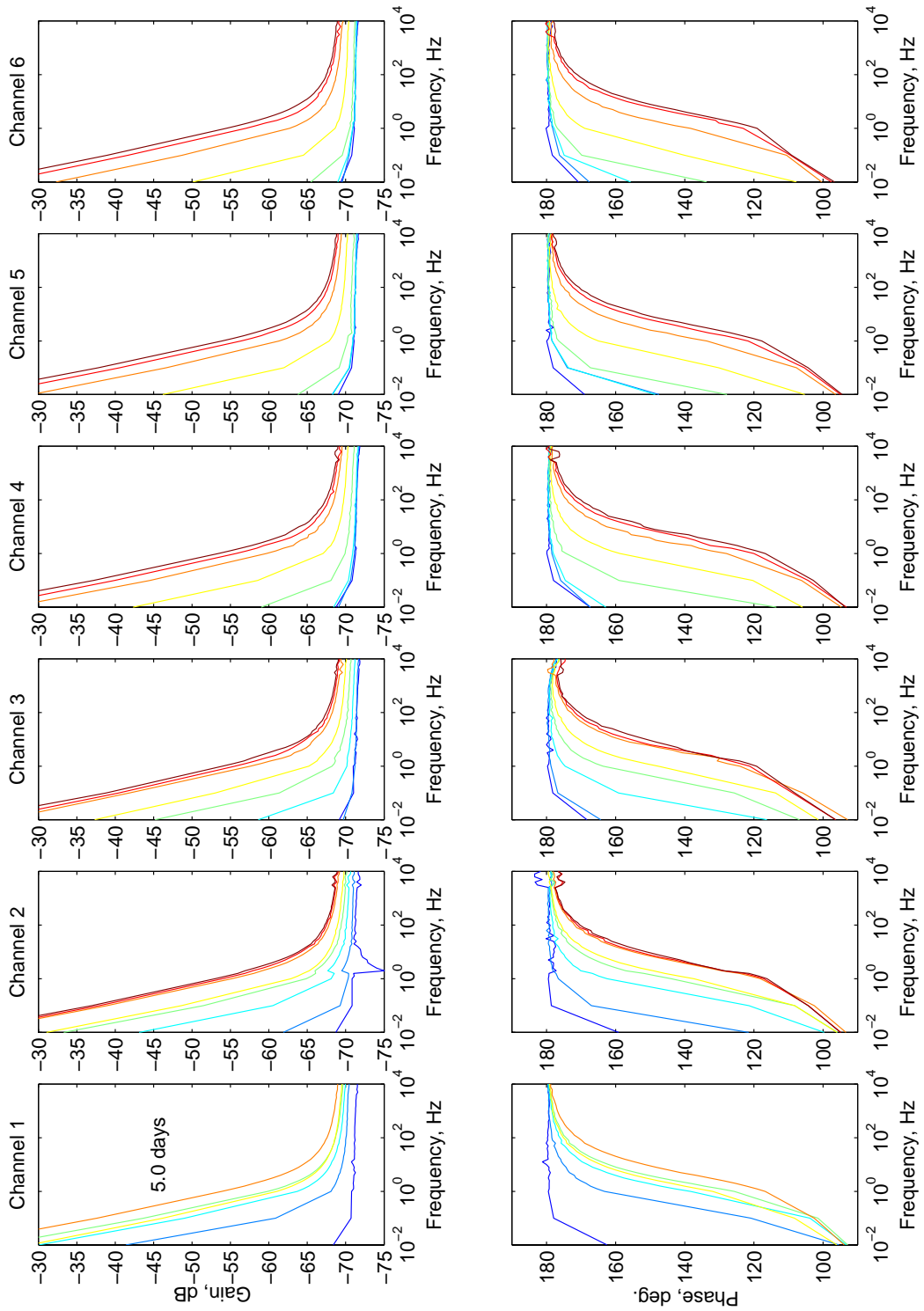


Figure 8-37: Maple rod frequency sweeps. Experiment temperature is 127 °F throughout. Measurement times shown are for 0.0 (dark blue), 0.2, 0.5, 1.0, 2.5, 5.0, 8.1, and 9.8 days (red).

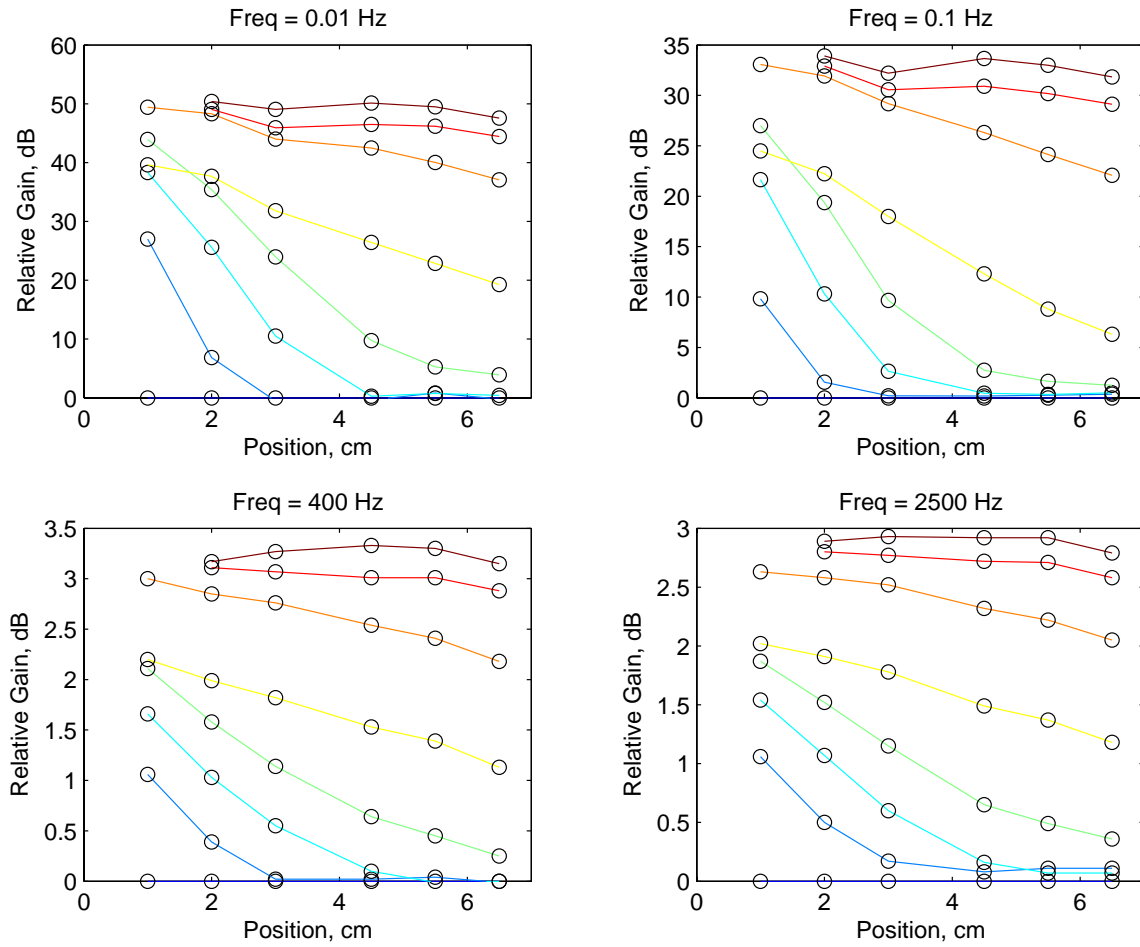


Figure 8-38: Maple rod relative gain profiles at 0.01, 0.1, 400, and 2,500 Hz. Gains have been normalized to 0 dB at time zero. Curve times are 0.0 (dark blue), 0.2, 0.5, 1.0, 2.5, 5.0, 8.1, and 9.8 days (red). Position 0 cm corresponds to the open face of the rod.

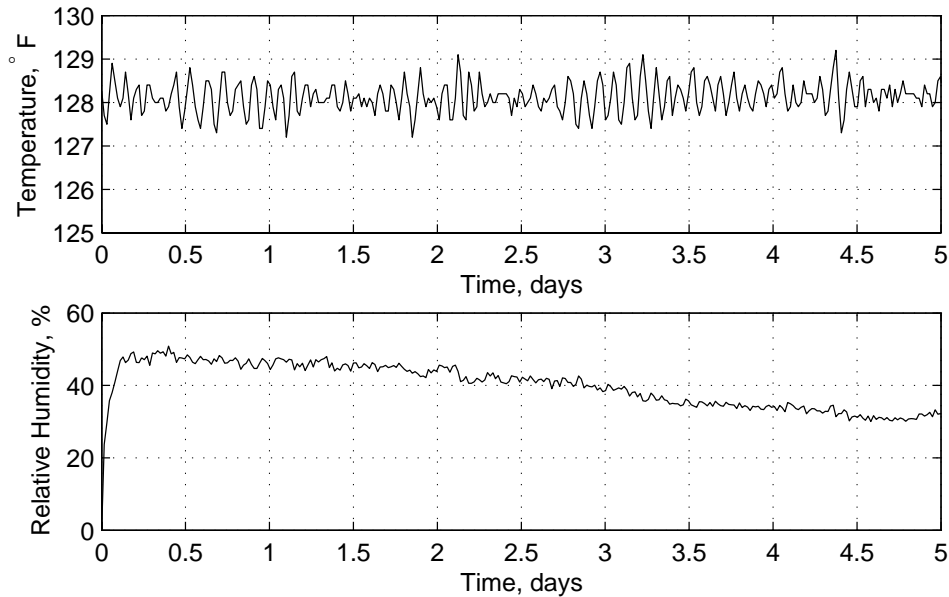


Figure 8-39: Transient % relative humidity during moisture diffusion into the single conductor cable using the z periodic sensor.

8.2.3 z Periodic Single Conductor Cable Transient Measurements

In this experiment the single conductor cable is placed in the measurement chamber and dried for four days. The z periodic sensor is wrapped around the cable using the sling clamp and all boundaries are sealed besides one end of the cable which is left exposed for moisture to enter the cable. During the experiment which lasted nearly 12 days the temperature averaged $128.1\text{ }^{\circ}\text{F}$ (standard deviation $0.40\text{ }^{\circ}\text{F}$). At time zero the relative humidity is raised by injecting 1 mL of tap water into the chamber. Shortly thereafter the humidity is rises to 51% and falls slowly to 25% on the eighth day when the chamber was evacuated. The temperature and relative humidity log for the experiment in shown in Fig. 8-39.

The gain and phase of the six channel measurements are plotted at selected frequencies in Fig 8-40. The 0.01 Hz sensor measurements saturates as a result of the feedback capacitance being too small. The saturated data is shown in the figure as a dotted line. Channel 5 had intermittent failures during the first three days of measurements.

The full frequency spectrum of the data at selected times is plotted in Fig. 8-41. It clearly shows that the measured gain and phase shifts in frequency as the moisture diffuses through the cable. Note that only times 0, 1, 3, 4, and 5 days are plotted for channel 5.

Relative gain profiles are plotted in Fig. 8-42 for four selected frequencies. It is seen that the

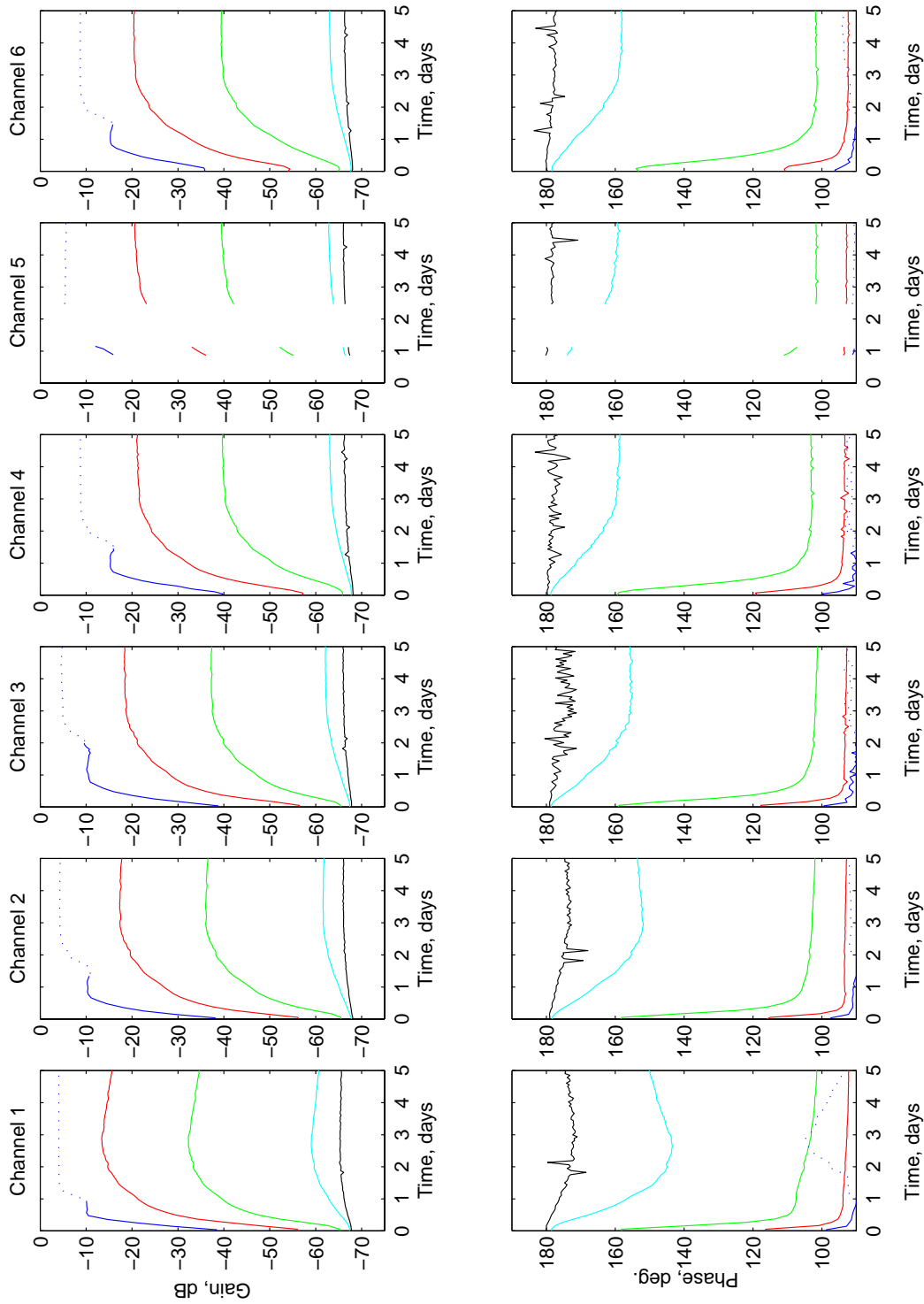


Figure 8-40: Single conductor cable measurements at 128 °F. Measurements are shown for frequencies of 0.01 (blue), 0.1 (red), 1.0 (green), 100 (cyan), and 10,000 (black) Hz. The dotted line indicates the 0.01 Hz measurements thought to saturate the controller box. *This measurement was conducted from January 25 to February 14, 2007.*

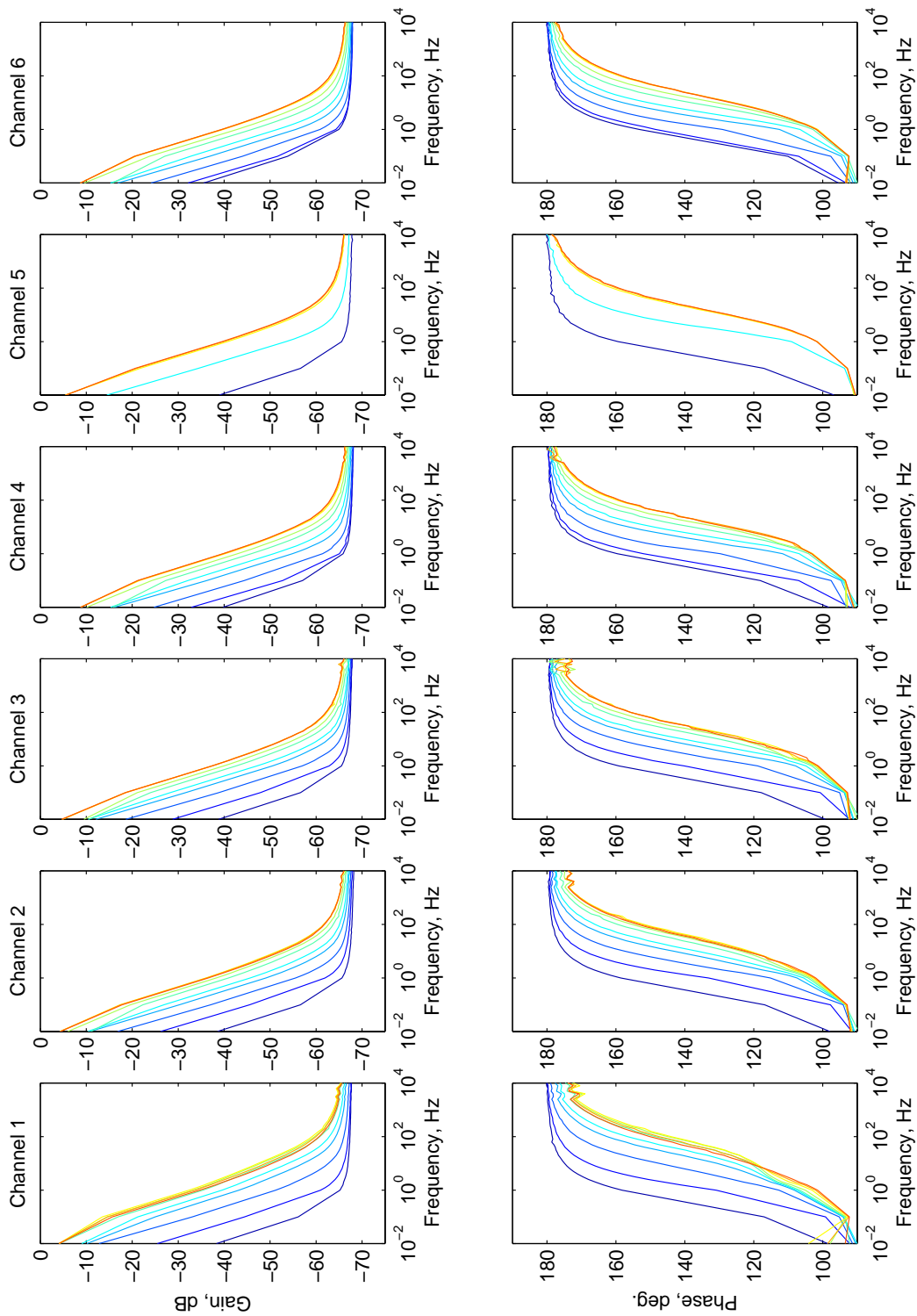


Figure 8-41: Single conductor cable at 128 °F. Measurement times shown are for 0.0 (dark blue), 0.2, 0.4, 0.7, 1, 1.5, 2, 3, 4, and 5 (red) days.

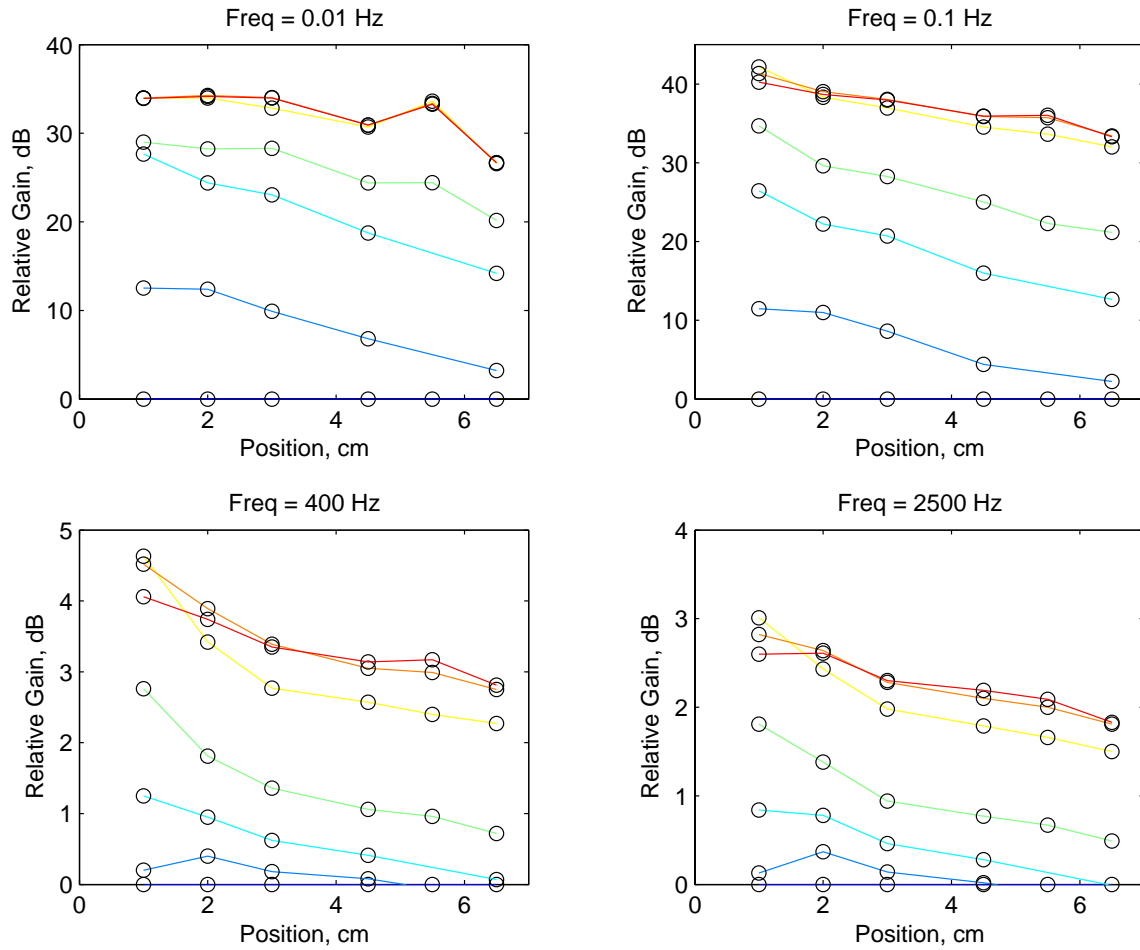


Figure 8-42: Single conductor cable relative gain profiles at 0.01, 0.1, 400, and 2,500 Hz. Gains have been normalized to 0 dB at time zero. Curve times are 0.0 (dark blue), 0.2, 0.5, 1.0, 2.5, 4.0, and 5.0 days (red). Position 0 cm corresponds to the open face of the cable.

gain shows a moderate slope downward, however the moisture diffuses quickly into the cable. It is expected that moisture may be able to move quickly through the stranded cable in the center or between the sensor and insulation. These measurements are analyzed further in Section 9.4.3.

8.3 Chapter Summary

In this chapter we have presented a series of moisture transient measurements for a variety of materials. Each experiment is conducted at a fixed temperature. Moisture is permitted into the measurement chamber and the dielectric response is recorded at several frequencies until steady state is reached. It was confirmed that Teflon is extremely hydrophobic (Section 8.1.1). On the

other hand, the wood and cable samples have responses that vary greatly with the environmental conditions.

Experiments have been organized by the sensor technology used. In Section 8.1 the ϕ periodic sensor is used. Experimental results were presented for Teflon, Birch, and the two PILC cable designs. In Section 8.2 the z periodic sensor is used. Experiments are presented for birch, maple, and the two PILC cable designs. Additional analysis for some measurements is also provided in Section B.2 as noted throughout the chapter.

In the following chapter we consider several of these measurements more closely and perform analysis to estimate the diffusion characteristics.

Chapter 9

Moisture Diffusion

A diffusion process is defined by the movement of a concentration at a rate proportional to the gradient of that concentration. The diffusion equation describes many physical phenomena such as transport of heat, magnetic field penetration into ohmic conductors, and charge transport in semiconductors. In this chapter the equation is applied to the movement of moisture. We begin with a derivation of the diffusion equation based on the definition of diffusion.

Having derived the diffusion equation we find the solution for diffusion problems in one linear dimension with Dirichlet, Neumann, or mixed boundary conditions. A similar treatment is made of cylindrical diffusion problems. Two dimensional diffusion is considered for the radial-angular case, and the radial-axial case. These problems provide insight into how moisture diffusion proceeds in cable geometries. More general problems cannot be solved analytically and require the use of the finite element method (FEM) for a numerical solution.

Estimating the diffusion process from dielectrometry measurements is then discussed. Some of the experiments conducted in Chapter 8 are analyzed and concentration profiles are estimated.

9.1 The Diffusion Equation

The diffusion equation describes processes where a concentration (moisture, heat, magnetic field, charge density, etc.) flows from areas of high concentration to low concentration at a rate proportional to the concentration gradient.

9.1.1 Derivation of the Diffusion Equation

We derive the diffusion equation by considering the flow of moisture in a body [98]. We begin by stating an observation: *moisture flows in the direction of decreasing concentration at a rate that is proportional to the gradient of the concentration.* Mathematically this can be written

$$\vec{v} = -D\nabla\psi \quad (9.1)$$

where D is the moisture diffusion coefficient of the object and has units of meters squared per second, \vec{v} is the velocity of moisture flow, and ψ is the dimensionless moisture concentration as a function of space and time. In general, D can be a function of ψ , time, and space, but in many cases, $D = D_o$ can be a constant. Let V be a volume with closed surface S . The rate of moisture leaving V through S is

$$\iint_S \vec{v} \cdot d\vec{a} = \iiint_V \nabla \cdot \vec{v} dV = - \iiint_V \nabla \cdot (D\nabla\psi) dV \quad (9.2)$$

The total volume of moisture, V_m , in the volume V is

$$V_m = \iiint_V \psi dV \quad (9.3)$$

The time rate of moisture entering the volume V must be equal to the rate of moisture entering through the surface S .

$$\frac{\partial V_m}{\partial t} = \iiint_V \frac{\partial \psi}{\partial t} dV = \iiint_V \nabla \cdot (D\nabla\psi) dV \quad (9.4)$$

This can be rewritten as

$$\iiint_V \left(\frac{\partial \psi}{\partial t} - \nabla \cdot (D\nabla\psi) \right) dV = 0 \quad (9.5)$$

Since the region V is arbitrary the integrand must be zero everywhere if continuous.

$$\frac{\partial \psi}{\partial t} = \nabla \cdot (D\nabla\psi) \quad (9.6)$$

The diffusion equation is a parabolic partial differential equation. In the steady state the equation reduces to an elliptical differential equation known as the Laplace equation which was used extensively in Chapter 3 to solve for the electric scalar potential. When the diffusion coefficient is constant, $D = D_o$, the diffusion equation 9.6 simplifies to the linear diffusion equation.

$$\frac{\partial \psi}{\partial t} = D_o \nabla^2 \psi \quad (9.7)$$

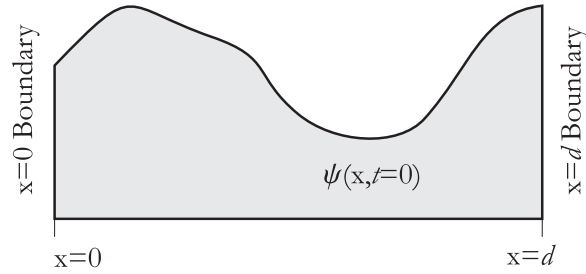


Figure 9-1: Illustration of the one dimensional diffusion problem. The problem is specified by the boundary conditions at $x = 0$ and $x = d$, the initial condition $\psi(x, t = 0)$, and the diffusion coefficient, D .

In one linear dimension this equation reduces to

$$\frac{\partial \psi}{\partial t} = D_o \frac{\partial^2 \psi}{\partial x^2} \quad (9.8)$$

9.1.2 Solution to the Linear 1D Diffusion Equation

We now derive the solution to the one dimensional linear diffusion equation (eq. 9.8) and provide illustrations through a series of examples. The basic problem scenario is shown in Fig. 9-1 when $D = D_o$. A region extending from $x = 0$ to $x = d$ has a known initial concentration $\psi(x, t = 0)$. A solution for ψ as a function of x and t can be found when appropriate boundary conditions are specified at $x = 0$ and $x = d$. Two types of boundary conditions are typically applied. A general Dirichlet boundary condition specifies the concentration, $\psi(x_o, t) = A_o(t)$, at the boundary for all time. A general Neumann boundary condition specifies the spatial derivative of the concentration, $\partial \psi(x, t) / \partial x|_{x=x_o} = B_o(t)$, at the boundary.

In steady state the problem reduces to the Laplace equation. Reducing eq. 9.8 to its steady state form we have

$$\frac{\partial^2 \psi_{ss}}{\partial x^2} = 0 \rightarrow \psi_{ss}(x) = Ax + B \quad (9.9)$$

The coefficients A and B can be found from the boundary conditions.

In cases of interest, the initial conditions will be different than the steady state form. To find the transient behavior we must solve the full diffusion equation of eq. 9.8. Given the similarity to the Laplace equation we are motivated to use the separation of variables solution technique for a homogeneous solution.

$$\psi_h(x, t) = X(x)T(t) \quad (9.10)$$

Substituting into eq. 9.8 and rearranging we have

$$\frac{1}{X} \frac{d^2 X}{dx^2} = \frac{1}{D_o T} \frac{dT}{dt} = -\alpha^2 \quad (9.11)$$

where $-\alpha^2$ is introduced as the separation constant. This equation can be rewritten as two ordinary differential equations so that $X(x)$ and $T(t)$ can be solved for separately.

$$\frac{d^2 X}{dx^2} + \alpha^2 X = 0 \quad (9.12)$$

$$\frac{dT}{dt} + \alpha^2 D_o T = 0 \quad (9.13)$$

The solutions to eq. 9.12 are complex exponentials, or equivalently sines and cosines.

$$X(x) = A_1 \sin \alpha x + A_2 \cos \alpha x \quad (9.14)$$

The solutions to eq. 9.13 are exponential.

$$T(t) = e^{-\alpha^2 D_o t} \quad (9.15)$$

We can now write the general solution.

$$\psi_h(x, t) = e^{-\alpha^2 D_o t} (A_1 \sin \alpha x + A_2 \cos \alpha x) \quad (9.16)$$

It is now clear that the choice of separation constant $-\alpha^2$ was made to insure α is real in the general solution, eq. 9.16. The solution remains bounded as $t \rightarrow \infty$. In most problems, the solution will involve an infinite series of solutions, each with different values of α , A_1 , and A_2 . We define the time constant of a process in terms of the smallest allowed value of α , and the diffusion coefficient.

$$\tau = \frac{1}{\alpha^2 D_o} \quad (9.17)$$

We also see that the initial condition is described entirely by $X(x)$. The boundary conditions will determine the allowed values of α . We now solve for the coefficients for representative case studies using various combinations of Dirichlet and Neumann boundary conditions.

Dirichlet Boundary Conditions

Consider the diffusion problem where the boundaries have a fixed concentration

$$\psi(0, t) = B_1 \quad (9.18)$$

$$\psi(d, t) = B_2 \quad (9.19)$$

The solution can be written as the homogeneous solution plus the steady state solution.

$$\psi(x, t) = \psi_h(x, t) + \psi_{ss}(x) \quad (9.20)$$

The steady state equation is found by applying the boundary conditions to eq. 9.9.

$$\psi_{ss}(x) = \left(\frac{B_2 - B_1}{d} \right) x + B_1 \quad (9.21)$$

The homogeneous solution is found by using homogeneous boundary conditions which imply $A_2 = 0$ and $\alpha = n\pi/d$ in eq. 9.16, where n is a positive integer. The homogeneous solution is a linear superposition of the individual harmonics.

$$\psi_h(x, t) = A_{1,1} \sin\left(\frac{\pi}{d}x\right) e^{-(\frac{\pi}{d})^2 D_o t} + A_{1,2} \sin\left(\frac{2\pi}{d}x\right) e^{-(\frac{2\pi}{d})^2 D_o t} + \dots \quad (9.22)$$

The coefficients will be determined by the initial condition, $\psi(x, t = 0)$, which must be given. We set the initial condition equal to the solution at time zero.

$$\psi(x, t = 0) = \psi_{ss}(x) + \sum_{n=1}^{\infty} A_n \sin\left(\frac{n\pi}{d}x\right) \quad (9.23)$$

Moving the steady state term to the left hand side, multiplying both sides by $\sin(m\pi x/d)$, and integrating, we find the coefficients.

$$A_n = \frac{2}{d} \int_0^d (\psi(x, t = 0) - \psi_{ss}(x)) \sin\left(\frac{n\pi}{d}x\right) dx \quad (9.24)$$

This result is found by making use of the orthogonality property of the sine functions for $m \neq n$.

Neumann Boundary Conditions

Neumann boundary conditions specify the derivatives at the boundaries.

$$\left. \frac{\partial \psi}{\partial x} \right|_{x=0} = C_1 \quad (9.25)$$

$$\left. \frac{\partial \psi}{\partial x} \right|_{x=d} = C_2 \quad (9.26)$$

The solution is again of the form in eq. 9.20. A steady state solution to eq. 9.9 can be found only if $C_1 = C_2$. We consider this case. The steady state equation is $\psi_{ss} = C_1x + B$, B to be found. B is found by setting the integrals of the initial condition and the steady state equation equal. The steady state solution is found to be

$$\psi_{ss}(x) = C_1x + \frac{\int_0^d \psi(x, t=0) dx - \frac{C_1 d^2}{2}}{d} \quad (9.27)$$

Notice that the steady state concentration will take negative values if the numerator is negative.

To find the homogeneous solution, we consider homogeneous Neumann boundary conditions which imply $A_1 = 0$ and $\alpha = n\pi/d$ in eq. 9.16, where n is a positive integer. The total solution is

$$\psi(x, t) = \psi_{ss}(x) + \sum_{n=1}^{\infty} e^{-\alpha_n^2 D_o t} A_n \cos \alpha_n x \quad (9.28)$$

where A_n is found by applying the orthogonality principle.

$$A_n = \frac{2}{d} \int_0^d (\psi(x, t=0) - \psi_{ss}(x)) \cos \left(\frac{n\pi}{d} x \right) dx \quad (9.29)$$

Dirichlet and Neumann Boundary Conditions

Finally we consider the case where the boundary conditions are

$$\psi(0, t) = B \quad (9.30)$$

$$\left. \frac{\partial \psi}{\partial x} \right|_{x=d} = C \quad (9.31)$$

The steady state concentration is $\psi_{ss}(x) = Cx + B$. To avoid negative values, $B > -Cd$. The solution is of the form

$$\psi(x, t) = \psi_{ss}(x) + \sum_{n=1}^{\infty} e^{-\alpha_n^2 D_o t} (A_n \sin \alpha_n x + B_n \cos \alpha_n x) \quad (9.32)$$

Table 9.1: One Dimensional Diffusion Examples. $D_o = 1$

Example	$\psi(x, t = 0)$	$x = 0$		$x = 1$	
		Dirichlet	Neumann	Dirichlet	Neumann
1	$\cos(\pi x/d + \pi/5) + 1$	0	×	0	×
2	$\cos(\pi x/d + \pi/5) + 1$	0	×	1	×
3	$\cos(\pi x/d + \pi/5) + 1$	×	0	×	0
4	$\cos(\pi x/d + \pi/5) + 1$	×	1	×	1
5	0	1	×	×	0
5	0	1	×	0	×

By applying the Dirichlet boundary condition we find $B_n = 0$. By applying the Neumann boundary condition we find $\alpha = \pi(2n - 1)/2d$. The coefficients solution is

$$A_n = \frac{2}{d} \int_0^d (\psi(x, t = 0) - \psi_{ss}(x)) \sin\left(\frac{2n - 1}{2d} \pi x\right) dx \tag{9.33}$$

We note that it is non-physical to impose two boundary conditions at the same boundary. For example consider the following conditions

$$\psi(0, t) = B \tag{9.34}$$

$$\frac{\partial \psi}{\partial x} \Big|_{x=0} = C \tag{9.35}$$

Setting the gradient, implies supplying any moisture level necessary to achieve that gradient. If at the same time the concentration is fixed, there is no means to maintain the gradient. The boundary conditions cannot be enforced simultaneously except for time independent cases which are trivial since there is no diffusion.

1D Diffusion Examples

Examples are given to illustrate the behavior of the concentration function for various boundary conditions. The examples in this section are summarized in Table 9.1. In all the examples $D_o = 1$, and $d = 1$. In examples 1 through 4 and 6, the time constant is $\tau = \pi^{-2} \approx 0.1013$, but in example 5, where the boundary conditions are mixed, the time constant is $\tau = 4\pi^{-2} \approx 0.4053$.

9.1.3 Small Time or Semi-Infinite Length Diffusion

A second pair of solutions to the diffusion equation exists in the form of the error function. Most often these solutions are applied in cases that can be modeled as semi-infinite. For example, early

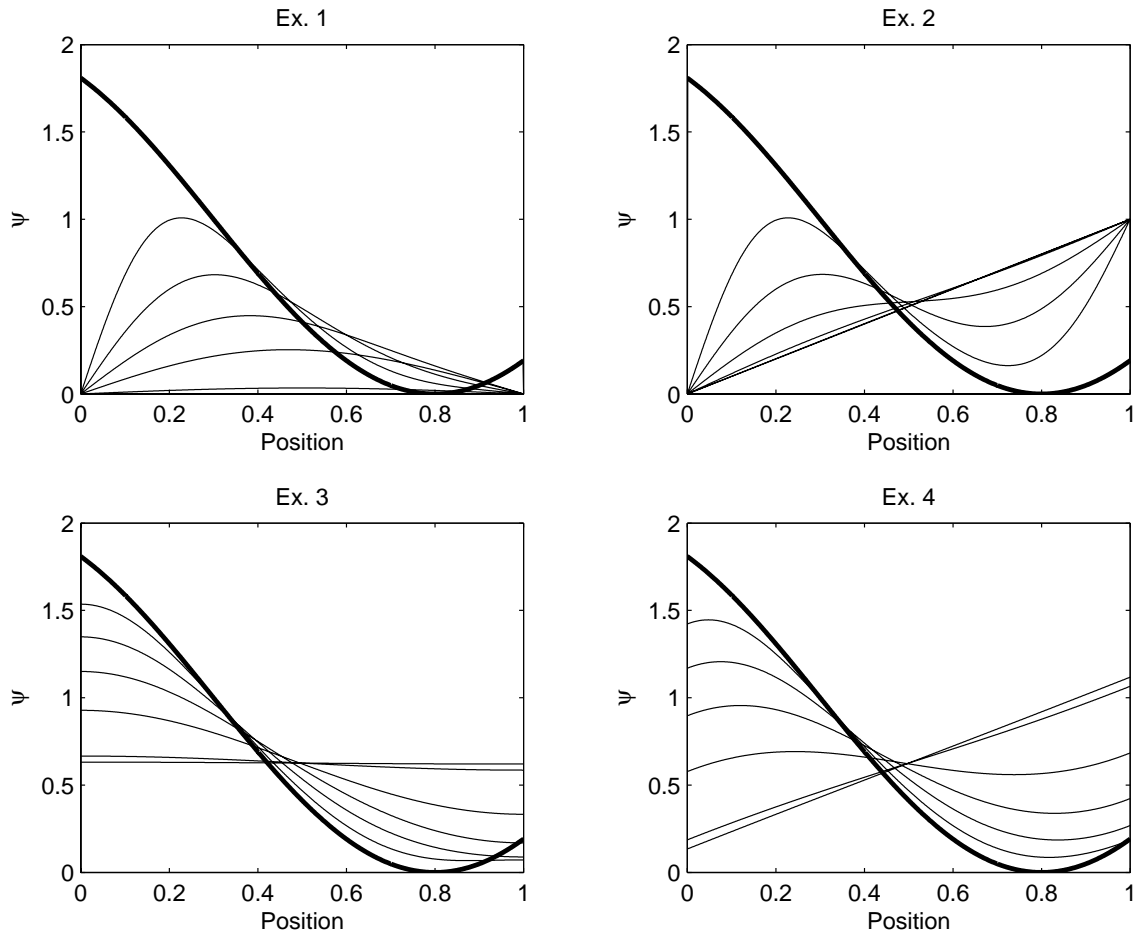


Figure 9-2: One dimension diffusion examples 1–4 in Table 9.1. The solid line indicates the initial condition. The concentration is plotted at 0.1τ , 0.25τ , 0.5τ , τ , 3τ , and 5τ , where τ is the diffusion time constant.

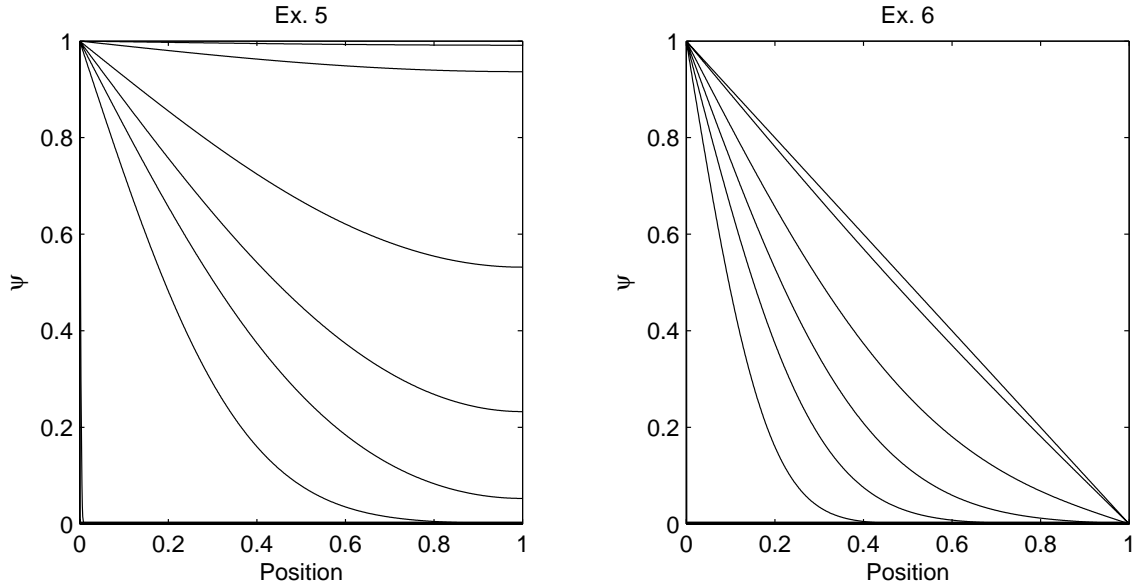


Figure 9-3: One dimension diffusion examples 5–6 in Table 9.1. The solid line indicates the initial condition. The concentration is plotted at 0.1τ , 0.25τ , 0.5τ , τ , 3τ , and 5τ , where τ is the diffusion time constant.

in a diffusion process the behavior near one end of the material is virtually unaffected by that at the other. In this window the domain can be modeled as semi-infinite with good results. The solution to the diffusion equation can be written in terms of the error function as

$$\psi(x, t) = A_1 \operatorname{erf}\left(\frac{L+x}{2\sqrt{Dt}}\right) + A_2 \operatorname{erf}\left(\frac{L-x}{2\sqrt{Dt}}\right) \quad (9.36)$$

L is a parameter. The error function is defined as [99]

$$\operatorname{erf}(x) = \frac{2}{\sqrt{\pi}} \int_0^x e^{-\xi^2} d\xi \quad (9.37)$$

Nonlinear Diffusion

If the diffusion coefficient is a function of the concentration the equation becomes nonlinear and in general there is no analytical solution for the concentration function. One special case of interest is a diffusion coefficient of the form suggested by Guidi and Fullerton for oil-impregnated kraft insulating paper [100].

$$D(\psi, T) = D_o e^{k\psi + E_a(1/T_o - 1/T)} \quad (9.38)$$

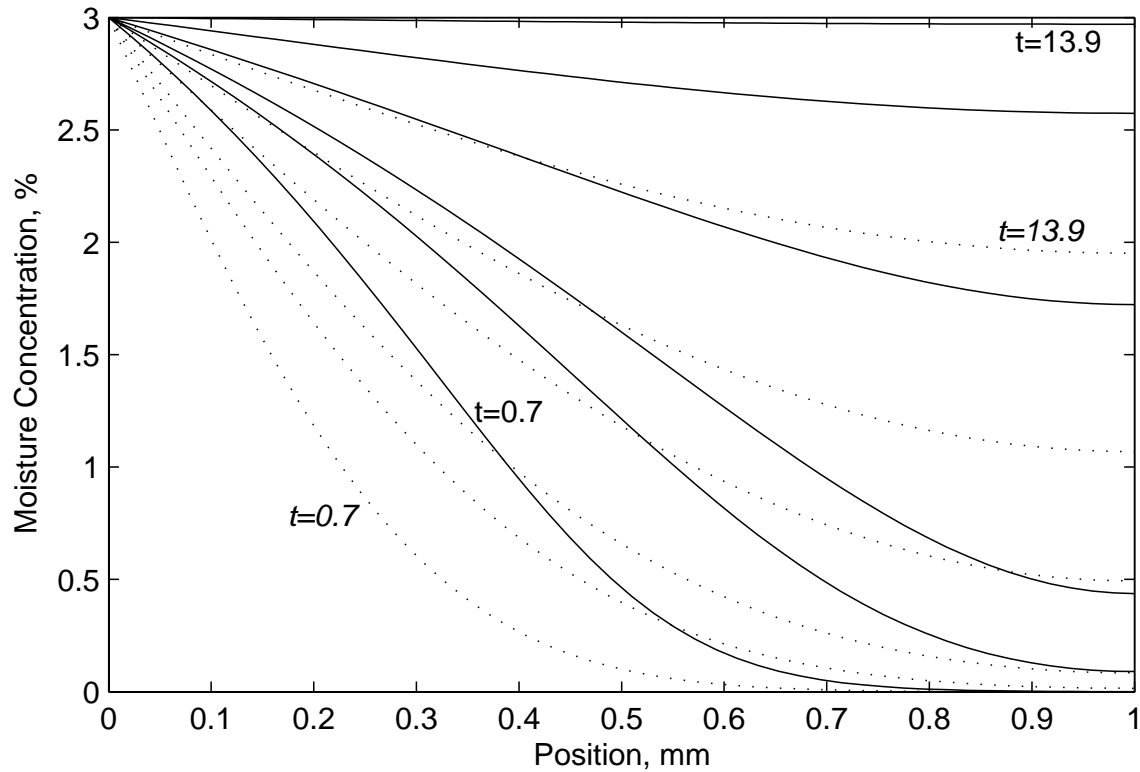


Figure 9-4: Comparison of a linear (dotted) and nonlinear (solid) diffusion process. The nonlinear diffusion coefficient is of the form in eq. 9.38 with $T = T_o$, $k = 0.5$, and $D_o = 2.62 \times 10^{-11} \text{ m}^2/\text{s}$. The linear problem is obtained by setting $k = 0$. Times plotted are 0.7, 1.5, 2.2, 4.4, 7.3, and 13.9 hours.

ψ is the moisture concentration in percent and T is the temperature in Kelvin. For analysis by Du et al., T_o is 298 K and $k = 0.5$ [101]. The coefficients D_o and E_a are determined from measurements. Du quotes values of $E_a = 8140 \text{ K}$, $D_o = 2.62 \times 10^{-11} \text{ m}^2/\text{s}$ for oil-free paper and $E_a = 8074 \text{ K}$, $D_o = 1.34 \times 10^{-13} \text{ m}^2/\text{s}$ for oil-impregnated paper. Other authors have also used this form for estimating nonlinear diffusion processes [39].

To illustrate the effect of the nonlinearity, one dimensional concentration profiles are plotted for a diffusion problem in Fig. 9-4. The properties of oil-free paper and eq. 9.38 are used for the nonlinear solution. For the linear problem k is set to zero. For this example, the moisture content at $x = 0 \text{ mm}$ is set to 3%, and at $x = 1 \text{ mm}$ a Neumann boundary condition is imposed ($\partial\psi/\partial x = 0$). The temperature is assumed to be T_o . The diffusion is faster when the governing diffusion coefficient is the nonlinear choice ($k > 0$). This is because for $k > 0$, the nonlinear diffusion coefficient is always larger than the linear diffusion coefficient. The exponential dependence of the diffusion coefficient on concentration accelerates the diffusion process at later time.

9.1.4 Radial Diffusion

We extend our study to consider diffusion in cylindrical geometries. The Laplacian in cylindrical coordinates is

$$\nabla^2\psi = \frac{1}{r} \frac{\partial}{\partial r} \left(r \frac{\partial\psi}{\partial r} \right) + \frac{1}{r^2} \frac{\partial^2\psi}{\partial\phi^2} + \frac{\partial^2\psi}{\partial z^2} \quad (9.39)$$

In the case of purely axial diffusion, $\psi = \psi(z, t)$ and the diffusion equation reduces to the linear form considered in Section 9.1.2. The case of angular diffusion in isolation is not studied because it cannot be achieved with simple boundary conditions. For the case of radial diffusion, $\psi = \psi(r, t)$, only the first term on the right in eq. 9.39 is non-zero. The diffusion equation reduces to

$$\frac{\partial\psi}{\partial t} = D_o \frac{1}{r} \frac{\partial}{\partial r} \left(r \frac{\partial\psi}{\partial r} \right) \quad (9.40)$$

Assuming a separable solution $\psi(r, t) = R(r)T(t)$ and the separation constant $-\alpha^2$ we have eq. 9.13 for $T(t)$ and the following for $R(r)$.

$$r^2 \frac{\partial^2 R}{\partial r^2} + r \frac{\partial R}{\partial r} + \alpha^2 r^2 R = 0 \quad (9.41)$$

We recognize this as a form of the Bessel equation when α is non-zero. If $\alpha = 0$ there is no diffusion process since the time dependence disappears. Making the substitution $\xi = \alpha r$ we can rewrite eq. 9.41.

$$\xi^2 \frac{\partial^2 R}{\partial \xi^2} + \xi \frac{\partial R}{\partial \xi} + \xi^2 R = 0 \quad (9.42)$$

This is the standard form of the Bessel function of order 0. It has solutions $J_o(\xi)$ and $Y_o(\xi)$. The transient part of the solution is then

$$\psi(r, t) = e^{-\alpha^2 D_o t} [A_1 J_o(\alpha r) + A_2 Y_o(\alpha r)] \quad (9.43)$$

Recall that $J_o(0) = 1$ and $Y_o(0) = -\infty$ so that problems involving $r = 0$ generally have $A_2 = 0$. The orthogonality condition for the Bessel functions is

$$\int_0^d r J_n(k_{mn}r) J_n(k_{jn}r) dr = 0 \quad m \neq j \quad (9.44)$$

where $k_{mn}d$ is the m th zero of the n th order Bessel function for a cylinder of radius d . The steady state equation is determined by setting the left hand side of eq. 9.40 to zero and integrating.

$$\psi_{ss}(r) = A \ln r + B \quad (9.45)$$

Table 9.2: The first nine zero's of the Bessel functions of the first kind of order 0 and 1.

$r =$	r_1	r_2	r_3	r_4	r_5	r_6	r_7	r_8	r_9
$J_0(r)$	2.4048	5.5201	8.6537	11.7915	14.9309	18.0711	21.2116	24.3525	27.4935
$J_1(r)$	3.8317	7.0156	10.1735	13.3237	16.4706	19.6159	22.7601	25.9037	29.0468

For problems that include $r = 0$, A must be zero to keep the concentration finite.

Homogeneous Dirichlet Boundary Condition

Consider the case of radial diffusion with the moisture concentration at radius, d , set to zero.

$$\psi(d, t) = 0 \quad (9.46)$$

It is necessary to formally state a second boundary condition: the concentration at $r = 0$ is finite.

$$|\psi(r = 0, t)| < \infty \quad (9.47)$$

Applying the boundary condition at $r = 0$ we find $A_2 = 0$. We also find from the boundary conditions that in the steady state, ψ goes to 0. Applying the boundary condition at $r = 0$ we have

$$\psi(d, t) = 0 = J_0(\alpha d) \quad (9.48)$$

We take $\alpha_n d$ to be the n th zero of the zero order Bessel function. Table 9.2 lists the first nine zeros of $J_0(r)$. We write the solution as a summation of terms.

$$\psi(r, t) = \sum_{n=1}^{\infty} A_n e^{-\alpha_n^2 D_o t} J_0(\alpha_n r) \quad (9.49)$$

Setting eq. 9.49 at $t = 0$ equal to the initial conditions and applying eq. 9.44 we solve for the coefficients, A_n .

$$A_n = \frac{\int_0^d r \psi(r, t=0) J_0(\alpha_n r) dr}{\frac{d^2}{2} [J_1(\alpha_n d)]^2} \quad (9.50)$$

Dirichlet Boundary Condition

We consider the boundary condition $\psi(r = d, t) = B_o$. The steady solution is $\psi_{ss}(r) = B_o$. The concentration is $\psi(r, t) = \psi_h(r, t) + \psi_{ss}(r)$, where ψ_h represents the homogeneous solution. The

coefficients are now

$$A_n = \frac{\int_0^d r(\psi(r, t=0) - B_o)J_o(\alpha_n r)dr}{\frac{d^2}{2} [J_1(\alpha_n d)]^2} \quad (9.51)$$

The solution is

$$\psi(r, t) = B_o + \sum_{n=1}^{\infty} A_n e^{-\alpha_n^2 D_o t} J_o(\alpha_n r) \quad (9.52)$$

Homogeneous Neumann Boundary Condition

Now we consider the Neumann boundary condition

$$\left. \frac{\partial \psi}{\partial r} \right|_{r=d} = 0 \quad (9.53)$$

The concentration in the steady state is a constant equal to the average initial concentration.

$$\psi_{ss}(r) = \frac{1}{\pi d^2} \int_0^{2\pi} \int_0^d \psi(r, t=0) r dr d\phi \quad (9.54)$$

$$= \frac{2}{d^2} \int_0^d r \psi(r, t=0) dr \quad (9.55)$$

Enforcing the boundary condition at $r = d$ we have

$$\left. \frac{\partial \psi}{\partial r} \right|_{r=d} = 0 = A_n e^{-\alpha_n^2 D_o t} \left. \frac{\partial J_o(\alpha r)}{\partial r} \right|_{r=d} \quad (9.56)$$

Using the identity

$$\frac{d}{dx} [x^{-\nu} J_\nu(x)] = -x^{-\nu} J_{\nu+1}(x) \quad (9.57)$$

we find

$$J_1(\alpha d) = 0 \quad (9.58)$$

This condition can only be satisfied if αd is a zero of $J_1(r)$. The n th zero of $J_1(r)$ is at $\alpha_n d$. Several values of r such that $J_1(r) = 0$, are listed in Table 9.2. We must now satisfy the initial condition.

$$A_n J_o(\alpha_n r) + \psi_{ss} = \psi(r, t=0) \quad (9.59)$$

$$A_n J_o(\alpha_n r) = \psi(r, t=0) - \psi_{ss} \quad (9.60)$$

Because $\alpha_n d$ corresponds to the zeros of J_1 and not J_0 , we need to manipulate the equation to make use of the orthogonality identity. We can do this by differentiating both sides with respect to r .

$$\frac{d}{dr} [A_n J_0(\alpha_n r)] = \frac{d}{dr} (\psi(r, t = 0) - \psi_{ss}) \quad (9.61)$$

$$-\alpha_n A_n J_1(\alpha_n r) = \frac{d}{dr} \psi(r, t = 0) \quad (9.62)$$

We now apply the orthogonality principle

$$-\alpha_n A_n J_1(\alpha_n r) r J_1(\alpha_m r) = r J_1(\alpha_m r) \frac{d}{dr} [\psi(r, t = 0)] \quad (9.63)$$

$$-\alpha_n A_n \int_0^d r J_1(\alpha_n r) J_1(\alpha_m r) dr = \int_0^d r J_1(\alpha_m r) \frac{d}{dr} [\psi(r, t = 0)] dr \quad (9.64)$$

The left integral equals zero for $n \neq m$. In the case that $n = m$, we can find the coefficient A_n .

$$-\alpha_n A_n \int_0^d r J_1(\alpha_n r) J_1(\alpha_n r) dr = \int_0^d r J_1(\alpha_n r) \frac{d}{dr} [\psi(r, t = 0)] dr \quad (9.65)$$

$$\alpha_n A_n \frac{d^2}{2} J_0(\alpha_n r) J_2(\alpha_n r) = \int_0^d r J_1(\alpha_n r) \frac{d}{dr} [\psi(r, t = 0)] dr \quad (9.66)$$

$$A_n = \frac{\int_0^d r J_1(\alpha_n r) \frac{d}{dr} [\psi(r, t = 0)] dr}{\alpha_n \frac{d^2}{2} J_0(\alpha_n r) J_2(\alpha_n r)} \quad (9.67)$$

The total solution is

$$\psi(r, t) = \psi_{ss} + \sum_{n=1}^{\infty} A_n e^{-\alpha_n^2 D_o t} J_0(\alpha_n r) \quad (9.68)$$

If the Neumann boundary condition was non-zero, a steady state concentration is never reached since a second boundary is needed to provide a source or sink.

Radial Diffusion Examples

We now present two examples of radial diffusion in Fig. 9-5 where in both cases the radius, d , and diffusion coefficient, D_o , are 1.0. In example 1, the cylinder is insulated (Neumann boundary condition) at the outer radius, d . The initial condition is $\psi(r, t = 0) = \cos(\pi r/d + \pi/5) + 1$. This example is very similar to example 3 for one dimensional linear diffusion. Note that the time constant $\tau \approx 0.0681$ is faster than for the linear problem.

In the second example, the initial concentration is zero, and the radius, d , has been fixed to a concentration of 1. This is similar to example 5 for one dimensional diffusion. The time constant $\tau \approx 0.1729$ is also substantially faster than the linear problem.

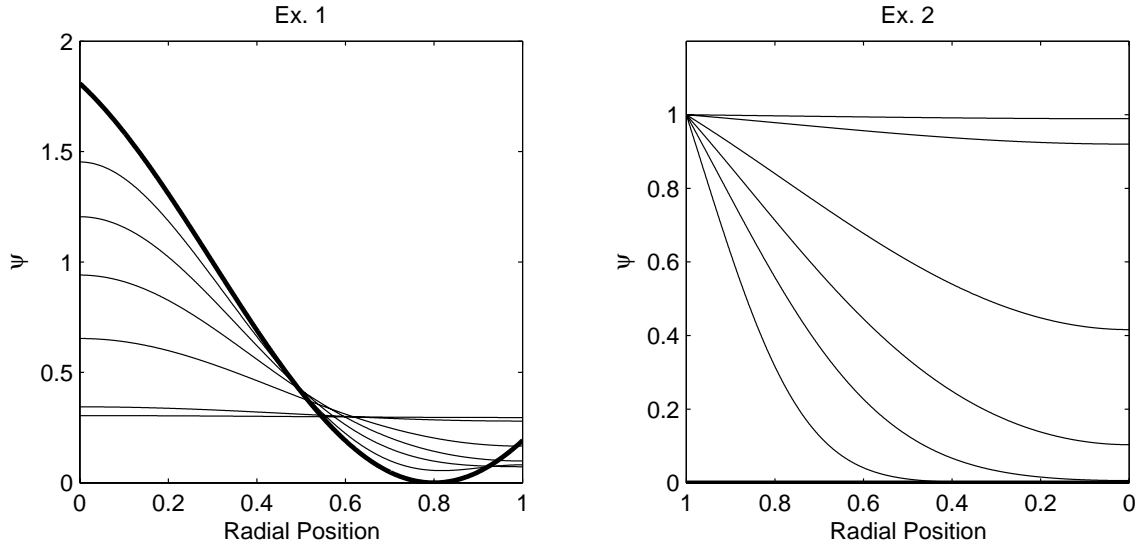


Figure 9-5: Radial diffusion examples plotted at times 0.1τ , 0.25τ , 0.5τ , τ , 3τ , and 5τ , where τ is the diffusion time constant.

9.1.5 Radial and Angular Diffusion

We consider the case where the concentration is allowed to vary with r , ϕ , and t . The diffusion equation reduces to

$$\frac{\partial\psi}{\partial t} = D_o \left[\frac{1}{r} \frac{\partial}{\partial r} \left(r \frac{\partial\psi}{\partial r} \right) + \frac{1}{r^2} \frac{\partial^2\psi}{\partial\phi^2} \right] \tag{9.69}$$

Attempting the separable solution $\psi(r, \phi, t) = R(r)Q(\phi)T(t)$, we have

$$RQ \frac{dT}{dt} = D_o \left[\frac{TQ}{r} \frac{d}{dr} \left(r \frac{dR}{dr} \right) + \frac{RT}{r^2} \frac{d^2Q}{d\phi^2} \right] \tag{9.70}$$

after substitution and division by ψ . Multiplying by r^2/ψ and moving $Q(\phi)$ to stand alone, we introduce the separation constant $-n^2D_o$.

$$\frac{r^2}{T} \frac{dT}{dt} - \frac{rD_o}{R} \frac{d}{dr} \left(r \frac{dR}{dr} \right) = \frac{D_o}{Q} \frac{d^2Q}{d\phi^2} = -n^2D_o \tag{9.71}$$

This forms an ordinary differential equation for $Q(\phi)$, the solution of which is

$$Q(\phi) = \begin{cases} A_n e^{jn\phi} + B_n e^{-jn\phi} & n \neq 0 \\ A_0 \phi + B_0 & n = 0 \end{cases} \tag{9.72}$$

The remaining terms are rearranged and the separation constant $-\alpha^2 D_o$ is introduced.

$$\frac{1}{T} \frac{dT}{dt} - \frac{D_o}{rR} \frac{d}{dr} \left(r \frac{dR}{dr} \right) = -\frac{n^2 D_o}{r^2} \quad (9.73)$$

$$\frac{1}{T} \frac{dT}{dt} = \frac{D_o}{rR} \frac{d}{dr} \left(r \frac{dR}{dr} \right) - \frac{n^2 D_o}{r^2} = -\alpha^2 D_o \quad (9.74)$$

Solving for $T(t)$ we find

$$T(t) = \begin{cases} C e^{-\alpha^2 D_o t} & \alpha^2 \neq 0 \\ C & \alpha^2 = 0 \end{cases} \quad (9.75)$$

Manipulating and expanding eq. 9.74 we reshape the equation.

$$\frac{D_o}{rR} \frac{d}{dr} \left(r \frac{dR}{dr} \right) - \frac{n^2 D_o}{r^2} = -\alpha^2 D_o \quad (9.76)$$

$$r D_o \frac{d}{dr} \left(r \frac{dR}{dr} \right) + (\alpha^2 r^2 D_o - n^2 D_o) R = 0 \quad (9.77)$$

$$r^2 \frac{d^2 R}{dr^2} + r \frac{dR}{dr} + (\alpha^2 r^2 - n^2) R = 0 \quad (9.78)$$

Making the substitution $u = \alpha r$ we find

$$u^2 \frac{d^2 R}{du^2} + u \frac{dR}{du} + (u^2 - n^2) R = 0 \quad (9.79)$$

Equation 9.79 is known as the Bessel equation of order n . The solutions are

$$R(r) = \begin{cases} A J_n(\alpha r) + B Y_n(\alpha r) & \alpha \neq 0 \\ A r^n + B r^{-n} & \alpha = 0 \quad n \neq 0 \\ A \ln r + B & \alpha = 0 \quad n = 0 \end{cases} \quad (9.80)$$

9.1.6 Radial and Axial Diffusion

We consider the case where the concentration is allowed to vary with r , z , and t . The diffusion equation reduces to

$$\frac{\partial \psi}{\partial t} = D_o \left[\frac{1}{r} \frac{\partial}{\partial r} \left(r \frac{\partial \psi}{\partial r} \right) + \frac{\partial^2 \psi}{\partial z^2} \right] \quad (9.81)$$

We try a separable solution of the form $\psi(r, z, t) = R(r)Z(z)T(t)$. Substituting and dividing by ψ we have

$$\frac{1}{T} \frac{dT}{dt} = D_o \left[\frac{1}{rR} \frac{d}{dr} \left(r \frac{dR}{dr} \right) + \frac{1}{Z} \frac{d^2 Z}{dz^2} \right] \quad (9.82)$$

Moving the R and T terms to the left hand side, and the Z term to the right, we introduce the separation constant $-k^2 D_o$.

$$\frac{1}{T} \frac{dT}{dt} - \frac{D_o}{rR} \frac{d}{dr} \left(r \frac{dR}{dr} \right) = \frac{D_o}{Z} \frac{d^2 Z}{dz^2} = -k^2 D_o \quad (9.83)$$

The right hand side is an ordinary differential equation, the solution of which is

$$Z(z) = \begin{cases} Ae^{jkz} + Be^{-jkz} & k \neq 0 \\ A_0 z + B_0 & k = 0 \end{cases} \quad (9.84)$$

The R and T terms can now be separated and a second separation constant, $-\alpha^2 D_o$, is introduced.

$$\frac{1}{T} \frac{dT}{dt} = \frac{D_o}{rR} \frac{d}{dr} \left(r \frac{dR}{dr} \right) - k^2 D_o = -\alpha^2 D_o \quad (9.85)$$

The solution for $T(t)$ is

$$T(t) = \begin{cases} Ce^{-\alpha^2 D_o t} & \alpha^2 \neq 0 \\ C & \alpha^2 = 0 \end{cases} \quad (9.86)$$

Equation 9.85 can be written for $R(r)$ as

$$r \frac{d}{dr} \left(r \frac{dR}{dr} \right) + \beta^2 r^2 R = 0 \quad (9.87)$$

where $\beta^2 = \alpha^2 - k^2$. Making the substitution $u = \beta r$ results in the Bessel equation of order zero.

$$u^2 \frac{d^2 R}{du^2} + u \frac{dR}{du} + u^2 R = 0 \quad (9.88)$$

The solutions to this equation are

$$R(r) = \begin{cases} AJ_o(\beta r) + BY_o(\beta r) & \beta \neq 0 \\ A \ln r + B & \beta = 0 \end{cases} \quad (9.89)$$

9.1.7 Normalized Diffusion Coefficient

The diffusion equation can be normalized to facilitate its manipulation.

$$\frac{\partial \psi}{\partial t} = D_o \nabla^2 \psi \quad (9.90)$$

This equation can be made non-dimensional by the following substitutions.

$$\tilde{\psi} = \frac{\psi}{\psi_{ss}} \quad (9.91)$$

$$\tilde{\nabla} = L\nabla \quad (9.92)$$

$$\tilde{t} = \frac{D_o t}{L^2} \quad (9.93)$$

ψ_{ss} is the steady state concentration, and L is a characteristic length. After the substitutions are made the non-dimensional moisture diffusion equation is

$$\frac{\partial \tilde{\psi}}{\partial \tilde{t}} = \tilde{\nabla}^2 \tilde{\psi} \quad (9.94)$$

Reducing this to a one dimensional diffusion process in z we have

$$\frac{\partial \tilde{\psi}}{\partial \tilde{t}} = \frac{\partial^2 \tilde{\psi}}{\partial \tilde{z}^2} \quad (9.95)$$

9.2 Measurements of Moisture Diffusion

Measuring moisture diffusion processes has been an area of study with a significant amount of research. In this section we briefly discuss the measurements available in the literature and then present the basic methodology used to interpret the results in Chapter 8.

Much of the early literature on moisture diffusion in papers deals with various forms of kraft paper. This was a topic of interest to General Electric in the 1960s and 70s and several studies were done. In 1966, Paul Ast investigated how moisture transfer through oil-free and oil-impregnated kraft (A50P281) paper is affected by temperature, moisture gradient and paper thickness [102]. Later in 1972 H.P. Fullerton investigated the concentration-dependent moisture diffusion coefficient in oil-free kraft (A50P260A) paper [103]. The form of the concentration-dependent diffusion coefficient is quite similar to that suggested by Guidi & Fullerton in 1974 [100]. In that study oil-impregnated kraft paper was studied for power transformer applications. The form of the diffusion coefficient given in eq. 9.38 was suggested.

In an study by B. Nettelblad, measurements were made at various temperatures showing how the moisture content of cellulose materials (paper and pressboard) affects the dielectric properties [86].

Moisture diffusion from oil into oil-impregnated pressboard was a major topic of research during the 90s at MIT, a period of sustained research and numerous investigators. Diffusion measurements seems to have been one of the driving motivations for the multi-wavelength dielectrometry sensor. In

one of the earlier publication von Guggenberg & Melcher measured moisture diffusion in a pressboard sample using the sensor [17]. They estimated the diffusion coefficient based on the delay in response of the 1 mm sensor compared to that of the 5.0 mm sensor. Yanqing Du, Alexander Mamishev and other students of M. Zahn, further developed the apparatus for measurements of moisture diffusion in oil-impregnated pressboard [40, 54, 64, 65] Du et al. estimated the diffusion coefficient using the same functional form as Guidi & Fullerton for oil-free transformer pressboard [39].

More recently moisture diffusion has been studied specifically in PILC cable insulation. As discussed in Section 7.3, Neimanis & Eriksson have investigated the effects of moisture on the insulation [1, 10]. Moisture diffusion in power cables has been studied with the use of dyes to monitor the diffusion process. Karl Fischer titration measurements are then used to determine the moisture content at various insulation layer depths [104, 105].

The diffusion coefficient can be estimated from the dielectrometry measurements taken in Chapter 8. Estimating the diffusion coefficient begins with establishing boundary conditions that yield as simple a formation of the problem as possible. In many of the transient measurements moisture is given access to only one end of the sample. The cylindrical side is covered by the sensor and rubber gasket, and held in place with a clamp. The opposite end is also sealed. If the diffusion coefficient is homogeneous in the MUT, and the boundary conditions are adequately enforced, the problem is essentially an axial diffusion problem and the diffusion equation simplifies to the cases studied in Section 9.1.2.

The boundary condition at the exposed end of the MUT is determined by the moisture content in the air. Ideally the boundary condition is stable throughout the experiment. The equilibrium relationship between the relative humidity in the air and the moisture content of the sample is needed to determine what the boundary condition actually is. Mappings have been done between various materials as presented in the following subsection.

The relationship between the moisture content and the effective permittivity is needed to interpret the dielectrometry measurements. In principle the response before the establishment of moisture at the boundary ($t < 0$) represents the 0% moisture content response. The steady state response represents the spectrum for the moisture content determined by the equilibrium curves. For our analysis, the spectrum is assumed to be shifted linearly on a logarithmic frequency scale for changes in moisture content. By shifting the initial spectrum until it reached the steady state spectrum a mapping is created between effective permittivity and moisture content.

For the z periodic sensor we can estimate the concentration profiles directly from the mapping for a particular frequency. For the ϕ periodic sensor the concentration profile must be assumed and the dielectric response calculated. The concentration profile must be adjusted until it produces a

sensor response that matches the measurement response. The profile is not a unique solution, but physical arguments assist in choosing a reasonable profile.

9.2.1 Air and Paper Moisture Equilibriums

In order to determine the absolute moisture content in the paper directly from the temperature and relative humidity equilibrium curves are needed. A number of studies have been done to determine moisture equilibriums with paper. For transformer applications, the equilibrium of moist oil and paper has been of significant interest [106–108], as has the solubility of various transformer oils [109].

Equilibrium curves between humidified air and cotton, spruce wood, and kraft paper, for various temperatures have been estimated by Piper [110]. Jeffries work in 1960 suggested a lower moisture content in kraft paper than Piper [111]. His data has been replotted in Fig. 9-6. Fessler et al. gathered the data from several publications and determined an empirical formula for water-paper equilibrium [112].

$$C = 2.173 \times 10^{-7} P_v^{0.6685} e^{4725.6/T} \quad (9.96)$$

C is the concentration of water in paper (g H₂O/g dry paper), P_v is the vapor pressure, and T is the temperature in Kelvin. The data in Table 5.2 is used to determine the relative humidity according to eq. 5.2, and the results are plotted in Fig. 9-7. A review of the literature has been done by Du [64] and Du et al. [65,101].

Moisture is entering the cable from air, and this is the equilibrium of interest. Further research has shown that the problem is much more difficult, and that the summary curves suggested here are simplifications of the problem. The equilibrium moisture content in paper has been shown to form a hysteresis loop [113–115]. Detailed studies have been conducted to model heat and mass transport in paper [116,117]. Relating the moisture content to material dielectric properties is also complicated by the highly dispersive and non-linear effective permittivity of water [118].

9.3 Diffusion Estimates from ϕ Periodic Measurements

The diffusion coefficient can be estimated from measurements using the ϕ periodic sensor. A mapping between the moisture concentration and the electrical properties of the medium is required. This mapping can be estimated by taking the moisture content in the MUT to be constant before the diffusion process, and after steady state is reached. As noted in Section 7.3, the presence of moisture in many materials causes a linear shift of the electrical properties on a logarithmic frequency scale. The shift is defined by the initial and final values of the measurement, eliminating the need for direct

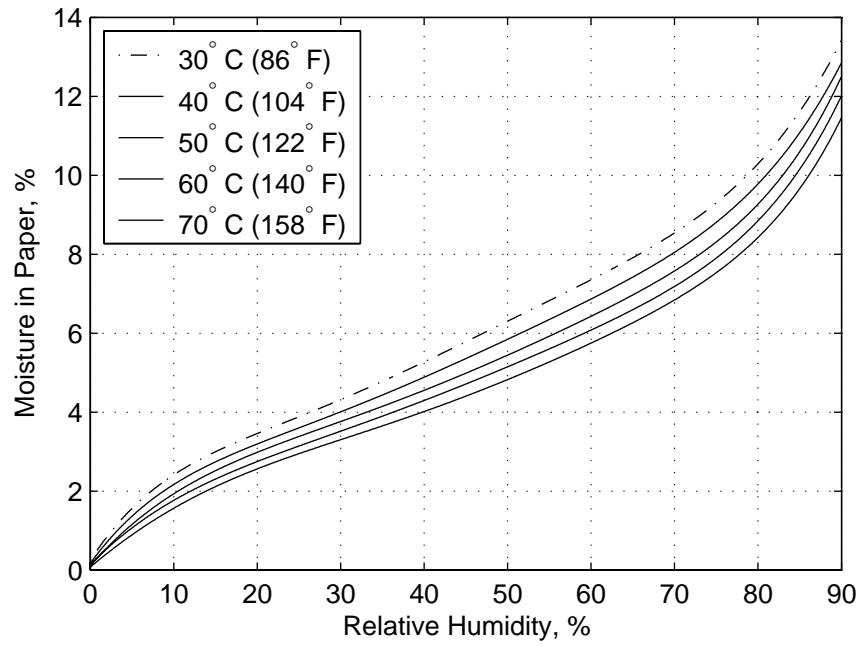


Figure 9-6: Jeffries curves for moisture in wood pulp as a function of relative humidity and temperature [111]. Sixth order polynomial fit coefficients provided by Du [39].

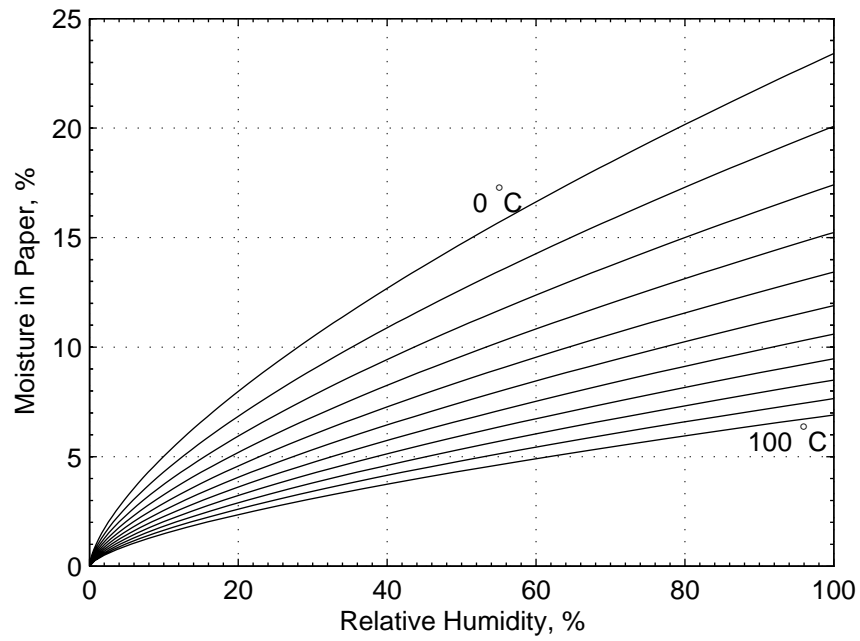


Figure 9-7: Fessler et al. curves of moisture in paper as a function of relative humidity for selected temperatures [112]. Curves have been plotted from 0 to 100 °C in 10 °C increments.

knowledge of the moisture content of the material in the estimation process. With the mapping function \mathcal{F} known, the permittivity is known for all moisture concentrations between the initial and final value.

The diffusion profile at select time, $\psi(z, t = t_n)$, can be determined based on mathematical simulation or theoretical calculation depending on the chosen form of the diffusion coefficient. The mapping is then used to determine the effective permittivity of the MUT at each point.

$$\epsilon^*(z, t) = \epsilon'(z, t) - j\epsilon''(z, t) = \mathcal{F}(\psi(z, t)) \quad (9.97)$$

The complex admittance measured by the dielectrometry sensor can be estimated by summing the differential contributions of each region of length δz over the entire surface of the sensor. The beauty of the ϕ periodic sensor in measuring diffusion along the axis of the cylinder (in the z direction) is that the sensor response can be determined using the analytical model.

9.3.1 Birch Rod Diffusion

We consider the transient experimental results presented in Section 8.1.2 on the birch rod using the 5 mm ϕ periodic sensor. In order to determine the diffusion coefficient we utilize the master curve presented in Section 7.2.2. We choose the frequency of 10 Hz to perform our analysis on because it is in the center of the master curve, providing a large frequency range of reliable data for shifting the curve. We assume that the birch rod has no moisture at the beginning of the experiment and that steady state has been reached at the end.

We begin by plotting the initial and final values of the effective permittivity in Fig. 9-8. Under the assertion that the logarithm of the frequency of the effective permittivity curve shifts linearly with moisture content, we estimate the shift needed to reach the final curve from the initial curve. The real part of the effective permittivity (left hand plot) is not measured over a sufficient frequency range to determine the shift. The value of $\log(\epsilon''/\epsilon_o)$ (right hand side) clearly has a distinct shape. A frequency shift of 4.8 decades causes the linear portions to overlap.

Having determined the frequency shift from the beginning of the experiment to the end, the moisture dependence of the effective permittivity is determined. The master curve in Fig. 7-15 is used for ϵ' . Because of the linear shape of the $\log(\epsilon''/\epsilon_o)$ curve, we assume a linear shift from the initial value to the final value. The moisture dependence of the effective permittivity used for calculations is shown in Fig. 9-9. Notice that the change in electrical properties is not linear with the moisture content. We cannot easily treat the problem as a “diffusion” of effective permittivity because of this nonlinear dependence.

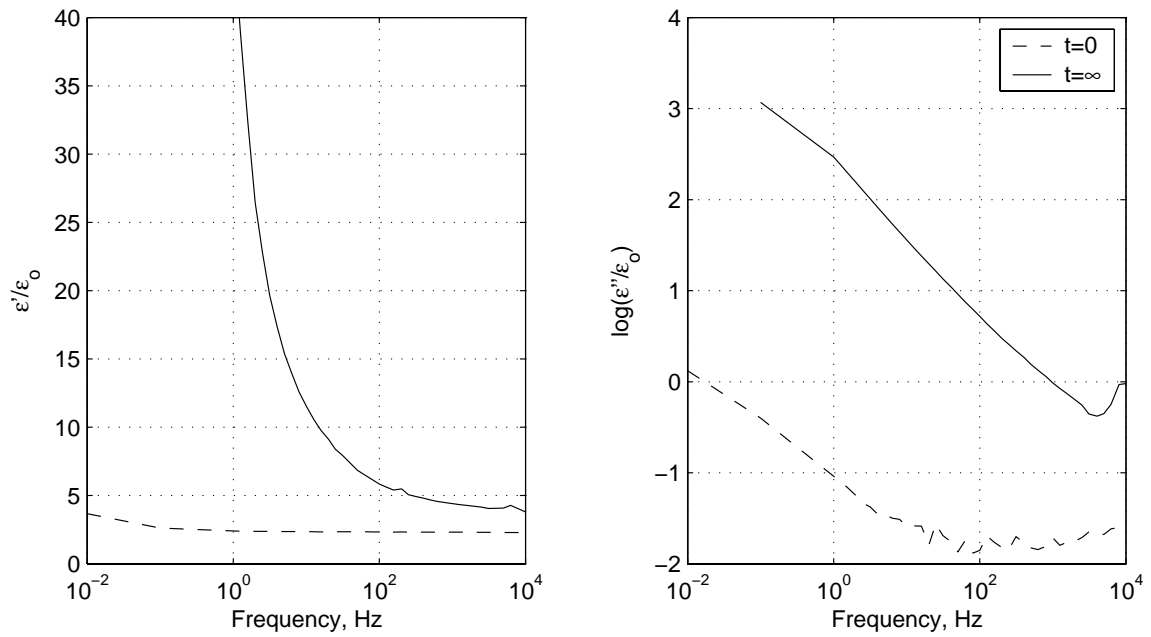


Figure 9-8: Birch rod initial (dashed) and final (solid) values of effective permittivity as measured by the 5 mm sensor in a ϕ periodic geometry.

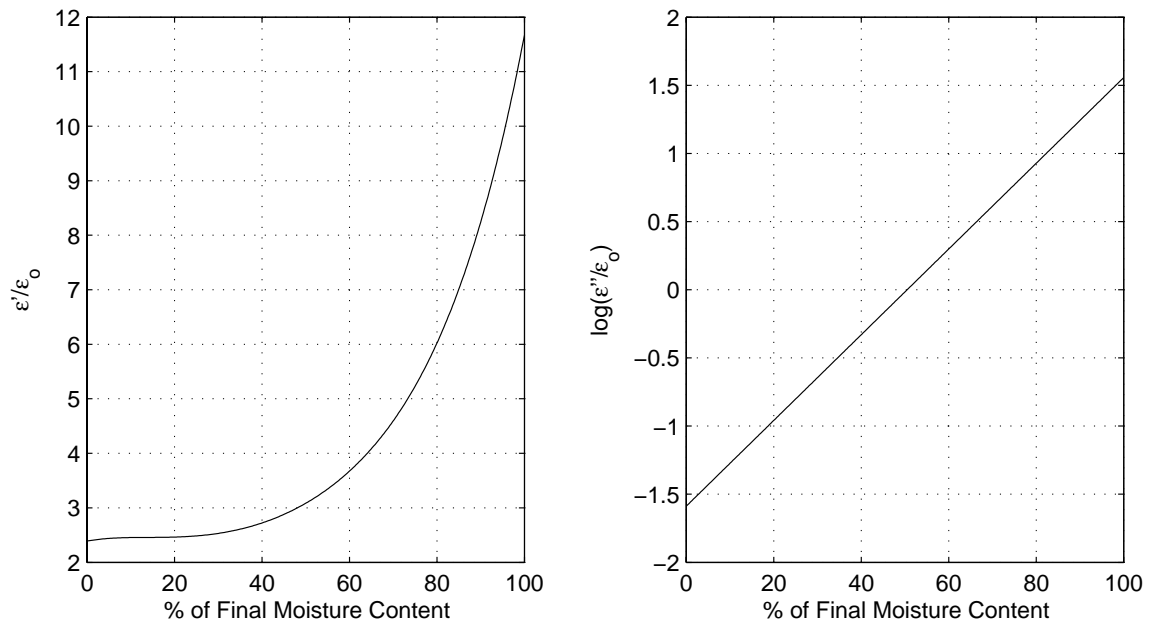


Figure 9-9: Birch rod effective permittivity as a function of the moisture content at 10 Hz as determined from the universal curve model for ϵ' . ϵ'' is determined based on a linear dependence on the plotted quantity.

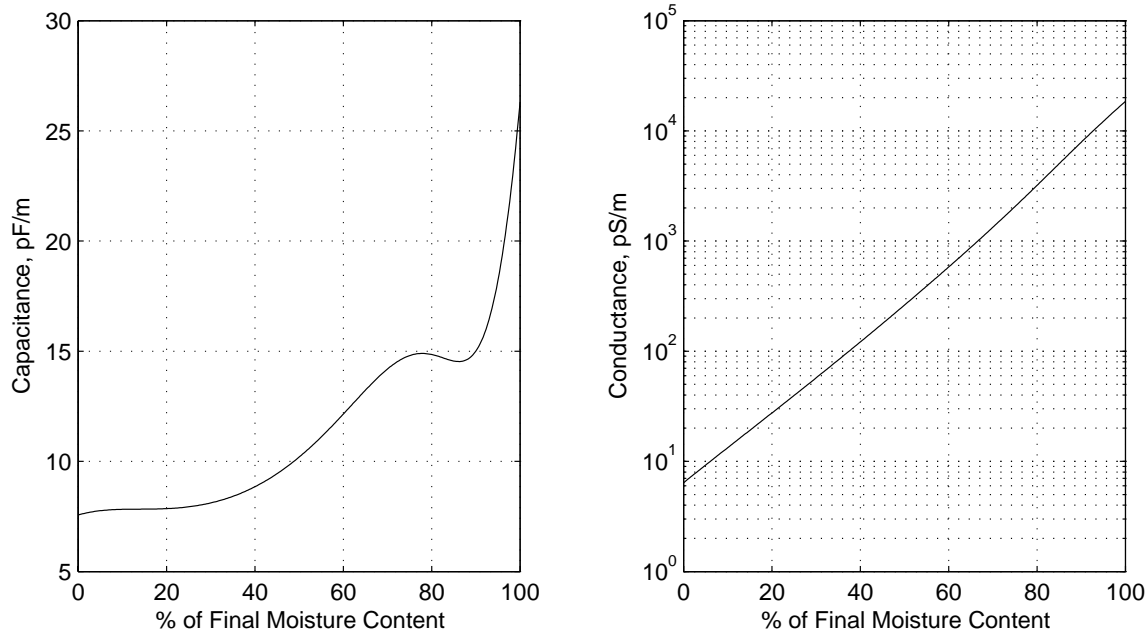


Figure 9-10: Calculated per unit length capacitance and conductance as a function of birch rod moisture concentration for the 5 mm ϕ periodic sensor. The calculation assumes the effective permittivity dependence in Fig. 9-9 at 10 Hz.

The permittivity as a function of moisture content is discretized into 300 intervals. For each interval the capacitance and conductance per unit length are found using the algorithm presented in Section 3.3. This acts as a mapping from moisture content to impedance. It serves as a lookup table to be used when calculating the total complex capacitance for each profile. The use of a lookup table significantly reduces the calculation time since it eliminates the need to use the forward problem when calculating the total capacitance. The calculated value of capacitance and conductance as a function of the moisture content is shown in Fig. 9-10.

The appearance of a local maximum at about 78% and a local minimum at 86% in the capacitance prompted further investigation to verify the accuracy of the algorithm. A full evaluation using my own MATLAB code for the *planar* problem exhibited the same behavior. Planar code was also produced by Y. Sheiretov [59]. We used this code to find the gain and phase at the maximum and minimum points. While the code does not produce capacitance and conductance directly, eqs. 3.6 and 3.7 can be used. The choice of the feedback capacitance need only be consistent. Again we find the drop in capacitance. Finally as a third test we produce the scenario in Maxwell 2D. While for 17 μm thick electrodes the decrease is not observed (at least at these two test points), but for 1 μm thick electrodes it is. The test details are summarized in Table 9.3. In the experimental setup

Table 9.3: Capacitance for Birch Diffusion Estimate

78%	Theory (0 μm)	$C=14.92$ pF/m
		$G=2.66$ nS/m
	Maxwell (1 μm)	$C=14.79$ pF/m
		$G=2.63$ nS/m
	Maxwell (17 μm)	$C=16.3$ pF/m
		$G=2.80$ nS/m
86%	Theory (0 μm)	$C=14.59$ pF/m
		$G=5.66$ nS/m
	Maxwell (1 μm)	$C=14.58$ pF/m
		$G=5.58$ nS/m
	Maxwell (17 μm)	$C=16.87$ pF/m
		$G=5.92$ nS/m

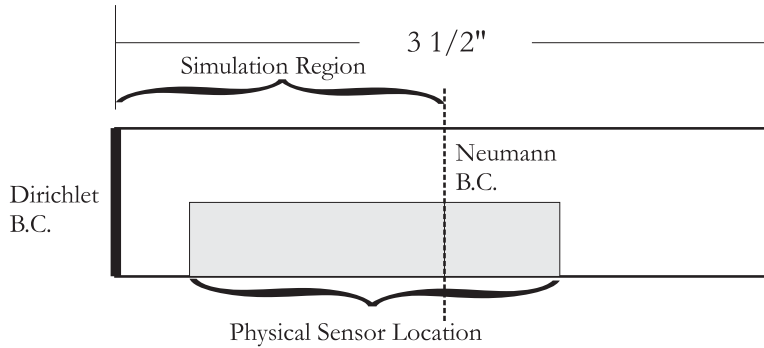


Figure 9-11: Side view of the birch rod and sensor for analysis purposes. A Neumann boundary condition is used to reduce the domain by a factor of two. The physical sensor is placed slightly inside the physical edge of the rod. The impedance profile is integrated over the surface of the sensor.

both ends of the 3 1/2 inch birch rod are exposed. For the purposes of numerical calculation we can reduce the domain by a factor of two to 1 3/4 inches and use a Neumann boundary condition at the border. This produces precisely the same diffusion profiles as would be achieved with a full simulation when the results are mirrored at the Neumann boundary. The remaining profile is identical to the calculated profile by the symmetry of the problem. This is illustrated in Fig. 9-11.

The diffusion profile is simulated at 50 times ranging from 0.001 to 10 time constants. The diffusion profiles give the moisture as a function of position and look qualitatively quite similar to the linear curves in Fig. 9-4. After the diffusion profiles are simulated the admittance (capacitance and conductance) associated with each profile is calculated by numerically integrating the capacitances over the sensor surface. The diffusion coefficient, $D_o = 1.3 \times 10^{-8}$ m²/sec., is selected to achieve the greatest similarity with the actual measurement results. Comparisons of the capacitance and

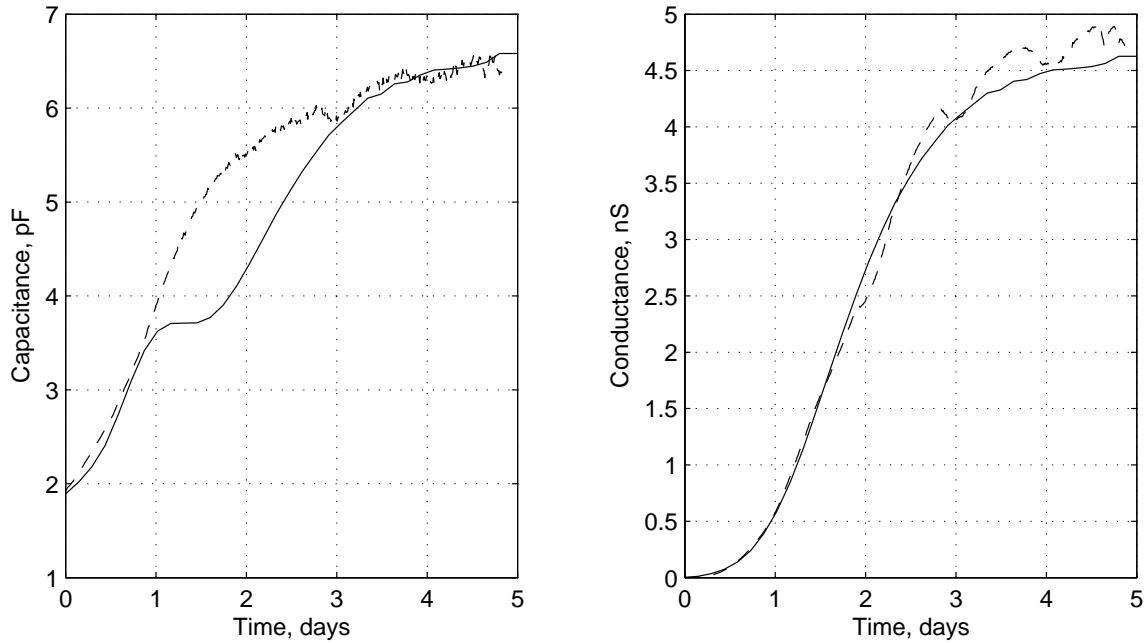


Figure 9-12: Comparison of the theoretical (solid) and experimental (dashed) capacitance and conductance at 10 Hz as a function of time for the birch rod. The simulation uses a diffusion coefficient of $D_o = 1.3 \times 10^{-8} \text{ m}^2/\text{sec}$. Notice that the conductance is in nano-Siemens and the capacitance is in pico-Farads.

conductance are shown in Fig. 9-12. The feature in the capacitance in Fig. 9-10 appears to lead to some discrepancy with the measured capacitance. The gain and phase from theory and experiment are compared in Fig. 9-13 show good agreement overall with slightly sharper transitions predicted in the phase. Overall the agreement is quite satisfactory.

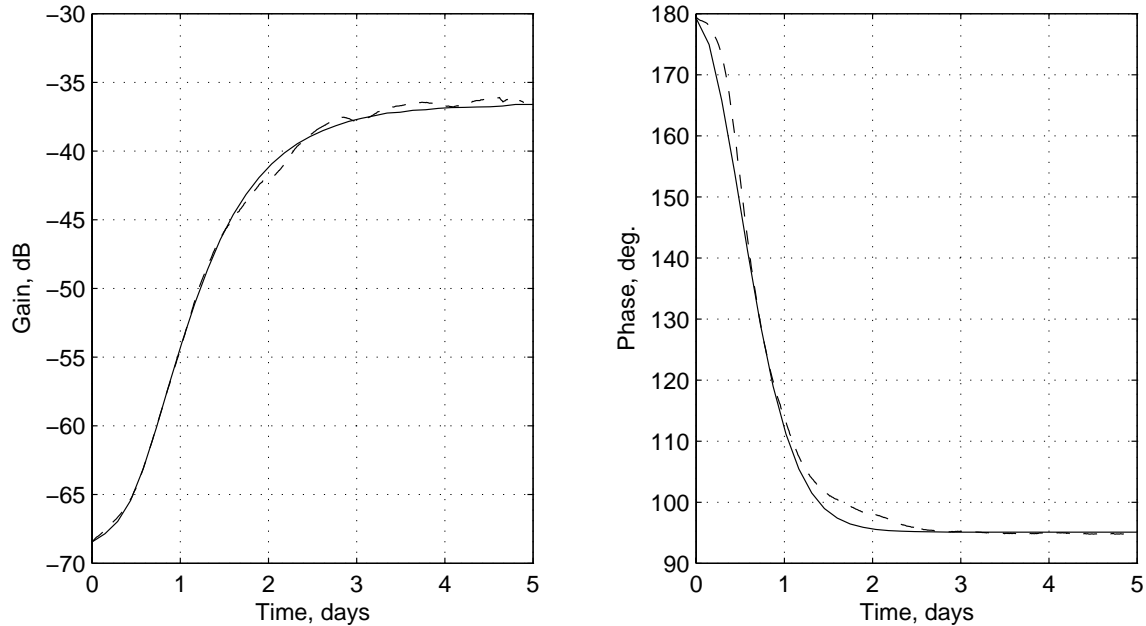


Figure 9-13: Comparison of the theoretical (solid) and experimental (dashed) gain and phase at 10 Hz as a function of time for the birch rod. The simulation uses a diffusion coefficient of $D_o = 1.3 \times 10^{-8} \text{ m}^2/\text{sec}$.

9.4 Diffusion Estimates from z Periodic Measurements

Quantifying the diffusion process from z periodic sensors can be done without assuming any form of the diffusion process. The profiles can be determined directly from the experimental measurements and a mapping between moisture content and the effective permittivity. We begin by assuming that the boundary conditions are constant for all time. This allows us to place a Dirichlet boundary at the exposed surface with the boundary condition of 100% final moisture content, and a Neumann boundary condition at the opposite end of the rod.

We then pick a frequency to evaluate the moisture content at and create a mapping to effective permittivity for that frequency. This is done by once again assuming the frequency spectrum is shifted linearly when frequency is plotted on a logarithmic scale. A vertical shift of the relative permittivity is seen in several materials. This is accounted for in the mapping by again assuming a linear shift in relative permittivity with the moisture content. No vertical shift is generally necessary for ϵ'' .

We now determine the effective permittivity of each measurement channel. Strictly speaking the effective permittivity is changing with z , that is across the sensor. The field solution to the z periodic sensor is only capable of considering profiles with variation perpendicular to the sensor,

that is in the r direction. Since the width of each channel on the sensor is small relative to the length of the rod, and the admittance is predominantly determined by the material properties closest to the measurement electrodes, we determine an effective permittivity of the material using the inverse problem solver. Further discussion of this issue is found in Chapter 10.

By this approximation we can determine moisture profiles from the measured gain and phase in very few steps. First the effective permittivity is determined using the inverse problem solver. The closest point on the mapping curve to the measured effective permittivity is then found. With the point on the mapping curve known, the relative moisture content is found. Repeating this for each channel and time give a moisture content profile. The only remaining task is to find a form of the diffusion coefficient that will fit the measured curves.

9.4.1 Maple Rod Diffusion

The maple rod measurements presented in Section 8.2.2 experiment 2, are analyzed at 1 Hz. The average temperature and relative humidity during the experiment are 126.6 °F and 27.2% respectively. A mapping of moisture content to permittivity is estimated based on spectrum shifting. A horizontal spectral shift of 3.8 decades is used. A vertical shift of 0.63 is also used for the real part of the relative permittivity. Only a horizontal shift is used for the imaginary component. The moisture mapping based on shifting is plotted in Fig. 9-14 along with the measured values of permittivity. There is excellent overlap between the mapping and the measured permittivity. This indicates that our assumption of a spectral shift is justified for this material. In order to get a sense of the permittivities dependence on the relative moisture content, the black squares indicate, in 10% increments, the moisture content.

The moisture content is estimated for each measurement by finding the closest point on the mapping and then using the moisture content associated with that position. In this way the diffusion profiles can be estimated. Figure 9-15 shows the diffusion profiles at selected times. The profile is extended to the boundary by the dashed lines.

The diffusion coefficient is estimated by fitting the theoretical sensor response to the measured sensor response. For each channel the gain and phase are estimated by taking the diffusion profiles, mapping the moisture content to effective permittivity, and then calculating the response. We find the diffusion coefficient is approximately $1.3 \times 10^{-8} \text{ m}^2/\text{sec.}$ The theoretical and measured gain and phase are shown in Fig. 9-16. Overall the agreement is excellent.

Using this diffusion coefficient, the diffusion profiles are plotted on Fig. 9-15 in red. Overall the agreement is exceptional.

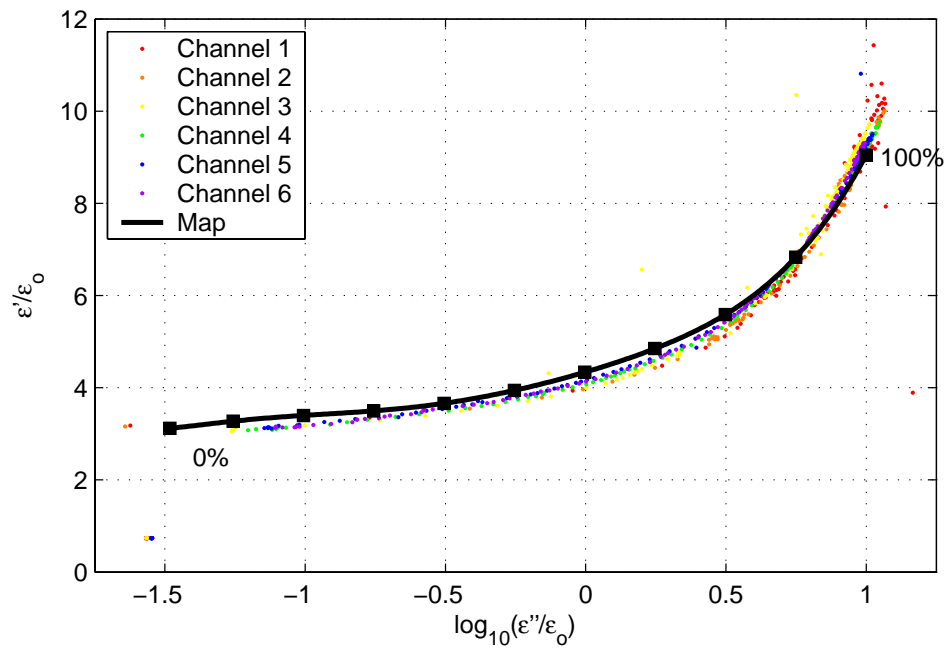


Figure 9-14: Maple rod moisture mapping at 1 Hz. The effective permittivity changes with the moisture content. The black curve shows the mapped permittivity as the moisture content changes from its initial (0%) to final(100%) value. Each block indicates a 10% increment. The channel measurements, plotted for all measurement times, show excellent agreement with the mapping. The final time shown is 12 days.

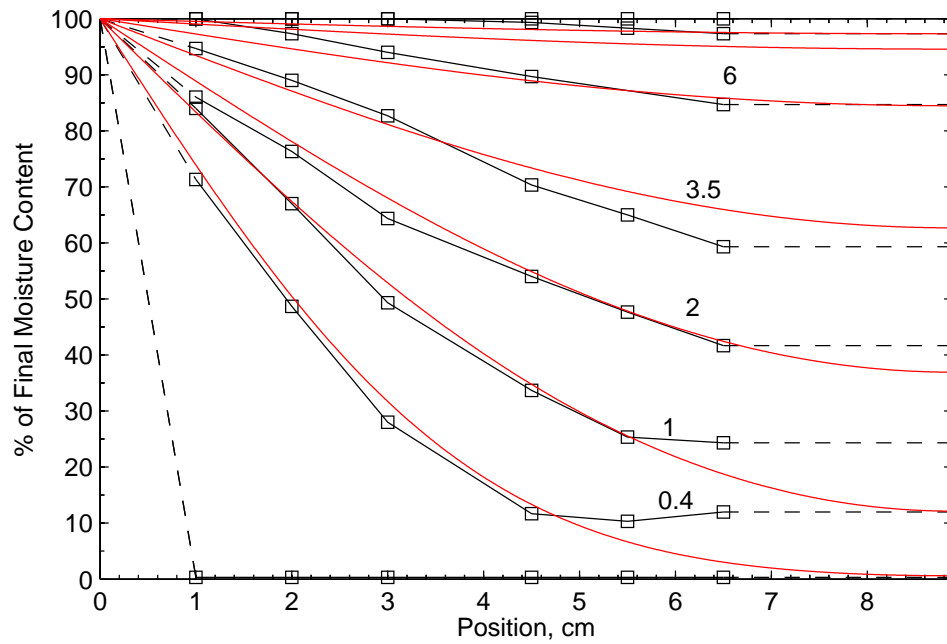


Figure 9-15: Maple rod moisture profiles measured using the z periodic sensor. The left side of the figure corresponds to the open face (Dirichlet boundary), and the right side to the blocked end (Neumann boundary). The profile times are 0, 0.4, 1, 2, 3.5, 6, 9, and 11 days. The red curves show the theoretical profiles at the corresponding times when $D_o = 1.3 \times 10^{-8} \text{ m}^2/\text{sec.}$

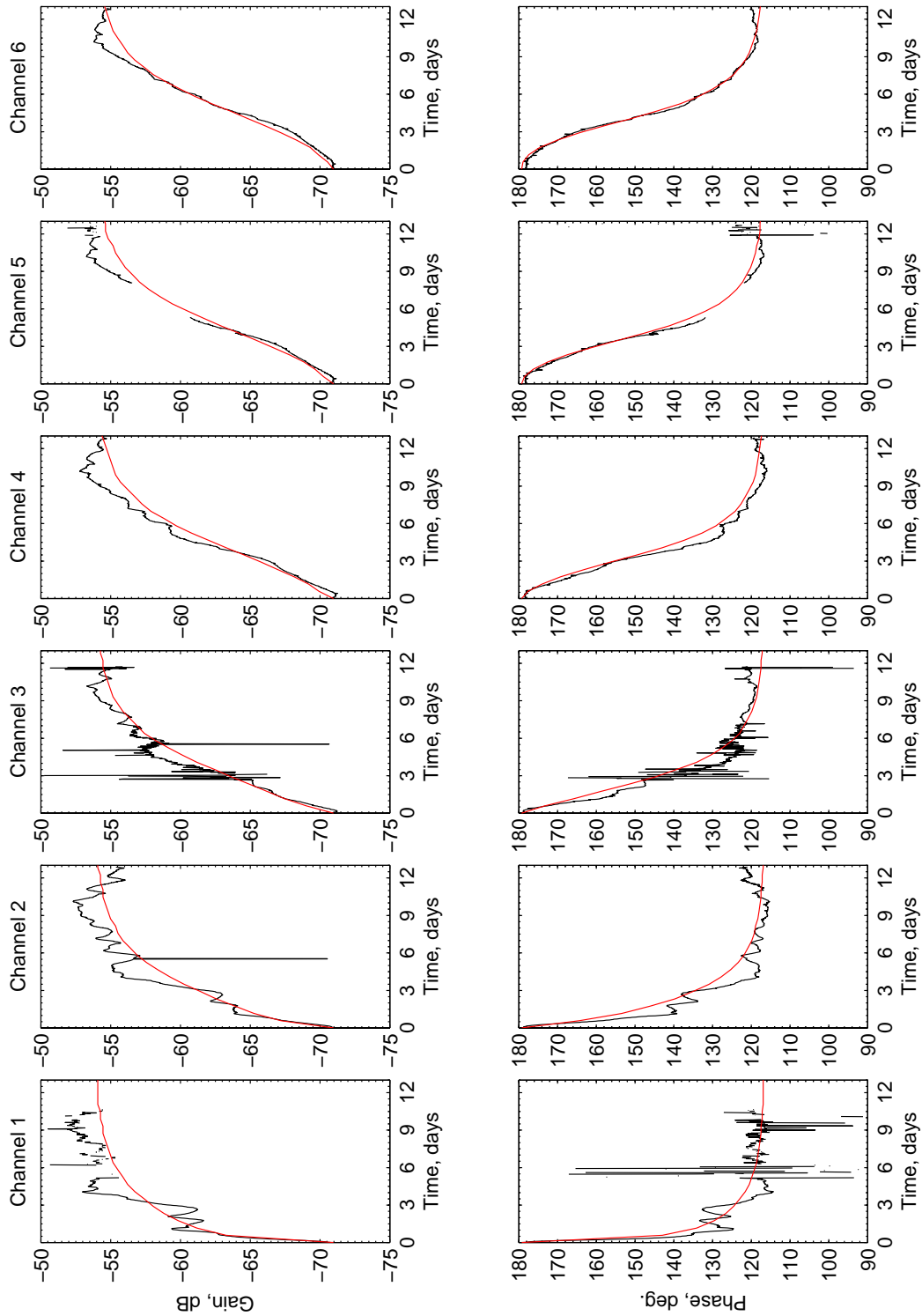


Figure 9-16: Maple rod: Measured (black) and theoretical (red) gain and phase at 1 Hz for moisture diffusion.

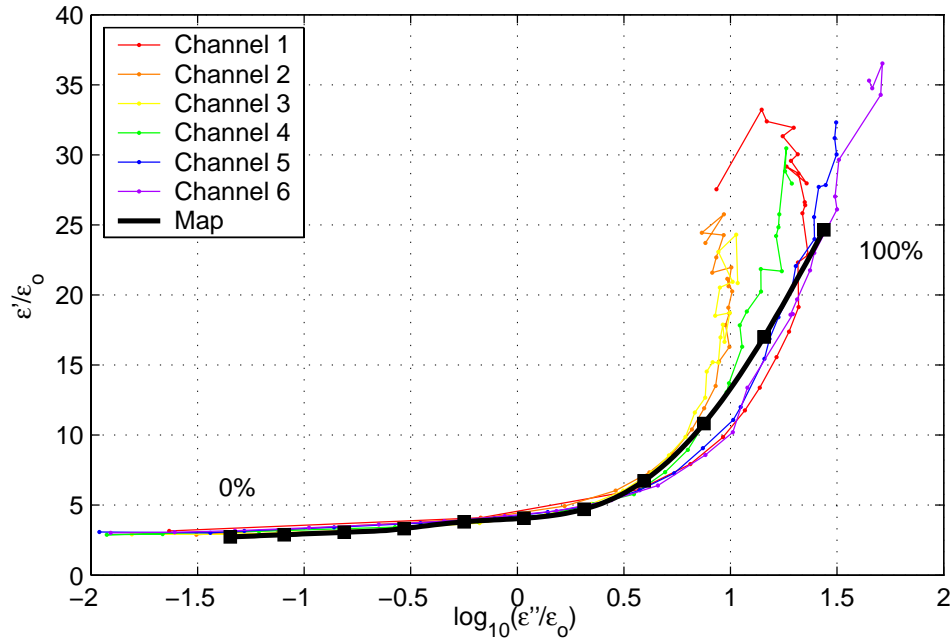


Figure 9-17: Birch rod moisture mapping at 10 Hz. The effective permittivity changes with the moisture content. The black curve shows the mapped permittivity as the moisture content changes from its initial (0%) to final(100%) value. Each block indicates a 10% increment. The channel measurements, plotted for all measurement times, show good agreement with the mapping through at least 70%. The final time shown is 2.5 days.

9.4.2 Birch Rod Diffusion

The birch rod in Section 8.2.1 shows a diffusion process in the z direction. The measurement temperature was 128 °F and the relative humidity was 60%. The mapping of the moisture content to effective permittivity is shown in Fig. 9-17. The channel measurements, plotted for all measurement times, indicate a strong overlap with the mapping through 70%. After 70% the behavior of the channels separates and is more difficult to track with the mapping.

We use the mapping to create a series of moisture profiles inside the material at selected times. These profiles are shown in Fig. 9-18. The profiles are similar to a one dimensional diffusion process, however, it is difficult to find acceptable agreement using a constant diffusion coefficient.

9.4.3 Single Conductor Cable Diffusion

The single conductor cable measurements in Section 8.2.3 are analyzed at 1 Hz. The presence of moisture is assumed to result in primarily a horizontal spectral shift. Because the moisture content varies significantly during the experiment (Fig. 8-39) the peak value of the cable moisture content

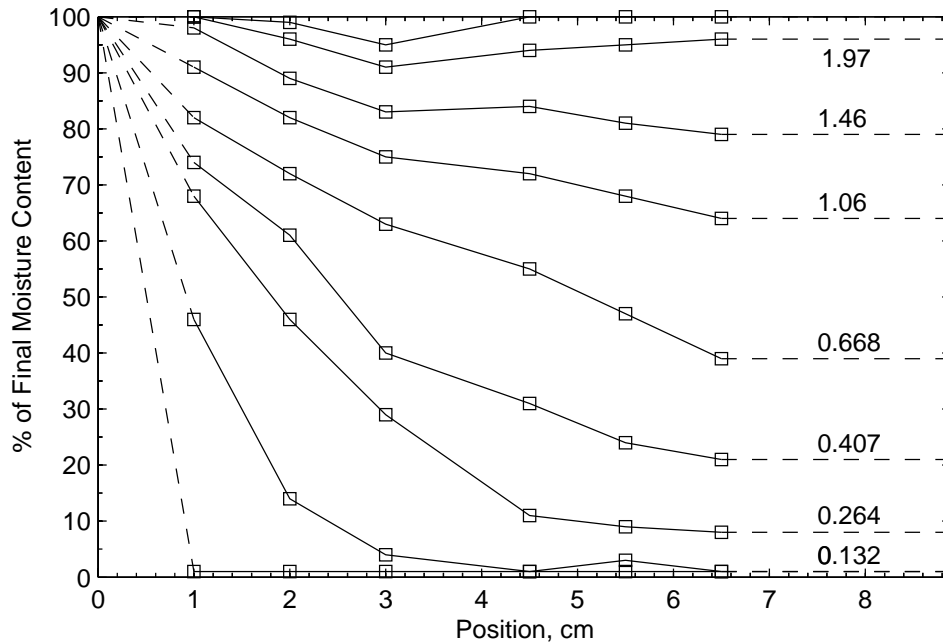


Figure 9-18: Birch rod moisture profiles measured using the z periodic sensor. The left side of the figure corresponds to the open face (Dirichlet boundary), and the right side to the blocked end (Neumann boundary). The times of the measurements are indicated in days.

is about 25% higher than the final value of the moisture. A mapping is formed for the entire range, not just from the initial to final value by shifting the real permittivity spectrum 3.2 decades. It appears that shifting ϵ'' 3.2 decades is too much and that a smaller shift is needed. For simplicity the initial and maximum values are used to define the limits of the ϵ'' dependence on moisture. The value of $\log_{10}(\epsilon''/\epsilon_o)$ is varied linearly between these two values with moisture content.

The resulting curve is shown in Fig. 9-19. The fit is of moderate quality. Notice for example the red curve, corresponding to channel 1. At time zero the moisture concentration is essentially zero. It quickly sweeps to the right as both parts of the permittivity increase. Then the permittivity decreases, but the relationship between the real and imaginary components of ϵ are clearly different. This doesn't necessarily imply that there is moisture hysteresis. A more significant contributor is that the moisture is diffusing axially and radially. The cable does not have a homogeneous cross-section. The stranded copper provides an alternative to moving through the oil impregnated paper, possibly at a much lower diffusion coefficient.

Figure 9-20 shows the "effective" diffusion profiles as estimated using the mapping in Fig. 9-19. The shape is somewhat unusual in that the curves are relatively flat. This further suggests that the stranded copper conductors serve as a conduit for moisture.

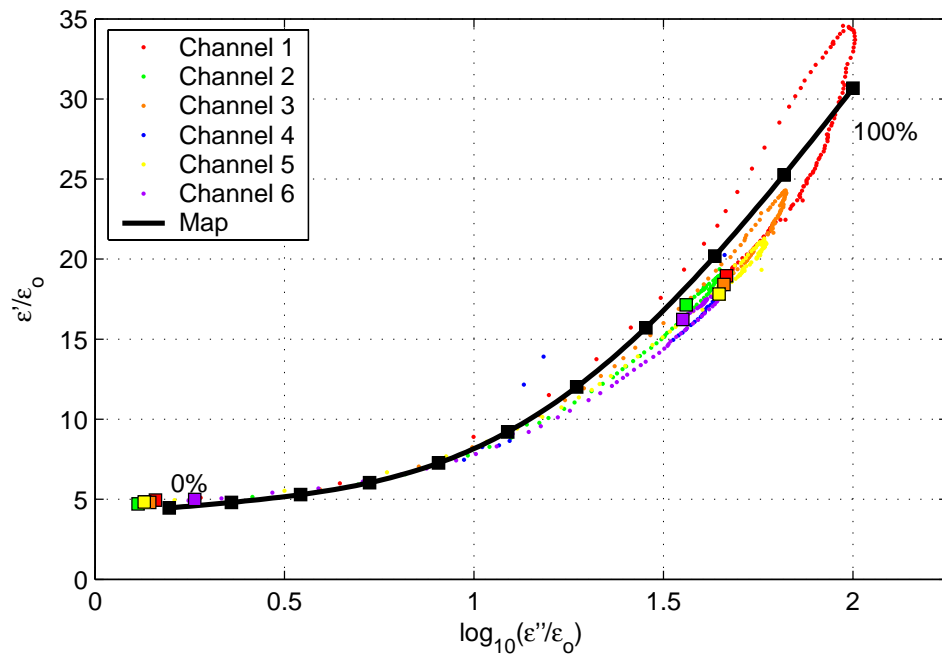


Figure 9-19: Single conductor cable moisture mapping at 1 Hz. The effective permittivity changes with the moisture content. The black curve shows the mapped permittivity as the moisture content changes from its initial (0%) to final (100%) value. Each block indicates a 10% increment in moisture content. The initial points and final points for each channel are noted by colored squares.

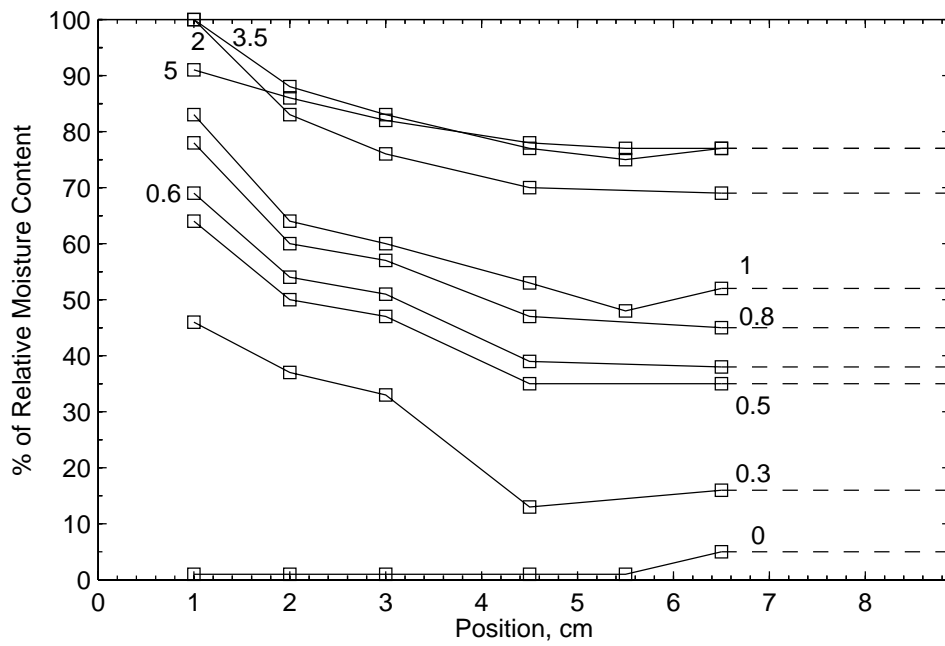


Figure 9-20: Single conductor cable moisture profiles measured using the z periodic sensor. The left side of the figure corresponds to the open face (Dirichlet boundary), and the right side to the blocked end (Neumann boundary). The profile times are 0, 0.3, 0.5, 0.6, 0.8, 1, 2, 3.5, and 5 days. After nearly 8 days the profiles is nearly uniform at 75%.

9.5 Three Dimensional Diffusion Problems

The boundary conditions determine the direction of moisture flow in a diffusion experiment. In our early transient measurements, much of the cylindrical side of the cable was exposed in addition to both cable ends. This resulted in a three dimensional diffusion process, the parameters of which require more degrees of freedom than our measurements provide. Figure 8-14 shows the clamping setup for one of these early experiments.

Complicating matters, the diffusion through the cable is direction dependent, *i.e.*, the diffusion coefficient is most accurately described by a tensor. Moisture moves along the axis of the cylinder considerably faster than it moves radially. This is expected since the paper tapes are helically wrapped; moisture can move more easily between the tapes than through the tapes. Also contributing to a faster rate of axial diffusion are the stranded copper phases of the cable. Moisture can move quickly between the gaps in the copper strands.

In this section we provide some preliminary analysis to illustrate the software tools available for approaching these types of problems. Here we use Comsol Multiphysics, a three dimensional finite element solver capable of addressing a plethora of physical phenomena described by partial differential equations.

In principle Multiphysics can address both the moisture diffusion and electrostatic aspects of the experiment. Unfortunately a three dimensional numerical solution is not practical for geometries of this size using modern personal computers. This is primarily due to the number of grid points required to accurately estimate the transadmittances between drive and sensing electrodes. The estimated transcapacitance from even the simplest three dimensional ring geometries is a considerable challenge. In Table 4.5 we reported a difference of 5.84% between the theoretical solution and a three dimensional simulation in Multiphysics. The Multiphysics simulation used the most precise grid possible with our computer. Increasing the grid size resulted in a memory related error. This was using the simplest conceivable geometry, with a homogenous material under test. To simulate the entire sensor with a moisture dependent effective permittivity would be unreasonable. We therefore only address the moisture diffusion process using the Multiphysics solver.

9.5.1 Example 3: Three Conductor Cable

We consider the geometry of the three conductor cable with boundary conditions similar to those pictured in Fig. 8-14. To reproduce the cable geometry in Multiphysics, the photograph of the three conductor cable shown in Fig. 2-1 is approximated by vector graphics using CorelDraw. The 2D vector graphic is imported by Multiphysics and extruded to produce the cable geometry shown in

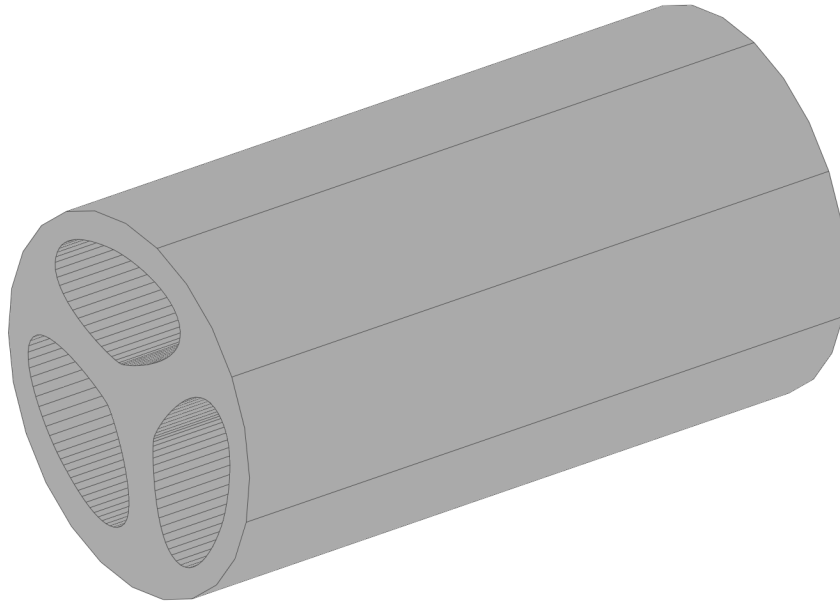


Figure 9-21: Three conductor cable geometry produced for analysis in Comsol Multiphysics. For these simulations the copper conductors are assumed to be hydrophilic to simplify the analysis.

Fig. 9-21. Notice that the copper conductors have been removed from the geometry. For this study we assume these regions are hydrophilic to simplify the analysis.

We then define the boundary conditions as either Dirichlet or Neumann. The Dirichlet boundary conditions are shaded in Fig. 9-22. Here the boundary condition is fixed to a particular concentration. Notice how both ends of the cable and a strip along the top are directly exposed to a fixed concentration. The remaining surfaces, including the inside surfaces along the copper conductors and the remaining exterior surface are specified by a zero flux, *i.e.*, a homogeneous Neumann boundary condition. Moisture cannot pass through these surfaces.

To complete the problem we choose the initial condition to be zero moisture concentration everywhere inside the insulation, and specify the insulation to have a constant diffusion coefficient. More sophisticated diffusion coefficients are possible, although the analysis is further complicated.

Using the transient solver, the diffusion process is simulated. The results are time dependent concentration profiles defined at each point inside the insulation. Because the geometry is three dimensional it is impossible to convey all the information in a single plot and a variety of methods can be used to illustrate the concentration.

We have chosen to illustrate the moisture concentration at an intermediate time where it varies substantially within the insulation. Figure 9-23 shows the moisture concentration at five “slices” within the cable. Each slice has a color plot indicating the concentration. Again the familiar *jet*

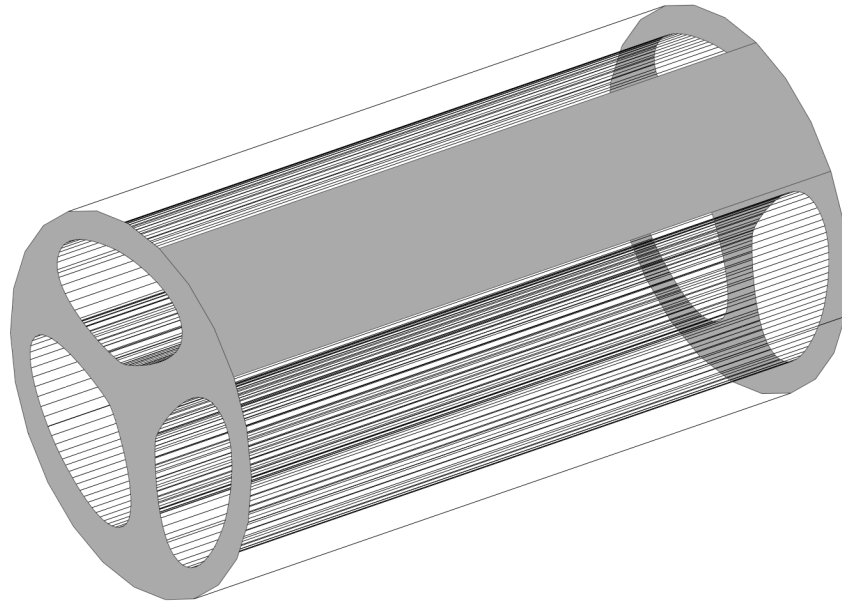


Figure 9-22: Dirichlet boundary conditions on the three conductor cable. The ends of the cable and a strip along the top are exposed to moisture. All other exterior surfaces are insulating, that is, moisture cannot enter nor exit through them.

colormap is used with dark red indicating the highest concentration, and dark blue indicating zero concentration. Recalling the boundary conditions from Fig 9-22, we see that the concentration is greatest along the Dirichlet boundary condition strip. If slices had been placed precisely on the ends of the cable, they would be solidly red as required by the boundary condition. The smallest concentration of moisture is found in the middle of the cable and directly opposite the exposed strip.

Another way of illustrating the moisture concentration is to plot surfaces where the concentration is constant. In Fig. 9-24 “isosurface” plots are made for moisture concentrations of 30%, 50%, 70%, and 90%. An animation of the isosurface location as time progresses would show the progression of the surfaces from the Dirichlet boundaries to the most remote point in the cable.

To use Multiphysics to predict the response of the dielectrometry sensor, the sensor electrodes and substrate must be included in the geometry. This complicates the simulation immensely. A mapping must then be supplied relating the moisture concentration to the effective permittivity. Finally the transmittance of each sensor must be calculated based on the effective permittivity at each location and each time. Computational limitations make such an exhaustive simulation impractical.

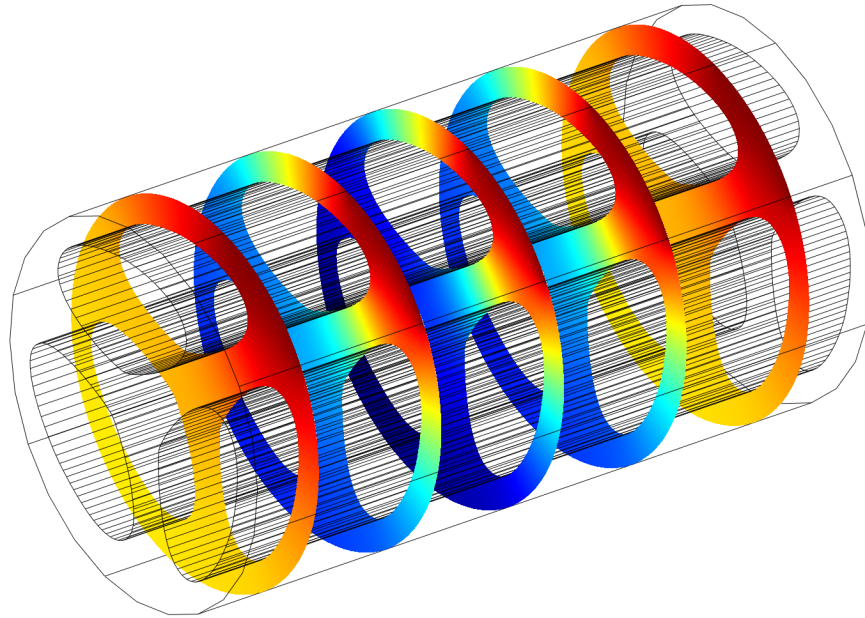


Figure 9-23: Slices of the moisture concentration in the three conductor cable. Concentration is represented by the jet colormap. High concentration (dark red) is found along the strip and cable ends, while the lowest concentration (dark blue) is in the center of the cable opposite the Dirichlet boundary condition strip.

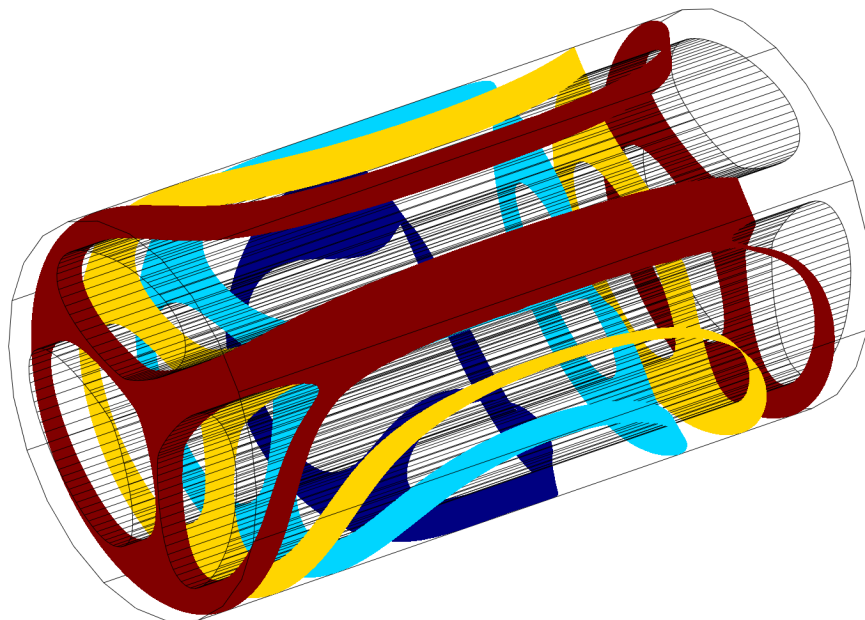


Figure 9-24: Moisture isosurfaces inside the three conductor cable. The concentrations plotted are 30% (dark blue), 50% (light blue), 70% (yellow), and 90% (red). Notice how the concentrations collapse to the most remote section of the cable, furthest from the surfaces of moisture ingress.

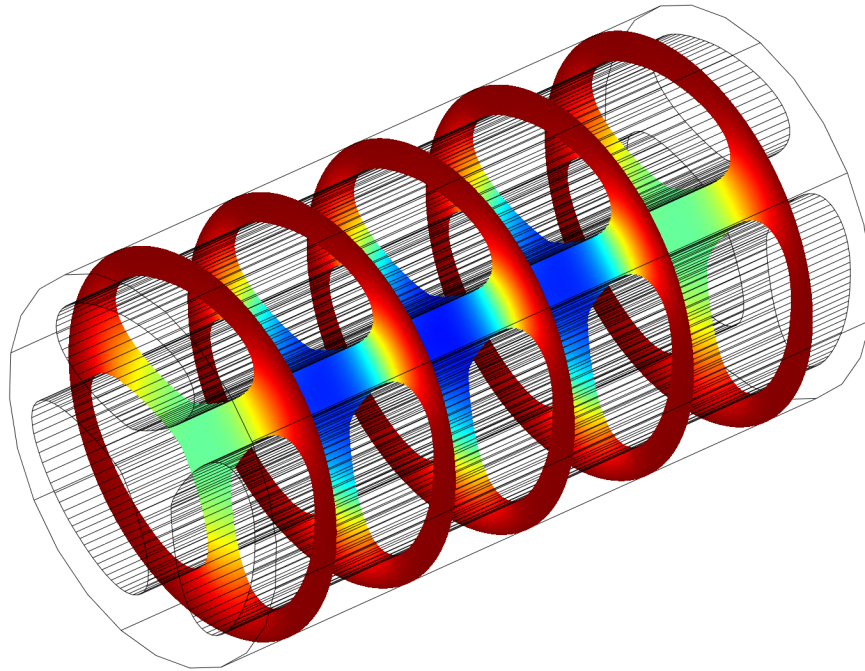


Figure 9-25: Slices of the moisture concentration in the three conductor cable. Concentration is represented by the jet colormap. High concentration (dark red) is found closest to the exterior surfaces of the cable. The lowest concentration (dark blue) is in the center of the cable and furthest from the ends.

9.5.2 Example 2: Three Conductor Cable

As a second example we consider the moisture diffusion process when the cylindrical side and both cable ends are exposed to moisture. These boundary conditions are of interest since they represent the case when the cable is not held by a clamping mechanism and there is no sensor in place. We again take the copper conductors to be hydrophobic. The Multiphysics simulation results are shown at an intermediate time in Fig. 9-25. Again slice plots have been used to illustrate the diffusion process. Notice that moisture is diffusing towards the center of the cable from the cylindrical side and both ends of the cable.

9.5.3 Example 3: Three Conductor Cable

In this example we simulate a crack in the cable sheath. This is done by setting a small patch on the cylindrical surface of the cable to a Dirichlet boundary condition with 100% relative moisture content. Zero flux boundary conditions are used elsewhere on the cylindrical surface. The cable ends also are zero flux boundaries to simulate a possible laboratory setup. The copper phases are again simulated as hydrophobic. The location of the “crack” is shown in Fig 9-26.

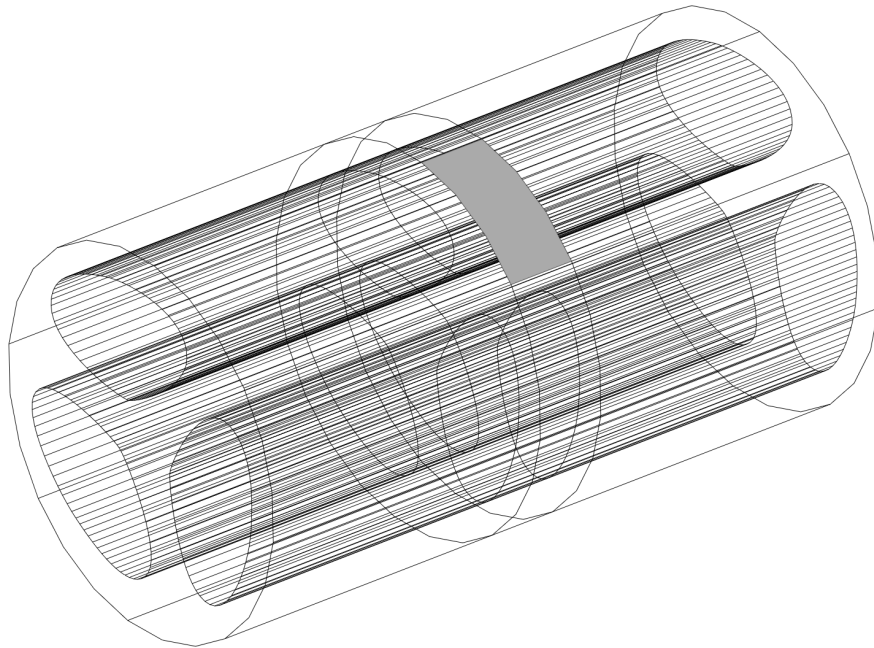


Figure 9-26: Dirichlet boundary conditions on the three conductor cable. The small patch is intended to simulate a crack in the cable sheath. All other exterior surfaces and the cable ends are insulating, that is, moisture cannot enter nor exit through them.

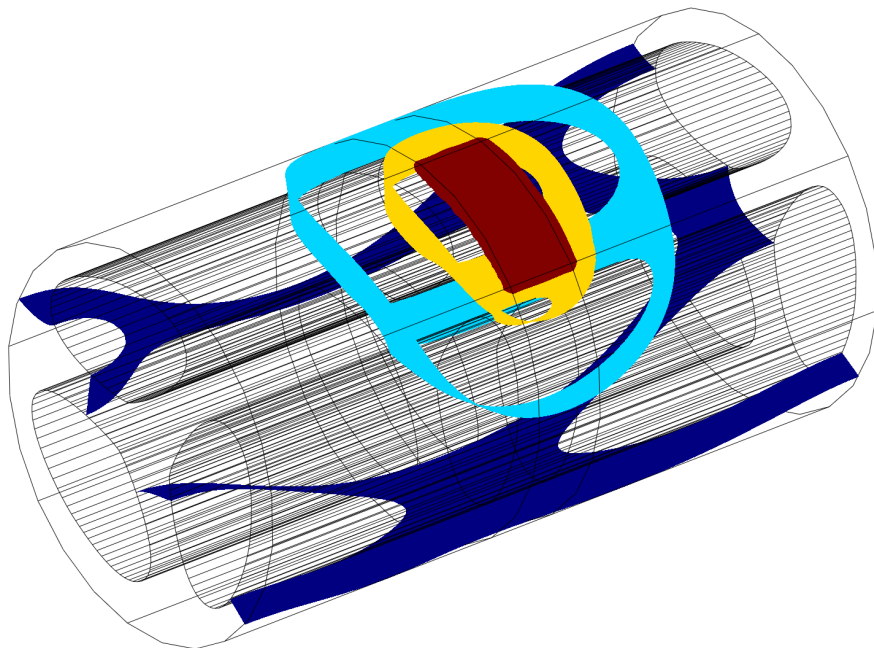


Figure 9-27: Moisture isosurfaces inside the three conductor cable. The concentrations plotted are 30% (dark blue), 50% (light blue), 70% (yellow), and 90% (red). Notice how the moisture diffuses away from the moisture source.

The simulation results are shown in Fig. 9-27 as isosurface plots. Moisture concentrations of 30%, 50%, 70%, and 90% are plotted. The length of a cable in the field will be considerably longer than that simulated in this example. While the same behavior is expected near the point of ingress, there are no cable ends to define boundary conditions at and the domain is practically of infinite length. The longer the cable sample, the more accurately the diffusion profiles will match those expected in the field.

9.6 Chapter Summary

This chapter has provided a detailed solution of the diffusion equation in several forms. The chapter began with a general derivation of the moisture diffusion equation (Section 9.1.1). The solution to the one dimensional linear problem with a constant diffusion coefficient was solved for various boundary conditions. Solutions to the linear diffusion equation for cylindrical geometries were considered in Section 9.1.4. The equilibrium relationship between moisture in air, and moisture in paper was the topic of Section 9.2. The case of a non-linear diffusion coefficient was also considered. Numerical techniques are used to obtain solutions to such problems.

In Sections 9.3 and 9.4, analysis was performed on diffusion measurements made with the ϕ and z periodic sensors respectively. The analysis provides an estimate of the diffusion coefficient or details of the diffusion profile. In the case of the z periodic sensor measurement on a maple rod in Section 9.4.1, the profiles are in good agreement with the choice of a constant diffusion coefficient. On the other hand, the moisture profiles for the single conductor cable measurements presented in Section 9.4.3 are not well fit by a simple diffusion coefficient and only the profiles are estimated.

Finally in Section 9.5 a three dimensional diffusion problem involving a model of the three conductor cable was solved numerically using Comsol Multiphysics. The capabilities and limitations of this solution technique were discussed.

Chapter 10

Multichannel Sensors

10.1 Introduction

The theoretical background for interdigital dielectrometry sensing was first formalized in a 1988 paper by Zaretsky, Mouayard, and Melcher in [37], where a solution is derived for a periodic sensor. Shortly thereafter Melcher and Zaretsky received a patent for a multi-wavelength dielectrometry sensing strategy for measuring permittivity in materials [119]. In the patent, a four wavelength sensor design is illustrated. The three wavelength design was then adapted by von Guggenberg and Melcher as a way to estimate the moisture diffusion coefficient in transformer pressboard [17].

The motivation for using a multiple wavelength sensor is to achieve multiple penetration depths, and therefore provide a spatial profile of the material under test (MUT). The typical multi-wavelength dielectrometry sensor is designed based on the assumption that material properties are only a function of z , the distance away from the surface of the sensor. Lateral variations (in x and y) must be negligible if the results from each wavelength are to be combined to provide a vertical profile. This assumption limits the types of problems multi-wavelength sensors can be applied to. In fact the multi-wavelength sensor presented in [119] is no more than a set of the single wavelength sensors developed in [37].

The multi-wavelength sensor has two primary limitations. First, the measurement strategy is fixed and wavelengths must be completely determined before manufacturing. If a larger penetration depth is required, the sensor has no ability to adjust. Second, the design assumes no lateral variations limiting applications to cases where such an assumption is valid. As a corollary to this, the sensor has no ability to measure lateral changes in MUT properties. Increasing the degrees of freedom implies increasing the number of single wavelength sensors that make up the multi-wavelength sensor. But

with each additional sensor the footprint of the sensor increases and more surface area must be available on the MUT.

In this chapter we develop a sensor technology that utilizes the same principles of the interdigital dielectrometry sensor, but eliminates the sensor limitations noted. The benefits come to us with a significant increase in hardware design complexity, but the sensor itself can be manufactured using the same technology as previous sensor designs.

The design features independently operated electrodes with a fixed periodicity. Each electrode finger is operated as a unique channel capable of being electronically switched between drive and sense mode. By conducting a series of measurements, a spatial profile of the MUT can be formed that varies in the direction perpendicular to the sensor, and in the direction of sensor periodicity. In principle, if a dual periodic sensor is used, MUT permittivity variations could be found in three directions.

The series of measurements consists of varying the effective sensor wavelength, and independently measuring the transcapacitance on every sensing electrode. In the following sections we provide a method to achieve multiple sensor wavelengths and lateral sensitivity. Theoretical evidence is used to provide performance estimates. Some experimental results are provided as a proof of concept.

10.2 The Multichannel Sensor

A simple multichannel sensor design featuring a series of electrode fingers independently excited and sensed is shown in Fig. 10-1. The sensor features 32 channels, which is sufficient to provide a number of *effective* wavelengths. The natural wavelength is the periodicity of alternating electrodes, and corresponds to the wavelength of a traditional sensor where alternating electrodes are excited. The choice of the natural wavelength should be made based on the number of channels desired, the size of the surface area to be measured, and the minimum penetration depth desired.

The sensor in Fig 10-1 is shown with two different excitations. The left side shows a “SD” or sense-drive excitation where the odd channels are driven and the even channels are sensed. The right side shows a “DS” or drive-sense excitation. Here the even channels are driven and the odd channels sensed. Each excitation results in as many as 16 independent measurements. Between the two measurements a total of 32 measurements are made. Assuming the measured capacitances are due only to the neighboring electrodes, 31 capacitances are determined, one for each set of neighboring electrodes. If the MUT properties vary in the direction of the electrode periodicity, the capacitance will reflect the MUT permittivity changes.

The penetration depth can be increased by increasing the number of electrodes in the excitation

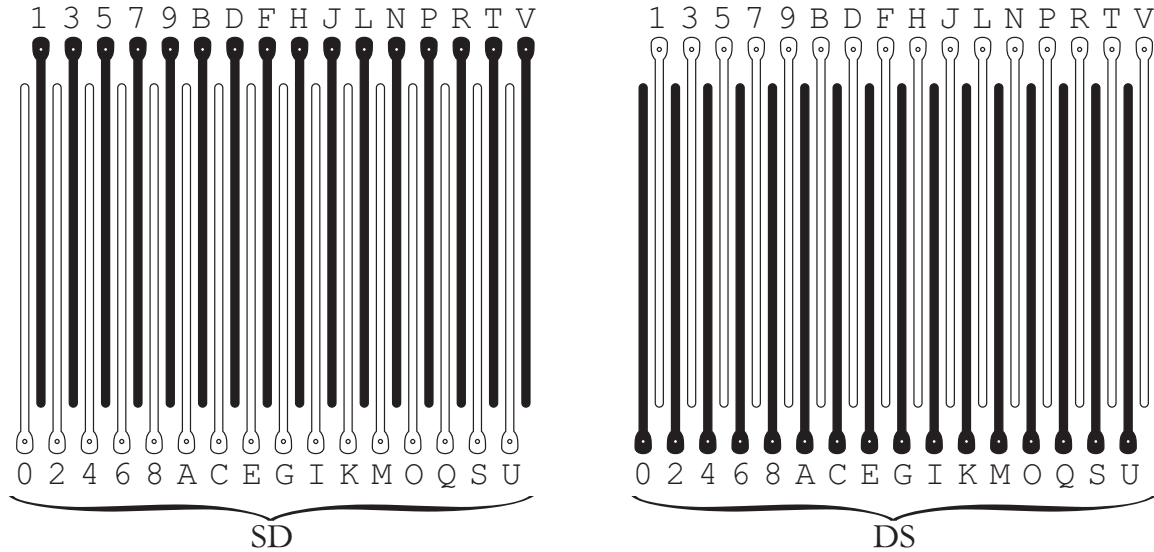


Figure 10-1: Multichannel sensor design featuring 32 channels. Each electrode has a separate connection to be connected to the appropriate switching hardware. The left sensor has a “SD” sense-drive excitation, while the right has a “DS” drive-sense excitation. Between the two excitations 32 measurements are possible. Colors: black – drive, white – sense.

periodicity. For example, a “DSSS” excitation has twice the effective wavelength as the “DS” excitation. Of course other excitations would provide the same effective wavelength, namely “DDSS” or “DDDS”. Because each finger is independently measured, each sense electrode provides different information, and has a different penetration depth associated with it.

We now investigate the issues of penetration depth and lateral changes in permittivity.

10.2.1 Penetration Depth

Penetration depth refers to the distance into the MUT that the sensor is capable of sensing. A change of material properties within the penetration depth is detected by the sensor, while a change in material outside the penetration depth goes undetected. Penetration depth is limited by noise in the measurement hardware. The sensitivity to changes in MUT properties decreases rapidly as the distance from the sensor increases. Properly designed, longer wavelength sensors are more sensitive to these changes than short wavelength sensors. Taking noise into account, sensitivity varies with the MUT properties, and therefore it is impossible to associate a single number with the penetration depth of a sensor design.

Penetration depth is best understood in terms of the electric field lines. The shape of the electric field lines is determined by all the physical parameters of sensor and MUT. Figure 10-2 shows a

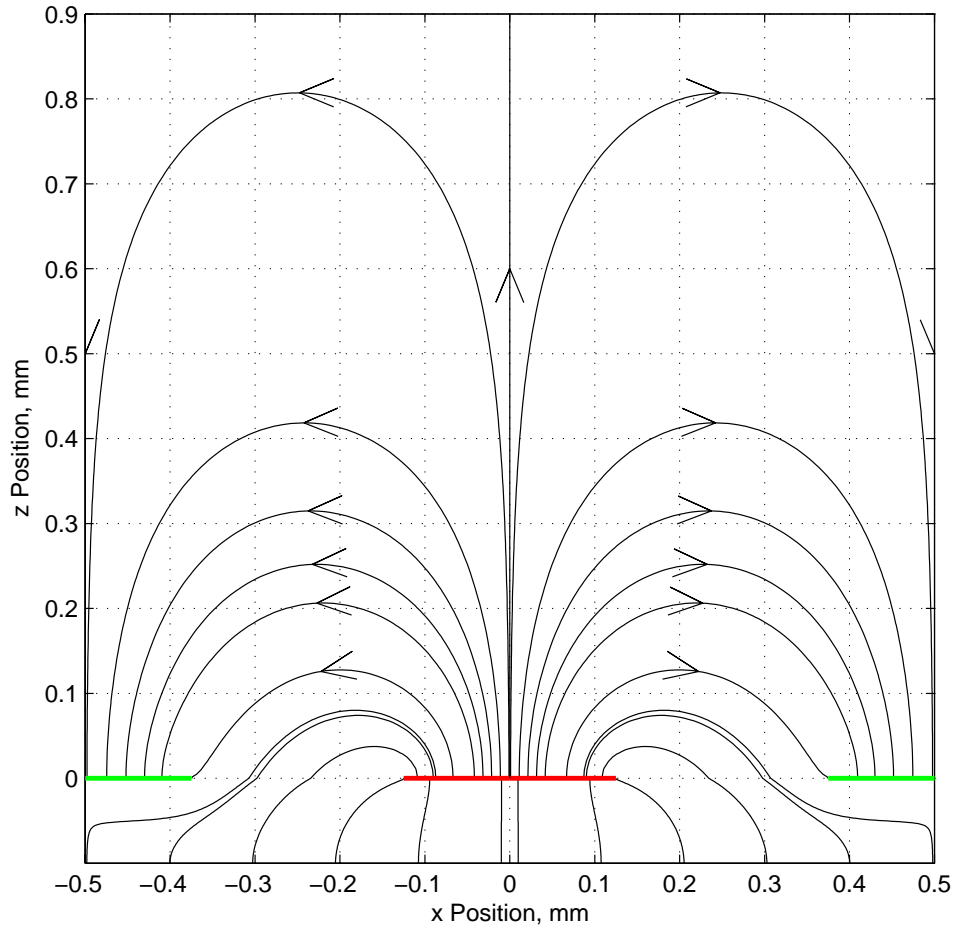


Figure 10-2: Field lines for a single period of a 1 mm wavelength sensor featuring a 4 mil Teflon substrate and a 50% metallization ratio. The MUT is vacuum.

selection of electric field lines for a 1 mm sensor featuring a 4 mil Teflon substrate, and a 50% metallization ratio. The MUT is vacuum. Electric field lines begin on the drive electrode (red), and terminate on the sense electrodes (green), or the back plane. The field line coming out of the center of the drive electrode ($x = 0$) extends to infinity and returns to terminate at the center of the sense electrodes ($x = \pm 0.5$).

The capacitance between the drive and sense electrode is affected by the MUT properties proportionally to the number of field lines that pass through a certain portion of the MUT. While only one field line passes through the MUT at infinity, the density of field lines is very high very close to the MUT. The majority of the surface of the sense electrode has electric field lines extending only a small distance into the MUT. The majority of the capacitance is “accumulated” on the edges closest to the drive electrodes where the currents in the sense electrode are largest. This capacitance

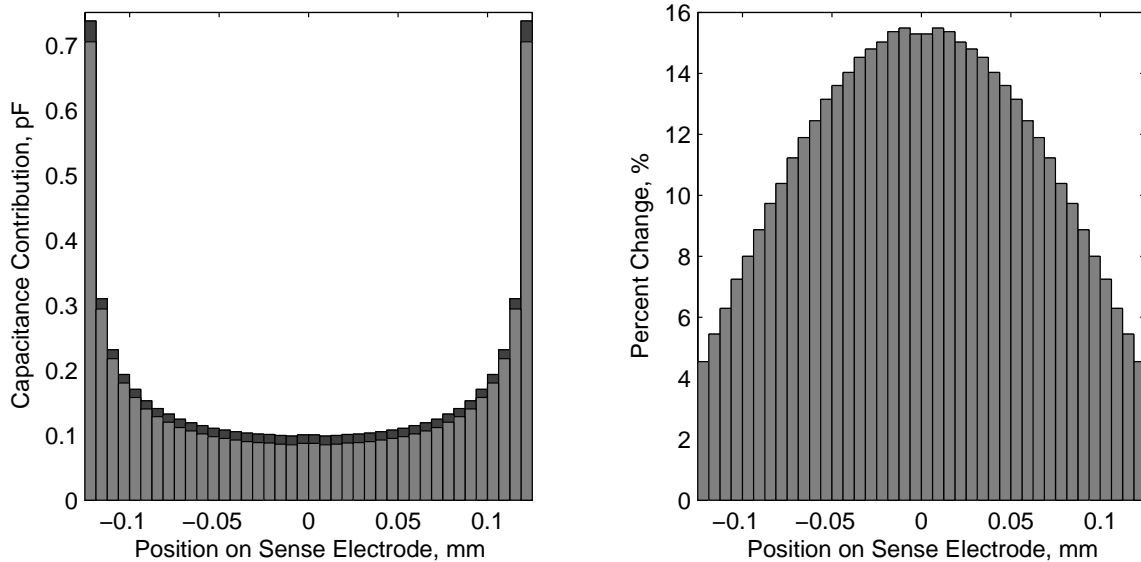


Figure 10-3: Comparison of discretized sense electrode capacitance for $\epsilon = \epsilon_0$, and $\epsilon = 10\epsilon_0$ with quarter wavelength air gap. The left figure shows the contribution of each $6.25 \mu\text{m}$ section of the sense electrode for ϵ_0 (light) and $10\epsilon_0$ (dark) cases. The percent difference between the two is plotted in the right figure. The percent change is greatest for those sections in the middle of the sense electrode. Theoretical analysis is done using the derivation in Section 3.5.

is determined primarily by the MUT properties in close vicinity to the electrode surface. The field lines ending at the center of the sense electrodes are of the greatest length and pass through the entire MUT. The capacitance is quite low because of the long length and low density of the field lines, but it is also sensitive to changes in the MUT properties very far away from the sensor.

To formalize this into a study we consider the same 1 mm sensor and discretize the sense electrode into 40 $6.25 \mu\text{m}$ subsections. The capacitance contribution for each subsection for an air MUT is calculated and plotted in Fig. 10-3. We then place an $\epsilon = 10\epsilon_0$ block at a quarter wavelength (.25 mm) from the sensor and assume it extends to infinity in z . The gap is air filled. The left figure shows the capacitance for each discrete subsection. The lighter blocks are for the air only case, and the dark blocks are with the $10\epsilon_0$ block in proximity. The capacitance for each subsection has increased slightly with the block in proximity of the sensor. The percent change is plotted in the left hand figure and clearly shows the proportionally larger effect the block has on the center section of the sense electrode.

With the ability to measure very small capacitances, a reasonable strategy is to isolate an electrode that is guarded by neighboring grounded electrodes to achieve a deep penetration depth. The shortest field lines are terminated by the guard electrodes, and the field lines passing deep into the

MUT will terminate on the measured sense electrode. Of course the trade off for this sensitivity is the much smaller capacitance that must be measured.

In light of this analysis, we see that among the excitation choices, “DSSS”, “DDSS”, and “DDDS” the first will provide the greatest sensitivity depth, particularly when the center sense electrode can be individually interrogated without contribution from the side sense electrodes. The “DDSS” choice offers only a little improvement in sensitivity depth since the deep electric field lines will terminate in-between the sense electrodes on the back plane (see Fig. 10-7). The “DDDS” excitation is the complement of the “DSSS” excitation and is the same as summing the three sense electrode capacitances in that case.

We now study the case of a 6 electrode periodicity.

Case Study: Six Electrode Periodicity

The depth sensitivity of the sensor can be adjusted by grouping electrodes to effectively increase the effective wavelength. For example, typically electrodes alternate between drive and sense, $\{\dots\text{DSDSDS}\dots\}$. If the electrodes are paired, $\{\dots\text{DDSSDDSS}\dots\}$, the effective wavelength is doubled, and the penetration depth increases. Generally there is a tradeoff between absolute capacitance and penetration depth. To achieve large penetration depths, the separation between the drive and sense electrodes for a given periodicity should be maximized. For example, there are nine practical ways to configure a six finger periodic sensor. They are given in Table. 10.1. We have used “D” and “S” as drive and sense, but now we introduce “G” to indicate that the electrode is grounded, and that the electrode current is ignored and not added to the sense electrodes measurement. Theoretically complementary configurations can be found by switching the drive and sense electrodes. In theory configurations 1 and 7 are complements and the same capacitance should be measured. The same can be said of configurations 2 and 5, and 4 and 8. Configurations 3, 6, and 9 are their own complements.

There are reasons to prefer configuration 7 over configuration 1, since configurations 7, 8, and 9 can all be calculated from a single measurement. Performing a measurement with configuration 1 only provides the same information as configuration 7.

To test the penetration depth for each configuration, numerical simulations have been done using Maxwell 2D. The penetration depth is tested by varying the height h of a glass block ($\epsilon_r = 7.8$) from the electrodes. The block extends to infinity and the gap between the block and the electrodes is air. The simulation parameters are summarized in Table 10.2.

When the height is zero, the capacitance is completely determined by the glass block. When the height approaches infinity the response is determined entirely by the background material, air. The

Table 10.1: Possible Sensor Configurations for a 6 Finger Periodicity. D-Drive, S-Sense, G-Ground.

(1)	D	D	D	D	D	S							
(2)	D	D	S	S	D	D							
(3)	D	D	D	S	S	S	(4)	D	D	D	G	S	G
(5)	D	S	S	S	S	D	(6)	D	G	S	S	G	D
(7)	D	S	S	S	S	S	(8)	D	G	S	S	S	G
							(9)	D	G	G	S	G	G

Table 10.2: Penetration Depth Study Simulation Parameters

Parameter	Value
Fundamental Wavelength	1.0 mm
Electrode Width	0.25 mm
Electrode Spacing	0.25 mm
Electrode Height	1 μ m
Glass Permittivity	7.8 ϵ_o
Gap Permittivity	ϵ_o

rate of convergence to the capacitance when the block is not present defines the penetration depth.

In order to compare the penetration depths without taking into account the absolute capacitance of the measurements, the measurements are normalized between 0, air only, and 1, glass only, by the following equation.

$$\text{Convergence}(h) = \frac{C_T(h) - C_T(h = 0)}{C_T(h = \infty) - C_T(h = 0)} \tag{10.1}$$

The results of the simulations are shown in Fig. 10-4. The “standard” case plotted represents the simulation results for a traditional 3 mm sensor with a 50% metallization ratio. The left figure shows that the measured capacitance will be very different for the “DDSSSS” configuration compared to the “DGGSGG” configuration. The right figure shows the convergence for each configuration. The convergence is the slowest for the “DGGSGG” configuration indicating that this setup has the deepest penetration depth of all the excitations considered. The smallest penetration depth is for the “DDDDDS” or equivalently “DSSSSS” configuration. The standard sensor finds itself in the middle ground.

Assuming the maximum penetration depth is desired, the choice of excitation is now determined by the sensitivity of the instruments measuring capacitance, and the actual electrode length. The capacitance of the “DGGSGG” configuration varies from 0.38 pF/m to 4.8 pF/m. For a typical electrode length of 5 cm, the theoretical capacitance measurements are 19 fF and 241 fF. Modern capacitance meters have femtoFarad accuracy such as the design presented in [120]. Because an air

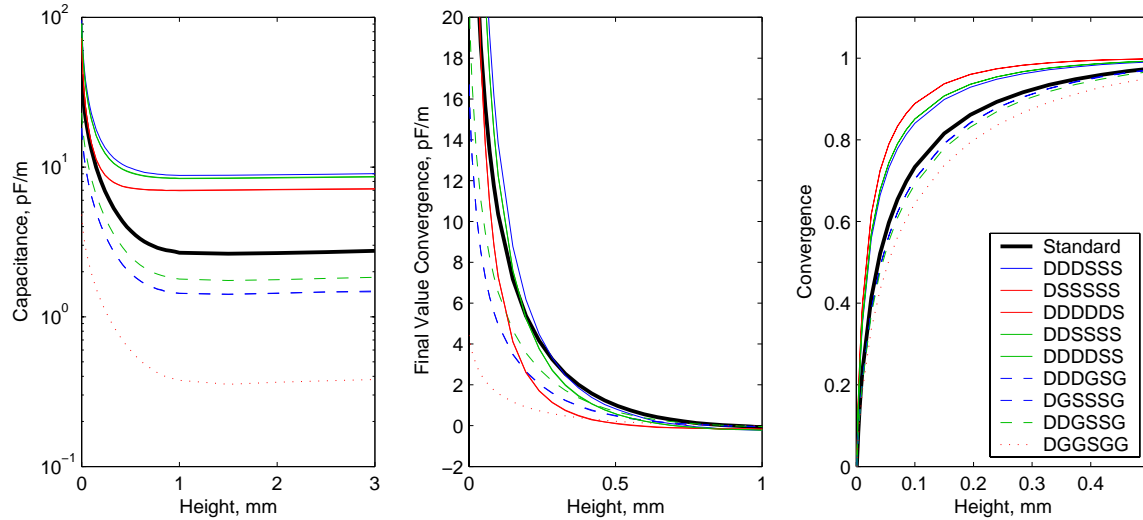


Figure 10-4: Simulation results for six electrode penetration depth study. Left: Capacitance measurement for each configuration as a function of the height of the block. Center: Convergence of the capacitance to the final value. Plotted is the capacitance minus its value at $h = \infty$. Right: Normalized convergence using eq. 10.1.

background has been used in these simulations an open top measurement should not have a lower capacitance. In the presence of a top ground plane the capacitance will approach zero as the ground plane moves closer to the electrodes. It is likely that any of the nine configurations in Table 10.2 could be used effectively with the capabilities of modern capacitance meters.

This study has looked at the special case of a six electrode excitation periodicity with a 1 mm fundamental periodicity. Longer periods will have a similar group of potential excitations and the choice of which excitation to use should reflect the ability to measure the air only capacitance. In general, the maximum penetration depth will be achieved with a single sense electrode in the center of guard electrodes.

Using the generalized planar periodic sensor solution we calculate the fields for case 7. Here we have used the fundamental wavelength of 5.0 mm. The field solutions for cases 8 and 9 are identical to case 7. Figure 10-5 is for the case when the material above the electrodes is air. The color map has been set at 20 colors to clearly indicate the equipotential surfaces which are at the boundaries between two colors. The electric field lines are normal to the equipotential surfaces. The voltage precisely at the surface of the electrodes is plotted in Fig. 10-6.

In Fig. 10-7 the field lines in air have been plotted in the lower figure. For comparison the top figures show the field lines for a $\{\dots DS\dots\}$ and $\{\dots DSSD\dots\}$ excitation. In all cases the test material is air. Notice how the deepest field lines terminate on the center electrode. The capacitances

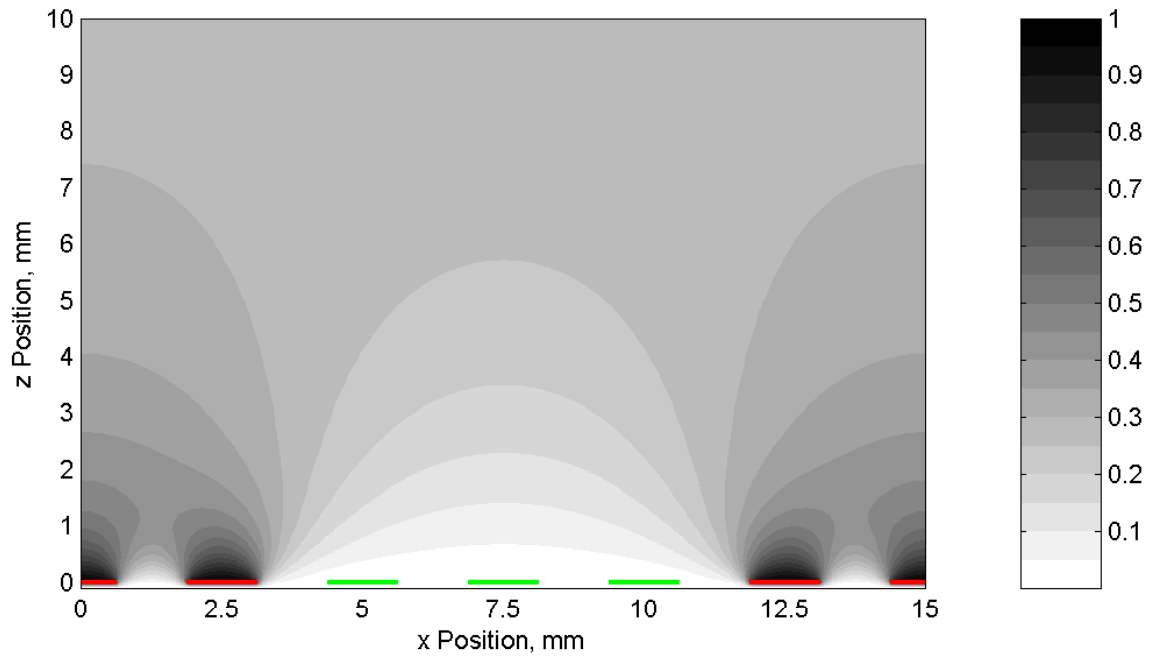


Figure 10-5: Potential field for the DDDSSS electrode configuration. The drive and sense electrodes are indicated by red and green lines respectively.

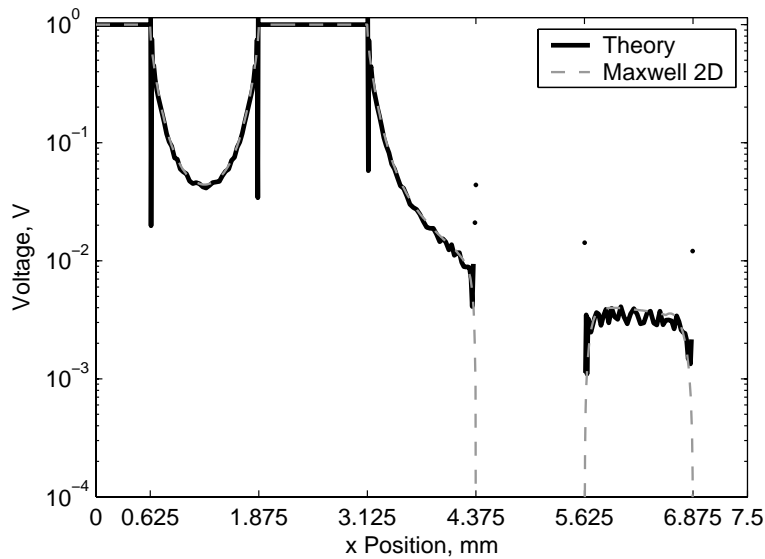


Figure 10-6: Voltage at the surface of the electrodes on a half wavelength with excitation DDDSSS. The black and gray curves show theoretical and Maxwell 2D results respectively. The ringing near the electrode edges is a consequence of the Fourier series method. As the number of terms is increased these spikes become narrower. Note that the voltage is on a logarithmic scale. Simulation parameters: $N = 700$, $K_1 = K_2 = K_3 = 50$.

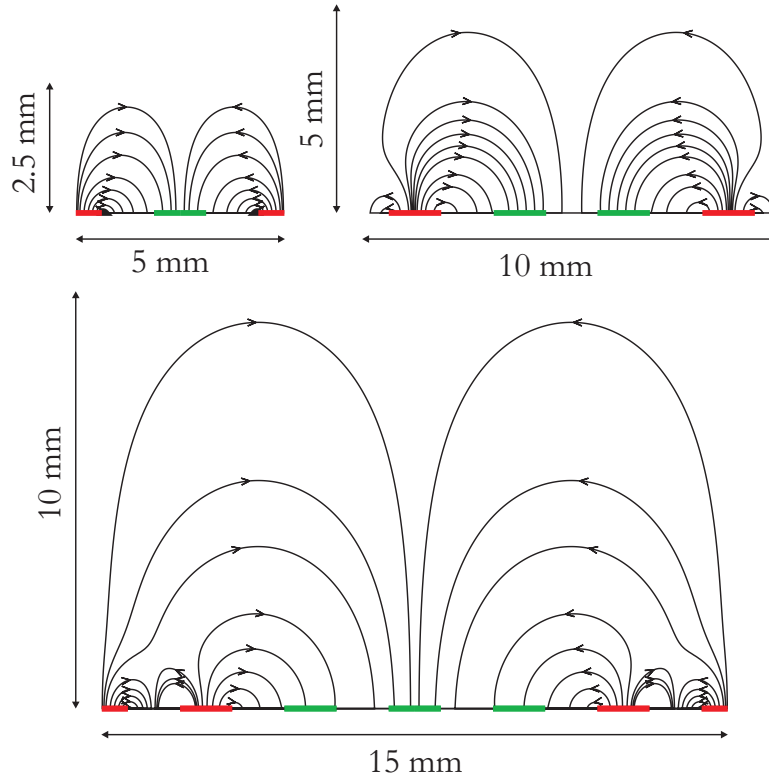


Figure 10-7: Field Lines for the 5, 10, and 15 mm effective wavelength sensors. The fundamental wavelength is 5 mm. Field lines are only drawn in the region above the substrate for clarity. The fields used for the 15 mm effective wavelength are the same plotted in Fig. 10-5.

for each of these configurations is summarized in Table 10.3

Table 10.3: Calculated Capacitance in pF/m for 5 mm Periodicity Example Problems

Electrode Configuration	Theory	Maxwell 2D Simulation
DS	2.68	2.68
DDSS	3.89	3.95
DDDSSS	4.49 (Outer: 1.77; Inner: 0.96)	4.68 Total, (O: 1.85; I: 0.98)

10.2.2 Lateral Changes in Permittivity

One of the primary benefits of the multichannel sensor is its ability to measure changes in the permittivity in the direction of sensor periodicity. This feature provides a valuable tool for monitoring diffusion processes where the direction of diffusion is in the direction of sensor periodicity. While a theoretical solution is not possible when ϵ is a function of x we find that the capacitance is primarily determined by the materials between the sense and adjacent drive electrodes.

Table 10.4: Table of Capacitances and Gains for 1, 2.5 and 5 mm sensors. Gain assumed 1 nF feedback capacitor and 5 cm electrode length.

Sensor Wavelength	Test ϵ_r	Capacitance pF/m	Gain, dB
1 mm	1	6.13	-70.3
	2	12.92	-63.8
	3	20.34	-59.9
	4	28.13	-57.0
	10	78.14	-48.2
2.5 mm	1	3.40	-75.4
	2	7.96	-68.0
	3	13.33	-63.5
	4	19.31	-60.3
	10	62.21	-50.1
5 mm	1	2.68	-77.5
	2	6.08	-70.3
	3	10.08	-66.0
	4	14.61	-62.7
	10	49.25	-52.2

The capacitance measured is related to the permittivity of the MUT. To demonstrate the multichannel sensors sensitivity to lateral changes in the permittivity profile, we begin by considering theoretical cases with a single MUT of fixed permittivity value. The theoretical capacitance measurements for a 1, 2.5 and 5 mm sensors of various MUTs is given in Table 10.4. The calculated gains assume a 1 nF feedback capacitor and a 5 mm electrode length. Since the materials are lossless the phase is 180° in all cases. They were calculated assuming a 4 mil Teflon substrate sensor with a 50% metallization ratio. The associated gains are quite reasonable and could be easily measured using our existing measurement equipment which has an open circuit gain around -100 dB.

We now present several simulation results for various permittivity profiles created in Maxwell 2D. We simulate a 10 wavelength section of a standard periodicity 1 mm sensor. To establish a baseline we simulate a homogenous MUT with permittivity, ϵ_o , and then with $2\epsilon_o$. The capacitance of each channel is calculated independently. Two profiles are also considered. The first is a ramp from $\epsilon_r = 1$ to $\epsilon_r = 2$ with endpoints at $x = .5$ mm to $x = 10.5$ mm. The second profile is a step change in permittivity from $\epsilon_r = 2$ to $\epsilon_r = 1$ at $x = 5.5$ mm. Note that because symmetric boundary conditions are used in the simulation, these profiles are mirrored in at the edges of the simulation space. The profiles and results are plotted in Fig. 10-8. The sensor response is able to follow the profile. At the limits the capacitance is very close to the nominal value.

A closer look at the capacitance values to the left and right of the step profile show that the measured capacitance is around 1% error in both cases. In fact when the step change in relative

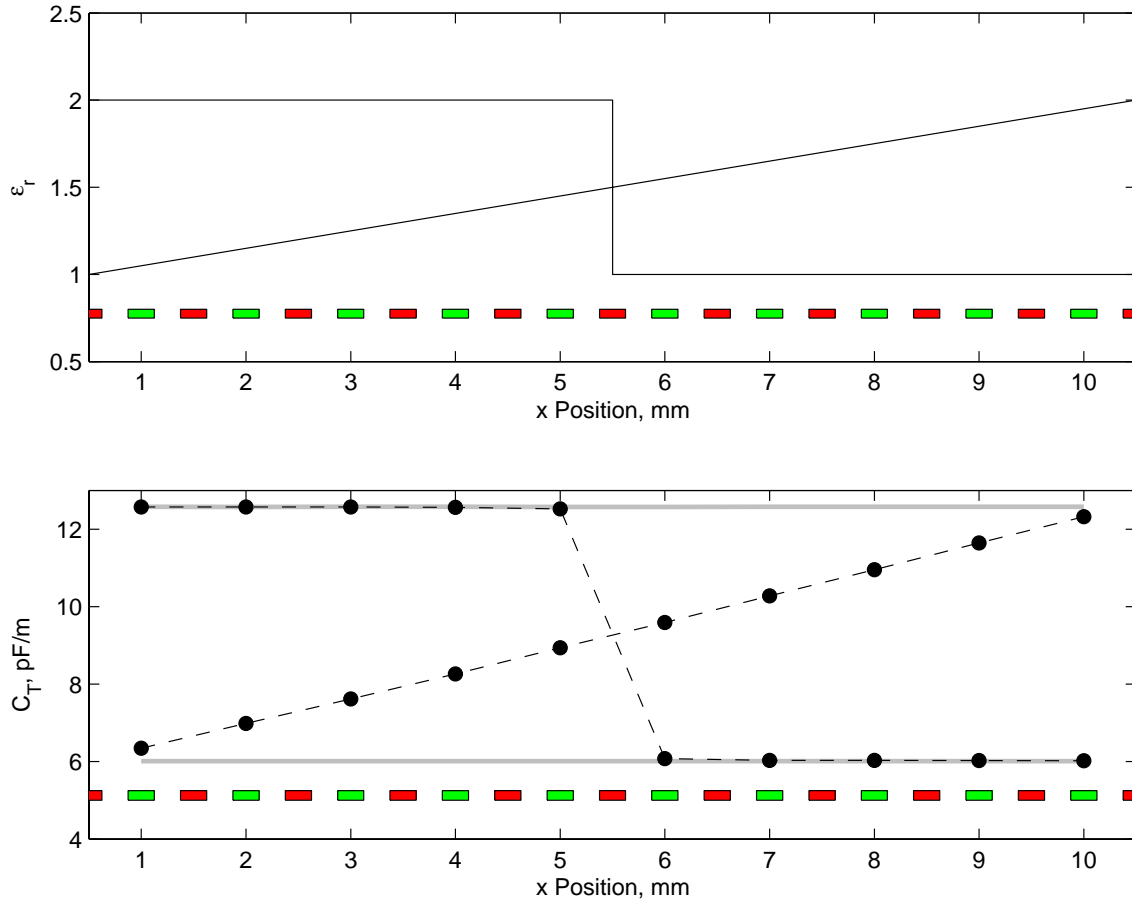


Figure 10-8: Multichannel sensor permittivity profile study using Maxwell 2D simulations. The top figure shows the step and ramp permittivity profiles. The lower figure shows the simulation results for the profiles (—•—) in comparison to the homogeneous profiles $\epsilon_r = 1$ and $\epsilon_r = 2$. The sense (green) and drive (red) electrodes are superimposed on each figure.

permittivity is from $\epsilon_r = 100$ to 1 the first sense electrode is within 7% of the nominal value. By the third sense electrode the capacitance is within 1% of the nominal value.

The resolution of these images could be nearly doubled by switching the drive and sense electrodes and measuring on the sense electrodes. This would give us a measurement after each half wavelength. We have also considered cases where the materials are lossy and similar results are achieved.

10.3 Sensing Hardware

The ability to control each electrode individually requires a small change fundamentally in the hardware but a rather large change in the scale of the system. In a traditional sensor the sense electrodes of a single wavelength are shorted and the current is fed into the inverting input of an operational amplifier. A feedback capacitance, C_f is connected between the output and the inverting input. The non-inverting input is grounded. The effect is to convert a current signal into a voltage signal, the proportionality of which is determined by C_f . The voltage signal is amplified, sampled digitally, and compared with the drive voltage to determine its relative amplitude and phase. After each measurement, the feedback capacitance is discharged by activating a reed relay in parallel with it. This is to eliminate any charge accumulated on the feedback capacitor which would result in a DC offset voltage. The presence of a DC offset voltage reduces the gain the voltage signal can receive prior to sampling. It reduces the reliability of the measurements. A reed relay is used because it offers a nearly perfect open circuit. The input impedance of solid state switches is too small for low frequency measurements but could be used in a higher frequency system.

A switch is needed to change a sense electrode to a drive electrode or drive to sense, depending on the electrodes place in the current excitation configuration. The presence of the switch must have a minimal effect on measurements during sense operation. If the switch is placed directly at the electrode any leakage currents typically found in CMOS switches are on the order of nano-Amperes could have a significant effect on sense current measurements. This problem is eliminated however by placing the switch on the non-inverting amplifier of the op-amp. In drive mode the switch is connected to the voltage source, and the feedback capacitance discharge switch is closed. This shorts the inverting input and the output, and the electrode is effectively connected to a voltage buffer. The technical challenge is limited choosing an op-amp with a very small input-bias current. The AD549 operational amplifier is designed with this issue specifically in mind, and currently is used in all the interface boxes [121]. The drive voltage, currently ± 10 V peak, is well within the specifications of the capabilities of this op-amp. A circuit diagram of the sense and drive switching configurations is shown in Fig. 10-9.

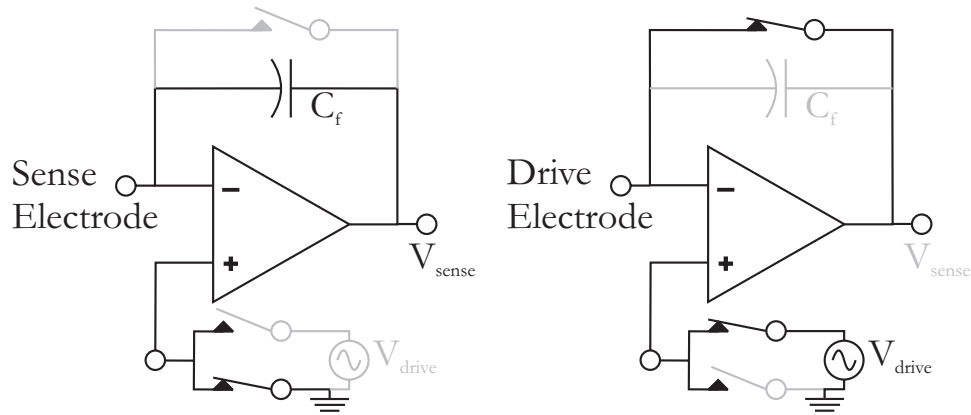


Figure 10-9: Sense (left) and drive (right) circuit configurations for the multichannel sensor. In the sense configuration the circuit acts as a current to voltage converter, and in the drive configuration as a voltage follower. The switch across C_f must be a reed type relay. A solid state switch may be used at the non-inverting op-amp terminal.

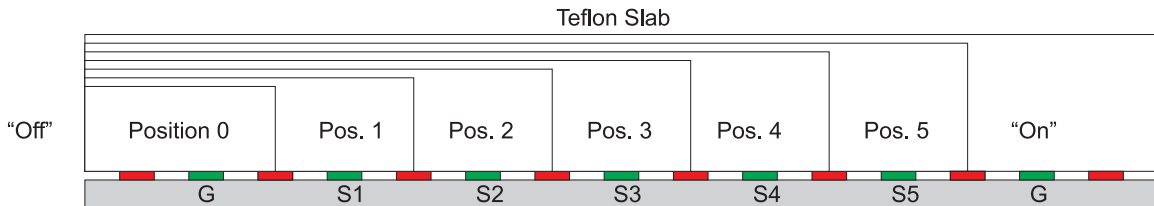


Figure 10-10: Measurement setup for Teflon slab motion. The red rectangles represent the drive electrodes and the green electrodes are the guard electrodes, labeled 'G', and the sense electrodes, 'S1' to 'S5'. Measurement positions of the slab are indicated. The thickness of the Teflon slab is constant at 7.20 mm and is held firmly in each place using a C clamp.

10.4 Experimental Verification

An experiment similar to the simulations is done using the 5 mm wavelength sensor on the three wavelength sensor introduced in Section 4.2.3. A 7.20 mm thick slab of Teflon is moved laterally across the periodicity of the sensor as shown in Fig. 10-10. Measurements are taken in with the Teflon slab completely removed, then sequentially with the Teflon slab edge centered on a drive electrode. A final measurement is made with the sensor completely covered. All measurements are made at 1 kHz.

In the first set of measurements all five sense electrodes are connected together as with a traditional sensor. Measurements are taken on channel 3 and repeated on channel 2 of interface box #1. The nominal value of the feedback capacitance is 5 nF on all channels. The measurement results are shown in Fig. 10-11. Ideally the measurements should be exactly the same. Differences are due

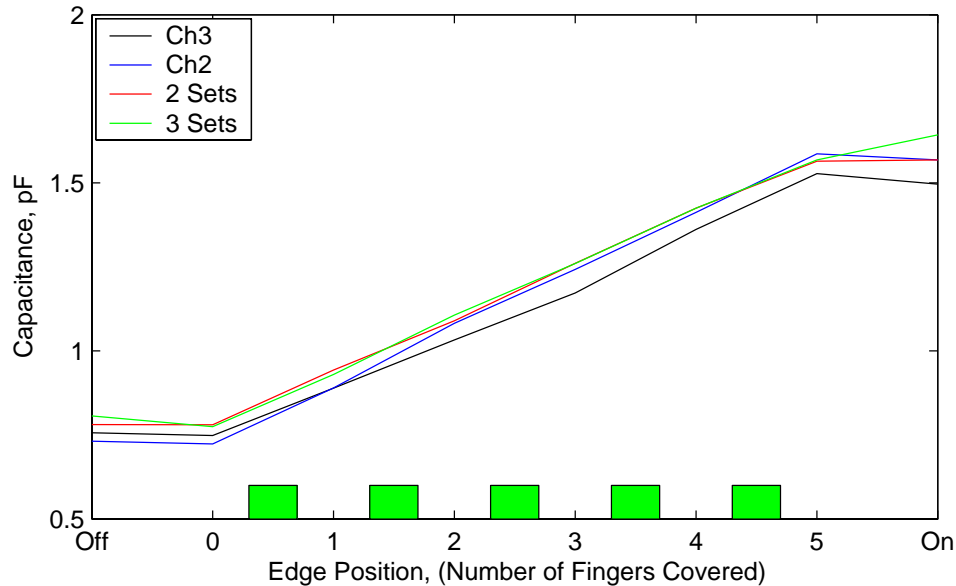


Figure 10-11: Capacitance measurements from lateral shifting of Teflon experiment for multichannel sensor proof of concept. Measurements “Ch3” and “Ch2” made prior to cutting the sensor. “2 Sets” and “3 Sets” are the sum of the measurements on the two and three channels respectively after the sensor has been divided. The green rectangles indicate the location of the sense electrodes.

to slight inconsistencies in the setup, liftoff, stray capacitances, etc.

In experiment ‘A’, the connection between ‘S3’ and ‘S4’ is breached as shown in Fig. 10-12. Sense fingers ‘S1,’ ‘S2,’ and ‘S3’ are connected to channel 3, and ‘S4’ and ‘S5’ are connected to channel 2. The measured capacitance in each position is plotted on the left side of Fig. 10-13. The measurement shows a step linear increase in capacitance as each electrode is covered. The sum of the two capacitances should be equal to the capacitance measured in the first experiments before the sensor had been cut. To verify this the capacitances are added and the sum for each measurement is plotted in Fig. 10-11 under the label ‘2 Sets’. The result is consistent with the previous two experiments.

In experiment ‘B’ the sensor is divided between electrodes ‘S4’ and ‘S5’ and a similar series of measurements are taken. Note that the electrodes have been renumbered to be consistent with Fig. 10-10. This is because the Teflon slap was slid in the opposite direction. The right side of Fig. 10-13 shows the measurement results. Electrodes ‘S1’ and ‘S2’ are connected to channel 1, electrodes ‘S3’ and ‘S4’ to channel 3, and ‘S5’ to channel 2. The capacitance are added and the sum for each measurement is plotted in Fig. 10-11 under the label ‘3 Sets’.

A similar measurement is performed but now the Teflon block is moved in the direction of the electrodes. Initially the block is completely off of the electrodes. It is moved in steps of 0.5 cm

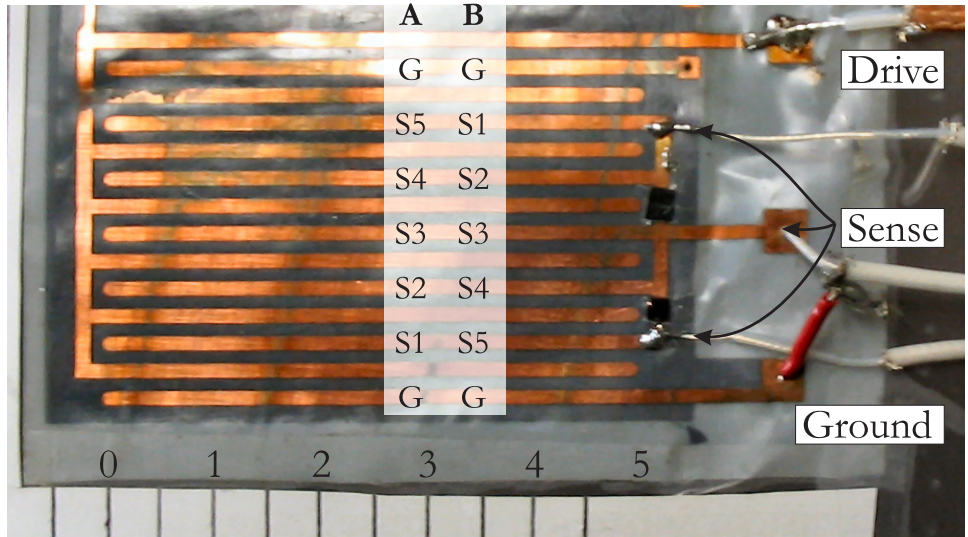


Figure 10-12: Final condition of the sensor used for experiment. The substrate and electroplating has been removed to separate the sense electrodes into 3 groups. The sense electrodes are named differently for experiment ‘A’ and ‘B.’The numbers on the bottom of the figure indicate the positions when the Teflon block is moved along the electrodes.

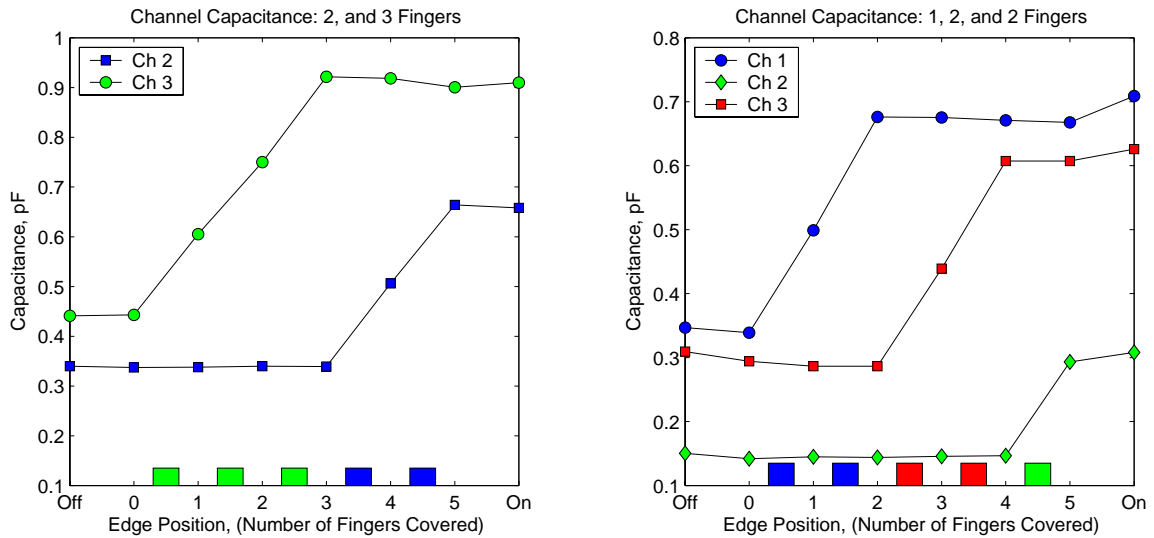


Figure 10-13: Multichannel capacitance measurements from lateral shifting of Teflon experiment for multichannel sensor proof of concept. The left figure shows the two channel experiment with fingers ‘S1-3’ connected to channel 3 and ‘S4-5’ on channel 2. The right figure shows the three channel experiment with fingers ‘S1-2’ connected to channel 1, ‘S3-4’ on channel 3, and ‘S5’ on channel 2. Measurements at 1 kHz.

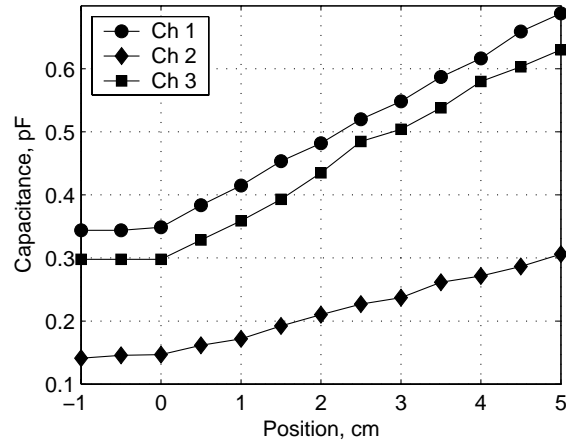


Figure 10-14: Experimental results for a Teflon block moved in the direction of the electrodes. Channels 1 and 3 are connected to pairs of electrodes ‘S1-2’, and ‘S3-4’ respectively. The discrepancy between the channel 1 and 2 measurements is due to different fixed amounts of stray capacitances which could be reduced significantly in a multichannel design. Difference in the feedback capacitance from the nominal value also contribute to an offset error. Channel 2 is connected to a electrode ‘S5’.

until the electrodes are completely covered. The measurement channels are unchanged. Results are plotted in Fig. 10-14. The sensor shows good sensitivity to the shifts. The measured capacitance is monotonically increasing, and approximately linear. It is impossible to distinguish the measurement from a material whose permittivity is increasing. It is important to develop experiments where this type permittivity change is either unexpected, or the form of the profiles are known a priori.

10.5 Capacitive Sensor Arrays

One of the interesting consequences of the generalized planar periodic sensor is that we can analytically solve for the capacitances in a one dimensional capacitive sensor array. In such an array a single electrode is driven and the capacitance is measured at each of the other electrodes. A series of measurements is taken. In Fig. 10-15 a five electrode configuration is considered. The five different excitations are shown. A total of 10 independent transcapacitance measurements can be made from the various excitations. In general for an N electrodes system the number of independent measurements that can be made is

$$M = \frac{N(N-1)}{2} \quad (10.2)$$

Figure 10-15 has been calculated using the generalized planar sensor theory described in Section 3.5. Because periodicity is assumed in the theory, we add a 4 mm buffer on both sides of the five finger array. A larger buffer would improve the accuracy of the theory at the expense of computational

complexity.

A nine electrode array is shown in Fig 10-16. Here we have calculated one wavelength of a larger sensor because of memory limitations. The space beyond the last electrode should be increased as much as possible to separate the drive electrodes to achieve the desired accuracy. The capacitance from the closest to furthest sense electrode from the drive is 2.55, 0.044, 0.026, and 0.016 pF/m. Of course the electrodes have the same capacitance on both sides of the drive electrode by symmetry.

10.6 Chapter Summary

In this chapter we explored the capabilities of the multichannel sensor using theory, simulation, and experiments. With the ability to dynamically change the excitation pattern, the sensor sensitivity depth can be adjusted during the course of a series of measurements. The choice of excitation pattern for a six electrode wavelength was considered in detail. A tradeoff exists between the sensitivity depth and transcapacitance. The choice of excitation should be made based on the capabilities of the experimental hardware.

It was verified numerically that the multichannel sensor is quite capable of resolving lateral variations in the permittivity profile. This feature was exploited in the six channel sensor design and the analysis done in Chapter 9.

In Section 10.3 a hardware setup involving a switch and relay was introduced that permits an individual electrode to be switched between drive and sense without sacrificing performance. Each channel requires its own switching hardware, feedback capacitance, and operational amplifier. Although this increases the complexity of the necessary hardware, the benefits are considerable.

A number of experiments were conducted by modifying a 5 mm wavelength sensor and sliding a Teflon slab laterally across the electrodes. The results were consistent with numerical analysis and expectation (Section 10.4). Finally we illustrated how the generalized planar sensor theory is used to simulate a finite capacitive array (Section 10.5). This same approach could be used to estimate the cross coupling between channels on the three wavelength sensor.

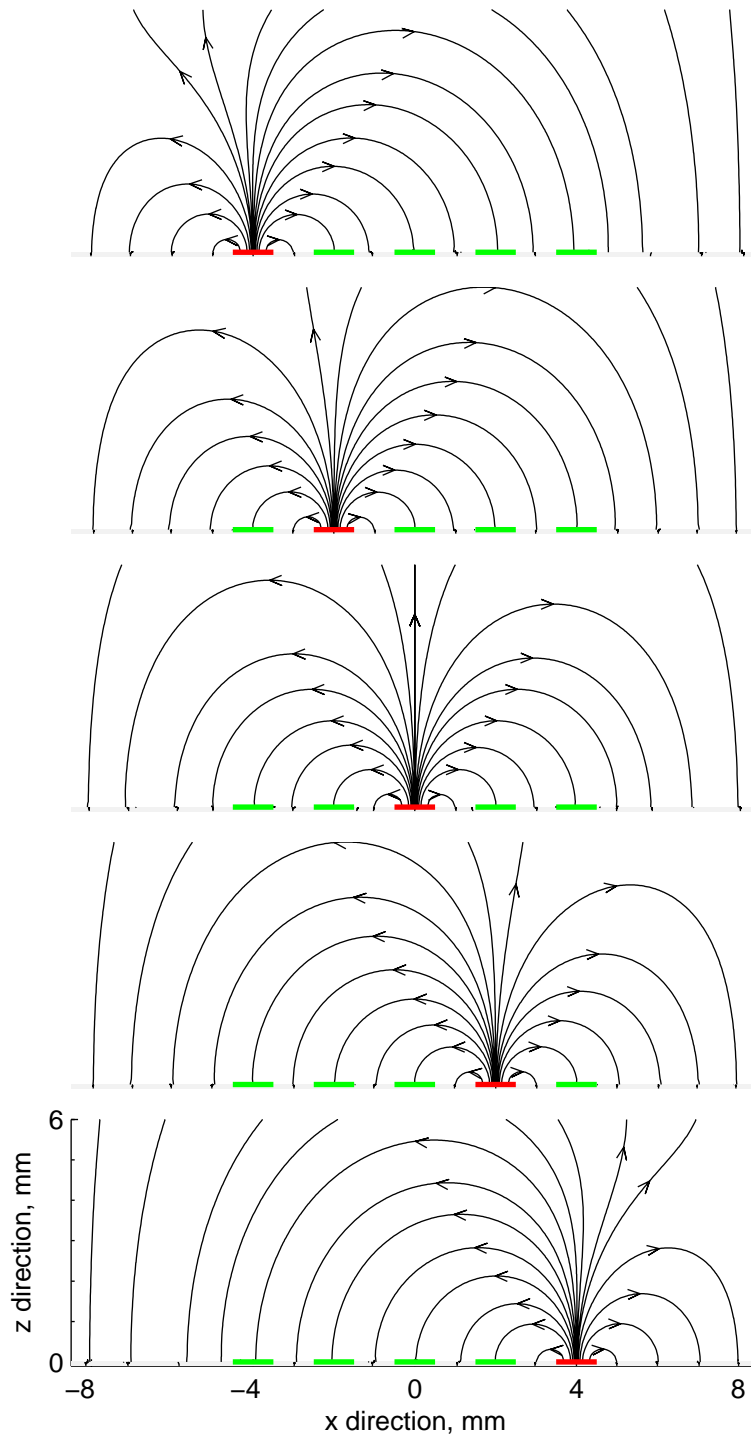


Figure 10-15: Five finger capacitive sensor array. The red electrode is drive while the green electrodes are sensed. The substrate is 4 mil thick Teflon. Electrodes are 1 mm wide with 1 mm spacing.

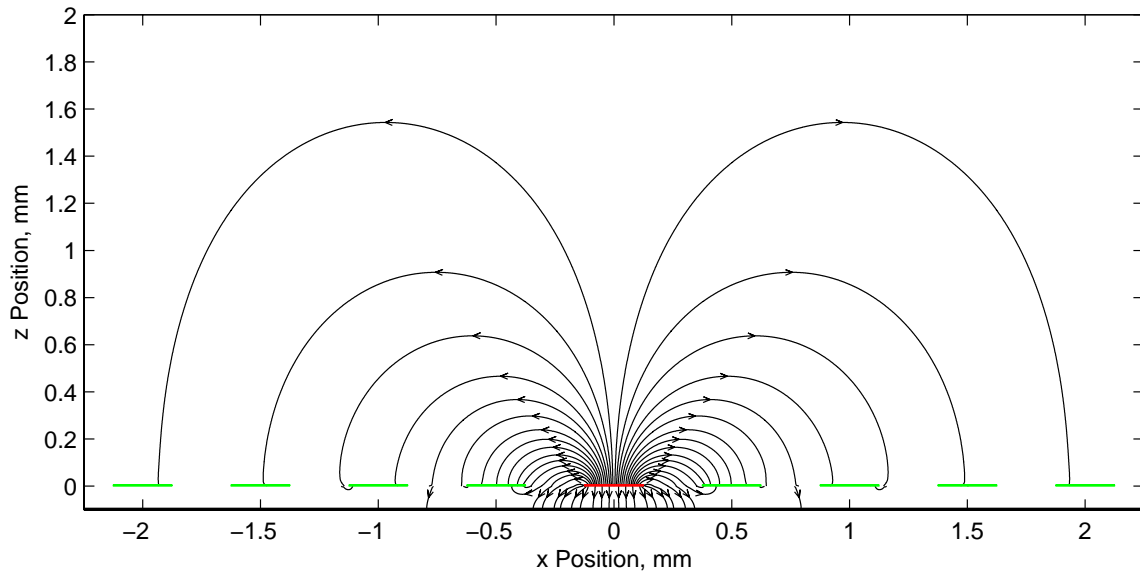


Figure 10-16: Capacitive sensor array with fifth electrode triggered. The red electrode is drive while the green electrodes are sensed. The substrate is 4 mil thick Teflon. Electrodes are 0.25 mm wide with 0.25 mm spacing.

Chapter 11

Summary, Conclusions and Suggestions for Future Work

11.1 Summary

This research has developed dielectrometry sensors for the purpose of measuring moisture and temperature dynamics in paper-insulated lead covered cables. Theoretical solutions to the electric field and impedance of the sensors have been derived analytically (Chapter 3), and have been used in the design of new sensors (Chapter 4). The practical differences between sensors in a planar geometry and a cylindrical geometry with electrodes periodic in angle (ϕ) or along the cylinders (z) axis is studied. New sensors have been designed based on the theoretical work and experiences with existing sensors designed for planar geometries.

The new sensor designs have been manufactured, and used to measure the temperature dependence of the permittivity for several plastics, woods, and the PILC cable samples (Chapter 6). Using the theoretical models the measured gain and phase is used to determine the effective permittivity of the material under test (Chapter 7). Transient moisture diffusion measurements are made (Chapter 8), and the measurements are interpreted in terms of calculated moisture profiles inside the material under test (Chapter 9).

Finally a multichannel sensor is introduced that can provide superior measurement capabilities over the current state of the art. Several studies are conducted (Chapter 10).

We briefly summarize each of the major contributions.

11.1.1 Sensor Theory

A semi-analytical solution to the electric field and related quantities has been found for several new geometries, extending and generalizing the previous research on planar sensors. This includes the ϕ periodic geometry and z periodic geometry, the solutions of which are analogous to the planar sensor solution. The planar periodic solution is generalized to provide the capability to solve any one dimensional planar topology. Also considered is a patch geometry, which extends the basic planar geometry from one to two dimensions. In all cases the solutions consist of a summation of Fourier modes. The primary assumptions made in developing the analytical solutions are:

1. the excitation frequency is sufficiently low, and the geometry is sufficiently small, that the EQS approximation is sufficiently accurate,
2. the sensor periodicity is infinite,
3. the electrodes have zero thickness,
4. the ϕ periodic sensor electrodes are of infinite length,
5. the z periodic sensor electrodes completely circumscribe the MUT, and
6. the circumference of the electrode circle is an integer multiple of the ϕ periodic sensor wavelength.

Within the assumptions of the analysis the accuracy that can be achieved by the solution is limited computationally and by the EQS approximation. In practice, the EQS approximation introduces a negligible error. The complete solution for the cylindrical and planar geometries is found including solutions for the electric field, the electric field lines, the electric potential, and impedance per unit length between drive and sense electrodes.

The solutions have been demonstrated by comparison with Maxwell 2D simulation results for the same geometries. The simulation results are in excellent agreement with the theoretical results, although some error exists due to the necessity of a non-zero electrode thickness for Maxwell 2D simulations. The cylindrical geometry sensors are compared to an equivalent planar sensor geometry. It is shown that as the radius becomes large relative to the wavelength, all three sensor responses become equivalent.

11.1.2 Sensor Designs

In the first series of measurements, sensors designed for planar geometries were wrapped around the cable in a ϕ periodic geometry. In general these sensors proved unreliable and failed either

immediately or after only a few uses. It is not believed this was related to the age of the sensors which was probably about five to ten years, but rather the designs themselves. Primarily of concern was the substrate thickness, and the electroplating thickness. All the sensor substrates of the Teflon based sensor designs before this project were 10 mils thick with $1/3$ oz copper cladding. Our conclusion was that the thick substrate in combination with the thin electrodes resulted in a brittleness inappropriate for the bending necessary for cylindrical geometries.

New ϕ and z periodic sensors were designed to take measurements on a variety of plastics, woods, and the cables themselves. The designs feature a 4 mil substrate and $1/2$ oz. copper cladding. The results have been exceptional; during the course of the research not a single sensor has failed due to broken electrodes or cracked electroplating.

11.1.3 Steady State Measurements and Analysis

The new sensor designs were used in a series of steady state temperature measurements. In these experiments the sensor was wrapped around the material under test (MUT) and placed in a temperature and humidity controlled vacuum chamber. Under most circumstances the chamber was thoroughly dried and moisture removed from the sample and chamber before measurements commenced. Measurements were taken at fixed temperatures from 0.01 to 10,000 Hz in logarithmic steps of 0.1 for a total of 61 measurements. In some cases the measurement range was extended as low as 0.005 Hz. After each frequency scan the temperature was changed to a new value and time was allowed for the temperature to stabilize in the chamber and material. The frequency scan was then repeated. Measurements were taken for each material in about 10°F increments from room temperature to 150°F and in some cases as high as 212°F .

The experimental results are analyzed to determine the effective permittivity of the measured materials as a function of frequency and temperature. Several of the plastics measured show only a small amount of dispersion and temperature dependence. The wood and cable measurements are highly dependent on frequency and temperature. The trend is for the relative permittivity and the dielectric loss to increase drastically at low frequency. As temperature increases the effective permittivity spectrum tends to shift towards higher frequency.

This shift of the dielectric spectrum with temperature is described by the Arrhenius temperature dependence. A master curve and activation energy are estimated based on the experimental measurements. In principle the master curve and activation energy completely describe the temperature dependence of the effective permittivity. Similar analysis is done on experimental measurements by Neimanis & Eriksson where moisture content was varied at fixed temperature [1]. The data suggests that changes in moisture content cause a shift of the dielectric spectrum much like changes

in temperature.

11.1.4 Transient Measurements and Analysis

Transient moisture measurements are taken with the ϕ and z periodic sensor. In these experiments the temperature is fixed and moisture is introduced into a dry chamber. The dielectric properties of the test material are continually monitored at several frequencies using the dielectrometry equipment. After sufficient time the chamber is evacuated and the drying process is also monitored.

Early experiments were done using the three conductor cable to demonstrate the effects of moisture on the cable insulation. The results show evidence of moisture entering the cable leading to an increase in insulation conductivity. The diffusion time varied greatly with the temperature and relative humidity of the chamber. For example at 100 °F and 80% relative humidity the response was changing for more than 30 days when the experiment was aborted. In another experiment at 180 °F and 50% relative humidity, steady state is reached in less than a week. The measurements suggest the diffusion process is a function of temperature and moisture concentration.

Subsequent to the initial three conductor experiments the exposed surface was limited to one or both ends of the cylindrical MUTs. If the material is homogeneous the diffusion process is completely axial and the diffusion coefficient can be estimated. Experiments conducted on birch, maple, and the cables, demonstrate that axial diffusion processes can be monitored by both the ϕ and z periodic sensors.

In the ϕ periodic case the response is assumed to be due to a moisture profile. A moisture profile is estimated by assuming a diffusion process and a mapping is used to convert the moisture content to an effective permittivity profile. The sensor response is calculated for each point of the permittivity profiles and the impedance is integrated over the surface of the electrodes. The gain and phase is then calculated based on this impedance and compared to the measured gain and phase. The diffusion process is adjusted until a good match is achieved.

For the z periodic sensor the gain and phase is measured at six locations in the direction of diffusion. With a moisture content to effective permittivity mapping the moisture profile is sampled at six locations at each time. The full profile can be interpolated or fit by the proper choice of a diffusion coefficient.

11.1.5 Multichannel Sensors

The experimental portion of the research demonstrates the utility of the sensors but does not fully exploit the possibilities of capacitive sensing technology. The multichannel sensor provides a method to achieve multiple penetration depths and greater sensor resolution without the need for separate

sensors of different wavelengths. The principle assumption of the three wavelength sensor utilized in vertical profiling is that all sensors observe the same MUT. In horizontal profiling or in more complicated situations, this is not the case. By utilizing the same sensor surface for several effective excitation wavelengths a more accurate profile can be formed.

Horizontal profiles can be estimated with many more points by measuring each sense electrode individually. The z periodic sensor paired sensing electrodes. In principle, each of these electrodes could be sensed individually doubling the number of data points in our profile. Furthermore, if the drive and sensing electrodes are switched, about four times as many measurement points could be recorded for the same periodicity and surface area as the six channel sensor.

11.2 Conclusion

The focus of this thesis work has been to develop dielectrometry sensors for PILC cable measurements. The effort has resulted in contributions to the theoretical treatment of dielectrometry sensors, a determination of the temperature dependence of the dielectric properties of the insulation, and the ability to produce profiles of moisture content inside the materials.

The original concept of the sponsor was to develop these sensors as a hand held cable moisture sensor for use in manholes. Technicians would measure the moisture content of the insulation in each cable where it is accessible in the manhole. If some critical moisture content was exceeded the cable would be replaced or its load adjusted appropriately.

It is evident from the design of the cables that without removing the lead sheath this application is not practical due to the high conductivity of lead. Our focus has therefore been to develop the technology for the cable geometry and to characterize the dielectric properties of the insulation under different temperature and moisture conditions.

The results and techniques developed in this thesis could be used in a laboratory setting for diagnostic testing of cable health. Current industry practice is to periodically remove a length of cable from the network and send it to the laboratory for a series of diagnostic tests. The health of the cable is quantified and this information is used to plan replacement for other cables in the network. Currently, testing techniques require about two months of laboratory time to assess the cable condition. Laboratory backlogs can result in delays of over a year. One of the potential benefits of dielectrometry is to provide an inexpensive health assessment mechanism that could be quickly conducted in house by each utility, providing initial feedback in days, long before a full report may be available from a third party laboratory. Due to the nature of the technology, dielectrometry sensors require only a few inches of cable, a trivial length compared to that typically provided for

full laboratory tests.

Because of the ability to determine the electrical properties of the cable under virtually any environmental condition, dielectrometry also serves as a powerful tool for predicting and interpreting field measurements of the cable. The major field test currently being conducted by industry is the VLF hipot test. This is an off-line pass/fail test where a very low frequency signal is applied to a cable at two to three times the normal operating voltage. If the cable can hold the voltage, it passes, if not, it fails. The VLF test is very limiting and a non-destructive field test is desirable. The development of more sophisticated field tests to quantify cable health is needed. Using dielectrometry measurements as part of a basis for interpretation of a new field test would be highly valuable. Because of the sheer number of manholes and the number of cables in each manhole, tests must be conducted quickly, at low costs, and with portable equipment. Real time interpretation of the experimental results is not necessary, and analysis of the measurement could be conducted at the end of the day.

Properly dealing with ageing PILC cable networks is a difficult problem that is slowly disappearing. As newer cable technology replaces PILC the amount of PILC infrastructure is reduced. Nevertheless the number of failures may be rising as much of the PILC cable network is approaching end of life. It is difficult to find statistics to quantify what stage the industry is in as the industry itself is only recently making collaborative efforts to document cable failures.

Cable failures pose the threat of huge financial losses for utilities; being able to replace PILC on a schedule rather than at failure presents the opportunity for tremendous cost reduction. Effectively scheduling replacement of PILC cable networks requires assessing the cables health to prioritize the weakest portions most likely to fail. Developing field tests to assess network health should be the focus of future research.

11.2.1 Laboratory Experience

The large component of laboratory work included in this thesis often proceeded by trial and error. A number of best practices have been developed from these efforts.

Our experimental samples were sealed in a vacuum chamber for measurements. A better choice might be a bench top humidity chamber which is capable of regulating temperature and relative humidity without additional hardware. The biggest problem with a vacuum chamber is that it takes about an hour to open and re-close. The vacuum flange is connected by numerous bolts and requires considerable strength to properly seal. The chamber will rotate if not held in place when tightening with a wrench. To avoid this a wood stage was built with recesses in it such that the heads of bolts on the bottom flange would sit in the recesses. The stage was then bolted to the table top.

The side ports and extremities of the vacuum chamber become cold spots for moisture to condense

in the chamber. While the bulk of the chamber is wrapped with heating tape, keeping each extremity at the correct temperature is not possible using this technique. In later experiments the side ports were sealed off as much as possible in the large chamber to prevent condensation. Plugs were used as opposed to valves for any unnecessary connections.

The SMA connections used inside and outside the chamber to connect the sensors to the interface box are not designed for use in water. It is best to avoid condensation on these parts. Since these were in the side ports of the large chamber, precisely where moisture was most likely to condense, they were often wrapped with electrical tape to limit the direct ingress of moisture into the connections. This was eventually done to all SMA connectors inside the chamber.

New sensors must be prepared prior to use by removing a brownish film from the surface. The film is slightly conductive and will disrupt measurements if left in place. We have addressed the issue of cleaning new sensors in Section A.2.

It is worth commenting on the choice of sensor orientation. The z periodic sensor orientation is quite useful in monitoring axial diffusion processes. The ϕ periodic sensor has limited applications since processes are not normally changing uniformly with angle. Axial diffusion processes can still be monitored using this orientation, however, more assumptions are necessary. Using a combination of the two may be useful in monitoring diffusion from a point, or localized source.

11.3 Suggestions for Future Work

During the course of the research, numerous avenues have presented themselves for further investigation, and at the end of the research one finds there is always more that could be done. Many of these avenues are explored briefly in the thesis, yet for reasons of time and resources only a preliminary effort may have been possible. In addition to the research that appears tangential to our efforts, continuing efforts are also suggested.

11.3.1 Theoretical Work

Several interesting theoretical problems could be solved to extend the current understanding.

- Generalize the planar solution to include both cosine and sine terms.

In Section 3.5 only the cosine terms were considered. While any geometry can be simulated using this formulation, it may be done more efficiently by considering both the sine and cosine terms. Consider Fig. 11-1 for example. The wavelength is not symmetric about any point. While the

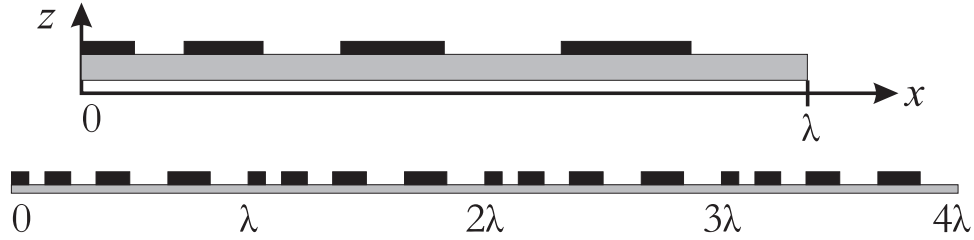


Figure 11-1: Asymmetric electrode configuration requiring both sine and cosine terms. The top shows a single wavelength, while the bottom shows four wavelengths. Because of the electrode layout, there is no symmetry point.

geometry can be approximated by simulating several wavelengths, this is computationally intensive. A more precise solution would be to include the sine terms as well as the cosine terms.

- Apply the generalized planar periodic formulation to the ϕ and z periodic cylindrical geometries.

The same approach used to generalize the planar periodic sensor could be used to generalize the ϕ and z periodic geometries. This would provide accurate solutions for arbitrary electrode configurations in the cylindrical geometries. The multichannel sensor techniques developed in Chapter 10 could then be applied.

- Include the effect of electrode thickness into ϕ , z , and generalized planar periodic sensor solutions using [49] as a foundation.

Electrode thickness is usually the largest disturbance factor.

One of the consequences of the generalized model is that the error introduced by a finite sensor periodicity can be analyzed. It would be interesting to compare the properties for a finite periodicity sensor to the infinite sensor. In principle, cross coupling can also be estimated. While these problems can be solved using the generalized planar formulation in Section 3.5, the computational requirements could be reduced in some cases by the inclusion of the sine terms.

It is interesting to note that finite electrode length could be partially addressed by the solution to the dual periodic sensor geometry. One could let the x periodicity be the same as for the one dimensional sensor, and the y periodicity be the physical length of the electrodes plus a sufficient buffer. Obviously this would not take into account that electrodes are typically rounded at one end, and connected together at the other.

11.3.2 Cylindrical Clamping

One of the primary technical challenges of the research has been to achieve a uniform pressure clamping of the sensor to the MUT. We have used the best technology available but the importance merits a serious investigation into the development of such a clamp. The use of pressure sensitive films could provide a feedback mechanism to the uniformity of the pressure applied. Since the clamp also serves as a moisture barrier it should completely circumscribe the cylinder.

11.3.3 Multichannel Sensing

Multichannel sensing has the broadest engineering implications with numerous applications. The instrumentation used in this research was originally designed for the three wavelength sensor, however the potential for the sensing technology extends beyond three channel sensing. We have utilized the hardware available essentially to its limits, often taking simultaneous measurements using all available hardware.

Multichannel sensing hardware must be developed to support far more individual channels, and these channels must be able to switch between drive and sense. An appropriate scale may be a 16, 32 or 64 channel system. The hardware should support the short circuit current mode and provide a means of increasing the feedback capacitance to avoid saturation. Using the inversion techniques frequently used for electrical capacitance tomography (ECT) should also be explored [34]. With these additional capabilities a new frontier of possibilities exists to perform experiments beyond consideration using the existing hardware.

11.3.4 Diffusion Experiments

Diffusion experiments have been conducted to provide information on how moisture diffuses inside the cable. It is not believed the utility industry has any immediate plans for such measurements, however, the basis developed in this thesis could be expanded upon if the need arose.

The diffusion experiments conducted for this research were all conducted in vacuum chambers however this choice was made mostly for legacy reasons, *i.e.*, the existence of such chambers at our disposal. Most of the experiments do not require positive or negative pressure but simply the ability to control and monitor temperature and relative humidity. Use of a vacuum chamber in principle permits for the control of the total moisture in the environment. It is generally preferable to control the boundary conditions by maintaining both the relative humidity and temperature at a constant level. Chambers of this type are commercially available although the cost is substantial. Future proposals should include an appropriate budget for such equipment.

While we have looked at the end diffusion problem, it is believed that moisture ingress usually originates at a crack in the sheath. Problems designed to simulate this situation should be studied with dielectrometry sensors such as that introduced in Section 4.2.6.

11.3.5 PILC Health Assessment

Assessing cable health and effectively scheduling replacement is the industrial motivation for this research. While extensive laboratory testing to assess cable health is available, a reliable field test would be far more valuable. Laboratory tests assume a cable sample is representative of some section of the network, an assumption that may not be justified. The ability to measure each cable on site would provide tremendous advantages in replacement and diagnosis efficiency. Very low frequency (VLF) tests are destructive, and provide only a binary assessment of health.

Development of a practical field test requires on site experience in the technicians environment, the manhole, to fully understand the practicality of any proposed measurement. Bridging the gap between the literature and the technician requires a more intimate understanding on the researchers part of the technicians environment. Any research effort for developing field tests would be greatly aided by collaboration between researchers and those with field experience.

Appendix A

Miscellanea

A.1 Terms and Nomenclature

absorption	A physical or chemical phenomenon or a process in which atoms, molecules, or ions enter some bulk phase - gas, liquid or solid material.
adsorption	A process that occurs when a gas or liquid solute accumulates on the surface of a solid or, more rarely, a liquid (adsorbent), forming a molecular or atomic film (the adsorbate).
degree of polymerization	The length of an average polymer chain. Increased mechanical strength is provided by longer chains. abbr. DP.
dielectric loss	Used to refer to the loss in dielectric measurements when plotted as $\log_{10}(\epsilon''/\epsilon_0)$.
fingers	synonymous with electrodes
guard electrode	grounded electrodes included in a sensor design to approximate a sensor with infinite periodicity.
hydrophile	A material that can transiently bond with water through hydrogen bonding. <i>Hydrophilic</i> .
hydrophobe	Physical property of a material that is repelled from water. <i>Hydrophobic</i> .
hygroscopy	the ability of a substance to attract water molecules from the surrounding environment through either absorption or adsorption.
metallization ratio	Ratio of the sum of drive electrode and sense electrode widths divided by the wavelength. Generally given under the assumption that the drive and sense electrodes have the same width.
partial discharge	Localized dielectric breakdown of a small portion of a solid or liquid electrical insulation system under high voltage stress. abbr. PD.

transcapacitance	the real capacitance between the drive and sense electrodes.
transconductance	the real conductance between the drive and sense electrodes.
wavelength	The fundamental spatial periodicity of the sensor electrode layout.

A.2 Temperature Conversion

Figure A-1 shows the conversion of temperature between Fahrenheit, Celsius, Rankine, and Kelvin.

The conversion equations are

$$^{\circ}\text{R} = ^{\circ}\text{F} + 459.67 \quad (\text{A.1})$$

$$^{\circ}\text{C} = (^{\circ}\text{F} - 32) \frac{5}{9} \quad (\text{A.2})$$

$$\text{K} = ^{\circ}\text{C} + 273.15 \quad (\text{A.3})$$

$$^{\circ}\text{F} = \left(\frac{9}{5}\right)^{\circ}\text{C} + 32 \quad (\text{A.4})$$

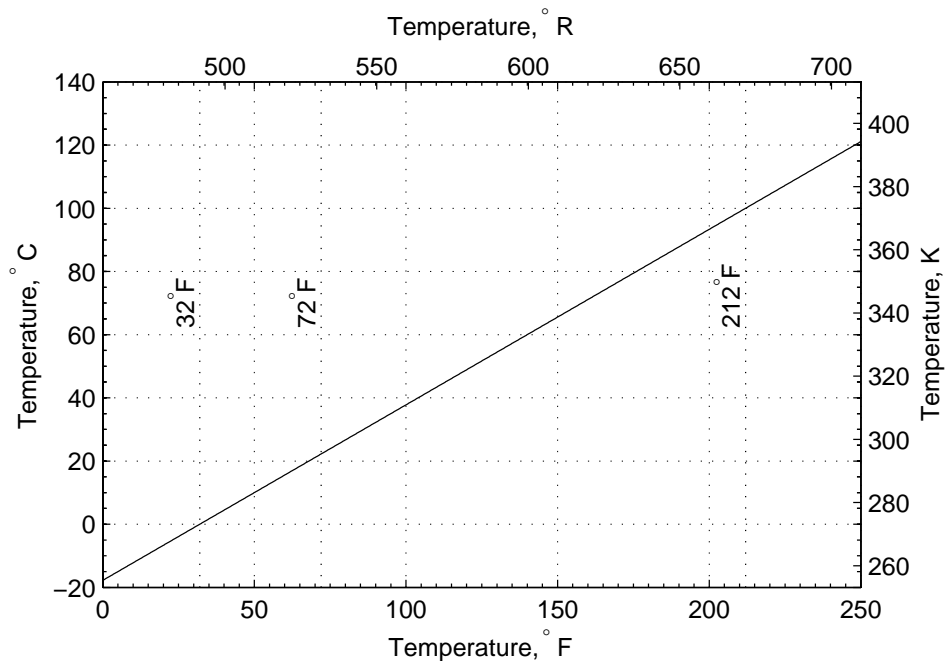


Figure A-1: Temperature conversion between Fahrenheit, Celsius, Rankine, and Kelvin. Conversion between Rankine and Fahrenheit are read vertically, and between Celsius and Kelvin are read horizontally. The line is used for all other conversions.

Table A.1: Supplies for Cleaning Sensors

Item	Description & Purpose
New Sensors	Trim to final size
Latex Gloves	Several Pairs
Cotton Balls	About 10 per sensor
Tissue Paper	Serves as backing to support sensor
Ultrasonic Cleaner	ULTRASONIK 104x by NEY used
Acetone	For cleaning sensors
Methanol	For cleaning sensors
Oven	For accelerated drying of sensors
Hot Plate	Heating bleach solution
Sink	For rinsing sensors
Catch Tray	To catch acetone and methanol during rinsing
Bleach	Undiluted, regular strength
Glass Stir Rod	For stirring while in bleach
Beaker	Large enough to fit largest sensor

Preparing Dielectrometry Sensors

The dielectrometry sensors manufactured by Polyflon Company arrive with a brownish layer on the top and bottom surfaces used to increase adhesion between the copper and Teflon substrate. This layer is removed before using the sensor. Mamishev gives a thorough description of the process he used in Appendix A of his thesis [54]. If the reader is unfamiliar with the cleaning process, this reference should be read.

The text is a bit too long to serve as a useful reference in the laboratory. The following outline was used. It lacks the thorough description of each step that can be found in [54]. Note that some steps have been removed, simplifying the procedure. It was found that the steps below are sufficient for cleaning our sensors.

1. Prepare a flat surface with tissue paper. Soak cotton in acetone and wipe down the sensor's top. Repeat with methanol. Repeat on the sensor's back. Rinse with acetone. Rinse with methanol. Best performed under an exhaust hood.
2. Place sensor in an oven set to 120 °F (50 °C) for 10 to 15 minutes.
3. Using the hot plate heat bleach in a beaker to 150 °F (65 °C).
4. Fill the ultrasonic cleaner with hot tap water. Turn the heater on and degas for 10 minutes on medium power and maximum degassing.
5. Set the ultrasonic cleaner power to low, degassing to medium, and float the bleach filled beaker

in the water. Place sensor in the bleach and stir using the glass stir rod for 30 seconds or until residue is removed.

6. Rinse sensor of the bleach with warm water in the sink. Rinse with acetone followed by methanol.
7. Return sensor to oven for 10 to 15 minutes.

A.3 Controller Box Commands

In this section we present an abridged listing of the controller box commands. For a full listing and detailed description see the reference manual [71]. If any parameters are to be given, all parameters must be given. Parameters are separated by a comma.

Command	Description and parameters.
[FP, parameters]	read/set fixed parameters. <ul style="list-style-type: none"> • not supported • not supported • channel 1 delay • channel 2 delay • channel 3 delay • channel 4 delay
[GP, parameters]	read/set Gain and Phase Meter parameters. <p>starting frequency</p> <ul style="list-style-type: none"> • ending frequency • excitation level • channel 1 enable • channel 2 enable • channel 3 enable • channel 4 enable • diagnostic enable • auto trigger enable
[TG]	trigger gain phase meter
[GD]	read GPM data
[CS]	check status
[AM]	abort any data logger and Gain Phase measurements in progress
[CM]	clear memory buffer
[DT, parameters]	read/set date and time <ul style="list-style-type: none"> • year (two digits) • month • day • hour • minute • second
[VE]	software version number
[DE, parameters]	enable(1)/disable(0) excite, discharge and attenuate

A.4 Acronyms

The following is an alphabetical listing of acronyms occurring in the thesis.

CDPVs	– Contaminants, Defects, Protrusions, Voids. (Cable imperfections) [12]
DP	– Degree of Polymerization
ECT	– Electrical Capacitance Tomography
ET	– Electrical Treeing
EQS	– Electroquasistatic
FVGrPM	– Floating Voltage with Ground Plane Mode
FVGPM	– Floating Voltage with Guard Plane Mode
HPPF	– High Pressure Fluid-Filled cable [122]
HPGF	– High Pressure Gas-Filled cable [122]
IRC	– Isothermal Relaxation Current [8, 15]
LTI	– Linear Time Invariant
MUT	– Material Under Test
PD	– Partial Discharges
PEC	– Perfect Electrical Conductor
PILC	– Paper-Insulated Lead Cable [6]
PILC	– Paper-Insulated Lead Covered cable [8, 12]
RVM	– Return Voltage Method [15, 20]
SCCM	– Short Circuit Current Mode
SCLF	– Self-Contained Liquid-Filled cable [122]
SCFF	– Self-Contained Fluid-Filled cable [12]
VLF	– Very Low Frequency
WT	– Water Treeing

A.5 Symbols & Constants

Symbol	Unit	Description & Value
Constitutive Parameters		
ϵ	F/m	permittivity
ϵ^*	F/m	effective permittivity
ϵ'	F/m	real part of the permittivity. $\mathbf{Re}\{\epsilon^*\}$
ϵ''	F/m	negative imaginary part of the permittivity. $-\mathbf{Im}\{\epsilon^*\}$
ϵ_r		relative permittivity
ϵ_o	F/m	permittivity of free space, $\epsilon_o = (c^2\mu_o)^{-1} = 8.854\dots \times 10^{-12}$
η_o	Ω	Intrinsic impedance of free space, $\eta_o = \sqrt{\mu_o/\epsilon_o} \approx 377 \Omega$
μ	H/m	magnetic permeability
μ_o	H/m	magnetic permeability of free space, $\mu_o = 4\pi \times 10^{-7}$
σ	S/m, $\Omega^{-1}\text{m}^{-1}$	electrical conductivity
τ	sec.	Relaxation time ϵ/σ
χ		electric susceptibility
Vector Quantities		
\vec{E}	V/m	electric field vector
\vec{D}	C/m ²	electric displacement vector
\vec{F}	V	electric vector potential
Other Quantities		
Γ		number of electrodes in half period of generalized planar sensor
λ	m	spatial wavelength
Φ	V	electric potential
$\Phi_n(r)$	V	n th Fourier mode of the electric potential
$\tilde{\Phi}_n$	V	n th Fourier mode of the electric potential at the electrode surface
c	m/s	speed of light in vacuum $c = 299,792,458$ (exact)
$C_n^*(r)$	F/m ²	n th Fourier mode surface capacitance density
C_f	F	feedback capacitance
C_T	F	transcapacitance
G_T	F	transconductance
H		number of unknowns
$I_n(kr)$		modified Bessel function of the first kind, order n
k	eV/K	Boltzmann's constant $k = 8.617343(15) \times 10^{-5}$
k	m ⁻¹	spatial "wavenumber"
K		number of collocation points
$K_n(kr)$		modified Bessel function of the second kind, order n
q		ratio of circumference to sensor wavelength for ϕ periodic sensor
σ_S^*	C/m ²	effective surface charge density
r_e	m	radius of electrodes in cylindrical configuration
r_g	m	radius of ground plane in cylindrical configuration
t_s	m	substrate thickness

A.6 MATLAB Code

We include a critical piece of MATLAB code for posterity and to serve as a model for numerical implementation of the theory. This code was written in MATLAB version 6 release 13 and is unlikely


```

%idx1 is el, idx1 = el+1 (el for 0 to K-1)
%idx2 is m, idx2 = m (m from 1 to K)
%idx3 is n, idx3 = n/q+1 (n from 0 to N*q in steps of q.)
%%%%%%%%Vector C_n is a vector length length(N) %%%%%%%%%
%idx1 is n, idx1 = n/q+1 (n from 0 to N*q in steps of q.)

%Cable Diameter (CALCULATED)
q = round(pi*trep/lambda); %Number of wavelengths around cable
r_e = q*lambda/(2*pi); % cable radius to be used.

% Voltage Plot Properties
numb = 150;           % Number of radial positions.
phimin = 0;          % Phi range min.
phimax = 2*pi;       % Phi range max.

N = 0:q:N*q;         %Fourier mode indexes. N = 0,q,2q,...,Nq
M = 0:K+1;           %Collocation point subscripts

%Collocation point positions
phi_m = (c/2 + (lambda-c-d)/4 * (1-cos(pi*M/(K+1))))/r_e;
theta_el2 = lambda/(2*r_e); %\theta_{\lambda/2}

%%Initial Print Out %%
cr = sprintf('\n');
% Some Outputs
disp(['Fourier Terms N = ' num2str(cyl.N) cr ...
      'Colocation Pts. K = ' num2str(cyl.K) cr ...
      'Original radius: ' num2str(trep/2) cr...
      'Adjusted radius: ' num2str(r_e) cr...
      'Number of Periods: ' num2str(q)])

%phi^{\prime}_{ell} positions
phip_el(1) = phi_m(1);
phip_el(2:K) = (phi_m(3:K+1) + phi_m(2:K))/2;
phip_el(K+1) = phi_m(K+2);

b_n = zeros(length(N),K);
Mlmm = zeros(K,K,length(N));

%Calculate b_n and Mlmm
for n = N
    for el = 0:K-1
        if n > 0 %b^{\prime}_n terms
            b_n(n/q+1,el+1) = 2/(n^3*theta_el2)*(cos(n*phi_m(2)) - cos(n*phi_m(1)))/...
                (phi_m(2) - phi_m(1)) * (sin(n*phip_el(el+2)) - sin(n*phip_el(el+1)));
        else %b^{\prime}_0 term
            b_n(1,el+1) = -1/(2*theta_el2)*(phi_m(1)+phi_m(2))*(phip_el(el+2)-phip_el(el+1));
        end
        for m = 1:K
            if n > 0 %M_{\ell,m}^{\prime} terms
                Mlmm(el+1,m,n/q+1) = -2/(n^3*theta_el2)*(sin(n*phip_el(el+2)) - ...

```

```

        sin(n*phip_el(el+1))*((cos(n*phi_m(m+2)) - cos(n*phi_m(m+1)))/...
        (phi_m(m+2)-phi_m(m+1)) - (cos(n*phi_m(m+1)) - cos(n*phi_m(m)))/...
        (phi_m(m+1)-phi_m(m)));
    else %M_{\ell,m}^0 term
        Mlmm(el+1,m,1) = 1/(2*theta_el2)*(phi_m(m+2)-phi_m(m))*...
            (phip_el(el+2)-phip_el(el+1));
    end %end if n
end % end m
end % end el
end %end n

mats = length(cyl.epsL); % Number of Solutions to solve for.
%%%% START LOOP FOR EACH MATERIAL SCENARIO !!!!
for cn = 1:mats
    epsL = cyl.epsL{cn};
    sigmaL = cyl.sigmaL{cn};
    %Calculate Surface Capacitance Density
    %%% START LOOP FOR EACH FREQUENCY!!!!
    for fidx = 1:length(freq)
        omega = 2*pi*freq(fidx);
        epsCL = epsL - i.*sigmaL./omega;
        %Find Final Thickness
        t(end+1) = r_e - (sum(t) + ccond*tcond);
        %Calculate Radius for all layers.
        for p = 1:(nlayer - ccond)
            if p > 1
                r(p) = r(p-1) + t(p);
            else % p == 1
                if ccond
                    r(1) = tcond + t(1);
                else
                    r(1) = t(1);
                end
            end
        end
    end
    %N = 0 TERMS!
    if ccond
        Cnh(1) = epsCL(1)/(r(1)*log(tcond/r(1)));
        for p = 2:(nlayer - 1)
            Cnh(1) = (epsCL(p)/r(p))/(epsCL(p)*(r(p-1)*Cnh(1))^-1+log(r(p-1)/r(p))); %1.11
        end
    else
        Cnh(1) = 0;
    end
    for n = N(2:end)
        %Find Cnh for most inward layer for n>0;
        if ccond
            Cnh(n/q+1) = -n*epsCL(1)/r(1)*...
                (1/(1-(tcond/r(1))^(2*n))+1/((r(1)/tcond)^(2*n)-1)); %1.11.
        else
            Cnh(n/q+1) = - n*epsCL(1)/r(1);
        end
    end
end

```



```

end
%Find Cnh for remaining layers;
for p = 2:(nlayer - ccond)
    an = 1 + (r(p-1)/r(p))^(2*n);
    bn = 1 - (r(p-1)/r(p))^(2*n);
    cn = 1 + (r(p)/r(p-1))^(2*n);
    dn = - 1 + (r(p)/r(p-1))^(2*n);
    Cnh(n/q+1) = -n*epsCL(p)/r(p)*(n*epsCL(p)*(1/(an*n*epsCL(p)-bn*r(p-1)*...
        Cnh(n/q+1)) - 1/(cn*n*epsCL(p)-dn*r(p-1)*Cnh(n/q+1)))...
        -r(p-1)*Cnh(n/q+1)*(1/(an*n*epsCL(p)-bn*r(p-1)*Cnh(n/q+1))...
        + 1/(cn*n*epsCL(p)-dn*r(p-1)*Cnh(n/q+1))));
end
if isnan(real(Cnh(n/q+1)))
    endN = n/q;
    break;
end
endN = n/q+1;
end % for n = N(2:end)
disp(['(' num2str(cn) ') Number of Fourier Terms Calculated for C_n for '...
    num2str(omega/(2*pi),4) ' Hz: ' num2str(endN)])
C_n(1) = eps_s/(r_e.*log((r_e+ts)/r_e)) -Cnh(1);
for n = N(2:endN)
    C_n(n/q+1) = -n*eps_s/r_e*(1/(1-((r_e+ts)/r_e)^(2*n))+...
        1/((r_e/(r_e+ts))^(2*n)-1))-Cnh(n/q+1);
end

Mx = zeros(K,K);
bx = zeros(K,1);
for n = N(1:endN)
    Mx = C_n(n/q+1).*Ml_mn(:, :, n/q+1)+Mx;
    bx = C_n(n/q+1).*b_n(n/q+1, :)' +bx;
end
v = Mx \ (Vd*bx);
v = [Vd; v; 0];

%CALCULATE TRANSCAPACITANCE
Y_t = 0;
for n = N(2:endN)
    sum1 = 0;
    for m = M(2:K+1)
        sum1 = v(m+1)/Vd*((cos(n*phi_m(m+2))-cos(n* phi_m(m+1)))/...
            (phi_m(m+2)-phi_m(m+1))-(cos(n*phi_m(m+1))-cos(n*phi_m(m)))/...
            (phi_m(m+1)-phi_m(m)))+sum1;
    end
    Y_t = Y_t-4*L*C_n(n/q+1)*sin(n*phi_m(K+2))*1/(n^3*theta_e12)*...
        ((cos(n*phi_m(2))-cos(n*phi_m(1)))/( phi_m(2)-phi_m(1))+sum1);
end
sum2 = 0;
for m = M(2:K+1)
    sum2 = v(m+1)/Vd * (phi_m(m+2) - phi_m(m)) + sum2;
end
end

```

```

Y_t = Y_t-(L/theta_el2)*C_n(1)*(theta_el2-phi_m(K+2) )*(phi_m(1)+phi_m(2)+sum2);
Y_t = Y_t*r_e*i*omega;
% FUNCTION OUTPUTS
C_t{cn}(fidx) = imag(Y_t)/omega;
G_t{cn}(fidx) = real(Y_t);
Gain{cn}(fidx) = 20*log10(sqrt(omega^2*C_t{cn}(fidx)^2+G_t{cn}(fidx)^2)/...
    (omega*(Cf)));
Phase{cn}(fidx) = mod((atan(-G_t{cn}(fidx)/(omega*C_t{cn}(fidx)))+pi)*...
    180/pi,180+1e-5);

```

```
%August 21th, Calculate the Full Field. Plot in Color
```

```

if vplot %FIND \tilde \Phi_n(r_e) for All $n$.
Phire = zeros(endN,1);
for n = N(1:endN)
    if n> 0 % n > 0 cases
        phi_re = zeros(1,K);
        for m = M(2:K+1)
            phi_re(m)= -2/(n.^2*theta_el2)*v(m+1)*((cos(n*phi_m(m+2))-...
                cos(n*phi_m(m+1)))/(phi_m(m+2)-phi_m(m+1))-...
                (cos(n*phi_m(m+1))-cos(n*phi_m(m)))/(phi_m(m+1)-phi_m(m)));
        end
        Phire(n/q+1) = sum(phi_re)-2/(n.^2*theta_el2)*Vd*(cos(n*phi_m(2))-...
            cos(n*phi_m(1)))/(phi_m(2)-phi_m(1));
    else %%% n = 0 case
        sum2 = 0;
        for m = M(2:K+1)
            sum2 = v(m+1)*(phi_m(m+2) - phi_m(m)) + sum2;
        end
        Phire(1) = 1/(2*theta_el2) *(Vd*(phi_m(1) + phi_m(2)) + sum2);
    end % if n> 0
end % for n = N(1:endN)

% FIND THE COEFFICIENT MATRIX, H
P = nlayer -ccond;
epsLp = [epsCL eps_s];
r = [r r_e+ts];
a = zeros(2*P+2,endN);
warning off MATLAB:nearlySingularMatrix
warning off MATLAB:singularMatrix
for n = N(2:endN)
    lastwarn('none');
    H = zeros(P);
    for p = 1:(P-1)
        H(2*p-1,2*p-1) = r(p)^n;
        H(2*p-1,2*p) = r(p)^(-n);
        H(2*p-1,2*p+1) = -r(p)^n;
        H(2*p-1,2*p+2) = -r(p)^(-n);
        H(2*p,2*p-1) = epsLp(p)/eps0*r(p)^n;
        H(2*p,2*p) = -epsLp(p)/eps0*r(p)^(-n);
    end
end

```

```

H(2*p,2*p+1) = -epsLp(p+1)/eps0*r(p)^(n);
H(2*p,2*p+2) = epsLp(p+1)/eps0*r(p)^(-n);
end
if ccond
H(2*P-1,1) = tcond^n;
H(2*P-1,2) = tcond^(-n);
else
H(2*P-1,2) = 1;
end
H(2*P,2*P-1) = r_e^n; % BC at r_e from top
H(2*P,2*P) = r_e^-n;
H(2*P+1,2*P+1) = r(P+1)^n; % BC at r_e+ts (ground plane)
H(2*P+1,2*P+2) = r(P+1)^(-n);
H(2*P+2,2*P+1) = r(P)^n; % BC at r_e from bottom
H(2*P+2,2*P+2) = r(P)^(-n);

c = zeros(2*P+2,1);
c(2*P) = Phire(n/q+1);
c(2*P+2) = Phire(n/q+1);
a(:,n/q+1) = H \ c;
if strcmp(lastwarn,'Matrix is singular to working precision.')
disp(['Number Of Fourier Terms for Color Voltage plot for '...
num2str(omega/(2*pi),4) ' Hz, is: ' num2str(n/q) '.'])
break;
end
end
a = a(:,1:n/q);
N2 = N(1:n/q);
%%N = 0 CASE!!!
H = zeros(P);
for p = 1:(P-1)
H(2*p-1,2*p-1) = 1;
H(2*p-1,2*p) = log(r(p));
H(2*p-1,2*p+1) = -1;
H(2*p-1,2*p+2) = -log(r(p));
H(2*p,2*p) = epsLp(p)/eps0;
H(2*p,2*p+2) = -epsLp(p+1)/eps0;
end
if ccond
H(2*P-1,1) = 1;
H(2*P-1,2) = log(tcond);
else
H(2*P-1,2) = 1;
end
H(2*P,2*P-1) = 1;
H(2*P,2*P) = log(r_e);
H(2*P+1,2*P+1) = 1;
H(2*P+1,2*P+2) = log(r(P+1));
H(2*P+2,2*P+1) = 1;
H(2*P+2,2*P+2) = log(r(P));

```

```

c = zeros(2*P+2,1);
c(2*P) = Phire(1);
c(2*P+2) = Phire(1);
a(:,1) = H \ c;

%%% Calculate Phi_n(r) for each r.
rs = [linspace(ccond*tcond,r_e+ts,numb) 1];
Phin = zeros(size(a,2),length(rs)-1);
m = 1;
for count = 1:length(r)
    while rs(m) <=r(count) & m <= numb
        if count == 1 & ccond
            Phin(1,m) = a(1,1) + a(2,1)*log(rs(m)); % Need a(2,1)
        elseif count == 1
            Phin(1,m) = a(2*count-1,1); %Avoid log(0)
        else
            Phin(1,m) = a(2*count -1,1) + a(2*count,1)*log(rs(m));
        end
        for n= N2(2:end)
            if a(2*count,n/q+1) ~= 0
                Phin(n/q+1,m) = a(2*count-1,n/q+1)*rs(m)^n + a(2*count,n/q+1)*rs(m)^(-n);
            else
                Phin(n/q+1,m) = a(2*count-1,n/q+1)*rs(m)^n;
            end
        end
        m = m + 1;
    end
end
rs = rs(1:end-1);
% CONVERT FROM Fourier Coef. (Phi_n(r)) to Phi
phi = linspace(phimin,phimax,200);
Phi = repmat(Phin(1,:)',1,length(phi));
tidx = isnan(Phin);
Phin(tidx) = 0;
for n = N2(2:end)
    Phi = Phi + Phin(n/q+1,:)'*cos(n*phi);
end
%%%%% PLOT PARAMETERS%%%%%%%%%%%%%
opengl neverselect
x = rs'*cos(phi);
y = rs'*sin(phi);
figure(4326); cfl;
set(gcf,'Position',[0 0 1000 1000])
pcolor(x,y,abs(Phi))
colormap(jet(1000))
shading interp
caxis([0 Vd])
colorbar
axis equal
hold on
plot(r,zeros(length(r),1),'r+')

```

```
hold off
if cyl.vplotS
    F(fidx+1) = getframe;
end
disp(['freq = ' num2str(freq(fidx))])
pause(.1)
end
clear r
end % END FREQUENCY LOOP!!!!
end % END MATERIALS LOOP!!!!
save datafull

if vplot & cyl.vplotS
    h = text(-.8*r_e,0,['DEMO: \lambda = ' num2str(lambda,3)...
        '. r_e = ' num2str(r_e,3) '.']);
    set(h,'FontSize',15);
    F(1) = getframe;
    movie2avi(F,cyl.moviename,'Compression','None')
end
warning on MATLAB:nearlySingularMatrix
warning on MATLAB:singularMatrix
```


Appendix B

Additional Figures




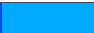








B.1 Steady State Measurements

B.1.1 Teflon Rod Constant Temperature Measurements

Additional Teflon Rod Experiment 1

A second dielectric spectroscopy scan of Teflon rod at constant temperature is shown in Fig B-1. Temperatures are given in Table B.1. All hardware in this setup is different than that presented in Sec. 6.1.1. Interface box 1 used.

Table B.1: Constant Temperature Information for Additional Steady State Teflon Measurement 1

Color						
Avg. Temp. °F	71.2	79.7	89.5	98.8	108.3	117.9
Std. Dev. °F	0.75	0.88	1.23	1.45	1.65	1.86
Color						
Avg. Temp. °F	127.7	137.2	147.1	156.6	166.2	175.8
Std. Dev. °F	2.04	2.01	2.19	1.46	1.32	1.09

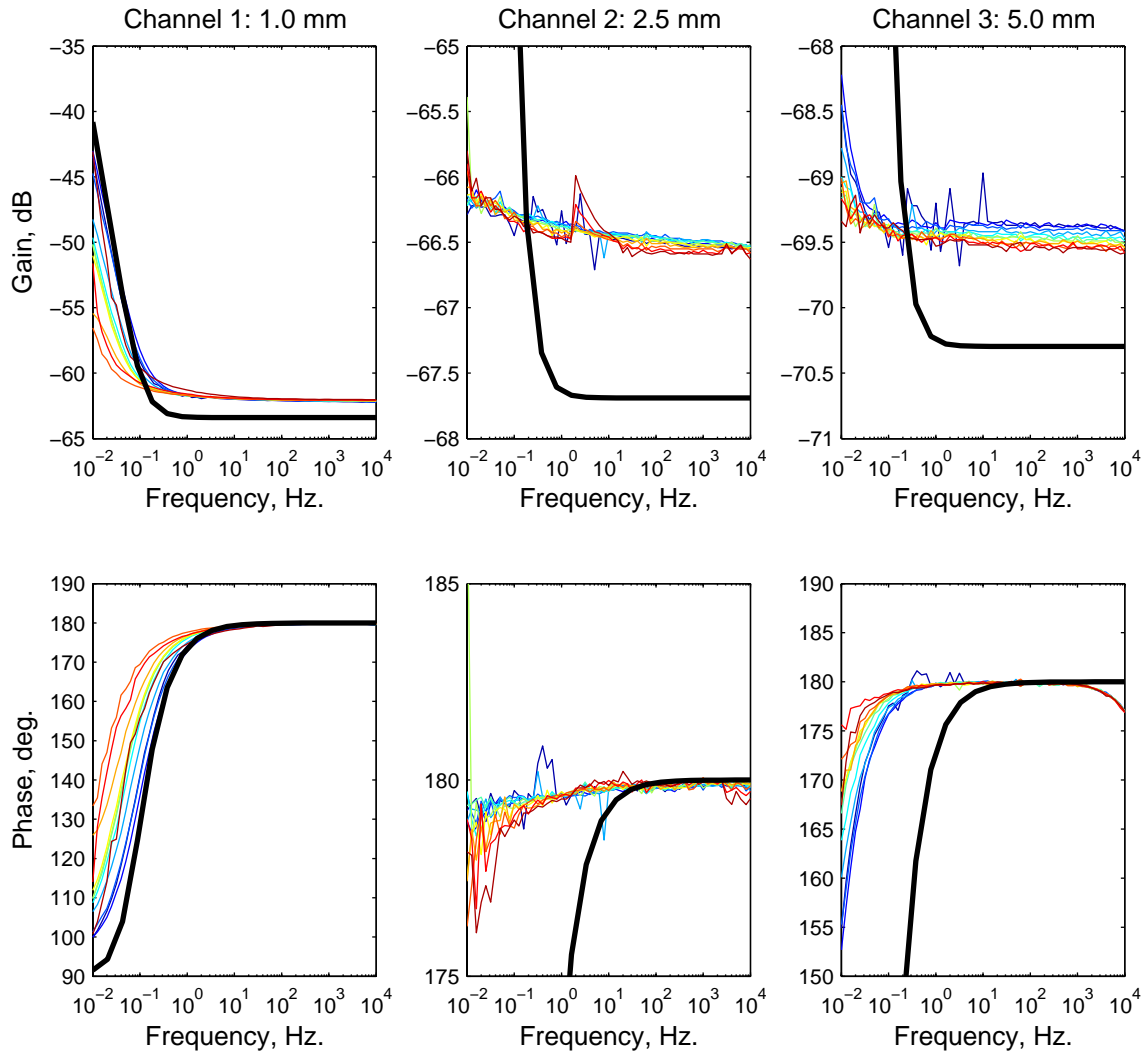


Figure B-1: Teflon constant temperature dielectric spectroscopy measurements for 12 temperatures using 1, 2.5, and 5 mm wavelength interdigital sensors. Measurements are in color (see Table B.1). Theoretical results in black. Interface box 1 is used. *This measurement was conducted from December 5 to December 6, 2006.*

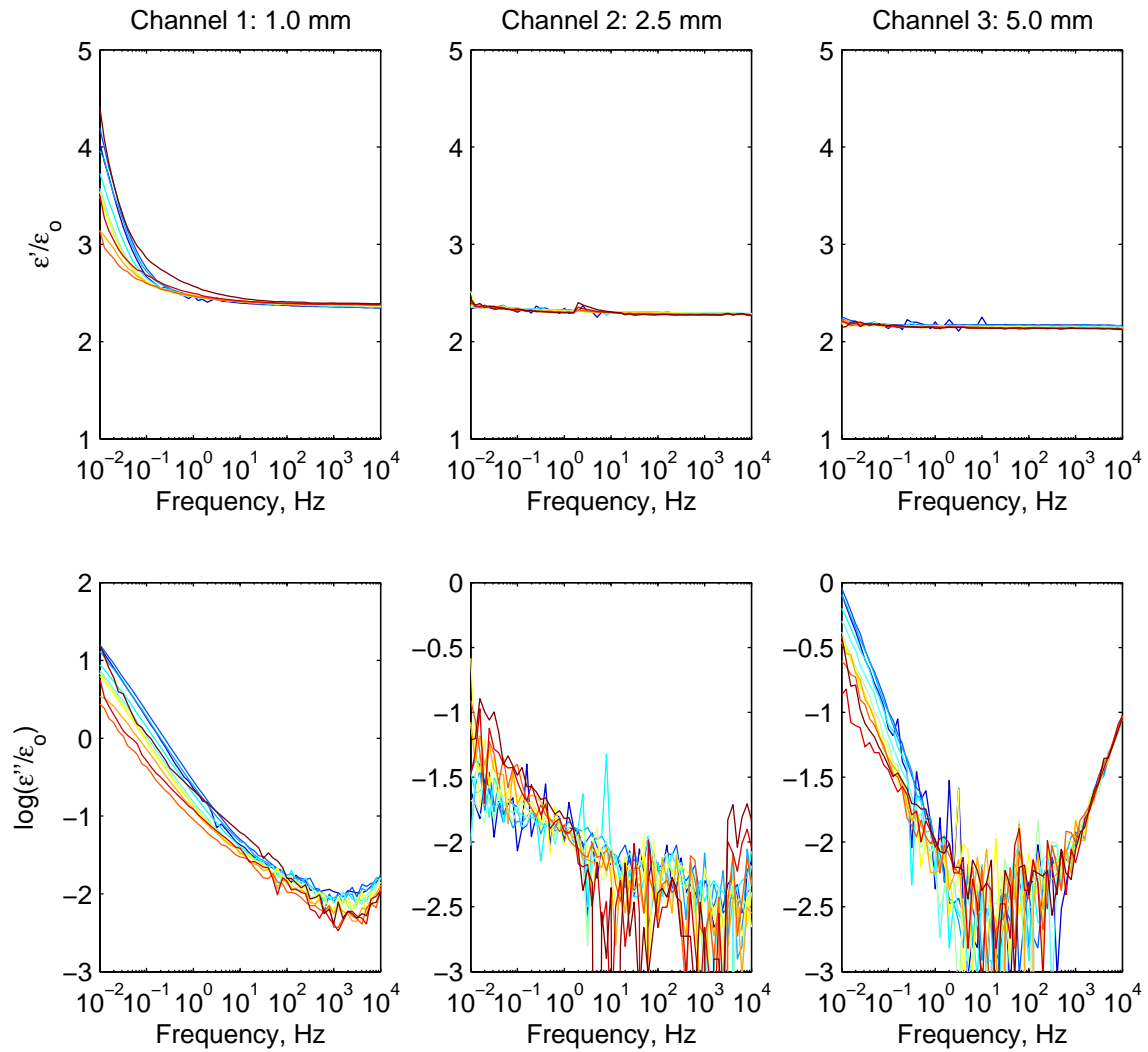


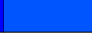


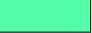








Figure B-2: Effective permittivity data for the Teflon rod from the steady state temperature measurements in Fig. B-1. Measurements are in colors corresponding to temperature as indicated in Table B.1.

Table B.2: Constant Temperature Information for Additional Steady State Teflon Measurement 2

Color						
Avg. Temp. °F	70.2	79.0	88.5	98.1	107.6	117.2
Std. Dev. °F	1.4	0.31	0.31	0.29	0.26	0.28
Color						
Avg. Temp. °F	126.6	136.1	145.6	155	164.4	173.7
Std. Dev. °F	0.21	0.26	0.21	0.18	0.23	0.2

Additional Teflon Rod Experiment 2

A third dielectric spectroscopy scan of Teflon rod at constant temperature is shown in Fig B-3. Temperatures are given in Table B.2.

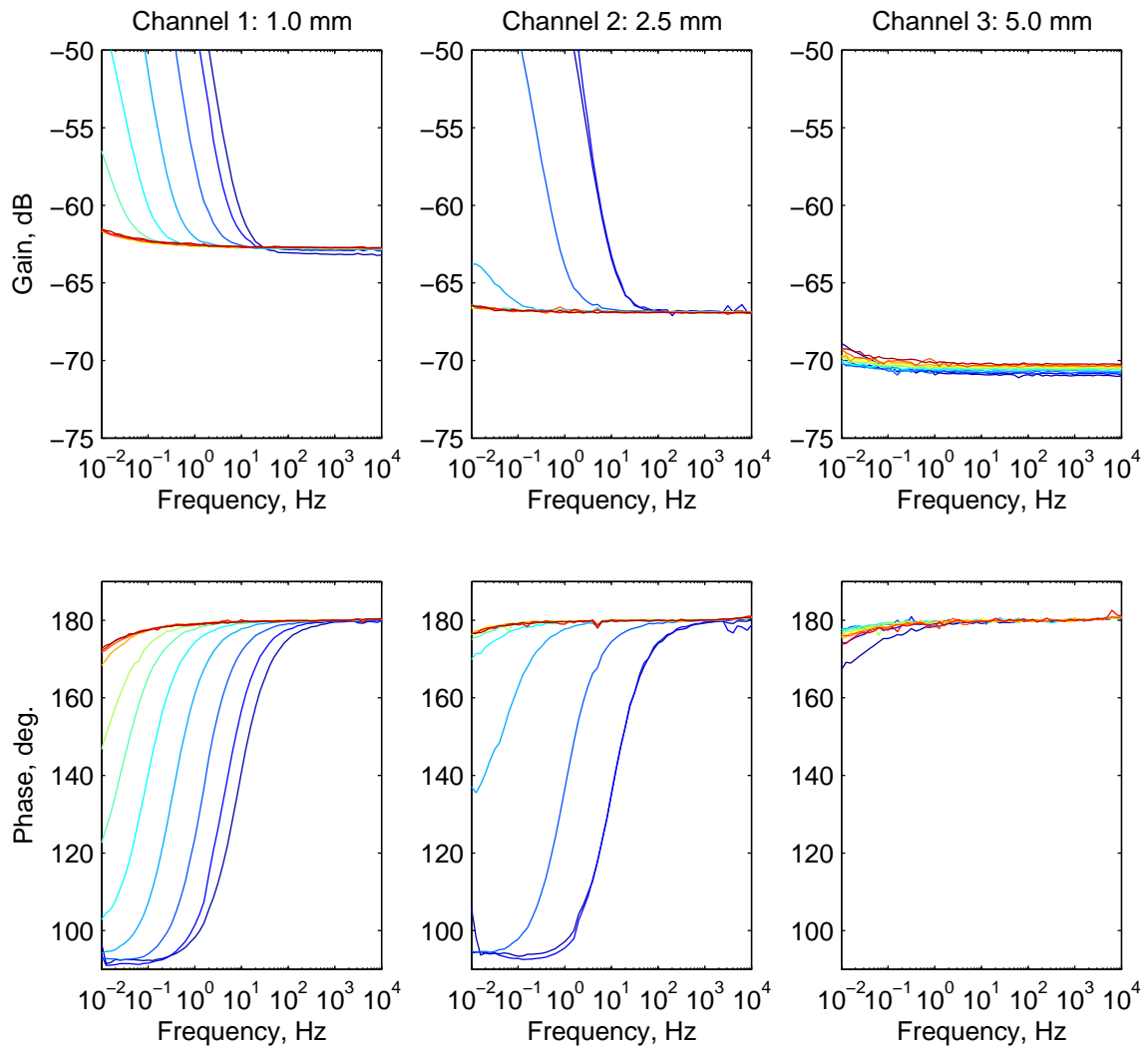


Figure B-3: Teflon constant temperature dielectric spectroscopy measurements for 12 temperatures using 1, 2.5, and 5 mm wavelength interdigital sensors. Measurements are in color (see Table B.2). Theoretical results in black. Interface box 3 is used. *This measurement was conducted from December 6 to December 7, 2006.*

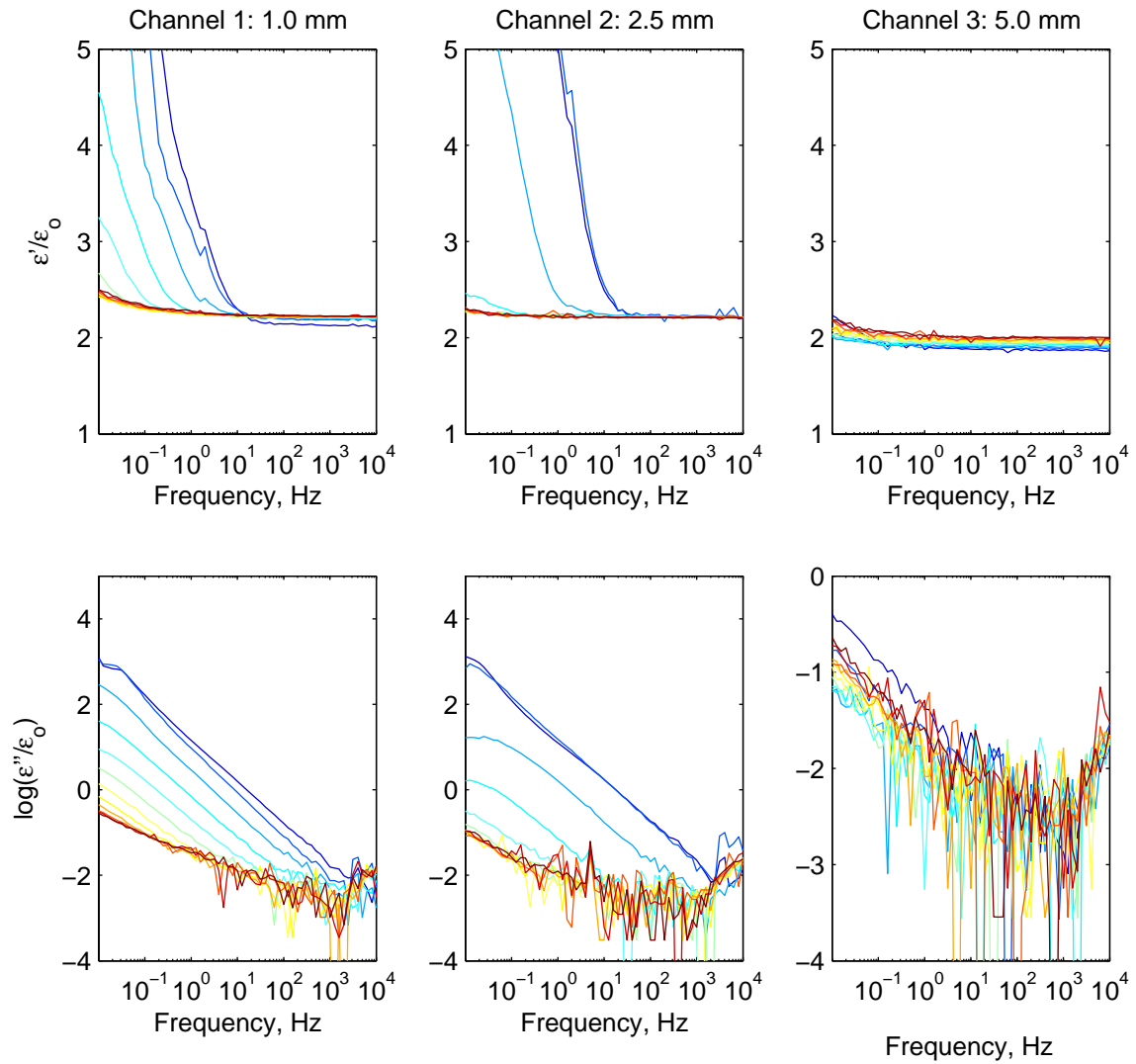


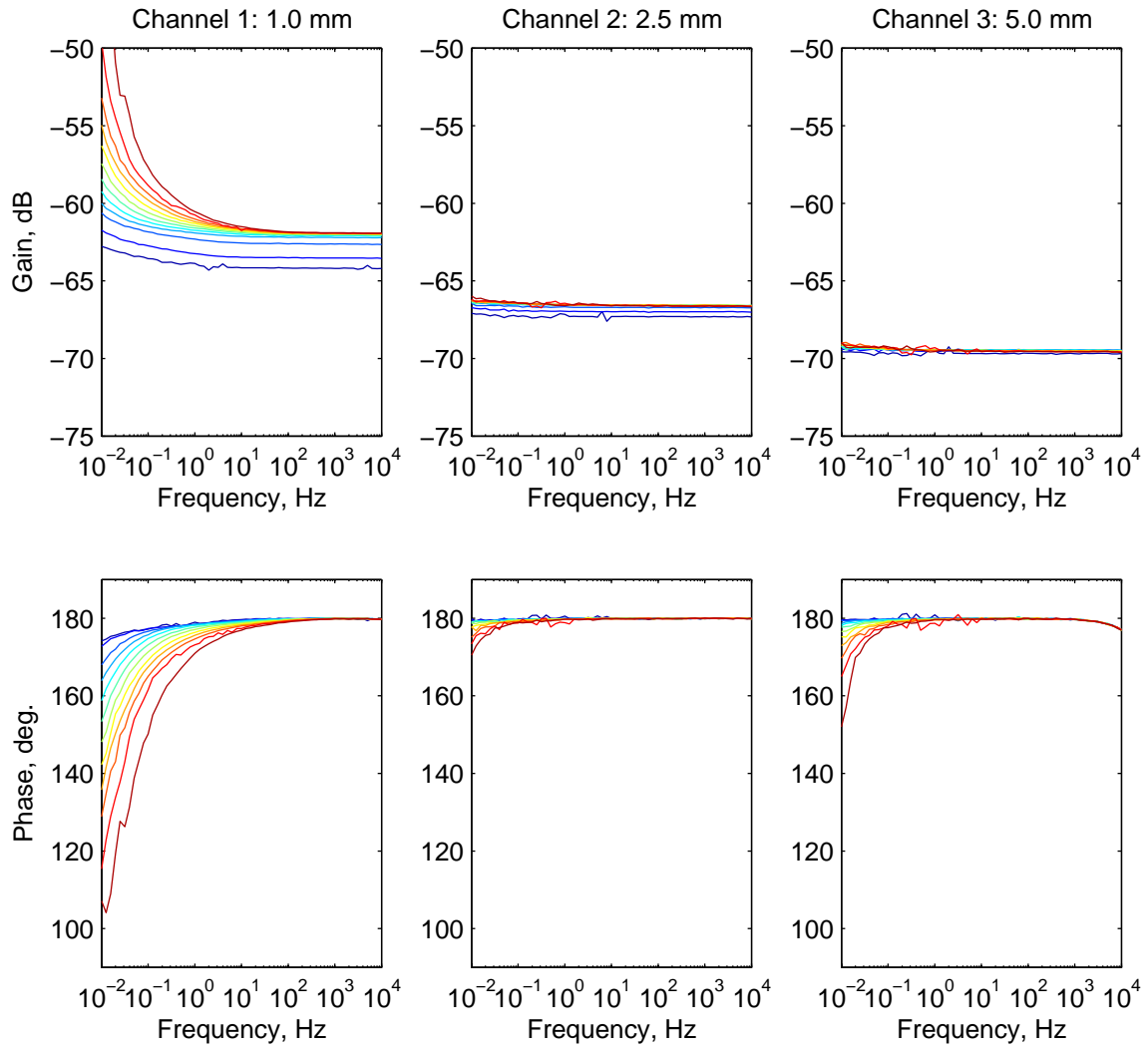
Figure B-4: Effective permittivity data for the Teflon rod from the steady state temperature measurements in Fig. B-3. Measurements are in colors corresponding to temperature as indicated in Table B.2.

Table B.3: Constant Temperature Information for Additional Steady State Teflon Measurement 3

Color						
Avg. Temp. °F	70.24	79.79	89.38	99.11	108.7	118.1
Std. Dev. °F	0.76	0.93	1.0	1.2	1.3	1.5
Color						
Avg. Temp. °F	127.6	137.5	147.2	156.7	166.3	176
Std. Dev. °F	1.6	1.8	1.8	1.7	1.0	0.61

Additional Teflon Rod Experiment 3

A fourth dielectric spectroscopy scan of Teflon rod at constant temperature is shown in Fig B-5. Temperatures are given in Table B.3.



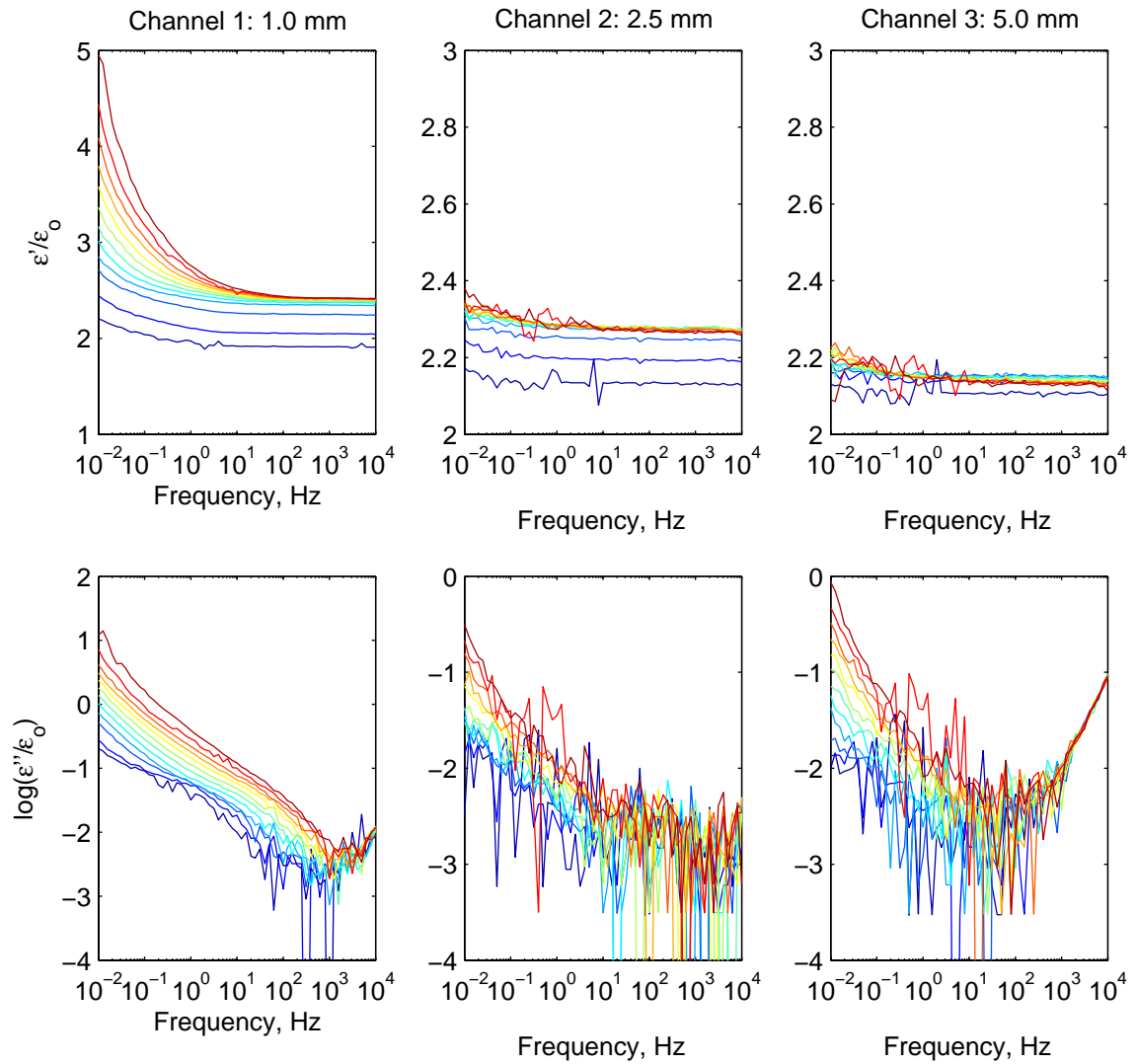


Figure B-6: Effective permittivity data for the Teflon rod from the steady state temperature measurements in Fig. B-5. Measurements are in colors corresponding to temperature as indicated in Table B.3.

Table B.4: Constant Temperature Information for Steady State Polycarbonate Measurements

Color						
Avg. Temp. °F	74.9	80.4	89.3	98.8	108.4	117.9
Std. Dev. °F	0.95	0.94	0.34	0.47	0.53	0.58
Color						
Avg. Temp. °F	127.4	136.8	146.2	155.7	165.1	174.2
Std. Dev. °F	0.66	0.71	0.66	0.76	0.70	0.25

B.1.2 Polycarbonate Rod Constant Temperature Measurements

A second dielectric spectroscopy scan of polycarbonate rod at constant temperature is shown in Fig B-7. Temperatures are given in Table B.4. The results are similar to those in Sec. 6.1.2. Interface box 3 used.

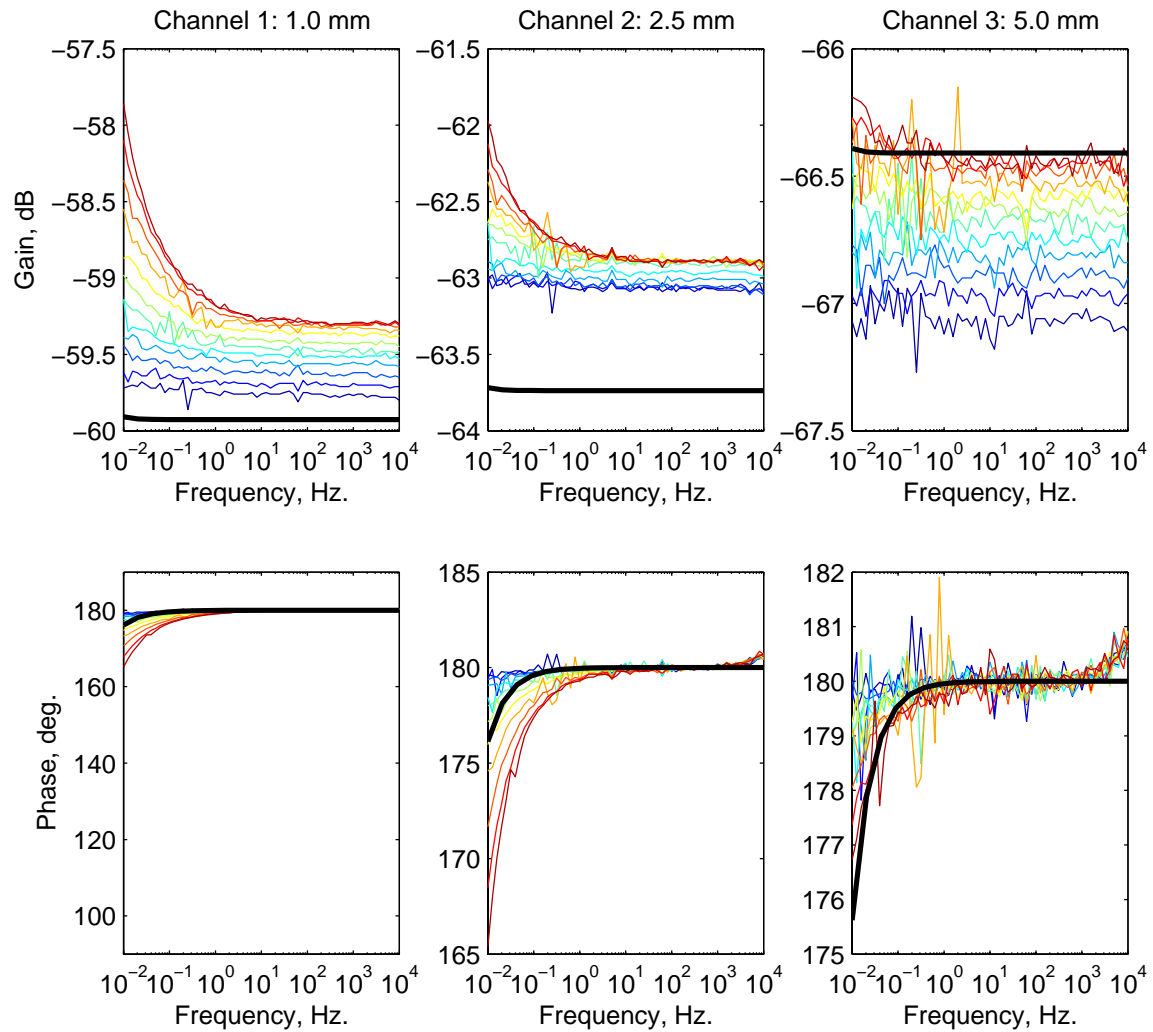


Figure B-7: Polycarbonate rod constant temperature dielectric spectroscopy measurements for 12 temperatures using 1, 2.5, and 5 mm wavelength interdigital sensors. Measurements are in color (see Table B.4). Theoretical results in black. Interface box 3 is used. *This measurement was conducted December 20, 2006.*

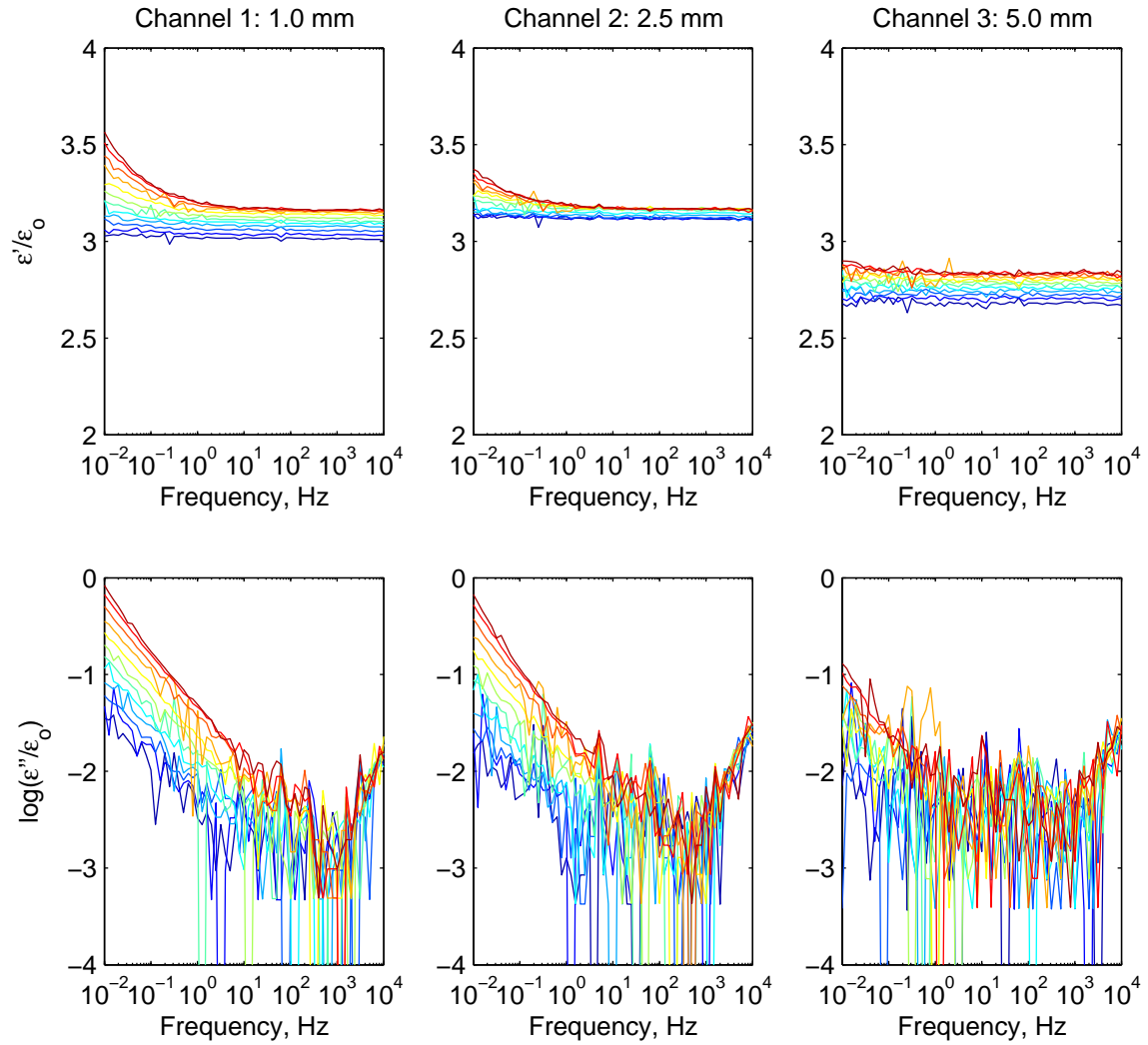


Figure B-8: Effective permittivity data for the polycarbonate from the steady state temperature measurements in Fig. B-7. Measurements are in colors corresponding to temperature as indicated in Table B.4.

Table B.5: Constant Temperature Information for Steady State Polyethylene Measurements

Color						
Avg. Temp. °F	73.8	80.1	89.2	98.8	108.4	118.0
Std. Dev. °F	0.87	0.73	0.38	0.43	0.46	0.63
Color						
Avg. Temp. °F	127.4	136.9	146.4	155.6	165.2	174.5
Std. Dev. °F	0.43	0.47	0.64	0.44	0.67	0.27

B.1.3 Constant Temperature Polyethylene Rod

A second dielectric spectroscopy scan of polyethylene rod at constant temperature is shown in Fig B-9. Temperatures are given in Table B.5. The results are similar to those in Sec. 6.1.3. Interface box 3 used.

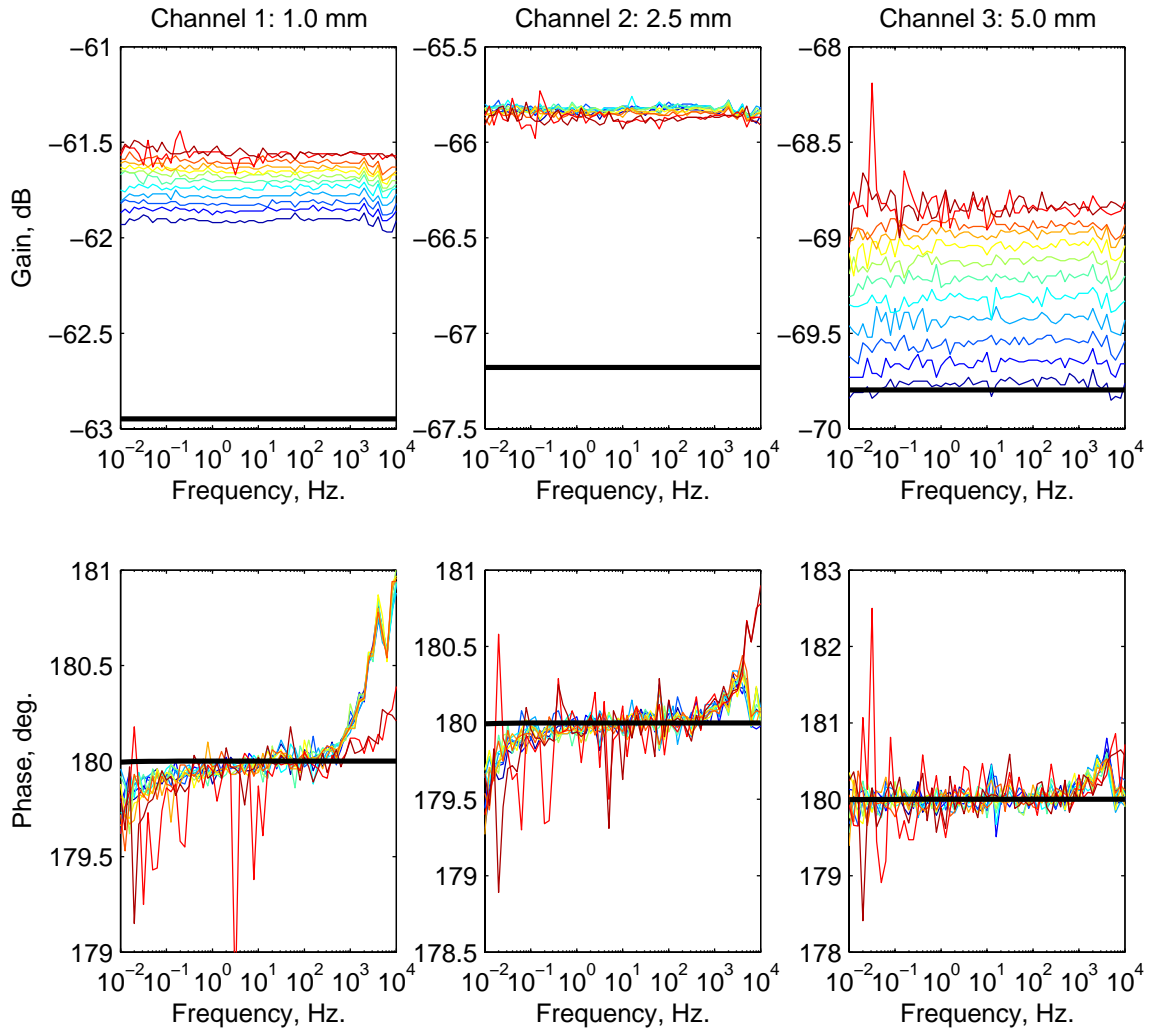


Figure B-9: Polyethylene rod constant temperature dielectric spectroscopy measurements for 12 temperatures using 1, 2.5, and 5 mm wavelength interdigital sensors. Measurements are in color (see Table B.5). Theoretical results in black. Interface box 3 is used. *This measurement was conducted January 1, 2007.*

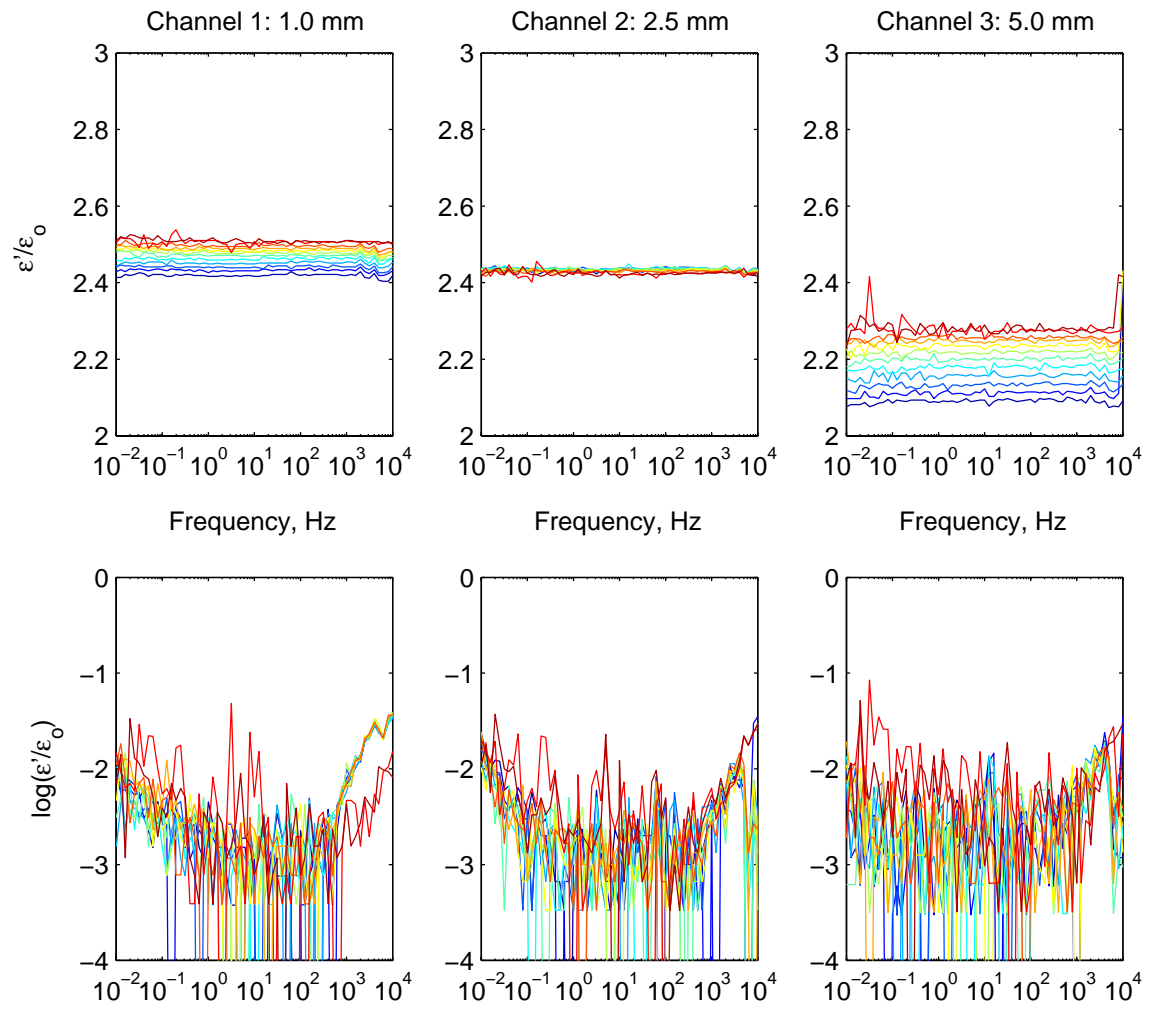


Figure B-10: Effective permittivity data for the polyethylene from the steady state temperature measurements in Fig. B-9. Measurements are in colors corresponding to temperature as indicated in Table B.5.

Table B.6: Constant Temperature Information for Steady State Acrylic Measurements

Color						
Avg. Temp. °F	74.4	80.1	89.2	98.8	108.3	118.0
Std. Dev. °F	0.83	0.77	0.30	0.39	0.50	0.59
Color						
Avg. Temp. °F	127.5	137	146.4	155.8	165.0	174.0
Std. Dev. °F	0.85	0.65	0.77	0.76	0.63	0.23

B.1.4 Acrylic Rod Constant Temperature

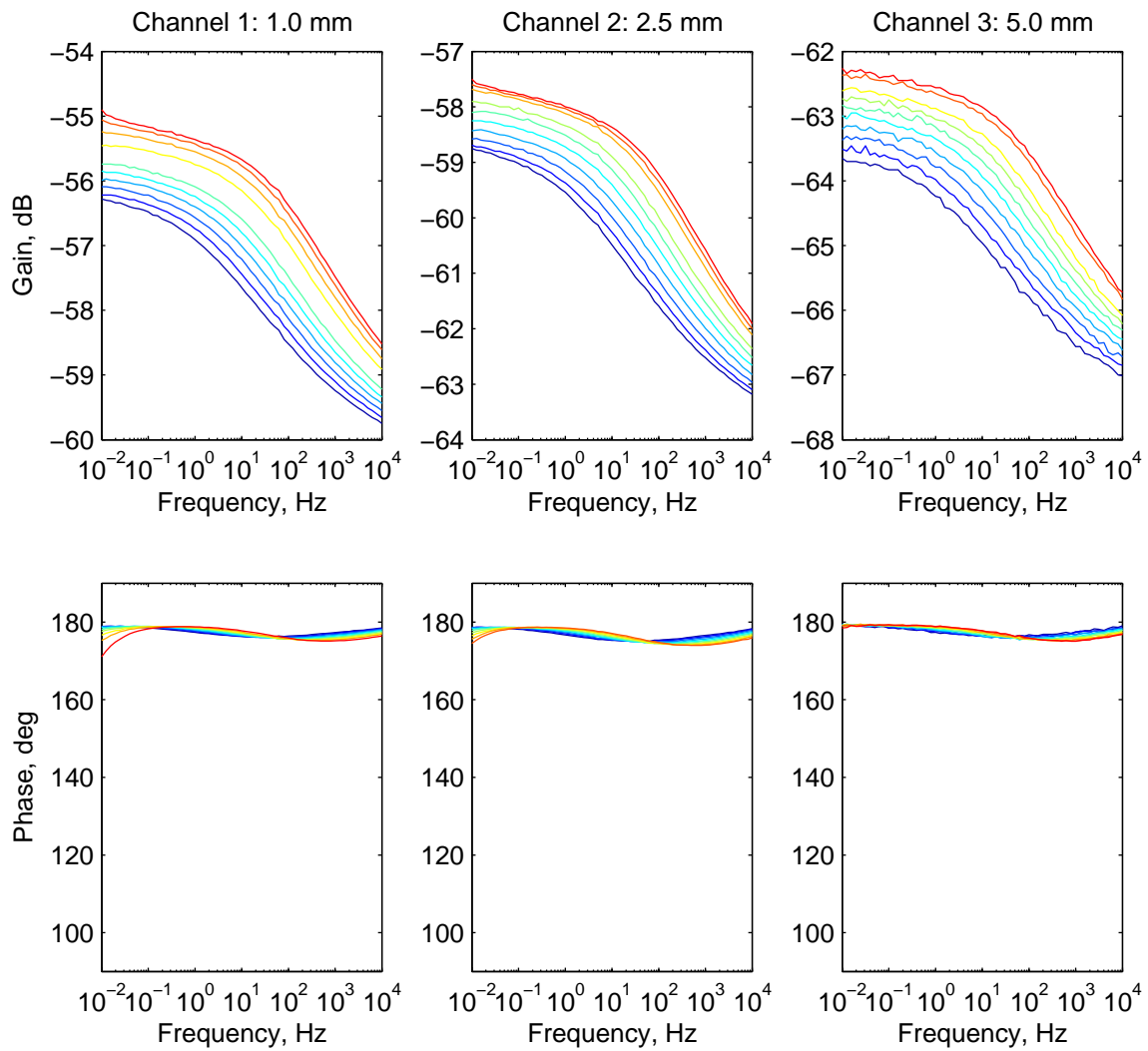


Figure B-11: Additional Acrylic rod constant temperature dielectric spectroscopy measurements for 12 temperatures using 1, 2.5, and 5 mm wavelength interdigital sensors. Measurements are in color (see Table B-11). Interface box 3 is used. *This measurement was conducted from January 3, 2006.*

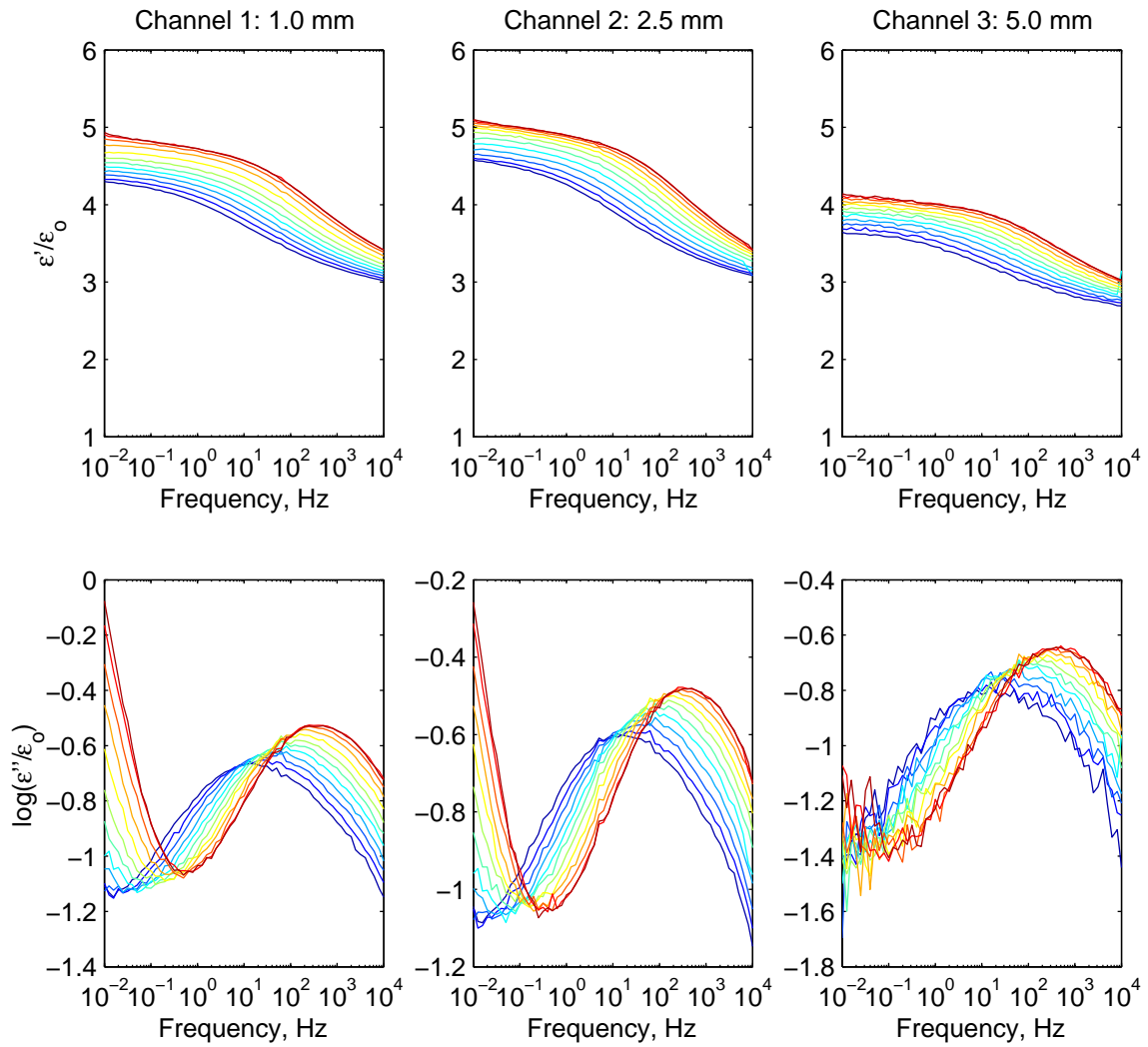


Figure B-12: Effective permittivity data for the acrylic from the steady state temperature measurements in Fig. B-11. Measurements are in colors corresponding to temperature as indicated in Table B-12.

Table B.7: Constant Temperature Information for Steady State Three Conductor Cable Measurements

Color							
Avg. Temp. °F	75.3	84.92	95.04	105.1	115.2	125.3	134.7
Std. Dev. °F	0.21	0.36	0.59	0.73	0.91	1.3	1.1
Color							
Avg. Temp. °F	144.3	154.4	163.9	183.4	193.3	203.1	212.9
Std. Dev. °F	1.2	1.4	1.4	1.4	1.2	1.1	0.52

B.1.5 Constant Temperature Three Conductor Cable

February 2006 Measurement

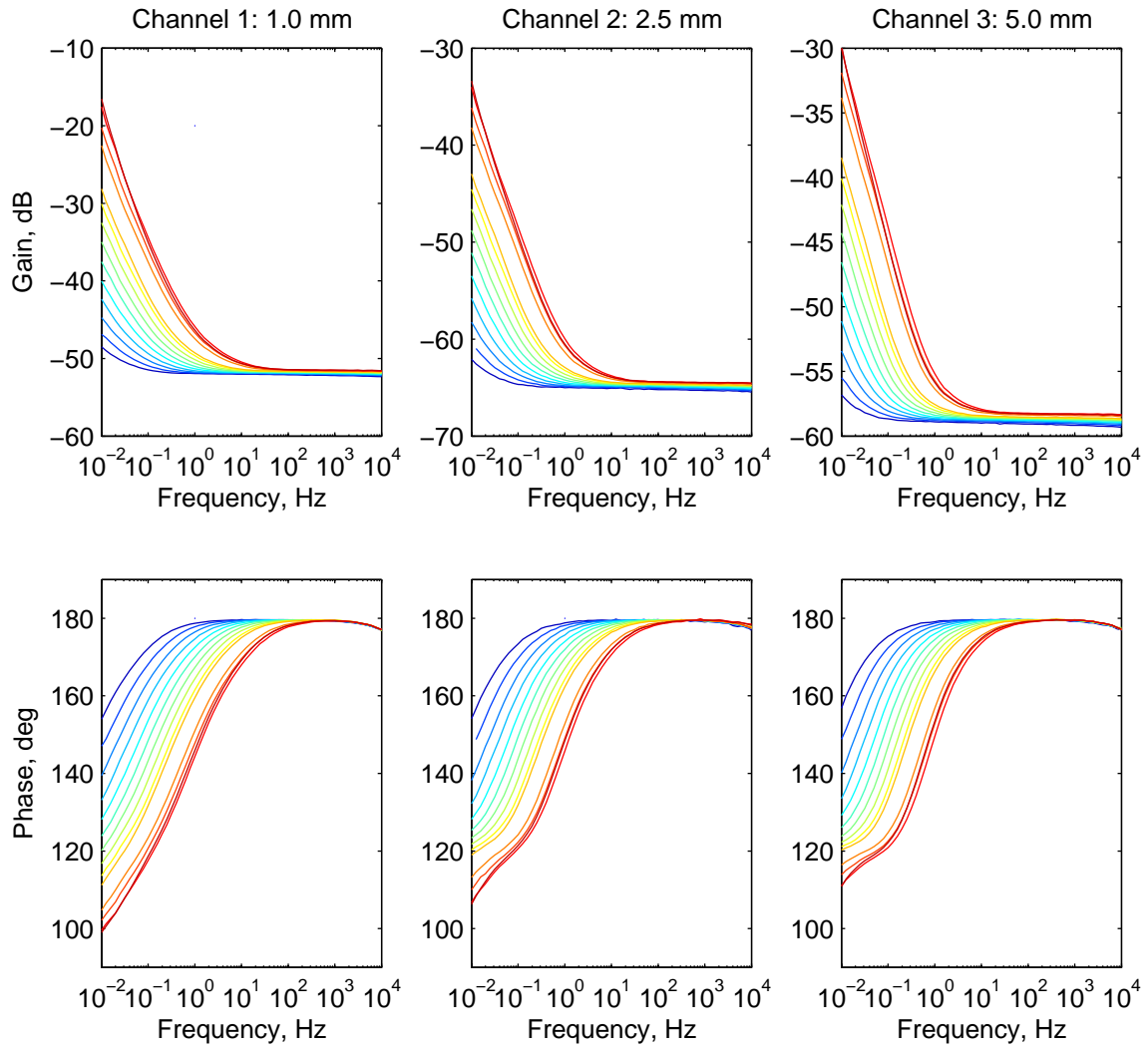


Figure B-13: Three conductor cable constant temperature dielectric spectroscopy measurements for 14 temperatures using 1, 2.5, and 5 mm wavelength interdigital sensors. Measurements are in color (see Table B.7). Interface box 2 is used. *This measurement was conducted from February 3 to February 4, 2006.*

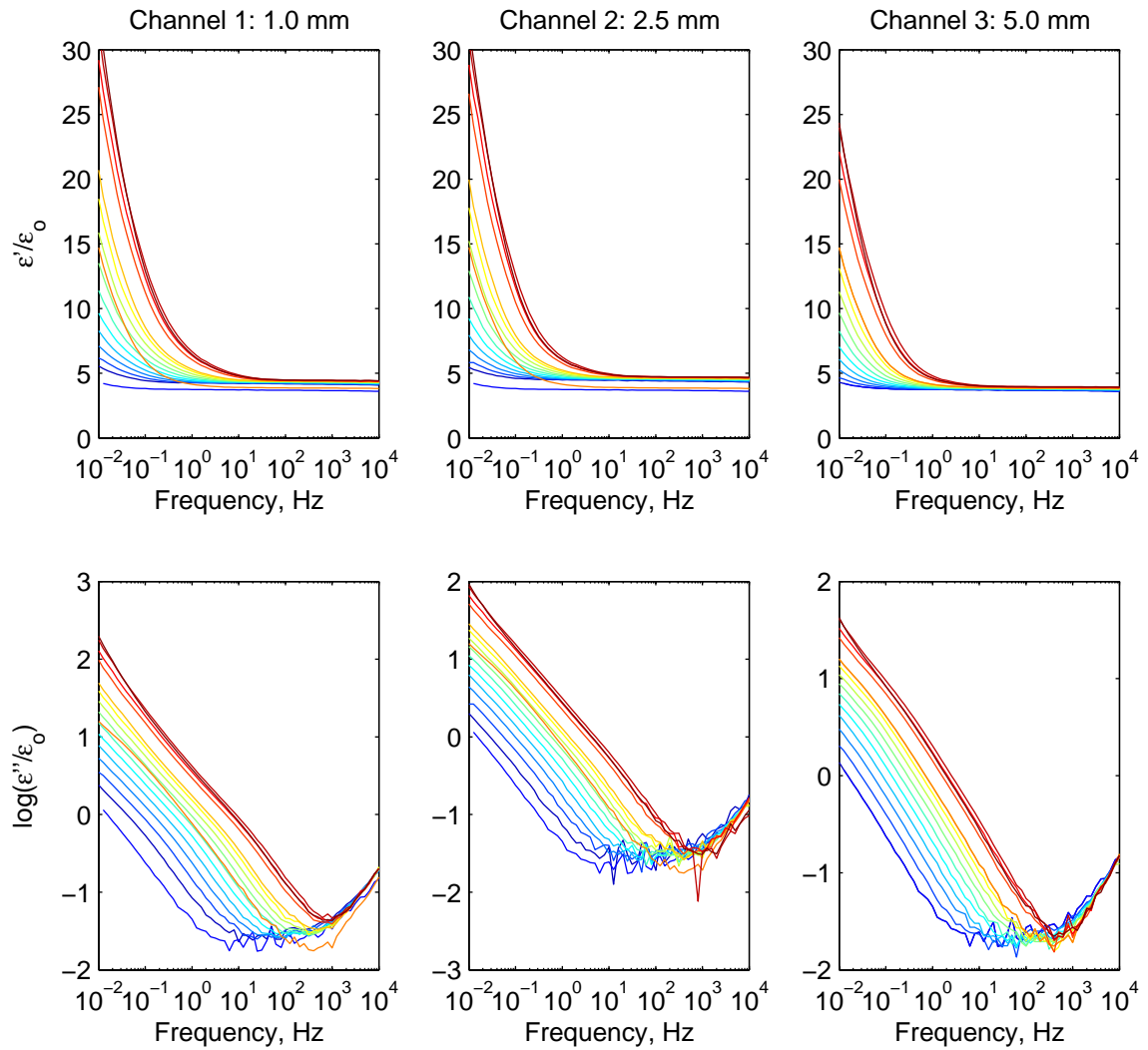


Figure B-14: Effective permittivity data for the three conductor cable from the steady state temperature measurements in Fig. B-13. Measurements are in colors corresponding to temperature as indicated in Table B.7.

Table B.8: Constant Temperature Information for Steady State Three Conductor Cable Measurements

Color						
Avg. Temp. °F	70.36	79.44	88.8	98.27	107.8	117.3
Std. Dev. °F	0.19	0.52	0.45	0.57	0.54	0.52
Color						
Avg. Temp. °F	126.8	136.3	145.9	155.5	164.8	
Std. Dev. °F	0.55	0.86	0.76	1.1	0.73	

June 2006 Measurement

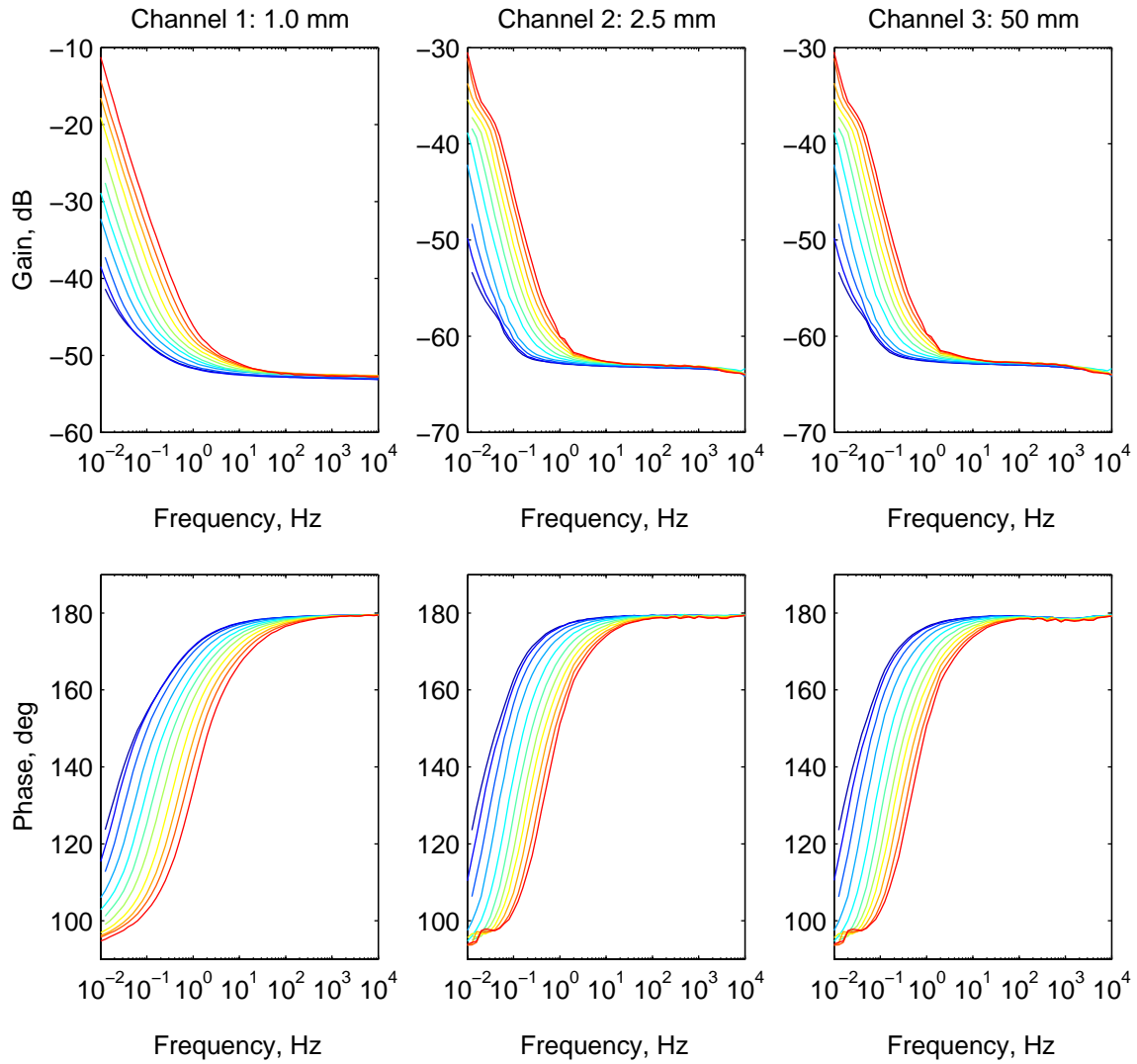


Figure B-15: Three conductor cable constant temperature dielectric spectroscopy measurements for 14 temperatures using 1, 2.5, and 5 mm wavelength interdigital sensors. Measurements are in color (see Table B.8). Interface box 2 is used. *This measurement was conducted from June 22 to June 23, 2006.*

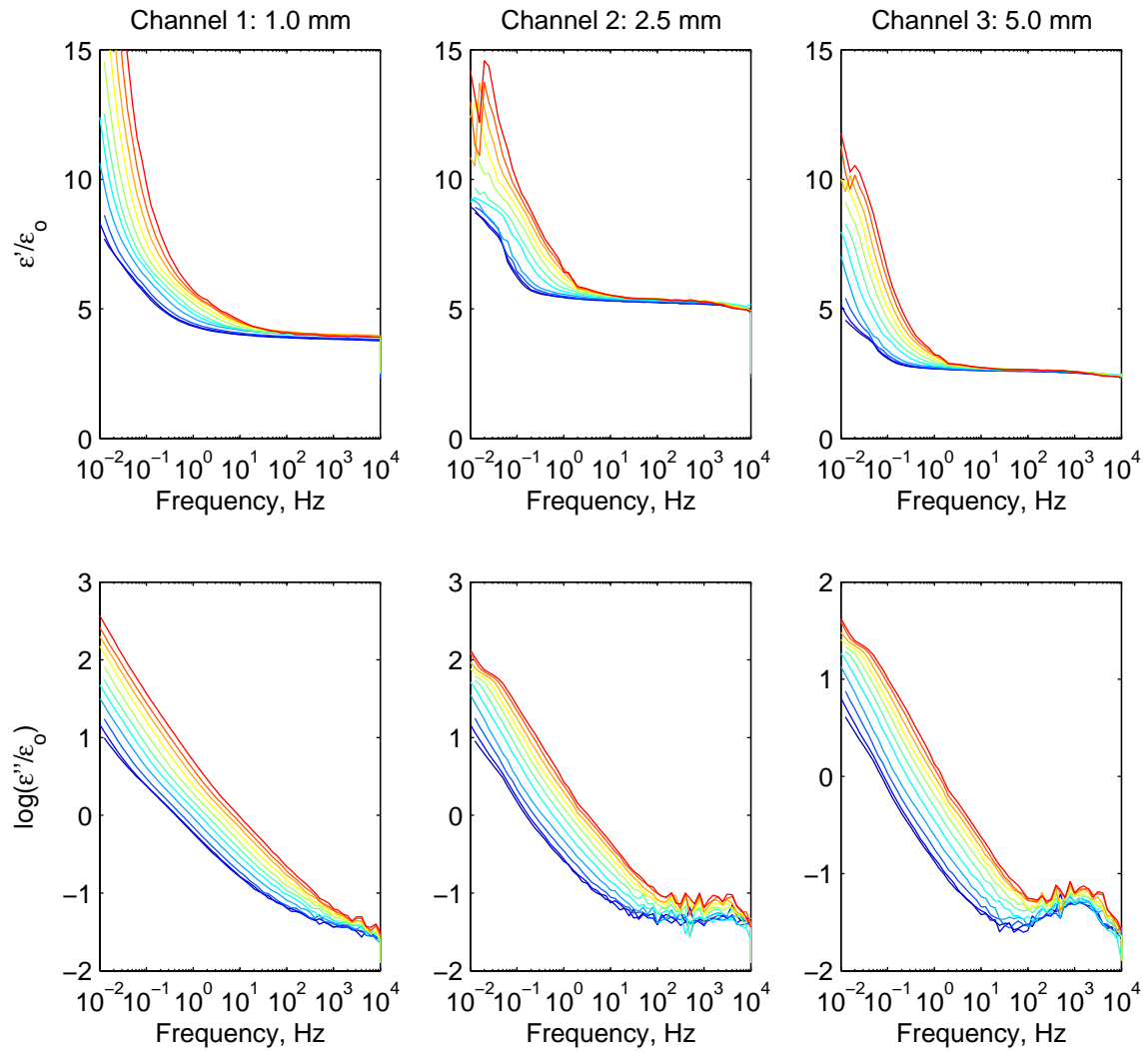


Figure B-16: Effective permittivity data for the three conductor cable from the steady state temperature measurements in Fig. B-15. Measurements are in colors corresponding to temperature as indicated in Table B.8.

B.2 Transient Measurements

B.2.1 ϕ Periodic Transient Measurements

Teflon Effective Permittivity

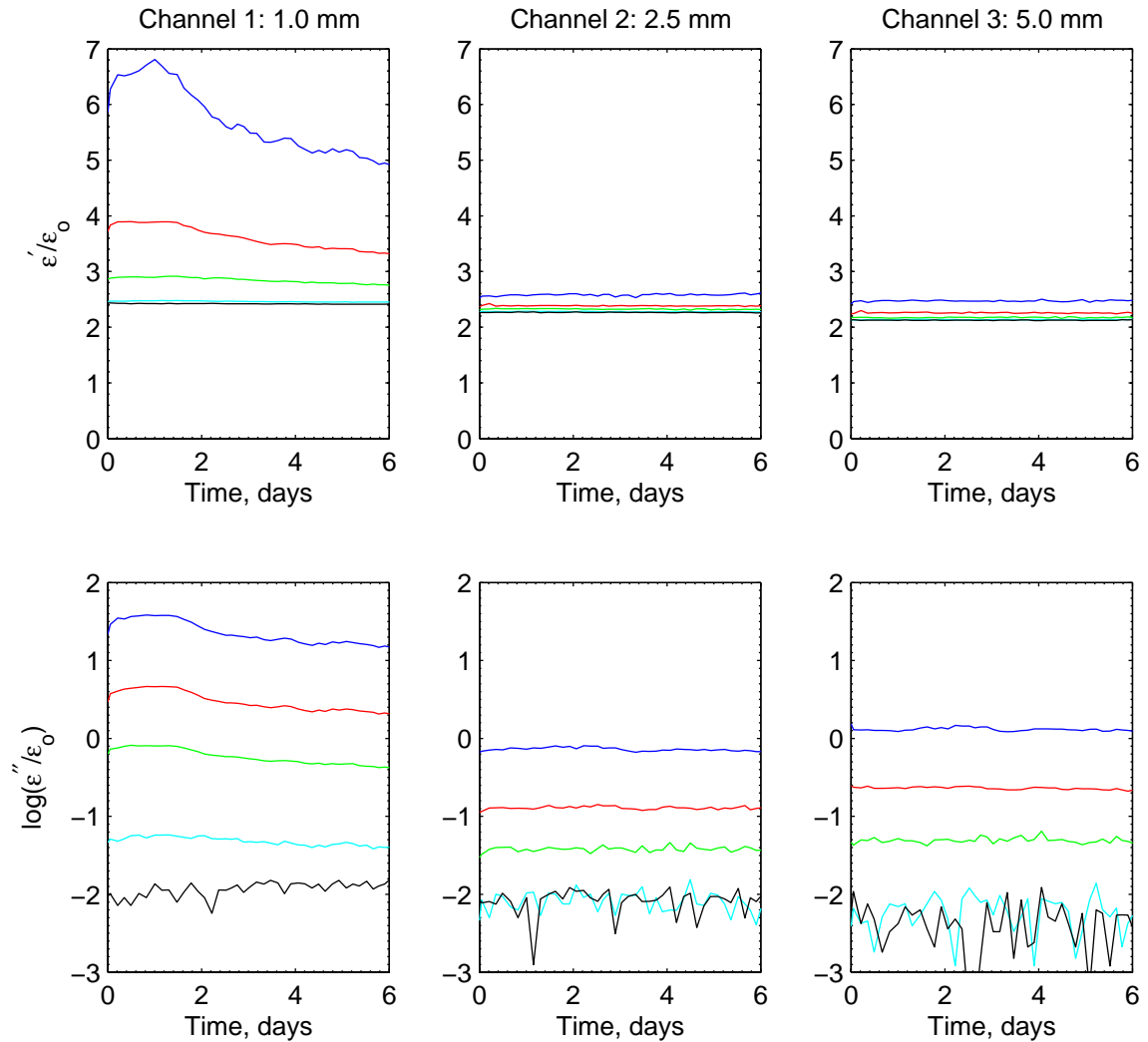


Figure B-17: Transient Teflon experiment calculated effective permittivity from measurements in Section 8.1.1. Frequencies shown are 0.01 (blue), 0.1 (red), 1.0 (green), 100 (cyan), and 10,000 (black) Hz.

Birch Rod Effective Permittivity

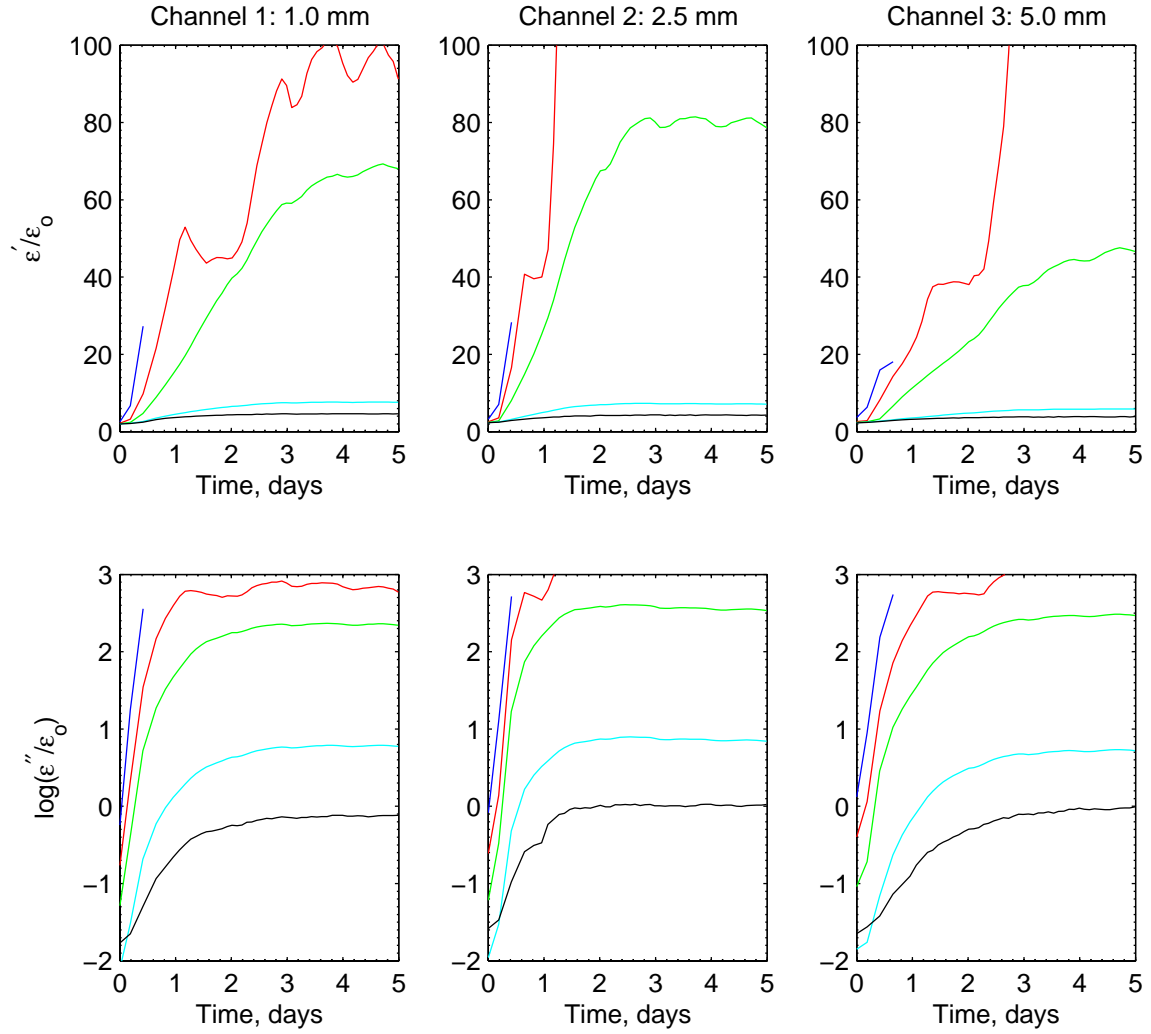


Figure B-18: Birch rod experiment calculated effective permittivity from measurements in Section 8.1.2. Frequencies shown are 0.01 (blue), 0.1 (red), 1.0 (green), 100 (cyan), and 10,000 (black) Hz.

Single Conductor Cable Effective Permittivity

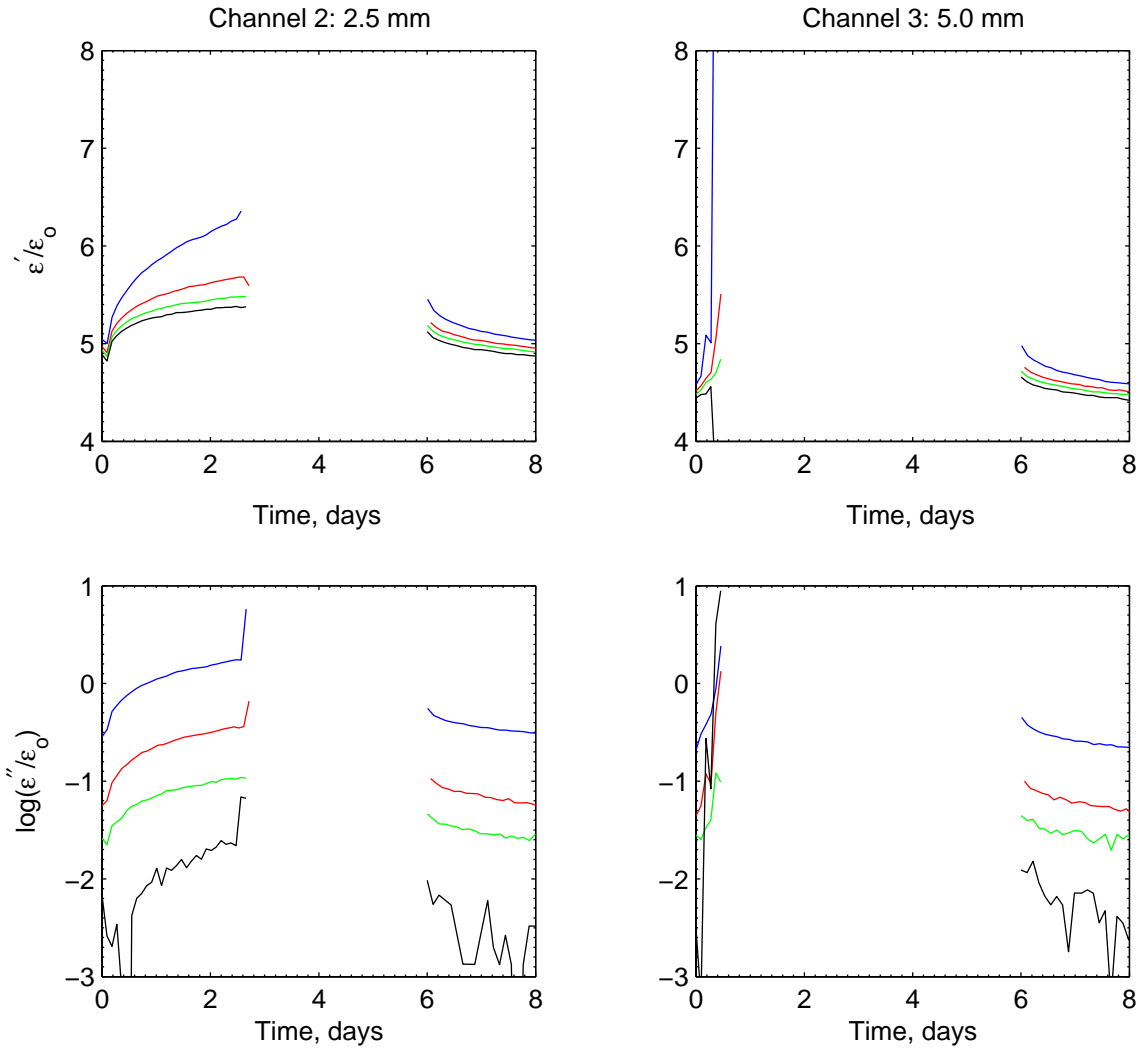


Figure B-19: Unwrapped single conductor cable experiment calculated effective permittivity from measurements in Section 8.1.3, Experiment 1. Frequencies shown are 10 (blue), 100 (red), 1,000 (green), and 10,000 (black) Hz.

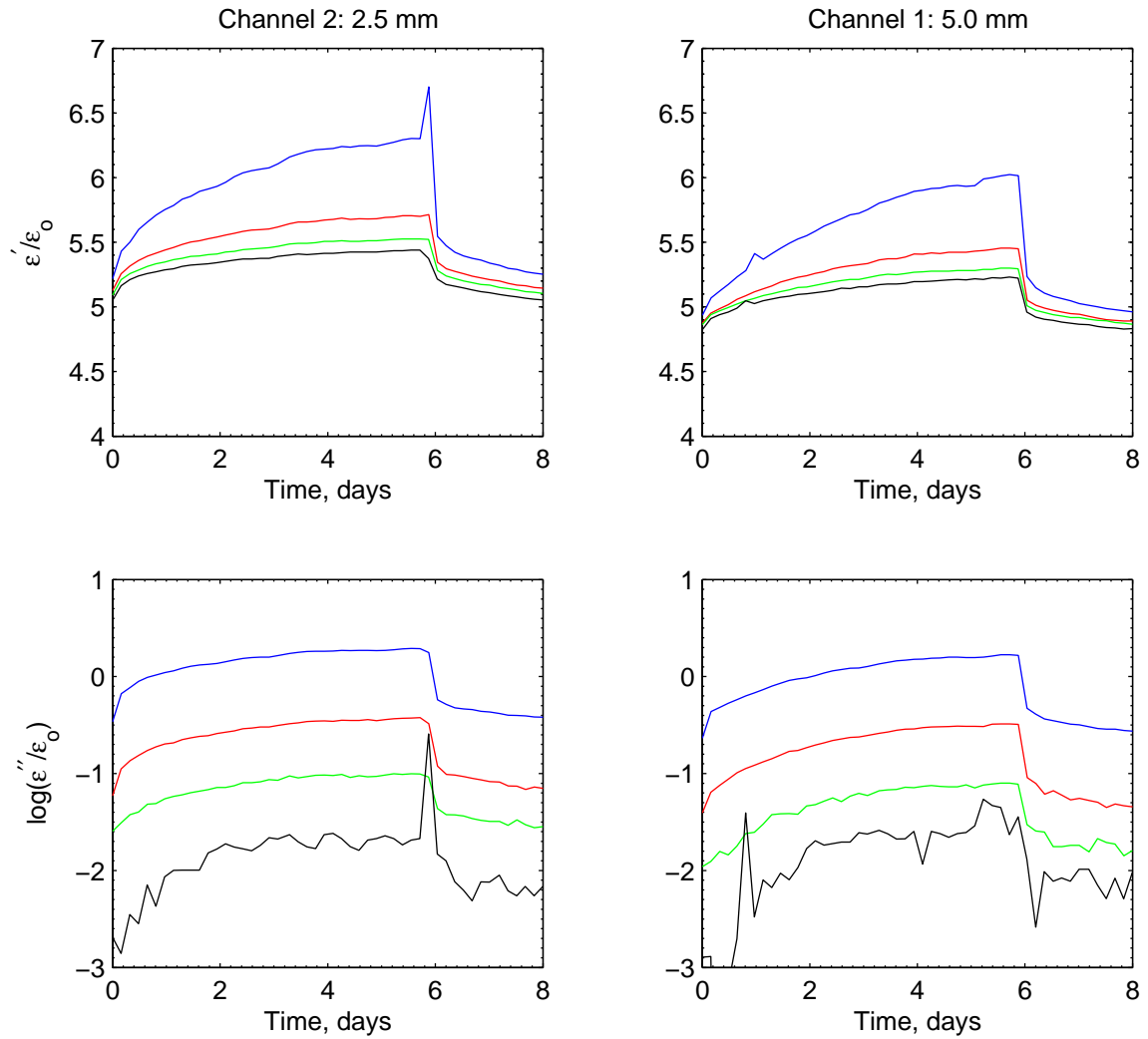


Figure B-20: Wrapped single conductor cable experiment calculated effective permittivity from measurements in Section 8.1.3, Experiment 1. Frequencies shown are 10 (blue), 100 (red), 1,000 (green), and 10,000 (black) Hz.

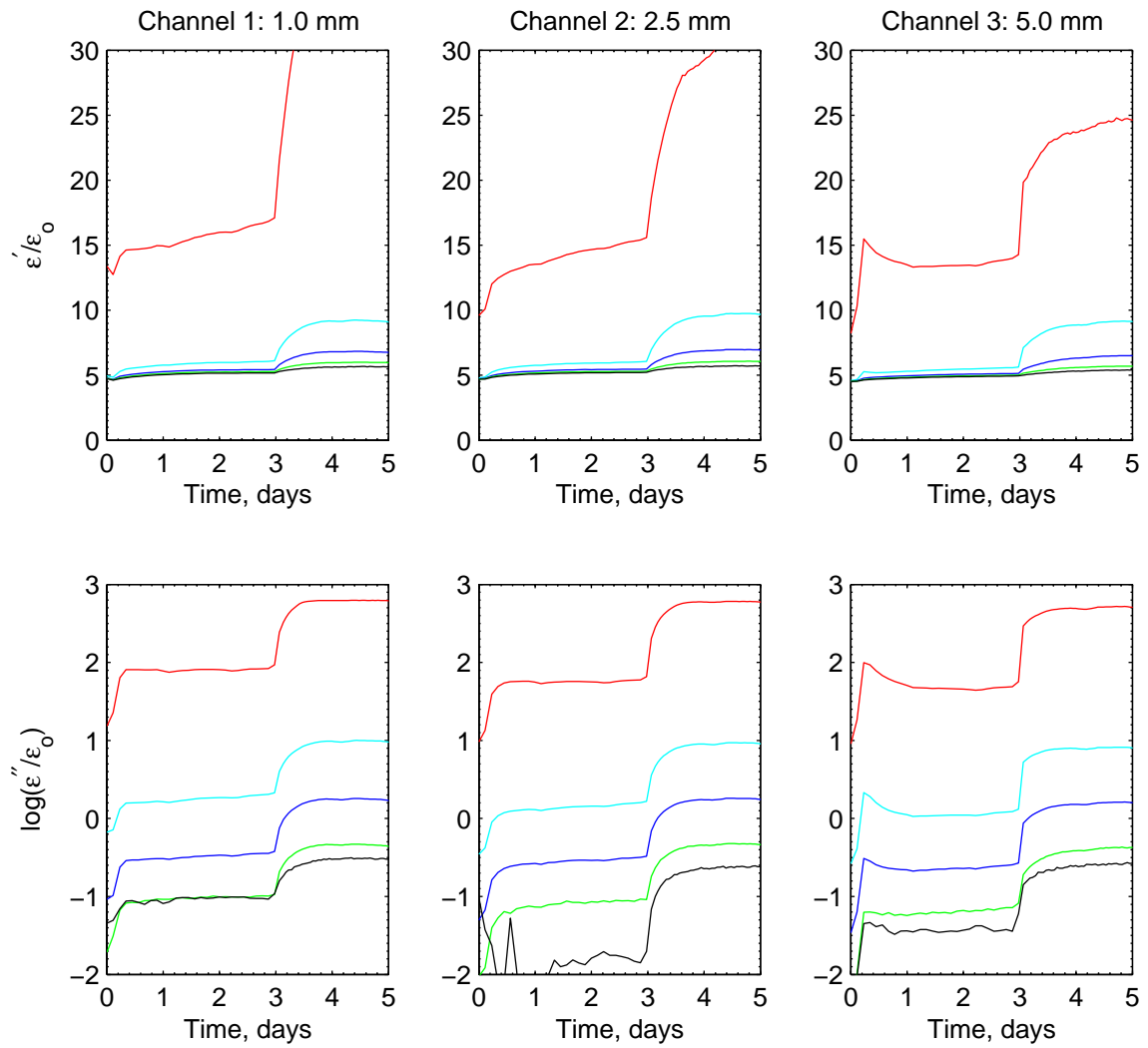


Figure B-21: Single conductor cable experiment calculated effective permittivity from measurements in Section 8.1.3, Experiment 2. Frequencies shown are 0.1 (red), 10 (cyan), 100 (blue), 1,000 (green), and 10,000 (black) Hz.

Three Conductor Cable Effective Permittivity

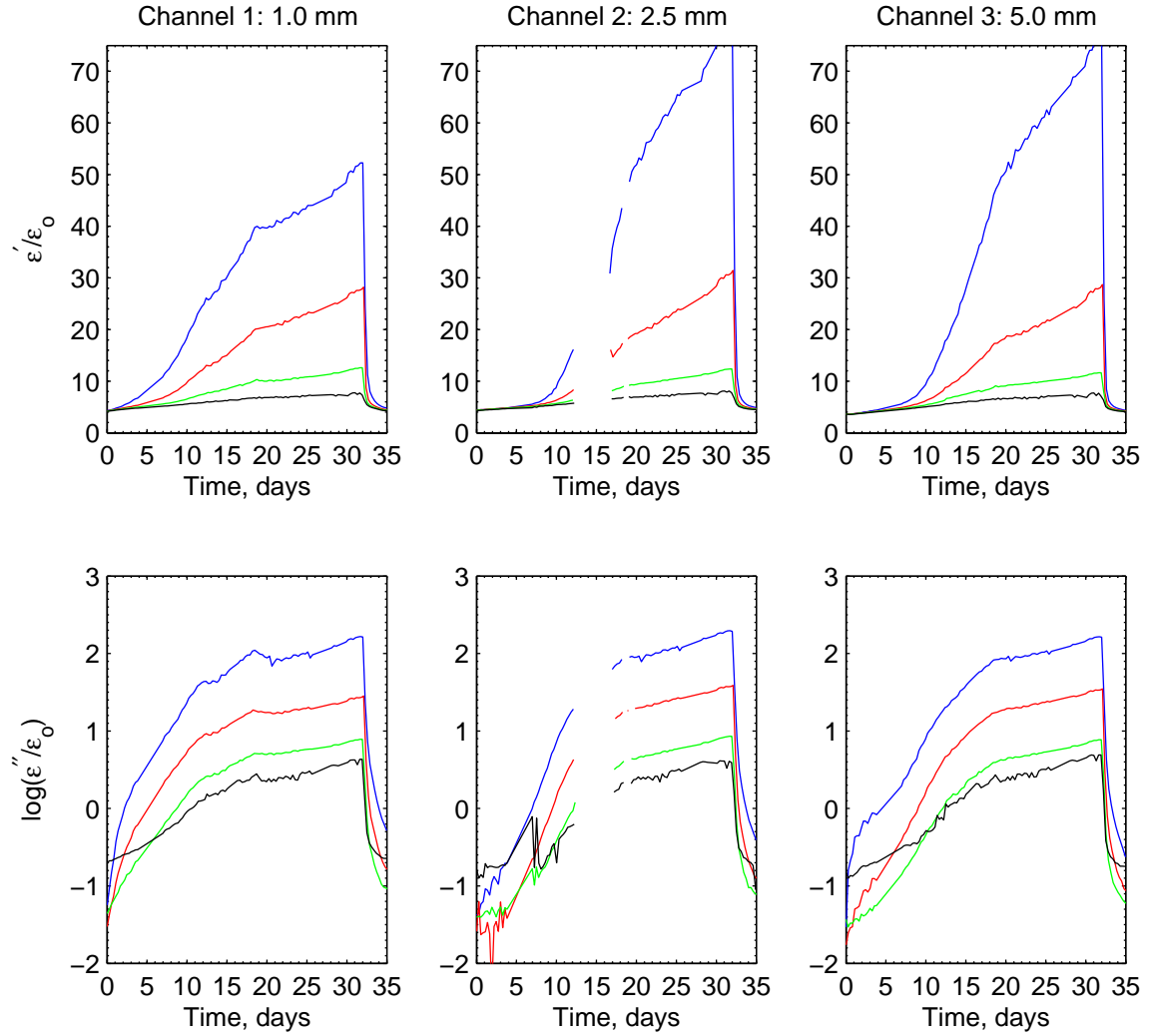


Figure B-22: Three conductor cable experiment calculated effective permittivity from measurements in Section 8.1.4, Experiment 1. Frequencies shown are 10 (blue), 100 (red), 1,000 (green), and 10,000 (black) Hz.

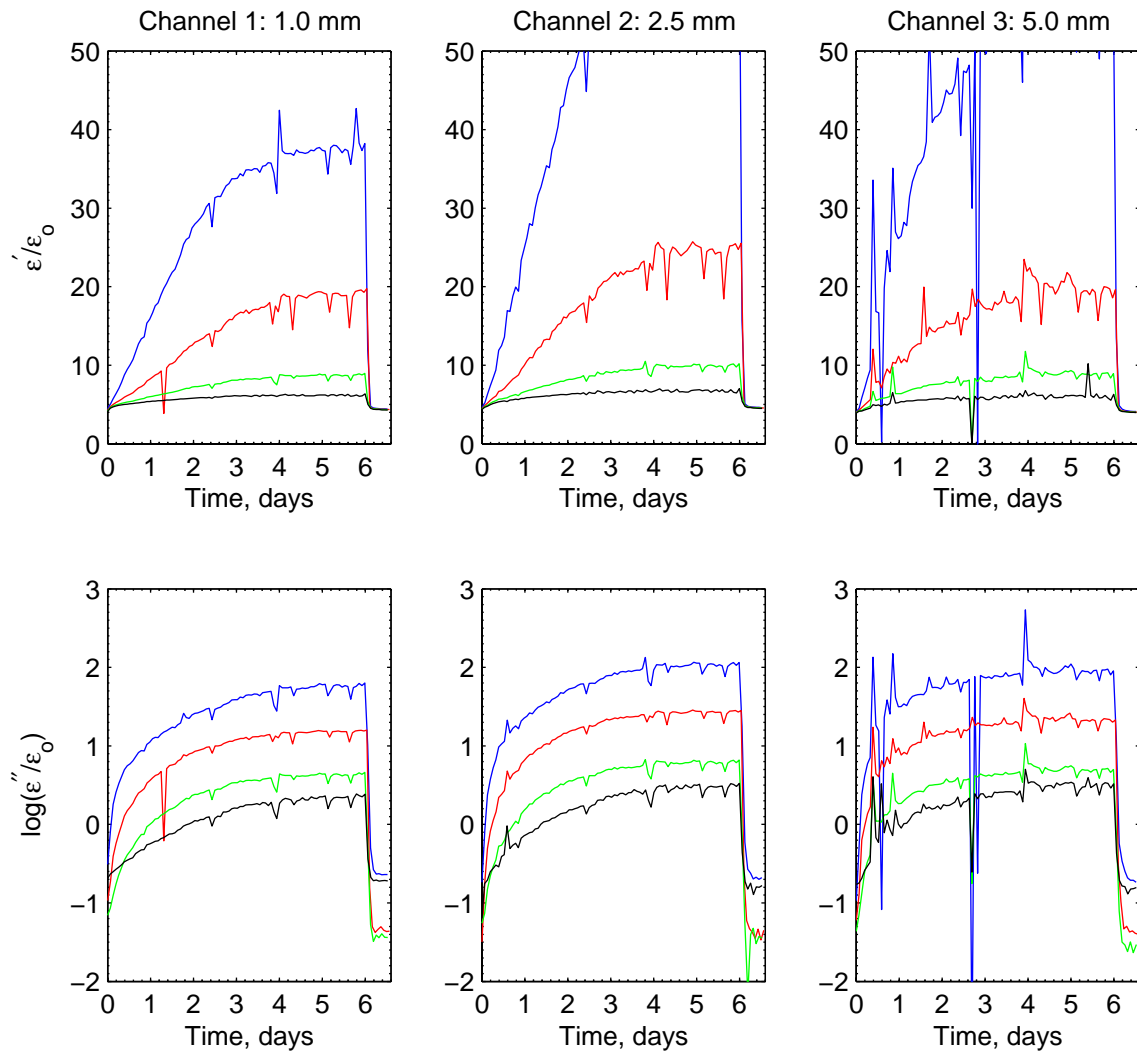


Figure B-23: Three conductor cable experiment calculated effective permittivity from measurements in Section 8.1.4, Experiment 2. Frequencies shown are 10 (blue), 100 (red), 1,000 (green), and 10,000 (black) Hz.

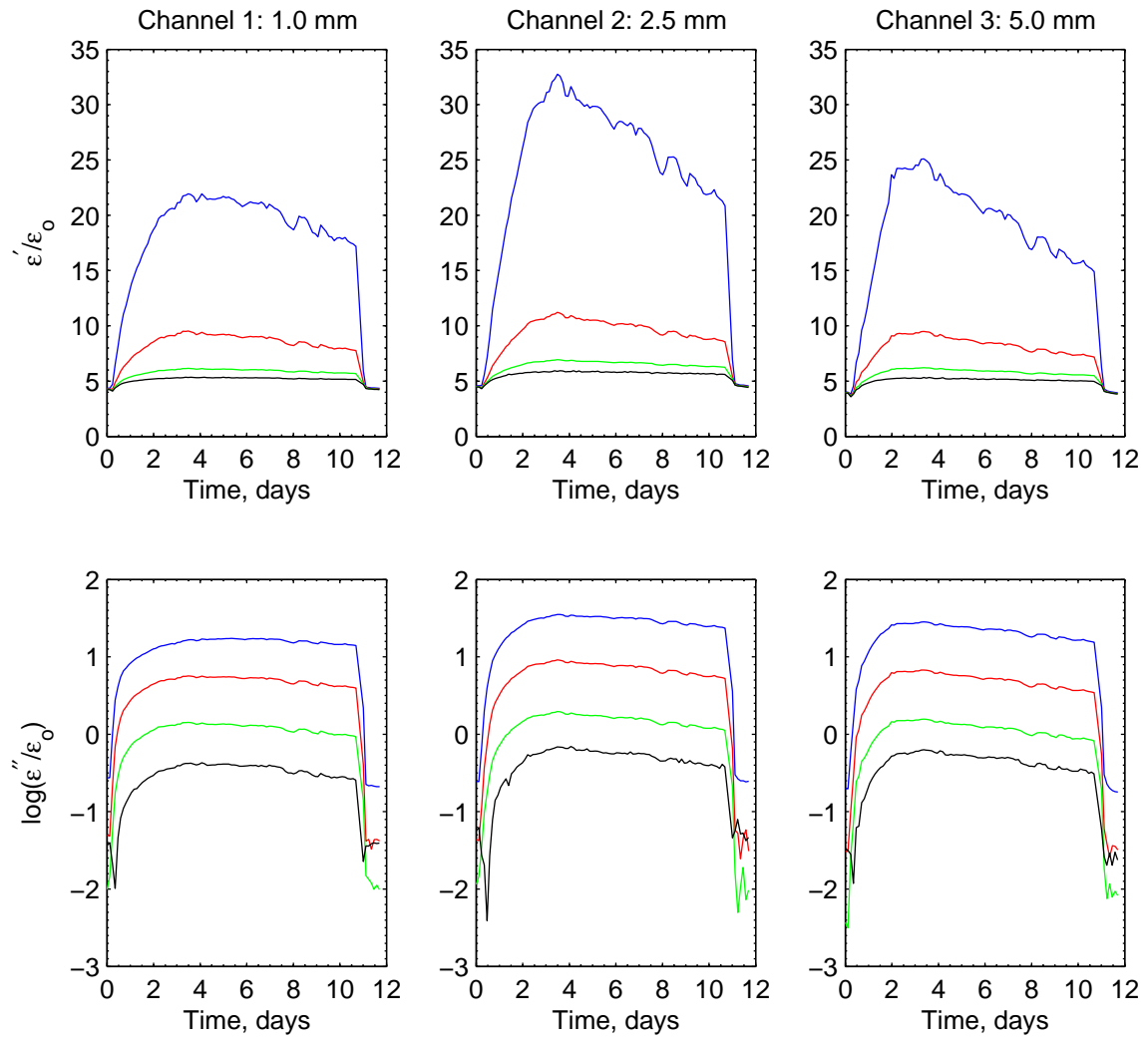


Figure B-24: Three conductor cable experiment calculated effective permittivity from measurements in Section 8.1.4, Experiment 3. Frequencies shown are 10 (blue), 100 (red), 1,000 (green), and 10,000 (black) Hz.

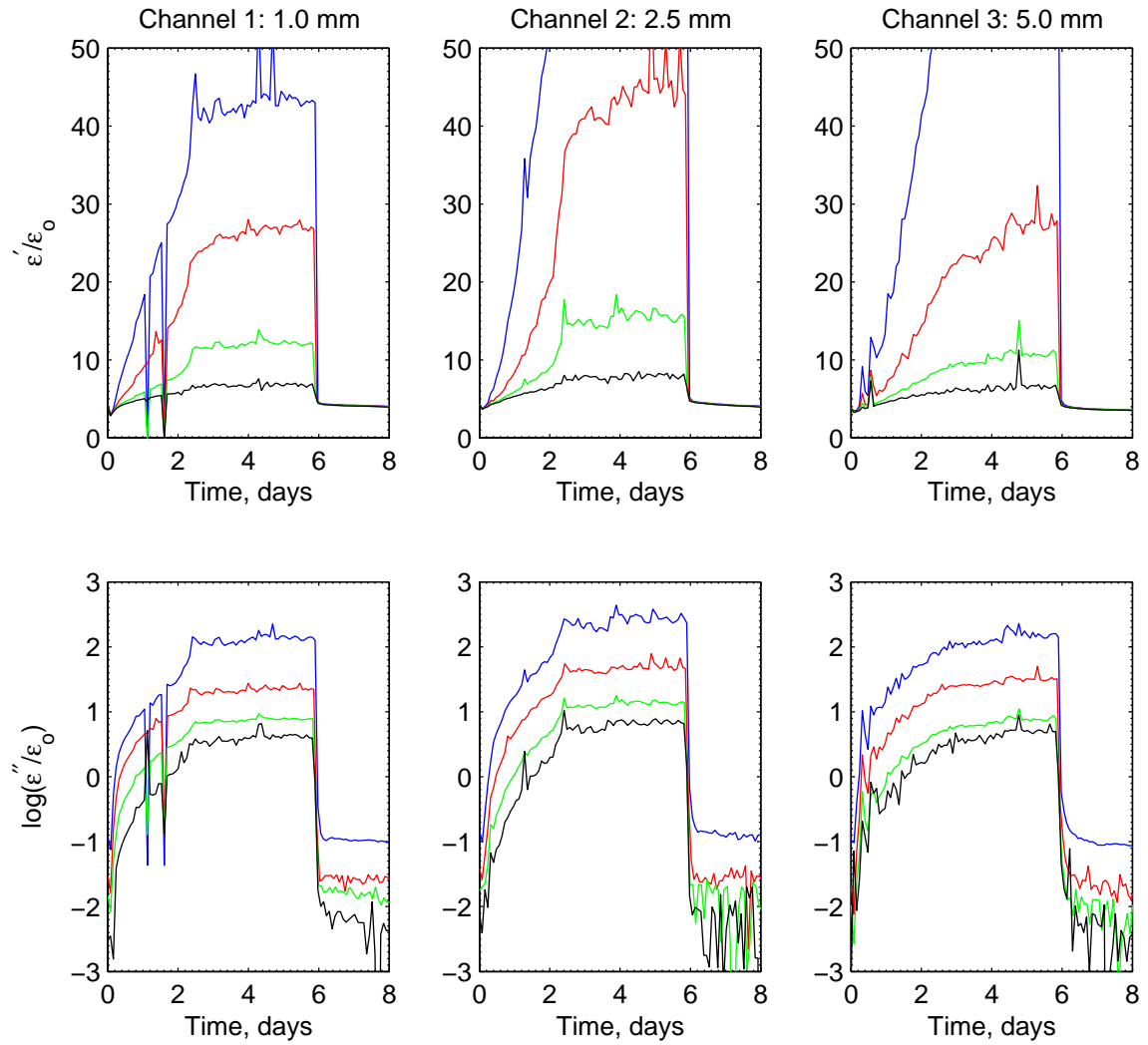


Figure B-25: Three conductor cable experiment calculated effective permittivity from measurements in Section 8.1.4, Experiment 4. Frequencies shown are 10 (blue), 100 (red), 1,000 (green), and 10,000 (black) Hz.

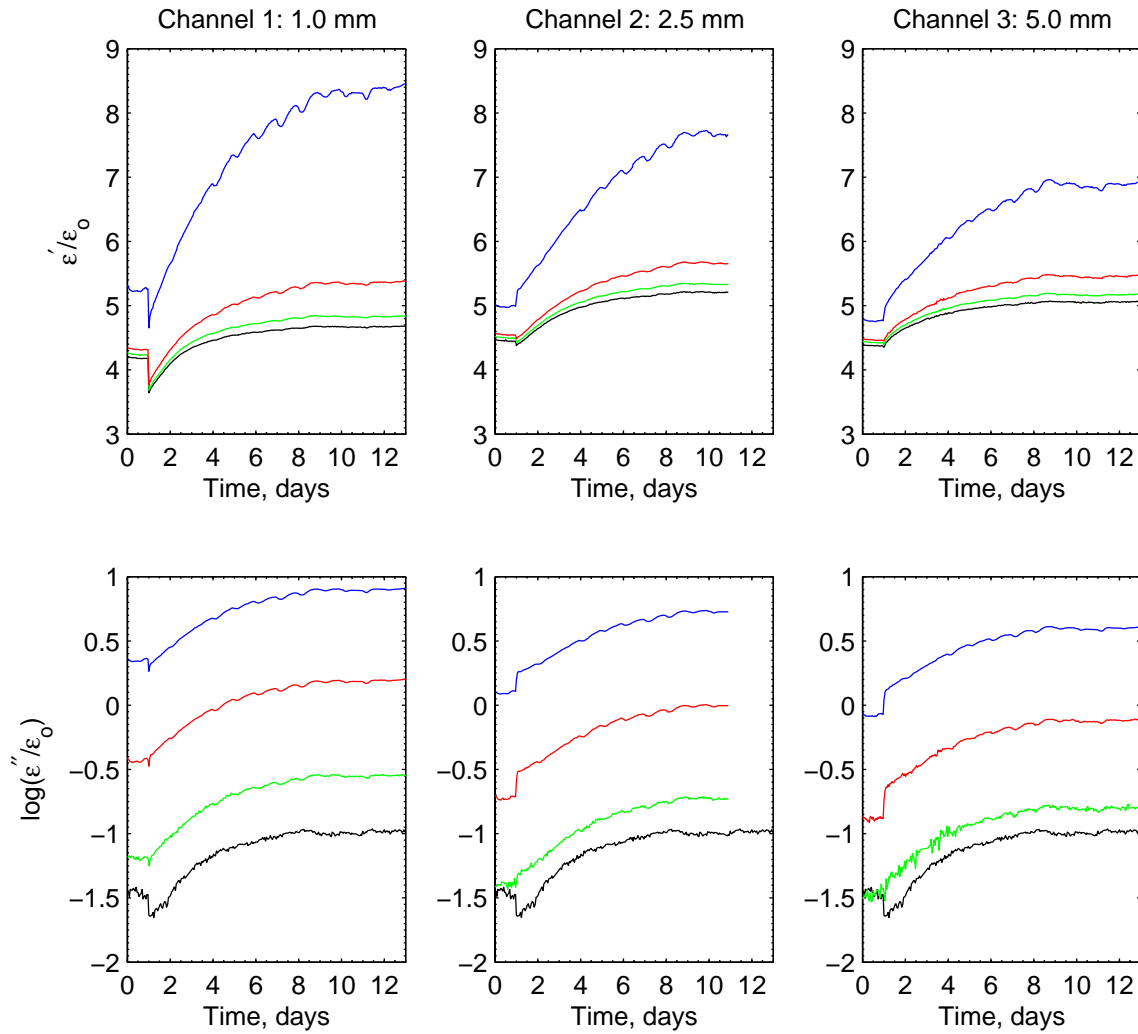


Figure B-26: Three conductor cable moisture ingress experiment calculated effective permittivity from measurements in Section 8.1.4, Experiment 5. Frequencies shown are 10 (blue), 100 (red), 1,000 (green), and 10,000 (black) Hz.

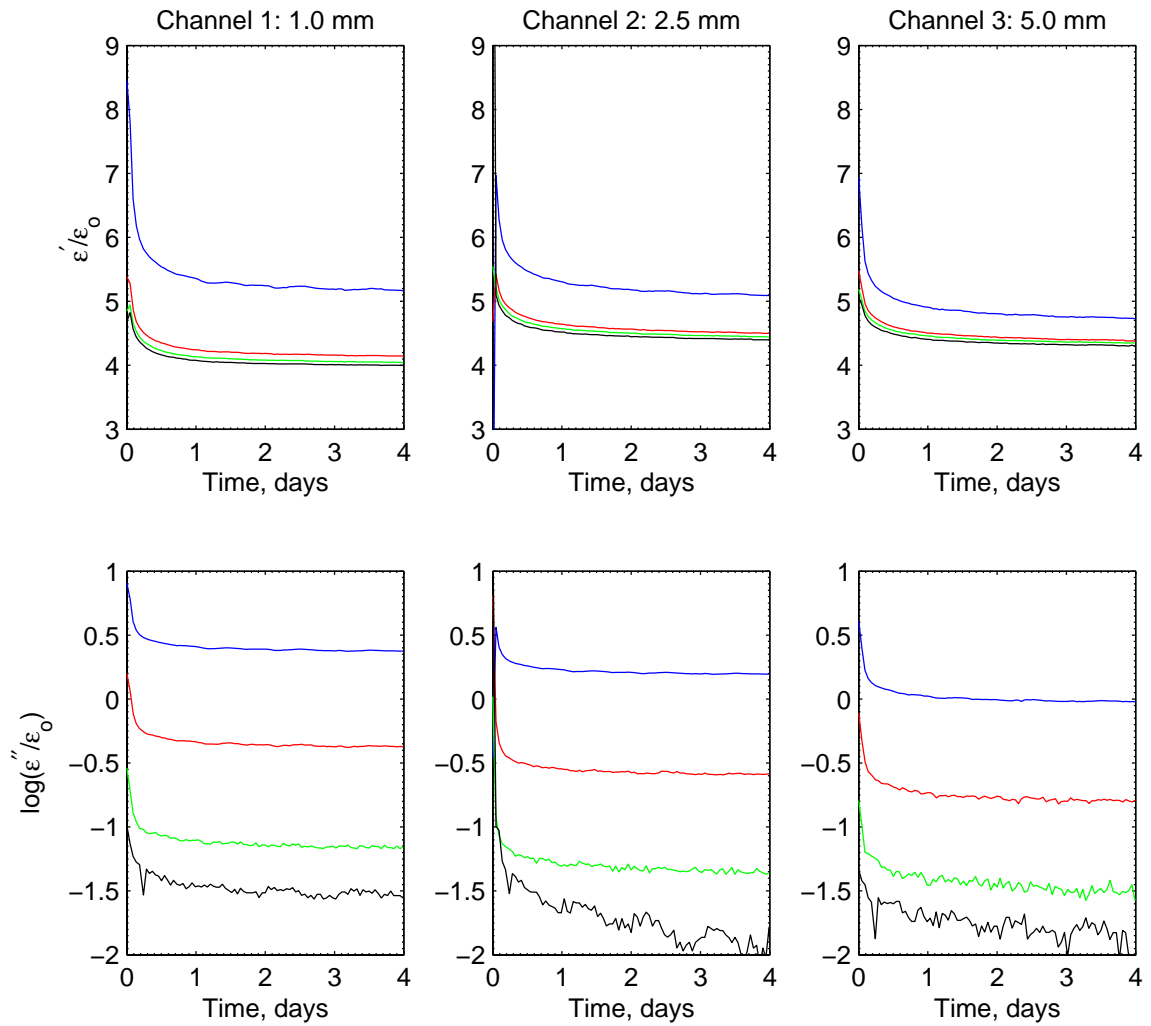


Figure B-27: Three conductor cable moisture egress experiment calculated effective permittivity from measurements in Section 8.1.4, Experiment 5. Frequencies shown are 10 (blue), 100 (red), 1,000 (green), and 10,000 (black) Hz.

Bibliography

- [1] R. Neimanis and R. Eriksson, "Diagnosis of moisture in oil/paper distribution cables - Part I: Estimation of moisture content using frequency-domain spectroscopy," *IEEE Transactions on Power Delivery*, vol. 19, no. 1, pp. 9–14, January 2004.
- [2] B. N. Taylor and P. J. Mohr, Eds., *The NIST Reference on Constants, Units, and Uncertainty*, 2007.
- [3] M. Zahn, *Electromagnetic Field Theory*. Krieger Publishing Company, 2003.
- [4] J. A. Kong, *Electromagnetic Wave Theory*. EMW Publishing, 2000.
- [5] A. Jonscher, *Dielectric Relaxation in Solids*, 2nd ed. Chelsea Dielectric Press Ltd, 1983.
- [6] J. Dyba, "The rise and decline in the United States of impregnated paper-insulated metallic sheathed cable, solid-type. I. The rise," *IEEE Electrical Insulation Magazine*, vol. 15, no. 4, pp. 13–16, Jul/Aug 1999.
- [7] W. R. Stagi, "Cable injection technology," in *Proc. IEEE Latin America Conf.*, 2006.
- [8] J. Crine, V. Buchholz, and M. Colwell, "Influence of aging on polarization currents and return voltage measured in PILC cables," in *Annual Report: Conference on Electrical Insulation and Dielectric Phenomena*. IEEE, 2001, pp. 188–191.
- [9] L. Olsson and G. Bengtsson, "PD-mapping of paper insulated MV cables in Gothenburg," in *Proc. CIGRE*, June 1997, p. 438.
- [10] R. Neimanis, R. Eriksson, and R. Papazyan, "Diagnosis of moisture in oil/paper distribution cables - part ii: Water penetration in cable insulation-experiment and modeling," *IEEE Transactions on Power Delivery*, vol. 19, no. 1, pp. 15–20, January 2004.

- [11] B. Hagstrom, R. Hampton, B. Helmesjo, and T. Hjertberg, "Disposal of cables at the 'end of life'; some of the environmental considerations," *IEEE Electrical Insulation Magazine*, vol. 22, no. 2, pp. 21–30, March/April 2006.
- [12] J. Densley, "Ageing mechanisms and diagnostics for power cables - an overview," *IEEE Electrical Insulation Magazine*, vol. 17, no. 1, pp. 14–22, January/February 2001.
- [13] W. Lawson, M. Simmons, and P. Gale, "Thermal ageing of cellulose paper insulation," *IEEE Trans. Diel. Elec. Insul.*, vol. EI-12, no. 1, pp. 61–66, February 1977.
- [14] F. Bitam-Megherbi, S. Osmani, and M. Megherbi, "The moisture effect on dielectric losses of insulating paper," in *Proceedings of the 2004 IEEE International Conference on Solid Dielectrics ICSD 2004*, 2004.
- [15] V. Buchholz, M. Colwell, S. Cherukupalli, J. Crine, and R. Keefe, "Comparison of moisture contents in PILC cables measured by chemical titration and determined from electrical and dielectric measurements," in *International Conference on Solid Dielectrics*. Toulouse, France: IEEE, July 2004.
- [16] E. LeGhait, "Dielectric losses in oil impregnated paper," *Electric Journal*, vol. 25, no. 4, pp. 187 – 193, 1928.
- [17] P. von Guggenberg and J. Melcher, "A three-wavelength flexible sensor for monitoring the moisture content of transformer pressboard." *Properties and Applications of Dielectric Materials*, 1991., Proceedings of the 3rd International Conference on, July 1991, pp. 1262–1265.
- [18] Y. Sheiretov and M. Zahn, "Dielectrometry measurements of moisture dynamics in oil-impregnated pressboard," *IEEE Trans. Diel. Elec. Insul.*, vol. 2, no. 3, pp. 329–351, June 1995.
- [19] A. Washabaugh, A. Mamishev, Y. Du, and M. Zahn, "Dielectric measurements of semi-insulating liquids and solids." Roma, Italy: International Conference Conduction and Breakdown in Dielectric Liquids (IDCL), July 1996, pp. 381–384.
- [20] A. Krivda, R. Neimanis, and S. Gubanski, "Assessment of insulation condition of 130 kV oil-paper current transformers using return voltage measurements and an expert system," in *Conference on Electrical Insulation and Dielectric Phenomena (CEIDP), Annual Report*, October 1997, pp. 210–213.

- [21] R. Van Brunt, K. Stricklett, J. Steiner, and S. Kulkarni, "Recent advances in partial discharge measurement capabilities at NIST," *IEEE Trans. Elec. Insul.*, vol. 27, no. 1, pp. 114–129, February 1992.
- [22] L. Lamarre, D. Fournier, and R. Morin, "Early detection of faults in underground distribution cable joints by partial discharge measurements," *Proceedings of the IEEE International Conference on Properties and Applications of Dielectric Materials*, vol. 2, pp. 864 – 867, 1994.
- [23] M. Vakilian, T. Blackburn, R. James, and B. T. Phung, "Semiconducting layer as an attractive PD detection sensor of XLPE cables," *IEEE Trans. Diel. Elec. Insul.*, vol. 13, no. 4, pp. 885–891, August 2006.
- [24] B. Jiang, A. P. Sample, R. M. Wistort, and A. V. Mamishev, "Autonomous robotic monitoring of underground cable systems," *2005 International Conference on Advanced Robotics, ICAR '05, Proceedings*, vol. 2005, pp. 673 – 679, 2005.
- [25] R. Neimanis, H. Lennholm, and R. Eriksson, "Determination of moisture content in impregnated paper using near infrared spectroscopy," in *Conference on Electrical Insulation and Dielectric Phenomena*, 1999, pp. 162–165.
- [26] P. Gervais, M. Duval, M. Merabet, and T. K. Bose, "The state of water in oil-impregnated paper insulation," *Conference Record of IEEE International Symposium on Electrical Insulation*, pp. 65 – 67, 1990.
- [27] R. Neimanis, T. K. Saha, and R. Eriksson, "Determination of moisture content in mass impregnated cable insulation using low frequency dielectric spectroscopy," in *Proceedings of the 2000 Power Engineering Society Summer Meeting*, 2000.
- [28] A. C. Gjaerde, L. Lundgaard, and E. Ildstad, "Effect of temperature and moisture on the dielectric properties of oil-impregnated cellulose," *9th International Symposium on High Voltage Engineering*, no. 1060, 1995.
- [29] J. Danvind and M. Ekevad, "Local water vapor diffusion coefficient when drying norway spruce sapwood," *Journal of Wood Science*, vol. 52, no. 3, pp. 195–201, June 2006.
- [30] G. Michael, "X-Ray computed tomography," *Physics Education*, pp. 442–451, 2001.
- [31] A. Mamishev, Y. Du, B. Lesieutre, and M. Zahn, "Development and applications of fringing electric field dielectrometry sensors and parameter estimation algorithms," *Journal of Electrostatics*, vol. 46, pp. 109–123, 1999.

- [32] J. Sears, "Interdigital dielectrometry based detection and identification of dangerous materials for security applications," Master's thesis, Massachusetts Institute of Technology, August 2003.
- [33] G. I. Rowe, J. H. Yi, K. G. Chiu, J. Tan, A. V. Mamishev, and B. Minaie, "Fill-front and cure progress monitoring for VARTM with auto-calibrating dielectric sensors," in *International SAMPE Symposium and Exhibition (Proceedings)*, 2005.
- [34] K. Alme and S. Mylvaganam, "Electrical capacitance tomography—sensor models, design, simulations, and experimental verification," *IEEE Sensors Journal*, vol. 6, no. 5, pp. 1256–1266, October 2006.
- [35] W. Stagi and F. E. Kimsey, "Case study: Rejuvenation fluid injection results from Duke Powers Little Rock retail tap line, a 115 kV XLPE, buried transmission circuit," in *Power Engineering Society: Transmission and Distribution*. IEEE, 2006.
- [36] R. Keefe and W. Zenger, "Electric cable samples specifications," Private Correspondence, October 2005.
- [37] M. C. Zaretsky, L. Mouayard, and J. R. Melcher, "Continuum properties from interdigital electrode dielectrometry," *IEEE Trans. Elec. Insul.*, vol. 23, no. 6, pp. 897–917, December 1988.
- [38] M. Zahn, "Optical, electrical and electromechanical measurement methodologies of field, charge and polarization in dielectrics," *IEEE Trans. Diel. Elec. Insul.*, vol. 5, no. 5, pp. 627–650, October 1998.
- [39] Y. Du, A. Mamishev, B. Lesieutre, and M. Zahn, "Measurement of moisture diffusion as a function of temperature and moisture concentration in transformer pressboard," in *Proceedings of the 1998 67th IEEE Annual Conference on Electrical Insulation and Dielectric Phenomena. Part 1 (of 2)*, 1998.
- [40] Y. Du, M. Zahn, and B. Lesieutre, "Dielectrometry measurements of effects of moisture and anti-static additive on transformer board," in *1997 IEEE Annual Report - Conference on Electric Insulation and Dielectric Phenomena*. IEEE, October 1997, pp. 226–229.
- [41] S. R. Cantrell, A. V. Mamishev, and M. Zahn, "Uncertainty analysis for multiple penetration depth dielectrometry." Inter. Conf. Advances in Processing, Testing and Application of Dielectric Materials, 2001, pp. 119–122.

- [42] A. V. Mamishev, K. Sundara-Rajan, F. Yang, Y. Du, and M. Zahn, "Interdigital sensors and transducers," *Proc. IEEE*, vol. 92, no. 5, pp. 808–845, May 2004.
- [43] I. Shay and M. Zahn, "Cylindrical geometry electroquasistatic dielectrometry sensors," *IEEE Trans. Diel. Elec. Insul.*, vol. 12, no. 1, pp. 41–49, February 2005.
- [44] A. Mamishev, B. Lesieutre, and M. Zahn, "Parameter estimation using an interdigital dielectrometry sensor," IEEE Conf. on Electrical Insulation and Dielectric Phenomena. Minneapolis, MN: IEEE, October, pp. 234–237.
- [45] P. A. von Guggenberg, "Applications of interdigital dielectrometry to moisture and double layer measurements in transformer insulation," Ph.D. dissertation, Massachusetts Institute of Technology, June 1993.
- [46] A. Mamishev and M. Zahn, "Techniques for semi-empirical characterization of material and sensor properties on interdigital dielectrometry," IEEE Inter. Symp. Elec. Insul. IEEE, June 1996, pp. 486–489.
- [47] A. Mamishev, B. Lesieutre, and M. Zahn, "Optimization of multi-wavelength interdigital dielectrometry instrumentation and algorithms," *IEEE Trans. Diel. Elec. Insul.*, vol. 5, no. 3, pp. 408–420, June 1998.
- [48] D. E. Schlicker, "Flow electrification in aged transformer oils," Master's thesis, Massachusetts Institute of Technology, September 1996.
- [49] B. Lesieutre, A. Mamishev, Y. Du, E. Keskiner, M. Zahn, and G. Verghese, "Forward and inverse parameter estimation algorithms of interdigital dielectrometry sensors," *IEEE Trans. Diel. Elec. Insul.*, vol. 8, no. 4, pp. 577–588, August 2001.
- [50] Y. Sheiretov and M. Zahn, "Modeling of spatially periodic dielectric sensors in the presence of a top ground plane bounding the test dielectric," *IEEE Trans. Diel. Elec. Insul.*, vol. 12, no. 5, pp. 993–1004, October 2005.
- [51] Y. Sheiretov, "Deep penetration magnetoquasistatic sensors," Ph.D. dissertation, Massachusetts Institute of Technology, June 2001.
- [52] F. B. Hildebrand, *Advanced Calculus for Applications*. Englewood Cliffs, New Jersey: Prentice-Hall, May 1965.
- [53] S. Hollos and R. Hollos, "Fourier series expansion of functions in two or more dimensions," May 2004, from <http://www.exstrom.com>.

- [54] A. V. Mamishev, "Interdigital dielectrometry sensor design and parameter estimation algorithms for non-destructive materials evaluation," Ph.D. dissertation, Massachusetts Institute of Technology, May 1999.
- [55] X. B. Li, S. D. Larson, A. S. Zyuzin, and A. V. Mamishev, "Design principles for multichannel fringing electric field sensors," *IEEE Sensors Journal*, vol. 6, no. 2, pp. 434–440, April 2006.
- [56] "MATLAB," The Mathworks Inc., Software, 2002, version 6.5.
- [57] "Mathematica," Wolfram Research, Software, 2006, version 5.2.
- [58] B. Barrowes, "Mathematica symbolic toolbox for MATLAB," October 2004.
- [59] Y. Sheiretov, "GETGP," Software, February 1997, version 3.
- [60] —, *Multidimensional Parameter Estimation Routines*, Massachusetts Institute of Technology, May 1997.
- [61] "CuFlon: Pure PTFE ultra low loss microwave substrates," Polyflon Corporation, Data Sheet, 1 Willard Road, Norwalk, CT 06851.
- [62] *Maxwell 2D Online Help*, 5th ed., Ansoft Corporation, 225 West Station Square Drive, Suite 200, Pittsburgh, PA 15219, 2005.
- [63] A. Mamishev, Y. Du, C. Lin, B. Lesieutre, and M. Zahn, "One-sided measurement of material dielectric properties using a liquid dielectric immersion technique." Nara, Japan: 13th Inter. Conf. Dielectric Liquids, July 1999, pp. 341–344.
- [64] Y. Du, "Measurements and modeling of moisture diffusion processes in transformer insulation using interdigital dielectrometry sensors," Ph.D. dissertation, Massachusetts Institute of Technology, May 1999.
- [65] Y. Du, B. Lesieutre, and M. Zahn, "Measurements and modeling of moisture dynamics in transformer insulation using interdigital dielectrometry sensors," Electric Power Research Institute, Tech. Rep., 2000.
- [66] "RG179B/U," Pasternack Enterprises, Online Drawing.
- [67] A. Mamishev, M. Zahn, B. Lesieutre, and B. Berdnikov, "Influence of geometric parameters on characteristics of an interdigital dielectrometry sensor," *Conference on Electrical Insulation and Dielectric Phenomena (CEIDP), Annual Report*, vol. 2, pp. 550 – 553, 1996.

- [68] “RG178B/U,” Pasternack Enterprises, Online Drawing.
- [69] M. C. Zaretsky, P. Li, and J. R. Melcher, “Estimation of thickness, complex bulk permittivity and surface conductivity using interdigital dielectrometry,” *IEEE Transactions on Electrical Insulation*, vol. 24, no. 6, pp. 1159 – 1166, 1989.
- [70] —, “Estimation of thickness, complex bulk permittivity and surface conductivity using interdigital dielectrometry.” *Conference Record of IEEE International Symposium on Electrical Insulation*, vol. 1988, pp. 162 – 166, 1988.
- [71] D. Otten, *Moisture Meter Reference Manual*, 1st ed., Laboratory of Electromagnetic and Electronic Systems, MIT, April 1991.
- [72] “IDS/ACS controller commands addendum,” April 1998.
- [73] *Meterman Model CR50 Component Tester Specifications*, Meterman Test Tools, 6920 Seaway Blvd. Everett, WA 98203, 2002.
- [74] Y. A. Cengel and M. A. Boles, *Thermodynamics: An Engineering Approach*, 4th ed. McGraw Hill, 2002.
- [75] *HIH-3610 Series Humidity Sensors*, Honeywell, Freeport, Illinois.
- [76] *HIH-4000 Series Humidity Sensors*, Honeywell, Freeport, Illinois, March 2005.
- [77] *EL-USB-2 Humidity, Temperature, and Dew Point USB Data Logger*, 5th ed., Lascar Electronics, Erie, PA, February 2007.
- [78] *Modern Plastics Encyclopedia*. McGraw-Hill/Modern Plastics.
- [79] J. Malecki, “Electrical conductivity and electret stability. Why electrets are so stable?” in *Electrets, 1996. (ISE 9), 9th International Symposium on*. IEEE, September 1996, pp. 110–116.
- [80] W. T. Shugg, Ed., *Handbook of Electrical and Electronic Insulating Materials*, 2nd ed. Wiley-IEEE Press, June 1995.
- [81] C. A. Harper, *Handbook of plastics, elastomers, and composites*, 4th ed., C. A. Harper, Ed. McGraw-Hill, 2002.
- [82] V. Adamec and J. H. Calderwood, “On the determination of electrical conductivity in polyethylene,” *Journal of Physics D: Applied Physics*, vol. 14, no. 8, pp. 1487–1494.

- [83] E. Lifshitz, L. Landau, and L. Pitaevskii, *Electrodynamics of Continuous Media*, 2nd ed., ser. Course of Theoretical Physics. Butterworth-Heinemann, January 1984, vol. 8.
- [84] A. K. Jonscher, "Dielectric relaxation in solids," *Journal of Physics D: Applied Physics*, vol. 32, no. 14, pp. R57–R70.
- [85] A. Mamishev, Y. Du, J. Bau, B. Lesieutre, and M. Zahn, "Evaluation of diffusion-driven material property profiles using three-wavelength interdigital sensors," *IEEE Trans. Diel. Elec. Insul.*, vol. 8, no. 5, pp. 785–798, October 2001.
- [86] B. Nettelblad, "Effect of moisture content on the dielectric properties of cellulose," in *NORD-IS*, 1992, p. 8.9.
- [87] H. Nyqvist, "Saturated salt solutions for maintaining specified relative humidities," *Int. J. Pharmaceutical Technology Product Manufacture*, vol. 4, pp. 47–48, 1983.
- [88] ASTM D1533-00, *Standard Test Method for Water in Insulating Liquids by Coulometric Karl Fischer Titration*, American National Standards Institute, 1819 L Street, NW, Washington, DC 20036, 2005.
- [89] ASTM D3277-95, *Standard Test Methods for Moisture Content of Oil-Impregnated Cellulosic Insulation*, 1st ed., American National Standards Institute, 1819 L Street, NW, Washington, DC 20036, 2001.
- [90] *CA-05 Mitsubishi Moisture Meter Instruction Manual*, Mitsubishi Kasei Corporation, Tokyo, Japan, June 1988, version 13.
- [91] Y. Sheiretov and M. Zahn, "A study of the temperature and moisture dependent dielectric properties of oil-impregnated pressboard," in *Conference on Electrical Insulation and Dielectric Phenomena*, Pocono Manor, PA, October 1993, pp. 487–492.
- [92] Y. K. Sheiretov, "Dielectrometry measurements of moisture dynamics in oil-impregnated pressboard," Master's thesis, Massachusetts Institute of Technology, May 1994.
- [93] C. Ekanayake, S. Gubanski, A. Graczkowski, and K. Walczak, "Frequency response of oil impregnated pressboard and paper samples for estimating moisture in transformer insulation," *IEEE Transactions on Power Delivery*, vol. 21, no. 3, pp. 1309–1317, July 2006.
- [94] C. Barnes, *Power Cables: Their Design and Installation*, 2nd ed. London, U.K.: Chapman & Hall, 1966.

- [95] G. Moore, *Electric Cables Handbook*, 3rd ed. Blackwell Publishing, 1997.
- [96] K. Tsuge and Y. Wada, "Effect of sorbed water on dielectric dispersion of cellulose at low frequencies," *J. Phys. Soc. Japan*, vol. 17, no. 1, p. 156, 1962.
- [97] P. Thärning, P. Werelius, B. Holmgren, and U. Gäfvert, "High voltage dielectric response analyser for cable diagnostics," in *Conf. on Electrical Insulation and Dielectric Phenomena Annual Reports*, 1993, pp. 745–750.
- [98] E. Kreyszig, *Advanced Engineering Mathematics*, 8th ed. John Wiley & Sons, Inc., 1999.
- [99] S. Haykin, *Digital Communications*. John Wiley & Sons Inc., 1988.
- [100] W. Guidi and H. Fullerton, "Mathematical methods for prediction of moisture take-up and removal in large power transformers," *Proceedings of IEEE Winter Power Meeting*, 1974.
- [101] Y. Du, M. Zahn, B. Lesieutre, A. Mamishev, and S. Lindgren, "Moisture equilibrium in transformer paper-oil systems," *IEEE Electrical Insulation Magazine*, vol. 15, no. 1, pp. 11–20, January/February 1999.
- [102] P. F. Ast, "Movement of moisture through A50P281 kraft paper (dry and oil-impregnated)," General Electric, Test Report HV-ER-66-41, June 1966.
- [103] H. Fullerton, "Determination of moisture diffusion coefficient of oil-free A50p260A paper," General Electric, Technical Information Series DF71ESP-23, January 1972.
- [104] M. Wang, S. Rowland, and P. Clements, "A mechanism of failure of oil-impregnated-paper low-voltage cables," in *Insucon Proceedings*, 2006.
- [105] S. Rowland, M. Wang, and M. Michel, "Effect of moisture diffusion and heat cycling on low voltage oil impregnated-paper insulated distribution lines," in *Conference on Electrical Insulation and Dielectric Phenomena Proceedings (CEIDP)*, 2006.
- [106] J. Fabre and A. Pichon, "Deterioration processes and products of paper and oil." in *Proceedings of the International Conference on Large High Voltage Electric Systems (CIGRE)*, Paris, France, June 1960, p. 137.
- [107] T. Oommen, "Moisture equilibrium in paper-oil insulation systems," in *Proceedings of the 16th Electrical/Electronics Insulation Conference*, Chicago, IL, October 1983, pp. 162–166.

- [108] T. V. Oommen, "Moisture equilibrium charts for transformer insulation drying practice," in *IEEE/PES 1984 Transmission and Distribution Conference (Power Engineering Society)*. Kansas City, MO, USA: IEEE, New York, NY, USA, 1984.
- [109] Y. Du, A. Mamishev, B. Lesieutre, M. Zahn, and S. Kang, "Moisture solubility for differential conditioned transformer oils," *IEEE Trans. Diel. Elec. Insul.*, vol. 8, no. 5, pp. 805–811, October 2001.
- [110] J. Piper, "Moisture equilibrium between gas space and fibrous materials in enclosed electric equipment," *Electrical Engineering*, vol. 65, no. 12, pp. 791 – 797, 1946.
- [111] R. Jeffries, "The sorption of water by cellulose and eight other textile polymers," *Journal of the Textile Institute Transactions*, vol. 51, no. 9, pp. 339–374, 1960.
- [112] W. Fessler, W. McNutt, and T. Rouse, "Bubble formation in transformers," EPRI, Tech. Rep. EL-5384, August 1987.
- [113] S. Chatterjee, B. Ramarao, and C. Tien, "Water-vapour sorption equilibria of a bleached-kraft paperboard - a study of the hysteresis region," *Journal of Pulp and Paper Science*, vol. 23, no. 8, pp. 366–373 –, 1997.
- [114] S. G. Chatterjee, "Comparison of domain and similarity models for characterizing moisture sorption equilibria of paper," *Industrial and Engineering Chemistry Research*, vol. 40, no. 1, pp. 188 – 194, 2001.
- [115] Y. Cöpür and H. Makkonen, "Moisture hysteresis in pine pulps," *Appita Journal*, vol. 59, no. 1, pp. 50 – 52, 2006.
- [116] W. R. Foss, C. A. Bronkhorst, and K. A. Bennett, "Simultaneous heat and mass transport in paper sheets during moisture sorption from humid air," *International Journal of Heat and Mass Transfer*, vol. 46, no. 15, pp. 2875–2886, 2003.
- [117] U. Nyman, P. Gustafsson, B. Johannesson, and R. Hägglund, "A numerical method for the evaluation of non-linear transient moisture flow in cellulosic materials," *International Journal for Numerical Methods in Engineering*, vol. 66, no. 12, pp. 1859 – 1883, 2006.
- [118] L. Rusiniak, "Dielectric properties and structure of water at room temperature. new experimental data in 5 Hz - 13 MHz frequency range." *Phys. Chem Earth (A)*, vol. 25, no. 2, pp. 201–207, 2000.

- [119] J. Melcher and M. Zaretsky, "Apparatus and method for measuring permittivity in materials," U.S. Patent No. 4,814,690, March 1989.
- [120] S. X. Yang and W. Q. Yang, "A portable stray-immune capacitance meter," *Review of Scientific Instruments*, vol. 73, no. 4, pp. 1958–1961, April 2002.
- [121] "AD549 ultralow input bias current operational amplifier," Analog Devices, Product Data Sheet, May 2006, Revision F.
- [122] "IEEE guide for the evaluation of the remaining life of impregnated paper-insulated transmission cable systems," IEEE, 3 Park Avenue, New York, NY 10016, Standard 1425, March 2002.

Biography

Zachary M. Thomas was born in North Tonawanda, New York in 1981. He attended high school at Saint Joseph's Collegiate Institute in Buffalo, NY. He was a four year member of the St. Joe's Jazz Lab Band where he played lead tenor saxophone for his junior and senior years. He also was a member of the Mock Trial team. He graduated in 1999.

From 1999 to 2003 Zachary Thomas attended Syracuse University in Syracuse, NY where he graduated with a Bachelor of Science degree in Electrical Engineering, summa cum laude, with honors. He was a four year member of the Syracuse University Marching Band, the Pride of the Orange, where he played alto saxophone. In 2001 he joined Tau Beta Pi, the engineering honor society. In 2002 he joined the Phi Kappa Psi fraternity and was subsequently initiated into the Order of Omega, the Greek leaders honor society. During his tenure at Syracuse, he served as president of the IEEE Student Branch, Tau Beta Pi, and Phi Kappa Psi, as well as vice president of the Alibrandi Catholic Centers Newman Association. He also served as a student member of the L.C. Smith EECS Student Council. He was a "physics coach" for PHY 211 and 212. During commencement ceremonies he served as a Class Marshal for the College of Engineering and Computer Science. He also served as the student speaker at the Convocation for the L.C. Smith College of Engineering and Computer Science.

From May 2002 through August 2003 he worked under the direction of Professor Lisa Osadciw on management algorithms for multiple radar sensors. The project was sponsored by Lockheed Martin. The work culminated in an undergraduate honors thesis entitled "The Application of Partially Ordered Sets to Sensor Management." During his senior year he developed an ultrasonic positioning system as part of a team effort in autonomous remote management of a mobile robot team.

In 2003 Zachary Thomas was accepted to the Massachusetts Institute of Technology. He is a 2003 National Science Foundation Graduate Research Fellow. From 2003 to 2005 he was a member of the Research Laboratory of Electronics, Center for Electromagnetic Theory and Applications, Professor Jin Au Kong, director. As a member of CETA he worked on several projects including "Sparse Satellite Radar for Ground and Airborne MTI," sponsored by Mitsubishi Co. and "Conformal An-

tenna Arrays (ACC 358),” sponsored by Lincoln Laboratories. His thesis work was on “left-handed metamaterial” (LHM) filter device designs and measurements. He received his Master of Science degree in Electrical Engineering in June 2005. His M.S. thesis, completed under the advisement of Dr. Tomasz Grzegorzczak and Professor Jin Au Kong, is entitled “Measurement and Device Design of Left-Handed Metamaterials.”

In June 2005 he joined the Laboratory for Electromagnetic and Electrical Systems (LEES) as a research assistant for Professor Markus Zahn. His research efforts as a student of Professor Zahn have culminated in the content of this thesis.